

Interactive buckling in thin-walled rectangular hollow section struts

by Jiajia Shen

MEng BEng

A thesis submitted to

Imperial College London

for the degree of

DOCTOR OF PHILOSOPHY

Department of Civil and Environmental Engineering
Imperial College of Science, Technology and Medicine
London SW7 2AZ, United Kingdom

July 2018

Declaration

This thesis is the result of my own original research that was carried out in the Department of Civil and Environmental Engineering at Imperial College London. The work of others described here in is acknowledged by appropriately referencing the published or unpublished sources. This thesis is submitted to Imperial College London for the degree of Doctor of Philosophy and has not been submitted for a degree or any other qualification at another university. The copyright of this thesis rests with the author and is made available under a Creative Commons Attribution Non-Commercial No Derivatives licence. Researchers are free to copy, distribute or transmit the thesis on the condition that they attribute it, that they do not use it for commercial purposes and that they do not alter, transform or build upon it. For any reuse or redistribution, researchers must make clear to others the licence terms of this work.

The publications based on this thesis are as follows:

Journal papers

J. Shen, M. A. Wadee and A. J. Sadowski. Interactive buckling in long thin-walled rectangular hollow section struts. *Int. J. Non-Linear Mech.*, 89 (2017), 43-58.

J. Shen & M. A. Wadee. (2017) Length effects on interactive buckling in thin-walled rectangular hollow section struts. *Thin-Walled Struct.* (In press) (doi:10.1016/j.tws.2017.04.006)

J. Shen & M. A. Wadee. Imperfection sensitivity of rectangular hollow section struts susceptible to interactive buckling. *Int. J. Non-Linear Mech.*, 99 (2018), 112-130.

J. Shen & M. A. Wadee. Sensitivity of elastic thin-walled rectangular hollow section struts to manufacturing tolerance level imperfections. *Eng. Struct.*, 170 (2018), 146-166.

Conference papers & abstract

J. Shen, M. A. Wadee and A. J. Sadowski. (2015) Numerical Study of Interactive Buckling in Thin-Walled Section Box Columns under Pure Compression. *Proc. of the 8th International Conference on Advances in Steel Structures (ICASS' 2015)*, Paper number: 44.

J. Shen, M. A. Wadee and A. J. Sadowski. (2016), Mode interaction in thin-walled box-section struts with semi-rigid flange–web joints. ASEC Engineering Mechanics Institute Conference 2016 (EMI 2016).

J. Shen, M. A. Wadee and A. J. Sadowski. (2016), Local-global mode interaction in box-section struts under axial compression. *Proc. of International Conference on Coupled Stability in Metal Structures (CIMS' 2016)*.

Abstract

Thin-walled rectangular hollow section (RHS) struts are widely used in current structural engineering practice due to their mass efficiency and relative ease of manufacture. Owing to their optimized geometric properties, they are vulnerable to local–global interactive buckling and exhibit highly unstable post-buckling behaviour with severe imperfection sensitivity when the local buckling load is close to the global buckling load. The current work investigates the underlying mechanism of local–global interactive buckling of RHS struts using both analytical and finite element (FE) approaches.

Variational models formulated using analytical techniques, describing the nonlinear local–global mode interaction in thin-walled RHS struts with varying flange–web joint rigidity, different strut lengths and geometric imperfections under pure compression, are presented. A system of nonlinear differential and integral equations subject to boundary conditions is formulated and solved using numerical continuation techniques. For the first time, the equilibrium behaviour of such struts with different cross-section joint rigidities is highlighted with characteristically unstable interactive buckling paths and a progressive change in the local buckling wavelength. Studies on the effects of strut length identify the boundaries for the four distinct length-dependent zones, where different characteristic post-buckling behaviour are exhibited. The most unstable zone is demonstrated to have a considerably narrower range than previously determined owing to the consideration of more realistic corner boundary conditions within the cross-section.

Imperfection sensitivity studies identify the high degree of sensitivity of struts exhibiting mode interaction. They also reveal that local and global imperfections are relatively more significant where global and local buckling are critical respectively. Moreover, a unified local geometric imperfection measurement based on equal local bending energy is proposed to determine the most severe local imperfection profile. It reveals that the most severe profile is modulated rather than periodically distributed along the strut length for purely elastic case.

For verification and extensive parametric study purposes, a nonlinear FE model, which considers material nonlinearity, geometric imperfections, and residual stresses, is developed within the commercial package ABAQUS. The classical solutions and experimental results from two independent studies are used to verify and validate the FE model, both of which show excellent comparisons. The validated FE model is then used to verify the variational model, which also shows excellent comparisons in local buckling wavelengths, cross-section deformation profile, ultimate load and the mechanical behaviour.

Finally, parametric studies on geometric properties, material nonlinearity and residual stresses are conducted using the developed FE model to understand the behaviour of RHS struts exhibiting mode interaction in more practically realistic scenarios. Based on the numerical results and existing experimental results from the literature, the current design rules for thin-walled welded RHS struts are assessed by means of reliability analysis in accordance with Annex D of EN1990. A modified Direct Strength Method (DSM) equation has been proposed and it is shown to provide a better ultimate load prediction than it does presently.

Acknowledgements

First of all, I would express my greatest gratitude and thanks to my first supervisor Professor Ahmer Wadee. He has always been very patient and kind and gave me lots of support and encouragement. As one of the top 100 UK practising scientists, Ahmer's expertise and strong background in nonlinear mechanics and mathematics has inspired me a great deal and always helped me achieve a deeper understanding of my research topic during discussion, which greatly enriched my research work.

Secondly, I would give my thanks to my second supervisor Dr Adam J. Sadowski. Working with him was a wonderful experience. His expertise in finite element analysis and programming made me more efficient during my work. He is always a good listener and always gave me the right directions.

Without both supervisors giving me the offer in 2014, I would not have the opportunity to spend the most wonderful 3 years working with the top engineering scientists at the one of the best universities in the world. Without them, the thesis will have never been realized.

I also would like to express my thanks to Professor Leroy Gardner, one of Ahmer's best friends in the department. He is a very successful researcher and educator. He was always very friendly and gave me some very helpful suggestions and advice.

I would also express my gratitude to all the staff and colleagues in the Department, who helped me during the past three years and half and made the daily college life more inter-

esting and enjoyable. Particularly, I would like to express my thanks and gratitude to Dr Merih Kucukler, Dr Jialiang Yu, Dr Fernando Madrazo-Aguirre, Dr Reuben Brambleby, Dr Elizabeth Liu, Dr Jie Wang, Bowen Xu, Oluwole Kunle Fajuyitan, Cagatay Demirci, Nicholas Hadjipantelis, Andreas Fieber, Bradley Pring and Sophie Day for their support and fruitful discussions throughout my PhD study; Professor Catherine O'Sullivan, Fionnuala Donovan and Sarah Willis for their support in the processes of the PhD assessments and daily issues.

Moreover, I am grateful for the financial support provided by the President's PhD Scholarship scheme from Imperial College London.

Finally, I would like to dedicate this thesis to my parents. It is very difficult for them to let their only child study in a country that is over 9 thousand kilometres from home. They sacrificed themselves a great deal by supporting me. It is their great love that makes the completion of this thesis possible. Therefore, I would like to express my enormous gratitude to them and hope they would feel happy and proud when they read this thesis.

Contents

List of Figures	16
List of Tables	32
Nomenclature	36
1 Introduction	47
1.1 Buckling analysis type	50
1.1.1 Linear buckling analysis	50
1.1.2 Nonlinear buckling analysis	53
1.2 Interactive buckling phenomena	57
1.2.1 Augusti model	57
1.2.2 Interactive buckling in real structures	60
1.3 Research Objectives	63
1.4 Outline of the thesis	64

1.4.1 Chapter 2: Literature review	64
1.4.2 Chapter 3: FE model development	65
1.4.3 Chapter 4: Behaviour of long struts with semi-rigid flange–web joints	65
1.4.4 Chapter 5: Variational modelling of practical cases	66
1.4.5 Chapter 6: Length effects	66
1.4.6 Chapter 7: Imperfection sensitivity	67
1.4.7 Chapter 8: Sensitivity to manufacturing tolerance level imperfections	67
1.4.8 Chapter 9: Parametric study and suggestions for improved design guidance	68
1.4.9 Chapter 10: Conclusions and future work	68
2 Literature Review	69
2.1 Analytical approaches	70
2.1.1 Engineering approaches	70
2.1.2 Theoretical approaches	75
2.2 Numerical approach to interactive buckling	84
2.2.1 Finite Element Method (FEM)	84
2.2.2 Generalized Beam Theory (GBT)	88
2.2.3 Finite Strip Method (FSM)	89
2.3 Imperfection sensitivity	92

2.3.1 Geometric imperfections measurement and modelling	94
2.3.2 Residual stresses measurement and modelling	98
2.3.3 Imperfection tolerance and modelling recommendations in Eurocode 3 (EC3)	101
2.3.4 Imperfection sensitivity studies	103
2.4 Experimental studies	111
2.5 Related design guidelines	116
2.5.1 Eurocode 3 approach	116
2.5.2 Direct Strength Method	119
2.6 Concluding remarks	120
3 Finite element model development and validation	122
3.1 Introduction	122
3.2 Development of finite element models	123
3.2.1 Strut modelling	123
3.2.2 Material Modelling	130
3.2.3 Geometric imperfection modelling	131
3.2.4 Residual stress modelling	132
3.3 Analysis type and solution strategy	134
3.3.1 Linear buckling analysis	135

3.3.2 Nonlinear analysis	137
3.4 Verification against classical solutions	140
3.4.1 Local buckling	140
3.4.2 Global buckling	142
3.5 Validation against experimental results	144
3.5.1 Test results from Usami & Fukumoto (1984)	144
3.5.2 Results from Yang <i>et al.</i> (2017)	146
3.6 Concluding remarks	149
4 Behaviour of long struts with semi-rigid flange–web joints	151
4.1 Introduction	151
4.2 Development of the variational model	152
4.2.1 Modal descriptions	153
4.2.2 Total potential energy	159
4.2.3 Governing equations	163
4.3 Numerical results	166
4.4 Verification and discussion	172
4.5 Simplified approach to predicting the location of secondary bifurcation	179
4.6 Parametric studies	183
4.6.1 Length variation	183

4.6.2	Cross-section aspect ratio variation	183
4.7	Concluding remarks	186
5	Variational modelling of practical cases	188
5.1	Modal descriptions	189
5.2	Geometric imperfections description	193
5.3	Potential energy formulation	195
5.3.1	Strain energy due to bending	195
5.3.2	Membrane strain energy	198
5.3.3	Work done by the load and total potential energy	200
5.4	Variational formulation and eigenvalue analysis	201
5.5	Concluding remarks	202
6	Length effects	204
6.1	Numerical solution strategy for variational model	205
6.2	Numerical results and verification	207
6.2.1	Long length strut	208
6.2.2	Transitional length strut	212
6.2.3	Intermediate length strut	214
6.2.4	Short length strut	217

6.3	Discussion and comparison with Van der Neut's model	222
6.4	Concluding remarks	229
7	Imperfection sensitivity	231
7.1	Numerical results, verification and discussion	232
7.1.1	Global imperfections ($q_{s0} \neq 0, w_0 = 0$)	235
7.1.2	Local imperfections ($w_0 \neq 0, q_{s0} = 0$)	238
7.1.3	Combined imperfections ($q_{s0} \neq 0, w_0 \neq 0$)	242
7.1.4	Verification and discussion	244
7.2	Variational model application and parametric study	247
7.2.1	Simplified method to predict load at pitchfork bifurcation ($q_{s0} \neq 0, w_0 = 0$)	247
7.2.2	Simplified method to predict the ultimate load ($q_{s0} = 10^{-3}, w_0 = 0$)	250
7.2.3	Simplified method to predict the ultimate load ($q_{s0} = 10^{-3}, A_0 = d/200$)	251
7.3	Concluding remarks	254
8	Sensitivity to manufacturing tolerance level imperfections	256
8.1	Imperfection description and modelling	257
8.2	Unified local imperfection measurement criterion	258
8.3	Effects of local imperfection profiles	260

8.3.1	Algorithm for determining most severe local imperfection profile . . .	262
8.3.2	Effects of number of sinusoidal half-waves β_i	268
8.3.3	Effects of the degree of localization α_i	271
8.3.4	Equilibrium paths for struts with the most severe imperfection profile	275
8.4	Discussion	276
8.4.1	Effects of localization on tangent stiffness and ultimate load	277
8.4.2	Most severe imperfection profile under amplitude tolerance constraint	279
8.4.3	Effects of superposing tolerance level global imperfections	281
8.5	Application and parametric study	283
8.5.1	Wavelength of most severe local imperfection profile	283
8.5.2	Global buckling loads of struts with tolerance level doubly-symmetric	
	cross-sectional local imperfections	285
8.6	Concluding remarks	289
9	Parametric study	292
9.1	Algorithm for Automated GMNIA	292
9.2	Geometric parameter	293
9.2.1	Plate width–thickness ratio	294
9.2.2	Cross-section aspect ratio	297
9.3	Material properties	298

9.3.1	Yielding stress levels	298
9.3.2	Effect of material strain-hardening	306
9.4	Residual stress	308
9.4.1	Effects on imperfection sensitivity	309
9.4.2	Effects on equilibrium paths	311
9.4.3	Simplified method to determine initial local imperfection amplitude	
	A_0^0	314
9.5	Comparison with the current design guidelines and reliability analysis	319
9.5.1	Assessment of the Effective Width Method in EC3 and reliability analysis	321
9.5.2	Assessment of the Direct Strength Method (DSM) and reliability analysis	326
9.6	Proposal and reliability analysis of a modified DSM procedure	327
9.7	Concluding remarks	329
10	Conclusions and future work	333
10.1	Conclusions	333
10.2	Future work	340
10.2.1	Further enhancements of variational model	340
10.2.2	Inclusion of other factors	341
10.2.3	Statistical analysis of geometric imperfections in welded RHS members	342

10.2.4 Extension of methodology to similar problems	343
Appendices	344
A Expressions for ODEs, integral and boundary conditions	344
B Zone 2–3 boundary determination from double modulus theory	355
C Buckling load, wavelength and cross-section profiles of pure local buckling mode	359
References	366

List of Figures

1.1	The Steve Jobs Theater in the Apple Campus in California, United States with the world's largest carbon fiber roof (Martin, 2017).	48
1.2	Applications of thin-walled structures.	49
1.3	(a) Simply-supported strut under pure compression. (b) The deflection and the curvature of the strut. (c) Equilibrium path of the strut under pure compression using linear buckling analysis.	51
1.4	Typical post-buckling behaviour and the corresponding example structural forms (Wadee, 2007).	53
1.5	Koiter's theory and its application in determining the post-buckling behaviour and the ultimate load of imperfect structural systems.	54
1.6	Rolling ball analogy for three types of stability of equilibrium for (a) single degree of freedom system and (b) system with more than one degree of freedom. Case (I) is stable but (II) and (III) are both unstable.	56
1.7	Augusti model (1964) and sketches of its typical equilibrium paths.	59
1.8	Effect of wavelength of individual buckling mode on the interactive buckling behaviour.	61

1.9	Interactive buckling in (a) build-up struts and (b) stiffened plates.	62
1.10	Link-spring model (Hunt, 1989) illustrating the effect of localized and periodic deformation on the equilibrium path.	63
2.1	Cross-section deformation profile at different stages. (a) Local buckling; (b) Interactive local-global buckling; (c) Local displacement change caused by the local-global mode interaction.	71
2.2	The Van der Neut model of an idealized thin-walled strut and the Van der Neut curve.	76
2.3	Discrete model for analysing the interaction between the global lateral-torsional buckling mode and the local flange buckling mode.	78
2.4	Decomposition of the global buckling mode into ‘sway’ and ‘tilt’ components.	80
2.5	Numerical continuation procedures for interactive buckling of perfect columns in AUTO.	83
2.6	Effective width of a plate under different stress distribution cases: (a) Uniform compression with $\sigma_{1,i} = \sigma_{2,i}$; (b) eccentric compression with $\sigma_{1,i} > \sigma_{2,i} > 0$; (c) eccentric compression with $\sigma_{1,i} > 0$ and $\sigma_{2,i} < 0$	85
2.7	Square box-section strut with initial local geometric imperfections: (a) Initial state. (b) Axial compressive strain Δ . (c) Axial compressive strain Δ and bending curvature ρ	90
2.8	Illustration of the influence coefficient method of beam-column in conjunction with the finite strip method of nonlinear elastic analysis of locally buckled ‘cell’ element.	91

2.9	Three types of structural imperfection sensitivity classified by Chilver (1976) from the view of design philosophy.	93
2.10	Definition of local geometric imperfections (Schafer & Peköz, 1998a).	95
2.11	Histograms of local imperfection amplitude normalized with respect to (a) plate width and (b) plate thickness in welded box-section columns in the existing literature.	97
2.12	Histogram of the local imperfection factor ρ in Eq. (2.17) determined based on the results in the existing literature.	98
2.13	ECCS residual stress distribution models for welded box sections (ECCS. TC 8, 1976).	100
2.14	Equivalent global and local imperfection modelling recommended by Eurocode 3 Part 1.5 (EN-1993-1-5:2006E, 2006).	102
2.15	Optimum design and efficiency chart of a square Van der Neut ideal two-flange strut with fixed length L and fixed cross-section area A	104
2.16	Summary of the normalized global slenderness $\bar{\lambda}_o^C = \sqrt{P_y/P_o^C}$ and local slenderness $\bar{\lambda}_1^C = \sqrt{P_y/P_1^C}$ of specimens in the existing literature.	114
2.17	Summary of the ultimate load from experimental studies in the existing literature and comparison with the Direct Strength Method (DSM) (Schafer, 2008) and the Effective Width Method (EWM) (EN-1993-1-1:2006E, 2006).	114
2.18	Interactive buckling observed in a stainless steel I-section strut (Becque, 2008).	115
3.1	Plan and cross-section view of the thin-walled rectangular hollow section strut of length L under an axial load P and the interactive buckling mode.	124

3.2	Illustration of the FE model for thin-walled RHS struts and the distrib-	
	tively applied load at the end-section.	124
3.3	Semi-rigid flange–web connection modelling in the FE model.	126
3.4	Shear locking for the four-noded bilinear plate element.	128
3.5	‘Hourglass’ mode in 2 by 2 four-noded bilinear elements.	129
3.6	Typical constitutive curve for structural carbon steel.	130
3.7	A typical nonlinear stress–strain relationship and the corresponding input	
	parameters in ABAQUS.	131
3.8	ECCS residual stress distribution for welded box-section members.	133
3.9	The orientation of local coordinates in perfect and imperfection struts within	
	different global coordinate systems.	134
3.10	Sketch for modified Riks arc-length method and other numerical incremental	
	techniques to trace the nonlinear equilibrium path.	138
3.11	Illustration of the effects of initial residual stresses on the initial geometric	
	imperfections introduced within the plate.	139
3.12	(a) Local buckling coefficient of the example strut using different mesh sizes.	
	(b) CPU (Intel Core i7-4790 CPU@3.60GHz) running time versus the num-	
	ber of elements along the web depth m_w .	141
3.13	Local buckling coefficient of struts with different length–web depth ratios.	142
3.14	Global buckling load of example struts from linear buckling analysis using	
	FE models and Euler buckling equation (Timoshenko & Gere, 1961).	143

3.15 Cross-section geometry of specimens from (a) Usami & Fukumoto (1984) and (b) Yang <i>et al.</i> (2017).	144
3.16 Residual stress distribution model adopted in FE models for columns tested in Usami & Fukumoto (Usami & Fukumoto, 1984).	146
3.17 Sensitivity of the local geometric imperfection size introduced in the FE models on the ultimate load and their comparison with the experimental results.	147
3.18 Load–end-shortening relationship for specimens (a) R-235-2 and (b) R-345-1 from experimental (Yang <i>et al.</i> , 2017) and FE results.	149
4.1 Plan view and cross-section geometry of the strut with semi-rigid joints under the concentric axial load P .	152
4.2 Global and local mode description in the variational model.	154
4.3 Semi-rigid joint with corresponding kinematic and static boundary conditions at the web–flange junctions.	156
4.4 Isolated model alongside the kinematic and static boundary conditions to determine the equivalent rotational spring stiffness on the more compressed web provided by the connecting flanges.	158
4.5 Numerical continuation procedure for determining the interactive buckling equilibrium path for perfect struts where global buckling is critical.	168
4.6 The influence of the rotational spring stiffness on the coefficient of the linear term in Eq. (4.43) for the example strut with the properties listed in Table 4.1.	169
4.7 Numerical equilibrium paths for struts with varying joint rigidity \bar{c}_θ .	170

4.8	Numerical solutions of the normalized local out-of-plane displacement in the more compressed web w_{wc}/t_w for the cases where: (a) $\bar{c}_\theta = 0$ (pinned), (b) $\bar{c}_\theta = 0.5$ and (c) $\bar{c}_\theta \rightarrow \infty$ (rigid).	172
4.9	3D visualization of the numerical solutions from the variational model, plotted using MATLAB (MATLAB, 2010).	173
4.10	Comparison of the post-buckling equilibrium paths for the cases where: (a) $\bar{c}_\theta = 0$ (pinned), (b) $\bar{c}_\theta = 0.5$, and (c) $\bar{c}_\theta \rightarrow \infty$ (rigid) from the variational and FE models.	174
4.11	Neutral axis shifting due to local buckling in the more compressed web and flanges.	175
4.12	Local deformation of the cross-section for the example struts at mid-span at different load levels for the cases where: (a) $\bar{c}_\theta = 0$ (pinned), (b) $\bar{c}_\theta = 0.5$, and (c) $\bar{c}_\theta \rightarrow \infty$ (rigid) from the variational and FE models.	175
4.13	Comparisons of the numerical solutions for the normalized local out-of-plane displacement in the more compressed web from the variational and FE models for $\bar{c}_\theta = 0$ (pinned), $\bar{c}_\theta = 0.5$ and $\bar{c}_\theta \rightarrow \infty$ (rigid) cases respectively.	176
4.14	Comparisons of the potential energy components from the example struts with joint rigidities $\bar{c}_\theta = 0$ (pinned), $\bar{c}_\theta = 0.5$ and $\bar{c}_\theta \rightarrow \infty$ (rigid) from the variational and FE models.	178
4.15	Deformed shape of the isolated plate element of the more compressed web under the critical buckling stress σ_{wcl}^C .	181
4.16	Comparison of the generalized coordinate of the sway mode at the secondary bifurcation point q_s^S using numerical continuation with AUTO for the full variational model alongside the presented simplified method.	184

4.17 The relationship between the local buckling coefficient k_p and the cross-section aspect ratio ϕ_c for the rigid joint case from the simplified method using Eq. (4.66) and the curve fit function given in Eq. (4.68).	186
5.1 Out-of-plane and in-plane local mode description.	190
5.2 Local out-of-plane displacement fields of the cross-section.	190
5.3 Pure local buckling mode and the corresponding kinematic and static boundary conditions at the web-flange junction.	192
5.4 Profile of local imperfection function, $w_{i0}(z)/A_{i0}$. (a) Localized imperfections introduced by varying the localization parameter α_i from zero to 10. (b) Periodic imperfections ($\alpha_i = 0$) with different numbers of half sine waves by varying the frequency parameter β_i from 1 to 9.	195
5.5 Introduction of the global imperfection. (a) The out-of-straightness sway component W_0 and (b) the pure rotation tilt component θ_0 .	196
6.1 The Van der Neut type curve for geometrically perfect struts.	204
6.2 Sketches of the equilibrium paths for struts of different lengths exhibiting mode interaction.	206
6.3 Sketch and flowchart of the numerical continuation procedure for determining the interactive buckling equilibrium path for perfect struts where local buckling is critical.	207
6.4 Nonlinear equilibrium paths for the example long length strut with $L = 4800$ mm from the variational and FE models.	209

6.5	Evolution of the numerical solutions for the normalized local out-of-plane displacement in the more compressed web w_{wc}/t_w and the less compressed web w_{wt}/t_w for the long length strut with $L = 4800$ mm.	210
6.6	Local deformation of the cross-section at mid-span for the long length strut with $L = 4800$ mm with the increase of the generalized sway mode coordinate q_s	211
6.7	Out-of-plane forces due to the large bending displacement and their effects on the local mode profile.	211
6.8	Nonlinear equilibrium paths for the transitional length strut with $L = 4500$ mm from the variational and FE models.	212
6.9	Evolution of the numerical solutions for w_{wc}/t_w and w_{wt}/t_w for the transitional length strut with $L = 4500$ mm.	213
6.10	Local deformation of the cross-section at mid-span for the transitional length strut with $L = 4500$ mm as q_s is increased.	213
6.11	Nonlinear equilibrium paths for the intermediate length strut with $L = 4000$ mm from the variational and FE models.	215
6.12	Evolution of the numerical solutions for w_{wc}/t_w and w_{wt}/t_w for the intermediate length strut with $L = 4000$ mm.	216
6.13	Local deformation of the cross-section at mid-span for the intermediate length strut with $L = 4000$ mm with the increase of q_s	217
6.14	Nonlinear equilibrium paths for the short length strut with $L = 3600$ mm from the variational and FE models.	218

6.15 Evolution of the numerical solutions for w_{wc}/t_w and w_{wt}/t_w for the short	
length strut with $L = 3600$ mm.	219
6.16 Local deformation of the cross-section at mid-span for the short length strut	
with $L = 3600$ mm with the increase of q_s .	219
6.17 In-plane displacements within the cross-section.	220
6.18 Normalized vertical in-plane displacement in the more compressed web $\Delta_{CR,MC}/d$	
at mid-span versus normalized load P/P_1^C and normalized global amplitude	
q_s .	221
6.19 The numerically obtained Van der Neut curve for struts with cross-section	
properties presented in Table 4.1.	222
6.20 The Van der Neut-type curve sketched with the competing buckling modes	
in zone 2 for three typical cross-section flange–web conditions.	224
6.21 Cross-section axial stiffness distribution schemes for struts exhibiting local–	
global mode interaction.	225
6.22 Relationship between $1/\Phi_r$ and $\bar{\eta}_w$ for the cross-section stiffness distributions	
presented in Figure 6.21 and the expression proposed by Van der Neut.	226
6.23 Cross-section deformation for the pure local buckling case (dot-dashed line)	
using Eqs. (5.2) and (5.3) and the global buckling induced local buckling case	
(solid line) using Eqs. (5.9)–(5.11). The deformation has been amplified by	
a factor of 20 to aid visualization.	227
7.1 The Van der Neut curve for the geometrically perfect and imperfect cases	
(van der Neut, 1969).	233

7.2	Sketches of the equilibrium paths and their numerical continuation procedures in AUTO for the imperfect struts primarily in zones 1 and 2.	234
7.3	Equilibrium paths and the imperfection sensitivity graph for the long length strut ($L = 4800$ mm) with different global imperfection sizes q_{s0} .	236
7.4	Equilibrium paths and the imperfection sensitivity graph for the transitional length strut ($L = 4500$ mm) with different global imperfection sizes q_{s0} .	237
7.5	Numerical solutions of the longitudinal profile of the local out-of-plane displacement in the more compressed web for the long length strut and the transitional length strut respectively.	238
7.6	Longitudinal component of initial local imperfections for the long length strut and the transitional length strut.	239
7.7	Equilibrium paths and the imperfection sensitivity graph for the long length strut with different local imperfection amplitudes A_0 .	240
7.8	Equilibrium paths and the imperfection sensitivity graph for the transitional length strut with different local imperfection amplitudes A_0 .	241
7.9	Evolution of the numerical solutions for the normalized local out-of-plane displacement in the more compressed web for the long length strut with different local imperfection amplitudes A_0 .	242
7.10	Equilibrium paths and the imperfection sensitivity graph for the long length strut with different normalized combined imperfection sizes $W_{\mathcal{E}0}$.	243
7.11	Equilibrium paths and the imperfection sensitivity graph for the transitional length strut with different normalized combined imperfection sizes $W_{\mathcal{E}0}$.	244

7.12	Membrane stress distributions along the strut corner line of the more compressed web at the ultimate load for the transitional length strut with the tolerance imperfection combination.	246
7.13	Comparison of the normalized load p^B using the simplified method and the full variational model against the normalized ultimate load p_u from the FE models for the long length and transitional length struts.	249
7.14	Length effects on the ultimate and pitchfork bifurcation load of thin-walled RHS struts with purely tolerance level global imperfections ($q_{s0} = 10^{-3}$).	250
7.15	Effects of tolerance level local imperfections, global imperfections and their combination on the ultimate load for thin-walled RHS struts with different lengths.	252
8.1	Global and local imperfection descriptions.	257
8.2	Algorithm for determining the most severe case periodic and modulated local imperfections under the constraint of the equal local bending energy of the initially imperfect geometry.	262
8.3	Algorithm for function to terminate the nonlinear analysis when the load begins to drop or the load-end-shortening curve reaches the plateau.	265
8.4	Sketch of two typical equilibrium paths describing failure for thin-walled RHS struts: (a) clearly unstable post-buckling behaviour; (b) weakly stable post-buckling behaviour.	266
8.5	Numerical illustration example for the Modified Southwell (MS) method to estimate the failure load from partial nonlinear analysis data and terminate the nonlinear analysis once certain failure criterion is met.	267

8.6	Normalized ultimate load of struts $p_u = P_u/P^C$ versus number of half-waves β_i with different local imperfection cases presented in Table 8.2 for different length struts.	268
8.7	Normalized amplitude of local imperfections versus number of half-waves β_i for different imperfection cases presented in Table 8.2.	269
8.8	Normalized amplitude of the local imperfection versus the degree of localization α_i for different imperfection cases as presented in Table 8.2.	271
8.9	Normalized ultimate load of the strut $p_u = P_u/P^C$ versus the degree of localization α_i for different local imperfection cases presented in Table 8.2.	272
8.10	Normalized longitudinal profile in the more compressed web of (a) most severe imperfection profile for the mono-symmetric imperfection (case 2), (b) most severe imperfection profile for the doubly-symmetric imperfection (case 4), (c) local buckling mode from linear buckling analysis and (d) interactive mode in the advanced post-buckling range of the perfect system where $q_s = 0.009$ for the long length strut with $L = 4800$ mm.	274
8.11	Equilibrium paths of example struts in zones 1–4 with the most severe imperfection profiles of the four cases presented in Table 8.2.	275
8.12	Cross-sectional axial tangent modulus and longitudinal component of the local buckling mode in the webs with the short length strut with increasing load level.	278
8.13	Longitudinal component of the most severe imperfection profile (case 4) w_{10} under the amplitude tolerance constraint (solid line) for different length struts.	280

8.14 Normalized wavelength of the most severe local imperfection profile with a doubly-symmetric cross-section profile for different length struts.	282
8.15 Effects of cross-section aspect ratio and normalized imperfection size on the normalized wavelength of the most severe imperfection profile.	284
8.16 Reduced global buckling load of struts with dimensionless local imperfection size $A_0/t = 0.6$ versus the normalized global buckling load from FE results and Eq. (8.5) for different cross-section aspect ratios and plate width–thickness ratios.	288
8.17 (a) Relationship of the normalized reduced global buckling load P_0^C/P_0^C versus P_0^C/P_1^C at different imperfection amplitude levels. (b) Ratio of the normalized reduced global buckling load of struts with different imperfection sizes from FE results and Eq. (8.5); the dashed line represents the average with the value being 0.993.	289
9.1 Algorithm for automated GMNIA for RHS struts. Codes were developed in MATLAB to achieve the entire process.	294
9.2 The effect of plate width–thickness ratio on the Van der Neut type curve for perfect rectangular hollow section struts.	295
9.3 Effect of the cross-section aspect ratio and web depth–thickness ratio on the zonal boundary of zones 2 and 3 for rectangular hollow section struts with pinned corners.	296
9.4 The effect of cross-section aspect ratio on the Van der Neut type curve.	297
9.5 The effect of yielding stress levels on the Van der Neut-type curve of strut with tolerance level geometric imperfections.	299

9.6 Imperfection sensitivity of four characteristic length struts to geometric imperfections at different cross-sectional local slenderness λ_p levels. Also shown are the fitted imperfection sensitivity curves, the details of which may be found in Table 9.1. Each family of curves represent zones 1 to 4 in sequence from right to left. 300

9.7 Equilibrium paths of four characteristic length struts with purely geometric imperfections with $q_{s0} = 1/1000$ and $A_0/d = 1/200$ at different λ_p levels. Dashed, solid, dotted and dot-dashed lines represent $\lambda_p=1, 1.225, 1.414,$ and 2 respectively; the outer thin dark solid line represents the purely elastic case. Graphs of normalized load ratio $p = P/P^C$ versus normalized end-shortening \mathcal{E}/L in the first row; the second row shows the normalized maximum amplitude of local deflection in the more compressed web $w_{wc,max}/t_w$ versus the normalized global amplitude q_s . Note that the point where loading commences is marked by $^{(*)}$ 304

9.8 Axial tangent modulus of a simply-supported plate with $d = 120$ mm, $t = 1$ mm and initial imperfection size $A_0 = d/200$ with increasing axial load level. 305

9.9 Effect of strain-hardening on the ultimate load of struts with tolerance level imperfections at different material yielding stress levels. 307

9.10 Ratio of compressive residual stresses σ_{rc} to local plate buckling stresses σ_1^C versus plate width–thickness ratios d/t in heavily welded box-section members for different (a) cross-sectional local slendernesses and (b) practically yielding stress levels. 308

9.11 Local imperfection sensitivity relationship for four characteristic length struts with residual stresses and the normalized global imperfection amplitude q_{s0} being $1/1000$ at different λ_p levels. Also shown are the fitted imperfection sensitivity curves, the details of which may be found in Table 9.4. 310

9.12 Equilibrium paths of four characteristic length struts with the ECCS residual stress distribution for welded box-section members with $d_t = 3t$ at different yielding stress levels.	312
9.13 Equilibrium paths of four characteristic length struts with the ECCS residual stress distribution for welded box-section members with $d_t = 6t$ at different yielding stress levels.	313
9.14 Equilibrium paths of the intermediate length strut ($L = 4000$ mm) with no residual stress (solid line), with the ECCS residual stress distribution with $d_t = 3t$ (dashed line) and $d_t = 6t$ (dot-dashed line).	314
9.15 Effects of residual stresses on the axial tangent modulus–axial load relationship of a simply-supported plate with $d = 120$ mm and $t = 1$ mm.	315
9.16 Relationship of the imperfection amplitude ratio before and after the self-equilibrating step A_0^0/A_0 and σ_{rc}/σ_1^C	317
9.17 Comparison of FE results with Eq. (9.5) for different cross-section aspect ratios, targeted imperfection sizes and compressive residual stress levels.	318
9.18 Ratio σ_{rc}/σ_1^C at the boundary of local geometric imperfection sensitivity range for practically realistic box-section members.	318
9.19 Comparison of ultimate loads between the experimental and FE results using the imperfection combination recommended by Degée <i>et al.</i> (Degée <i>et al.</i> , 2008).	320
9.20 Comparison of the ultimate loads for lightly welded and heavily welded struts from the validated FE model and the design equation from EC3.	322

9.21 Relationship between V_{rt}^2 and P_o^C/P_1^C at different plate slendernesses determined based on Eq. (9.9) for heavily welded RHS struts with $d=120$ mm, $b = 60$ mm and $t = 1$ mm.	324
9.22 Comparison of the ultimate loads for lightly welded and heavily welded struts from the validated FE model and the DSM.	326
9.23 Column buckling curves. Solid and the dashed lines represent the column strength curve in the DSM and the five curves, a ₀ -d, in EC3 respectively.	327
9.24 Comparison of the ultimate load for lightly and heavily welded struts from the validated FE model and the modified DSM.	329
B.1 ‘Double modulus’ theory in determining the effective bending stiffness of struts undergoing global-local mode interaction.	356
C.1 Deformed shape of an isolated thin-walled RHS strut element under pure compression with corresponding kinematic and static boundary conditions at the web-flange junctions.	360
C.2 Ratio of the local buckling modal amplitude in the web and flange for thin-walled RHS struts with different cross-section aspect ratios $\phi_c=d/b$	361
C.3 Comparisons in the local buckling coefficient-cross-section aspect ratio and the normalized longitudinal wavelength-cross-section aspect ratio relationship for thin-walled rectangular hollow section struts from FE, analytical models and the fitted functions.	364
C.4 Cross-section profile of linear buckling mode for different cross-section aspect ratios ranging from 1 to 3.	365

List of Tables

2.1	Types of bifurcation defined by Van der Neut (1969).	77
2.2	Numerically estimated cumulative distribution function (CDF) values for maximum magnitude of local imperfections (Schafer & Peköz, 1998a).	96
2.3	Design values of global imperfections recommended by Eurocode 3 Part 1.1 (EN-1993-1-1:2006E, 2006).	102
2.4	Buckling curve types for hollow section columns in Eurocode 3 Part 1.1 (EN-1993-1-1:2006E, 2006).	102
2.5	Imperfection factors for the separate buckling curves for compression members made from steel (EN-1993-1-1:2006E, 2006) in EC3.	118
2.6	Comparison of the ultimate load from experimental studies in the existing literature with the Effective Width Method (EWM) with the column buckling curve being b (EN-1993-1-1:2006E, 2006) and the Direct Strength Method (DSM) (Schafer, 2008).	118
3.1	Summary of analysis types and their objectives.	135
3.2	Material and cross-section properties of square box section strut for mesh sensitivity analysis and verification.	140

3.3	Material and geometric properties of the welded box section columns (Usami & Fukumoto, 1984).	144
3.4	Geometric imperfections and residual stresses in the welded box section columns (Usami & Fukumoto, 1984).	145
3.5	Ultimate load of columns from the tests of Usami & Fukumoto (1984) and FE results.	146
3.6	Geometric properties and geometric imperfection sizes of two specimens from Yang <i>et al.</i> (2017).	147
3.7	Material properties of two specimens from Yang <i>et al.</i> (2017).	148
4.1	Geometric properties of the rectangular hollow section strut in the numerical example, selected to ensure global buckling is critical.	166
4.2	Theoretical values of the global and local critical buckling stresses for the pinned cross-section case.	167
4.3	Rotational stiffness c_θ and the corresponding normalized stiffness \bar{c}_θ values used in the numerical studies.	169
4.4	Geometric properties of the rectangular hollow section struts in the parametric study, selected to ensure global buckling is critical. The flange width $b = 60$ mm and the wall thickness $t_f = t_w = 1$ mm throughout.	184
4.5	Comparison of the local buckling coefficient k_p for the more compressed web at the secondary bifurcation point from the full variational model, $k_{p,AUTO}$, solved using numerical continuation with AUTO and the simplified method, $k_{p,EQ}$, using Eq. (4.66) from the pinned case ($\bar{c}_\theta = 0$) to the rigid case ($\bar{c}_\theta \rightarrow \infty$) for different cross-section aspect ratios.	185

6.1	Theoretical values of the global (P_0^C) and local (P_1^C) buckling loads for the four representative length cases.	208
7.1	Theoretical values of the global and local buckling loads for the two separate lengths studied.	234
8.1	Number of half-waves β_0 in the local buckling mode for the struts in four characteristic length-dependent zones.	260
8.2	Initial local imperfection parameters for the most severe local imperfection case study.	261
8.3	Ultimate load and local imperfection amplitude of the most severe local periodic imperfection profile.	271
8.4	Ultimate load and local imperfection amplitude of the most severe local modulated imperfection profile.	273
8.5	Normalized ultimate loads of struts with the most severe modulated local imperfection and its approximation using periodic profiles under the amplitude tolerance constraint.	280
9.1	Constants for the fitted imperfection sensitivity curves and their comparison with FE results for four characteristic struts.	302
9.2	Parameters for different elastic-plastic material models.	306
9.3	Ratio σ_{rc}/σ_1^C for the example struts with the ECCS residual stress distribution model for welded box-section members with two different uniform tensile range lengths at different plate slenderness levels.	309

9.4	Constants for the fitted imperfection sensitivity curves Eq. (9.1) and their comparison with FE results for four characteristic struts with ECCS welding residual stress distributions.	311
9.5	Effect of residual stress on the ultimate load of example struts with global imperfection $q_{s0} = 1/1000$ and local imperfection $A_0 = d/1000$	314
9.6	Principal parameters and their ranges for the parametric study for the guideline reliability assessment. Note that the critical buckling load ratio is altered by varying the strut length.	319
9.7	Coefficient of variation (COV) for geometric and material property parameters based on the data presented in (Schillo, 2017).	325
9.8	Summary of reliability analysis results for the Effective Width Method in EC3. Note that $k_{d,n}$ is the fractile factor, which is related to the number of tests in each data set; b_m and V_δ are the mean value and the COV of the correction factor for the ultimate load from the tests, FE models and design equation.	325
9.9	Summary of reliability analysis results for the DSM with quantities being defined in Table 9.8.	327
9.10	Summary of reliability analysis results for the modified DSM equations with quantities being defined in Table 9.8.	328

Nomenclature

In this thesis, the following nomenclature is adopted. In the cases where more than one meaning has been assigned to a symbol, the correct use should be obvious from the context.

Coordinates, stress, strains, loads and energy

x	Transverse direction along flange width
y	Transverse direction along web depth
z	Longitudinal direction along strut
\bar{z}	Normalized longitudinal coordinate
ζ	Normalized transverse coordinate
C	Critical bifurcation point
S	Secondary bifurcation point
U	Point of ultimate load
$\sigma_{z,wc}$	Direct stress in the more compressed web
$\sigma_{l,w}^C, \sigma_{l,f}^C$	Local buckling stress for webs and flanges respectively
σ_{wcl}^C	Critical buckling stress of the more compressed web

σ_o^C	Global buckling stress
k_p	Plate buckling coefficient
$k_{p,AUTO}, k_{p,EQ}$	k_p solved using AUTO and simplified equation respectively
γ_{xz}, γ_{yz}	Shear strains in the planes xz and yz respectively
$\varepsilon_{z,f}, \varepsilon_{z,wc}, \varepsilon_{z,wt}$	Direct strains in flanges, the more compressed web and less compressed web respectively
$\varepsilon_{z,wco}, \varepsilon_{z,wto}$	Direct strains in the more compressed web and less compressed web from the global mode respectively
P	Applied axial load
P_E	Euler buckling load
P_o^C	Global buckling load
P_1^C	Local buckling load
P^C	Critical buckling load
P^B	Load at the bifurcation point
P^S	Load at the secondary bifurcation point
P_u	Ultimate load
$P_{u,FE}, P_{u,exp}$	Ultimate load from FE and experimental results respectively
$P_{u,perf}, P_{u,imp}$	Ultimate load of perfect and imperfect struts respectively
p	Normalized axial load applied, $p = P/P^C$
p_u	Normalized ultimate load, $p_u = P_u/P^C$
$p_{u,perf}, p_{u,imp}$	p_u for perfect and imperfect struts respectively

M	Moment
M_f, M_{wc}	Bending moments in the flange and the more compressed web at the junction respectively
V	Total potential energy
$U_{b,o}$	Global bending strain energy
$U_{b,f}, U_{b,wcl}, U_{b,wtl}$	Local bending strain energy in both flanges, the more compressed web and less compressed web respectively
$U_{m,f}, U_{m,wc}, U_{m,wt}$	Membrane strain energy in both flanges, the more compressed web and less compressed web respectively
U_f, U_{wc}, U_{wt}	Total strain energy in both flanges, the more compressed web and less compressed web respectively
U_{sp}	Strain energy in rotational springs
\mathcal{L}	Lagrangian
\mathbf{V}_{ij}	Hessian matrix

Geometric and material properties

b	Flange width
d	Web depth
t_f	Thickness of flange plate
t_w	Thickness of web plate
t	Thickness of plate

L	Strut length
l_e	Effective length of the isolated plate element
A	Cross-sectional area
ϕ_c	Cross-section aspect ratio d/b
ϕ_t	Ratio of flange plate thickness to web plate thickness t_f/t_w
I_e	Effective second moment of area of the cross-section owing to local buckling
r	Radius of gyration
E	Young's modulus
G	Shear modulus
ν	Poisson's ratio
D_f, D_w	Flexural rigidities of the individual flanges and webs respectively
EI_w	Flexural rigidity about the local weak neutral axis of the web
c_i	Rotational spring stiffness in the Augusti model
c_θ	Stiffness of rotational spring connecting flanges and webs
\bar{c}_θ	Normalized c_θ
c_f	Equivalent rotational stiffness on the more compressed web provided by the connecting flange
$c_{\theta f}$	Equivalent rotational stiffness, $1/c_{\theta f} = 1/c_\theta + 1/c_f$
$\bar{\lambda}_o$	Normalized global slenderness, $\bar{\lambda}_o = \sqrt{P_y/P_o^C}$

$\bar{\lambda}_1$	Normalized local slenderness, $\bar{\lambda}_1 = \sqrt{P_y/P_1^C}$
η	Reduction factor in the longitudinal stiffness owing to local buckling of plate
$\bar{\eta}_w$	Equivalent axial stiffness reduction factor in the more compressed web
Φ_r	Bending stiffness reduction factor due to local buckling in the more compressed web and flanges determined using double-modulus theory
Φ_m	Equivalent bending stiffness reduction factor for the transitional state

Generalized coordinates and displacements

Q_i	Generalized coordinates
$W(z)$	Lateral displacement (sway component)
$\theta(z)$	Rotation of plane sections (tilt component)
χ	Curvature of the deflected strut
q_s, q_t	Generalized coordinates defining the normalized amplitude of the sway and tilt modes respectively
q_s^S	q_s at the secondary bifurcation point
Δ	Purely in-plane compressive strain
\mathcal{E}	Total end-shortening

$\eta(z)$	Displacement of the centroid of the cross-section owing to plate local buckling
$w_f(x, z)$	Local out-of-plane displacement of the flanges
$w_{wc}(y, z)$	Local out-of-plane displacement of the more compressed web
$w_{wt}(y, z)$	Local out-of-plane displacement of the less compressed web
$w_{wc,max}$	Maximum out-of-plane displacement of the more compressed web
$u_f(x, z)$	Local in-plane displacement of the flanges
$u_{wc}(y, z)$	Local in-plane displacement of the more compressed web
$u_{wt}(y, z)$	Local in-plane displacement of the less compressed web
$f_f(x), f_{wc}(y), f_{wt}(y)$	Cross-section component of $w_f(x, z)$, $w_{wc}(y, z)$ and $w_{wt}(y, z)$ respectively
$g_f(x), g_{wc}(y), g_{wt}(y)$	Cross-section component of $u_f(x, z)$, $u_{wc}(y, z)$ and $u_{wt}(y, z)$ respectively
$w(z), u(z)$	Longitudinal component of local out-of-plane and in-plane displacement respectively
θ_f, θ_w	Rotations of the flange and the more compressed web at the junction respectively

Geometric imperfections and residual stresses

$W_0(z)$	Initial out-of-straightness of the global mode
$\theta_0(z)$	Initial rotation of the plane-section

q_{s0}	Amplitude of W_0
q_{t0}	Amplitude of θ_0
$w_{f0}(x, z)$	Initial out-of-plane deflection in flanges
$w_{wc0}(y, z)$	Initial out-of-plane deflection in the more compressed web
$w_{wt0}(y, z)$	Initial out-of-plane deflection in the less compressed web
$w_{i0}(z)$	Longitudinal component of local imperfections
A_{i0}	Amplitude of w_{i0}
α_{i0}	Degree of localization of w_{i0}
β_{i0}	Number of sinusoidal half waves of w_{i0}
\mathcal{E}_0	Total end-shortening of the initial imperfection
$\bar{W}_{\mathcal{E}0}$	Combined geometric imperfection scaling factor
$\mathbf{W}_{\mathcal{E}0}$	Combined measure of geometric imperfections $\mathbf{W}_{\mathcal{E}0} = \bar{W}_{\mathcal{E}0} \{q_{s0, \text{tol}} L, A_{0, \text{tol}}\}$
$U_{b,l}^0$	Total local bending energy in the entire strut due to the local imperfections
$U_{b,lf}^0, U_{b,lwc}^0, U_{b,lwt}^0$	Local bending energy in both flanges, the more compressed web and the less compressed web due to local imperfections respectively
A_{i0}^0	Initial A_{i0} input for determining the worst imperfection profile
ϵ_0	Normalized imperfection size
δ_0	Amplitude of global imperfection measured from tests
σ_{rc}	Initial compressive residual stress

σ_{rt}	Initial tensile residual stress
$\sigma_{w,rc}, \sigma_{w,rt}$	Initial compressive and tensile residual stresses in the webs
d_t	Length of the uniform tensile range in the ECCS residual stress model for welded box-section members

Numerics

\mathbf{f}	Vector defining system of first order differential equations
\mathbf{y}	Vector of variables
η	Continuation parameter
\mathbf{J}	Jacobian matrix

Finite element modelling and analysis

m_l	Number of elements along the strut length
m_w	Number of elements along the web depth
k_θ	Equivalent rotational stiffness in the FE model
M_z, M_x	In-plane and out-of-plane bending moment of shell element
E_h	Strain hardening modulus
$\sigma_{true}, \sigma_{nom}$	True and nominal stresses
$\varepsilon_{true}, \varepsilon_{nom}$	True and nominal strains
$\varepsilon_{true,pl}$	True plastic strain

f_y	Material yield stress
f_u	Material ultimate stress
ε_y	Yield strain
ε_{sh}	Strain value at which strain hardening commences
ε_u	Ultimate strain
LBA	Linear buckling analysis
GNA	Geometric nonlinear analysis
GNIA	Geometric nonlinear analysis with imperfections
GMNIA	Geometric and material nonlinear analysis with imperfections
$\{\mathbf{P}\}_{ref}$	Reference level of external load
$[\mathbf{K}_\sigma]_{ref}$	Stress stiffness matrix associate $\{\mathbf{P}\}_{ref}$
$[\mathbf{K}]$	Stiffness matrix of the structure
λ	Load proportion factor
λ_{cr}	Load proportion factor at the critical buckling point
$\{\mathbf{d}\}$	Displacement vector
$\{\delta\mathbf{d}\}$	Buckling displacement vector
\bar{u}	Generalized displacement

Design guidelines

Eurocode 3

A_{eff}	Effective area of cross-section owing to local buckling
χ	Buckling reduction factor
N_{cr}	Elastic buckling load for the relevant buckling mode based on the gross cross-section
$N_{\text{c,Rd}}$	Cross-section resistance under uniform compression
$N_{\text{b,Rd}}$	Member buckling resistance
$N_{\text{u,Rd}}$	Member resistance $N_{\text{u,Rd}} = \min\{N_{\text{c,Rd}}, N_{\text{b,Rd}}\}$
γ_{M0}	Partial safety factor for cross-section resistance
γ_{M1}	Partial safety factor for member buckling resistance
ρ	Area reduction factor for plate owing to local buckling

Direct strength method

P_{ne}	Nominal axial strength for flexural, torsional or flexural-torsional buckling
P_{nl}	Nominal axial strength for local buckling
P_{n}	Nominal axial strength $P_{\text{n}} = \min\{P_{\text{ne}}, P_{\text{nl}}\}$

Subscripts

1, 2	Cases where local and global buckling is critical respectively
f	Flanges
w	Webs
wc	More compressed web
wt	Less compressed web
l	Local buckling
o	Global buckling
AUTO	Solved from AUTO
ABAQUS	Solved from ABAQUS
EQ	Solved from the equation using the simplified method
FE	Solved from the finite element method
tol	Tolerance level
imp	Imperfect case
perf	Perfect case

Chapter 1

Introduction

Sustainable design and construction has gradually become the mainstream in the structural engineering discipline. Engineers are increasingly required to take full advantage of every piece of material to design efficient structural systems so as to minimize the adverse effects on the environment owing to construction. The advance in material science and manufacturing technology makes many light weight and high performance materials available for structural purposes (Ashby, 2011), such as high strength steel, Carbon Fiber Reinforced Polymers (CFRP) and Glass Fiber Reinforced Polymers (GFRP). Moreover, better understanding in nonlinear mechanics (Thompson & Hunt, 1973; Thompson & Hunt, 1984) as well as advances in computational mechanics (Belytschko *et al.*, 2000; Bathe, 2006) and optimization theory (Xie & Steven, 1993; Rozvany, 2009), have enabled structural forms to become increasingly slender, as shown in Figure 1.1. However, buckling instability is practically always the governing failure mode of such structures under compression (Bleich, 1952; Timoshenko & Gere, 1961; Bulson, 1970; Bažant & Cedolin, 2010).

Thin-walled structures are one of the most favourable and material efficient structural forms. Thin plates can be efficiently manufactured to almost any imaginable structural forms through a variety of different manufacturing methods, such as cold-forming, hot-



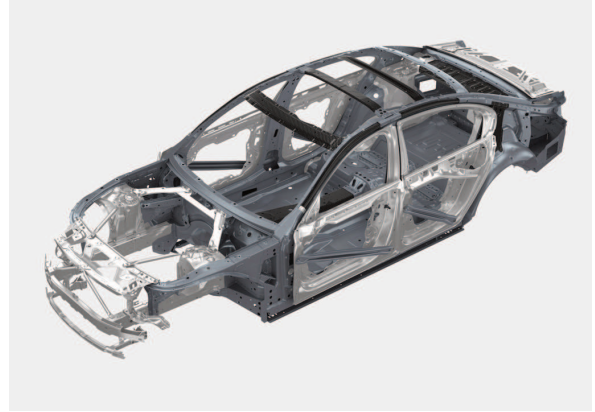
Figure 1.1: The Steve Jobs Theater in the Apple Campus in California, United States with the world's largest carbon fiber roof (Martin, 2017).

rolling, welding and bolting. Therefore, it has wide applications in engineering structures particularly where the self-weight of the structure is a key design constraint factor, such as in aircraft, automotive applications, long-span bridge decks and even computer cases, as shown in Figure 1.2. However, manufacturing processes and handling can introduce significant imperfections in structures, such as geometric imperfections, residual stresses, material strength enhancement and plastic strains. These imperfections have been reported to have significant effects on the equilibrium behaviour and load-carrying capacity (van der Neut, 1973; Thompson & Supple, 1973; Thompson & Hunt, 1973; Gioncu, 1994b; Wadee, 2000; Becque & Rasmussen, 2009a; Quach *et al.*, 2010; Bai & Wadee, 2015a; Liu & Wadee, 2016b).

The term 'thin-walled' is defined by the relative thickness of plates in comparison with other dimensions of the structures or the relatively high local slenderness in comparison with the global slenderness. Unlike members with stocky cross-sections or low local slenderness, thin-walled plated structural systems are likely to exhibit local buckling. When it comes to thin-walled plated structures made of high strength materials, local buckling is almost always permitted in order to take full advantage of the material strength. Therefore, the



(a) Fuselage section of C919 jetliner (Comac C919, 2014).



(b) Frame structure of BMW-7 series (Howard, 2015).



(c) Steel box girders of A380 Thame Valley Viaduct (MISTRAS group, 2017).



(d) Computer case (Powercase Technology (Shenzhen) Co., Ltd., 2015).

Figure 1.2: Applications of thin-walled structures.

interaction between local and global buckling may influence a very large range of geometric proportions.

According to linear theory (Bleich, 1952), a given structural form is optimum if the local buckling and global buckling loads are equal, *i.e.* local and global buckling modes are triggered simultaneously. However, the general theory of elastic stability (Thompson & Hunt, 1973) has demonstrated that such an approach is not appropriate. Even though these modes may be stable when triggered in isolation, the interaction between individual

modes can lead to completely unstable post-buckling behaviour and severe imperfection sensitivity (Thompson & Lewis, 1972; Thompson & Supple, 1973; Tvergaard, 1973; van der Neut, 1973; Thompson & Hunt, 1974; Koiter & Pignataro, 1976a; Byskov & Hutchinson, 1977; Loughlan, 1983; Hunt *et al.*, 1988; Kołakowski, 1989; Kołakowski, 1993; Gioncu, 1994b; Hunt & Wadee, 1998; Wadee, 2000; Teter, 2007; Bai & Wadee, 2015a; Wadee & Farsi, 2015; Bai & Wadee, 2016; Liu & Wadee, 2016b). In particular, the load-carrying capacity erosion from initial imperfections tends to be maximum near the so-called ‘naive optimum’ point (van der Neut, 1969; Thompson & Hunt, 1973).

The current work aims to investigate the nonlinear behaviour of thin-walled rectangular hollow-section struts under compression at a fundamental level and then use this to provide design recommendations.

1.1 Buckling analysis type

1.1.1 Linear buckling analysis

Linear buckling theory or analysis is well known and widely accepted. There are a great number of textbooks (Bleich, 1952; Timoshenko & Gere, 1961; Bulson, 1970; Bažant & Cedolin, 2010) dealing with the theory and their application in different types of structural systems. Compared with nonlinear buckling theory, linear buckling analysis neglects higher order terms in formulating the governing equations or the total potential energy of the system and thus requires a relatively limited computational effort. For instance, for an in-compressible, simply-supported strut under pure compression, as shown in Figure 1.3, the complete relationship between the strut curvature χ and the deflection W is presented as (Bažant & Cedolin, 2010):

$$\chi = \frac{\ddot{W}}{(1 + \dot{W}^2)^{3/2}} = \ddot{W} \left(1 - \frac{3}{2}\dot{W}^2 + \frac{15}{8}\dot{W}^4 - \dots \right), \quad (1.1)$$

where dots represent derivatives with respect to the strut length coordinate z . In linear

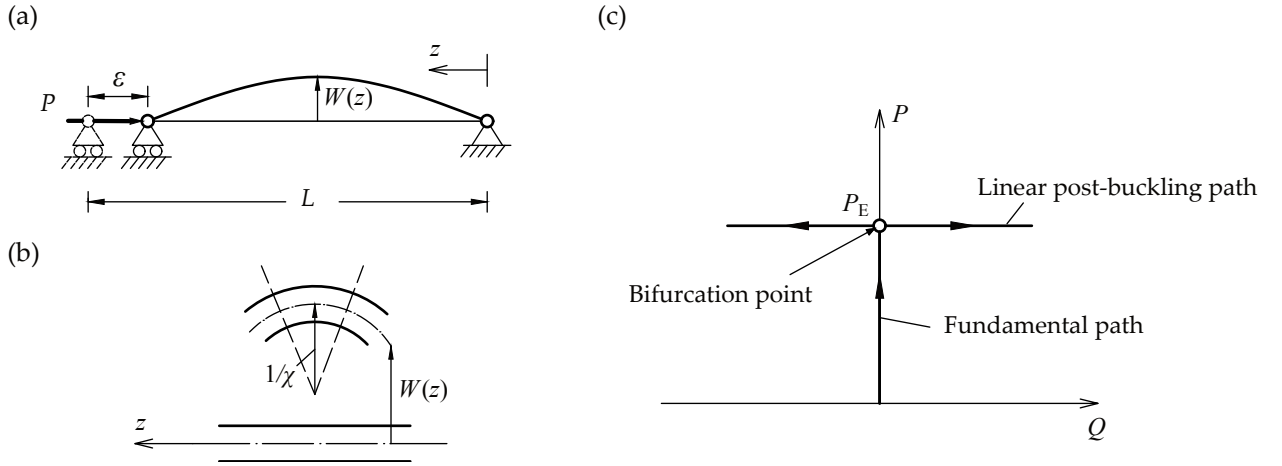


Figure 1.3: (a) Simply-supported strut under pure compression. (b) The deflection and the curvature of the strut. (c) Equilibrium path of the strut under pure compression using linear buckling analysis.

buckling analysis, it is assumed that the slope of W with respect to z is small and thus Eq. (1.1) can be reduced to a linearized version:

$$\chi \approx \ddot{W}. \quad (1.2)$$

The governing differential equation for the strut is given thus:

$$EI \frac{d^4 W}{dz^4} + P \frac{d^2 W}{dz^2} = 0, \quad (1.3)$$

with the boundary conditions being:

$$W(0) = W(L) = \dot{W}(0) = \dot{W}(L) = 0. \quad (1.4)$$

The trivial solution for the equation is $W(z) = 0$ and the non-trivial solutions are given thus:

$$W_n(z) = Q \sin \frac{n\pi z}{L}, \quad P_n = \frac{n^2 \pi^2 EI}{L}, \quad (1.5)$$

where n is an integer and Q is the amplitude of the deflection. The lowest load of the non-trivial solution, *i.e.* where $n = 1$, corresponds to the famous Euler buckling load, P_E :

$$P_E = \frac{\pi^2 EI}{L^2}. \quad (1.6)$$

The load–deflection relationship, *i.e.* the equilibrium path, is shown in Figure 1.3(c). The strut is stable when $Q = 0$ and $P < P_E$; it becomes unstable and branches at $P = P_E$ with equal probability of exhibiting deflection in the positive or negative direction. This type of problem is also known as a bifurcation problem. With a similar approach, which neglects the membrane components, the critical buckling load of plates under pure compression can be obtained using linear buckling analysis. The detailed derivation can be also found in many classical text books (Timoshenko & Gere, 1961; Bulson, 1970; Brush & Almroth, 1975).

As can be seen from Figure 1.3(c) and Eq. (1.5), linear buckling analysis can only provide the critical buckling load and the corresponding buckling mode at which point the structures initially lose stability. No further information about the post-buckling behaviour is provided. Therefore, linear buckling analysis can only give a good estimate of the ultimate load for structures exhibiting neutral or weakly stable post-buckling behaviour, such as columns with stocky cross-sections. For structures exhibiting strongly stable post-buckling behaviour, such as simply-supported plates under pure compression, they can sustain a significantly greater load than the critical buckling load, as sketched in Figure 1.4(a). In practice, local buckling is often permitted in order to take full advantage of the material strength; the critical buckling load from linear buckling analysis would underestimate the actual load-carrying capacity in such an example. On the other hand, for structures exhibiting unstable post-buckling behaviour, such as shells under axial compression and struts on softening elastic foundations, the critical buckling load from linear buckling analysis provides an upper bound estimate of the ultimate load, *i.e.* reaching the critical buckling load is accompanied by stiffness loss and erosion in load capacity, as sketched

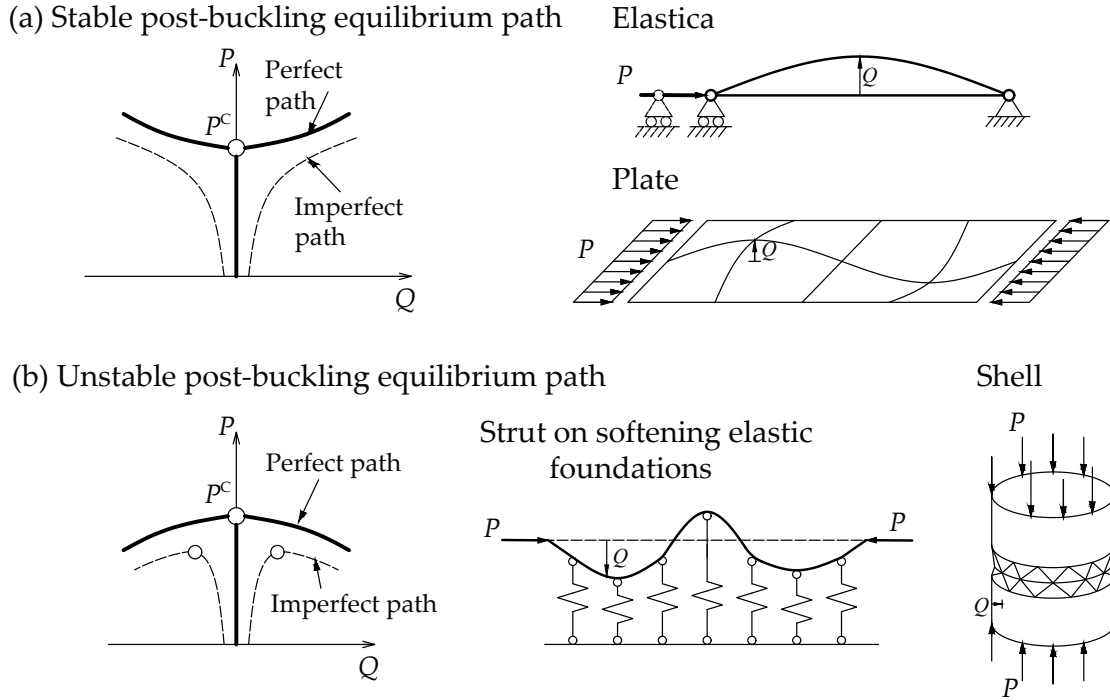


Figure 1.4: Typical post-buckling behaviour and the corresponding example structural forms (Wadee, 2007).

in Figure 1.4(b). Moreover, since such structures are very sensitive to imperfections, the perfect critical buckling load cannot be reached in practice. Therefore, higher order terms need to be included in the analysis and hence nonlinear analysis is required so as to obtain information about the post-buckling behaviour and understand some potentially highly nonlinear post-buckling behaviour, such as interactive buckling.

1.1.2 Nonlinear buckling analysis

Since Euler's work on the classical elastica problem (Euler, 1744), an actual theoretical framework was only formulated for the nonlinear post-buckling analysis when W. T. Koiter devised the general approach to post-buckling analysis of continuous elastic systems (Koiter, 1945) using the perturbation method. A concise introduction of the theory can be found in the review by Budiansky and Hutchinson (1979). In Koiter's theory, as shown in Figure 1.5(a), the fundamental and post-buckling paths are denoted by $u_0(\lambda)$ and

$u_0(\lambda) + v(\lambda)$ respectively, the latter deviating from the fundamental path at the bifurcation point with the load factor $\lambda = \lambda_c$. The normalized bifurcation mode may be defined by:

$$u_1 = \lim_{\lambda \rightarrow \lambda_c} v / \|v\|, \tag{1.7}$$

where $\|v\| = \langle v, v \rangle^{1/2}$ and $\langle v, v \rangle$ is the inner-product functional. By introducing the scalar parameter $\xi = \langle v, u_1 \rangle$, the post-buckling path can be expressed using power series expansions, thus:

$$u = u_0(\lambda) + \xi u_1 + \xi^2 u_2 + \dots, \quad \text{where } n \geq 2, \langle u_n, u_1 \rangle = 0, \tag{1.8}$$

and

$$\lambda = \lambda_c + \lambda_1 \xi + \lambda_2 \xi^2 + \dots. \tag{1.9}$$

Following the standard perturbation procedure, $u_1, u_2, \text{ etc.}$ and $\lambda_c, \lambda_1, \lambda_2, \text{ etc.}$ can be deduced by solving the governing equations of equilibrium. In particular, the governing equation is derived based on application of the calculus of variations on the nonlinear potential energy functional V , where:

$$\delta V = 0, \tag{1.10}$$

and δV is the first variation of V . The generalized theory can consider both perfect and

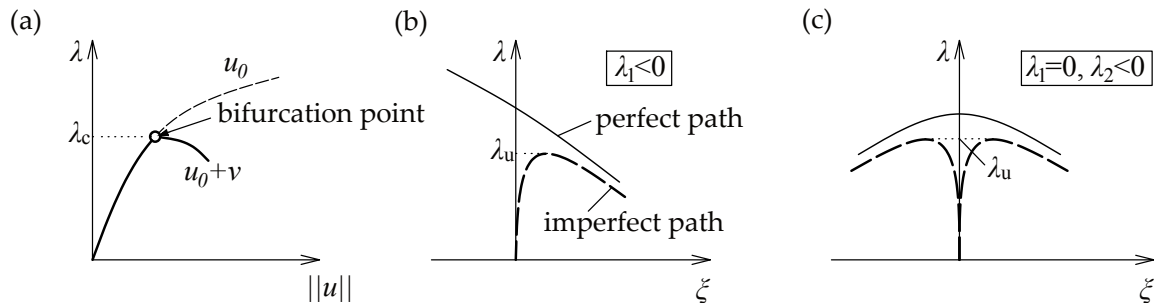


Figure 1.5: Koiter's theory and its application in determining the post-buckling behaviour and the ultimate load of imperfect structural systems.

imperfect structural systems, as shown in Figure 1.5(b, c). It can not only provide a qualitative prediction of the post-buckling behaviour of the structural system, but also an accurate quantitative estimate of the ultimate load, particularly for imperfect structural systems. The application of the theory for interactive buckling in thin-walled structures will be introduced in Chapter 2.

Independently, the Stability Research Group at University College London, headed by A. H. Chilver and J. M. T. Thompson, developed a general theory of elastic stability based on the perturbation method in the context of discrete elastic systems (Thompson & Hunt, 1973; Thompson & Hunt, 1984). The fundamentals of the work are based on two axioms (Thompson & Hunt, 1973) for elastic systems under conservative loading:

Axiom 1. *A stationary value of the total potential energy with respect to the generalized coordinates is necessary and sufficient for the equilibrium of the system.*

Axiom 2. *A complete relative minimum of the total potential energy with respect to the generalized coordinates is necessary and sufficient for the stability of an equilibrium state.*

The first axiom provides the governing equation for determining the equilibrium state:

$$V_i = \frac{\partial V}{\partial Q_i} = 0, \quad (1.11)$$

where V is the total potential energy and defined in terms of generalized coordinates Q_i and the external load P :

$$V = V(Q_1, Q_2, \dots, Q_i, \dots, Q_n, P). \quad (1.12)$$

The second axiom provides the governing criterion to determine the stability of the equilibrium state. It can also be expressed as the second derivative of V with respect to the generalized coordinates:

$$V_{ij} = \frac{\partial^2 V}{\partial Q_i \partial Q_j}. \quad (1.13)$$

The stability of the equilibrium can also be visualized with the rolling ball analogy. Figure 1.6(a) presents the analogy for stability of single degree of freedom (DOF) systems. In case (a-I), the ball is in a local minimum and perturbation in both directions will make it return to its original position eventually, which implies that the original position is stable. In case (a-II), the ball is in a local maximum and perturbation in both directions will make it permanently move away from the original position, which implies that the original position is unstable. In case (a-III), the ball is at the point of inflexion and a small perturbation will make it effectively move away from the original position, which implies that the original position is unstable. For systems with n -DOFs, the potential energy profile

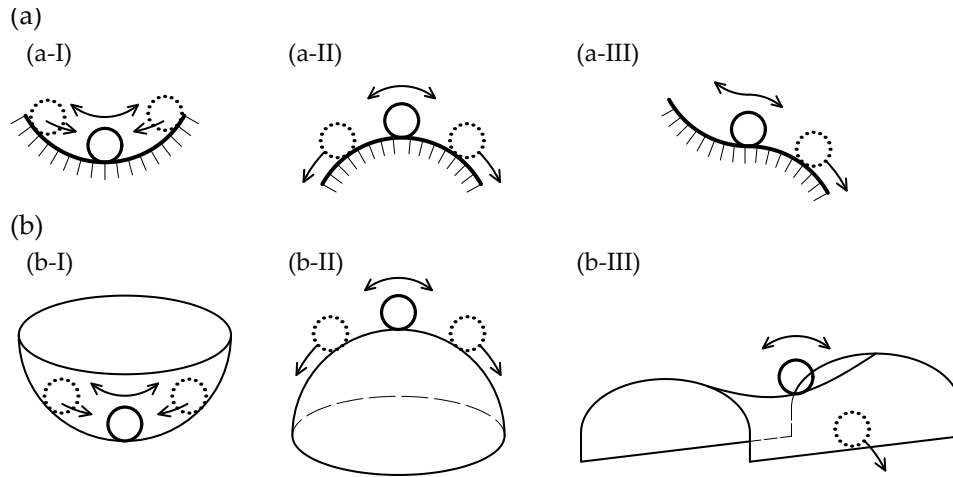


Figure 1.6: Rolling ball analogy for three types of stability of equilibrium for (a) single degree of freedom system and (b) system with more than one degree of freedom. Case (I) is stable but (II) and (III) are both unstable.

becomes an $n + 1$ -dimensional surface. Figure 1.6(b) presents the analogy for stability for systems with two DOFs. Cases (b-I) and (b-II) are essentially the same as (a-I) and (a-II) for SDOF system. Case (b-III) illustrates the case where the surface in one direction is a minimum but one of the other directions is a maximum, which is known as *saddle point*—it is essentially unstable also.

For multiple degrees of freedom (MDOF) systems, the stability of the equilibrium state

should be determined by calculating the determinant of the Hessian matrix \mathbf{V}_{ij} , where

$$\mathbf{V}_{ij} = \begin{bmatrix} V_{11} & V_{12} & \cdots & V_{1j} & \cdots & V_{1n} \\ V_{21} & V_{22} & \cdots & V_{2j} & \cdots & V_{2n} \\ \cdots & \cdots & \cdots & \cdots & \cdots & \cdots \\ V_{i1} & V_{i2} & \cdots & V_{ii} & \cdots & V_{in} \\ \cdots & \cdots & \cdots & \cdots & \cdots & \cdots \\ V_{n1} & V_{n2} & \cdots & V_{nj} & \cdots & V_{nn} \end{bmatrix}. \quad (1.14)$$

The equilibrium state is stable if \mathbf{V}_{ij} is positive-definite and vice versa. In particular, when \mathbf{V}_{ij} becomes singular, it corresponds to the bifurcation state. Higher derivatives of V are required to determine the stability at the bifurcation point.

Catastrophe theory provides another theoretical tool to classify types of bifurcation in a more theoretically strict way and facilitated a better overall understanding of the physical phenomena mathematically (Thompson *et al.*, 1978; Thompson, 1979; Hunt, 1981; Thompson, 1982; Gioncu, 1994a).

More recently, with the development of computational techniques, nonlinear post-buckling analysis can be readily performed using general purpose numerical analysis packages, such as the finite element package ABAQUS (2014). More details about the numerical approaches will be introduced in Chapter 2.

1.2 Interactive buckling phenomena

1.2.1 Augusti model

Since the full modelling of the local-global buckling mode interaction in actual structures is relatively complex, many efforts have been made to use phenomenological models to

understand the underlying mechanism of interactive buckling. A systematic review of the related mechanical models, which are devised using rigid bars and springs, can be found in Gioncu's review paper (Gioncu, 1994b). Even though these models are simple and generally have a small number of degrees of freedom, their behaviour are essentially equivalent to those of real and complex structures at least qualitatively.

One of the most famous models is the 2-DOF Augusti model (1964), as shown in Figure 1.7, which is used to understand the interactive buckling of modes that both have stable symmetric post-buckling paths when considered in isolation. The model is made up of a rigid cantilever with length L that is pinned at its base but restrained by two rotational springs with stiffnesses c_1 and c_2 that provide the structural integrity. The deflected profile of the cantilever is described by the angles spanned by the springs, Q_1 and Q_2 . The detailed energy formulation and the corresponding equilibrium path solution of the model can be found in Thompson and Hunt (1973).

Figure 1.7(c, d) present the sketches of the equilibrium paths of the Augusti model with $c_1 > c_2$ and $c_1 = c_2$ respectively. When Q_1 and Q_2 are triggered in isolation, *i.e.* the cantilever purely deflects either in the xz plane or the yz plane, the system exhibits symmetrically stable post-buckling behaviour. However, in realistic scenarios, there is an interaction between Q_1 and Q_2 since there is only a finite restraint in the non-critical plane of deflection. For instance, the cantilever initially remains undeflected in the fundamental path until P reaches the critical load $P^C = c_1/L$. After that, the cantilever starts to deflect in the direction Q_1 corresponding to the relatively smaller spring stiffness c_1 . When P reaches the buckling load at the secondary bifurcation point $P^S = (3c_1 + c_2)/4L$, the cantilever starts to deflect Q_2 in addition to Q_1 , *i.e.* interactive buckling is triggered. The triggering of interactive buckling also leads to unstable post-buckling behaviour. From the perspective of energy, the unstable interactive buckling path requires less energy compared with the primary stable post-buckling path (Timoshenko & Gere, 1961; Hunt *et al.*, 1989). In particular, when $c_1 = c_2$, the critical and secondary bifurcation points coincide, the post-

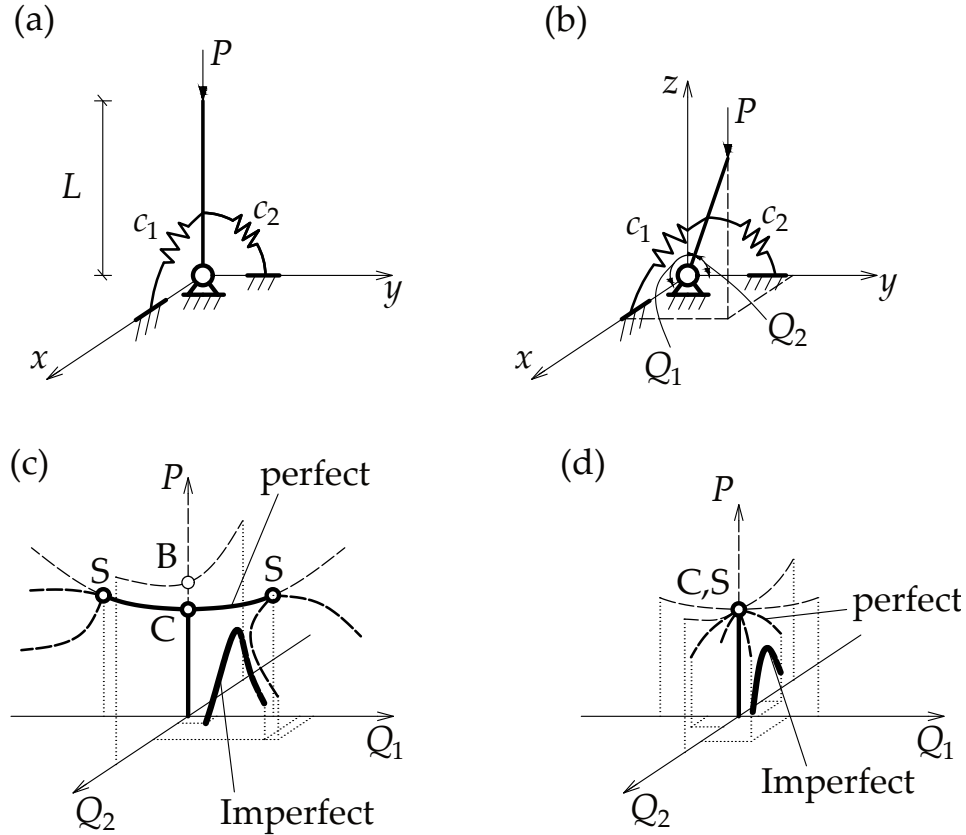


Figure 1.7: Augusti model (1964) and sketches of its typical equilibrium paths. (a) The initial configuration with rotational spring of stiffness c_1 and c_2 acting in the xz and the yz planes respectively. (b) The buckled configuration with generalized angular coordinates Q_1 and Q_2 representing the rotational deformation in the springs. Equilibrium paths for the cases where (c) $c_2 > c_1$ and (d) $c_1 = c_2$. Symbols C, B, and S represent the critical buckling point, the higher buckling load point, and the secondary bifurcation point respectively. The equilibrium paths of the model with initial geometric imperfections are also shown to demonstrate the erosion in the ultimate load due to geometric imperfections.

buckling behaviour is highly unstable, as shown in Figure 1.7(d); the critical buckling load is followed by a negative post-buckling stiffness and hence a reduction in the load-carrying capacity.

Moreover, the model also exhibits sensitivity to geometric imperfections, which is maximized for the case where $c_1 = c_2$. Closed-form expressions for the imperfection sensitivity relationship for cases with $c_1 \neq c_2$ and $c_1 = c_2$ are provided in Thompson and Hunt (1973), which both follow the well-known two-thirds power law, *i.e.* $p_{u,imp} = p_{u,perf}(1 - a\epsilon_0^{2/3})$ with

$p_{u,imp}$ and $p_{u,perf}$ being the ultimate load of imperfect and perfect struts, a being constant and ϵ_0 being the normalized imperfection size.

The Augusti model demonstrates that the interaction of two stable-symmetric buckling modes leads to an unstable-symmetric buckling mode as well as an introduction of imperfection sensitivity. It reflects the interactive buckling behaviour of real structures qualitatively, such as built-up columns (Thompson & Hunt, 1973), I-section struts (Wadee & Bai, 2014; Bai & Wadee, 2015a), stiffened plates (Wadee & Farsi, 2014a; Wadee & Farsi, 2015). However, the phenomenological models cannot provide the physical similitude of the real structures. Discrete structural models, which have more DOFs to simulate the most important aspects of the real structures, are required. Related work will be introduced in Chapter 2.

1.2.2 Interactive buckling in real structures

Mode interaction in real structures is generally derived from the chosen geometric properties such that the critical buckling loads of several different buckling modes are equal or in proximity, since linear theory (Bleich, 1952) and perhaps some study (Maquoi & Massonnet, 1976) has suggested that such a scheme is most economical. From the wavelength of the individual buckling mode, Gioncu (1994b) classified the interactive buckling in structures into three main categories, as shown in Figure 1.8.

The first case represents where the wavelengths of the individual modes, *i.e.* modes 1 and 2, are of the same order and the post-buckling behaviour of each mode is either neutral or weakly stable, as shown in Figure 1.8(a). The interactive buckling behaviour of such structures is weakly unstable and their sensitivity to imperfections is minor or moderate. An example for such a case is the interaction between flexural buckling and flexural-torsional buckling in struts with mono-symmetrical sections.

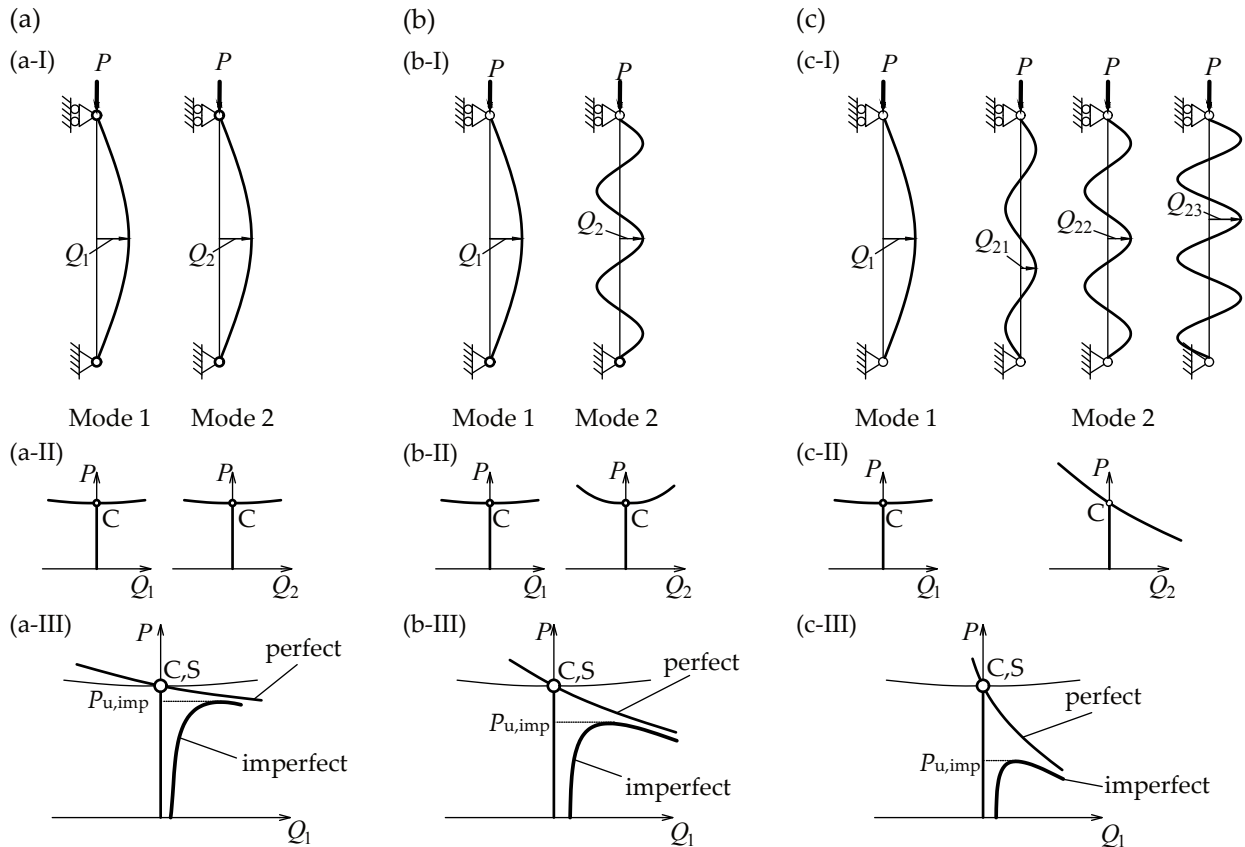


Figure 1.8: Effect of wavelength of individual buckling mode on the interactive buckling behaviour (Gioncu, 1994b). Sub-graphs (I) and (II) present the longitudinal wavelength and typical equilibrium paths of individual mode; (III) presents the interactive buckling equilibrium path of perfect and imperfect structures.

The second case represents where the wavelength of mode 2 is significantly smaller than that of mode 1, as shown in Figure 1.8(b), the unstable interactive buckling path shows a relatively larger gradient than in the first case, *i.e.* exhibiting moderate-to-strong interaction. Accordingly, such types of structures exhibit relatively higher sensitivity to imperfections. There are many examples for the type of mode interaction, such as the interaction of element member buckling with global buckling of the whole strut in built-up columns and the interaction of plate local buckling with Euler buckling in thin-walled section struts, as shown in Figure 1.9. It should be noted that the phenomena investigated in the current research belongs to this type of mode interaction.

The third case is a specialized case of the second one. In particular, there are a large number

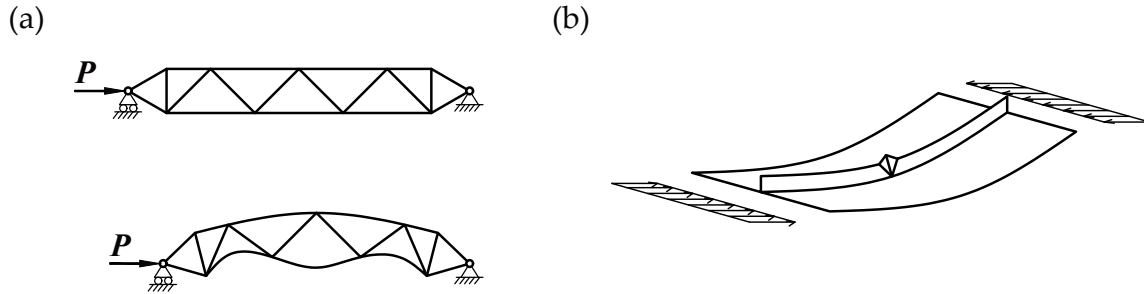


Figure 1.9: Interactive buckling in (a) build-up struts and (b) stiffened plates.

of local buckling modes with the same buckling load in mode 2. The interaction between the local modes gives rise to unstable post-buckling behaviour. Further interaction with the global mode leads to extremely unstable behaviour and high imperfection sensitivity, as shown in Figure 1.8(c). An example for such case is the cylindrical shells (Lord *et al.*, 1997).

In practice, the effects of mode interaction and imperfections on the load-carrying capacity in the first case is considered by the safe coefficients (Gioncu, 1994b) because erosion in the load-carrying capacity due to the imperfection sensitivity is mild, *i.e.* under 10%. However, for cases 2 and 3, special design methods have been developed based on experimental and numerical studies to consider the adverse effects in the load-carrying capacity due to imperfections. Specifically, for thin-walled plated structural systems, the effective width method (EWM) (EN-1993-1-5:2006E, 2006) and direct strength method (DSM) (Schafer & Peköz, 1998b) are used to determine the load-carrying capacity of members susceptible to interactive buckling.

Localization of buckling pattern due to interactive buckling

In contrast to the periodic buckling modes in the purely local buckling cases, interactive buckling also leads to the localization of the local mode, which has been widely observed in both analytical (Hunt & Wadee, 1998; Wadee, 1998; Wadee & Gardner, 2012; Wadee &

(Bai, 2014; Wadee & Farsi, 2014a) and experimental studies (Gardner & Nethercot, 2004a; Becque & Rasmussen, 2009a; Wadee & Gardner, 2012; Pavlovčič *et al.*, 2012) on interactive buckling of thin-walled metallic structures and sandwich panels. Hunt (1989) adopted simplified rigid-link and springs systems to illustrate the mechanism of the formation of the localization pattern, as shown in Figure 1.10. If the post-buckling behaviour is stable,

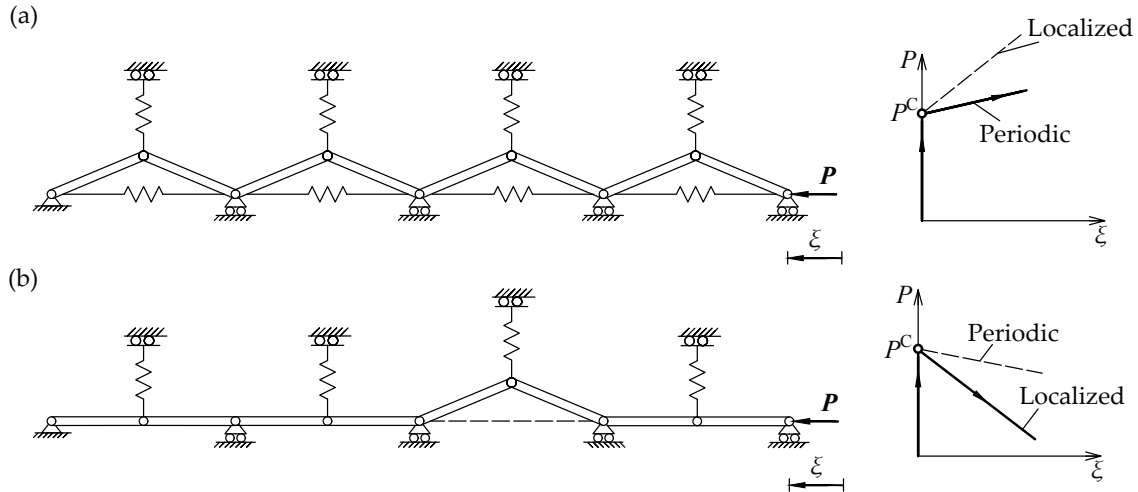


Figure 1.10: Link-spring model (Hunt, 1989) illustrating the effect of localized and periodic deformation on the equilibrium path.

the localized pattern requires more energy to trigger and thus the practically-observed post-buckling mode is periodic. If the post-buckling behaviour is unstable, the periodic pattern requires more energy to trigger and thus the post-buckling mode is localized. In such cases, a periodic profile assumption on the local mode would overestimate the post-buckling stiffness and strength and therefore would be unsafe.

1.3 Research Objectives

The aim of the present project is to develop a series of variational and FE models to investigate the mechanism of interactive buckling of thin-walled rectangular hollow section (RHS) struts under pure compression and to investigate the influence of different flange-

web joint rotational rigidities, geometric properties, initial geometric imperfections and material properties on the nonlinear interactive buckling behaviour. The aim is to provide practising structural engineers with safe and appropriate design recommendations on designing hollow-section struts with geometries that are susceptible to modal interactions.

1.4 Outline of the thesis

There are nine further chapters in the current thesis and a brief outline is given below.

1.4.1 Chapter 2: Literature review

This chapter aims to provide a systematic and detailed review of the literature on topics relevant to interactive buckling of thin-walled RHS struts. Firstly, both analytical and numerical approaches to modelling the interactive buckling of thin-walled structures are reviewed. Secondly, imperfection measurement and modelling, the imperfection modelling recommendations in the Eurocode 3 (EC3) as well as the imperfection sensitivity studies are reviewed and discussed. Moreover, the review summarises the experimental studies on mode interaction in thin-walled RHS columns. The ultimate loads of these specimens are summarized in the framework of current design guidelines. Related results on thin-walled section beams (Wadee & Gardner, 2012) and struts (Becque & Rasmussen, 2009a) of other cross-sections, which exhibit mode interaction, are also discussed. Finally, current design methodologies considering the effects of mode interaction, such as the effective width method (von Karman *et al.*, 1932) and the Direct Strength Method (DSM) (Schafer & Peköz, 1998b), are introduced.

1.4.2 Chapter 3: FE model development

In this chapter, nonlinear FE models for thin-walled RHS struts are developed in the commercial package ABAQUS (ABAQUS, 2014). The modelling details, such as element types, meshing scheme, strut modelling, boundary and loading conditions as well as geometric imperfection and residual stress modelling are introduced. Moreover, the analysis type, procedure and solution strategy are introduced. The verification and validation of the FE models using some classical solutions and experimental results in the existing literature are presented, which shows excellent comparisons. The developed FE models are used to verify variational models developed in the later chapters and to conduct extensive parametric studies to understand the interactive buckling of thin-walled rectangular hollow section columns in practically realistic scenarios.

1.4.3 Chapter 4: Behaviour of long struts with semi-rigid flange–web joints

A variational model formulated using analytical techniques describing the nonlinear interaction of global and local buckling modes in long thin-walled RHS struts with semi-rigid flange–web joints under pure compression is presented. A system of nonlinear differential and integral equations subject to boundary conditions is formulated and solved using numerical continuation techniques. For the first time, the equilibrium behaviour of such struts with different cross-section joint rigidities is highlighted with characteristically unstable interactive buckling paths and a progressive change in the local buckling wavelength. The results from the variational model are verified using the nonlinear FE model developed in Chapter 3 and show excellent comparisons. A simplified method to calculate the local buckling load of the more compressed web undergoing global buckling and the corresponding global mode amplitude at the secondary bifurcation is also developed.

1.4.4 Chapter 5: Variational modelling of practical cases

The variational model in Chapter 4 is further developed to include the cases where local buckling is critical as well as introducing the possibility of both local and global geometric imperfections existing. Two independent sets of in-plane and out-of-plane local displacement fields, which represent the pure local buckling mode and global buckling induced interactive buckling mode respectively, are introduced to describe the interactive buckling of struts with different lengths. Global and local imperfections, the profiles of which correspond to the global and local modal descriptions adopted in the variational model, are introduced. The total potential energy is determined based on the modal description and the newly introduced geometric imperfections using a very similar formulation adopted in Chapter 4. By performing the calculus of variations on the total potential energy, the governing equations for the longitudinal components of the local post-buckling modes subject to boundary and integral conditions are obtained.

1.4.5 Chapter 6: Length effects

The variational model developed in Chapter 5 is used to investigate how different strut lengths affect the nonlinear mode interaction of perfect struts. The nonlinear behaviour of four struts with representative lengths are investigated, which are characterized by the post-buckling equilibrium paths. The numerical results from the variational model are verified using nonlinear FE models. Moreover, the van der Neut-type (van der Neut, 1969) curve for the example thin-walled RHS struts is presented. The four length-dependent zones are identified and a detailed discussion is made based on the results.

1.4.6 Chapter 7: Imperfection sensitivity

The variational model developed in Chapter 5 is used to investigate the imperfection sensitivity of RHS struts where global and local buckling loads are in close proximity. The equilibrium behaviour of struts with varying imperfection sizes is presented and compared. The numerical results are validated using the nonlinear FE models. A simplified method to calculate the pitchfork bifurcation load where mode interaction is triggered for struts with a global imperfection is developed for the first time. The simplified method is calibrated to predict the ultimate load for struts with tolerance level global imperfections and combined imperfections based on a parametric study. The relative significance of local and global imperfections on the load-carrying capacity of struts with different lengths is investigated.

1.4.7 Chapter 8: Sensitivity to manufacturing tolerance level imperfections

This chapter is an enhancement on the work developed in Chapter 7. The main focus is on the response of the struts with tolerance level imperfections. A unified local imperfection measurement based on equal local bending energy is proposed. The effects of the cross-section profile, the number of half-waves and the degree of localization of the local imperfections on the ultimate load and equilibrium path are investigated. A framework to determine the most severe local imperfection is proposed and a program is developed in MATLAB, which makes it feasible to conduct an automated parametric study in an efficient way. A semi-empirical equation to determine the most severe imperfection profile is proposed based on the parametric study results. Since struts with tolerance level doubly-symmetric cross-section local imperfections exhibit neutral post-buckling behaviour, a semi-empirical equation to calculate the corresponding global buckling load is proposed since this would provide a reliable strength prediction.

1.4.8 Chapter 9: Parametric study and suggestions for improved design guidance

Parametric studies on cross-section geometric properties, material yielding stress level and strain hardening, as well as residual stresses are conducted using the FE approach to understand the behaviour of RHS struts exhibiting mode interaction in more practically realistic scenarios. Based on the numerical results and existing experimental results in the literature, the current design rules for thin-walled welded RHS struts are assessed by means of reliability analysis, in accordance with Annex D of EN1990 (BS EN 1990, 2002).

1.4.9 Chapter 10: Conclusions and future work

The principal work conducted and discoveries are summarized in Chapter 10. The original contributions and practical significance is also explained and highlighted. Suggestions are made for extending the current work and the potential application of the present methodology.

Chapter 2

Literature Review

In the preceding chapter, a brief introduction about the general theory of elastic buckling and the nonlinear coupled instability phenomena was presented. In the current chapter, the focus moves on to the interactive buckling of thin-walled structures. Previous studies and corresponding design guidelines related to the interactive buckling of thin-walled plated structures are reviewed, which aims at providing essential background information and placing the contribution of the current work into context as well as its relationship with previous work. Firstly, the analytical approaches to interactive buckling of thin-walled plated structures are presented. Specifically, both strict theoretical and approximate engineering approaches are introduced. After that, numerical approaches to modelling interactive buckling, *i.e.* the Finite Element Method (FEM), Generalized Beam Theory (GBT) and the Finite Strip Method (FSM), are discussed. Since thin-walled plated structures susceptible to mode interaction have been found to be quite sensitive to imperfections, related work on imperfection measurement and modelling, studies on imperfection sensitivity as well as imperfection modelling recommendations in current design guidelines are presented. Moreover, experimental studies on determining the ultimate load of thin-walled box-section struts exhibiting local–global mode interaction alongside some experimental results on the local–global interactive buckling behaviour of open section struts are pre-

sented. Finally, related parts about the ultimate load prediction of thin-walled struts susceptible to local–global mode interaction in current guidelines are introduced. A comparison between experimental results from the existing literature and the design equations is also presented.

2.1 Analytical approaches

In terms of analytical approaches, they can be classified into two categories (Gioncu, 1994b). The first one is the engineering method, based on approximate approaches, which use the concept of reduced stiffness or a reduced cross-section to consider the effects of local buckling. The engineering method is relatively simple but can only provide a prediction on the ultimate load. The second is the theoretical method, based on the general theory of elastic stability (Koiter, 1945; Thompson & Hunt, 1973). This method establishes the fully nonlinear governing equations based on energy principles or from direct equilibrium. The post-buckling behaviour and imperfection sensitivity can be predicted using Koiter’s theory (Koiter, 1945), numerical continuation techniques (Wadee, 1998), or some combination of the two.

2.1.1 Engineering approaches

Bijlaard and Fisher (1952; 1953) investigated the global buckling load of locally buckled square box-section columns using the method of split rigidities (Bijlaard, 1951a; Bijlaard, 1951b) in conjunction with the principle of virtual work. The stress distribution and the cross-section profile change, as shown in Figure 2.1, were solved based on energy methods. The stress–strain relationship of plates in the post-buckling range as well as the kinematic conditions of the perturbed profile, as shown in Figure 2.1(c), were adopted to establish the corresponding internal and external virtual work terms. With the stress distribution,

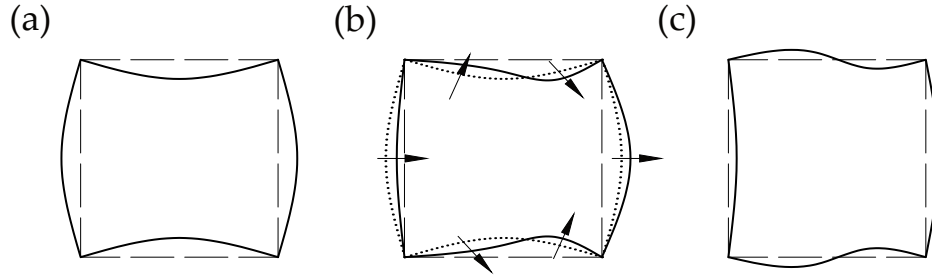


Figure 2.1: Cross-section deformation profile at different stages. (a) Local buckling. (b) Interactive local–global buckling. Note that the arrows represent the deformation direction of plate components. Dotted and solid lines represent the cross-section profiles during the pure local buckling and local–global interactive buckling stages respectively. (c) Local displacement change caused by the local–global mode interaction.

the bending moment on the section can be obtained, which can be used to determine the effective bending rigidity of the section and the effective global buckling load, *i.e.* the ultimate load. The results from the theoretical model showed good comparisons with experimental results. However, it was assumed that the post-buckling stiffness of square box-section columns was constant with the buckling progression, which in fact has been shown in later work to be decreasing (Hancock, 1981). This assumption overestimated the ultimate load. Moreover, the method can only be used for predicting the ultimate load and no information about the behaviour after that can be obtained.

Little (1979) proposed an approximate solution method to study the local–global mode interaction of thin-walled square box-section struts by transforming the geometric nonlinear problem due to local buckling of plates to a nonlinear material problem. Based on the assumption that the strain distribution is linear over the cross-section width, the theoretical moment–rotation–axial load (M – ϕ – P) relationship for a strut element with length being equal to the half-wavelength of the local buckling mode was calculated. The stiffness loss due to local buckling in the more compressed part was considered by applying a suitable average nonlinear stress–strain relationship. This was taken from the load–end-shortening curve of a simply-supported rectangular plate under pure compression up to failure using large deflection elastic-plastic analysis. Since the stress distribution in the webs is

not uniform, they were divided into 10 elements, in which the stress and strain condition was assumed to be constant. Then, the M - ϕ - P relationship was incorporated into an iterative numerical method for an inelastic complete column, which was an assembly of such half-wavelength elements. By integrating along the member axis, the load versus deflection curves of locally buckled columns was obtained. Moreover, local and global geometric imperfections, as well as residual stresses, were considered in the model. However, as noted by the author, the average stress-strain relationship to consider the effects of local buckling in plates neglected the interaction between individual plates. Moreover, the assumption about the strain distribution over the cross-section, as well as the average strain-stress relationship for the flanges, which are in combined compression and bending, is also theoretically baseless.

Djubek *et al.* (1983) proposed a semi-analytical approach to compute the ultimate load of thin-walled box-section struts susceptible to local-global mode interaction. The effects of the plate local buckling on the bending rigidity of the cross-section were considered by using the effective width concept. The expressions of the effective width for uniformly and non-uniformly compressed plates were provided, which are used for determining the effective width in webs and flanges respectively. In particular, the Winter empirical equation (Winter, 1968) was used to determine the effective width for the uniformly compressed web. In the formulation, the variation of the effective cross-section along the length of the strut owing to different ratios of compression and bending moment was considered. Moreover, the neutral axis movement due to the buckling of the more compressed section was also included. The governing equation for the local-global mode interaction of struts was given thus:

$$\{EI_e [z, W(z, P)] W''(z, P)\}'' + P \{W''(z, P) + \eta'' [z, W(z, P)] + W_0''(z)\} = 0, \quad (2.1)$$

where $I_e [z, W(z, P)]$ is the effective second moment of area of the cross-section, which is the function of the coordinate z and the column deflection $W(z, P)$; P is the axial force

applied to the strut; $\eta[z, W(z, P)]$ represents the displacement of the centroid of the cross-section owing to the plate local buckling; $W_0(z)$ is the initial global imperfection of the strut and primes represent derivatives with respect to z . Since the governing differential equation is nonlinear with coefficients being functions of P , a combination of numerical continuation and the Runge–Kutta method (Press *et al.*, 2007) was adopted to obtain the numerical solution. Moreover, the limit state of the strut was defined by the onset of yielding in the plate. The numerical results identified the erosion in the load-carrying capacity due to the geometric imperfections. However, as noted by the authors, there is no theoretical basis for the method to determine the effective stiffness in flanges, where there is a combination of axial compression and bending. A systematic investigation should be conducted to obtain the actual effective area distribution. It should also be noted that the effective width equation proposed by Winter (1968) is mainly used for the ultimate strength prediction. Therefore, it may not have been reasonable to describe the effective stiffness distribution in the buckled plate without verification from experimental results.

Graves Smith (1968) developed analytical models based on variational principles in conjunction with the Rayleigh–Ritz method to investigate the effects of material yielding stress level, cross-section aspect ratio, local–global mode interaction on the ultimate load of perfect thin-walled box-section columns. The analysis of local–global mode interaction consisted of two parts: firstly, analysis was conducted to obtain the post-buckling behaviour of columns under pure compression; secondly, a perturbation analysis, by applying an infinitesimal bending strain, was conducted based on the results of the first part. The corresponding ultimate load was determined by computing the effective bending stiffness of the section in the post-buckling range. The results revealed that the global–local interactive failure mode has little effect on the ultimate load of square box-section columns when the slenderness ratio is half of the critical slenderness ratio, defined where the local buckling load is equal to the global buckling load. An excellent comparison in the ultimate load was observed between the analytical and test results.

Using a very similar approach to that proposed by Little (1979), Lee and his collaborators (Shanmugam *et al.*, 1987; Chiew *et al.*, 1987) investigated the ultimate load of thin-walled welded box columns susceptible to local–global mode interaction. The effect of plate local buckling was considered by adopting a unified and simplified piecewise linear stress–strain relationship, which could represent the typical load–end-shortening curves of unwelded plates with plate width–thickness ratios being between 30 and 80 alongside an initial imperfection of $b/1000$, where b is the plate width. The analytical model was validated using experimental results of 17 welded box-section columns under pure compression. It revealed that the analytical model could provide a reasonably accurate prediction of the ultimate load. Based on the validated analytical model, a parametric study on the column and plate slenderness was conducted. The load-carrying capacity erosion due to geometric imperfections and residual stresses was identified, particularly for columns with intermediate lengths. As for the effect of plate slenderness on the interactive buckling, it revealed that the column strength is independent of column global slenderness $\bar{\lambda}_o$ in the lower range of $\bar{\lambda}_o$ and this range increases with the increasing plate width to thickness ratio b/t . Moreover, at low b/t ratios, interactive buckling failure mode governs for the whole range of $\bar{\lambda}_o$, whereas the failure is mainly due to local buckling up to a certain value of $\bar{\lambda}_o$ for larger b/t .

It should be noted that the engineering method becomes practically less significant for research purposes with the advance and availability of computational mechanics tools, such as commercially available FE packages. However, they played an important role in understanding the key parameters that affect the physical phenomena. Moreover, owing to its simplicity and reasonable accuracy, it is acceptable for practical engineering purposes and some of these studies have played important roles in the development of the codes of practice.

2.1.2 Theoretical approaches

Van der Neut model

As far as the author is aware, the Van der Neut model (van der Neut, 1969) is the first work to apply the general elastic stability theory to the interactive buckling of thin-walled structures. The Van der Neut model is an idealized column, which consists of two load-carrying flanges with width b and thickness h and an unspecified web with height $2c$ that is rigid in shear and only offers a simple support to the flanges without contributing to the transmission of the axial force, see Figure 2.2(a). With the idealized web assumption, the force in the flanges is very easy to calculate; Van der Neut investigated the ultimate load and initial post-buckling behaviour of perfect columns, columns with a pure local imperfection, and columns with both local and global imperfections with varying lengths. The application of the model to imperfection sensitivity and load-carrying capacity erosion study is discussed in a later section specifically about imperfections (§2.3).

In the model, the interaction between local and global modes is considered by introducing the reduction factor in the longitudinal stiffness η in the post-buckling range of the flanges. The reduction factor η is given by:

$$\eta = \frac{d(P/P_1^C)}{d(\varepsilon/\varepsilon_1)}, \quad (2.2)$$

where P and ε are the applied compressive load and the direct strain in the flanges respectively and P_1^C and ε_1 are the local buckling load and the corresponding direct strain in the flanges. For the perfect case, η decreases with the increase of P/P_1 , but it remains approximately 0.4083 for $\varepsilon/\varepsilon_1 < 3$ (Hemp, 1945). The governing differential equation was established using direct equilibrium.

Using Koiter's theory (Koiter, 1945), Van der Neut investigated the characteristics of the equilibrium response at the buckling load and classified the post-buckling properties

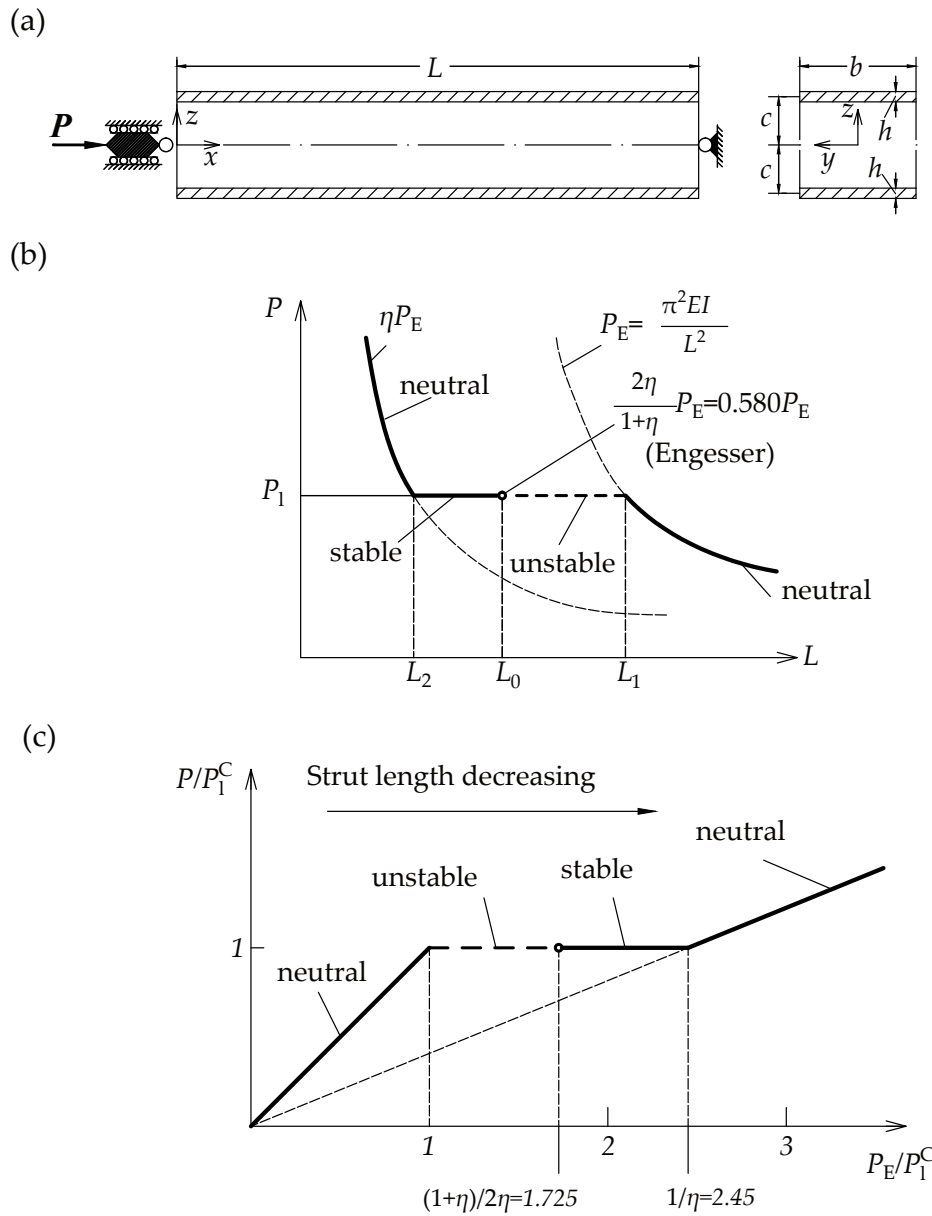
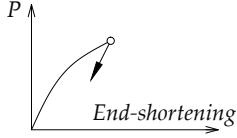
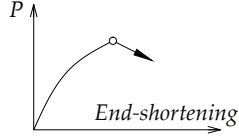
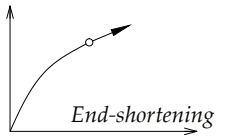


Figure 2.2: (a) The Van de Neut model of an idealized thin-walled strut (van der Neut, 1969). The strut comprises two load-carrying flanges with width b , thickness h , length L with a pair of rigid webs of depth $2c - h$ with no longitudinal stiffness; P is the concentric axial load applied to the entire strut. (b, c) The Van de Neut curves for the geometrically perfect case: η is the stiffness reduction factor, $L_0 = [2\eta/(1 + \eta)]^{1/2} L_1$, $L_2 = \eta^{1/2} L_1$ and L_1 is defined when $P_E = P_1^C$; P_1^C and P_E are the plate local buckling load and the column Euler global buckling load respectively.

Table 2.1: Types of bifurcation defined by Van der Neut (1969), where P is the axial load and P_1^C is the local buckling load. The quantity $(W_0/c)^2$ is the same order of the deflection at mid-span and $-\Delta L$ is the end-shortening; $\frac{dP/P_1^C}{d(W_0^2/c^2)}$ represents the slope of the load versus mid-span deflection curve and $\frac{dP/P_1^C}{d(-\Delta L/\varepsilon_1 L)}$ represents the slope of the load versus end-shortening curve.

Bifurcation at P_b			
			
$\frac{dP/P_1^C}{d(W_0^2/c^2)}$	< 0	< 0	> 0
$\frac{dP/P_1^C}{(-\Delta L/\varepsilon_1 L)}$	> 0	< 0	> 0
Post-buckling characteristic	Unstable & explosive	unstable	stable

into three categories, as presented in Table 2.1. Moreover, as shown in Figure 2.2(b), four distinct length-dependent zones were identified, *i.e.* the column is approximately neutrally stable when $L < L_2$, strongly stable when $L_2 < L < L_0$, strongly unstable when $L_0 < L < L_1$ and approximately neutrally stable once again when $L > L_1$. By an axis transformation, Figure 2.2(b) can be presented as the more well-known diagram comprising three straight lines as shown in Figure 2.2(c). The boundary for each characteristic zone was determined based on the Engesser ‘double-modulus’ theory (Bažant & Cedolin, 2010), where the effective axial stiffness of the buckled plate is assumed to be ηE .

Using almost the same methodology, Van der Neut (1976) also studied the mode interaction in stiffened plates used in aircraft wing structures, where the cross-section is unsymmetrical, *i.e.* the area of the plate side is larger than the stiffener topside. In particular, the rotational constraint from adjacent plate elements were included in the analytical model. Unstable post-buckling behaviour due to mode interaction was also observed but the severity was mollified. Moreover, compared with the two-flange Van der Neut idealized column, it was found that the unstable range for the stiffened plate was much smaller.

Discrete models

Menken *et al.* (1991; 1994) developed a discrete model (see Figure 2.3) involving a limited number of degrees of freedom to analyse the interaction between the local flange buckling and the overall lateral-torsional buckling in a cantilever T-section beam. Using the general theory of elastic stability (Thompson & Hunt, 1973), the interactive buckling behaviour was reproduced and it agreed well with the experimental results qualitatively. Although discrete models reproduce qualitative behaviour, analytical approaches based on continuous models are generally superior for reproducing quantitative behaviour.

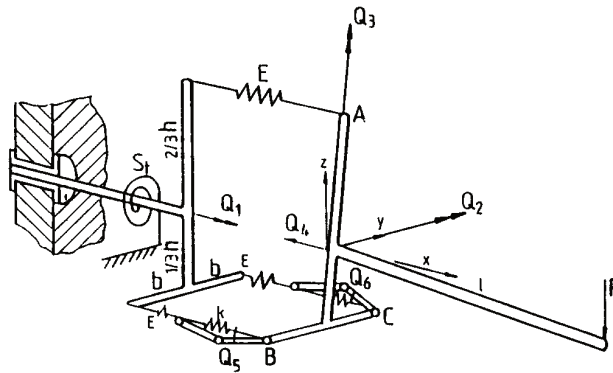


Figure 2.3: Discrete model for analysing the interaction between the global lateral-torsional buckling mode and the local flange buckling mode; Q_1 is the rotation and Q_3 is the lateral deflection, both describing the global lateral-torsional buckling mode. The independent angles Q_5 and Q_6 represent the local buckling mode of flanges; Q_2 characterizes the vertical deflection and Q_4 is the end-shortening. Reproduced from Menken *et al.* (1994).

Continuous models

Based on the concept of slowly varying functions, Koiter and Pignataro (1976a) formulated a relatively simple and approximate potential energy expression to describe the local-global mode interaction in stiffened panels. As for the description of the local mode, a simple but sufficiently accurate approximation based on the solution of initial post-buckling of long flat plates was adopted. Specifically, the cross-section component of the local out-of-plane

displacement was given as a piecewise function:

$$g_w(\zeta) = \begin{cases} q \sin(\pi\zeta) + (1 - q) [1 - \cos(3\pi\zeta)] / 3 & \text{for } 0 \leq \zeta \leq 1/6, \\ q \sin(\pi\zeta) + (1 - q) [1 + 2 \sin(3\pi\zeta/2 - \pi/4)] / 3 & \text{for } 1/6 < \zeta < 5/6, \\ q \sin(\pi\zeta) + (1 - q) [1 + \cos(3\pi\zeta)] / 3 & \text{for } 5/6 \leq \zeta \leq 1, \end{cases} \quad (2.3)$$

where $\zeta=y/b$ is the normalized transverse coordinate with b being the plate element width between stiffeners, q is the parameter reflecting the effects of rotational restraints in the longitudinal edges, the variation of which can mimic a variety of different rotational boundary conditions from the simply-supported ($q=0$) to clamped cases ($q=1$). The longitudinal component of the out-of-plane displacement was assumed to be a sine function, the wavelength of which depended on the rotational restraint at both longitudinal edges. Moreover, the modulation in the local mode amplitude owing to local–global mode interaction was considered by introducing a modulated function. As for the in-plane local mode, both axial and transverse displacement fields were considered, the wavelength of which in the longitudinal direction was assumed to be half of the out-of-plane component a . The cross-section components for axial and transverse local modes were assumed to be:

$$g_u = \frac{\pi}{8a} g_w^2(\zeta), \quad g_v = \frac{\pi}{8b} g_w(\zeta) g_w'(\zeta), \quad (2.4)$$

where the prime represents the derivative with respect to ζ . By reducing the functional in terms of a dimensionless quantity, it revealed that the expression only depends on the ratio of the global buckling load to the local buckling load as well as the cross-section properties, the latter of which was found to vary in a relatively narrow range for practically significant sections. Based on the analytical model, it was found that the unstable post-buckling behaviour of stiffened panels was less severe than that for the Van der Neut's two-flange simplified model.

Recently, the group led by Wadee has developed a series of mathematical models based on

variational principles to simulate the nonlinear local–global interactive buckling behaviour in thin-walled structural components under compression (Wadee & Bai, 2014; Wadee & Farsi, 2014a; Liu & Wadee, 2015) and bending (Wadee & Gardner, 2012). The fundamental methodology for the series of works is essentially the same, which was firstly proposed while studying localized buckling in sandwich structures (Wadee, 1998). Timoshenko beam theory was used to model the global behaviour of the structure because Hunt and Wadee (1998) demonstrated that the shear strains within each individual element were essential to preserve the energy terms necessary for modelling the interaction. Specifically, the global mode was divided into two components: a pure lateral displacement W and a pure rotation θ (see Figure 2.4), known as the ‘sway’ and ‘tilt’ modes respectively (Hunt *et al.*, 1988; Hunt & Wadee, 1998). The local mode was estimated by appropriate boundary conditions,

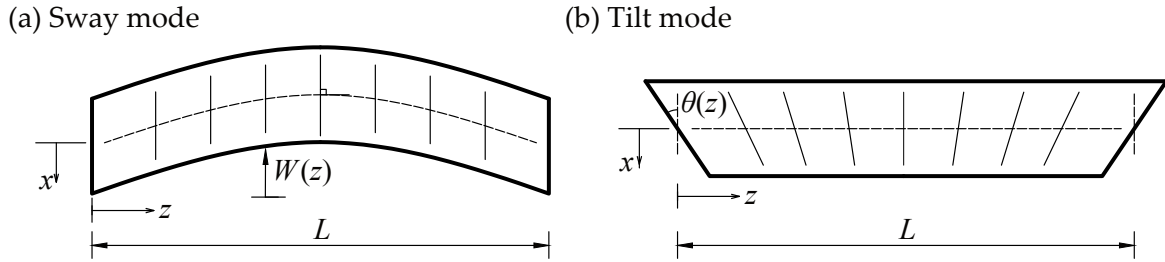


Figure 2.4: Decomposition of the global buckling mode into ‘sway’ and ‘tilt’ components.

in conjunction with the Rayleigh–Ritz method. Geometric nonlinearities were considered by using large-deflection plate theory (Timoshenko & Woinowsky-Krieger, 1959). Based on the modal description, the total strain energy and work done by load terms were determined. The global buckling load of the compression member was determined by considering the condition where the Hessian matrix of the total potential energy V is singular on the fundamental path, where all local and global buckling modes are null. With variational principles, the total potential energy V was then minimized with respect to the continuous variables, the longitudinal local out-of-plane component w and in-plane component u , to obtain a system of nonlinear differential and integral equations that define the equilibrium states.

Since the governing equations are too complex to solve analytically, the numerical continuation software, AUTO (Doedel & Oldeman, 2009), was used to solve the governing equations. AUTO is generally used to solve the following problem using numerical continuation:

$$\mathbf{f}(\mathbf{y}, \eta) = 0, \quad (2.5)$$

where \mathbf{f} and \mathbf{y} denote n -dimensional vectors, and η is the continuation parameter, *i.e.* a free parameter introduced to observe how the solution of \mathbf{f} evolves. The method for orthogonal collocation (De Boor & Swartz, 1973) was adopted to discretize the problem using piecewise polynomials with 2–7 collocation points per mesh interval (Doedel & Oldeman, 2009). Moreover, the mesh is automatically adapted to the solution so as to distribute the error from local discretization (Russell & Christiansen, 1978). Although AUTO is principally designed for autonomous systems (hence the name), n^{th} -order non-autonomous equations can be solved by introducing a further variable, f_{n+1} , where

$$\dot{f}_{n+1} = 1, \quad (2.6)$$

with the boundary condition being:

$$f_{n+1} = 0. \quad (2.7)$$

As for the numerical continuation routine, pseudo-arclength continuation is adopted in combination with the modified Newton–Raphson method is adopted (Riks, 1979). It can trace the limit points (or *folds*), which is very helpful to trace the highly nonlinear equilibrium paths in current study.

Despite the advantage in tracing highly nonlinear equilibrium paths, the modified Newton–Raphson method cannot detect and identify bifurcation points in the solution space (Crisfield & Wills, 1988). Since the rank of the Jacobian matrix of the system of equations, \mathbf{J} , reduces by at least one at a bifurcation point, AUTO can locate bifurcation points by examining it (Doedel & Oldeman, 2009). Moreover, from evaluating the derivative of \mathbf{J} at

the bifurcation point, the trajectories of different post-bifurcation paths can be computed by finding the roots of the resulting algebraic bifurcation equation (Keller, 1977). The well-defined trajectories of the post-bifurcation branch paths also makes it possible to switch between different post-bifurcation branches. It should be noted that AUTO can also detect other kinds of critical points, such as torus bifurcations and Hopf bifurcations. However, in the current thesis, the detection of limit points and bifurcation points is deemed sufficient.

AUTO has been shown in previous studies to be a powerful numerical solver of nonlinear problems without losing the intrinsic mathematical structure of the solutions and to switch between, as well as trace, equilibrium paths (Wadee & Bai, 2014; Wadee & Farsi, 2014a; Wadee & Farsi, 2014b; Bai & Wadee, 2015b; Liu & Wadee, 2015). This puts it to somewhat of an advantage to the commercial FE package ABAQUS in the sense that the perfect nonlinear behaviour can be investigated without resorting to perturbing the system to by-pass the bifurcation. The fourth-order and second-order governing equations are firstly non-dimensionalized and then transformed into a system of first order differential equations (Wadee, 1998) so as to be solved within AUTO. Moreover, it should be mentioned that the principal parameters used in the continuation process in AUTO are interchangeable. For the case where global buckling is critical, see Figure 2.5(a), the global buckling load P_0^C is obtained explicitly from the analytical model. Using the continuation method, the normalized amplitude of the global mode q_s is then varied to obtain the secondary bifurcation point S, where local buckling is triggered. Subsequently, the second run is started at the bifurcation point S using the branch switching facility within the package and the applied load P is varied to compute the interactive buckling paths. For the case where local buckling is critical, the first run starts from zero load and the local buckling load P_1^C is obtained numerically. Using the branch switching function, the post-buckling path of the local buckling mode is computed. The second run is stopped and the branch is switched in the third run when a secondary bifurcation point S is found. From this point, the interactive buckling path is found; the procedure is shown in Figure 2.5(b).

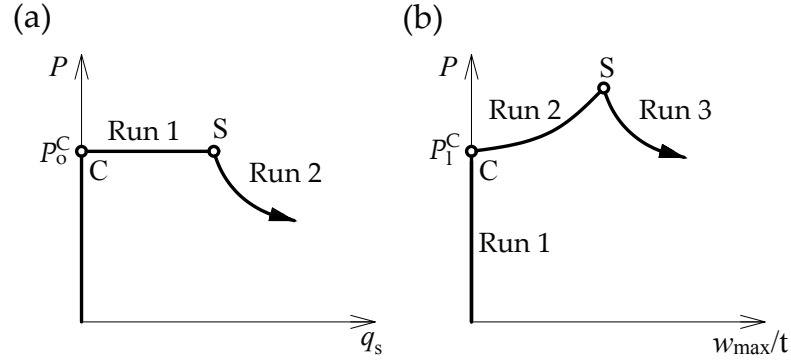


Figure 2.5: The numerical continuation procedures for interactive buckling of perfect columns: (a) global buckling being critical and (b) local buckling being critical. The thicker line shows the actual solution path. Circles marked C and S represent the critical and secondary bifurcation points respectively; q_s and w_{\max}/t represent the respective normalized amplitudes of the global and local buckling modes.

Highly unstable cellular buckling (Hunt *et al.*, 2000) due to the instability of the mode interaction in combination with the strong post-buckling stability of the local mode was observed in I-section struts (Wadee & Bai, 2014), beams (Wadee & Gardner, 2012), stiffened plates (Wadee & Farsi, 2014a) and angles (Bai *et al.*, 2017). Snap-backs in the equilibrium paths and evolution of the local mode profile from localized to distributed were captured, which was not well reproduced in the numerical verification (Wadee & Bai, 2014; Wadee & Farsi, 2014a) using ABAQUS, but were observed in physical experiments.

The analytical models for stiffened plates and I-section columns were extended to include rotational springs at junctions within the cross-sections (Wadee & Farsi, 2014b; Bai & Wadee, 2015b). In both cases, a rapid erosion of the snap-backs in the equilibrium paths was observed with the increase of the rotational rigidity at junction. However, the evolution of the local mode profile from localized to being more distributed and the wavelength change was still captured. Moreover, based on the analytical models, parametric analysis was conducted to investigate the effects of changing the global and local slenderness on the post-buckling behaviour, thus providing the important practical sizing information to structural designers (Bai, 2014; Wadee & Farsi, 2015). Compared with Van der Neut’s ‘three-straight line’ $P_u/P_1^C - P_o^C/P_1^C$ diagrams, as shown in Figure 2.2, the diagrams in

present works (Bai, 2014; Wadee & Farsi, 2015) present quantitative information about the behaviour of structural components in the interactive buckling range.

The results from these studies reveal amongst other things that progressive cellular buckling (Hunt *et al.*, 2000) arises from the nonlinear interaction between the weakly stable global buckling mode and the strongly stable local buckling mode. Moreover, experimental results from other research groups (Fok *et al.*, 1976; Becque & Rasmussen, 2009a) have been useful in validating the analytical work (Wadee & Bai, 2014; Wadee & Farsi, 2014b) with excellent agreement. It should be noted that these models were also extended to include geometric imperfections. The related work will be discussed in a later section specifically about imperfection sensitivity.

2.2 Numerical approach to interactive buckling

2.2.1 Finite Element Method (FEM)

Owing to the popularity of general-purpose finite element (FE) packages with powerful modelling and solution functions, FEM has become a critically important and accessible method in analysing the nonlinear behaviour of thin-walled structures. Compared with analytical methods, it can model nearly all the actual physical scenarios, including items such as residual stresses, initial imperfections and plasticity. Therefore, it is often used for verifying analytical models (Wadee & Farsi, 2014a; Becque, 2014; Bai & Wadee, 2015b; Liu & Wadee, 2015), expanding the original simplified analytical model to more general and actual cases (Kiymaz, 2005) and conducting parametric studies based on FE models validated by experiments (Becque & Rasmussen, 2009b; Yuan *et al.*, 2014). Related studies using commercial packages with the FE models calibrated by experimental results are reviewed later in §2.4.

However, compared with analytical methods, it takes more time to run a nonlinear FE analysis with a fine-mesh scheme. Nevertheless, high precision in the solution was obtained in nearly all these numerical studies except for the aforementioned cases. In the current study, the FE method is used as a verification tool for the analytical model, to give hints for refining the analytical models and to conduct parametric studies to increase the understanding of the behaviour of thin-walled RHS in practical scenarios.

Apart from the usage of generalized FE packages, some researchers have also developed some specific finite elements to study the local–global mode interaction. Usami and Fukumoto (1984) adopted an updated Lagrangian formulation for elastic large displacement analysis of beam-columns (Cook *et al.*, 2007) to simulate the global response of welded box-section struts exhibiting mode interaction within the FEM framework. Local buckling was considered by introducing the effective width concept, as shown in Figure 2.6. The effective member sections were determined using the effective width formula at every loading stage. For uniformly compressed plates, *i.e.* webs, the expression for the effective

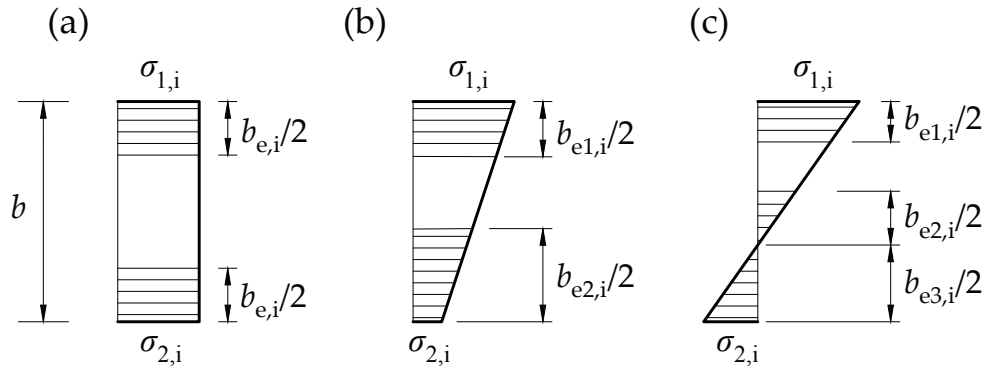


Figure 2.6: Effective width of a plate under different stress distribution cases: (a) Uniform compression with $\sigma_{1,i} = \sigma_{2,i}$; (b) eccentric compression with $\sigma_{1,i} > \sigma_{2,i} > 0$; (c) eccentric compression with $\sigma_{1,i} > 0$ and $\sigma_{2,i} < 0$.

width at step i was given thus:

$$\frac{b_{e,i}}{b} = C \sqrt{\frac{\sigma_{cr}}{\sigma_i}} \leq 1, \quad (2.8)$$

where b is the total width; C is a constant determined based on the stub column tests; σ_{cr}

is the local buckling load of a simply supported plate under pure compression; σ_i is the edge stress at step i . It should be noted that by substituting σ_i with the yielding stress f_y in Eq. (2.8), it is equivalent to the effective width equation to determine the ultimate load of locally buckled plates. For non-uniformly compressed plates, the following expressions were used. When $\sigma_{1,i}, \sigma_{2,i} \geq 0$:

$$\frac{b_{e1,i}}{b} = \frac{C}{2} \sqrt{\frac{\sigma_{cr}}{\sigma_{1,i}}}, \quad (2.9)$$

$$\frac{b_{e2,i}}{b} = \left[1 + 0.44 \left(1 - \frac{\sigma_{2,i}}{\sigma_{1,i}} \right) \right] \frac{b_{e1,i}}{b}, \quad (2.10)$$

$$b_{e1,i} + b_{e2,i} \leq b. \quad (2.11)$$

When $\sigma_{1,i} \geq 0$ and $\sigma_{2,i} \leq 0$, the expression for $b_{e1,i}$ is the same as that given by Eq. (2.9) and

$$\frac{b_{e2,i}}{b} = 1.44 \frac{b_{e1,i}}{b}, \quad (2.12)$$

with

$$b_{e1,i} + b_{e2,i} \leq b - b_{e3,i}, \quad (2.13)$$

where $\sigma_{1,i}$ and $\sigma_{2,i}$ are the maximum and minimum edge stresses respectively, as shown in Figure 2.6. As for the FE formulation for the beam-column element, the shape function for the axial and lateral displacements was adopted as first and third order polynomials. Half of each column was discretized into six elements and four point Gaussian quadrature was adopted to integrate the element stiffness matrix. As for the imperfections, an initial deflection of a half sinusoidal wave was introduced as the global geometric imperfection.

Ali and Sridharan (1988) developed a one-dimensional finite element model, which can simulate the interactive buckling of thin-walled columns with an arbitrary cross-section. In particular, the displacement field of the model includes amplitude modulation of the local modes and the global mode. As for the global mode, both purely flexural and flexural-torsional buckling modes were considered; as for the local mode description, a primary local mode and two relevant secondary local modes with the same wavelength were considered.

All the modes were determined using the finite strip method. Some examples on channel-section columns were presented; it revealed that there is a nonlinear coupling between flexural and flexural–torsional buckling through the local buckling mode. Moreover, highly imperfection sensitive behaviour of channel-section columns was identified, which is more severe than the cases with doubly-symmetric cross-sections.

Degée *et al.* (2007) developed a new special beam finite element to analyse the local and interactive post-buckling of Rectangular Hollow Section (RHS) thin-walled members. The newly developed element was based on the superposition of a displacement field of a classical strut (global mode) and a field describing local effects (local mode). The nonlinear analysis results for beams of moderate local and global slenderness matched well with the results obtained using shell elements. However, the simplified assumption that neglected some nonlinear local terms in the strain energy expression makes the element only valid in cases where the geometric nonlinear effect is relatively small.

Since the full nonlinear post-buckling analysis of thin-walled structures requires a considerable computational effort, Lanzo and Garcea (1996) developed an asymptotic approach based on a finite element implementation of Koiter’s general theory of stability. Compared with the previous approach using the analytical method in conjunction with Koiter’s theory, this method overcame the limitation from the displacement field assumption and limited boundary condition cases. Compared with the standard nonlinear incremental path-tracing approach, it was much faster and computationally efficient. The numerical results also demonstrated that this method can provide a reasonably accurate prediction of ultimate load and initial post-buckling behaviour. It was also reported that the method could capture some complex strong modal interaction phenomena, which was difficult to predict by some, more standard, nonlinear analysis techniques. However, since the selection of the number of buckling modes is crucial for the accuracy of the method, an *a posteriori* study on the number of selected modes should be performed, otherwise all critical modes must be taken into account. Moreover, owing to the limitation of Koiter’s theory, this

method is only reliable in the initial post-buckling stage. Therefore, this method has been more widely used on the imperfection sensitivity studies (Zagari *et al.*, 2016), where only the ultimate load is of interest.

2.2.2 Generalized Beam Theory (GBT)

GBT was first developed by Schardt (1994) but was only valid for linear buckling theory initially. Silvestre and Camotim (2003) developed a geometrically nonlinear GBT, which is valid in the large deformation range but still keeps the advantage of the modal decomposition feature. Compared with traditional GBT, two additional sets of cross-section deformation modes, namely shear and transverse modes, were introduced, thus making complex cross-section analysis possible. A finite element beam was developed for the solution of the GBT equations. A predictor–corrector technique based on the Newton–Raphson method and arc-length control was used to solve the nonlinear equations. In the three illustrative examples on the post-buckling behaviour of a plate, a lipped channel and a Z-section column under pure compression, the equilibrium paths calculated by the nonlinear GBT match well with those from ABAQUS using shell elements. The decomposition feature of GBT helped explain the mechanism of some cross-section modes which cannot be provided by conventional numerical methods directly. Moreover, the method discretized the system in terms of modes and hence the number of degrees of freedom is substantially reduced when compared with shell FE models, which has a marked effect on reducing computing time.

In recent years, nonlinear GBT has been further extended to solve a variety of different problems by Camotim and his collaborators, such as the post-buckling behaviour of thin-walled structures made of nonlinear materials using the active elastic moduli predicted by deformation and flow plasticity theories (Gonçalves & Camotim, 2004); the elastic post-buckling behaviour of imperfect thin-walled steel members with arbitrary cross-section pro-

files with non-standard support conditions (*e.g.* localised restraints) under general loading conditions (Basaglia *et al.*, 2011); the interaction between local and distortional buckling of thin-walled lipped channel columns (Silvestre & Camotim, 2006) and beams (Martins *et al.*, 2018).

2.2.3 Finite Strip Method (FSM)

The FSM was first developed by Cheung (1968) alongside Graves Smith and Sridharan (1978) to reduce the computational efforts. The basic methodology and theory is essentially identical to FEM. The only difference is the discretization. In the finite strip method, only a single element is used to model the longitudinal direction. It greatly reduces the number of degrees of freedom in the model compared with FEM. However, it may also introduce errors for the cases where the longitudinal displacement field varies and deviates from the predefined shape function. Hancock *et al.* (1990) proposed the spline finite strip method by discretizing the longitudinal direction as well and using spline functions to describe the longitudinal displacement field. It can somewhat make up the shortcomings of the original version of FSM but with the price of additional complexity and increased computational efforts.

Using the FSM, Hancock (1981) studied the effective global bending rigidity of square box-section columns with initial local imperfections. As shown in Figure 2.7, a perturbation in global bending was applied by adding a small curvature to the locally deformed sections due to axial compression and initial geometric imperfections. The resulting stress distribution was integrated to obtain the bending moment applied on the section. To simulate the actual stress distribution, half of the cross-section was subdivided into 16 equal width strips. The effective global bending rigidity of the section then was determined by dividing the bending moment by the curvature. With this methodology, the effective bending rigidity of struts with different local imperfection sizes under different compressive stress

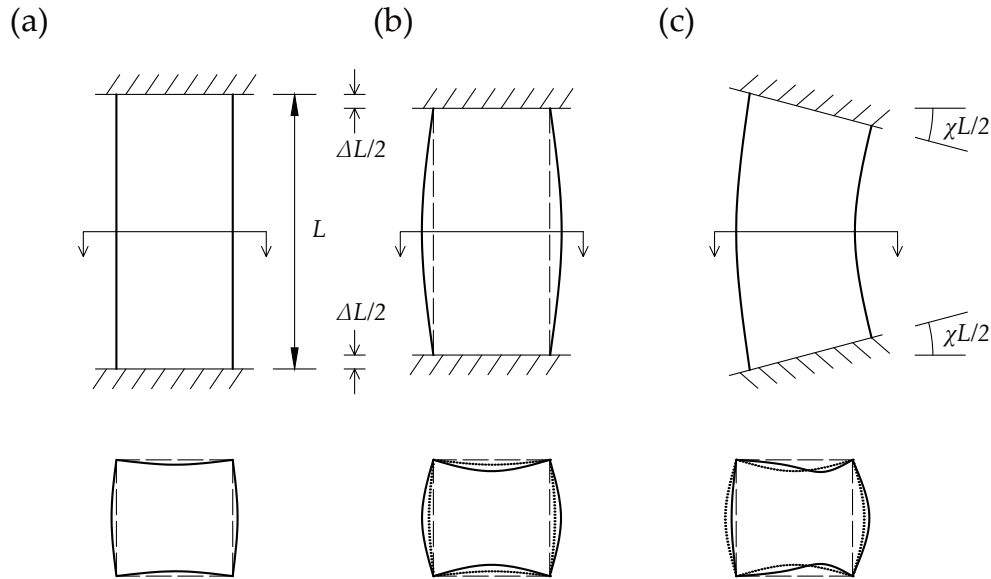


Figure 2.7: Square box-section strut with initial local geometric imperfections: (a) Initial state. (b) Axial compressive strain Δ . (c) Axial compressive strain Δ and bending curvature χ . The dotted line in the cross-section graphs represents the deformed profile in the preceding stage.

levels was determined. A comparison was made with previous studies (Bijlaard & Fisher, 1953; Dewolf *et al.*, 1974), which verified the effectiveness of the methodology. Moreover, it revealed that the effective bending rigidity is sensitive to imperfection size when the initial compressive load is smaller than the local buckling load.

Sridharan and his collaborators (Sridharan, 1983; Benitot & Sridharan, 1984; Sridharan & Ali, 1986) used the finite strip method in conjunction with Koiter's theory to analyse the mode interaction of thin-walled structural members with different cross-sections. As for the global mode, both purely flexural and flexural-torsional buckling were considered. The numerical results (Benitot & Sridharan, 1984) matched the available experimental results well. However, greater focus was placed on the imperfection sensitivity study. The evolution or progress of the interactive buckling behaviour was not presented.

Dauids and Hancock (1987) combined the influence coefficient method (Han & Chen, 1983) for beam-columns with the FSM for nonlinear elastic analysis of locally buckled thin-walled sections to analyse the local-global interactive buckling in beam-columns, as shown

in Figure 2.8. This method takes advantage of both analysis methods and thus is very computationally efficient. Moreover, the effects of local and global geometric imperfections, residual stresses, general boundary conditions as well as the general applied loads were included in the model. As for the analysis procedure, the column was first replaced by a series of ‘cell’ elements, the lengths of which were equal to the half-wavelength of the pure local buckling mode. The moment and axial force resisted by a cell subjected to the defined curvature and axial strain were determined using the nonlinear elastic FSM. The average values of moment and axial force then were used for the nonlinear analysis of the beam-column. The numerical results showed good comparisons with experimental results.

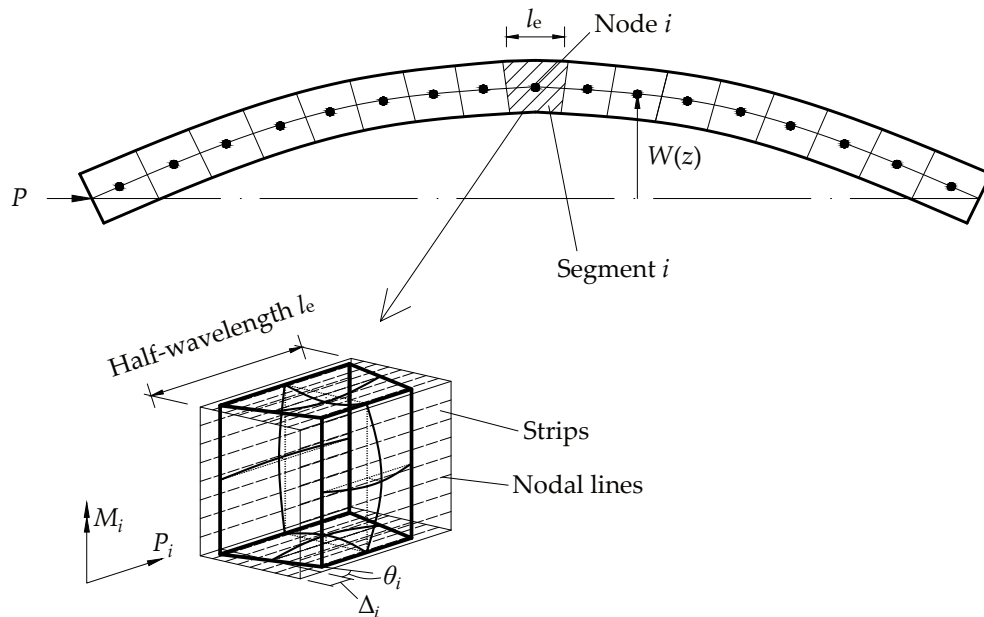


Figure 2.8: Illustration of the influence coefficient method of beam-column in conjunction with the finite strip method of nonlinear elastic analysis of locally buckled ‘cell’ element.

In particular, the post-ultimate equilibrium path could be traced well and the amplitude modulation in the local mode could be captured. The numerical results also revealed that columns exhibiting mode interaction are sensitive to geometric imperfections. Compared with previous approximate methods (Bijlaard & Fisher, 1952; Bijlaard & Fisher, 1953; Dewolf *et al.*, 1974; Djubek *et al.*, 1983) in considering the reduced stiffness owing to local buckling, this method is more accurate. However, it should be stressed that the wavelength

of the local mode in the local–global interactive post-buckling range in fact varies along the strut length and with the interaction progression, which was not considered by the method due to technical complexity.

Møllmann and Goltermann (Møllmann & Goltermann, 1989; Goltermann & Møllmann, 1989) also used the finite strip method in conjunction with Koiter’s theory to investigate the interactive buckling behaviour of an I-section beam under pure bending and a box-section column under pure compression. Substantial reductions (up to 50%) in the load-carrying capacity were observed in both examples due to the mode interaction. Guo and Chen (1991) extended the method by including plasticity. The method was validated by their experiments on channel columns under compression.

Hancock *et al.* (1990) reviewed the application of FSM in buckling and nonlinear analysis of thin-walled structural members. Compared with the FEM, the FSM is more computationally efficient. However, in order to make the computation process simplified, some assumptions or simplifications have to be made, which have been shown to have significant effects on the post-buckling behaviour prediction. With the popularity of powerful commercial FE packages, the principal role of FSM in the nonlinear buckling analysis was replaced by the FEM. More recently, fewer papers have been forthcoming with FSM used for nonlinear analysis; it has become more popular as a linear buckling analysis tool (Schafer *et al.*, 2010) to facilitate design using the so-called the Direct Strength Method (Schafer & Peköz, 1998b).

2.3 Imperfection sensitivity

Previous studies (van der Neut, 1969; Thompson & Hunt, 1973; Svensson & Croll, 1975; Gioncu, 1994b) have shown that structures susceptible to mode interaction can be extremely sensitive to imperfections, *i.e.* a tiny imperfection in the initial geometry may lead

to a significant erosion in the load-carrying capacity. In view of the design philosophy, Chilver (1976) classified the imperfection sensitivity of structures into three categories, as shown in Figure 2.9. In his opinion, the imperfection sensitivity should be avoided but

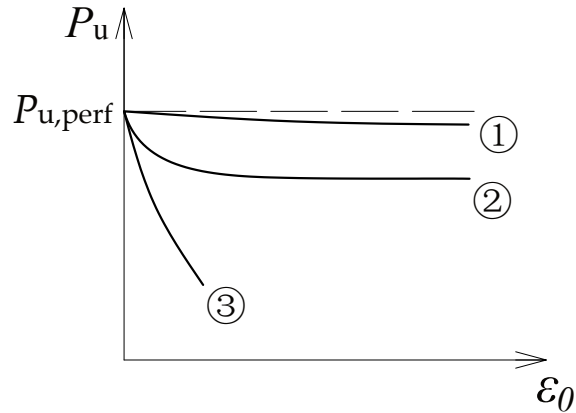


Figure 2.9: Three types of structural imperfection sensitivity classified by Chilver (1976) from the view of design philosophy. Quantities P_u , $P_{u,\text{perf}}$, ε_0 represent the ultimate load, the ultimate load of perfect structures and the generalized imperfection size respectively. Type 1 represents the structures exhibiting mildly imperfection sensitivity; Type 2 represents structures exhibiting initial sensitivity to micro imperfections but are mildly sensitive to imperfections over a wide range of practical imperfection size; Type 3 represents structures showing strong sensitivity to imperfections.

relatively mild sensitivity can be accommodated. In particular, those structures that are initially sensitive to micro-imperfections but showing mild sensitivity over a wide range of practical imperfections, *i.e.* there is a ‘plateau’ of the ultimate load in the P_u - ε_0 relationship in the practical imperfection range (see curve 2 in Figure 2.9), can also be useful in structures. The main issue for such cases is to determine the load-carrying capacity erosion due to imperfections.

In this section, imperfection measurement methods in test and modelling techniques are reviewed. After that, the imperfection tolerance level and modelling suggestions within the current Eurocode are presented. Finally, imperfection sensitivity studies on thin-walled members susceptible to interactive buckling are presented.

2.3.1 Geometric imperfections measurement and modelling

Geometric imperfections of thin-walled section members are affected by a series of factors, such as variations in material properties and geometry, the manufacturing method and fabrication techniques. Moreover, additional geometric imperfections may arise due to transportation, storage and erection, which are almost always localized, such as dents (Cruise & Gardner, 2006). The existing literature (Schafer & Peköz, 1998a; Wadee, 2000; Zeinoddini & Schafer, 2012; Wadee & Farsi, 2015; Bai & Wadee, 2015a; Liu & Wadee, 2016b; Zagari *et al.*, 2016) has identified that both magnitude and distribution of geometric imperfections affect the load carrying capacity of the structural members. Hence, a great deal of effort has been made on geometric imperfection measurement and developing a consistent and unified method to determine the geometric imperfection distribution and the magnitudes that reflect actual cases in practice.

Schafer and Peköz (1998a) measured the local imperfection distribution along the length for eleven nominally identical cold-formed specimens using a milling machine with a direct current differential transformer (DCDT) and proposed the concept of the imperfection spectrum to describe the measured results. Based on the test results, they also explained the use of the imperfection spectrum for modal and generalized imperfections. The methodology was widely used by later researchers working on imperfection measurement and modelling (Cruise & Gardner, 2006; Theofanous & Gardner, 2009; Schafer *et al.*, 2010; Zeinoddini & Schafer, 2012; Trouncer & Rasmussen, 2015).

Recently, Zhao *et al.* (2015) developed a novel imperfection measurement platform, which can measure the full three-dimensional (3D) imperfect geometry of a cold-formed steel member with good accuracy using a laser sensor mounted on transitional and rotary stages. The data processing system can transform the raw data into a complete 3D numerical model (point cloud), which provides the basis for further analysis on imperfections or numerical simulations, such as FE analysis.

As for the magnitude of local imperfections in cold-formed sections, Schafer and Peköz (1998a) proposed rules of thumb for two types of imperfections for cold-formed sections based on the collected test data, as shown in Figure 2.10. For internal elements, two ap-

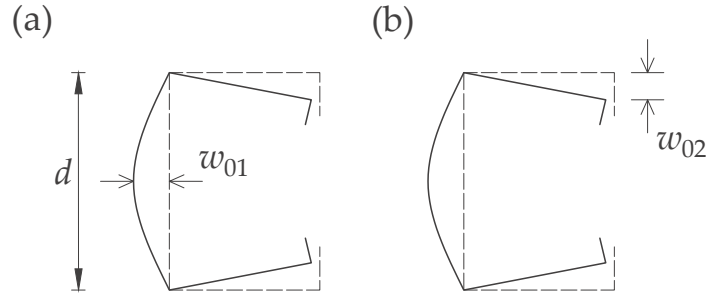


Figure 2.10: Definition of local geometric imperfections (Schafer & Peköz, 1998a).

proximate expressions based on linear regression and exponential curve fitting respectively were given:

$$w_{01} \approx 0.006d, \quad (2.14)$$

$$w_{01} \approx 6te^{-2t}, \quad (2.15)$$

where d and t are the width and thickness of the plate respectively. The unit in the equation should be millimetres. For outstand elements, the magnitude of the imperfections can be predicted by:

$$w_{02} \approx t. \quad (2.16)$$

It should be stressed that the above rules of thumb are only valid for a plate width–thickness ratio (d/t) less than 200 for internal members and less than 100 for outstand members; thicknesses should also be less than 3 mm.

Since large variations exist in the magnitude of local imperfections and the rules of thumb do not provide a complete characterization of imperfection magnitude, Schafer and Peköz (1998a) also suggested a probabilistic treatment, which ignores any trend in the data attributed to plate width or thickness. The numerically estimated cumulative distribution function (CDF) values and the summary statistics are given in Table 2.2. A CDF value is

Table 2.2: Numerically estimated cumulative distribution function (CDF) values for maximum magnitude of local imperfections (Schafer & Peköz, 1998a). Note that $\mathbf{P}(w_0 < w_{0i})$ represents probability that a randomly selected local imperfection maximum magnitude, w_0 , is less than a discrete deterministic one, w_{0i} .

$\mathbf{P}(w_0 < w_{0i})$	Type 1	Type 2
	w_{01}/t	w_{02}/t
0.25	0.14	0.25
0.50	0.34	0.50
0.75	0.66	0.75
0.95	1.35	0.95
0.99	3.87	0.99
Mean	0.50	1.29
St. dev.	0.66	1.07

written as $\mathbf{P}(w_0 < w_{0i})$ and indicates that the probability that a randomly selected local imperfection maximum magnitude, w_0 , is less than a discrete deterministic value, w_{0i} . For instance, $\mathbf{P}(w_0 < w_{0i}) = 0.75$ corresponds to $w_{01}/t = 0.66$ for internal elements and $w_{02}/t = 1.55$ for outstand elements. The maximum magnitude of the local imperfection for a typical member, w_0 , is expected to less than these values 75% of the time.

As for the magnitude of local imperfections in welded sections, a summary of the measured data in existing literature (Pavlovčič *et al.*, 2012; Shi *et al.*, 2014; Schillo, 2017; Yang *et al.*, 2017) is presented in Figure 2.11. It reveals that $\mathbf{P}(A_0/d < 1/200)=0.8$ and $\mathbf{P}(A_0/d < 1/125)=0.91$, the latter of which corresponds to the functional manufacturing tolerances for welded box sections (EN, 2008). As for the local imperfection normalized with respect to plate thickness, it reveals that the imperfection amplitude is generally smaller than that for cold-formed sections presented in Table 2.2, *i.e.* $\mathbf{P}(A_0/t < 0.3)=0.83$ and $\mathbf{P}(A_0/t < 0.5)=0.96$. This may be attributed to the fact that the plate slenderness in welded sections is relatively higher than that for cold-formed sections.

Mateus and Witz (2001) proposed an equation to determine the initial imperfection amplitude based on the regression analysis of data gathered from surveys of ship and welded box girder bridge plates:

$$\frac{w_0}{t} = \frac{\rho d^2 f_y}{t^2 E}, \quad (2.17)$$

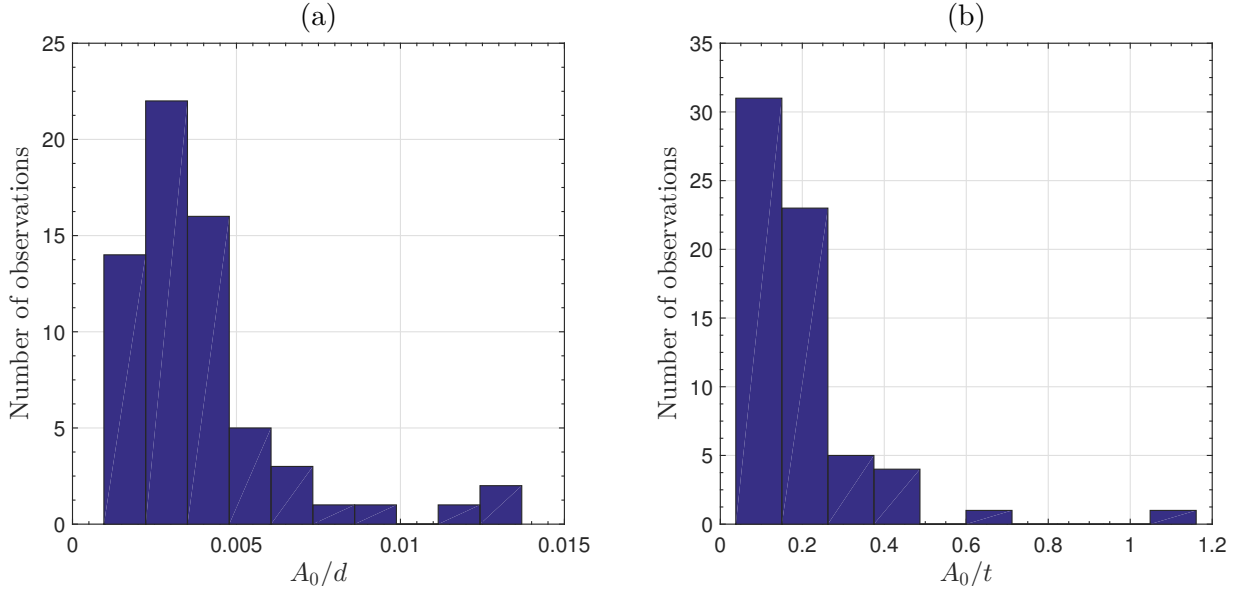


Figure 2.11: Histograms of local imperfection amplitude normalized with respect to (a) plate width and (b) plate thickness in welded box-section columns in the existing literature.

where d and t are plate width and thickness respectively; f_y and E are material yielding stress and Young's modulus respectively; ρ is the fitted factor. It was suggested that $\rho = 0.1$ would be most adequate; $\rho = 0.3$ and 0.025 would give the related upper and lower bound of the imperfection amplitude. Figure 2.12 shows the histogram of ρ determined based on the measured local imperfection amplitude in welded box section column in the existing literature. It reveals that Eq. (2.17) could provide a relatively reasonable prediction of the local imperfection amplitude in welded box-section struts.

Compared with the magnitude, there seems to be no real consensus on a consistent or unified method for the distribution of local geometric imperfections. A great deal of effort has been made in analysing the measurement data using the signal-spectrum analysis method (Schafer & Peköz, 1998a; Cruise & Gardner, 2006; Truncer & Rasmussen, 2015) and developing methodologies such that the artificially generated local imperfections can reflect those in physical reality (Zeinoddini & Schafer, 2012). However, since local imperfections are essentially stochastic parameters, a large number of analyses are necessary to obtain statistically significant results in terms of the ultimate load (Sarawit *et al.*, 2003).

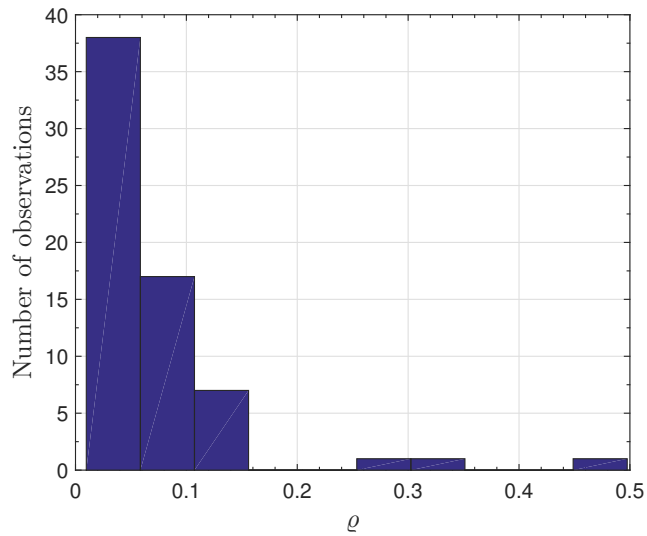


Figure 2.12: Histogram of the local imperfection factor ρ in Eq. (2.17) determined based on the results in the existing literature.

Therefore, for convenience, the majority of the previous studies adopted the profile of the lowest local buckling mode as the distribution profile of local imperfections (van der Neut, 1969; Degée *et al.*, 2008; Yang *et al.*, 2017). The details of related work on the imperfection distribution modelling and the effects on the ultimate load prediction will be introduced later in the current chapter.

2.3.2 Residual stresses measurement and modelling

Residual stresses are internal stresses existing in structural sections in the externally unloaded state (Cruise & Gardner, 2008), which are primarily established during the uneven cooling of a welded or hot-rolled steel member or during non-uniform plastic deformation due to cold-work (Trahair *et al.*, 2007). They must be distributed through the section such that all equilibrium conditions are satisfied. The magnitude and distribution of residual stresses in sections are closely related with the corresponding manufacturing process (Tebedge & Tall, 1973; Abambres & Quach, 2016). Generally, the existence of residual stresses in structural members will cause premature yielding, thus leading to stiffness loss

and erosion in the load-carrying capacity.

The current study focuses on residual stresses in welded cross-sections. However, it should be noted that systematic experimental and theoretical studies on residual stresses in cold-formed sections have been conducted, *i.e.* development of measuring techniques (Weng & Peköz, 1990), test results (Schafer, 1997; Schafer & Peköz, 1998a), mechanism of residual stress formation with its numerical and analytical simulation (Quach *et al.*, 2004; Moen *et al.*, 2008; Quach *et al.*, 2010; Pastor *et al.*, 2013), and modelling methodologies in computational models (Schafer & Peköz, 1998a; Schafer *et al.*, 2010). Compared with welded sections and cold-formed sections, work on residual stress distributions and magnitude in hot-rolled sections is relatively more mature and related studies can be found (Lay & Ward, 1969; Tebedge & Tall, 1973; ECCS. TC 8, 1976). Moreover, owing to post-manufacturing treatment, residual stresses in hot-rolled sections are relatively small in comparison with cold-formed and welded sections.

As for the measurement of residual stresses in welded sections, it is mainly conducted using the sectioning method (Abambres & Quach, 2016). This technique is based on the measurement of residual strains that are released when test sections are cut into small coupon strips (Tebedge *et al.*, 1973). The residual stresses can then be obtained by multiplying the change in the longitudinal strains in each strip coupon surface with the Young modulus. It should be noted that there are also some non-destructive methods to measure residual stresses, such as X-ray diffraction, ultrasonic and magnetic methods, but they are very expensive and not often practical (Yuan *et al.*, 2014).

As for residual stresses in welded sections, it has been observed that only the axial membrane component is of significance (ECCS. TC 8, 1976). The membrane stress magnitude depends on the plate cutting method and welding techniques. The distribution for normal strength steel (NSS) has been investigated extensively and there are some widely-accepted models (ECCS. TC 8, 1976; Abambres & Quach, 2016). The ECCS model for four typical cases is shown in Figure 2.13. The tensile stresses at the corners are assumed to be

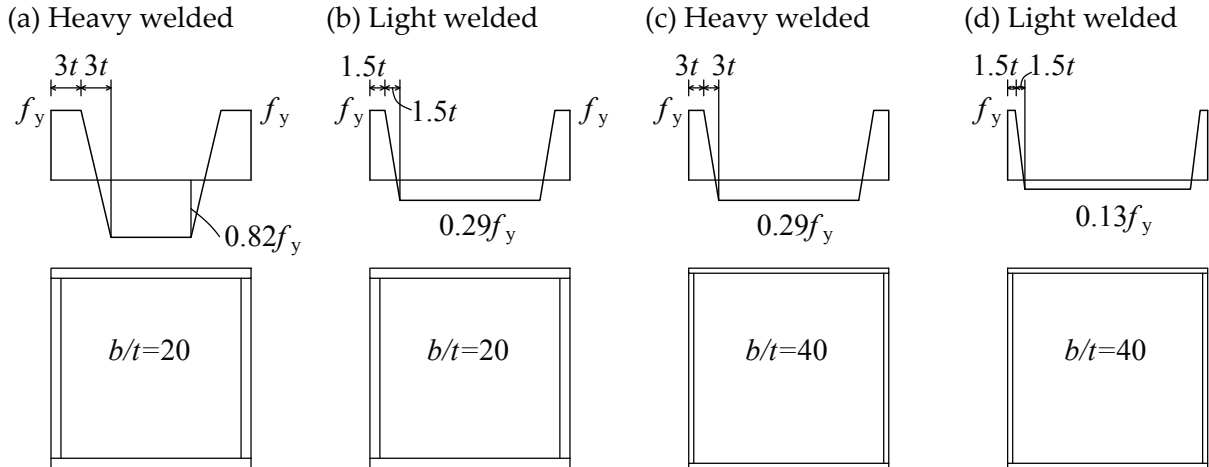


Figure 2.13: Residual stress distribution model for welded box sections (ECCS. TC 8, 1976), where f_y is the yielding stress, t is the plate thickness and b is the plate width.

constant with the value equal to the material yielding stress. The length of the tensile range is related to the welding method. The compressive residual stresses are assumed to be uniformly distributed in the central part of the section, with the value determined from the self-equilibrating conditions. With the increase of the plate width–thickness ratio, the ratio of compressive residual stress to yielding stress decreases. In the current study, the ECCS model is adopted for modelling the residual stresses.

Recently, as the use of high strength steel (HSS) has increased, numerous studies have been conducted on residual stress distributions on welded HSS box-section members. Ban *et al.* (2013) investigated the residual stress distribution in HSS welded box sections with a yield stress of 460 MPa via experimental studies on 6 welded square box sections with various width–thickness ratios and plate thickness. It was found that the residual stress distribution profile over the sections is very similar to that of NSS sections, which can also be described using piecewise functions. Moreover, the compressive residual stress was significantly correlated with the sectional dimensions, unlike the tensile stress. As for the compressive residual stress in the central portion, it decreased with the increase of the width-to-thickness ratio. Moreover, no residual stress interaction among four component plates was identified, *i.e.* the compressive and tensile residual stresses were self-equilibrating

for each plate independently. Based on the test results, a prediction model and its simplified form were proposed to describe the residual stress distribution. However, as noted by the authors, the model is only valid for sections with the same steel grade and manufactured using the same method, in this case from butt welds.

Somodi and Kövedi (2018) measured the residual stresses of welded box-section specimens with a variety of different steel grades (S235 to S960) and plate width–thickness ratios (14 to 60.5) using the sectioning method. A residual stress distribution model was proposed based on the test results and some results in the existing literature, which were applicable for various steel grades between S235 and S960. However, as noted by the authors, since the residual stress distribution is closely related to the manufacturing method, the proposed model is only valid for the sections manufactured by the MAG (Metal Active Gas) welding process.

2.3.3 Imperfection tolerance and modelling recommendations in Eurocode 3 (EC3)

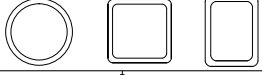
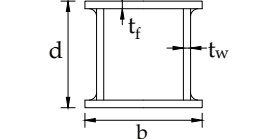
In Eurocode 3 (EN-1993-1-5:2006E, 2006), it is recommended that both geometric and structural imperfections should be included in the FE model where imperfections are considered. However, equivalent geometric imperfections may be used when a more refined analysis, which includes both geometric and structural imperfections, is unavailable. The recommended equivalent initial global imperfection (local bow imperfection) amplitude e_0 of hollow section members for nonlinear analysis depends on the many factors, *i.e.* material properties, manufacturing method and analysis type, as shown in Tables 2.3 and 2.4.

As for the local equivalent geometric imperfections, the magnitude is the minimum of $a/200$ and $b/200$, where a and b is the shorter span of the panel or subpanel, as shown in Figure 2.14(b). The imperfection shape for global and local imperfections are the corresponding linear buckling modes.

Table 2.3: Design values of global imperfections recommended by Eurocode 3 Part 1.1 (EN-1993-1-1:2006E, 2006).

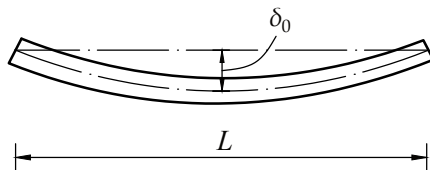
Buckling curve	elastic analysis	plastic analysis
	δ_0/L	δ_0/L
a ₀	1/350	1/300
a	1/300	1/250
b	1/250	1/200
c	1/200	1/150
d	1/150	1/100

Table 2.4: Buckling curve types for hollow section columns in Eurocode 3 Part 1.1 (EN-1993-1-1:2006E, 2006).

Cross-section type	manufacturing method	buckling about axis	Buckling curve	
			S235, S275, S355, S420	S460
hollow sections				
	hot finished	any	a	a ₀
	cold-formed	any	c	c
	general welds (except below)	any	b	b
	thick welds: $a > 0.5t_f$			
	$d/t_w < 30$	any	c	c
	$b/t_f < 30$			

Moreover, the sign of the applied imperfection should be such that it leads to the lowest resistance. In combining imperfections, a dominant imperfection shape should be chosen and the accompanying imperfections may have their values reduced to 70%.

(a) Global imperfection



(b) Local imperfection

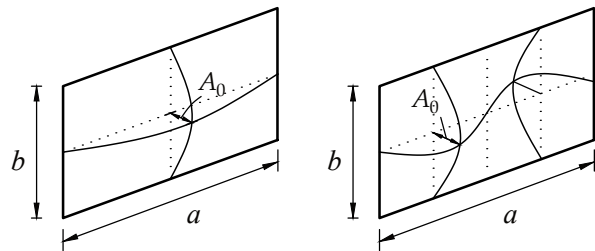


Figure 2.14: Equivalent global and local imperfection modelling recommended by Eurocode 3 Part 1.5 (EN-1993-1-5:2006E, 2006).

As for modelling residual stresses explicitly, it is recommended that the imperfection shape should be based on the critical buckling modes and the amplitudes are 80% of the geometric

fabrication tolerance. The residual stresses may be represented by a pattern from the fabrication process with the amplitude equal to the mean values.

However, according to previous studies (Johansson *et al.*, 2007; Degée *et al.*, 2008), adopting tolerance level imperfections as the imperfection introduced in the model would lead to an overly conservative prediction of the ultimate load. Therefore, it may not be a reasonable choice in the context of a probabilistic analysis. Moreover, the measured local imperfection amplitude from the specimens also revealed that the actual local geometric imperfection amplitude is generally much smaller than the tolerance level (Degée *et al.*, 2008; Pavlovčič *et al.*, 2012; Yang *et al.*, 2017; Schillo, 2017). Numerical results (Johansson *et al.*, 2007) also showed that the ultimate load of a plate with a tolerance geometric imperfection level and the compressive residual stress being $0.2f_y$ under pure compression is more than 15% lower than calculated from the well known Winter formula (Winter, 1947). In order to make them consistent, a reduced imperfection combination should be adopted.

2.3.4 Imperfection sensitivity studies

Based on the idealized ‘two-flange’ model, Van der Neut (1969; 1973) investigated the imperfection sensitivity and post-buckling behaviour of such an idealized column with local and global imperfections using the theory developed by Koiter (1945). For the local imperfection function, Van der Neut assumed that the ‘worst’ imperfection corresponds to the mode pertaining to the smallest buckling load. The stiffness reduction factor η for the column with the local imperfection was determined by using a Ritz–Galerkin approximate solution of the nonlinear plate equation. Unlike the perfect case, η is a nonlinear function and would vary with the local imperfection amplitude A_0 and the axial load P . The governing differential equation was established with direct equilibrium as it was for the perfect case. From the numerical results with different values of A_0 , it was found that the instability phenomenon would vanish with the increase of the imperfection amplitude.

Moreover, it was found that struts are sensitive to both global and local imperfections. In particular, the global imperfection was found to be more significant in the range where local buckling is critical. However, the validity of the results was restricted to small global imperfections of amplitudes less than 2% of the web depth due to the approximation from the Taylor series expansion of the load, $P(\varepsilon)$.

Based on Van der Neut's idealized column with local imperfections, Thompson and his collaborators (Thompson & Lewis, 1972; Thompson & Hunt, 1974) investigated an efficiency chart of such an idealized column, which shows the relationship of the ultimate load for thin-walled struts versus the ratio of the global and local buckling loads under a constant weight constraint for optimum design purposes, as shown in Figure 2.15. It

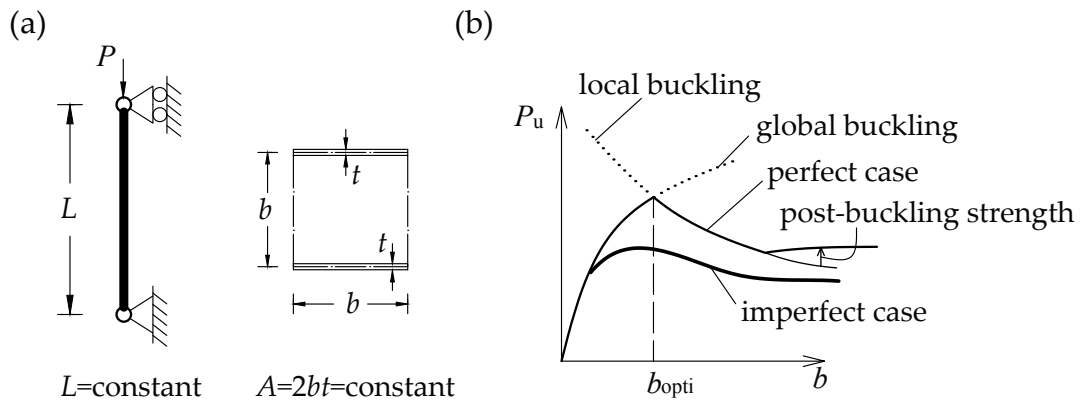


Figure 2.15: Optimum design and efficiency chart of a square Van der Neut ideal two-flange strut with fixed length L and fixed cross-section area A .

was found that the optimum point shifted to one side of the ideal optimum point, *i.e.* to where $P_o^C/P_1^C|_{\text{opt}} < 1$. More importantly, it was demonstrated that reaching the so-called ‘naive optimum’ load, where the local buckling load is equal to the global buckling load, was practically unachievable for such components with realistically sized initial imperfections. Moreover, using the asymptotic approach, they determined the local imperfection sensitivity law in each zones and found that the imperfection sensitivity is fundamentally more severe for the case where local buckling is critical than it is for case where the global buckling is critical. This discovery was contrary to the received wisdom at the time where

local buckling is permissible due to its stable post-buckling behaviour, but this is due to the consideration of mode interaction.

Since the Van der Neut model did not include the contribution of both webs, Maquoi and Massonnet (1976) investigated the efficiency chart for thin-walled square hollow section columns with various different sizes of geometric imperfections using the software developed by Klöppel and Schubert (1971). A significant erosion in the load-carrying capacity near the naive optimum point was also observed. Moreover, it was also found that the profile of the efficiency chart curve was affected by the imperfection size. When the imperfection size is tiny, the maximum efficiency is located to one side of the naive optimum point ($P_o^C/P_1^C = 1$), where $P_o^C/P_1^C < 1$; with increasing imperfection size, it moves to the other side and is finally located at some point where $P_o^C/P_1^C > 1$. However, they found that the respective curves were very flat in the vicinity where the local and global buckling loads are equal. Therefore, it was concluded that the optimum scheme based on the equal local and global buckling loads was still valid, even though the design load should be reduced based on the imperfection sensitivity study results. It should also be noted that the effects of material nonlinearity were investigated in their work. This affected the profile of the efficient curve significantly, *i.e.* the capacity erosion was even larger and the efficiency curve was essentially flat when the local buckling stress was close to the yielding stress.

Using the finite strip method with mode interaction theory, Sridharan (1983) found that in the case of narrow stiffened plates supported along the longitudinal edges, no catastrophic failure was observed where interactive buckling occurred for stiffened plates with initial imperfections. It was also pointed out that previous research (Tvergaard, 1973) ignored some key terms in the energy function that would affect the imperfection sensitivity results. Moreover, it was highlighted that the severity of the imperfection sensitivity depended on the structural profiles; cross-sections with unstiffened plate elements were more sensitive than those with stiffened (mutually interconnected) elements.

Kiyamaz (2005) investigated the effects of column out-of-straightness, plate imperfections,

residual stresses and material plasticity on the ultimate load and post-buckling behaviour of square hollow section columns exhibiting mode interaction using the FE package ABAQUS. Three example columns with typical slendernesses were analysed, where (i) global buckling was clearly critical, (ii) global and local buckling were triggered simultaneously, and (iii) local buckling was clearly critical. The severe erosion in the load-carrying capacity due to imperfections in the case where the local and global buckling loads were the same was again observed.

Degée *et al.* (2008) investigated the effects of various imperfections, *i.e.* residual stresses, local and global geometric imperfections, on the load-carrying capacity of slender welded RHS columns exhibiting mode interaction through experimental and numerical methods. Since the residual stress is relatively complex to model, they proposed an equivalent geometric imperfection modelling method by amplifying the local and global geometric imperfections based on the parametric study results. They found that a model with a local imperfection of $1/250$ of the cross-section width and a global imperfection of $1/725$ of the column length showed good agreement with a model including residual stresses.

Based on a validated FE model from experimental results of two heavily welded box-section struts, Pavlovčič *et al.* (2012) studied the effects of different measured imperfections (local imperfection, global imperfection and residual stresses) and their combinations on the ultimate load. It revealed that the residual stresses appeared to have the most significant effect on the capacity erosion among all three imperfections, which reduces the column capacity up to 37%. It was also found that the equivalent geometric imperfection modelling suggestion given by Degée *et al.* (2008), *i.e.* global imperfection $L/725$ plus local imperfection $d/200$ (L and d are the strut length and web depth respectively), may underestimate the effects of actual imperfections on the heavily welded box-section struts. Moreover, it was reported that the imperfection combination with pure geometric imperfections and residual stresses, *i.e.* global imperfection $L/1000$ plus local imperfection $d/1000$ plus residual stresses, provided a safe, yet accurate, prediction of the ultimate load. However, the

parametric study only focused on the two specimens. A more extensive parametric study would have been required to draw general conclusions.

Since the Van der Neut's idealized 'two-flange' model is only limited to the purely elastic case, Becque (2014) introduced material nonlinearity into the classical model and studied its effects on the imperfection sensitivity and ultimate load. The Von Mises yield criterion was adopted with an associated flow rule and isotropic hardening to model the material plasticity. The governing equations, derived based on equilibrium conditions, were written in an incremental form. Moreover, compared with elastic plate theory, the stress resultants were used instead of the stresses at mid-span because the stress distribution is no longer linear in the inelastic range. The finite difference method was adopted to solve the governing equations. The theoretical model was verified using the FE package ABAQUS and showed good comparisons. With the verified theoretical model, the effects of material strain hardening and yielding stress level on the profile of the Van der Neut-type curve and the strut imperfection sensitivity were investigated. As for the nonlinear material model, the Ramberg–Osgood model was adopted. Two values of the Ramberg–Osgood parameter n were considered, *i.e.* $n = 7$ and $n = 50$ corresponding to a strain-hardening material similar to stainless steel and an approximately two-stage piecewise linear stress-strain relationship. It was found that when the proof stress was significantly higher than the local buckling stress of the cross-section ($\sigma_{0.2} > 2\sigma_{cr}$), plasticity curtailed the Van der Neut curve for short length struts (Zone 4) into a plateau with low to moderate imperfection sensitivity; when the proof stress was the same order as the local buckling stress ($\sigma_{0.2} < 1.5\sigma_{cr}$), the plateau in zone 4 would extend and merge with that for transitional length struts (zone 2) and struts would exhibit high imperfection sensitivity. Indeed, the length of the extended plateau depended on the amount of strain hardening. At the same value of $\sigma_{0.2}/\sigma_{cr}$, the width of plateau for $n = 50$ is much larger than that for $n = 7$.

Based on the developed variational model, Wadee and his collaborators investigated the imperfection sensitivity analysis of I-section columns (Bai & Wadee, 2015a; Liu & Wadee,

(2016b) and stiffened plates (Wadee & Farsi, 2015) under compression. The effects of local imperfections, global imperfections and their combination on the ultimate load and post-buckling behaviour were investigated. It was found that the compression members susceptible to local–global mode interaction are very sensitive to imperfections. Moreover, with the increase of imperfection size, the severity of unstable post-buckling behaviour is mollified to some degree, but cellular buckling phenomena could still be observed (Wadee & Farsi, 2015; Bai & Wadee, 2015a).

Effect of imperfection profile

Owing to its relative simplicity and the lack of efficient and advanced computational tools, early researchers mainly adopted a local imperfection profile that was affine to the lowest local buckling eigenmode to investigate the imperfection sensitivity of thin-walled compression members susceptible to mode interaction (van der Neut, 1969; Koiter & Pignataro, 1976a; Koiter & Pignataro, 1976b). These works identified serious erosion in the load-carrying capacity for the cases where the local and global buckling loads are in close proximity. Moreover, these provided the ultimate load prediction with good accuracy for the cases studied. Therefore, it is still one of the most widely used methodologies (Schafer *et al.*, 2010).

In spite of its convenience, local imperfections modelled with this approach may not reflect the actual imperfection profiles in physical reality. Equally importantly, they may not represent the most severe local imperfection profile (Wadee, 2000; Schafer *et al.*, 2010). With the advance of computational tools and physical testing techniques, numerous investigations on the effects of local imperfection profiles on the ultimate load and post-buckling behaviour have been conducted. Rasmussen and Hancock (1988) proposed an analytical technique to expand the range of measured geometric imperfections in the longitudinal and cross-sectional dimensions based on the buckling modes. In particular, the secondary local buckling components triggered by the interaction of global and local buckling modes were

also considered, *i.e.* the modulated longitudinal profile and the mono-symmetric cross-section profile.

Dubina and Ungureanu (2002) studied the effects of cross-section imperfection profiles on the load erosion of channel section columns susceptible to mode interaction using the FE method. They found that the ultimate loads for example struts with symmetrical and asymmetrical cross-section imperfection profiles, which are affine to the lowest and higher local buckling modes, were 12% lower and 15% higher than the test results respectively. They also emphasized that using the sinusoidal shape from linear buckling analysis may not represent the most appropriate imperfection mode introduced in nonlinear analysis.

Zeinoddini and Schafer (2012) introduced three methods to simulate the geometric imperfections in cold-formed steel members and compared their effects for predicting the peak load and final failure mode using geometric and materially nonlinear FE models. All three methods were based on the imperfection spectra (Schafer & Peköz, 1998a), which is built on a large number of imperfection measurement tests. It was found that the ‘1D Modal Spectra Method’, which adopted the cross-section imperfection component from linear buckling analysis and the longitudinal component from spectral analysis, provided the most accurate prediction for the ultimate load and the final failure mode.

Trouncer and Rasmussen (2015) conducted a spectral analysis of the ultimate load as a function of imperfection spectra for 20 storage rack columns susceptible to mode interaction. From a large number of FE simulations, they found that local imperfections in the shape of higher order modes with half-wavelengths in close proximity to the half-wavelength of the critical buckling mode have little effect on the ultimate load; this also applies if the local imperfections were introduced to the cross-section non-symmetrically, which would naturally break the symmetry and hence trigger mode interaction.

Zagari *et al.* (2016) investigated the imperfection sensitivity of thin-walled perforated rack members in compression using an FE implementation of the Koiter method in conjunction

with a Monte Carlo simulation. The most severe combination of imperfections and the erosion of the ultimate load due to imperfections were identified. From the probability distribution of the ultimate load for specimens exhibiting mode interaction, it was found that the deviation is very small, which implies that the imperfection profile has very minor effects on the ultimate load for such cases. However, even though a great number of imperfection combinations were adopted in the study, only the geometric imperfections in the space of the linear buckling modes were considered.

Wadee and his collaborators investigated the most severe imperfection profile of thin-walled I-section struts (Bai & Wadee, 2015a; Liu & Wadee, 2016b) and stiffened panels (Wadee & Farsi, 2015) exhibiting mode interaction using an analytical approach. By introducing a local imperfection function that matches the least stable localized post-buckling mode for the strut on a softening foundation – derived from a first order approximation of a multiple scale perturbation analysis (Wadee *et al.*, 1997), the most severe local imperfection profiles have been determined in terms of the wavelength of the oscillating component and the degree of localization. Unlike preceding work that compared different imperfection profiles with the same amplitude, a unified and consistent approach was implemented adopting the concept of initial end-shortening of the extreme fibre of flange plate \mathcal{E}_0 . This was initially proposed by Wadee (2000) for identifying the most severe local imperfection profile in sandwich panels under compression that are susceptible to local–global mode interaction. Based on the unified and consistent imperfection measurement approach, these works determined that the most severe local imperfection profiles correspond to a localized profile with a smaller wavelength of the oscillating component than that for the local buckling eigenmodes. It was also found that the most severe imperfection profile is related to imperfection size, *i.e.* the wavelength of the longitudinal component of local imperfection decreases with the increasing imperfection size.

2.4 Experimental studies

Experimental studies are essential to validate the effectiveness of the existing theoretical or numerical models and to provide suggestions for more reasonable or accurate models that reflect the actual underlying physical mechanisms. In this section, experimental studies on the interactive buckling of box-section columns are reviewed. Since the existing experimental studies on box-section columns principally focus on the ultimate load-carrying capacity, very limited information about the mode interaction mechanism is generally provided. Some experimental studies on members with other cross-sections under pure compression or pure bending, which provide more information on local–global mode interaction and facilitate a better understanding of the underlying mechanism, are introduced.

Usami and Fukumoto (1982) tested 24 welded box struts made from high strength steel (nominal yielding stress $f_y = 690 \text{ N/mm}^2$) and with various slenderness ratios ($L/r=10, 35, 50$ and 65) and width–thickness ratios ($d/t = 22, 27, 33, 38, 44$). Both global geometric imperfection and residual stresses were measured before the test. From the test, it was observed that the triggering of local–global mode interaction did not lead to the ultimate state of specimens. Moreover, the tested specimens exhibited a large deformation capacity even after reaching the ultimate load, which implies that the failure mode was ductile.

Chiew *et al.* (1987) performed experimental studies on a series of 17 steel welded box-section struts with square and rectangular hollow sections with various column and plate slendernesses. Local–global mode interaction was observed in long columns with high plate slendernesses. The final failure mode was gradual in most cases, even though in some specimens, the failure occurred rapidly with almost no visible warning, which was followed by very rapid unloading.

Degée *et al.* (2008) presented the test results of six welded rectangular hollow section columns that failed by local–global mode interaction. The initial imperfections of the test columns were measured before the test and it was found that all of them were below the

tolerance level recommended by Eurocode 3. The ultimate loads of all the specimens were found to be higher than that predicted by the current Eurocode 3 provisions. Based on the test results, FE models were developed and calibrated. Since the current Eurocode 3 was shown to be relatively conservative, a proposal was made about the modification of the non-dimensional slenderness used in the global buckling calculation and the selection of the buckling curve a instead of b in the Eurocode 3.

Pavlovčič *et al.* (2010; 2012) conducted full-scale tests on four welded and cold-formed box-section columns subject to concentric compression. Material properties, local and global geometric imperfections and residual stress distributions were measured before loading tests. As for the test results, the ultimate loads of the four example struts were all higher than those predicted by the current Eurocode 3 provisions. In particular, the displacement in the mid-line of the more compressed flange was provided in two specific stages, *i.e.* the ultimate load and the ultimate displacement stages. It revealed that the amplitudes of the local and global mode were the same magnitude in both stages. The profile of the local mode was modulated before and at the ultimate load point and became highly localized due to the development of plasticity at some specific location.

Kwon and Seo (2013) conducted a series of compression tests on welded rectangular hollow section columns fabricated from 6.0 mm thick steel plates with a nominal yielding stress of 315 MPa and susceptible to local–global interactive buckling. A significant erosion in the load-carrying capacity due to imperfections was identified in the specimens. The local–global mode interaction was also observed in the tests, with the final failure mode being a localized kink in the plate due to plasticity. It was also found that localized imperfections may lead to a premature localized failure at the loaded end. Since most of the example struts clearly had local buckling being critical ($P_o^C/P_1^C > 1.5$), a significant post-buckling reserve was observed before the visible local–global mode interaction, which occurred before the ultimate load was reached. However, when the ultimate load was reached, it was always followed by a sharp drop in the load-carrying capacity. Moreover, the ultimate load of the

test columns was compared against the current design guidelines, such as the DSM based on the American Institute of Steel Construction (AISC) guidelines and the effective width method given in Eurocode 3, which showed that these guidelines can predict the ultimate load properly and safely.

Yang *et al.* (2017) tested 12 steel medium-length welded steel box-section columns. Before the tests, the geometric imperfections were measured and were revealed to be smaller than the recommended tolerance level in the current design guidelines. The failure mode of all specimens was observed in a form of local–global buckling, *i.e.* local buckling occurred initially and then the global mode was triggered. The test results were compared against Eurocode 3 and showed that the current guidelines slightly overestimate the ultimate load, with the average ratio of the design equation to the test results being 1.05. Moreover, FE models calibrated based on the experimental results were developed and parametric studies were conducted in a wider range of parameters, such as material strength, column slenderness, plate width to thickness ratio, geometric imperfection size and residual stress levels. The numerical results further confirmed the potentially unsafe prediction of the current guidelines. A design proposal on the buckling curve selection for designing box-section columns susceptible to local–global interactive buckling was presented. A summary of the slenderness range and the ultimate load of box-section columns in the literature are presented in Figures 2.16 and 2.17 respectively. A discussion about the comparison is presented in the following section specifically about design guidelines (§2.5).

Several experiments, more related with the mechanism investigation, were conducted on T-section beams under pure bending (Menken *et al.*, 1991), I-section columns under compression (Davids & Hancock, 1986; Becque & Rasmussen, 2009a) and I-section beams under uniform bending (Wadee & Gardner, 2012). In the experiments of the simply-supported T-section beams under pure bending (Menken *et al.*, 1991), the interactive buckling between the local flange buckling and the overall lateral–torsional buckling was observed. In particular, a wavelength change in the local mode was captured.

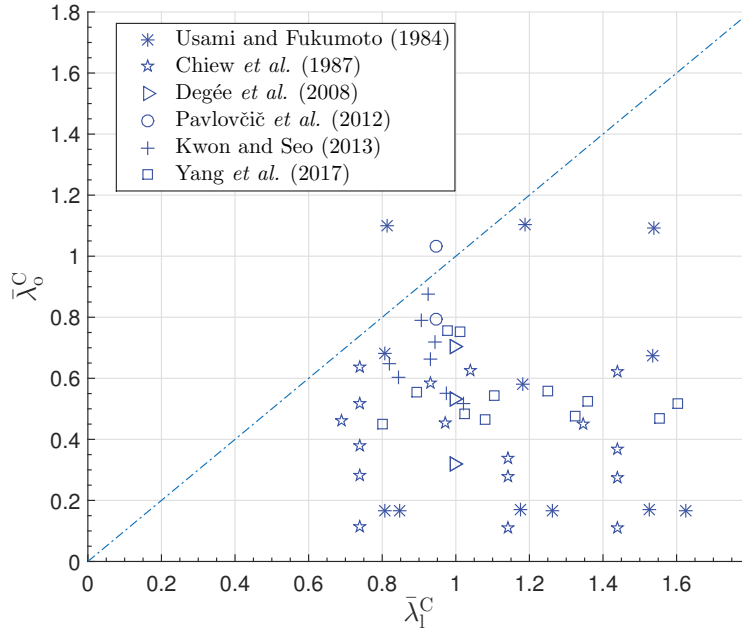


Figure 2.16: Summary of the normalized global slenderness $\bar{\lambda}_0^C = \sqrt{P_y/P_0^C}$ and local slenderness $\bar{\lambda}_1^C = \sqrt{P_y/P_1^C}$ of specimens in the existing literature, where P_y , P_0^C and P_1^C represent the squash load, the global buckling load and the local buckling load respectively.

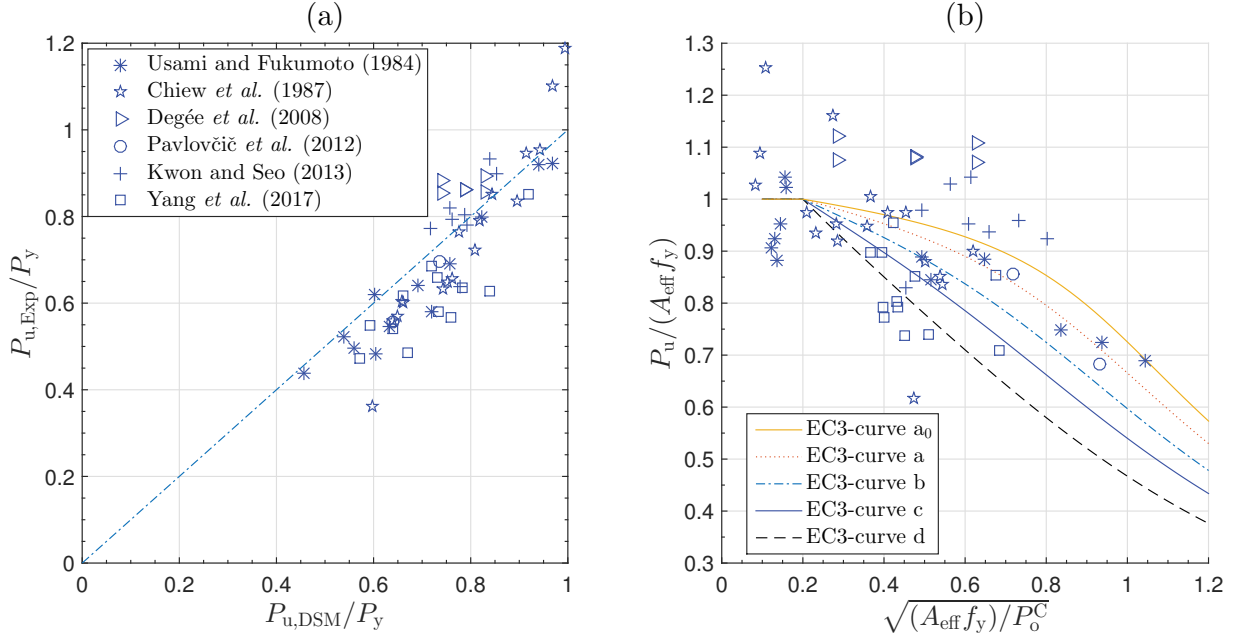


Figure 2.17: Summary of the ultimate load from experimental studies in the existing literature and comparison with the Direct Strength Method (DSM) (Schafer, 2008) and the Effective Width Method (EWM) (EN-1993-1-1:2006E, 2006). Note that the symbol legend in graph (b) is the same as that in (a).

Dauids and Hancock (1986) conducted an experimental study on interactive buckling of long I-section columns under compression, a local buckling mode with uniform wavelength and amplitude along the full length of the column was first observed with a decrease in axial stiffness. When global buckling was triggered, modulation in the maximum amplitude of the local buckling mode along the length was observed, accompanied by an increase in the number of local buckle halfwaves and a decrease in the wavelength. Moreover, the equilibrium path of the load–end-shortening relationship also showed a rapid unloading, indicating the unstable post-buckling behaviour.

Tests to investigate the interactive buckling behaviour of pin-ended thin-walled stainless steel I-columns under the concentric compressive load were conducted by Becque (2008). Compared with previous research, more details about the interactive buckling behaviour, *i.e.* the evolution of the local buckling mode, were presented (see Figure 2.18). Amplitude modulation in the local mode with the increase of the load was clearly observed in the tests.



Figure 2.18: Interactive buckling observed in a stainless steel I-section strut (Becque, 2008).

In the tests presented by Wadee and Gardner (2012) on I-section beams under uniform bending, a highly unstable response was observed once interactive buckling was triggered. In particular, cellular buckling was observed in some of the tests, *i.e.* a new local buckling peak appearing soon after the initial one. Amplitude modulation, with the peak at the mid-span and decaying to the lateral restraints, was also clearly observed, particularly for

the cases where lateral torsional buckling was critical. Some of the test results showed good comparisons for cases where global lateral buckling was critical with those from a variational model developed using analytical techniques.

2.5 Related design guidelines

Current design guidelines mainly focus on the load-carrying capacity erosion at the interaction point of material yielding and pure global buckling (Perry–Robertson formula) or pure local buckling (Winter formula) due to imperfections. The basic methodology to consider the effects of mode interaction is to replace the yielding stress or squash load with the limiting stress of a mode that may interact with the original buckling mode or to adopt reduced cross-section properties, with calibrated factors for the original design equations based on experimental or numerical results.

2.5.1 Eurocode 3 approach

In the current version of EC3 ([EN-1993-1-1:2006E, 2006](#); [EN-1993-1-5:2006E, 2006](#)), the effect of local buckling on the ultimate load is considered by using an effective cross-section instead of the gross cross-section properties. Both cross-section and member buckling resistance checks are required. The cross-section resistance under uniform compression is given thus:

$$N_{c,Rd} = A_{\text{eff}} f_y / \gamma_{M0}, \quad (2.18)$$

where γ_{M0} is a partial safety factor for cross-section resistance with a recommended value of 1.0; $A_{\text{eff}} = \sum A_{c,\text{eff}}$, which is the summation of all the effective areas of compression elements within the cross-section. The effective area of each individual plate $A_{c,\text{eff}}$ is given by:

$$A_{c,\text{eff}} = \rho A_c, \quad (2.19)$$

where A_c is the gross area of each individual plate, and for box-section members under pure compression the expression for the factor ρ is given by:

$$\rho = \frac{(\bar{\lambda}_{ps} - 0.22)}{\bar{\lambda}_{ps}^2} \leq 1, \quad (2.20)$$

with the normalized plate slenderness $\bar{\lambda}_{ps}$ defined as:

$$\bar{\lambda}_{ps} = \sqrt{\frac{f_y}{\sigma_{cr}}}, \quad (2.21)$$

where $\sigma_{cr} = k_p \pi^2 E / [12(1 - \nu^2)(b/t)^2]$ is the local buckling stress of a rectangular plate with width b , thickness t and the adopted value of the buckling coefficient k_p is 4, which is a safe assumption. It implies that the interaction between individual plates within the cross-section is neglected.

For member buckling design resistance, $N_{b,Rd}$, the expression is given thus:

$$N_{b,Rd} = \chi A_{eff} f_y / \gamma_{M1}, \quad (2.22)$$

where γ_{M1} is a partial safety factor for member buckling; χ is the buckling reduction factor and is given by the following expression from the Perry–Robertson model (Trahair *et al.*, 2007):

$$\chi = \begin{cases} 1 & \text{for } \bar{\lambda} \leq 0.2, \\ \left(\Phi + \sqrt{\Phi^2 - \bar{\lambda}^2} \right)^{-1} & \text{for } \bar{\lambda} > 0.2, \end{cases} \quad (2.23)$$

where

$$\Phi = 0.5 [1 + \alpha (\bar{\lambda} - 0.2) + \bar{\lambda}^2], \quad \bar{\lambda} = \sqrt{\frac{A_{eff} f_y}{N_{cr}}}, \quad (2.24)$$

with N_{cr} being the elastic buckling load for the relevant mode based on the gross cross-section and α being an imperfection factor that determines a distinct buckling curve; in EC3, there are five separate buckling strength curves, as presented in Table 2.5. The buckling curve is assigned on the basis of the cross-section type, material properties and

the axis of buckling. In particular, the column buckling curves for generally welded and

Table 2.5: Imperfection factors for the separate buckling curves for compression members made from steel (EN-1993-1-1:2006E, 2006) in EC3.

Buckling Curve	a ₀	a	b	c	d
Imperfection factor α	0.13	0.21	0.34	0.49	0.76

heavily welded steel sections are recommended as b and c respectively (EN-1993-1-1:2006E, 2006). The nominal ultimate load $N_{u,Rd}$ is thus given as the minimum of $N_{c,Rd}$ and $N_{b,Rd}$.

The comparison of experimental results in the existing literature with the effective width method can be seen in Figure 2.17(b). The scatter in the comparison is quite large. The range, mean and the coefficient of variation (COV) of $P_{u,Exp}/P_{u,EC3,b}$ are presented in Table 2.6. Generally, the test results from some researchers (Degée *et al.*, 2008; Pavlovčič *et al.*, 2012; Kwon & Seo, 2013) showed that the current EC3 formulae can provide a conservative prediction of the ultimate load but it can be overly conservative for some specimens. However, some test results from Yang *et al.* (2017) showed that the Eurocode 3 provisions may provide unconservative predictions under certain circumstances. The

Table 2.6: Comparison of the ultimate load from experimental studies in the existing literature with the Effective Width Method (EWM) with the column buckling curve being b (EN-1993-1-1:2006E, 2006) and the Direct Strength Method (DSM) (Schafer, 2008).

Tests	$P_{u,Exp}/P_{u,EC3,b}$			$P_{u,Exp}/P_{u,DSM}$		
	Range	Mean	COV	Range	Mean	COV
U. & F. (1984)	0.882→1.210	1.016	9.66%	0.799→1.029	0.921	7.69%
Chiew <i>et al.</i> (1987)	0.688→1.253	1.020	11.73%	0.604→1.195	0.937	13.87%
Degée <i>et al.</i> (2008)	1.110→1.347	1.222	7.26%	1.034→1.189	1.106	5.01%
Pavlovčič <i>et al.</i> (2012)	1.066→1.104	1.085	2.50%	0.868→0.943	0.906	5.87%
Kwon & Seo (2013)	0.917→1.206	1.164	10.05%	0.820→1.114	1.024	8.91%
Yang <i>et al.</i> (2017)	0.816→1.071	0.915	9.03%	0.722→0.954	0.844	9.72%

reason for the scatter of the data mainly comes from the welding method and the local imperfection size. Currently, the effective width in each plate is determined by Eq. (2.20), which is only related to the plate slenderness. However, the actual effective width is also related with the local imperfection size, which can vary considerably between different cases (Schillo, 2017). This may explain that the scatter for each set of experimental data

is relatively small. Therefore, in order to describe the load-carrying capacity of thin-walled welded box-section struts better, a calibration of the Winter curve, *i.e.* Eq. (2.20), should be conducted. Moreover, it should be noted that the abnormally low data point in Chiew *et al.* (1987) may be resulting from defects in the specimen, since the rest of the data all range from 0.95 to 1.20.

2.5.2 Direct Strength Method

The Direct Strength Method (DSM) was developed by Schafer and Peköz (Schafer & Peköz, 1998b) for considering the local, distortional and global buckling of cold-formed carbon steel sections (Schafer, 2006c; Schafer, 2006b; Schafer, 2008). It has been included in Appendix 1 of the AISI specification (AISI:S100-2007, 2007). Instead of determining the effective width for each individual plate and calculating the effective cross-section properties, only the critical buckling loads of the member with gross section properties are required for the DSM, which can be obtained very conveniently using available free software, such as CUFSM (Schafer, 2006a) based on the so-called constrained finite strip method or GBTUL (Bebiano *et al.*, 2008) based on Generalized Beam Theory.

The nominal axial strength, P_n , is the minimum of P_{ne} and P_{nl} as given below. The nominal axial strength, P_{ne} , for flexural, torsional or flexural–torsional buckling is:

$$\frac{P_{ne}}{P_y} = \begin{cases} 0.658\bar{\lambda}_o^2 & \text{for } \bar{\lambda}_o \leq 1.5, \\ 0.877/\bar{\lambda}_o^2 & \text{for } \bar{\lambda}_o > 1.5, \end{cases} \quad (2.25)$$

where the global slenderness $\bar{\lambda}_o = \sqrt{P_y/P_o^C}$, the squash load of the gross cross-section $P_y = A_g f_y$, P_o^C is the minimum of the critical elastic buckling loads in flexural, torsional, or flexural–torsional buckling and A_g is the gross cross-sectional area. As for local buckling,

the nominal axial strength, P_{nl} is given by:

$$\frac{P_{nl}}{P_{ne}} = \begin{cases} 1 & \text{for } \bar{\lambda}_l \leq 0.776, \\ \left[1 - 0.15 (P_1^C/P_{ne})^{0.4}\right] (P_1^C/P_{ne})^{0.4} & \text{for } \bar{\lambda}_l > 0.776, \end{cases} \quad (2.26)$$

where $\bar{\lambda}_l = \sqrt{P_{ne}/P_1^C}$ with P_1^C being the critical elastic local buckling load and P_{ne} being defined in Eq. (2.25).

Compared with the effective width method currently in EC3, the DSM is more simple and straightforward. The comparison of experimental results on welded box-section columns in the existing literature with the DSM prediction can be seen in Figure 2.17(a) and Table 2.6. It can be seen that the scatter in the comparison is large. Generally, the DSM provides an unconservative prediction of the ultimate load. This is in fact reasonable since the DSM is mainly based on fitting the test and numerical results of cold-formed thin-walled columns. As for welded sections, the effects of residual stress may have a detrimental effect on the ultimate load. Therefore, in order to make the DSM valid for the welded sections, further calibration is necessary with respect to experimental or validated numerical results.

2.6 Concluding remarks

In the current chapter, a literature review about the interactive buckling of thin-walled plated structures has been presented. Analytical approaches, including both approximate engineering and strict theoretical approaches, alongside their advantages, disadvantages and findings have been introduced. In particular, the seminal work by Van der Neut as well as the extensive work by Wadee and his collaborators, the methodology of which is adopted in the current work is introduced in detail. Subsequently, related studies using numerical approaches to the local–global mode interaction, *i.e.* from FE, GBT and FSM approaches, are presented. Moreover, imperfection measurement and modelling, the imper-

fection modelling recommendations in EC3 as well as the imperfection sensitivity studies have been reviewed and discussed. Furthermore, existing experimental studies on thin-walled box-section columns exhibiting local–global mode interaction were reviewed. The ultimate load of these specimens were also summarized in the framework of current design guidelines. It is revealed that the DSM formulae based on the cold-formed steel sections generally provides an unconservative ultimate load prediction for the welded box-section struts. As for the effective width method in the current EC3 methodology, it is revealed that it can provide a conservative ultimate load prediction for most tested specimens. However, a large scatter in the results is observed, which suggests that the current simplified design equation may be improved.

Chapter 3

Finite element model development and validation

3.1 Introduction

In order to verify the variational models developed in the study, a robust and accurate numerical method should be adopted. Owing to the popularity of general-purpose finite element (FE) packages with powerful modelling and accurate solution functions, the FE method has become an important and accessible technique in analysing the nonlinear behaviour of thin-walled structures (Schafer *et al.*, 2010). Compared with other numerical methods, it can model relatively easily nearly all the actual physical scenarios, including items such as residual stresses, initial geometric imperfections and plasticity. Therefore, it is often used for verifying analytical models (Wadee & Farsi, 2014a; Bai & Wadee, 2015b), expanding an originally simplified analytical model to more general and actual cases (Kiymaz, 2005) and conducting parametric studies based on the FE model validated by experiments (Degée *et al.*, 2008; Becque & Rasmussen, 2009b; Yuan *et al.*, 2014; Yang *et al.*, 2017).

In the current chapter, details of models, developed within the commercial general purpose FE package ABAQUS (2014), are presented. Firstly, the strut modelling details, *i.e.* boundary conditions, the use of symmetry to improve computational efficiency, semi-rigid flange–web joint modelling, the chosen element type and mesh scheme, are described. The material model, geometric imperfection modelling and the introduction of residual stresses are also presented. Moreover, the analysis types and the corresponding solution strategy as well as the analysis objectives are described. Finally, the verification of finite element models against classical solutions and validation against experimental results from the literature are presented.

3.2 Development of finite element models

A thin-walled rectangular hollow section strut of length L with simply-supported boundary conditions under an axial load P is considered, as shown in Figure 3.1.

3.2.1 Strut modelling

Boundary conditions

As shown in Figure 3.1(c), there are two planes of symmetry in the interactive buckling mode. Therefore, the current FE model exploits symmetry for computational efficiency, as shown in Figure 3.2(a). As for the boundary condition at the loaded-end, the displacements and rotations of the end section ($z = 0$) of the strut are linked to a reference point at the centre of the cross-section through rigid body kinematic coupling. This ensures that all the boundary conditions, defined at the reference point, are uniformly transmitted to the entire cross-section. The translational degrees of freedom (DOFs) in the x and y directions at the reference point are restrained and thus the pinned-roller support assumption is

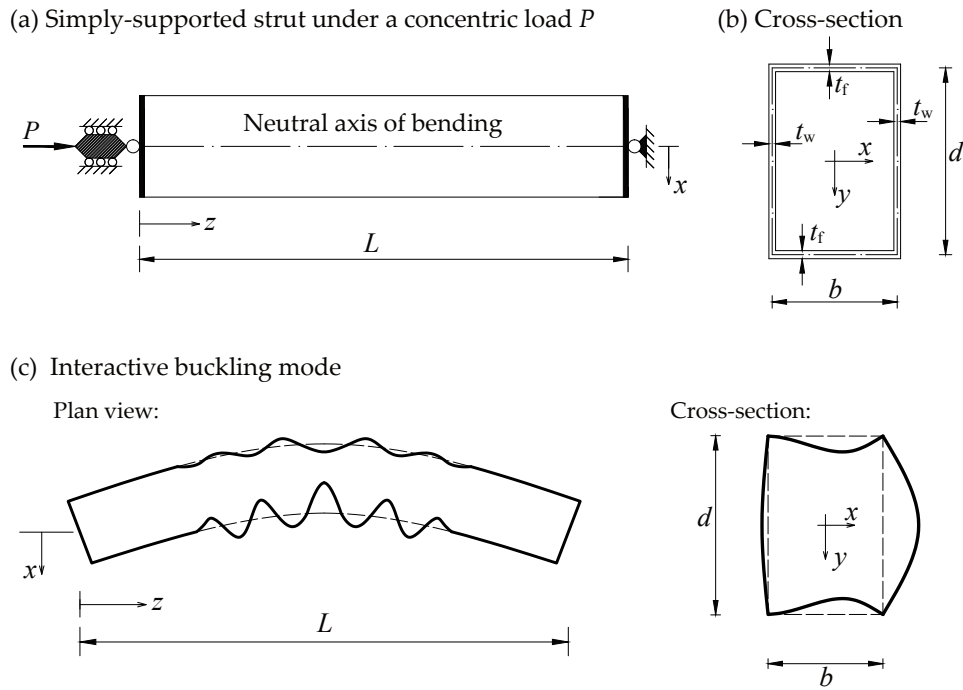


Figure 3.1: (a) Plan view of the thin-walled rectangular hollow section strut of length L under an axial load P . Lateral and longitudinal coordinates are x and z respectively. (b) Cross-section properties of the strut; the vertical coordinate is y . (c) Plan and cross-section view of the interactive buckling mode.

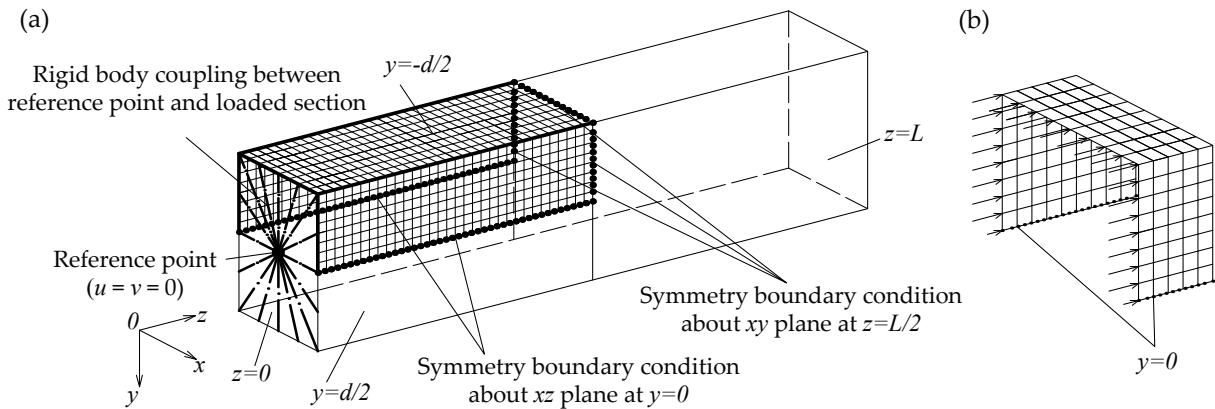


Figure 3.2: (a) Illustration of the FE model for thin-walled RHS struts. Global buckling bends the strut about the weak axis y . (b) Distributively applied load at the end-section; the magnitude of the load on the nodes at the symmetric line ($y = 0$) is half of that in the other nodes. Note that the mesh in the figure is only for illustration purposes and does not represent the mesh scheme implemented in actual analyses.

satisfied. The axial load P is applied distributively to each node of the end section in the z -direction, as shown in Figure 3.2(b). In particular, the magnitude of the applied load on the two nodes on the symmetric line ($y = 0$) is half of those on the other nodes. It should be noted that the choice of double symmetry and the way the load was applied was made after careful verification against the half-strut (Shen & Wadee, 2018b) and full-strut models, where it was found that they produce identical results.

It should also be noted that the symmetric boundary condition at mid-span makes the number of half-waves in the local mode always be odd, which may lead to large errors in the cases where the strut length is within a factor of 5 of the half wavelength of the local buckling mode. In such cases, the symmetric boundary condition at mid-span is removed and full-length strut model is adopted, as can be seen in §3.4.1. However, such cases are not significant for strut design in term of practical geometries.

Semi-rigid flange–web connection modelling

Compared with open sections, the interaction between individual plates in closed cross-sections is more significant. Therefore, a study on the effects of flange–web joint rigidity is conducted in Chapter 4. To capture the local deformation of each individual plate and the effects of the rotational stiffness at the junction, each plate is modelled separately. The nodes at the junctions of the webs and the flanges are defined and labelled separately but share the same coordinates. The translational DOFs of these nodes are then tied together but the rotational DOFs are not, thus approximating a pinned joint. A rotational spring element, ‘SPRING2’ in the ABAQUS element library, is then introduced to connect the end nodes of each flange and web, as shown in Figure 3.3(a).

With the varying stiffness of the spring element, cross-section joint properties ranging from pinned to rigid can be modelled. Since the rotational springs are discretely distributed in the FE model, as shown in Figure 3.3(b), in order to make them equivalent to that in the

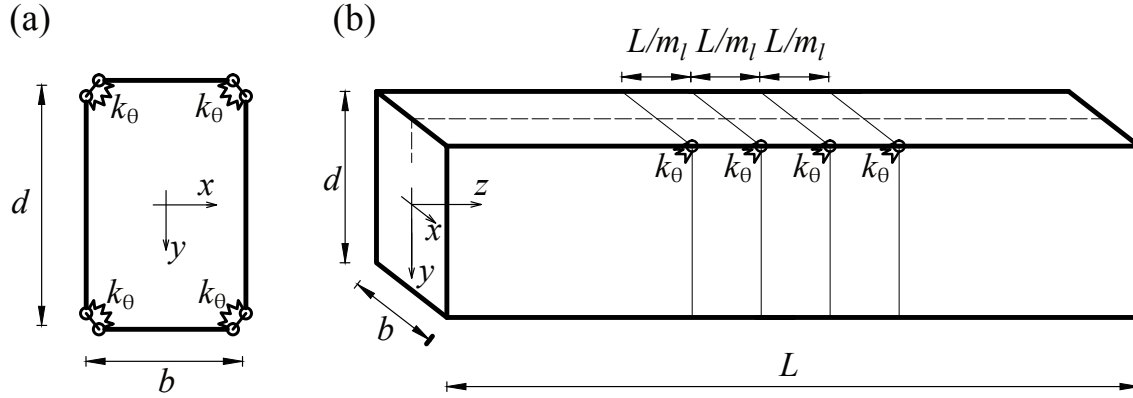


Figure 3.3: Semi-rigid flange–web connection modelling in the FE model. (a) Node-to-node rotational springs in the cross-section; (b) Springs along the length of the strut; m_1 represents the number of elements along the length of the strut; k_θ is the stiffness of an individual rotational spring.

variational model, which is continuous, the following relationship is applied:

$$k_\theta = \frac{c_\theta L}{m_1 + 1}, \quad (3.1)$$

where c_θ is the rotational stiffness of the rotational spring at flange–web joints in the analytical model defined in the analytical formulation in Chapter 4; L is the strut length; k_θ is the rigidity of an individual rotational spring in the FE model with its units being Nmm and m_1 is the number of elements along the length of strut. For the two limiting joint cases, *i.e.* the pinned and rigid cases, special treatments are adopted. In the FE model, if k_θ were set to be zero, the strut would in fact be a mechanism and hence would not satisfy static equilibrium. Therefore, k_θ is set to be a very small nominal value of 10^{-6} Nmm such that potential kinematic mechanisms can be avoided and the pinned case is essentially satisfied numerically. As for the rigid joint case, the rotational DOFs at the junctions of the webs and flanges are tied together in the same way as the translational DOFs.

It should be noted that since there are two nodes at the flange–web joints that share the same coordinate and all the translational DOFs are tied, the distributed load is only applied on one of the nodes – currently being the nodes on the top edges of both webs. Moreover,

in order to make the model more concise, only one node is defined at the junction for FE models used in the remaining chapters.

Element choice

Owing to the geometry of the thin-walled rectangular hollow section struts, 3D finite elements are not suitable for the analysis. If the 3D elements were made very thin only in the thickness direction, there would be problems of shear locking and ill-conditioning. In order to overcome the problem, a great number of 3D elements should be used. Therefore, three dimensional conventional shell elements were used, which take full advantage of the geometric property conditions to discretize the structure by defining the geometry at a reference surface and the thickness being defined through the section property definition.

Specifically, the 4-node general-purpose, reduced integration shell element with hourglass control S4R (ABAQUS, 2014) was adopted. The general-purpose element can provide robust and accurate solutions in all loading conditions for both thin (Kirchhoff plate theory) and thick shear flexible (Mindlin plate theory) plates. It should be noted that 4-node bilinear elements suffer from shear locking in both the in-plane (membrane) and the out-of-plane (transverse) dimension, as shown in Figure 3.4. Spurious shear strains are introduced due to the bilinear displacement field assumption. However, it has been demonstrated that the problem can be solved using reduced integration (Cook *et al.*, 2007), since the shear strain at the integration point, the solid square symbol in Figure 3.4, is zero. The reduced integration method can overcome the shearing lock problem but it introduces the ‘zero strain’ or ‘hourglass’ mode, as shown in Figure 3.5. These modes would lead to zero strain in the integration point and hence zero energy in the element, thus making the stiffness matrix singular. In ABAQUS, there is an hourglass control/stabilization procedure for both transverse and in-plane displacement (ABAQUS, 2014). Therefore, the type of element chosen does not suffer from shear locking, nor does it have any unconstrained hourglass modes.

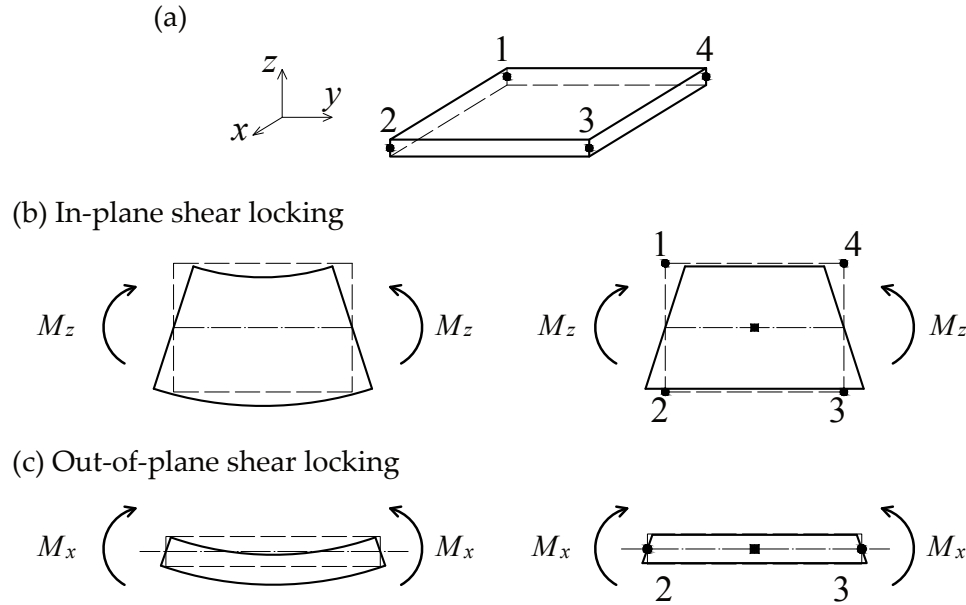


Figure 3.4: Shear locking for the four-noded bilinear plate element. (a) Four-noded bilinear shell element and its coordinate system. (b) Deformation of plate and the four-noded bilinear plate element under in-plane bending moment M_z . (c) Deformation of plate and four-noded bilinear shell element under out-of-plane bending moment M_x .

About the cross-sectional properties of the shell element, Simpson's rule is adopted for the numerical integration. The default number of the integration points for a homogeneous section is five, which is sufficient for predicting the response of an elastic-plastic shell up to the limit load (ABAQUS, 2014). However, for the cases with more complex nonlinear behaviour involving strain reversals or cases with complex residual stresses and strain distributions (Schafer *et al.*, 2010), more section points would be required, but normally no more than nine.

It should also be noted that the S4R element is capable of handling large strains and large rotations, which is suitable for modelling the geometric nonlinearity due to the mode interaction. Moreover, numerous previous research studies (Becque & Rasmussen, 2009b; Schafer *et al.*, 2010; Sadowski & Rotter, 2013; Yuan *et al.*, 2014; Wadee & Farsi, 2014a; Bai & Wadee, 2016; Liu & Wadee, 2016b) have demonstrated this element can model plate buckling problems with very good accuracy.

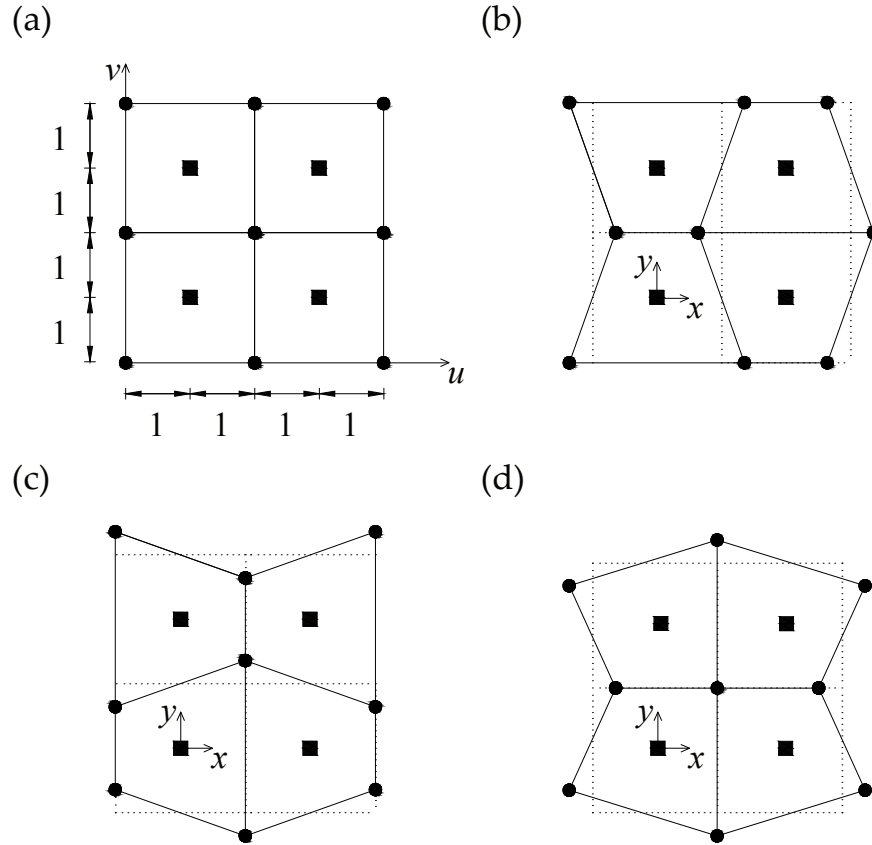


Figure 3.5: (a) Undeformed 2 by 2 four-noded bilinear elements. Solid circle and square symbols represent the nodes and integration points respectively. The horizontal and vertical displacements are u and v respectively. Hourglass modes (Cook, 1994) with (b) $u = -cxy$, $v = 0$; (c) $u = 0$, $v = cxy$; and (d) $u = cy(1 - x)$, $v = cx(1 - y)$, where c is a non-zero constant.

Meshing scheme

Since the wavelength of the local buckling mode is considerably smaller than that of the global mode, a meshing scheme suitable for capturing the local buckling mode naturally would be sufficiently good for the global and local-global interactive buckling mode. Moreover, to increase computational accuracy, the shape of the elements is made to be as square as possible (Cook *et al.*, 2007). A mesh sensitivity study has been conducted to find an acceptable meshing scheme that not only yields accurate results but also is computational efficient, which may be found in §3.4.1. Currently, the meshing scheme of 20 elements per wavelength has been adopted.

3.2.2 Material Modelling

Apart from models formulated in Chapter 9, the material is assumed to be linear elastic, homogeneous and isotropic with Young's modulus E , Poisson's ratio ν and shear modulus $G = E/[2(1 + \nu)]$. In Chapter 9, where the effects of material nonlinearity is considered, the idealized piecewise linear elastic–plastic stress–strain relationship, presented in Figure 3.6(b), is employed to simulate the actual engineering stress–strain relationship for carbon steel, as shown in Figure 3.6(a). The parameters f_y and ε_y are the yielding stress

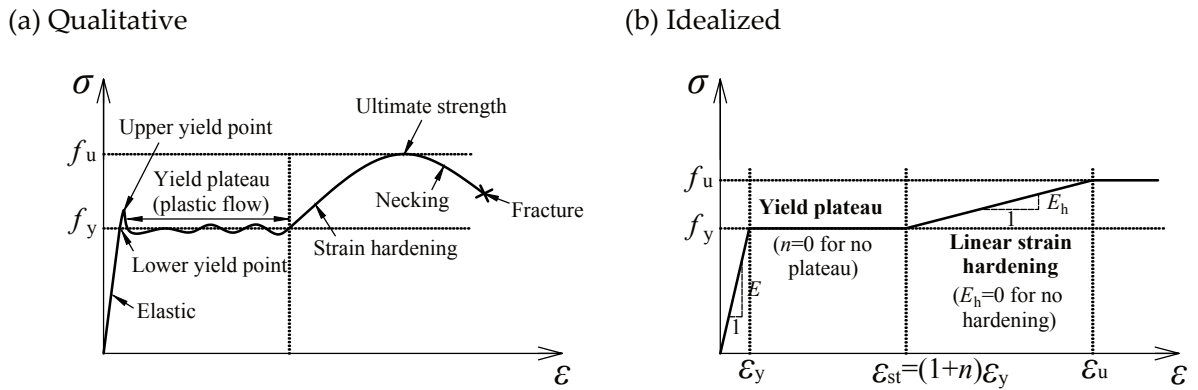


Figure 3.6: Typical constitutive curve for structural carbon steel: (a) qualitative description of actual stress–strain relationship and (b) idealized piecewise linear relationship. In particular, $n = 0$ and $E_h = 0$ represents the elastic–perfectly plastic model; $n = 0$ but $E_h > 0$ represents the elastic–linear strain-hardening model; $n > 0$ and $E_h > 0$ represents the model that has a yielding plateau before the linear strain hardening. Note that the strains and stresses are both engineering strains and stresses.

and strain respectively; $(1 + n)\varepsilon_y$ is the strain value, at which the strain hardening begins; E_h is the modulus in the strain hardening range; f_u and ε_u are the ultimate stress and strain respectively. Moreover, the isotropic hardening and the Von Mises yield criterion with associated plastic flow are adopted in the material model.

It should be noted that the graphs presented in Figure 3.6 are for nominal values of strain and stress, where the cross-section area reduction during the loading is not included. However, the constitutive formulations are based on the true ‘Cauchy’ stress–strain relationship in ABAQUS. Therefore, the transformation of data from nominal stress σ_{nom} and strain

ε_{nom} to true stress σ_{true} and strain $\varepsilon_{\text{true}}$ is required, thus:

$$\sigma_{\text{true}} = \sigma_{\text{nom}}(1 + \varepsilon_{\text{nom}}), \quad (3.2)$$

and

$$\varepsilon_{\text{true}} = \ln(1 + \varepsilon_{\text{nom}}). \quad (3.3)$$

Moreover, in defining the data on the stress–strain curves, ABAQUS also requires that the plastic strains rather than the total strains, as shown in Figure 3.7. The true plastic strain

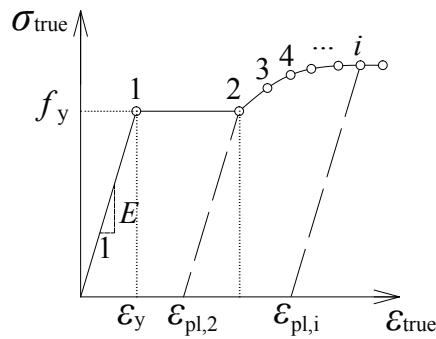


Figure 3.7: A typical nonlinear stress–strain relationship and the corresponding input parameters in ABAQUS.

can be expressed as:

$$\varepsilon_{\text{true,pl}} = \varepsilon_{\text{true}} - \frac{\sigma_{\text{true}}}{E}. \quad (3.4)$$

3.2.3 Geometric imperfection modelling

There are two different methods to introduce the geometric imperfections in FE models in ABAQUS. The first is to use the keyword ‘*IMPERFECTION’ to introduce the shape of eigenmodes from linear buckling analysis, which is very straightforward and convenient. Currently, it is used for introducing the necessary geometric perturbation to simulate the post-buckling behaviour response of the perfect case and the cases where only a global

imperfection exists. However, it should be stressed that this approach is quite cumbersome and inefficient in cases where local buckling is clearly critical, since a large number of less important local modes would also be produced apart from the target local and global modes. Moreover, since the sequence order of the global mode is not known in advance, a post-processing script would need to be written to distinguish the target modes for the nonlinear analysis. Therefore, the approach is not suitable for automation and naturally limits the number of cases that can be considered.

The second approach is to use MATLAB (MATLAB, 2010) to generate the nodal coordinates input file for the FE model with pre-defined global or local imperfections respectively, which can model more general imperfection cases. In particular, this approach can be used for the investigation of the most severe local imperfection profile. Moreover, it can improve the computational efficiency since no linear buckling analysis is required before the nonlinear analysis, which also makes an automated parametric study possible. It should be noted that the local and global imperfection profiles in the this approach is based on the local and global buckling mode obtained from the variational model, which is introduced in Chapter 7.

3.2.4 Residual stress modelling

Residual stresses are modelled as initial conditions in the current FE models in ABAQUS. Currently, only membrane residual stresses are considered. Unless otherwise specified, the ECCS (1976) residual stress distribution pattern for welded box-section members is adopted, as shown in Figure 3.8. The tensile residual stresses at the corners are assumed to be equal to yielding stress f_y . The compressive residual stress in the flanges and webs are determined based on the equilibrium condition. For instance, the compressive residual

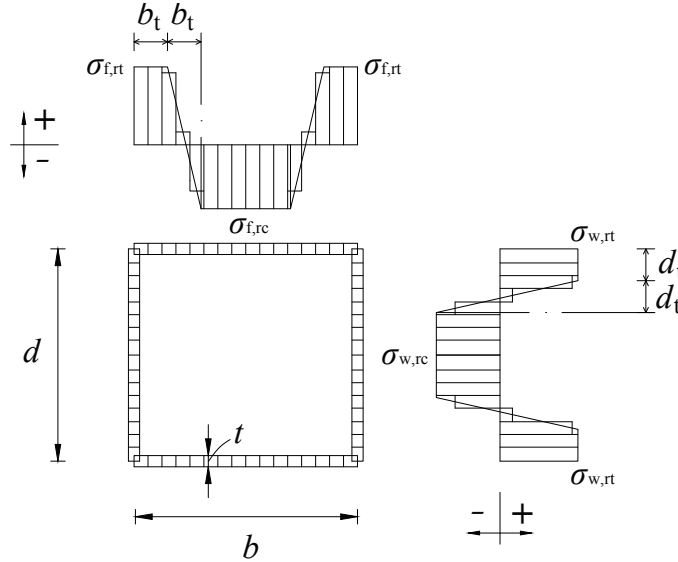


Figure 3.8: ECCS residual stress distribution for welded box-section members. Note that the uniform tensile range length d_t for heavily-welded and lightly-welded box-section members are $3t$ and $1.5t$ respectively; $\sigma_{f,rc}$ and $\sigma_{w,rc}$ are compressive residual stresses in the flanges and webs respectively; $\sigma_{f,rt}$ and $\sigma_{w,rt}$ are tensile residual stresses in the flanges and webs respectively.

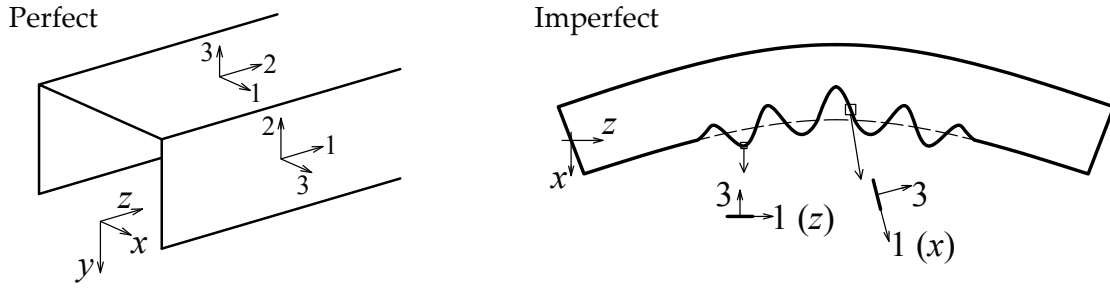
stresses in the webs can be determined as:

$$\sigma_{w,rc} = \frac{3d_t\sigma_{w,rt}}{d - 3d_t}. \quad (3.5)$$

A script has been developed in MATLAB to produce the residual stress distribution in the FE model automatically.

Moreover, it should be noted that for the models including residual stresses, the coordinate system is re-defined such that the longitudinal direction of the strut parallels to the x coordinate, as shown in Figure 3.9(b). In ABAQUS, the local coordinate orientation of shell elements, which is related to the residual stress components, is defined by the projection of the global axis on the surface, as shown in Figure 3.9. Owing to the local imperfections introduced in both webs, the local coordinate orientation, particularly the local 1-direction, would vary along the length with the curvature of the initially deformed plate if the global coordinate orientation in Figure 3.2 is adopted, as shown in Figure 3.9(a). It would make

(a) Local coordinate direction before transformation



(b) Local coordinate direction after transformation

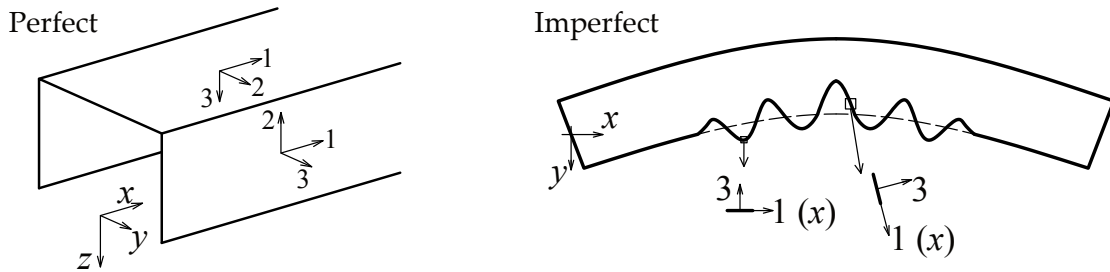


Figure 3.9: The orientation of local coordinates in perfect and imperfection struts within different global coordinate systems.

the introduction of residual stresses in the model very complex. Therefore, the x -direction of the global coordinate transformed to be the same as the longitudinal direction of the plate, as shown in Figure 3.9(b), which makes the local 1-direction in all plates be the same and consistent along the length.

3.3 Analysis type and solution strategy

As presented in Table 3.1, four different types of analyses are adopted in the current study for specific objectives. The solution strategy and objective of each type of analysis is introduced in this section.

Table 3.1: Summary of analysis types and their objectives.

Abbreviation	Geometric nonlinearity	Material model	Imperfections	Analysis objective
LBA	None	Linear elastic	None	Critical buckling load and eigenmodes for nonlinear analysis (Chapters 4, 6, 7)
GNA	Yes	Linear elastic	None	Interactive buckling behaviour of perfect elastic RHS struts (Chapters 4, 6)
GNIA	Yes	Linear elastic	Geometric imperfections only	Interactive buckling behaviour of elastic RHS struts with geometric imperfections (Chapters 7, 8)
GMNIA	Yes	Piecewise linear with yielding	Geometric imperfections and/or residual stresses	Ultimate load of imperfect RHS struts susceptible to local-global buckling with different material yielding stress levels (Chapter 9)

3.3.1 Linear buckling analysis

As mentioned in §3.2.3, the linear buckling analysis in the current study is conducted principally to acquire the critical buckling load and the corresponding eigenmodes to be introduced as perturbations or imperfections for further nonlinear analyses. Moreover, it is used to provide guidance on the proposal of cross-section shape functions for the variational model and to verify the linear buckling analysis of the variational model.

As for the solution process of linear buckling analysis, the first step is to load the structure by an arbitrary reference level of external load, $\{\mathbf{P}\}_{\text{ref}}$, and then a standard linear static analysis is conducted to determine element stresses. For the stress associated with load $\{\mathbf{P}\}_{\text{ref}}$, the stress stiffness matrix is $[\mathbf{K}_\sigma]_{\text{ref}}$. Since it is assumed that the problem is linear, the stiffness matrix of the structure $[\mathbf{K}]$ remains the same and the stress stiffness matrix would be proportional to the load level with respect to the reference external load, *i.e.* $[\mathbf{K}_\sigma] = \lambda [\mathbf{K}_\sigma]_{\text{ref}}$, where $\lambda = \{\mathbf{P}\} / \{\mathbf{P}\}_{\text{ref}}$. Therefore, at the bifurcation point, the following

relationship should be satisfied:

$$([\mathbf{K}] + \lambda_{\text{cr}}[\mathbf{K}_{\sigma}]_{\text{ref}}) \{\mathbf{d}\} = \{\mathbf{P}\}_{\text{cr}} = \lambda_{\text{cr}}\{\mathbf{P}\}_{\text{ref}}, \quad (3.6)$$

where $\{\mathbf{d}\}$ is the displacement of nodes at reference configuration of the primary path. From the concept of perturbation, let the buckling displacement $\{\delta\mathbf{d}\}$ occur relative to the displacement $\{\mathbf{d}\}$ of the reference configuration with the load level remaining unchanged:

$$([\mathbf{K}] + \lambda_{\text{cr}}[\mathbf{K}_{\sigma}]_{\text{ref}}) \{\mathbf{d} + \delta\mathbf{d}\} = \lambda_{\text{cr}}\{\mathbf{P}\}_{\text{ref}}. \quad (3.7)$$

By subtracting Eq. (3.6) from Eq. (3.7), the classical eigenvalue problem can be obtained:

$$([\mathbf{K}] + \lambda_{\text{cr}}[\mathbf{K}_{\sigma}]_{\text{ref}}) \{\delta\mathbf{d}\} = \{\mathbf{0}\}. \quad (3.8)$$

The smallest root λ_{cr} defines the level of the critical buckling load, *i.e.* $\lambda_{\text{cr}} = \{\mathbf{P}\}_{\text{cr}}/\{\mathbf{P}\}$. The eigenvector $\{\delta\mathbf{d}\}$ associated with λ_{cr} is the buckling mode. Since the magnitude of $\{\delta\mathbf{d}\}$ is indeterminate in a linear buckling problem, it would be output as a normalized shape with the amplitude being unity.

In order to model the interactive buckling behaviour, both the local and global buckling buckling mode is required to be introduced as geometric perturbations. Particularly, for short struts with larger ratios of global buckling load to local buckling load P_0^C/P_1^C , the eigenvalue of the global buckling mode would be much larger than that of the critical local buckling mode. A large number of eigenvalues and eigenmodes are required to be output. Therefore, the Lanczos method (Bathe, 2006) is adopted to extract the eigenvalues and eigenmodes. It is generally much faster when a large number of eigenmodes are required for a system with many degrees of freedom compared with the subspace iteration method, the latter of which is faster for the cases where only a small number of (fewer than 20) eigenmodes are required (ABAQUS, 2014).

3.3.2 Nonlinear analysis

The linear buckling analysis can only provide the critical buckling load and the corresponding buckling mode. In order to obtain the nonlinear post-buckling behaviour and the behaviour of struts with imperfections and nonlinear material properties, nonlinear analysis should be conducted.

Geometric Nonlinear Analysis (GNA)

GNA is mainly used to analyse the local–global mode interaction of perfect struts. Owing to the discontinuous pitchfork bifurcation response at the initial instability, it is not possible to analyse the interactive post-buckling behaviour of perfect struts as well as struts with only global imperfections or only symmetric local imperfections exist, in ABAQUS directly, unless imperfections exist naturally from the discretization. Therefore, an initial perturbation in the geometry is introduced to transform the discontinuous bifurcation problem into a continuous one (Belytschko *et al.*, 2000). In the current study, the eigenmode shapes from linear buckling analysis are adopted as the profiles for the initial local or global geometric perturbations and the scale factors for the local and global perturbations are set to $10^{-3}t_w$ and $10^{-6}L$ respectively. These sufficiently small sizes ensure that the response essentially mimics the perfect cases as far as possible, without encountering the pitchfork bifurcations that would have led to convergence problems.

As for the solution method, the modified Riks arc-length method (Riks, 1979) is adopted. Compared with the load-controlled or displacement-controlled methods, the method can allow the load or displacement to increase and decrease, as shown in Figure 3.10(a). Previous studies on thin-walled compression members (van der Neut, 1969; Wadee & Farsi, 2014a; Wadee & Bai, 2014) have demonstrated that there is a snap-back and sharp dynamic drop in the load-carrying capacity after the ultimate load for perfect members and members with tiny imperfections, where local buckling load is close to global buckling load.

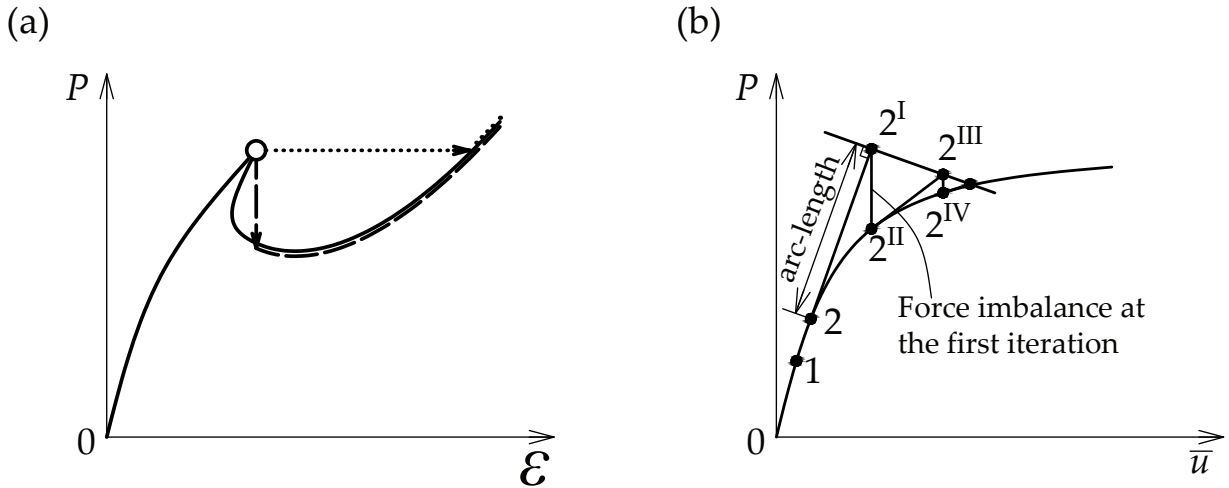


Figure 3.10: (a) Comparison of equilibrium paths with a snap back after the ultimate load from different nonlinear solution strategies. Dotted, dashed and solid lines represent the load-controlled, displacement controlled and Riks arc-length method respectively. Note that P and \mathcal{E} represent the load and end-shortening respectively. (b) Sketch for the modified Riks arc-length method. Note that \bar{u} represents the generalized displacement.

Therefore, the highly unstable nonlinear response can be traced accurately. Moreover, it should be noted that the basic algorithm of the Riks method remains the Newton–Raphson method. However, compared with the Newton–Raphson method, it can overcome the convergence difficulties for the cases where there is a ‘limit’ point (Cook *et al.*, 2007), which is very common in the current study.

As for the incremental step size control, the initial step size is set to be 0.05 of the critical buckling load. Moreover, the step size can be automatically adjusted with the progression of the analysis and the step size limit is also 0.1. All of these can avoid the problem of overshooting and make the computation efficient as far as possible.

Nonlinear Analysis with Imperfections

Geometric Nonlinear Analysis with Imperfections (GNIA) principally deals with the imperfection sensitivity of purely elastic struts susceptible to local–global mode interaction, which is used for the verification of the variational model that includes geometric imperfec-

tions. Geometric and Material Nonlinear Analysis with Imperfections (GMNIA) is mainly used to analyse the ultimate load of imperfect struts (including geometric imperfections and residual stresses) with different yielding stress levels. It helps understand the actual nonlinear behaviour of struts in practice and facilitates the establishment of robust design guideline for such members.

Both GNIA and GMNIA adopt the same nonlinear solution method, *i.e.* the Riks arclength method, as that of the GNA. Therefore, the analysis procedure is essentially the same. The only difference is that geometric imperfections, residual stresses and material nonlinearity are introduced into the FE models. It should be noted that for the cases where both geometric imperfections and residual stresses are introduced in the FE model, a pre-analysis is required before the nonlinear analysis, since the strut with the predefined geometric local imperfections and residual stresses may not be in equilibrium (Little, 1980). The pre-analysis step may amplify the initial geometric imperfection amplitude significantly where the compressive residual stress is close to the plate buckling load, as shown in Figure 3.11. Therefore, an iterative solution process needs to be conducted to determine the initial

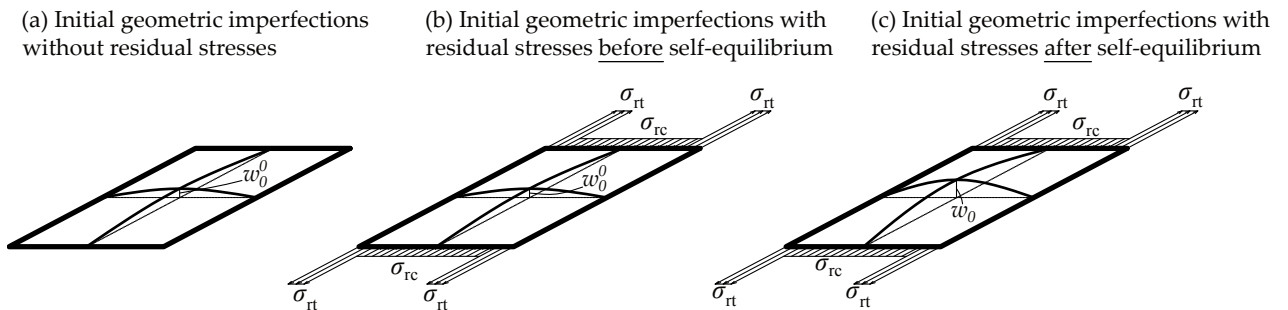


Figure 3.11: Illustration of the effects of initial residual stresses on the initial geometric imperfections introduced within the plate.

imperfection amplitude A_0^0 introduced in the FE model so that the initial imperfection amplitude after the pre-analysis step is the same as the prescribed value A_0 .

Automated termination of analyses

Currently, ABAQUS does not provide a satisfactory facility for automatically terminating a nonlinear analysis when the failure criterion is met. This can make the parametric study inefficient. Recently, Sadowski *et al.* (2017a) developed a FORTRAN code for an ABAQUS user subroutine, which is able to terminate the nonlinear Riks arc-length analysis automatically once certain criteria are met. In the current study, a code with similar functions is developed within MATLAB, the details of which can be found in Chapter 8.

3.4 Verification against classical solutions

In this section, linear buckling analysis is conducted to obtain the local and global buckling load of square box-section columns and comparisons are made with the classical solutions.

3.4.1 Local buckling

Firstly, the mesh sensitivity study is presented. Since the wavelength of the local buckling mode is much smaller than that of the global one, a good meshing scheme suitable to capture the local buckling mode naturally would be satisfactory to capture the global one.

A mesh sensitivity analysis was conducted for an example square box section strut where local buckling was critical. The cross-section geometric properties are shown in Table 3.2.

Owing to the square section, each plate would essentially buckle independently. Therefore,

Table 3.2: Material and cross-section properties of square box section strut for mesh sensitivity analysis and verification.

E (kN/mm ²)	ν	b (mm)	d (mm)	t (mm)
210	0.3	90	90	1

the unloaded edges of each plate can be treated as simply-supported. Moreover, the length

of the example strut is 3890 mm, which makes the strut length sufficiently long such that the local buckling coefficient k_p can be treated as 4, which appears in the local critical buckling stress of a plate σ_{cr} expression thus:

$$\sigma_{cr} = \frac{k_p \pi^2 E}{12(1 - \nu^2)(b/t)^2}. \quad (3.9)$$

The mesh sensitivity results are presented in Figure 3.12. Considering both the accuracy

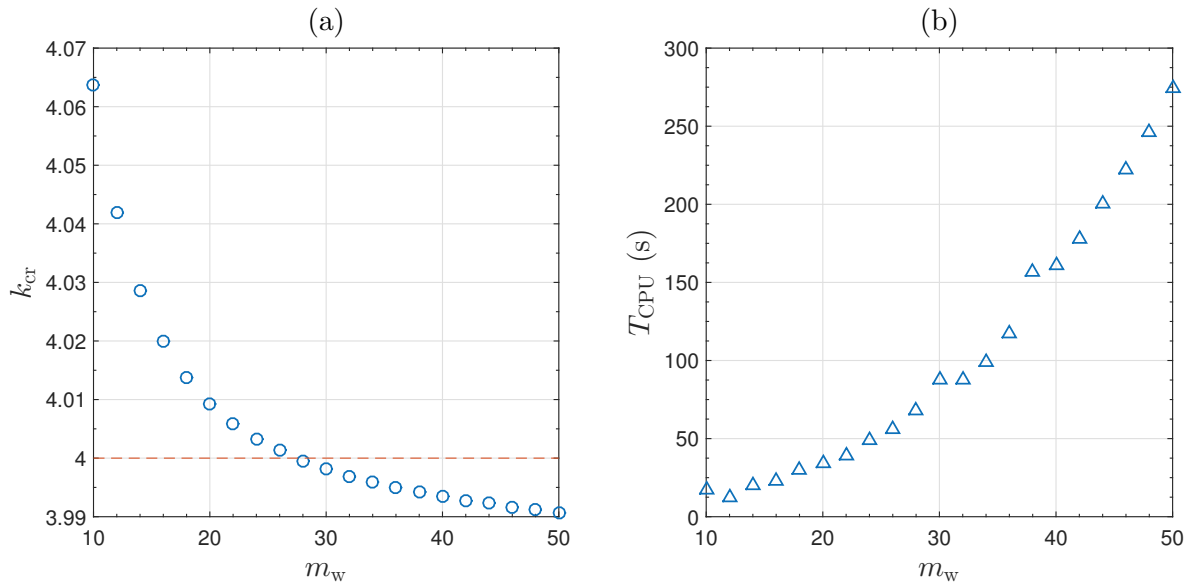


Figure 3.12: (a) Local buckling coefficient of the example strut using different mesh sizes. (b) CPU (Intel Core i7-4790 CPU@3.60GHz) running time versus the number of elements along the web depth m_w . Note that the material and cross-section properties of the example strut are presented in Table 3.2, and the strut length is 3890 mm.

and computational effort, it was deemed that 20 elements for per half wave, *i.e.* $m = 20$, was sufficient to simulate the local buckling mode currently.

Based on the mesh sensitivity study, the strut length is varied to obtain the local buckling coefficient of square box-section struts with different length to width ratios, as shown in Figure 3.13. It should be noted that the symmetric boundary condition at mid-span, as shown in Figure 3.2, is removed and the whole length strut is modelled so as to capture the even number of half-waves in the longitudinal direction. The results from linear buckling

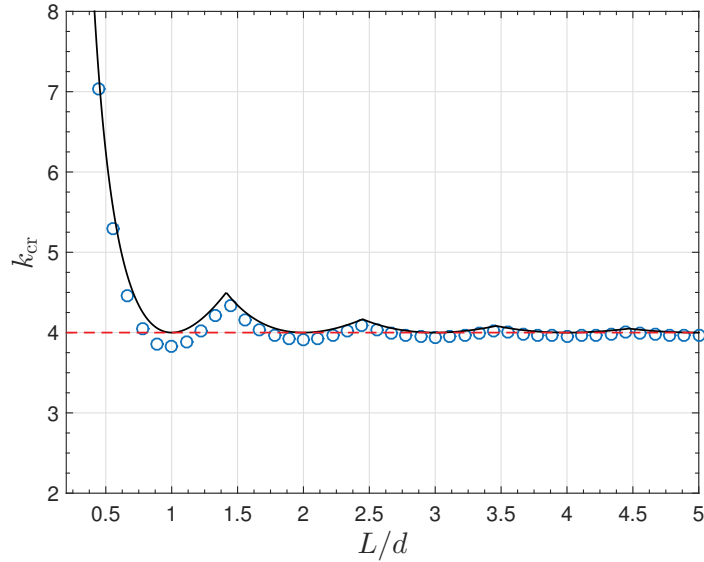


Figure 3.13: Local buckling coefficient of struts with different length–web depth ratios. Solid line represents the analytical solutions from Bulson (1970) and circles represent the results from FE models using linear buckling analysis. Note that the material and cross-section properties of the example strut are presented in Table 3.2.

analysis show good comparisons with the analytical solutions from Bulson (1970), particularly in the practically significant range where the strut length is at least 5 times greater than the flange width. Finally, it should be noted that the buckling coefficient $k_p = 4$ is obtained based on classical Kirchhoff plate theory (Timoshenko & Woinowsky-Krieger, 1959), where shearing effects are neglected. However, the FE model for struts is modelled using S4R shell elements, where shearing effects are included. This explains the critical buckling coefficient from FE model being smaller than that from the classical solution since the former has more degrees of freedom.

3.4.2 Global buckling

The comparison with the Euler buckling equation is mainly to verify the effectiveness of the simply-supported condition at the ends and symmetric boundary conditions adopted at mid-span and the mid-lines of the webs. The material and cross-section geometric

properties are the same as those in the previous subsection. The strut length is varied from the case where the local buckling load is equal to the global buckling load, *i.e.* $P_o^C/P_1^C = 1$, to the cases where global buckling is clearly critical, *i.e.* $P_o^C/P_1^C < 0.4$. As

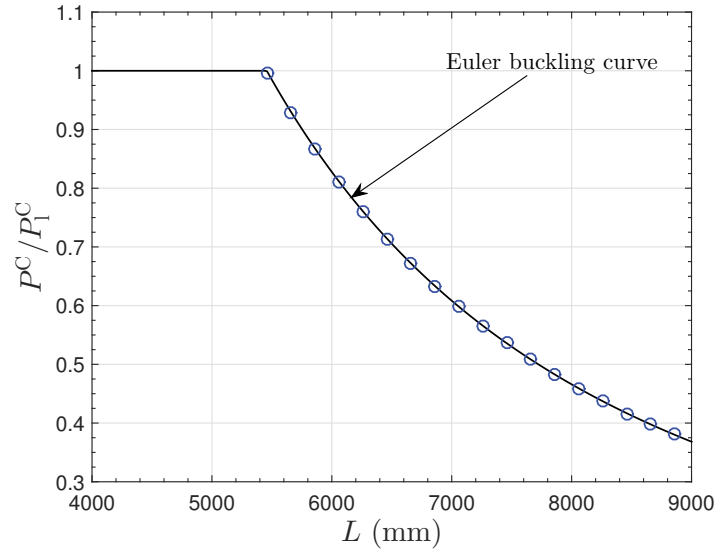


Figure 3.14: Global buckling load of example struts from linear buckling analysis using FE models (circles) and Euler buckling equation (Timoshenko & Gere, 1961). Note that the material and cross-section geometric properties of example struts are presented in Table 3.2.

shown in Figure 3.14, the results from the FE models show excellent comparisons with those predicted by the classical Euler buckling equation.

Based on the excellent comparisons with the classical solutions on plate local buckling and strut global buckling, it may be concluded that the current developed FE models are verified. However, it should be noted that the comparison with the classical solutions only verify the ‘linear’ behaviour of the perfect models. Therefore, in the next section, existing experimental results from literature are adopted to validate the nonlinear behaviour of FE models, where the geometric imperfections as well as residual stresses are included.

3.5 Validation against experimental results

In order to validate the FE model, experimental results on welded box-section columns susceptible to local–global mode interaction under pure compression from two independent sources (Usami & Fukumoto, 1984; Yang *et al.*, 2017) were adopted. The cross-section geometries of the specimens are shown in Figure 3.15.

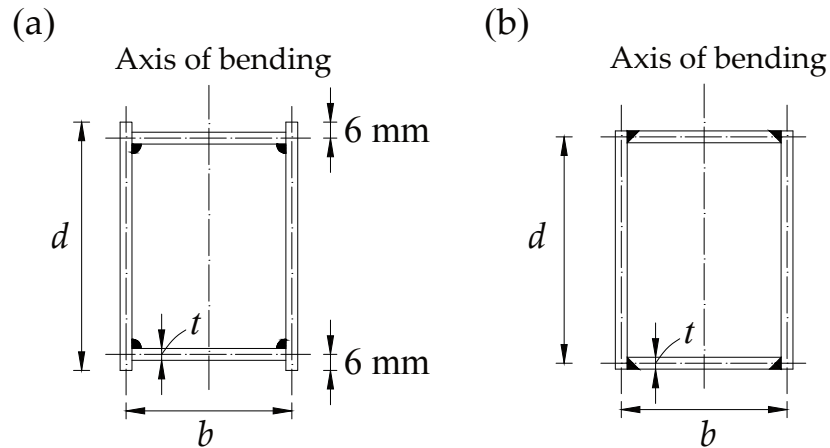


Figure 3.15: Cross-section geometry of specimens from (a) Usami & Fukumoto (1984) and (b) Yang *et al.* (2017).

3.5.1 Test results from Usami & Fukumoto (1984)

The geometric and material properties of the columns are presented in Table 3.3. As for

Table 3.3: Material and geometric properties of the welded box section columns (Usami & Fukumoto, 1984).

Specimen No.	E (kN/mm ²)	ν	f_y (N/mm ²)	b (mm)	d (mm)	t (mm)	L (mm)
R-40-29				93	147	4.46	1650
R-40-44				143	214	4.46	2150
R-40-58	213	0.225	568	191	277	4.47	3310
R-65-29				94	147	4.44	2690
R-65-44				143	214	4.44	4080
R-65-58				191	277	4.46	5370

the global imperfection, the deflected shapes in the perpendicular direction to the buckling axis were determined by measuring the deflection at nine sections along the members. The shapes were reported to be close to the half-sine wave shape and the maximum values of initial deflection δ_0 are listed in Table 3.4. Therefore, in the FE model, it was assumed that the global mode is a half sine wave with the amplitude being δ_0 . As for the local imperfection, the amplitude and distribution were not presented. The amplitude of the local imperfection was adopted from the manufacturing tolerance recommended by EC3, *i.e.* $A_0=d/200$, and its distribution was assumed to be affine to the lowest local buckling mode.

Table 3.4: Geometric imperfections and residual stresses in the welded box section columns (Usami & Fukumoto, 1984).

Specimen No.	A_0/d	δ_0/L	$R_c = \sigma_{rc}/f_y$	$R_t = \sigma_{rt}/f_y$
R-40-29		3.02×10^{-4}	0.32	
R-40-44		2.06×10^{-4}	0.22	
R-40-58	1/200	1.46×10^{-4}	0.15	0.8
R-65-29		2.42×10^{-4}	0.32	
R-65-44		2.48×10^{-4}	0.22	
R-65-58		1.18×10^{-4}	0.15	

As for the residual stresses, the sectioning method was adopted to measure the distribution and it showed that there are rather high tensile stresses (about $0.8f_y$) near the web-flange junctions and the compressive residual stresses remain constant over the central portion of each plate with the normalized magnitude being listed in Table 3.4. Therefore, the residual stress model, as presented in Figure 3.16, is adopted in the FE model.

As for material modelling, since the material is mild steel, an elastic-perfectly plastic model was adopted in the material modelling. The comparison in the ultimate load from FE and experimental results is shown in Figure 3.5. For the six tested specimens, the ratio of the ultimate load from FE to the experimental results ranged from 0.939 to 1.001, with the average value and the coefficient of variation (COV) being 0.972 and 2.62% respectively. Moreover, a sensitivity study on the local imperfection size in the FE model was conducted. As shown in Figure 3.17, $P_{u,FE}/P_{u,Exp}$ is always in the range of [0.9, 1.1] with the normalized

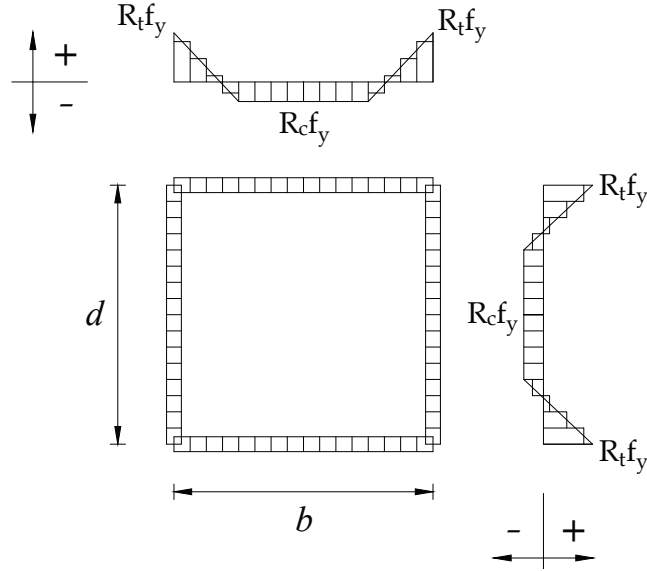


Figure 3.16: Residual stress distribution model adopted in FE models for columns tested in Usami & Fukumoto (Usami & Fukumoto, 1984). The values of R_c and R_t for different specimens are presented in Table 3.4.

Table 3.5: Ultimate load of columns from the tests of Usami & Fukumoto (1984) and FE results. Also shown are the ratios of the column global buckling load P_o^C and the squash load P_y to the local buckling load P_1^C .

Specimen No.	P_o^C/P_1^C	P_y/P_1^C	$P_{u,exp}$ (kN)	$P_{u,FE}$ (kN)	$P_{u,FE}/P_{u,exp}$
R-40-29	1.40	0.64	970.0	960.4	0.991
R-40-44	4.14	1.38	1160.0	1093.6	0.943
R-40-58	5.21	2.32	1180.0	1158.6	0.982
R-65-29	0.54	0.65	753.0	754.0	1.001
R-65-44	1.16	1.39	939.0	881.9	0.939
R-65-58	1.99	2.33	1040.0	1015.6	0.977
				Average	0.972
				COV	2.62%

local imperfection size varying from 1/1000 to 1/200.

3.5.2 Results from Yang *et al.* (2017)

Since the results from Usami & Fukumoto (1984) only provided the ultimate load, test results from Yang *et al.* (2017), where the load–end-shortening relationship was provided, are adopted to validate the FE models further. The geometric properties and initial ge-

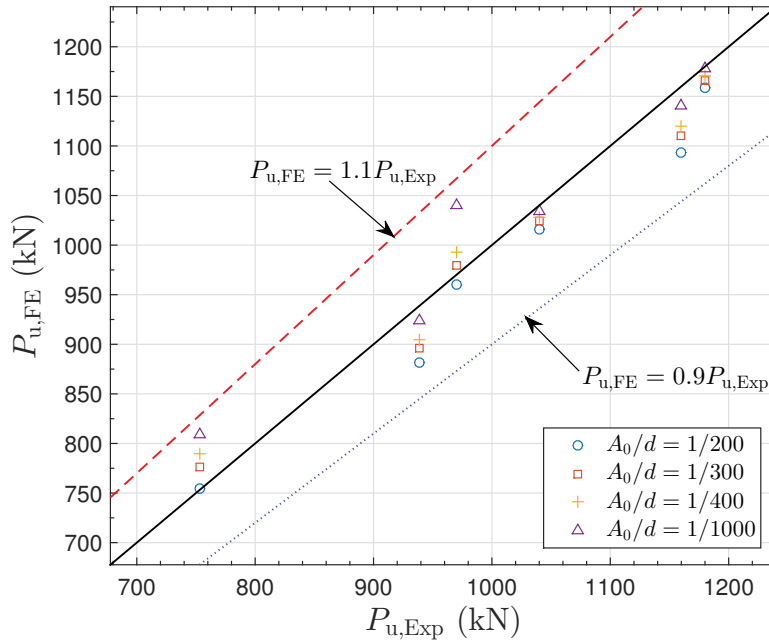


Figure 3.17: Sensitivity of the local geometric imperfection size introduced in the FE models on the ultimate load and their comparison with the experimental results.

ometric imperfection size of the two specimens are shown in Table 3.6. The initial local

Table 3.6: Geometric properties and geometric imperfection sizes of two specimens from Yang *et al.* (2017).

Specimen No.	b (mm)	d (mm)	t (mm)	L_e (mm)	A_0/d	δ_0/L_e
R-235-2	155.25	305.35	5.45	2780.4	0.340%	0.063%
R-345-1	125.39	245.89	5.81	2250.0	0.479%	0.114%

out-of-plane deformation of cross-sections at five different sections were measured in the test (Yang *et al.*, 2017). It revealed that the largest amplitude often occur in the webs but cross-section profiles did not resemble the local buckling mode and showed significant scatter. The initial out-of-straightness deformation of the columns was measured at the quarter-points of the span and the largest value was recorded as δ_0 . In the FE modelling, the maximum displacement in the web A_0 was adopted as the amplitude of the local imperfection and the imperfection profiles were assumed to be affine to the lowest local buckling mode; the global imperfection was modelled as a half-sine wave and the amplitude was set to be δ_0 .

Although only one detailed stress–strain curve for the material of a specimen was provided in Yang *et al.* (2017), the key parameters in the stress–strain curves for each specimen are presented in Table 3.7. A preliminary sensitivity study on the effects of material strain-

Table 3.7: Material properties of two specimens from Yang *et al.* (2017).

Specimen no.	E (kN/mm ²)	f_y (N/mm ²)	f_u (N/mm ²)	ε_{st}	ε_u
R-235-2	207	315.30	462.48	0.0265	0.210
R-345-1	203	416.25	575.91	0.0145	0.132

hardening has shown that strain-hardening has little effect before the ultimate load is reached. Therefore, the piecewise linear model with yielding, the parameters of which were based on tests, was adopted in the FE models.

As for the residual stresses, the actual distribution was not provided in Yang *et al.* (2017). Therefore, the ECCS residual stress distribution model was adopted, as presented in Figure 3.8. It was assumed that specimens were heavily welded, *i.e.* the width of the uniformly residual tensile stress range is $3t$ and the tensile residual stresses at edges $\sigma_{rc} = f_y$.

The comparisons in the load–end-shortening relationship between experimental and FE results are presented in Figure 3.18. Generally, the FE results show a good comparison with the experimental results, particularly the initial stiffness. As for the specimen R-235-2, the FE model can capture the stiffness change in the entire loading history well, with the FE model exhibiting a slightly stiffer response. The ultimate load ratio $P_{u,FE}/P_{u,Exp}=1.038$. As for the specimen R-345-1, there is stiffness reduction near $P=1000$ kN for the FE model but the FE model shows a slightly higher ultimate load with $P_{u,FE}/P_{u,Exp}=1.029$.

Based on the good comparisons with two independent experimental studies, it may be concluded that the developed FE model has been validated and may be used to verify the variational models developed in later chapters and be implemented to perform extensive parametric studies.

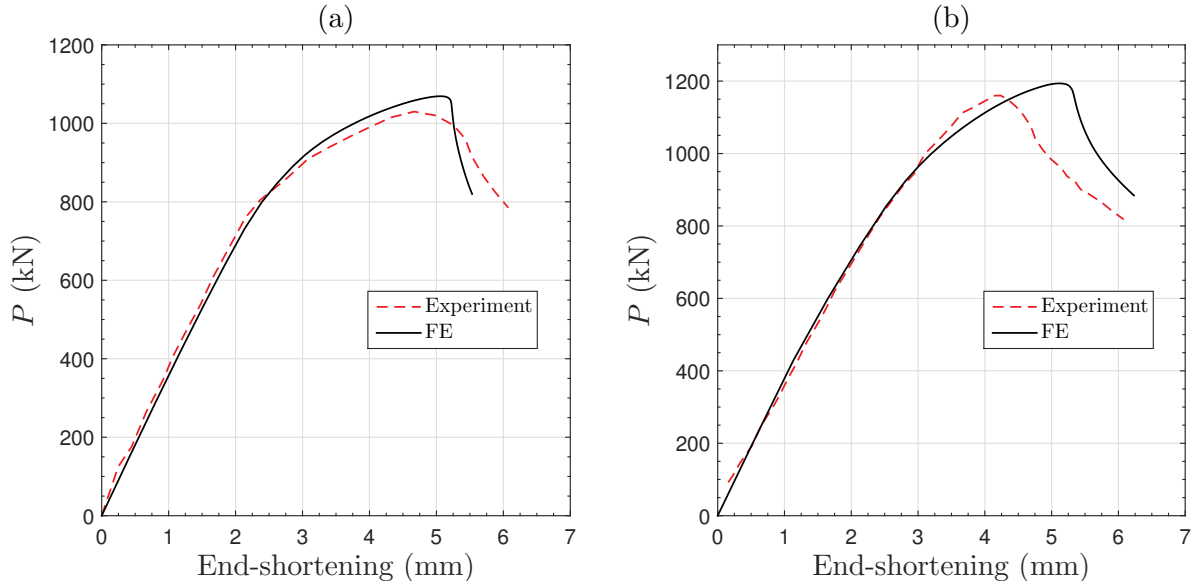


Figure 3.18: Load–end-shortening relationship for specimens (a) R-235-2 and (b) R-345-1 from experimental (Yang *et al.*, 2017) and FE results.

3.6 Concluding remarks

In the current chapter, the details of finite element modelling, the solution strategy alongside their verification and validation were presented. Firstly, strut modelling details, *i.e.* simply-supported boundary conditions, semi-rigid flange–web joints, usage of symmetry to improve computational efficiency, the selected element type and the meshing scheme, were described. Moreover, the adopted material model, geometric imperfections and residual stresses introduced in the models were presented. The analysis types: the linear buckling analysis (LBA), geometric nonlinear analysis (GNA), geometric nonlinear analysis with imperfections (GNIA) and geometric and material nonlinear analysis with imperfections (GMNIA) were introduced alongside their solution strategies and application scenarios.

The developed FE models were firstly verified against the classical solutions from the linear buckling of simply-supported plates under pure compression and the Euler buckling load of a simply-supported column, which show excellent comparisons. This verifies the effectiveness of the boundary conditions, element type and mesh scheme adopted in the current

FE model. Subsequently, the verified FE models were validated against experimental results from two independent studies, which also shows good comparisons. It validates the effectiveness of nonlinear material modelling, geometric imperfections and residual stress modelling as well as the nonlinear solution strategy. Therefore, it may be concluded that the developed FE model has been validated. In the following chapters, the validated FE models will be used to verify the developed variational models and to conduct extensive parametric studies to provide suggestions on the establishment of robust guidance for thin-walled rectangular hollow section columns.

Chapter 4

Behaviour of long struts with semi-rigid flange–web joints

4.1 Introduction

The current chapter investigates global–local mode interaction in rectangular hollow section struts with semi-rigid flange–web joints. It aims at providing a quantitative description of the interaction between flanges and webs in the interactive post-buckling stage, which has not been addressed well in previous studies due to technical complexity (van der Neut, 1969). It facilitates a better understanding of the underlying mechanics of local–global mode interaction in practical cross-sections. A variational model describing the behaviour of a thin-walled rectangular hollow section strut with semi-rigid flange–web joints under axial compression is developed using analytical techniques. The primary aim is to analyse the interaction of global and local buckling modes for the case where global buckling is critical. A relationship describing how the cross-section joint rigidity affects the properties of the system is obtained explicitly from the developed equilibrium equations. These equations are solved using numerical continuation techniques through the well-known software

AUTO-07P (Doedel & Oldeman, 2009). The resulting equilibrium paths are presented for various different cases and potentially dangerous unstable interactive buckling is found. The numerical results from the variational model show excellent comparisons throughout the post-buckling range with numerical results obtained using a nonlinear finite element (FE) model developed within the commercial package ABAQUS (2014). A simplified method to predict the local buckling load of the more compressed web undergoing global buckling and the corresponding amplitude at the secondary bifurcation point is developed based on the verified variational model. A couple of parametric studies concerning the geometric properties are also presented that successfully verify the simplified methodology.

4.2 Development of the variational model

A thin-walled simply supported rectangular hollow section strut of length L , loaded by an axial force P at the centroid of the cross-section is considered, as shown in Figure 4.1. The

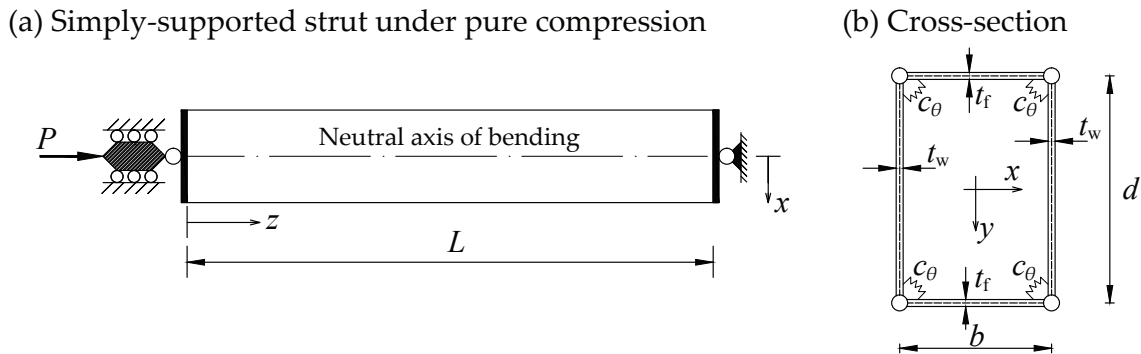


Figure 4.1: (a) Plan view of the rectangular hollow section strut of length L under the concentric axial load P . The lateral and longitudinal coordinates are x and z respectively. (b) Cross-section geometry of the strut with semi-rigid joints including definitions of the rotational stiffness at junctions; the vertical axis coordinate is y .

web depth and thickness are d and t_w respectively; the flange width and thickness are b and t_f respectively. The joints between the webs and the flanges are assumed to be semi-rigid and connected by a rotational spring with stiffness c_θ . It should be stressed that as $c_\theta \rightarrow \infty$,

the joints tend to full rigidity; when $c_\theta \rightarrow 0$, the joints tend to being pinned, *i.e.* there is no rotational interaction between individual plate and they buckle individually. The strut material is assumed to be linearly elastic, homogeneous and isotropic with Young's modulus E , Poisson's ratio ν and shear modulus $G = E/[2(1 + \nu)]$. It is assumed that global buckling occurs about the weak axis of bending.

4.2.1 Modal descriptions

The formulation begins with the definition of both the global and the local modal displacements based on a recent purely numerical study (Shen *et al.*, 2015). Since previous studies (Hunt & Wadee, 1998; Wadee *et al.*, 2010; Wadee & Bai, 2014; Wadee & Farsi, 2014a; Wadee & Farsi, 2014b; Bai & Wadee, 2015b) have clearly demonstrated that it is essential to include the shear strain contributions into the total potential energy formulation to model the interactive buckling behaviour, Timoshenko beam theory is assumed currently. The global mode is decomposed into two components: a purely lateral displacement W and a pure rotation of the plane sections θ , see Figure 4.2, known as the ‘sway’ and ‘tilt’ modes (Hunt *et al.*, 1988; Hunt & Wadee, 1998) respectively. The global buckling lateral displacement W and the corresponding rotation θ are defined by the following expressions:

$$W(z) = -q_s L \sin\left(\frac{\pi z}{L}\right), \quad \theta(z) = -q_t \pi \cos\left(\frac{\pi z}{L}\right), \quad (4.1)$$

where q_s and q_t are the generalized coordinates defining the normalized amplitudes of the sway and tilt modes respectively. The shear strain in the flanges from global buckling is given by the following expression:

$$\gamma_{xz} = \frac{dW}{dz} - \theta = -(q_s - q_t) \pi \cos\left(\frac{\pi z}{L}\right). \quad (4.2)$$

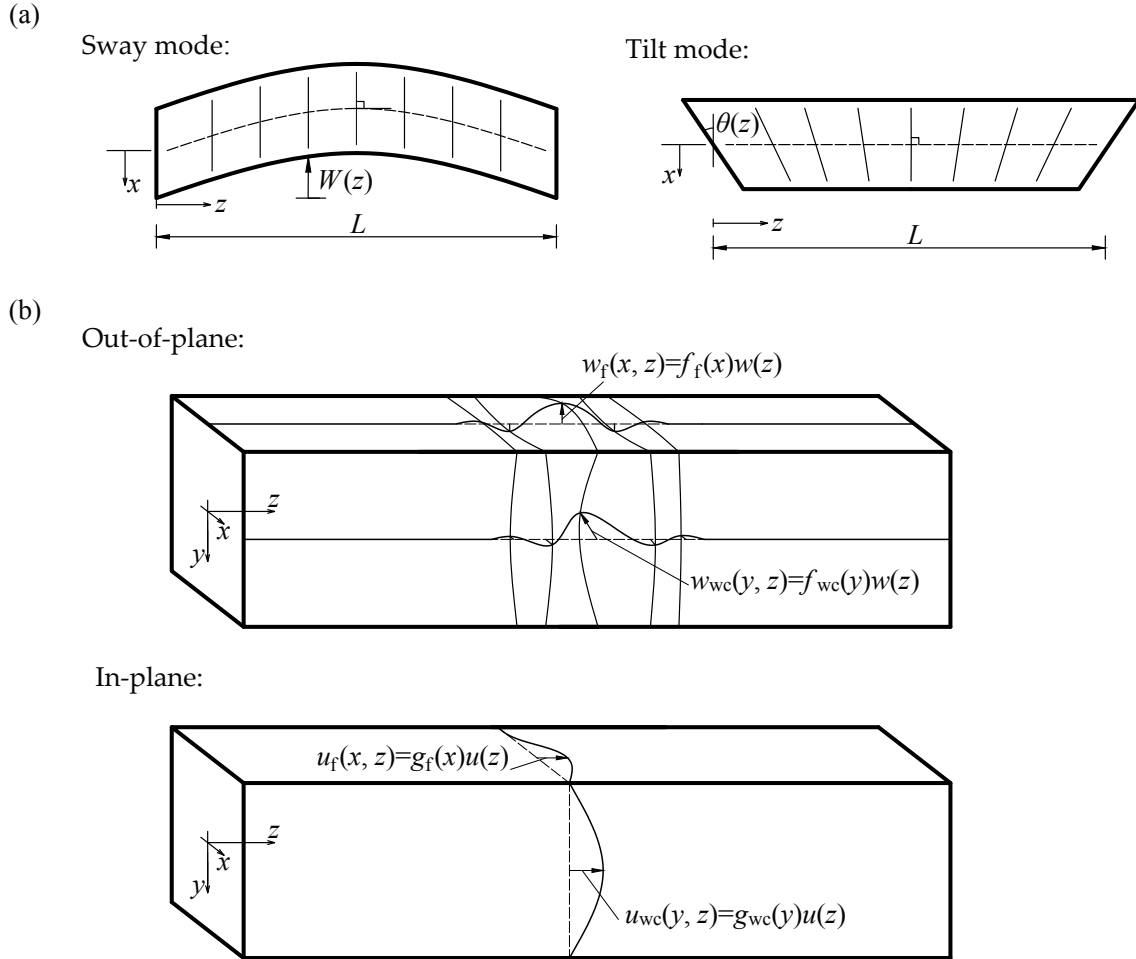


Figure 4.2: (a) Sway and tilt components of the global buckling mode bending about the weak axis y . (b) Out-of-plane local mode in the flanges $w_f(x, z)$ and in the more compressed web $w_{wc}(y, z)$. Also shown are the in-plane local mode in the flanges $u_f(x, z)$ and in the more compressed web $u_{wc}(y, z)$.

In the current study, the focus is on the cases where global buckling occurs first and so the local displacement in the less compressed web is assumed to be zero. The local buckling mode, including out-of-plane and in-plane displacement components, shown in Figure 4.2(b), is defined with the following variables:

$$w_f(x, z) = f_f(x)w(z), \quad w_{wc}(y, z) = f_{wc}(y)w(z), \quad (4.3)$$

$$u_f(x, z) = g_f(x)u(z), \quad u_{wc}(y, z) = g_{wc}(y)u(z), \quad (4.4)$$

where f and g are the cross-section components for the out-of-plane and in-plane displacement components respectively; $w(z)$ and $u(z)$ are the longitudinal out-of-plane and in-plane displacement components respectively.

From an earlier numerical study (Shen *et al.*, 2015), it was determined that the cross-section shape functions for the out-of-plane and the in-plane components, f and g , are approximately the same. Therefore, currently, these components are in fact assumed to be the same, *i.e.* $g_f(x) = f_f(x)$ and $g_{wc}(y) = f_{wc}(y)$. The cross-section components, $f_f(x)$ and $f_{wc}(y)$, as shown in Figure 4.3(a), are estimated by applying appropriate kinematic and static boundary conditions for each plate in conjunction with the Rayleigh–Ritz method. It is assumed that f_{wc} has the functional form that is derived from the conditions of a simply-supported strut (a cosine wave) and a beam under pure bending (a parabola) such that the cases for a fully pinned joint or a joint that rotates as a rigid body can be modelled, thus:

$$f_{wc} = B_0 \cos\left(\frac{\pi y}{d}\right) + (1 - B_0) \left(1 - \frac{4y^2}{d^2}\right). \quad (4.5)$$

For f_f , the functional form is derived from a beam with one end clamped and the other end simply-supported with an end moment arising from the transfer of moment at a non-pinned joint. This naturally leads to a cubic polynomial form:

$$f_f = A_0 \left(x + \frac{b}{2}\right) + A_1 \left(x + \frac{b}{2}\right)^2 + A_2 \left(x + \frac{b}{2}\right)^3. \quad (4.6)$$

The coefficients B_0 in f_{wc} and A_0 , A_1 and A_2 in f_f are determined by applying appropriate boundary conditions at the junctions. The form of f_{wc} automatically satisfies the natural boundary conditions for the web displacement function, *i.e.* $f_{wc}(\pm d/2) = 0$. Since global buckling occurs first and the resulting less compressed web is assumed to have zero out-of-plane displacement, the flanges near the less compressed side also have zero out-of-plane displacement. Therefore, the junction between the less compressed web and the flanges is assumed to be rigid, as shown in Figure 4.3(a). At the junction between the less compressed

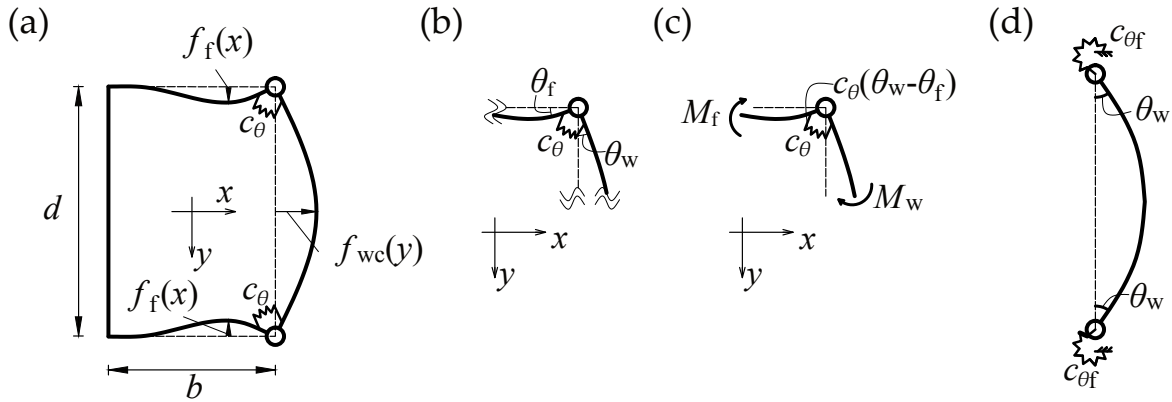


Figure 4.3: Semi-rigid joint with corresponding kinematic and static boundary conditions at the web–flange junctions. (a) Cross-section component of the local mode in the flanges $f_f(x)$ and the more compressed web $f_{wc}(y)$; the stiffness of the rotational spring at the joints is c_θ . (b) Kinematic boundary condition at the junction; θ_f and θ_w are the rotations of the flange and the more compressed web at the junction respectively. (c) Equilibrium condition at the junction; M_f and M_w are the bending moments in the flange and the more compressed web at the junction respectively. (d) Equivalent rotational springs with stiffness $c_{\theta f}$ attached to the more compressed web.

web and flanges, $x = -b/2$ and $y = \pm d/2$, the boundary condition for the flanges are:

$$f_f(-b/2) = f'_f(-b/2) = 0, \quad (4.7)$$

where the prime denotes differentiation with respect to x .

Another boundary condition can be obtained by considering moment continuity at the junction between the flanges and the more compressed web given that there is a rotational spring of stiffness c_θ present, as shown in Figure 4.3(b–c). Hence, the following boundary conditions need to be satisfied:

$$M_f(x = b/2) + M_{wc}(y = -d/2) = c_\theta(\theta_w - \theta_f), \quad (4.8)$$

where:

$$M_f(x = b/2) = \left[D_f \left(\frac{\partial^2 w_f}{\partial x^2} + \nu \frac{\partial^2 w_f}{\partial z^2} \right) \right]_{x=b/2}, \quad (4.9)$$

$$M_{\text{wc}}(y = -d/2) = \left[D_{\text{w}} \left(\frac{\partial^2 w_{\text{wc}}}{\partial y^2} + \nu \frac{\partial^2 w_{\text{wc}}}{\partial z^2} \right) \right]_{y=-d/2}, \quad (4.10)$$

$$\theta_{\text{w}} = \frac{df_{\text{wc}}}{dy} \Big|_{y=-d/2}, \quad \theta_{\text{f}} = \frac{df_{\text{f}}}{dx} \Big|_{x=b/2}, \quad (4.11)$$

with $D_{\text{f}} = Et_{\text{f}}^3/[12(1 - \nu^2)]$ and $D_{\text{w}} = Et_{\text{w}}^3/[12(1 - \nu^2)]$ being the flexural rigidities of the individual flanges and webs respectively.

As for the purely pinned or rigid joint, one more boundary condition at the more compressed web and flange junction can be obtained. For the purely pinned joint case, the flanges do not buckle, hence:

$$\theta_{\text{f}} = f'_{\text{f}}(x = b/2) = 0. \quad (4.12)$$

For the case where the joint rotates as a rigid body, the rotation of the more compressed web and flange are the same, hence:

$$\theta_{\text{f}} = f'_{\text{f}}(x = b/2) = \theta_{\text{w}} = f'_{\text{wc}}(y = -d/2). \quad (4.13)$$

These four equations above, *i.e.* Eqs. (4.7–4.8), (4.12) and (4.13), can resolve the four undetermined coefficients in f_{wc} and f_{f} for the pinned and rigid joint cases respectively.

However, for the semi-rigid joint case, the fourth boundary condition cannot be obtained directly as for the pinned and rigid joint cases above. When the more compressed web buckles, both the flanges and the joint rotational springs provide the web with restraints. Therefore, by isolating the more compressed web plate, the total rotational stiffness provided by the flanges together with the rotational spring can be replaced by an equivalent rotational spring $c_{\theta\text{f}}$, as shown in Figure 4.3(d). Moreover, since the flanges and the rotational springs are effectively in series, the following standard relationship can be used:

$$\frac{1}{c_{\theta\text{f}}} = \frac{1}{c_{\theta}} + \frac{1}{c_{\text{f}}}, \quad (4.14)$$

where c_{f} is the equivalent rotational stiffness accounting for the rotational restraint provided

by the flanges, as shown in Figure 4.4(a). In the rigid joint case, where $c_\theta \rightarrow \infty$ and $c_{\theta f} = c_f$,

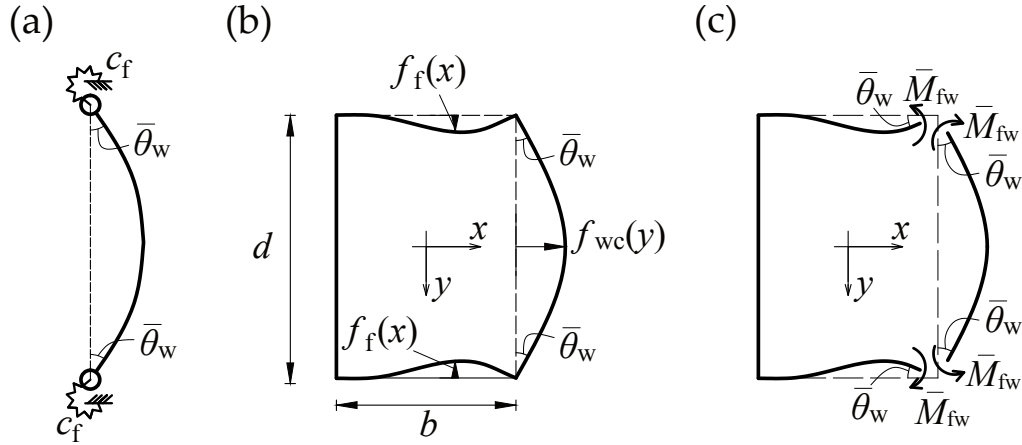


Figure 4.4: (a) Equivalent rotational springs with stiffness c_f on the more compressed web provided by the connecting flange. (b) Cross-section component of the local mode in the flanges $f_f(x)$ and the more compressed web $f_{wc}(y)$ for the rigid joint case due to the rotation of the flange and the more compressed web at the junction, $\bar{\theta}_w$. (c) Free-bodies of the more compressed web–flange junctions; \bar{M}_{fw} is the bending moment within the flange and the more compressed web at the junction.

the rotational stiffness c_f can be determined by considering the continuity of moment and rotation at the junctions, as shown in Figure 4.4(b–c), hence:

$$\bar{M}_{fw} = c_f \bar{\theta}_w = \left[D_w \left(\frac{\partial^2 w_{wc}}{\partial y^2} + \nu \frac{\partial^2 w_{wc}}{\partial z^2} \right) \right]_{y=-d/2}, \quad (4.15)$$

where:

$$\bar{\theta}_w = \frac{\partial w_{wc}}{\partial y} \Big|_{y=-d/2} = w [f'_{wc}(y = -d/2)], \quad (4.16)$$

$$\frac{\partial^2 w_{wc}}{\partial y^2} \Big|_{y=-d/2} = w [f''_{wc}(y = -d/2)], \quad (4.17)$$

$$\frac{\partial^2 w_{wc}}{\partial z^2} \Big|_{y=-d/2} = \ddot{w} [f_{wc}(y = -d/2)] = 0. \quad (4.18)$$

Substituting the displacement function for the more compressed web in the rigid joint case,

the rotational stiffness c_f can be obtained:

$$c_f = \frac{4D_f}{b} \quad (4.19)$$

and an expression for the equivalent rotational spring stiffness $c_{\theta f}$ can be expressed thus:

$$c_{\theta f} = \frac{c_\theta}{c_\theta/c_f + 1}. \quad (4.20)$$

Therefore, the final boundary condition to determine the undetermined parameters is given by the relationship:

$$c_{\theta f}\theta_w = \left[D_w \left(\frac{\partial^2 w_{wc}}{\partial y^2} + \nu \frac{\partial^2 w_{wc}}{\partial z^2} \right) \right]_{y=-d/2}. \quad (4.21)$$

Based on these conditions, the coefficients A_i , where $i = \{0, 1, 2\}$ and B_0 can be determined:

$$\begin{aligned} A_0 &= 0, \\ A_1 &= -\frac{2\pi\bar{c}_\theta(\bar{c}_\theta + 2)}{b^2\phi_c(\bar{c}_\theta + 1)(\pi\phi_c\phi_t^3\bar{c}_\theta - 4\phi_c\phi_t^3\bar{c}_\theta - 2\bar{c}_\theta - 2)}, \\ A_2 &= \frac{2\pi\bar{c}_\theta(\bar{c}_\theta + 2)}{b^3\phi_c(\bar{c}_\theta + 1)(\pi\phi_c\phi_t^3\bar{c}_\theta - 4\phi_c\phi_t^3\bar{c}_\theta - 2\bar{c}_\theta - 2)}, \\ B_0 &= -\frac{2(2\phi_c\phi_t^3\bar{c}_\theta + \bar{c}_\theta + 1)}{\pi\phi_c\phi_t^3\bar{c}_\theta - 4\phi_c\phi_t^3\bar{c}_\theta - 2\bar{c}_\theta - 2}, \end{aligned} \quad (4.22)$$

where $\bar{c}_\theta = c_\theta/c_f$, $\phi_t = t_f/t_w$ and $\phi_c = d/b$. It should be stressed that when $c_\theta \rightarrow \infty$, f_f and f_{wc} converge to the rigid joint case, *i.e.* $\theta_f = f'_f(x = b/2) = \theta_w = f'_{wc}(y = -d/2)$; when $c_\theta \rightarrow 0$, f_f and f_{wc} converge to the pinned joint case, *i.e.* $f_f = 0$ and $f_{wc} = \cos(\pi y/d)$.

4.2.2 Total potential energy

The total potential energy V comprises the contributions from the strain energy U stored from the global bending of the strut, axial and shear stresses in the whole cross-section,

the local bending of the flanges and the more compressed web, the rotational springs and the work done by the external load $P\mathcal{E}$, where \mathcal{E} is the total end-shortening.

The only contribution to the global bending strain energy $U_{b,o}$ is from the webs through the sway mode, since the membrane strain energy contributions from the flanges and webs account for the effect of global bending through the tilt mode, as shown in Figure 4.2(a).

Therefore, the global bending strain energy, $U_{b,o}$, can be expressed thus:

$$U_{b,o} = 2 \int_0^L \frac{EI_w}{2} \ddot{W}^2 dz = EI_w \int_0^L q_s^2 \frac{\pi^4}{L^2} \sin^2 \frac{\pi z}{L} dz, \quad (4.23)$$

where $EI_w = Edt_w^3/12$ is the flexural rigidity about the local weak neutral axis of the web and dots represent differentiation with respect to z . The factor of 2 is included to account for both webs.

The local bending strain energy stored in both flanges and the more compressed web can be determined with the following standard expressions:

$$U_{b,fl} = D_f \int_0^L \int_{-b/2}^{b/2} \left\{ \left(\frac{\partial^2 w_f}{\partial z^2} + \frac{\partial^2 w_f}{\partial x^2} \right)^2 - 2(1-\nu) \left[\frac{\partial^2 w_f}{\partial z^2} \frac{\partial^2 w_f}{\partial x^2} - \left(\frac{\partial^2 w_f}{\partial z \partial x} \right)^2 \right] \right\} dx dz, \quad (4.24)$$

$$U_{b,wcl} = \frac{D_w}{2} \int_0^L \int_{-d/2}^{d/2} \left\{ \left(\frac{\partial^2 w_{wc}}{\partial z^2} + \frac{\partial^2 w_{wc}}{\partial y^2} \right)^2 - 2(1-\nu) \left[\frac{\partial^2 w_{wc}}{\partial z^2} \frac{\partial^2 w_{wc}}{\partial y^2} - \left(\frac{\partial^2 w_{wc}}{\partial z \partial y} \right)^2 \right] \right\} dy dz. \quad (4.25)$$

Since it is assumed that there is no buckling displacement in the less compressed web, it naturally follows that there is zero local bending strain energy in that element.

The membrane strain energy in the flanges $U_{m,f}$ is derived from considering the direct strains (ε) and the shear strains (γ). The complete direct strain expression for the flanges can be written as:

$$\varepsilon_{z,f} = \frac{\partial u_t}{\partial z} + \frac{\partial u_f}{\partial z} + \frac{1}{2} \left(\frac{\partial w_f}{\partial z} \right)^2 - \Delta, \quad (4.26)$$

where the first term is from the global mode and $u_t = x\theta(z)$, being the ‘tilt’ in-plane displacement; the second and third terms are the local components obtained based on von Kármán plate theory; the final term is the purely in-plane compressive strain. The corresponding shear strain component can be written thus:

$$\gamma_{xz,f} = \frac{\partial u_f}{\partial x} + \frac{\partial W}{\partial z} - \theta + \frac{\partial w_f}{\partial x} \frac{\partial w_f}{\partial z}. \quad (4.27)$$

From the previous numerical study (Shen *et al.*, 2015), the transverse stress component was shown to be very small when compared with the other two components, a finding that also coincides with earlier analytical work (Koiter & Pignataro, 1976a), hence it is not included presently. The complete expression for the membrane strain energy stored in both flanges can be written thus:

$$U_{m,f} = 2 \int_0^L \int_{-t_f/2}^{t_f/2} \int_{-b/2}^{b/2} \frac{1}{2} (E\varepsilon_{z,f}^2 + G\gamma_{xz,f}^2) dx dy dz. \quad (4.28)$$

The membrane strain energy stored in the more compressed web also comprises direct and shear strain energy contributions. As for the less compressed web, the expression is more straightforward since it is assumed that there are no local buckling related terms. The complete expressions for the direct strain in the more and less compressed webs are:

$$\varepsilon_{z,wc} = \varepsilon_{z,wco} - \Delta + \frac{\partial u_{wc}}{\partial z} + \frac{1}{2} \left(\frac{\partial w_{wc}}{\partial z} \right)^2, \quad (4.29)$$

$$\varepsilon_{z,wt} = \varepsilon_{z,wto} - \Delta, \quad (4.30)$$

where the direct strains from the global mode, *i.e.* $\varepsilon_{z,wco}$ and $\varepsilon_{z,wto}$, can be written thus:

$$\varepsilon_{z,wco} = -\frac{b}{2} \dot{\theta} = -q_t \frac{b\pi^2}{2L} \sin \frac{\pi z}{L}, \quad (4.31)$$

$$\varepsilon_{z,wto} = +\frac{b}{2} \dot{\theta} = q_t \frac{b\pi^2}{2L} \sin \frac{\pi z}{L}. \quad (4.32)$$

Unlike the flanges, the shear strain within the webs only contain terms from the local mode. The shear strain in the less compressed web is zero and the shear strain in the more compressed web can be written thus:

$$\gamma_{yz,wc} = \frac{\partial u_{wc}}{\partial y} + \frac{\partial w_{wc}}{\partial y} \frac{\partial w_{wc}}{\partial z}. \quad (4.33)$$

The transverse stress is once again neglected in the current formulation for the same reasons as outlined above, thus the membrane strain energy contributions from the webs $U_{m,wc}$ and $U_{m,wt}$ can be given respectively thus:

$$U_{m,wc} = \int_0^L \int_{-t_w/2}^{t_w/2} \int_{-d/2}^{d/2} \frac{1}{2} (E\varepsilon_{z,wc}^2 + G\gamma_{yz,wc}^2) dy dx dz, \quad (4.34)$$

$$U_{m,wt} = \int_0^L \int_{-t_w/2}^{t_w/2} \int_{-d/2}^{d/2} \frac{1}{2} E\varepsilon_{z,wt}^2 dy dx dz. \quad (4.35)$$

The strain energy stored in the rotational springs, U_{sp} , accounting for the web–flange joints in the side of the more compressed web, is given by the following expression:

$$U_{sp} = 2 \int_0^L \frac{1}{2} c_\theta \left(\left. \frac{\partial w_f}{\partial x} \right|_{x=b/2} - \left. \frac{\partial w_{wc}}{\partial y} \right|_{y=-d/2} \right)^2 dz. \quad (4.36)$$

The factor of 2 is included to account for the rotation of both corners, as shown in Figure 4.3(a).

The total end-shortening \mathcal{E} comprises components from pure squash, the global sway mode and the local in-plane displacement. Hence, the work done by the external load P is given by the expression:

$$P\mathcal{E} = P \int_0^L \left(q_s^2 \frac{\pi^2}{2} \cos^2 \frac{\pi z}{L} + \Delta - \Delta_m \right) dz, \quad (4.37)$$

with:

$$\Delta_m = \frac{[2\phi_t \{g_f\}_x + \{g_{wc}\}_y] \dot{u}}{2b(\phi_t + \phi_c)}, \quad (4.38)$$

where $\{g_f\}_x$ and $\{g_{wc}\}_y$ are definite integrals with respect to their corresponding subscript

x or y , thus:

$$\{g_f\}_x = \int_{-b/2}^{b/2} g_f dx, \quad \{g_{wc}\}_y = \int_{-d/2}^{d/2} g_{wc} dy. \quad (4.39)$$

In summary, the total potential energy V can be expressed by the summation of all the strain energy terms minus the work done by the external load:

$$V = U_{b,o} + U_{m,f} + U_{m,wc} + U_{m,wt} + U_{b,fl} + U_{b,wcl} + U_{sp} - P\mathcal{E}. \quad (4.40)$$

4.2.3 Governing equations

By performing the calculus of variations on the total potential energy V , the governing equations of equilibrium can be obtained. The integrand of the total potential energy V can be written as a Lagrangian (\mathcal{L}) of the form thus:

$$V = \int_0^L \mathcal{L}(\ddot{w}, \dot{w}, w, \dot{u}, u, z) dz. \quad (4.41)$$

The equilibrium states of the system can be obtained by invoking the condition that V is stationary by setting the first variation of V , *i.e.* δV , to zero, where:

$$\delta V = \int_0^L \left(\frac{\partial \mathcal{L}}{\partial \ddot{w}} \delta \ddot{w} + \frac{\partial \mathcal{L}}{\partial \dot{w}} \delta \dot{w} + \frac{\partial \mathcal{L}}{\partial w} \delta w + \frac{\partial \mathcal{L}}{\partial \dot{u}} \delta \dot{u} + \frac{\partial \mathcal{L}}{\partial u} \delta u \right) dz. \quad (4.42)$$

Since $\delta \ddot{w} = d(\delta \dot{w})/dz$, $\delta \dot{w} = d(\delta w)/dz$ and $\delta \dot{u} = d(\delta u)/dz$, integration by parts allows the development of the Euler–Lagrange equations for w and u , resulting in a fourth order nonlinear ordinary differential equation (ODE) in w and a second order nonlinear ODE in

u :

$$\begin{aligned}
& D_w \left[2\phi_t^3 \{f_f^2\}_x + \{f_{wc}^2\}_y \right] \ddot{w} - \frac{3Et_w}{2} \left[2\phi_t \{f_f^4\}_x + \{f_{wc}^4\}_y \right] \dot{w}^2 \ddot{w} \\
& - Gt_w \left[2\phi_t \{f_f'^2 f_f^2\}_x + \{f_{wc}'^2 f_{wc}^2\}_y \right] (\ddot{w}w^2 + \dot{w}^2 \dot{w}) \\
& - Et_w \left[2\phi_t \{g_f f_f^2\}_x + \{g_{wc} f_{wc}^2\}_y \right] (\ddot{u} \dot{w} + \dot{u} \ddot{w}) \\
& + \frac{\pi^2 Et_w b q_t}{2L} \left[\frac{4\phi_t}{b} \{x f_f^2\}_x + \{f_{wc}^2\}_y \right] \left(\sin \frac{\pi z}{L} \ddot{w} + \frac{\pi}{L} \cos \frac{\pi z}{L} \dot{w} \right) \\
& + \left\{ 2D_w \nu \left[2\phi_t^3 \{f_f f_f''\}_x + \{f_{wc} f_{wc}''\}_y \right] - 2D_w (1 - \nu) \left[2\phi_t^3 \{f_f'^2\}_x + \{f_{wc}'^2\}_y \right] \right. \\
& \left. + Et_w \Delta \left[2\phi_t \{f_f^2\}_x + \{f_{wc}^2\}_y \right] \right\} \ddot{w} - Gt_w \left[2\phi_t \{g_f' f_f' f_f\}_x + \{g_{wc}' f_{wc}' f_{wc}\}_y \right] \dot{u} w \\
& - \frac{2\pi^2 Gt_f}{L} \{f_f' f_f\}_x (q_s - q_t) \sin \frac{\pi z}{L} w + K w = 0,
\end{aligned} \tag{4.43}$$

$$\begin{aligned}
& Et_w \left[2\phi_t \{g_f^2\}_x + \{g_{wc}^2\}_y \right] \ddot{u} + Et_w \left[2\phi_t \{g_f f_f^2\}_x + \{g_{wc} f_{wc}^2\}_y \right] \dot{w} \ddot{w} \\
& - Gt_w \left[2\phi_t \{g_f' f_f' f_f\}_x + \{g_{wc}' f_{wc}' f_{wc}\}_y \right] \dot{w} w + 2Gt_f \{g_f'\}_x (q_s - q_t) \pi \cos \frac{\pi z}{L} \\
& - \frac{\pi^3 Et_w b q_t}{2L^2} \left[\frac{4\phi_t}{b} \{x g_f\}_x + \{g_{wc}\}_y \right] \cos \frac{\pi z}{L} - Gt_w \left[2\phi_t \{g_f'^2\}_x + \{g_{wc}'^2\}_y \right] u = 0,
\end{aligned} \tag{4.44}$$

where K is the coefficient of the linear term w , sometimes also referred to as the foundation term, which is well known to affect the local buckling load ([Hunt & Wadee, 1998](#)). Currently, it comprises a plate-related term K_p and a spring-related term K_s , *i.e.* $K = K_p + K_s$, where:

$$K_p = D_w \left[2\phi_t^3 \{f_f''^2\}_x + \{f_{wc}''^2\}_y \right], \quad K_s = 2c_\theta (f_{wc}'|_{y=d/2} - f_f'|_{x=b/2})^2. \tag{4.45}$$

Moreover, equilibrium also requires the minimization of V with respect to the generalized coordinates q_s , q_t and Δ , leading to three integral equations:

$$\begin{aligned}
\frac{\partial V}{\partial q_s} &= \pi^2 Gt_f b L (q_s - q_t) + \frac{\pi^4 EI_w q_s}{L} - P \frac{\pi^2 L q_s}{2} \\
& - 2\pi Gt_f \int_0^L \left[\{g_f'\}_x u + \{f_f' f_f\}_x \dot{w} w \right] \cos \frac{\pi z}{L} dz = 0,
\end{aligned} \tag{4.46}$$

$$\frac{\partial V}{\partial q_t} = \frac{\pi^4 E t_w b^2 d q_t}{4L} \left[1 + \frac{\phi_t}{3\phi_c} \right] - \pi^2 G t_f b L (q_s - q_t) \quad (4.47)$$

$$\begin{aligned} & + 2\pi G t_f \int_0^L \left[\{g'_f\}_x u + \{f'_f f_f\}_x \dot{w} \right] \cos \frac{\pi z}{L} dz \\ & - \frac{\pi^2 E b t_w}{2L} \int_0^L \left\{ \left[\{g_{wc}\}_y + \frac{4\phi_t}{b} \{x g_f\}_x \right] \dot{u} \right. \\ & \quad \left. + \left[\frac{1}{2} \{f_{wc}^2\}_y + \frac{2\phi_t}{b} \{x f_f^2\}_x \right] \dot{w}^2 \right\} \sin \frac{\pi z}{L} dz = 0, \\ \frac{\partial V}{\partial \Delta} & = -E t_w \int_0^L \left\{ \left[\{g_{wc}\}_y + 2\phi_t \{g_f\}_x \right] \dot{u} + \left[\frac{1}{2} \{f_{wc}^2\}_y + \phi_t \{f_f^2\}_x \right] \dot{w}^2 \right\} dz \\ & + 2E t_w d L \Delta \left(1 + \frac{\phi_t}{\phi_c} \right) - P L = 0. \end{aligned} \quad (4.48)$$

Since the strut is an integral member, Eq. (4.47) provides a relationship between q_s and q_t before the local mode is triggered, *i.e.* when $u = w = \dot{w} = 0$:

$$q_s = (1 + s) q_t, \quad (4.49)$$

where:

$$s = \frac{\pi^2 E b^2}{4G L^2} \left(\frac{1}{3} + \frac{\phi_c}{\phi_t} \right). \quad (4.50)$$

The boundary conditions for w and u and their derivatives are for a simple-support at $z = 0$ and for symmetry at $z = L/2$:

$$w(0) = \dot{w}(0) = \dot{w}(L/2) = \ddot{w}(L/2) = u(L/2) = 0. \quad (4.51)$$

A further boundary condition can be obtained from minimizing V and it is a condition that relates to matching the in-plane strain at the ends:

$$\begin{aligned} \dot{u}(0) & \left[\{g_{wc}^2\}_y + 2\phi_t \{g_f^2\}_x \right] + \frac{\dot{w}^2(0)}{2} \left[\{g_{wc} f_{wc}^2\}_y + 2\phi_t \{g_f f_f^2\}_x \right] \\ & - \Delta \left[\{g_{wc}\}_y + 2\phi_t \{g_f\}_x \right] + \frac{P \left[\{g_{wc}\}_y + 2\phi_t \{g_f\}_x \right]}{2E t_w d (1 + \phi_t / \phi_c)} = 0. \end{aligned} \quad (4.52)$$

Linear eigenvalue analysis for the perfect column is conducted to determine the critical load for global buckling P_o^C . This is achieved by considering the condition where the Hessian matrix \mathbf{V}_{ij} is singular when $q_s = q_t = w = u = 0$, where:

$$\mathbf{V}_{ij} = \begin{bmatrix} \frac{\partial^2 V}{\partial q_s^2} & \frac{\partial^2 V}{\partial q_s \partial q_t} \\ \frac{\partial^2 V}{\partial q_t \partial q_s} & \frac{\partial^2 V}{\partial q_t^2} \end{bmatrix}, \quad (4.53)$$

which produces the following expression:

$$P_o^C = \frac{2\pi^2 EI_w}{L^2} + \frac{\pi^2 Et_f b^3}{2(1+s)L^2} \left(\frac{1}{3} + \frac{\phi_c}{\phi_t} \right). \quad (4.54)$$

Note that if Euler–Bernoulli bending theory had been assumed, the shear modulus $G \rightarrow \infty$, which implies that $s \rightarrow 0$, and P_o^C would reduce to the classical Euler load, as would be expected.

4.3 Numerical results

In this section, representative numerical examples from the variational model with a varying rotational stiffness c_θ are presented. The geometric properties of the example strut are presented in Table 4.1. The Young’s Modulus E and Poisson’s ratio ν of the material are

Table 4.1: Geometric properties of the rectangular hollow section strut in the numerical example, selected to ensure global buckling is critical.

Length	Flange width	Web depth	Flange thickness	Web thickness
L	b	d	t_f	t_w
5250 mm	60 mm	120 mm	1 mm	1 mm

chosen to be 210 kN/mm² and 0.3 respectively. For the case where $c_\theta = 0$, the theoretical buckling stresses and critical mode are presented in Table 4.2. The global buckling stress is calculated using Eq. (4.54) where $\sigma_o^C = P_o^C/A$ and A is the total area of the cross-section. The local buckling stress is estimated by using the classical plate buckling stress

Table 4.2: Theoretical values of the global and local critical buckling stresses for the pinned cross-section case.

σ_o^C (N/mm ²)	$\sigma_{1,w}^C$ (N/mm ²)	$\sigma_{1,f}^C$ (N/mm ²)	Critical mode
52.70	52.72	210.88	Global

$\sigma_{1,w}^C = k_p D_w \pi^2 / (d^2 t_w)$ for the webs and $\sigma_{1,f}^C = k_p D_f \pi^2 / (b^2 t_f)$ for the flanges (Bulson, 1970).

Since it is initially assumed that $c_\theta = 0$, all the plates have effectively pinned edges and the length of the strut is much larger than the width of the plate, $k_p = 4$ is adopted for the plate buckling coefficient to obtain a lower bound. With the increase of the rotational stiffness c_θ , the local buckling load P_1^C would also increase whereas the global buckling load P_o^C would remain the same. Therefore, the selected geometric dimensions and material properties ensure that global buckling is always critical for any positive value of c_θ in the examples presented.

The system of nonlinear differential equations, *i.e.* Eqs. (4.43)–(4.44), subject to the corresponding integral (Eqs. (4.46)–(4.48)) and boundary conditions (Eqs. (4.51) and (4.52)), is solved numerically using the continuation and bifurcation software AUTO (Doedel & Oldeman, 2009). The software is not only capable of solving the nonlinear ordinary differential equations numerically, but it also maintains the intrinsic bifurcational structure of the solutions. Moreover, importantly, the software can switch between, as well as trace, different equilibrium paths, allowing the evolution of the geometrically perfect cases to be studied.

The solution strategy for using AUTO is shown diagrammatically in Figure 4.5. The critical load P_o^C is obtained explicitly from Eq. (4.54). Using the continuation method, the generalized global sway mode amplitude q_s is first varied, while $P = P_o^C$, to obtain the secondary bifurcation points S_i , where the first one ($S_1 \equiv S$) pinpoints the location where interactive buckling is practically triggered. Subsequently, the second run is started at the secondary bifurcation point S using the branch switching facility within the software and P is varied to compute the interactive buckling path. With the increase of c_θ , the value

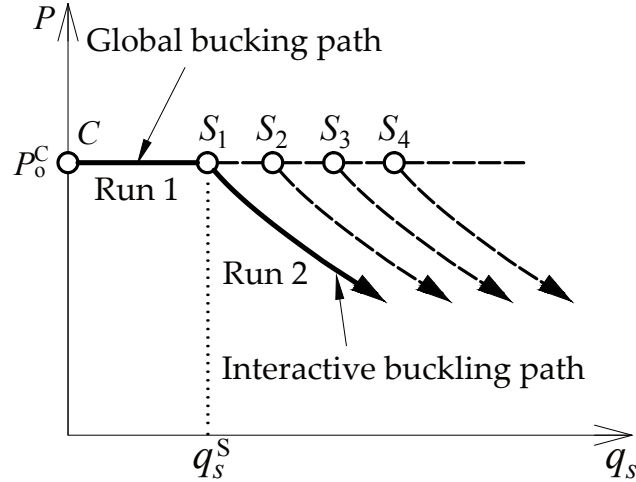


Figure 4.5: Numerical continuation procedure for determining the interactive buckling equilibrium path for perfect struts where global buckling is critical. The thicker solid line shows the actual solution path. Circles marked C and S_i represent the critical and secondary bifurcation points respectively. The generalized coordinate of the sway mode at the secondary bifurcation point is defined as q_s^S .

of q_s at the secondary bifurcation point q_s^S increases due to the higher local buckling stress for the more compressed web relative to the constant global buckling load.

However, before conducting numerical continuation in AUTO, the effects of the rotational springs on the nonlinear ODEs are investigated. The explicit spring related term in the ODEs is the coefficient of linear term w , K , in Eq. (4.43). Figure 4.6(a) shows the relationship between the individual components of K , *i.e.* K_p and K_s defined in Eq. (4.45), while varying the normalized joint rigidity \bar{c}_θ . It can be seen that the plate-related term K_p rises with the increase of the rotational spring stiffness. Moreover, it reaches a plateau with the value being the same as the rigid joint case when the normalized joint stiffness \bar{c}_θ is close to 7. As for the spring-related term K_s , it reaches a peak and then decays to zero as \bar{c}_θ is increased further. This can be attributed to the fact that the rotation of the flange and the more compressed web at the joint are approximately the same and thus $f'_{wc}(y=d/2) = f'_{wt}(x=b/2)$. Based on this analysis, struts with the cross-section joint stiffness c_θ listed in Table 4.3 are used in the subsequent numerical study.

Unstable post-buckling behaviour arising from the triggering of interactive buckling is

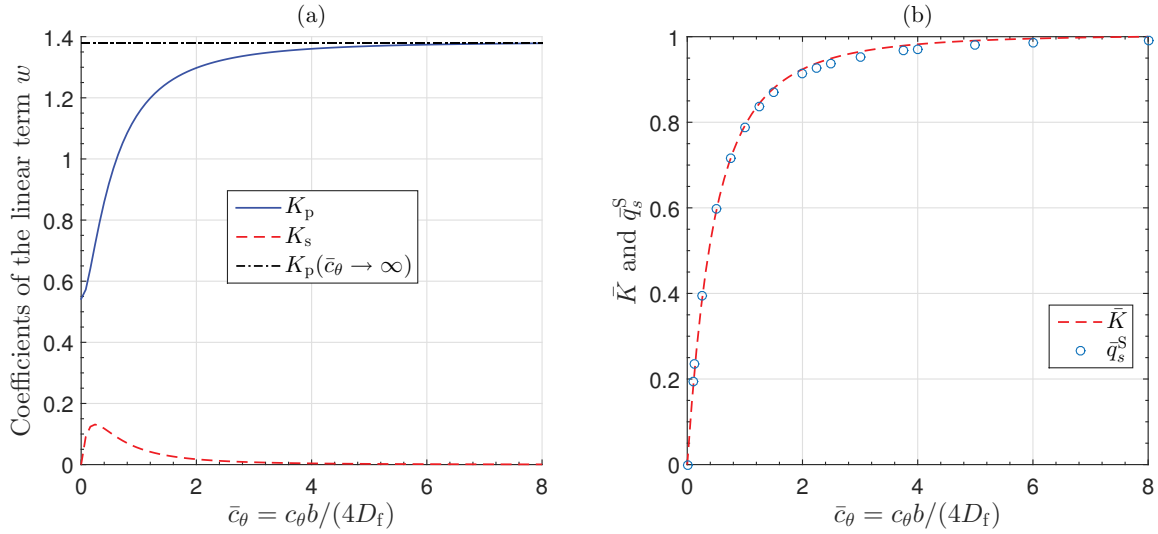


Figure 4.6: (a) The influence of the rotational spring stiffness on the coefficient of the linear term w in Eq. (4.43) for the example strut with the properties listed in Table 4.1. The quantities K_p and K_s are the plate and spring related terms respectively, given in Eq. (4.45). (b) The normalized values of the coefficient of the linear term \bar{K} and the generalized coordinate of the global sway mode \bar{q}_s^S versus the normalized joint rigidity \bar{c}_θ .

Table 4.3: Rotational stiffness c_θ and the corresponding normalized stiffness \bar{c}_θ values used in the numerical studies.

c_θ (Nm/m)	0	160.26	641.03	2564.10	∞
\bar{c}_θ	0	0.125	0.5	2	∞

observed in all example struts presented in Figure 4.7. Figure 4.7(a) shows that the severe

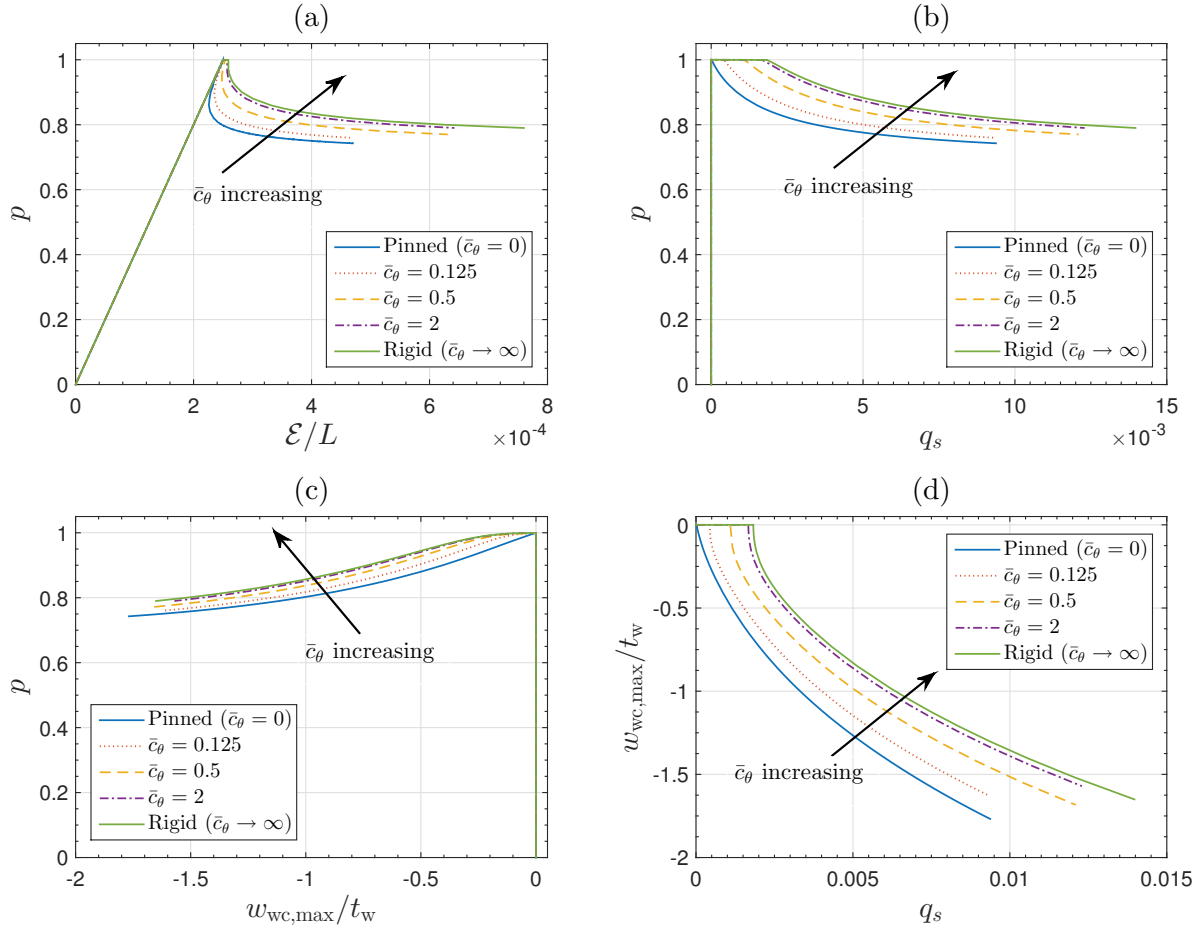


Figure 4.7: Numerical equilibrium paths for struts with varying joint rigidity \bar{c}_θ . Graphs of the normalized load $p = P/P_o^C$ versus (a) the normalized end-shortening \mathcal{E}/L , (b) the generalized coordinate of the sway mode q_s and (c) the normalized peak amplitude of local deformation in the more compressed web $w_{wc,max}/t_w$; (d) $w_{wc,max}/t_w$ versus q_s .

snap-back phenomenon in the normalized load $p = P/P_o^C$ versus the normalized end-shortening \mathcal{E}/L relationship is mollified with the increasing joint rigidity \bar{c}_θ . Moreover, stiffer joints within the cross-section also lead to a higher residual post-buckling capacity. A gradual transition from highly unstable behaviour to less unstable behaviour can be observed. At the same load level in the post-buckling range, a higher joint rigidity case corresponds to larger global and local mode amplitudes, as shown in Figure 4.7(b, c). The generalized global mode amplitude to trigger the mode interaction q_s^S increases significantly especially between $\bar{c}_\theta = 0$ and $\bar{c}_\theta = 0.5$. The rate of increase in q_s^S , however, begins to reduce

significantly as \bar{c}_θ is increased further; for example, the equilibrium path of the case with $\bar{c}_\theta = 2$ is very similar to the rigid case. By normalizing K and q_s^S between the pinned and rigid cases, thus:

$$\bar{K} = \frac{K - K_0}{K_R - K_0}, \quad \bar{q}_s^S = \frac{q_s^S - q_{s0}^S}{q_{sR}^S - q_{s0}^S}, \quad (4.55)$$

where K_0 is the coefficient of the linear term for the pinned case ($\bar{c}_\theta = 0$); K_R is the coefficient of the linear term for the rigid case ($c_\theta \rightarrow \infty$); q_{s0}^S is the value of q_s^S for the pinned case ($\bar{c}_\theta = 0$); and q_{sR}^S is the value of q_s^S for the rigid case ($c_\theta \rightarrow \infty$). It can be observed in Figure 4.6(b) that the respective distributions of \bar{K} and \bar{q}_s^S with respect to \bar{c}_θ are practically identical, which is understandable since K is known to control the local buckling load (Hunt & Wadee, 1998) and that in turn controls when the secondary bifurcation occurs.

From the solutions of the out-of-plane components of the local mode w , a wavelength variation is observed with the progress of interactive buckling, as shown in Figure 4.8. The initially localized buckling mode spreads outwards from the mid-span of the column, developing with more peaks and troughs alongside a clear reduction in wavelength as the modal amplitude becomes larger and the load drops in the post-buckling range. Since the global buckling mode amplitude at the secondary bifurcation is relatively larger for struts with a higher joint rigidity, the local buckling profile is initially more localized at mid-span at $p = 0.995$. Moreover, the higher joint rigidity also leads to a smaller wavelength at the same load level. This is in accord with results in previous work on I-section struts (Bai & Wadee, 2015b) and on struts on elastic softening–hardening foundations (Budd *et al.*, 2001).

Three dimensional representations of the numerical solutions with $\bar{c}_\theta = 0$, $\bar{c}_\theta = 0.5$ and the rigid case ($\bar{c}_\theta \rightarrow \infty$) at load levels $p = 0.995$ and $p = 0.790$ in the post-buckling range are shown in Figure 4.9. It should be emphasized that there is no buckle in the flanges for the

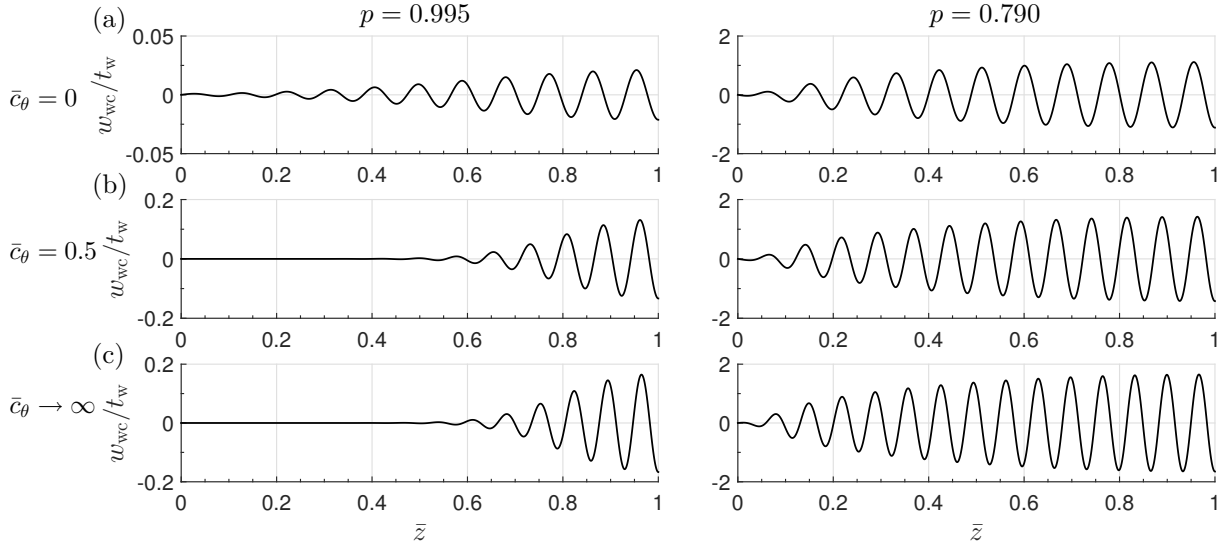


Figure 4.8: Numerical solutions of the normalized local out-of-plane displacement in the more compressed web w_{wc}/t_w for the cases where: (a) $\bar{c}_\theta = 0$ (pinned), (b) $\bar{c}_\theta = 0.5$ and (c) $\bar{c}_\theta \rightarrow \infty$ (rigid). The left and right columns correspond to the normalized load in the post-buckling range $p = 0.995$ and $p = 0.790$ respectively. Note that the longitudinal coordinates are normalized with respect to half the strut length $\bar{z} = 2z/L$ and that the buckling wavelengths are reduced at the lower load.

$\bar{c}_\theta = 0$ case, as shown in Figure 4.9(a), owing to the lack of interaction between adjacent plates within the cross-section.

4.4 Verification and discussion

The validated FE model developed in Chapter 3 was used to verify the variational model. A linear eigenvalue analysis is first conducted in ABAQUS to obtain the global buckling load of the FE model with the same geometric properties as the variational model. The global critical load is found to be 18.90 kN, approximately 0.21% smaller than the analytical solution P_o^C using Eq. (4.54). The insignificant error is postulated to be derived from the global mode displacement field assumption in Eq. (4.1), which comprises only a single term.

In terms of the nonlinear behaviour, equilibrium paths obtained from both the variational and FE models show excellent agreement for all rotational stiffness cases listed in Table 4.3,

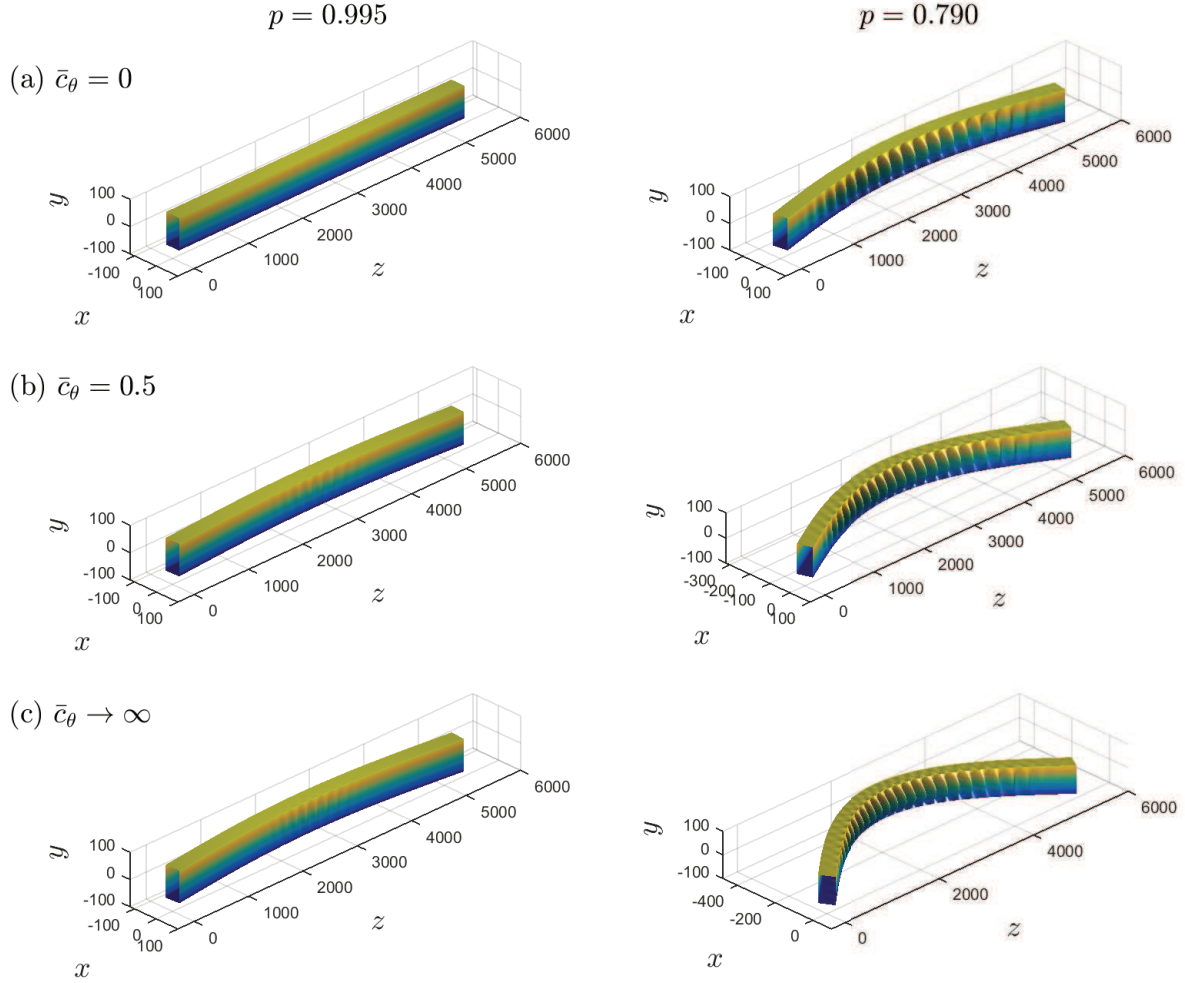


Figure 4.9: 3D visualization of the numerical solutions from the variational model, plotted using MATLAB (MATLAB, 2010). The results are shown for the post-buckling equilibrium states for the cases where: (a) $\bar{c}_\theta = 0$ (pinned), (b) $\bar{c}_\theta = 0.5$ and (c) $\bar{c}_\theta \rightarrow \infty$ (rigid) from the top to the bottom row respectively. The left and right columns correspond to the normalized load in the post-buckling range $p = 0.995$ and $p = 0.790$ respectively. Note that the deformations shown have been amplified by a factor of 5 and the longitudinal coordinate (z) has been scaled by a factor of 0.25, both to aid visualization. All dimensions are in millimetres.

with the variational model exhibiting a very slightly stiffer response in the advanced post-buckling range. Three typical cases, *i.e.* $\bar{c}_\theta = 0$ (pinned), $\bar{c}_\theta = 0.5$ and $\bar{c}_\theta \rightarrow \infty$ (rigid), are presented and discussed currently, as shown in Figure 4.10. From both the p - q_s and $w_{wc,max}$ - q_s equilibrium diagrams, it can be observed that the values of q_s^S for all cases are extremely close between the two models. As for the local–global mode relationship, the present model matches better with the FE results, when compared to previous studies on

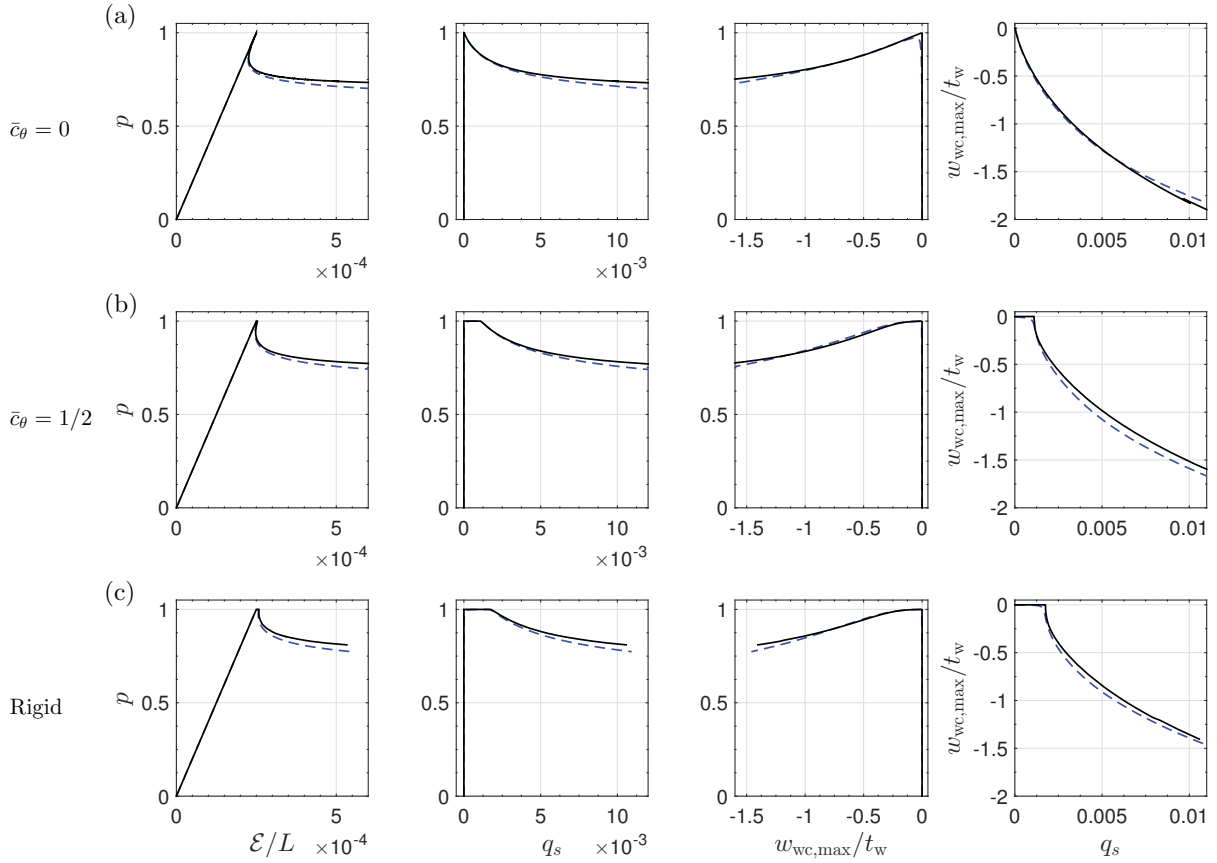


Figure 4.10: Comparison of the post-buckling equilibrium paths for the cases where: (a) $\bar{c}_\theta = 0$ (pinned), (b) $\bar{c}_\theta = 0.5$, and (c) $\bar{c}_\theta \rightarrow \infty$ (rigid) from the variational (solid line) and FE (dashed line) models. Graphs of the normalized load ratio $p = P/P_o^C$ versus the normalized end-shortening \mathcal{E}/L in the first column, the generalized coordinate of the sway mode q_s in the second column, and the normalized maximum amplitude of local deflection in the more compressed web $w_{wc,max}/t_w$ in the third column; the fourth column shows $w_{wc,max}/t_w$ versus q_s .

I-section struts (Bai & Wadee, 2015b; Liu & Wadee, 2015) using the same methodology. Apart from the fact that the cross-section functions f_f , f_{wc} , g_f and g_{wc} have assumed forms, an additional source for the stiffer response of the variational model is derived from the underlying assumption that the neutral axis location remains unchanged. In fact, the neutral axis of bending would move to the less compressed web side when local buckling occurs in the more compressed web and flanges, as shown in Figure 4.11; however, it is worth emphasising presently that the errors are fundamentally small.

Figure 4.12 shows the evolution of the cross-section deformation at mid-span for the cases

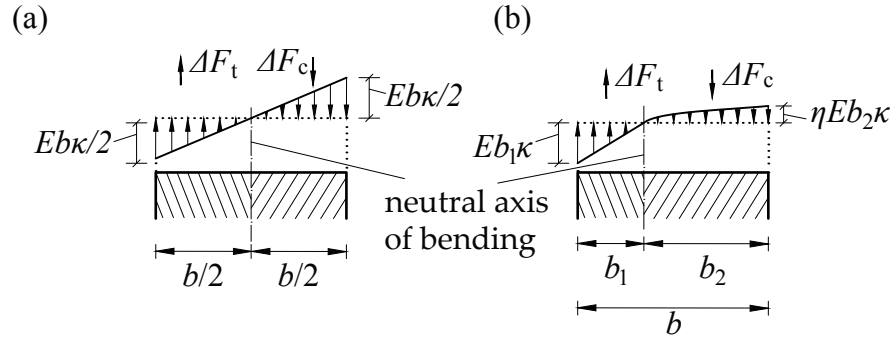


Figure 4.11: Neutral axis shifting due to local buckling in the more compressed web and flanges. The variation in the normal stress due to the global curvature κ (a) before local buckling and (b) after local buckling in the more compressed web and flanges; δF_t and δF_c are the relative load changes in the less and more compressed sides of the cross-section respectively, which include the unloading and loading of the flanges and webs; η is the stiffness reduction factor for the more compressed web due to local buckling.

where $\bar{c}_\theta = 0$ (pinned), $\bar{c}_\theta = 0.5$, and $\bar{c}_\theta \rightarrow \infty$ (rigid). The excellent comparisons through-

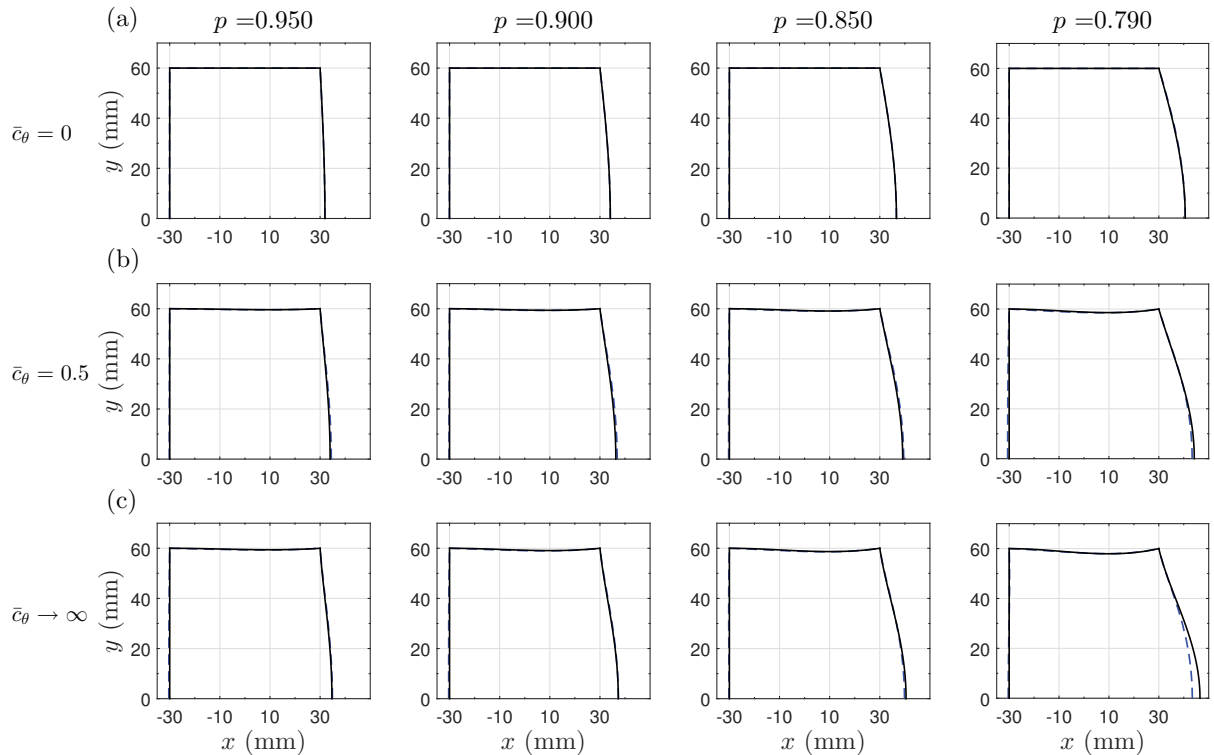


Figure 4.12: Local deformation of the cross-section for the example struts at mid-span at different load levels for the cases where: (a) $\bar{c}_\theta = 0$ (pinned), (b) $\bar{c}_\theta = 0.5$, and (c) $\bar{c}_\theta \rightarrow \infty$ (rigid) from the variational (solid line) and FE (dashed line) models. Note that the displacements shown have been amplified by a factor of 20 to aid visualization.

out verify the effectiveness of the assumed cross-sectional shape functions. At $\bar{c}_\theta = 0$, there is no out-of-plane displacement in the flanges. With the increase of the joint rigidity \bar{c}_θ , the flanges bulge increasingly and finish with the rotation at the joint being equal to the more compressed web, *i.e.* $\theta_f(x = b/2) = \theta_{wc}(y = d/2)$, as shown in Figure 4.12(c). A small difference in the more compressed web deflection can be observed between the FE and the variational results in the advanced post-buckling range; the difference increases as \bar{c}_θ is increased, as shown in the fourth column of Figure 4.12(b, c). Moreover, the discrepancy in the less compressed web is caused by the large amount of bending in that web (Shen *et al.*, 2015), which is currently not included as an extra local displacement function in the variational model.

Figure 4.13 shows the comparison for the normalized solutions of the out-of-plane displacement in the more compressed web w_{wc}/t_w for the cases where $\bar{c}_\theta = 0$ (pinned), $\bar{c}_\theta = 0.5$, and $\bar{c}_\theta \rightarrow \infty$ (rigid), at $p = 0.950$ and $p = 0.790$ respectively. An excellent comparison

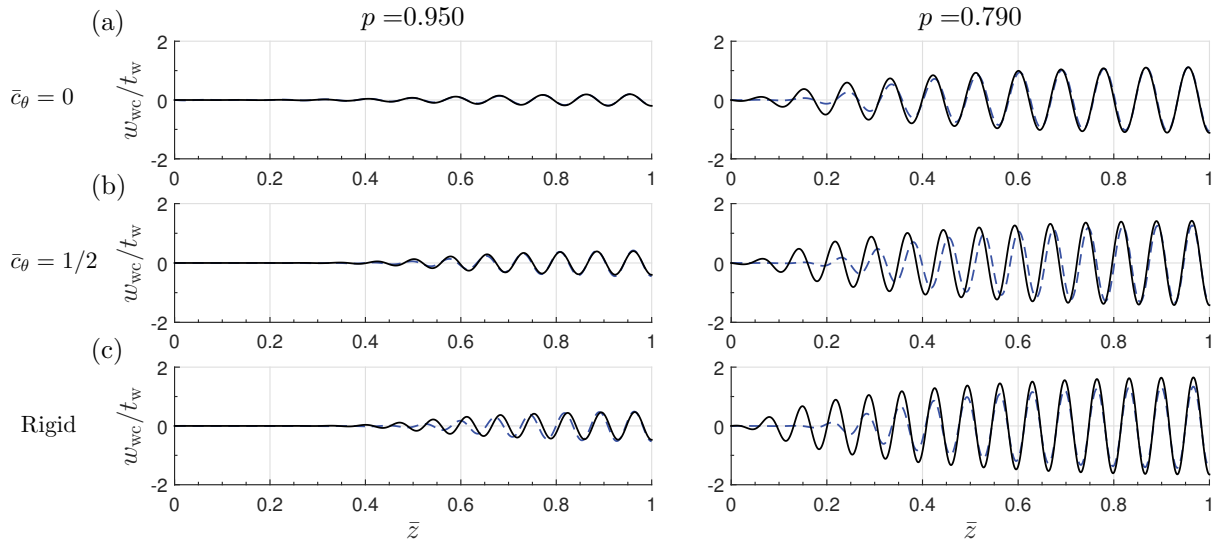


Figure 4.13: Comparisons of the numerical solutions for the normalized local out-of-plane displacement w_{wc}/t_w in the more compressed web from the variational (solid line) and FE (dashed line) models for $\bar{c}_\theta = 0$ (pinned), $\bar{c}_\theta = 0.5$ and $\bar{c}_\theta \rightarrow \infty$ (rigid) cases respectively. Note that the longitudinal coordinate is normalized with respect to half of the strut length $\bar{z} = 2z/L$.

is observed in all the cases, especially for the case where $\bar{c}_\theta = 0$. However, the slight

error increases with the commensurate increase of the joint rigidity and the progression of interactive buckling, as described for Figure 4.12. In the variational model, the profile of the local mode is assumed to be the same in the whole strut and the amplitude is allowed to vary, see Eqs. (4.3) and (4.4). This assumption holds true for the $\bar{c}_\theta = 0$ case, where the profile is always the sine function, since the flanges provide no rotational restraints to the buckled web. For the cases where $\bar{c}_\theta > 0$, the cross-section profile depends on the bending moment at the web–flange junctions, which varies along the length. Figure 4.12 demonstrates that the currently assumed shape function matches well with the cross-section deformation at mid-span. Therefore, the errors, although very small, become increasingly larger towards the ends, where the profile is slightly different from that at mid-span.

Since the FE package ABAQUS can automatically calculate and output the strain energy in individual plates and the work done by load as standard, it provides an additional perspective for validating the variational model. Figure 4.14 presents the comparisons between the components of the potential energy during the loading for the cases where $\bar{c}_\theta = 0$ (pinned), $\bar{c}_\theta = 0.5$ and $\bar{c}_\theta \rightarrow \infty$ (rigid). As for the energy in the variational model, the strain energy in the flanges U_f comprises the local bending energy $U_{b,f}$, given in Eq. (4.24), and the membrane strain energy $U_{m,f}$, given in Eq. (4.28). The strain energy in the more compressed web U_{wc} comprises half of the total global bending energy $U_{b,o}/2$, given in Eq. (4.23), the local bending energy $U_{b,wcl}$, given in Eq. (4.25), and the membrane strain energy $U_{m,wc}$, given in Eq. (5.28). The strain energy in the less compressed web U_{wt} comprises half of the total global bending energy $U_{b,o}/2$, given in Eq. (4.23), and the membrane strain energy $U_{m,wt}$, given in Eq. (4.35). The work done by load term $P\mathcal{E}$ is given in Eq. (4.37).

There are three individual stages that may be observed in the energy relationships versus the generalized coordinate of the sway mode q_s . The first stage corresponds to the purely axial deformation of the struts under compression before the buckling load is reached. The

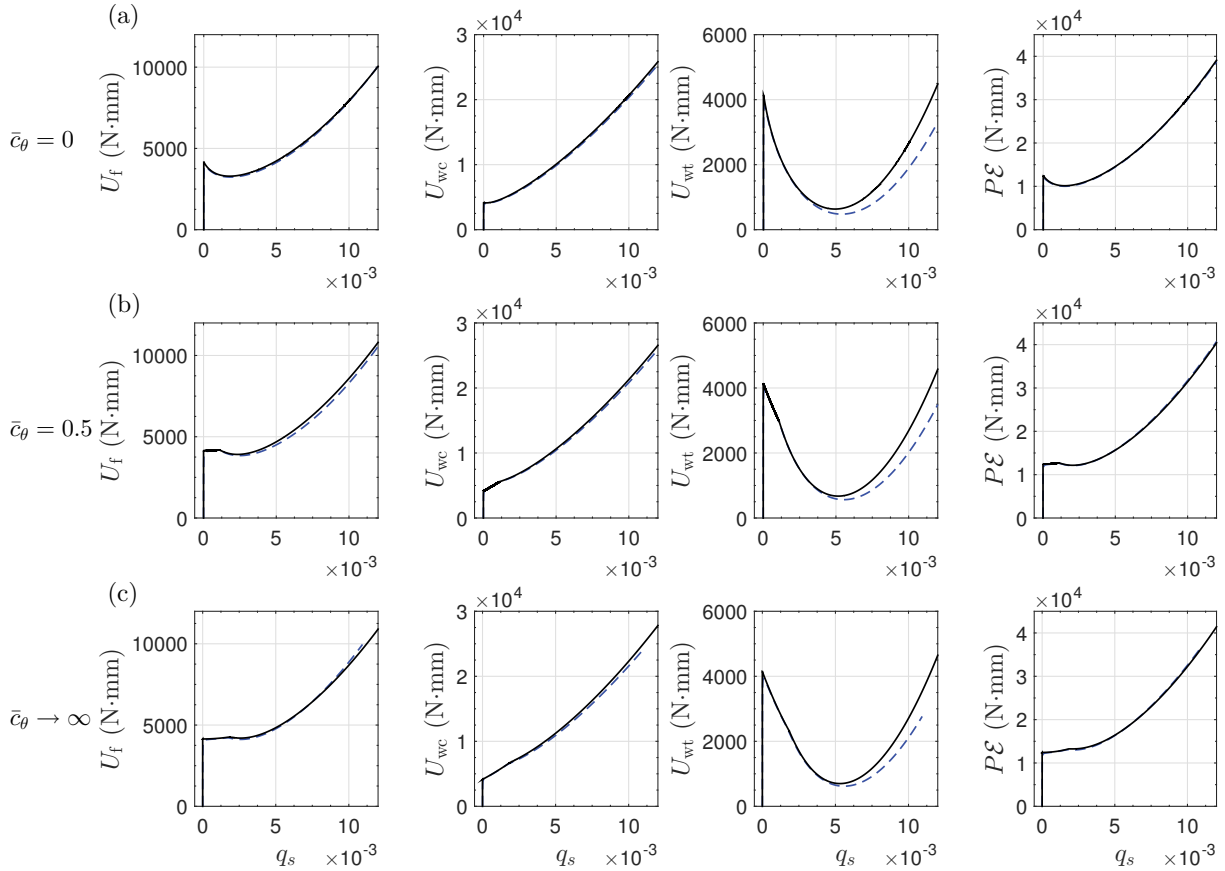


Figure 4.14: Comparisons of the potential energy components from the example struts with joint rigidities $\bar{c}_\theta = 0$ (pinned), $\bar{c}_\theta = 0.5$ and $\bar{c}_\theta \rightarrow \infty$ (rigid) from the variational (solid line) and FE (dashed line) models. Graphs of the total strain energy stored in the flanges U_f , more compressed web U_{wc} , less compressed web U_{wt} and the work done by the load $P\mathcal{E}$ respectively, all versus the generalized coordinate of the sway mode q_s .

second stage is where pure global buckling is triggered and the third stage is where interactive buckling progresses with the simultaneous increase of the global and local modes. Except for the strain energy in the more compressed web, an energy reduction can be observed at the initial stage of interactive buckling. For the strain energy in the flanges and the work done by the load, the reduction corresponds to the ‘snap-back’ that features in the load–end-shortening relationship shown in Figure 4.7(a) for small values of \bar{c}_θ . With the increase of the joint rigidity, the reduction diminishes; for the rigid joint case, the energy reduction is essentially negligible, which perhaps explains why no snap-back is observed for that case.

The comparisons of the strain energy terms and the work done by the load between the FE and the variational models are generally excellent for all values of \bar{c}_θ . The main source of discrepancy resides in the strain energy stored in the less compressed web U_{wt} , with the relative errors being 40%, 33% and 28% at $q_s = 0.01$ for $\bar{c}_\theta = 0$ (pinned), $\bar{c}_\theta = 0.5$ and $\bar{c}_\theta \rightarrow \infty$ (rigid) cases respectively. However, the proportion of the strain energy stored in the less compressed web compared to the total strain energy stored in the rectangular hollow section strut, U_{wt}/U , is relatively small; for the rigid joint case, $U_{\text{wt}}/U \approx 0.07$ when $q_s = 0.01$. Therefore, the errors for the entire system due to errors from the less compressed web are in fact below 3%. Referring to Figure 4.7(d), at the same value of q_s , the local mode amplitude is higher for smaller values of \bar{c}_θ . Therefore, any neutral axis movement would be larger for smaller values of \bar{c}_θ . This contributes to the reason why the error in the strain energy stored in the less compressed web is the largest in the effective pinned joint case at the same value of q_s . The neutral axis movement due to the plate buckling and the assumed cross-section shape functions (see Figure 4.12) are the two principal factors that are postulated to be responsible for the small overall discrepancy in the strain energy of the more compressed and less compressed webs. All of these factors taken together lead to a very marginally stiffer response in the variational model, but it is not particularly large and is only really significant in the far-field post-buckling range. Hence, it may be concluded that the developed variational model has been satisfactorily verified and may now be exploited further.

4.5 Simplified approach to predicting the location of secondary bifurcation

From the numerical results, as presented in Figure 4.7, unstable post-buckling equilibrium paths were observed after the secondary bifurcation point and the severely unstable behaviour is somewhat mollified with the increase of \bar{c}_θ , which in turn shows an increase in

the generalized coordinate of the sway mode at the secondary bifurcation point q_s^S . Earlier studies (van der Neut, 1969; van der Neut, 1973; Thompson & Hunt, 1973; Thompson & Hunt, 1984; Wadee & Farsi, 2015) on thin-walled structures susceptible to mode interaction suggest that the imperfection sensitivity decreases with the relative increase of q_s^S since the proximity of the critical and secondary bifurcation points is reduced. A simplified approach for predicting q_s^S based on the verified variational model is presented currently since this quantity provides a valuable indication of the potential sensitivity to imperfections.

When the strut buckles in a purely global mode, the direct strain $\varepsilon_{z,wc}$ can be written as Eq. (4.29) by assuming the local buckling components are zero:

$$\varepsilon_{z,wc} = \varepsilon_{z,wco} - \Delta, \quad (4.56)$$

where $\varepsilon_{z,wco}$ is obtained from Eq. (4.31); Δ is also obtained by assuming the local buckling components in Eq. (4.48) are zero. Since the transverse strain is neglected, the compressive stress in the more compressed web $\sigma_{z,wc}$ can be written thus:

$$\sigma_{z,wc} = E\varepsilon_{z,wc} = -\frac{\pi^2 Ebq_t}{2L} \sin \frac{\pi z}{L} - \frac{P_o^C}{2t_w d (1 + \phi_t/\phi_c)}. \quad (4.57)$$

From the numerical results in Figure 4.8, the local mode is initially localized. Instead of analysing the whole web with the entire strut length, a plate element at mid-span with length l_e is isolated to compute the approximate local buckling coefficient k_p , as shown in Figure 4.15. It is assumed that within this plate element, the axial stress is constant along the length with the value of the direct stress at mid-span. Therefore, when the direct stress in the more compressed web $\sigma_{z,wc}$ reaches the local buckling stress, $\sigma_{wcl}^C = k_p \pi^2 E / [12(1 - \nu^2)(d/t_w)^2]$, it may be assumed that interactive buckling will also be triggered.

Since the cross-section shape function for the more compressed web has already been obtained, with reference to Eq. (4.5) and Figure 4.3(d), the local buckling coefficient k_p

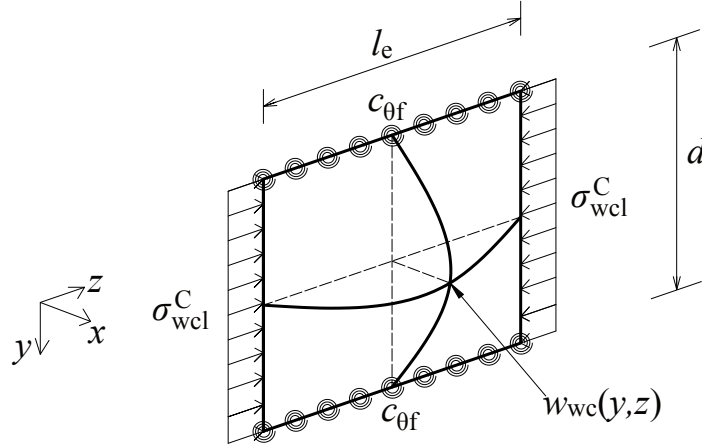


Figure 4.15: Deformed shape of the isolated plate element of the more compressed web under the critical buckling stress σ_{wcl}^C . The effective length of the element is l_e with depth d and thickness t_w . The equivalent rotational stiffness provided by the flanges and the rotational springs at the web–flange joints is $c_{\theta f}$.

may be calculated by applying minimum potential energy principles on the isolated plate element of the more compressed web. The buckled displacement field is thus assumed to be:

$$w_{wc}(y, z) = Q f_{wc}(y) \sin \frac{\pi z}{l_e}, \quad (4.58)$$

where Q is a new generalized coordinate representing the amplitude of the local buckling mode within the plate element shown in Figure 4.15.

The strain energy U in the plate element comprises two components: the strain energy stored from local buckling $U_{b,wcl}$ and the strain energy stored in the equivalent rotational springs $U_{sp,\theta f}$:

$$U_{b,wcl} = \frac{D_w}{2} \int_0^{l_e} \int_{-d/2}^{d/2} \left\{ \left(\frac{\partial^2 w_{wc}}{\partial z^2} + \frac{\partial^2 w_{wc}}{\partial y^2} \right)^2 - 2(1 - \nu) \left[\frac{\partial^2 w_{wc}}{\partial z^2} \frac{\partial^2 w_{wc}}{\partial y^2} - \left(\frac{\partial^2 w_{wc}}{\partial z \partial y} \right)^2 \right] \right\} dy dz, \quad (4.59)$$

$$U_{sp,\theta f} = 2 \int_0^{l_e} \frac{1}{2} c_{\theta f} \left(\frac{\partial w_{wc}}{\partial y} \Big|_{y=-d/2} \right)^2 dz, \quad (4.60)$$

where the expression for $c_{\theta f}$ was presented in Eq. (4.20). The work done by load term is given by the following standard expression:

$$P\Delta = \frac{\sigma_{\text{wcl}}^{\text{C}} t_{\text{w}}}{2} \int_0^{l_e} \int_{-d/2}^{d/2} \left(\frac{\partial w_{\text{wc}}}{\partial z} \right)^2 dy dz. \quad (4.61)$$

The total potential energy can thus be written as:

$$V = U_{\text{b,wcl}} + U_{\text{sp,\theta f}} - P\Delta, \quad (4.62)$$

and by setting $dV/dQ = 0$ for equilibrium, the following expression for k_p is obtained:

$$k_p = a_0 + a_1 \phi_1^2 + \frac{1}{\phi_1^2}, \quad (4.63)$$

where $\phi_1 = l_e/d$ with a_0 and a_1 being constants that are functions of ϕ_c , ϕ_t and \bar{c}_θ , thus:

$$a_0 = \frac{10 \{ 4\phi_c \phi_t^3 \bar{c}_\theta [\phi_c \phi_t^3 \bar{c}_\theta (5\pi^2 - 48) + 3(\pi^2 - 8)(\bar{c}_\theta + 1)] + 3\pi^2 (\bar{c}_\theta + 1)^2 \}}{4\phi_c \phi_t^3 \bar{c}_\theta [\phi_c \phi_t^3 \bar{c}_\theta (\pi^4 + 15\pi^2 - 240) + 15(\pi^2 - 8)(\bar{c}_\theta + 1)] + 15\pi^2 (\bar{c}_\theta + 1)^2}, \quad (4.64)$$

$$a_1 = \frac{15 \{ 4\phi_c \phi_t^3 \bar{c}_\theta [\phi_c \phi_t^3 \bar{c}_\theta (\pi^2 - 8) + (\pi^2 - 4)(\bar{c}_\theta + 1)] + \pi^2 (\bar{c}_\theta + 1)^2 \}}{4\phi_c \phi_t^3 \bar{c}_\theta [\phi_c \phi_t^3 \bar{c}_\theta (\pi^4 + 15\pi^2 - 240) + 15(\pi^2 - 8)(\bar{c}_\theta + 1)] + 15\pi^2 (\bar{c}_\theta + 1)^2}. \quad (4.65)$$

Defining $\phi_1 = (a_1)^{-1/4}$, an expression for the minimum value of k_p is found:

$$k_p = a_0 + 2\sqrt{a_1}. \quad (4.66)$$

By referring to the relationship between q_s and q_t given in Eq. (5.37), an explicit expression for the secondary bifurcation point q_s^{S} is duly obtained:

$$q_s^{\text{S}} = \frac{2(\sigma_{\text{wcl}}^{\text{C}} - \sigma_o^{\text{C}})(1+s)L}{\pi^2 Eb}. \quad (4.67)$$

4.6 Parametric studies

To verify the simplified approach, a couple of parametric studies are presented where the length and the cross-section aspect ratios are varied. The results from the simplified approach are compared to the full variational model solved using numerical continuation in AUTO.

4.6.1 Length variation

The strut geometries have the same cross-section properties as shown in Table 4.1 and the joint rigidity values are $\bar{c}_\theta = \{0, 0.5, 1, \infty\}$. The length of the struts is varied from the case where global buckling is marginally critical to $L = 7200$ mm.

The comparison of the generalized coordinate of the sway mode at the secondary bifurcation point q_s^S between the full variational model using numerical continuation and the simplified approach using Eq. (4.67) is shown in Figure 4.16. With the increase of the length L , q_s^S increases; the simplified approach predicts q_s^S with good accuracy and is always on the safe side. The source of error arises from the fact that the simplified model assumes that the stress is constant along the length of the plate element. However, the stress distribution is effectively a combination of the uniform stress from the axial load and the superposition of the sine function from global buckling, as given in Eq. (4.57).

4.6.2 Cross-section aspect ratio variation

For the cross-section aspect ratio parametric study, the geometric properties of the struts are shown in Table 4.4. The cross-section aspect ratio ϕ_c ranges from 1 to 2.5; the width of the flange b is fixed and the wall thickness is fixed and uniform throughout the cross-section. The length of each strut is selected to ensure that global buckling is marginally

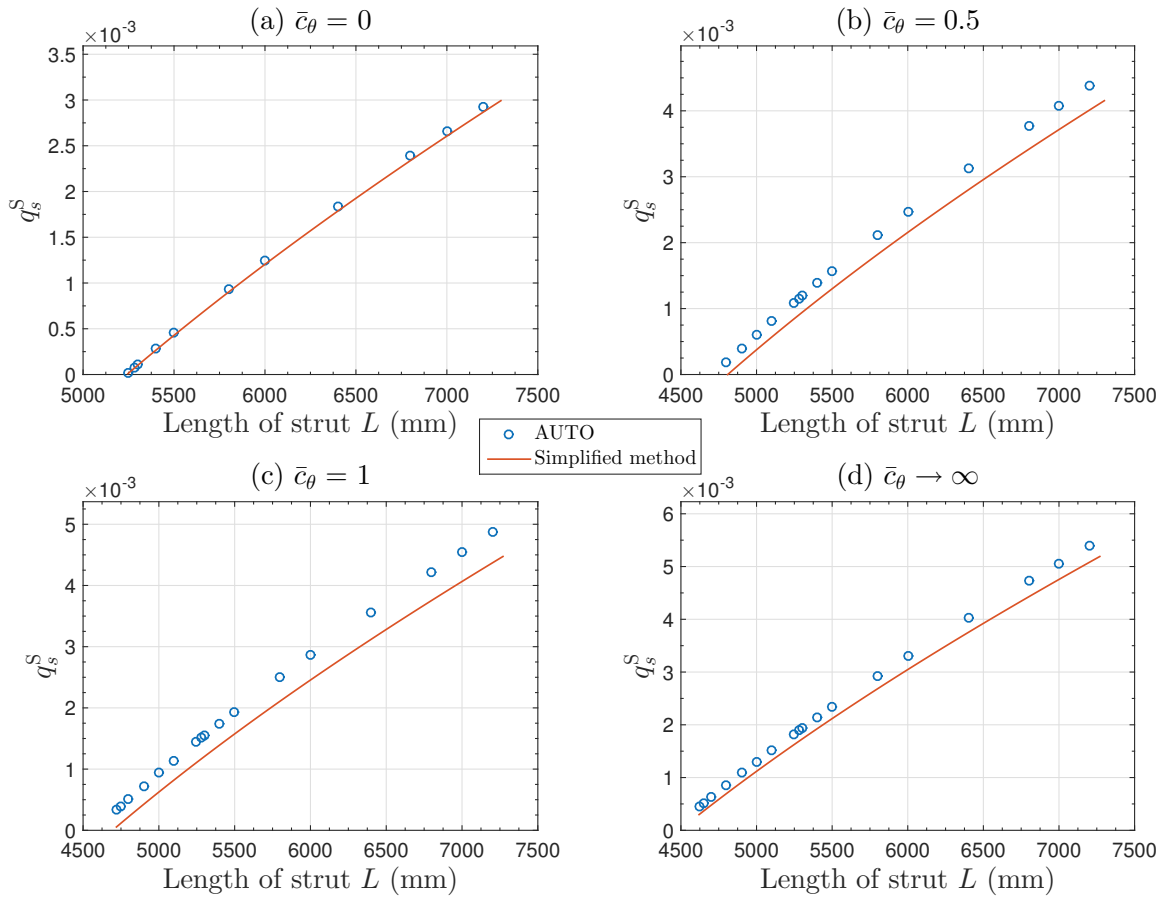


Figure 4.16: Comparison of the generalized coordinate of the sway mode at the secondary bifurcation point q_s^S using numerical continuation with AUTO for the full variational model alongside the presented simplified method.

Table 4.4: Geometric properties of the rectangular hollow section struts in the parametric study, selected to ensure global buckling is critical. The flange width $b = 60$ mm and the wall thickness $t_f = t_w = 1$ mm throughout.

Cross-section aspect ratio	Web depth d	Length L
ϕ_c	(mm)	(mm)
1	60	2430
1.25	75	3120
1.5	90	3830
1.75	105	4540
2	120	5250
2.5	150	6700

critical ($P_o^C/P_1^C \approx 0.995$) for the pinned joint case. Since q_s^S is related to the strut length, the current focus is on the local buckling coefficient k_p at the secondary bifurcation point.

Table 4.5 shows the comparisons between the evaluation of the local buckling coefficient

Table 4.5: Comparison of the local buckling coefficient k_p for the more compressed web at the secondary bifurcation point from the full variational model, $k_{p,AUTO}$, solved using numerical continuation with AUTO and the simplified method, $k_{p,EQ}$, using Eq. (4.66) from the pinned case ($\bar{c}_\theta = 0$) to the rigid case ($\bar{c}_\theta \rightarrow \infty$) for different cross-section aspect ratios.

ϕ_c	Ranges		$k_{p,EQ}/k_{p,AUTO}$	
	$k_{p,AUTO}$	$k_{p,EQ}/k_{p,AUTO}$	Mean	COV
1	4.01 → 5.03	0.968 → 0.998	0.980	1.16%
1.25	4.01 → 5.32	0.941 → 0.998	0.959	2.22%
1.5	4.01 → 5.47	0.936 → 0.997	0.956	2.38%
1.75	4.01 → 5.56	0.938 → 0.998	0.957	2.31%
2	4.01 → 5.63	0.941 → 1.000	0.960	2.28%
2.5	4.01 → 5.76	0.947 → 0.998	0.964	1.93%

k_p at the secondary bifurcation point from the full variational model solved by numerical continuation and the approximation presented in Eq. (4.66).

In the same way, as shown in the length parameter study results, the simplified method is demonstrated to predict k_p with very good accuracy yet being always on the safe side for the cases studied. Defining $k_{p,EQ}$ as the prediction of k_p from the simplified method using Eq. (4.66) and $k_{p,AUTO}$ as the value of k_p from the full variational model, for each cross-section case, the mean value of $k_{p,EQ}/k_{p,AUTO}$ ranges between 0.956 and 0.980 and the maximum COV (coefficient of variation) is 2.38%. With the increase of the aspect ratio ϕ_c , an increase in k_p is observed due to the rotational restraint provided by the relatively narrower flanges. Therefore, a larger cross-section aspect ratio would lead to a relatively higher post-buckling strength.

Since cases with rigid joints ($\bar{c}_\theta \rightarrow \infty$) and uniform thickness ($\phi_t = 1$) are most common in practice, a power series approximation for Eq. (4.66) can be derived to order ϕ_c^2 for such cases:

$$k_p = 4.33 + 0.76\phi_c - 0.10\phi_c^2. \quad (4.68)$$

The comparison between this function and Eq. (4.66) is shown in Figure 4.17 and can be seen to be practically perfect for the range shown.

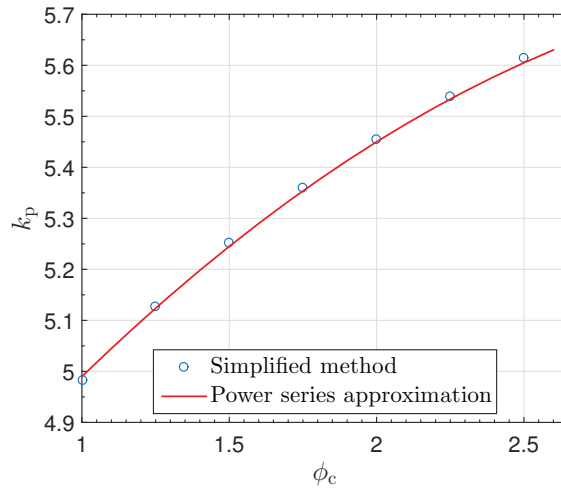


Figure 4.17: The relationship between the local buckling coefficient k_p and the cross-section aspect ratio ϕ_c for the rigid joint case from the simplified method using Eq. (4.66) and the curve fit function given in Eq. (4.68).

4.7 Concluding remarks

A nonlinear variational model describing the interactive buckling of a thin-walled rectangular hollow section strut with varying rigidities of the web–flange joints under pure compression has been developed using variational principles. Numerical examples, focusing on cases where global buckling is critical, have been presented and verified using the FE package ABAQUS. Unstable post-buckling behaviour due to mode interaction was observed. A progressive change in the local buckling mode is identified in terms of both the wavelength and the amplitude. As far as the author is aware, it is the first time that this has been demonstrated in rectangular hollow section struts. With the increase of the cross-section joint rigidity, a transition from highly unstable to more mildly unstable post-buckling behaviour is observed. The excellent comparisons between the variational and FE results verified the effectiveness of the presented methodology.

A simplified method to predict the local buckling coefficient in the more compressed web and the global buckling amplitude at the secondary bifurcation point is proposed based on the verified variational model; it is demonstrated to be simple, yet safe and accurate for the cases studied.

The study in this chapter verifies the analytical methodology adopted and provides a preliminary understanding of the highly nonlinear system. The following chapters build on the findings in this chapter and extend them to analyse cases where local buckling is critical and flange–web joints are rigid alongside more practically realistic cases with initial geometric imperfections.

Chapter 5

Variational modelling of practical cases

The previous chapter introduced a variational model for RHS struts with semi-rigid flange–web joints, but the model was only valid for long length struts where global buckling is critical. Moreover, no geometric imperfections were introduced in the variational model. However, in practice, a large proportion of thin-walled RHS struts are designed with local buckling being critical so as to take full advantage of the high strength to self-weight ratio. The actual flange–web joint properties are rigid more often than not. More importantly, there is always some imperfection in real structures, either in the geometry or in the loading. Previous studies (Koiter & Pignataro, 1976a; Thompson *et al.*, 1976; Loughlan, 1983; Goltermann & Møllmann, 1989; Wadee, 2000; Bai & Wadee, 2015a; Wadee & Farsi, 2015; Liu & Wadee, 2016b) have identified that thin-walled plated structures susceptible to interactive buckling tend to be highly sensitive to imperfections; a tiny imperfection may lead to a significant erosion in the load-carrying capacity. Therefore, in the current chapter, the variational model is extended to include the scenarios where local buckling is critical as well as where both local and global geometric imperfections exist.

The material and cross-section geometric properties of the RHS struts in this chapter are almost the same as those presented in Chapter 4. The only difference is that the joints between the webs and the flanges are assumed to be rigid, hence the following two assumptions are satisfied (Bulson, 1970): (i) the webs and the flanges at their common edges remain orthogonal during buckling; (ii) the wavelengths of the local buckling mode, which simultaneously appear in all constituent plates, are the same. Recalling the variational model in Chapter 4, the same definitions for material and geometric properties are adopted and shown in Figure 4.1.

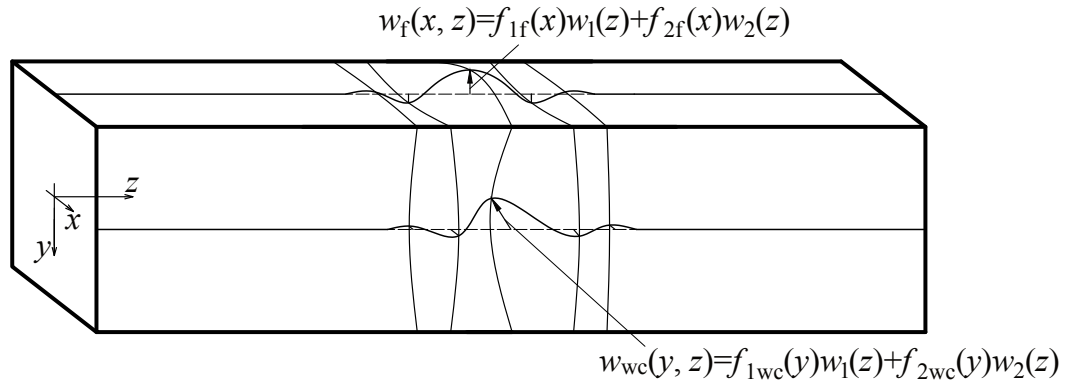
5.1 Modal descriptions

The formulation begins with the description of both the global and the local modal displacements. The global mode description is the same as that in Chapter 4, which is decomposed into two components, a pure lateral displacement W and a pure rotation of the plane sections θ , as presented in Eq. (4.1) and Figure 4.2(a).

The local buckling mode, including out-of-plane and in-plane displacement components, shown in Figure 5.1, is expressed as a combination of the local modes in the pure local buckling case and the case where global buckling is critical, as shown in Figures 5.1 and 5.2, which can be expressed as:

$$\begin{aligned}
 w_f(x, z) &= f_{1f}(x)w_1(z) + f_{2f}(x)w_2(z), \\
 w_{wc}(y, z) &= f_{1wc}(y)w_1(z) + f_{2wc}(y)w_2(z), \\
 w_{wt}(y, z) &= f_{1wt}(y)w_1(z) + f_{2wt}(y)w_2(z), \\
 u_f(x, z) &= g_{1f}(x)u_1(z) + g_{2f}(x)u_2(z), \\
 u_{wc}(y, z) &= g_{1wc}(y)u_1(z) + g_{2wc}(y)u_2(z), \\
 u_{wt}(y, z) &= g_{1wt}(y)u_1(z) + g_{2wt}(y)u_2(z),
 \end{aligned} \tag{5.1}$$

(a) Out-of-plane



(b) In-plane

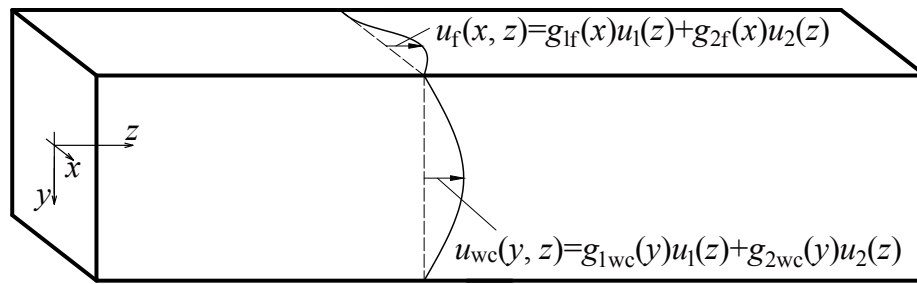
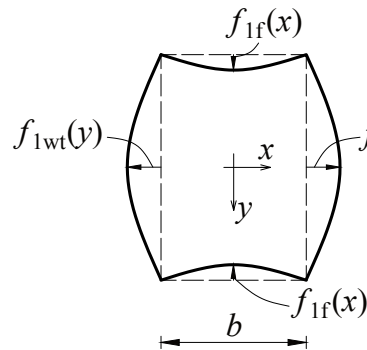


Figure 5.1: (a) Out-of-plane local mode in the flanges $w_f(x, z)$ and in the more compressed web $w_{wc}(y, z)$. (b) In-plane local mode in the flanges $u_f(x, z)$ and in the more compressed web $u_{wc}(y, z)$.

(a) Local mode 1



(b) Local mode 2

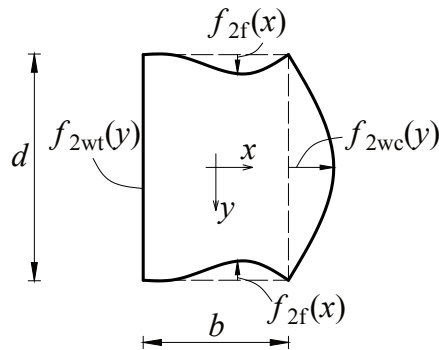


Figure 5.2: Local out-of-plane displacement fields of the cross-section. (a) Pure local buckling case. (b) Interactive buckling case where global buckling is critical.

where f and g are the cross-section components for the out-of-plane and in-plane components respectively; w_i and u_i , where $i = \{1, 2\}$, are the longitudinal out-of-plane and in-plane displacement components respectively. Subscripts 1 and 2 represent the cases where local and global buckling are critical respectively, as shown in Figure 5.2. The subscripts ‘f’ and ‘w’ represent the flanges and webs respectively; subscripts ‘c’ and ‘t’ represent the more and less compressed webs respectively.

The cross-section out-of-plane components f , as shown in Figure 5.2, are estimated by applying kinematic and static boundary conditions for each plate. For the pure local critical mode, as shown in Figure 5.2(a), it is assumed that the out-of-plane displacement in the webs f_{1w} has the functional form that is derived from the conditions of a simply-supported strut (a cosine wave with the current coordinate system) and a beam under pure bending (a parabola from applying Euler–Bernoulli beam theory), thus:

$$f_{1wc} = f_{1wt} = A_{10} \cos \frac{\pi y}{d} + (1 - A_{10}) \left(1 - \frac{4y^2}{d^2} \right). \quad (5.2)$$

For the out-of-plane displacement in the flanges f_{1f} , the functional form is derived from a simply-supported beam with equal and opposite end moments arising from the transfer of moment at the flange–web joints. This naturally leads to the following parabolic form:

$$f_{1f} = B_{10} \left(\frac{x^2}{b^2} - \frac{1}{4} \right). \quad (5.3)$$

The coefficients A_{10} in f_{1wc} and B_{10} in f_{1f} are determined by applying appropriate boundary conditions at the junctions, as shown in Figure 5.3. The form of f_{1wc} and f_{1f} automatically satisfies the natural boundary conditions at the junctions, *i.e.* $f_{1wc}(\pm d/2) = 0$ and $f_{1f}(\pm b/2) = 0$. Owing to the symmetric form of the functions, the junction between the flange and the web with the coordinate $(x = b/2, y = d/2)$ is considered. For rotational

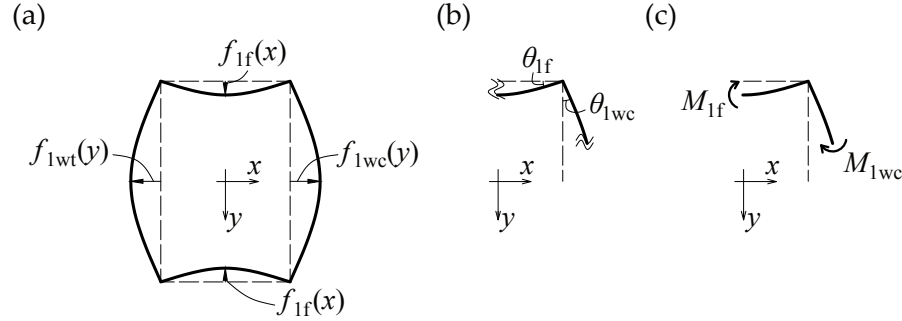


Figure 5.3: (a) Pure local buckling mode. (b) Kinematic boundary condition at the junction; θ_{1f} and θ_{1wc} are the rotations of the flange and the web at the junction respectively. (c) Equilibrium condition at the junction; M_{1f} and M_{1wc} are the bending moments in the flange and the more compressed web at the junction respectively.

continuity, the following boundary condition also needs to be satisfied:

$$\theta_{1f} = \left. \frac{df_{1f}}{dx} \right|_{x=b/2} = \theta_{1wc} = \left. \frac{df_{1wc}}{dy} \right|_{y=d/2}. \quad (5.4)$$

Moreover, moment equilibrium at the junction leads to a further condition:

$$M_{1f}(x = b/2) + M_{1wc}(y = d/2) = 0, \quad (5.5)$$

where:

$$M_{1f}(x = b/2) = \left[D_f \left(\frac{\partial^2 w_{1f}}{\partial x^2} + \nu \frac{\partial^2 w_{1f}}{\partial z^2} \right) \right]_{x=b/2} = D_f w_1 \left. \frac{d^2 f_{1f}}{dx^2} \right|_{x=b/2}, \quad (5.6)$$

$$M_{1wc}(y = d/2) = \left[D_w \left(\frac{\partial^2 w_{1wc}}{\partial y^2} + \nu \frac{\partial^2 w_{1wc}}{\partial z^2} \right) \right]_{y=d/2} = D_w w_1 \left. \frac{d^2 f_{1wc}}{dy^2} \right|_{y=d/2}, \quad (5.7)$$

where $D_f = Et_f^3/[12(1 - \nu^2)]$ and $D_w = Et_w^3/[12(1 - \nu^2)]$ are the flexural rigidities of the individual flange and web plates respectively. The terms related to the Poisson's ratio ν disappear due to the fact that $f_{1f} = f_{1wc} = 0$ at the junction. Based on the boundary conditions presented in Eqs. (5.4) and (5.5), the coefficients A_{10} and B_{10} are thus:

$$A_{10} = \frac{4(\phi_c \phi_t^3 + 1)}{4 + \phi_c \phi_t^3(1 - \pi)}, \quad B_{10} = \frac{4\pi}{\phi_c [4 + \phi_c \phi_t^3(1 - \pi)]}, \quad (5.8)$$

where the cross-section aspect ratio $\phi_c = d/b$, and the flange–web thickness ratio $\phi_t = t_f/t_w$. It should be stressed that the above assumption for f_{1f} and f_{1w} is only valid for rectangular sections ($d > b$), where the critical stress in the webs is smaller than in the flanges. A set of shape functions, which is valid from a square to a rectangular hollow section, is derived from a semi-analytical method, the details of which may be found in Appendix C.

The cross-section components describing mode interaction, where global buckling is critical, can be determined by letting $c_\theta \rightarrow \infty$ in the cross-section shape functions Eqs. (4.5)–(4.6) and (4.22) in Chapter 4:

$$f_{2wc} = \frac{2(2\phi_c\phi_t^3 + 1)}{2 + \phi_c\phi_t^3(4 - \pi)} \cos \frac{\pi y}{d} - \frac{\pi\phi_c\phi_t^3}{2 + \phi_c\phi_t^3(4 - \pi)} \left(1 - \frac{4y^2}{d^2}\right), \quad (5.9)$$

$$f_{2f} = \frac{-2\pi}{\phi_c[2 + \phi_c\phi_t^3(4 - \pi)]} \left(\frac{x}{b} + \frac{1}{2}\right)^2 + \frac{2\pi}{\phi_c[2 + \phi_c\phi_t^3(4 - \pi)]} \left(\frac{x}{b} + \frac{1}{2}\right)^3, \quad (5.10)$$

$$f_{2wt} = 0. \quad (5.11)$$

As for the cross-section shape functions for the in-plane components, g , it was determined that they are same as those of out-of-plane components currently, *i.e.* $g_{if} = f_{if}$, $g_{iwc} = f_{iwc}$ and $g_{iwt} = f_{iwt}$, based on the same assumption adopted in §4.2.1. It should be noted that this assumption may not be consistent with classical theory (Koiter, 1945) for an in-plane displacement field, but the shape function forms do satisfy the kinematic boundary conditions. Moreover, since the energy would be minimized by the longitudinal components of the in-plane displacement, *i.e.* $u_1(z)$ and $u_2(z)$, the approximate nature of the shape function should be mitigated somewhat.

5.2 Geometric imperfections description

An initial out-of-straightness in the x -direction, W_0 , and an initial pure rotation of the plane section θ_0 , corresponding to the sway and tilt components of the global buckling

mode in Eq. (4.1), are introduced to the whole strut respectively as components that form the global imperfection:

$$W_0(z) = -q_{s0}L \sin\left(\frac{\pi z}{L}\right), \quad \theta_0(z) = -q_{t0}\pi \cos\left(\frac{\pi z}{L}\right), \quad (5.12)$$

with q_{s0} and q_{t0} being the respective normalized amplitudes.

The local imperfection is introduced by defining an initial out-of-plane deflection in both flanges and webs, corresponding to the local mode description in Eq. (5.1):

$$\begin{aligned} w_{f0}(x, z) &= f_{1f}(x)w_{10}(z) + f_{2f}(x)w_{20}(z), \\ w_{wc0}(y, z) &= f_{1wc}(y)w_{10}(z) + f_{2wc}(y)w_{20}(z), \\ w_{wt0}(y, z) &= f_{1wt}(y)w_{10}(z) + f_{2wt}(y)w_{20}(z), \end{aligned} \quad (5.13)$$

where the cross-section components f are the same as described in Eqs. (5.2)–(5.3) and (5.9)–(5.11); the longitudinal component of the local imperfection $w_0(z)$ is derived from a first-order approximation from a multiple scale perturbation analysis of a strut on a nonlinear softening foundation, which has been demonstrated to match the least stable localized post-buckling mode shape very well (Wadee *et al.*, 1997):

$$w_{i0}(z) = A_{i0} \operatorname{sech}\left[\alpha_i\left(\frac{z}{L} - \eta\right)\right] \cos\left[\beta_i\pi\left(\frac{z}{L} - \eta\right)\right], \quad (5.14)$$

where $i = \{1, 2\}$, $z \in [0, L]$ and the imperfection is symmetric about $z/L = \eta$. Since previous work on sandwich panels (Wadee, 2000), I-section struts (Bai & Wadee, 2015a), stiffened plates (Wadee & Farsi, 2015) and functionally graded carbon nanotube-reinforced composite beams (Wu *et al.*, 2016) have demonstrated that the drop in the stiffness is largest when the local imperfection is symmetric about midspan, *i.e.* $\eta=1/2$, the value of η is selected to be $1/2$ in the current study. The quantity A_{i0} controls the amplitude of the imperfection component. The parameters α_i and β_i control the degree of localization of the imperfection and the number of sinusoidal half waves of the longitudinal imperfection

component respectively, as shown in Figure 5.4. When $\alpha_i = 0$, the function is periodic; with the increase of α_i , the function becomes increasingly localized. Moreover, in order to be in accord with the boundary condition at ends, β_i has to be an odd number.

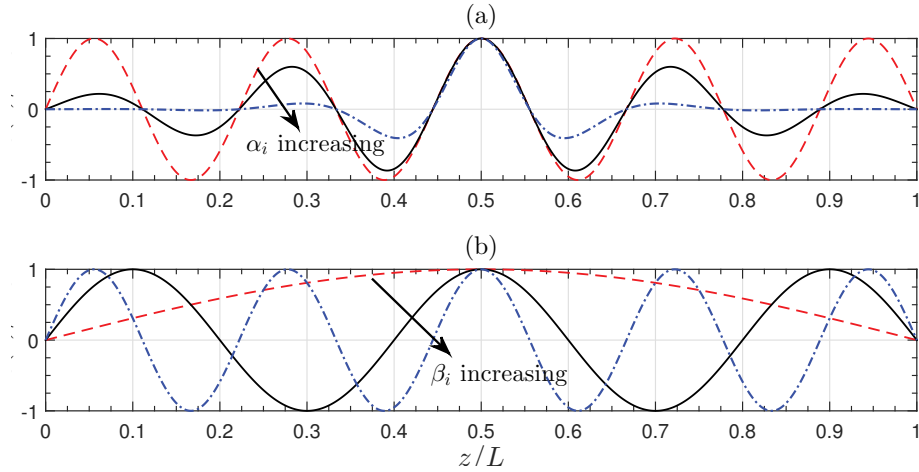


Figure 5.4: Profile of local imperfection function, $w_{i0}(z)/A_{i0}$. (a) Localized imperfections introduced by varying the localization parameter α_i from zero to 10. (b) Periodic imperfections ($\alpha_i = 0$) with different numbers of half sine waves by varying the frequency parameter β_i from 1 to 9.

5.3 Potential energy formulation

The formulation of the total potential energy functional follows a similar approach as that in Chapter 4, but currently accounts for the scenarios where local buckling may also be critical as well as where both global and local geometric imperfections exist.

5.3.1 Strain energy due to bending

The unloaded strut with initial global and local imperfections is assumed to be stress-relieved (Thompson & Hunt, 1984; Wadee, 2000; Bai & Wadee, 2015a; Wadee & Farsi, 2015). The case of the global imperfection W_0 is illustrated in Figure 5.5. For the local

imperfection case, w_0 would replace W_0 and the flexural rigidity of the flanges $D_f = Et_f^3/[12(1-\nu^2)]$ or the webs $D_w = Et_w^3/[12(1-\nu^2)]$ would replace the flexural rigidity of the web about the local weak neutral axis $EI_w = Edt_w^3/12$.

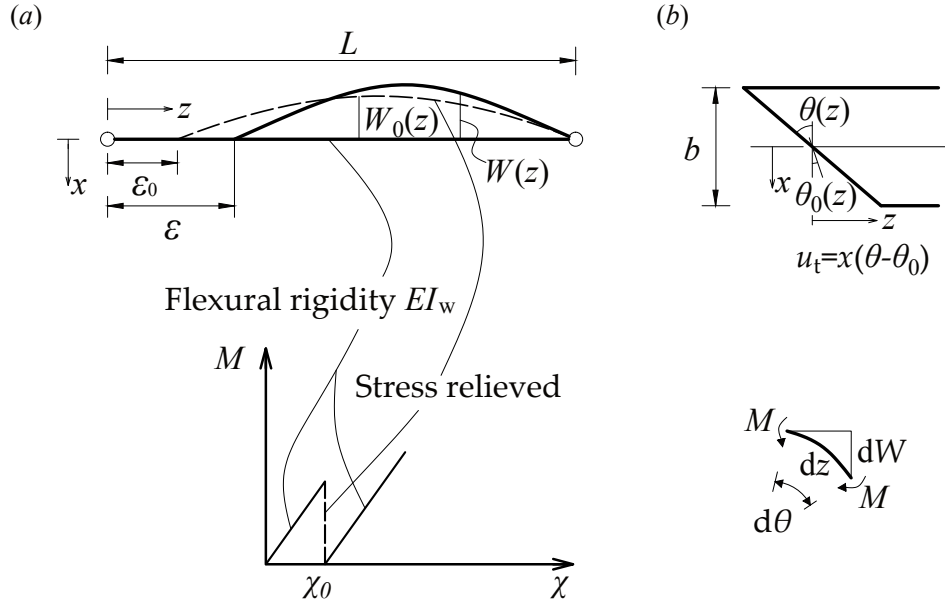


Figure 5.5: Introduction of the global imperfection. (a) The out-of-straightness sway component W_0 and (b) the pure rotation tilt component θ_0 .

Therefore, the global bending energy, $U_{b,o}$, can be expressed thus:

$$U_{b,o} = 2 \int_0^L \frac{EI_w}{2} (\chi - \chi_0)^2 dz = EI_w \int_0^L (q_s - q_{s0})^2 \frac{\pi^4}{L^2} \sin^2 \frac{\pi z}{L} dz, \quad (5.15)$$

with $\chi = \ddot{W}$ and $\chi_0 = \ddot{W}_0$, where dots represent derivatives with respect to z . The factor of 2 is included to account for both webs.

The local bending energy stored in both flanges, the more compressed web and the less compressed web can be determined by the standard expression for the strain energy of bending of a plate (Timoshenko & Woinowsky-Krieger, 1959), hence:

$$U_{b,f} = D_f \int_0^L \int_{-b/2}^{b/2} \left\{ \left[\frac{\partial^2 (w_f - w_{f0})}{\partial z^2} + \frac{\partial^2 (w_f - w_{f0})}{\partial x^2} \right]^2 \right. \quad (5.16)$$

$$- 2(1 - \nu) \left[\frac{\partial^2 (w_f - w_{f0})}{\partial z^2} \frac{\partial^2 (w_f - w_{f0})}{\partial x^2} - \left(\frac{\partial^2 (w_f - w_{f0})}{\partial z \partial x} \right)^2 \right] \Bigg\} dx dz,$$

$$U_{b,wcl} = \frac{D_w}{2} \int_0^L \int_{-d/2}^{d/2} \left\{ \left[\frac{\partial^2 (w_{wc} - w_{wc0})}{\partial z^2} + \frac{\partial^2 (w_{wc} - w_{wc0})}{\partial y^2} \right]^2 - 2(1 - \nu) \left[\frac{\partial^2 (w_{wc} - w_{wc0})}{\partial z^2} \frac{\partial^2 (w_{wc} - w_{wc0})}{\partial y^2} - \left(\frac{\partial^2 (w_{wc} - w_{wc0})}{\partial z \partial y} \right)^2 \right] \right\} dy dz, \quad (5.17)$$

$$U_{b,wtl} = \frac{D_w}{2} \int_0^L \int_{-d/2}^{d/2} \left\{ \left[\frac{\partial^2 (w_{wt} - w_{wt0})}{\partial z^2} + \frac{\partial^2 (w_{wt} - w_{wt0})}{\partial y^2} \right]^2 - 2(1 - \nu) \left[\frac{\partial^2 (w_{wt} - w_{wt0})}{\partial z^2} \frac{\partial^2 (w_{wt} - w_{wt0})}{\partial y^2} - \left(\frac{\partial^2 (w_{wt} - w_{wt0})}{\partial z \partial y} \right)^2 \right] \right\} dy dz. \quad (5.18)$$

By substituting w_f from Eqs. (5.1) and (5.13) into Eq. (5.16), the explicit expression for the local bending energy in the flanges is written thus:

$$U_{b,fl} = D_f \int_0^L \left\{ \{f_{1f}^2\}_x (\ddot{w}_1 - \ddot{w}_{10})^2 + \{f_{2f}^2\}_x (\ddot{w}_2 - \ddot{w}_{20})^2 + \{f_{1f}''^2\}_x (w_1 - w_{10})^2 + \{f_{2f}''^2\}_x (w_2 - w_{20})^2 + 2 \{f_{1f} f_{2f}\}_x (\dot{w}_1 - \dot{w}_{10}) (\dot{w}_2 - \dot{w}_{20}) + 2 \{f_{1f}'' f_{2f}''\}_x (w_1 - w_{10}) (w_2 - w_{20}) + 2\nu \{f_{1f} f_{1f}''\}_x (\ddot{w}_1 - \ddot{w}_{10}) (w_1 - w_{10}) + 2\nu \{f_{2f} f_{2f}''\}_x (\ddot{w}_2 - \ddot{w}_{20}) (w_2 - w_{20}) + 2\nu \{f_{1f} f_{2f}''\}_x (\ddot{w}_1 - \ddot{w}_{10}) (w_2 - w_{20}) + 2\nu \{f_{1f}'' f_{2f}\}_x (w_1 - w_{10}) (\ddot{w}_2 - \ddot{w}_{20}) + 2(1 - \nu) \left[\{f_{1f}''^2\}_x (\dot{w}_1 - \dot{w}_{10})^2 + \{f_{2f}''^2\}_x (\dot{w}_2 - \dot{w}_{20})^2 + 2 \{f_{1f}' f_{2f}'\}_x (\dot{w}_1 - \dot{w}_{10}) (\dot{w}_2 - \dot{w}_{20}) \right] \right\} dz. \quad (5.19)$$

The respective expanded expressions for the local bending strain energy stored in the more

and less compressed webs are obtained in the same way and have a very similar format. The total local bending energy $U_{b,l}$ can be written as:

$$U_{b,l} = U_{b,fl} + U_{b,wcl} + U_{b,wtl}. \quad (5.20)$$

5.3.2 Membrane strain energy

The membrane strain energy in the flanges $U_{m,f}$ is derived from considering the direct strains (ε_z) and the shear strains (γ_{xz}) in the flanges. The direct strains comprise three contributions, the first term from the global tilt mode, the next three terms from the local mode obtained based on von Kármán plate theory and finally a purely in-plane compressive strain Δ :

$$\begin{aligned} \varepsilon_{z,f} &= \frac{\partial u_t}{\partial z} + \frac{\partial u_f}{\partial z} + \frac{1}{2} \left(\frac{\partial w_f}{\partial z} \right)^2 - \frac{1}{2} \left(\frac{\partial w_{f0}}{\partial z} \right)^2 - \Delta \\ &= -x(q_t - q_{t0}) \frac{\pi^2}{L} \sin \frac{\pi z}{L} + \{g_{1f}\}_x \dot{u}_1 + \{g_{2f}\}_x \dot{u}_2 + \frac{1}{2} \{f_{1f}^2\}_x (\dot{w}_1^2 - \dot{w}_{10}^2) \\ &\quad + \frac{1}{2} \{f_{2f}^2\}_x (\dot{w}_2^2 - \dot{w}_{20}^2) + \{f_{1f}f_{2f}\}_x (\dot{w}_1\dot{w}_2 - \dot{w}_{10}\dot{w}_{20}) - \Delta. \end{aligned} \quad (5.21)$$

The shear strain component can be written thus:

$$\begin{aligned} \gamma_{xz,f} &= \frac{\partial u_f}{\partial x} + \frac{\partial (W - W_0)}{\partial z} - (\theta - \theta_0) + \frac{\partial w_f}{\partial x} \frac{\partial w_f}{\partial z} - \frac{\partial w_{f0}}{\partial x} \frac{\partial w_{f0}}{\partial z} \\ &= \{g'_{1f}\}_x u_1 + \{g'_{2f}\}_x u_2 - [(q_s - q_t) - (q_{s0} - q_{t0})] \pi \cos \frac{\pi z}{L} \\ &\quad + \{f'_{1f}f_{1f}\}_x (\dot{w}_1 w_1 - \dot{w}_{10} w_{10}) + \{f'_{2f}f_{2f}\}_x (\dot{w}_2 w_2 - \dot{w}_{20} w_{20}) \\ &\quad + \{f'_{1f}f_{2f}\}_x (w_1 \dot{w}_2 - w_{10} \dot{w}_{20}) + \{f_{1f}f'_{2f}\}_x (\dot{w}_1 w_2 - \dot{w}_{10} w_{20}). \end{aligned} \quad (5.22)$$

From the previous numerical study (Shen *et al.*, 2015), the transverse stress component was shown to be tiny when compared with the longitudinal stress, a finding that also coincides with earlier work (Koiter & Pignataro, 1976a). Therefore, the complete expression for the membrane strain energy stored in the flanges can be written thus if the transverse strain

is simplified to be $\varepsilon_{x,f} = -\nu\varepsilon_{z,f}$:

$$U_{m,f} = U_{fd} + U_{fs} = 2 \int_0^L \int_{-t_f/2}^{t_f/2} \int_{-b/2}^{b/2} \frac{1}{2} (E\varepsilon_{z,f}^2 + G\gamma_{xz,f}^2) dx dy dz. \quad (5.23)$$

The membrane strain energy in the webs also comprises direct and shear strain energy contributions. The complete expressions for the direct strain in the more compressed and less compressed webs are very similar to those for the flanges presented in Eq. (5.21), thus:

$$\begin{aligned} \varepsilon_{z,wc} &= \frac{\partial u_{t,wc}}{\partial z} + \frac{\partial u_{wc}}{\partial z} + \frac{1}{2} \left(\frac{\partial w_{wc}}{\partial z} \right)^2 - \frac{1}{2} \left(\frac{\partial w_{wc0}}{\partial z} \right)^2 - \Delta \\ &= -(q_t - q_{t0}) \frac{b\pi^2}{2L} \sin \frac{\pi z}{L} + \{g_{1wc}\}_y \dot{u}_1 + \{g_{2wc}\}_y \dot{u}_2 + \frac{1}{2} \{f_{1wc}^2\}_y (\dot{w}_1^2 - \dot{w}_{10}^2) \\ &\quad + \frac{1}{2} \{f_{2wc}^2\}_y (\dot{w}_2^2 - \dot{w}_{20}^2) + \{f_{1wc}f_{2wc}\}_y (\dot{w}_1\dot{w}_2 - \dot{w}_{10}\dot{w}_{20}) - \Delta, \end{aligned} \quad (5.24)$$

$$\begin{aligned} \varepsilon_{z,wt} &= \frac{\partial u_{t,wt}}{\partial z} + \frac{\partial u_{wt}}{\partial z} + \frac{1}{2} \left(\frac{\partial w_{wt}}{\partial z} \right)^2 - \frac{1}{2} \left(\frac{\partial w_{wt0}}{\partial z} \right)^2 - \Delta \\ &= (q_t - q_{t0}) \frac{b\pi^2}{2L} \sin \frac{\pi z}{L} + \{g_{1wt}\}_y \dot{u}_1 + \{g_{2wt}\}_y \dot{u}_2 + \frac{1}{2} \{f_{1wt}^2\}_y (\dot{w}_1^2 - \dot{w}_{10}^2) \\ &\quad + \frac{1}{2} \{f_{2wt}^2\}_y (\dot{w}_2^2 - \dot{w}_{20}^2) + \{f_{1wt}f_{2wt}\}_y (\dot{w}_1\dot{w}_2 - \dot{w}_{10}\dot{w}_{20}) - \Delta. \end{aligned} \quad (5.25)$$

Unlike the flanges, the shear strains in the webs only contain the terms from the local mode owing to their relatively small thickness, thus:

$$\begin{aligned} \gamma_{yz,wc} &= \frac{\partial u_{wc}}{\partial y} + \frac{\partial w_{wc}}{\partial y} \frac{\partial w_{wc}}{\partial z} - \frac{\partial w_{wc0}}{\partial y} \frac{\partial w_{wc0}}{\partial z} \\ &= \{g'_{1wc}\}_y u_1 + \{g'_{2wc}\}_y u_2 + \{f'_{1wc}f_{1wc}\}_y (\dot{w}_1 w_1 - \dot{w}_{10} w_{10}) \\ &\quad + \{f'_{2wc}f_{2wc}\}_y (\dot{w}_2 w_2 - \dot{w}_{20} w_{20}) + \{f'_{1wc}f_{2wc}\}_y (w_1 \dot{w}_2 - w_{10} \dot{w}_{20}) \\ &\quad + \{f_{1wc}f'_{2wc}\}_y (\dot{w}_1 w_2 - \dot{w}_{10} w_{20}), \end{aligned} \quad (5.26)$$

$$\begin{aligned}
\gamma_{yz,wt} &= \frac{\partial u_{wt}}{\partial y} + \frac{\partial w_{wt}}{\partial y} \frac{\partial w_{wt}}{\partial z} - \frac{\partial w_{wt0}}{\partial y} \frac{\partial w_{wt0}}{\partial z} \\
&= \{g'_{1wt}\}_y u_1 + \{g'_{2wt}\}_y u_2 + \{f'_{1wt} f_{1wt}\}_y (\dot{w}_1 w_1 - \dot{w}_{10} w_{10}) \\
&\quad + \{f'_{2wt} f_{2wt}\}_y (\dot{w}_2 w_2 - \dot{w}_{20} w_{20}) + \{f'_{1wt} f_{2wt}\}_y (w_1 \dot{w}_2 - w_{10} \dot{w}_{20}) \\
&\quad + \{f_{1wt} f'_{2wt}\}_y (\dot{w}_1 w_2 - \dot{w}_{10} w_{20}).
\end{aligned} \tag{5.27}$$

Again, assuming that $\varepsilon_{y,wc} = -\nu\varepsilon_{z,wc}$ and $\varepsilon_{y,wt} = -\nu\varepsilon_{z,wt}$, the membrane strain energy stored in both webs is given thus:

$$U_{m,w} = \frac{1}{2} \int_0^L \int_{-d/2}^{d/2} \int_{-t_w/2}^{t_w/2} \left[E (\varepsilon_{z,wc}^2 + \varepsilon_{z,wt}^2) + G (\gamma_{yz,wc}^2 + \gamma_{yz,wt}^2) \right] dx dy dz. \tag{5.28}$$

5.3.3 Work done by the load and total potential energy

The total end-shortening \mathcal{E} comprises terms from pure squash, the global sway mode and the local in-plane displacement. The expression for the work done by the external load is given by:

$$P\mathcal{E} = P \int_0^L \left[\Delta + (q_s^2 - q_{s0}^2) \frac{\pi^2}{2} \cos^2 \frac{\pi z}{L} - \Delta_m \right] dz, \tag{5.29}$$

where:

$$\Delta_m = \frac{(2\phi_t \{g_{1f}\}_x + \{g_{1wc}\}_y + \{g_{1wt}\}_y) \dot{u}_1 + (2\phi_t \{g_{2f}\}_x + \{g_{2wc}\}_y + \{g_{2wt}\}_y) \dot{u}_2}{2b(\phi_t + \phi_c)}. \tag{5.30}$$

In summary, the total potential energy V can be expressed by the summation of all the strain energy terms minus the work done by the external load:

$$V = U_{b,o} + U_{b,l} + U_{m,f} + U_{m,w} - P\mathcal{E}. \tag{5.31}$$

5.4 Variational formulation and eigenvalue analysis

The governing equations for equilibrium are obtained by performing the calculus of variations on the total potential energy V following the same procedure for the case in Chapter 4. The integrand of the total potential energy V can be expressed as a Lagrangian (\mathcal{L}) of the form:

$$V = \int_0^L \mathcal{L}(\ddot{w}_i, \dot{w}_i, w_i, \dot{u}_i, u_i, z) dz, \quad (5.32)$$

where $i = \{1, 2\}$. Equilibrium of the system requires that V is stationary for any small changes in w_i and u_i . Therefore, the governing equilibrium equations can be obtained by setting the first variation of V to zero:

$$\delta V = \int_0^L \left[\frac{\partial \mathcal{L}}{\partial \ddot{w}_i} \delta \ddot{w}_i + \frac{\partial \mathcal{L}}{\partial \dot{w}_i} \delta \dot{w}_i + \frac{\partial \mathcal{L}}{\partial w_i} \delta w_i + \frac{\partial \mathcal{L}}{\partial \dot{u}_i} \delta \dot{u}_i + \frac{\partial \mathcal{L}}{\partial u_i} \delta u_i \right] dz = 0. \quad (5.33)$$

Since $\delta \ddot{w}_i = d(\delta \dot{w}_i)/dz$, $\delta \dot{w}_i = d(\delta w_i)/dz$ and $\delta \dot{u}_i = d(\delta u_i)/dz$, integration by parts allows the development of the Euler–Lagrange equations for w_i and u_i , which comprise a fourth order ordinary differential equation (ODE) for w_i and second order ODE for u_i , thus:

$$\frac{d^2}{dz^2} \left(\frac{\partial \mathcal{L}}{\partial \ddot{w}_i} \right) - \frac{d}{dz} \left(\frac{\partial \mathcal{L}}{\partial \dot{w}_i} \right) + \frac{\partial \mathcal{L}}{\partial w_i} = 0, \quad (5.34)$$

$$\frac{d}{dz} \left(\frac{\partial \mathcal{L}}{\partial \dot{u}_i} \right) - \frac{\partial \mathcal{L}}{\partial u_i} = 0. \quad (5.35)$$

Moreover, equilibrium also requires the minimization of V with respect to the generalized coordinates q_s , q_t and Δ , leading to three integral equations:

$$\frac{\partial V}{\partial q_s} = 0, \quad \frac{\partial V}{\partial q_t} = 0, \quad \frac{\partial V}{\partial \Delta} = 0. \quad (5.36)$$

The first expression in Eq. (5.36) provides a relationship between the global imperfection parameters q_{s0} and q_{t0} that is obtained by setting global mode amplitudes q_s and q_t , and

local buckling mode functions, *i.e.* u_i , w_i and their derivatives with respect to z , to zero:

$$q_{s0} = (1 + s) q_{t0}, \quad (5.37)$$

where s is the shear correction factor and the expression is the same as presented in Eq. (4.50). Moreover, it should be mentioned that the corresponding relationship, $q_s = (1+s)q_t$, also applies before local buckling is triggered as it did for the perfect long strut length cases presented in Chapter 4.

The boundary conditions for w_i , u_i and their derivatives are for simply-supported conditions at $z = 0$ and for symmetry conditions at $z = L/2$:

$$w_i(0) = \ddot{w}_i(0) = \dot{w}_i(L/2) = \ddot{w}_i(L/2) = u_i(L/2) = 0. \quad (5.38)$$

Two further boundary conditions can be obtained from the variational formulation with regards to the in-plane displacements u_i , hence:

$$\left[\frac{\partial \mathcal{L}}{\partial \dot{u}_i} \delta u_i \right]_0^L = 0. \quad (5.39)$$

The global buckling load P_o^C can be determined by conducting linear buckling analysis for the imperfect strut with the same methodology adopted in Chapter 4 by considering the Hessian matrix \mathbf{V}_{ij} being singular, where $q_s = q_t = 0$ and $w_1 = w_2 = u_1 = u_2 = 0$. It turns out that the expression for P_o^C is the same as Eq. (4.54). Moreover, it should be noted that the full expressions for Eqs. (5.34)–(5.36) and (5.39) may be found in Appendix A.

5.5 Concluding remarks

The nonlinear variational model in Chapter 4 has been extended to describe the interactive buckling of elastic thin-walled RHS struts in scenarios where local buckling may be

critical as well as where both local and global geometric imperfections exist. Two independent sets of in-plane and out-of-plane local displacement fields, which represent the pure local buckling mode and global buckling induced interactive buckling mode respectively, are introduced to describe the interactive buckling mode of struts with different lengths. In particular, the cross-section components of these local modes are approximated by applying approximate kinematic boundary conditions for each plate in conjunction with the Rayleigh–Ritz method. The total potential energy was determined based on the modal description and introduced geometric imperfections. By performing the calculus of variations on the total potential energy, the governing equations for the longitudinal components of the local post-buckling modes subject to boundary and integral conditions are obtained. The verification of the variational model and a series of parametric studies for both perfect and imperfect cases are presented in Chapters [6](#) and [7](#) respectively.

Chapter 6

Length effects

In the current chapter, the variational model developed in Chapter 5 is used to investigate how different strut lengths affect the nonlinear modal coupling of perfect struts, *i.e.* $q_{s0}=q_{t0}=w_{10}=w_{20}=0$. The interactive buckling responses of four representative struts, which are defined qualitatively in sequence as the length is progressively reduced as ‘long’, ‘transitional’, ‘intermediate’ and ‘short’ length struts, thus corresponding to the four different zones shown in Figure 6.1 respectively, are studied. The characteristic post-buckling

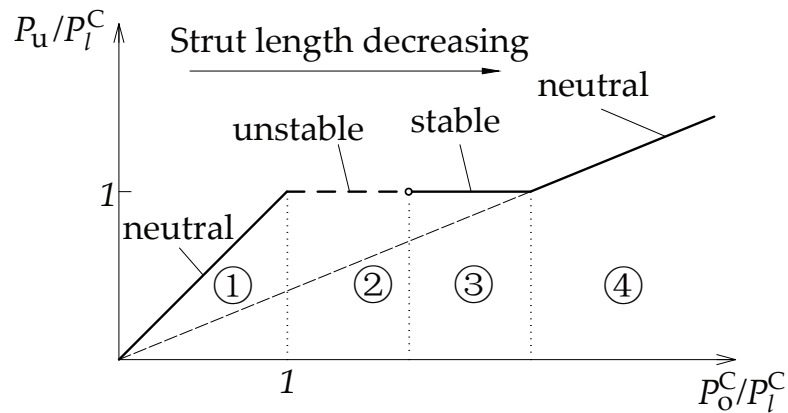


Figure 6.1: The Van der Neut type curve (see Figure 2.2) for geometrically perfect struts. The quantities P_u , P_0^C , P_l^C are the ultimate, the global buckling and the local buckling loads respectively, also each part of the curve has a specific post-buckling characteristic behaviour.

equilibrium paths are determined and a progressive change in the local buckling wave-

length is found in each case. The numerical results from the variational model largely show excellent comparisons with numerical results obtained using a nonlinear FE model developed within ABAQUS (2014) in terms of the ultimate load and the initial post-buckling behaviour. A parametric study on the strut length identifies the boundaries of the four distinct length-dependent domains and places the current results within the context of the classical work by Van der Neut (1969).

6.1 Numerical solution strategy for variational model

Since the complete system of the nonlinear coupled ordinary differential equations is too complicated to be solved analytically, it is therefore solved numerically using the continuation and bifurcation software AUTO-07P (Doedel & Oldeman, 2009). According to previous studies on mode interaction in thin-walled compression members (van der Neut, 1969; Koiter & Pignataro, 1976a; Wadee & Farsi, 2015; Bai & Wadee, 2016; Liu & Wadee, 2016a), the behaviour can be classified into four distinct zones that are related to the strut length L . Currently, these have been assigned the qualitative names ‘long’, ‘transitional’, ‘intermediate’ and ‘short’ length struts and respectively correspond to the zones labelled 1–4, as shown in Figure 6.1. The different equilibrium diagrams alongside the numerical continuation procedures to compute the equilibrium paths of the four representative struts using AUTO are shown diagrammatically in Figure 6.2. Figure 6.2(a) depicts the equilibrium behaviour for the case where global buckling is critical and was described in Chapter 4

However, for the cases where local buckling is critical, *i.e.* for zones 2–4, as presented in Figure 6.1, there is known to be some numerical difficulty in switching from the pure local buckling path to the interactive buckling path (Wadee & Bai, 2014; Liu & Wadee, 2016b; Yiatros *et al.*, 2015). Therefore, the numerical continuation strategy known as ‘homotopy’ was adopted to obtain the solution, as described in Figure 6.3. The solution begins from

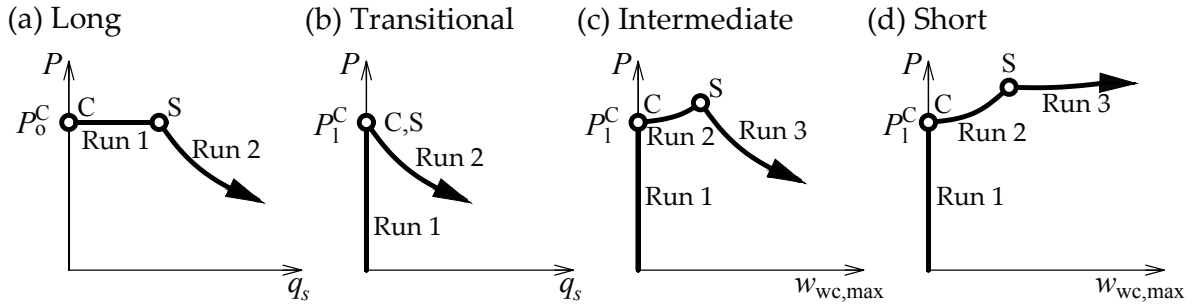


Figure 6.2: Sketches of the equilibrium paths for struts of different lengths exhibiting mode interaction. Graphs (a)–(d) correspond to the zones labelled 1–4, as presented in the Van der Neut type curve in Figure 6.1. Circles marked C and S represent the critical and secondary bifurcation points for each case respectively. Note that the abscissa changes from q_s in (a–b) to $w_{wc,max}$ in (c–d), which reflects the appropriate measure of the critical buckling mode.

determining the equilibrium path for a strut with length L_1 , a case where global buckling is critical, referring to Runs 1 and 2 depicted in Figure 6.3. Then by replacing q_s with L as the principal varying parameter in AUTO, the interactive buckling equilibrium states of struts with different lengths can be obtained, referring to Run 3, depicted in Figure 6.3, which begins at point R_1 . The interactive buckling path of the strut with the new length L_2 , where local buckling is critical, can be computed from the point R_2 by re-setting the principal varying parameter back to q_s and keeping L constant. The solution of this branch ends at the new secondary bifurcation point S_2 .

As for the fundamental and pure local buckling equilibrium path, as shown in Run 1 in Figure 6.2(b) and Runs 1 and 2 in Figure 6.2(c–d), the continuation process initiates from zero load and the local buckling load P_1^C is obtained numerically. The post-buckling path is then computed by using the branch switching facility and the local buckling equilibrium path ends at the secondary bifurcation point S, where critical local buckling is initially destabilized due to contamination from the global buckling mode.

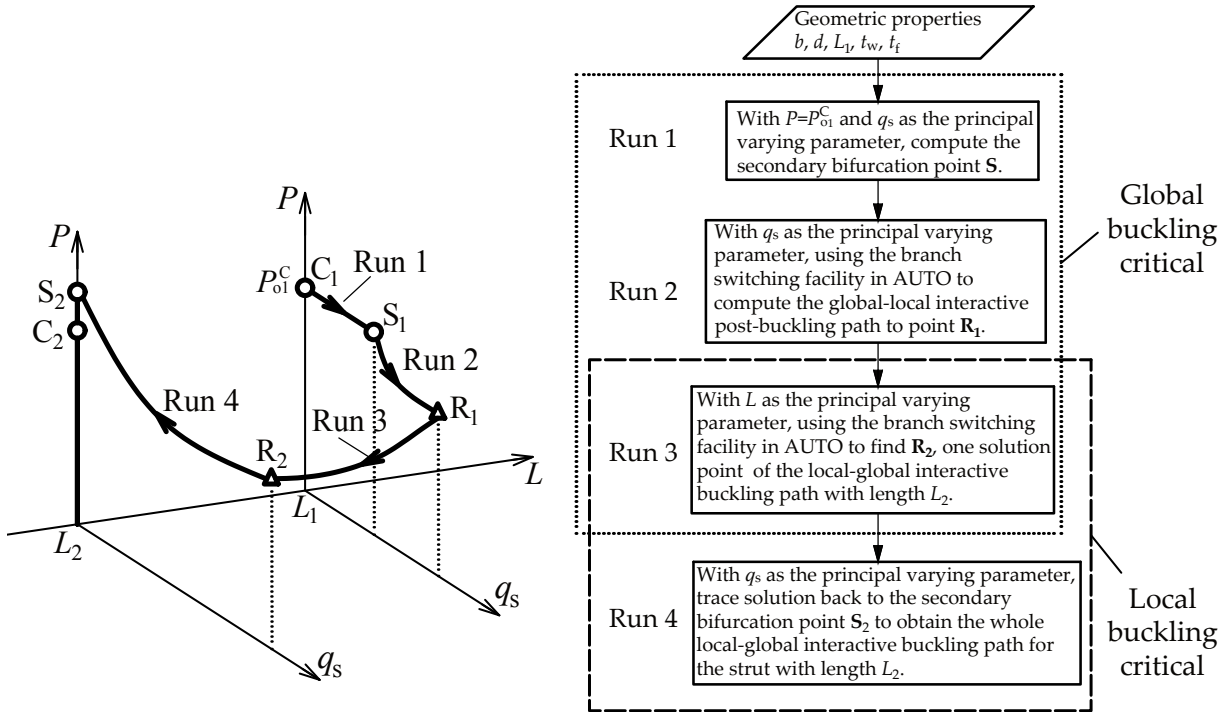


Figure 6.3: Sketch and flowchart of the numerical continuation procedure for determining the interactive buckling equilibrium path for perfect struts where local buckling is critical. Circles marked C_i and S_i represent the critical and secondary bifurcation points respectively; triangles marked R_i represent generic equilibrium states on the interactive buckling paths with strut lengths L_i . Strut lengths L_1 and L_2 represent the cases where global buckling and local buckling are critical respectively; P_{01}^C is the global buckling load of the strut with length L_1 .

6.2 Numerical results and verification

Four representative numerical examples from the variational model with the same cross-section properties but different lengths are presented. The cross-section geometric and material properties of the example struts are the same as the example strut presented in §4.3. The same material and cross-section properties are used throughout the current chapter. The length, critical buckling loads and corresponding zones of the example struts are presented in Table 6.1.

Table 6.1: Theoretical values of the global (P_o^C) and local (P_1^C) buckling loads for the four representative length cases.

L (mm)	P_o^C (kN)	$P_{1,AUTO}^C$ (kN)	$P_{1,ABAQUS}^C$ (kN)	P_o^C/P_1^C	Zone	Length description
4800	22.67	24.61	24.57	0.92	1	‘Long’
4500	25.79	24.61	24.58	1.05	2	‘Transitional’
4000	32.54	24.57	24.58	1.32	3	‘Intermediate’
3600	40.30	24.67	24.58	1.63	4	‘Short’

6.2.1 Long length strut

The interactive buckling behaviour of long struts has been investigated in Chapter 4, which showed excellent comparisons with the FE model. For the present long length strut, where $L = 4800$ mm, a sharp snap-back in the load–end-shortening relationship is observed, as shown in Figure 6.4(a). Severely imperfection sensitive behaviour would be expected for such a strut with P_o^C/P_1^C being close to unity (Bai & Wade, 2015a; Wade & Farsi, 2015).

From the solutions of the out-of-plane components of the local mode in the more compressed web w_{wc} , the increase of the global buckling mode amplitude not only leads to an increase in the local mode amplitude, as shown in Figure 6.4(d), but also forces a change of the local buckling profile from being localized to being more distributed alongside a corresponding reduction in the local buckling mode wavelength, as shown in Figure 6.5.

Compared with the FE model, the variational model shows a slightly stiffer post-buckling response, as shown in Figure 6.4. One of the sources for the stiffer response is derived from the assumption that the location of the neutral axis remains unchanged in the variational model. In fact, the neutral axis would move towards the less compressed web as the effective stiffness of the more compressed web drops due to it buckling locally, as shown in Figure 4.11. Moreover, in the variational model, the cross-section profile of the local mode is assumed to be the same along the length of strut and throughout the post-buckling range with the only variable being the modal amplitude of local buckling. However, the profile is in fact affected by the bending moment and axial stress on the cross-section, which varies along the strut length and with the progression of mode interaction. This may explain

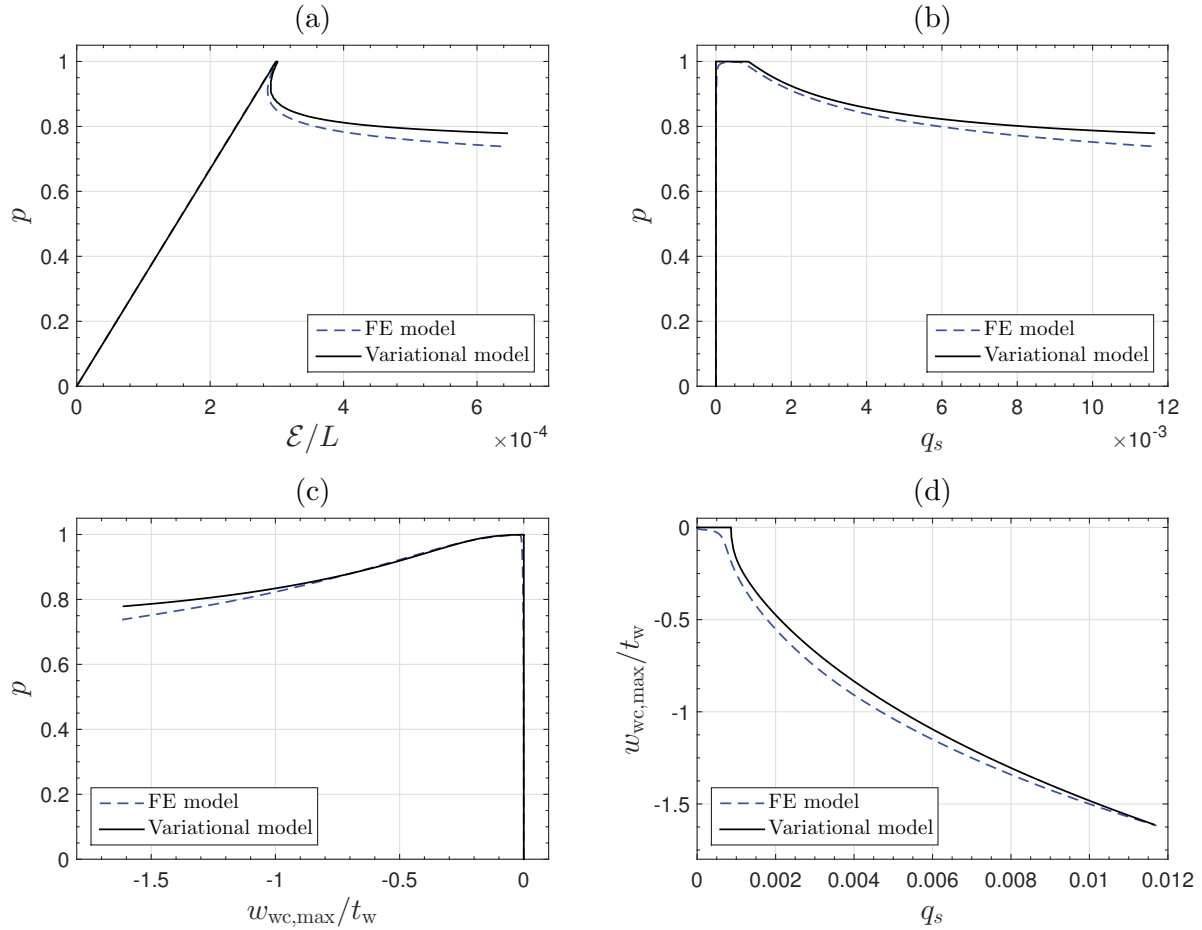


Figure 6.4: Nonlinear equilibrium paths for the example long length strut with $L = 4800$ mm from the variational and FE models. Graphs of the normalized load ratio $p = P/P^C$, where P^C is the critical buckling load, versus (a) the normalized end-shortening \mathcal{E}/L , (b) the generalized coordinate of the sway mode q_s , and (c) the normalized maximum amplitude of the local buckling deflection in the more compressed web $w_{wc,max}/t_w$; (d) $w_{wc,max}/t_w$ versus q_s .

the small discrepancy in the longitudinal solutions of the local deflection amplitude in the more compressed web w_{wc}/t_w , as shown in Figure 6.5, and the ‘bulging-out’ effect due to the high axial stress in the more compressed web in Figure 6.6(d). It should be mentioned that there is a tiny out-of-plane displacement in the less compressed web in the initial post-buckling stage of the FE results, as shown in Figure 6.5(e–h) and Figure 6.6(a). With the increase of the global mode amplitude, the change in the profile of the local mode nearly follows the same pattern as that in the more compressed web, *i.e.* from localized to more distributed, but its amplitude remains approximately the same. The kinematic

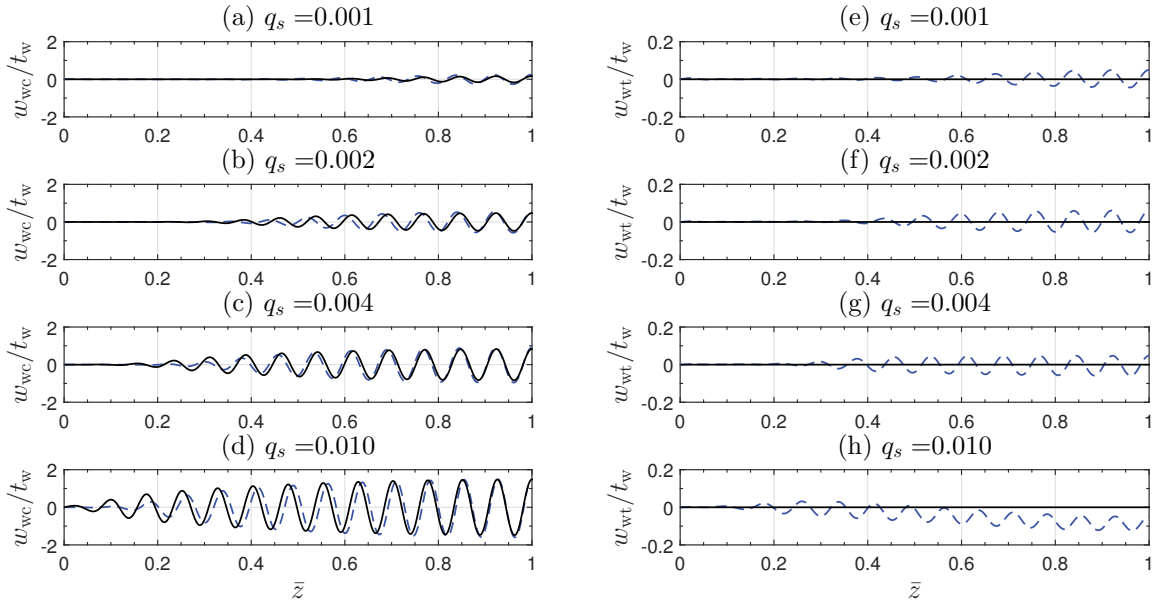


Figure 6.5: Evolution of the numerical solutions for the normalized local out-of-plane displacement in (a–d) the more compressed web w_{wc}/t_w and (e–h) the less compressed web w_{wt}/t_w for the long length strut with $L = 4800$ mm. The dashed and solid lines represent the numerical results from the FE and the variational model respectively. Note that the longitudinal coordinate is normalized with respect to half of the strut length $\bar{z} = 2z/L$ and that w_{wc}/t_w is an order of magnitude greater than w_{wt}/t_w .

compatibility between the buckled flanges and the less compressed web leads to the tiny deformation. When the generalized coordinate of the global mode q_s is relatively larger, the entirety of the less compressed web deforms inwards slightly, as shown in Figures 6.5(h) and 6.6(d). This is caused by the out-of-plane force introduced by the global mode that is identical to the phenomenon that causes the ‘Brazier effect’ in cylindrical shells under uniform bending (Brazier, 1927; Wadee *et al.*, 2006), as shown in Figure 6.7, which is not included in the current variational model. All of these factors taken together lead to the very marginally stiffer response in the variational model for the long strut, but it is, in fact, very small.

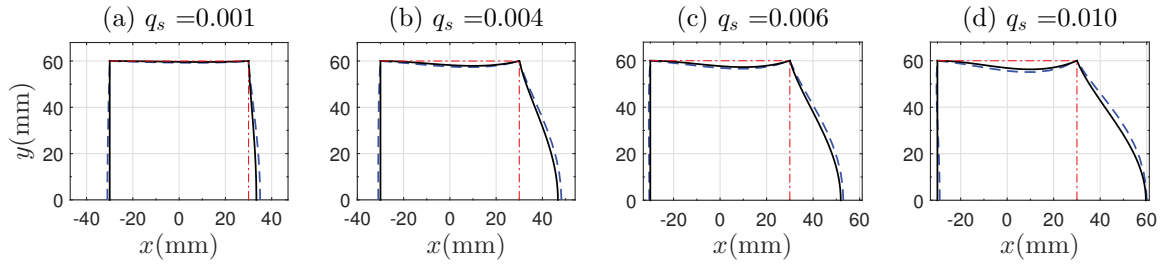


Figure 6.6: Local deformation of the cross-section at mid-span for the long length strut with $L = 4800$ mm with the increase of the generalized sway mode coordinate q_s . The dashed and solid lines represent the numerical results from the FE and variational models respectively. The dot-dashed line represents the undeformed shape. Note that the displacements shown have been amplified by a factor of 20 to aid visualization.

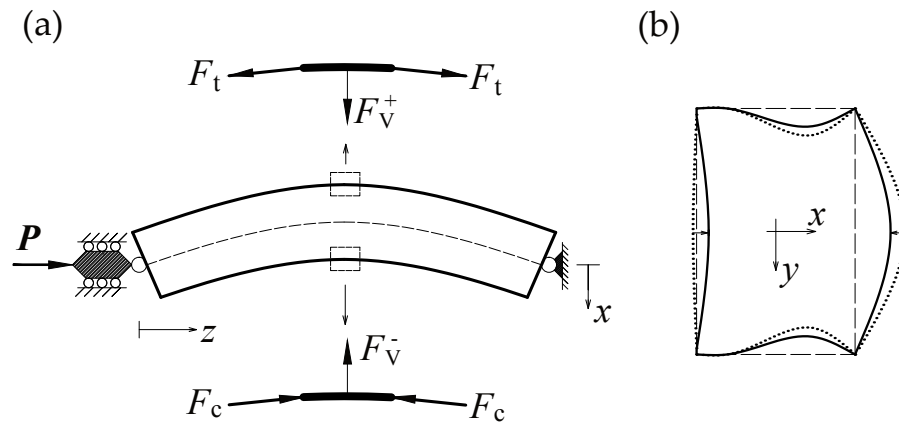


Figure 6.7: (a) Out-of-plane forces due to the large bending displacement with F_V representing the effective vertical component, as shown, of the axial force within each web (F_c or F_t). (b) Corresponding effects on the local mode profile – the dotted line and the thick solid line represent the cross-section profile before and after considering the global bending effects respectively.

6.2.2 Transitional length strut

For the transitional length strut considered, where $L = 4500$ mm, an even more severe snap-back is observed in the load–end-shortening relationship, as shown in Figure 6.8(a). This is caused by the fact that when local buckling initially occurs, the actual stiffness of

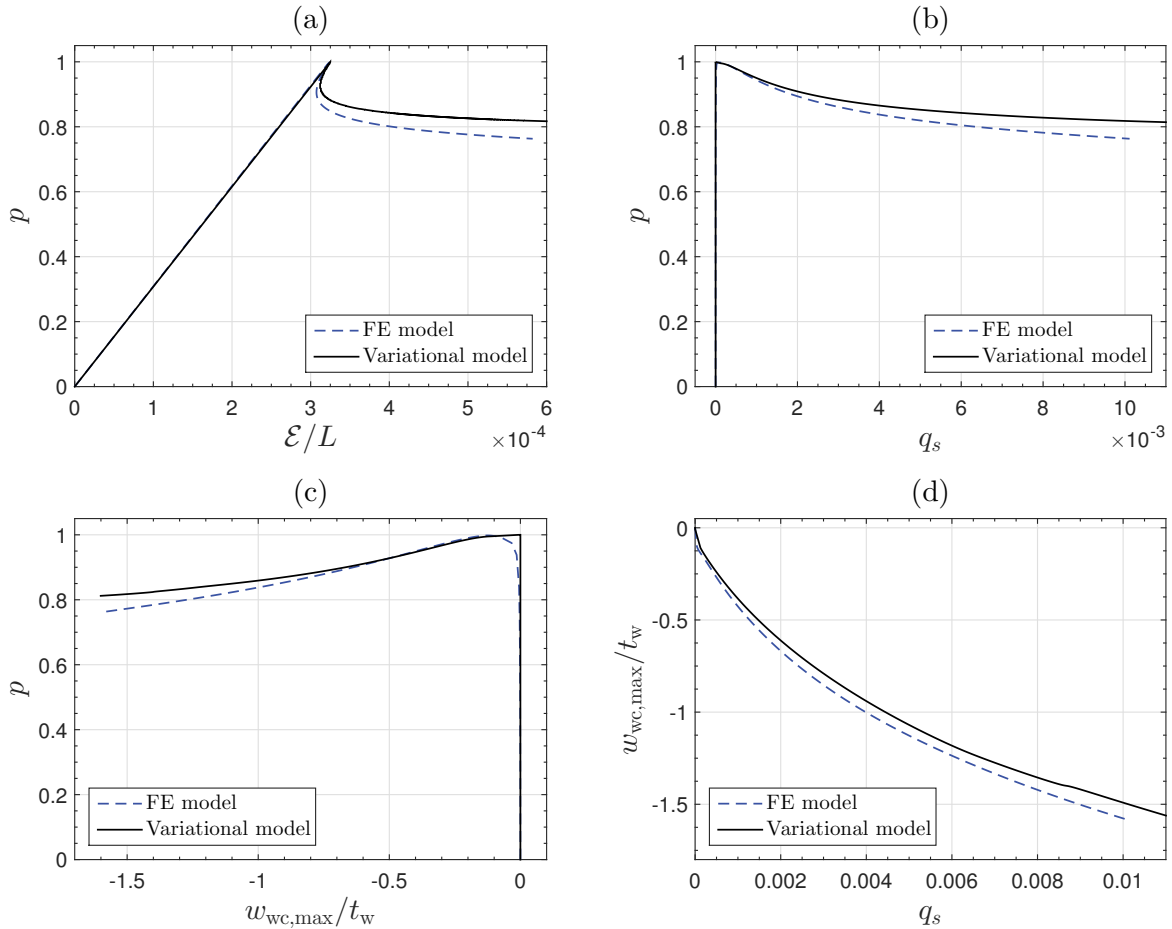


Figure 6.8: Nonlinear equilibrium paths for the transitional length strut with $L = 4500$ mm from the variational and FE models. Graphs (a)–(d) are as described in Figure 6.4.

the strut is reduced, effectively leading to a reduced global buckling load, which becomes instantaneously smaller than the critical local buckling load P_1^C . Hence, both buckling modes are effectively triggered simultaneously, as shown in Figure 6.8(d).

The solutions of the local deflection in the more and less compressed webs are shown in Figure 6.9. The amplitude in the more compressed web increases with the progression of

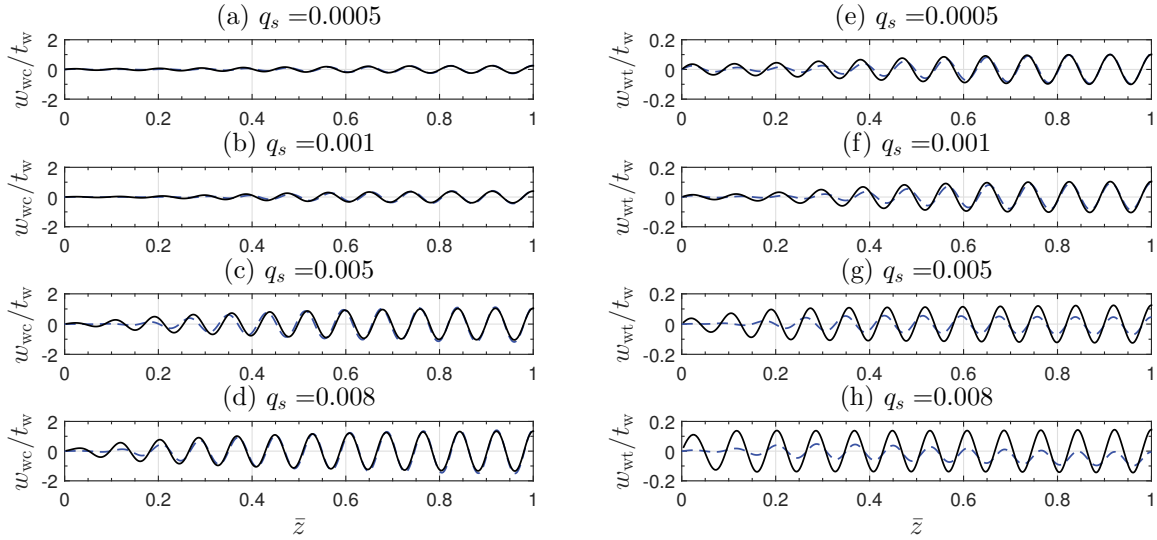


Figure 6.9: Evolution of the numerical solutions for (a–d) w_{wc}/t_w and (e–h) w_{wt}/t_w for the transitional length strut with $L = 4500$ mm. Graphs are as described in Figure 6.5.

mode interaction, while the amplitude in the less compressed web remains approximately unchanged. This leads to a transition of the cross-section deformation from being close to the pure local mode (symmetrical about the y -axis) to being dominated by the global mode (asymmetrical about the y -axis), as shown in Figure 6.10. Since local buckling is

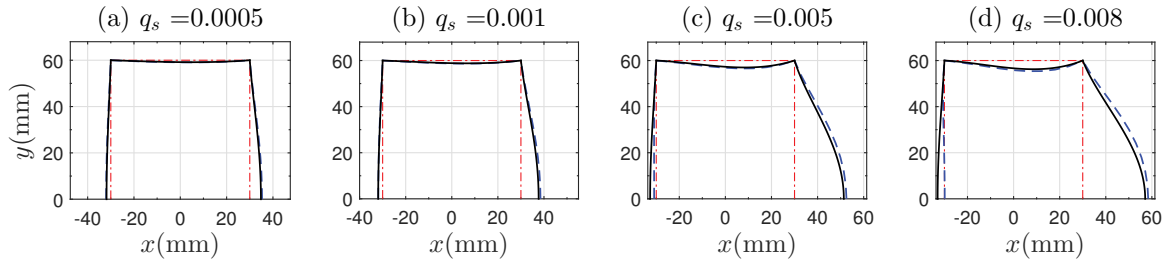


Figure 6.10: Local deformation of the cross-section at mid-span for the transitional length strut with $L = 4500$ mm as q_s is increased. The graphs are as described in Figure 6.6.

critical for the transitional length strut, the longitudinal profile of the local mode is initially distributed rather than localized. However, a reduction in the local buckling wavelength with the increase of the global mode amplitude is also observed as the axial end-shortening is increased.

The variational model for the transitional length strut also shows a stiffer post-buckling response when compared to the corresponding FE model, as can be seen from the equilibrium

path comparison in Figure 6.8; the reasons listed for the long strut also apply presently. The excellent comparisons between the solution of the out-of-plane displacement in the more compressed web and the cross-section deformation, particularly when q_s is relatively small, verify the current methodology. As shown in Figure 6.7, with the increase of the global buckling amplitude, the less compressed web bulges inwards. It can be seen clearly from the solution of the out-of-plane displacement in the less compressed web from the FE model in Figure 6.9(g–h), where the solution wave drifts to the negative direction. This can also help to explain the discrepancy in the cross-section deformation for the less compressed web at mid-span when q_s is large, as shown in Figure 6.10(c–d).

6.2.3 Intermediate length strut

For the intermediate length strut, where $L = 4000$ mm, there are three stages in the equilibrium paths for the load versus end-shortening and versus the local buckling amplitude, as shown in Figure 6.11(a,c). The first stage involves purely axial deformation of the strut before the critical buckling load P_1^C is reached ($p < 1$). The second stage is the local buckling of the whole cross-section and the third stage is the local–global mode interaction. Before the secondary bifurcation, the strut is stable; however, the triggering of the global mode leads to unstable post-buckling behaviour. In the interactive buckling range, there are several snap-backs in the equilibrium path, which correspond to the local mode increasing its number of peaks hence reducing its wavelength, as shown in Figure 6.12. This type of cellular buckling (Hunt *et al.*, 2000) has also been observed in previous studies on I-section beams (Wadee & Gardner, 2012), I-section struts (Wadee & Bai, 2014), stiffened panels (Wadee & Farsi, 2014a) and struts with equal angle cross-sections (Bai *et al.*, 2017).

From the solutions of the out-of-plane displacements in the more and less compressed webs, the progression of mode interaction forces a reduction in wavelength. Since the local buckling mode is well developed before mode interaction occurs, the wavelength

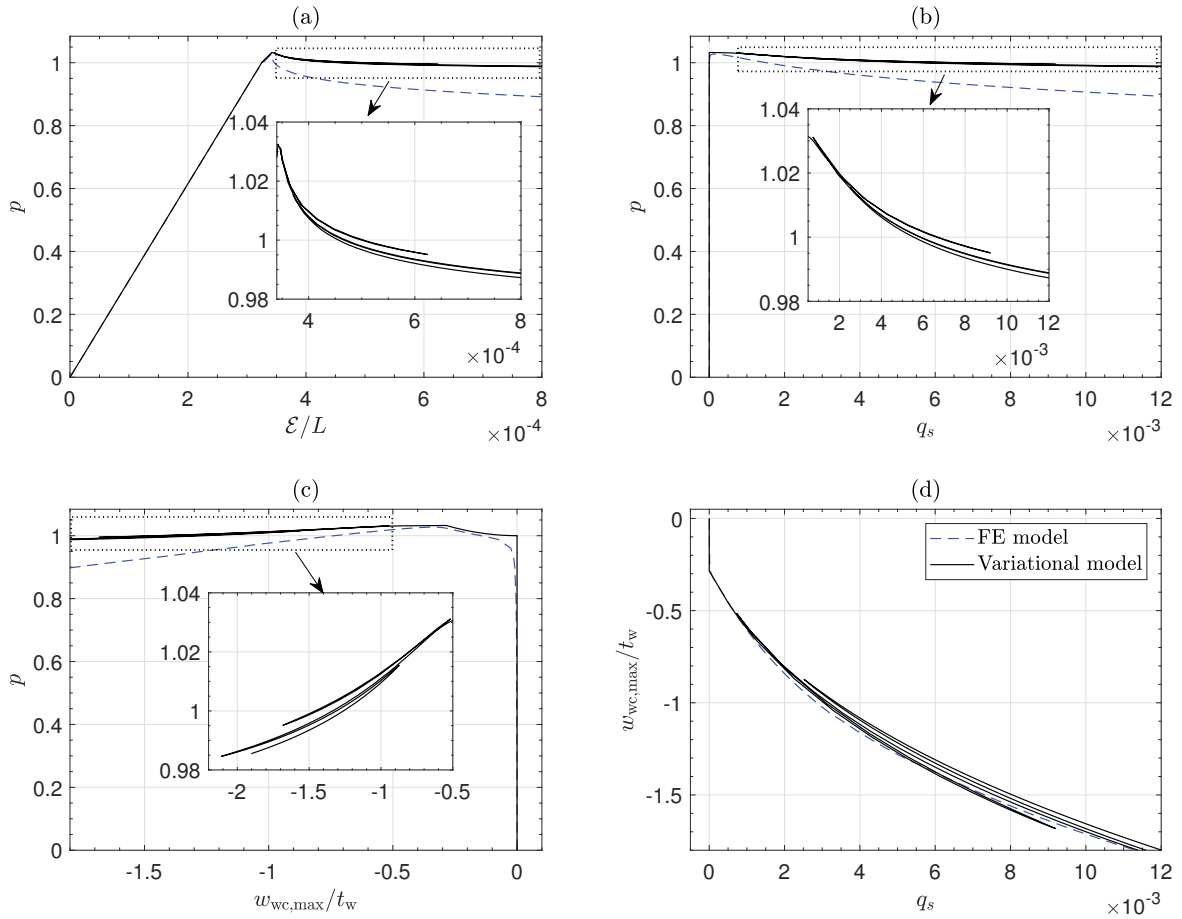


Figure 6.11: Nonlinear equilibrium paths for the intermediate length strut with $L = 4000$ mm from the variational and FE models. Graphs (a)–(d) are as described in Figure 6.4. Insets in (a)–(c) present close-ups of graphs that show the snap-backs in the interactive post-buckling range.

reduction leads to an increase in the number of peaks and troughs, as shown in Figure 6.12, which is not observed in the previous two relatively slender example struts. Moreover, the displacement amplitude increases at mid-span but remains approximately unchanged at the ends, leading to the profile changing from periodic to being more localized. The mode interaction makes the relative contributions from local modes 2 and 1, *i.e.* w_2/w_1 , increase, thus breaking the initial symmetric deformation of the local mode gradually, as can be seen in Figure 6.13.

Compared with the long and transitional length struts, the numerical results from the variational model for the intermediate length strut shows a relatively stiffer post-buckling

response when compared with the FE model. The reason is partly due to local buckling being more developed before the triggering of the secondary instability; for example, the assumed cross-section profile of the local mode, which fits well with the FE results at mid-span, is not necessarily valid for the whole length. The errors would be relatively small for slender struts, since the longitudinal deflection profile is more localized. However, for the intermediate length strut, the longitudinal component is further distributed and the error therefore would be significantly larger.

However, it should be emphasized that the current model can capture the evolution of the longitudinal and cross-section components of the local mode well, as shown in Figures 6.12 and 6.13. It should also be noted that even though the progressive change in the local mode

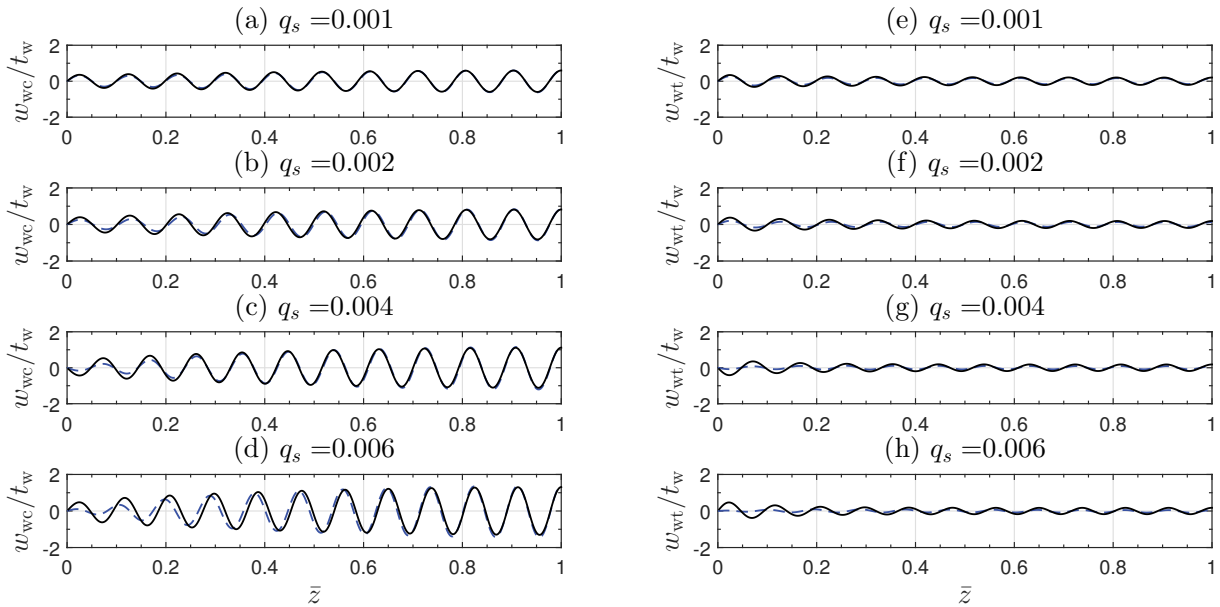


Figure 6.12: Evolution of the numerical solutions for (a–d) w_{wc}/t_w and (e–h) w_{wt}/t_w for the intermediate length strut with $L = 4000$ mm. Graphs are as described in Figure 6.5. Note that w_{wc}/t_w is now less than an order of magnitude greater than w_{wt}/t_w .

is also captured by the FE model, there are no snap-backs observed in the corresponding equilibrium paths. The variational model shows a stiffer response after the secondary bifurcation, but the predictions of the critical and secondary bifurcations agree well with the FE model and provide the correct trend for the post-buckling behaviour after the secondary instability.

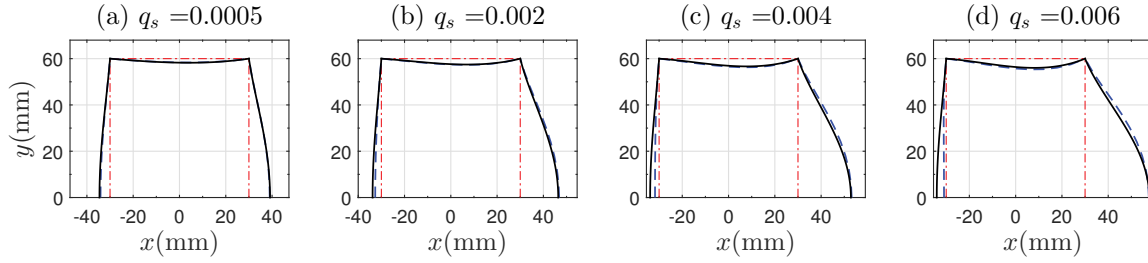


Figure 6.13: Local deformation of the cross-section at mid-span for the intermediate length strut with $L = 4000$ mm with the increase of q_s . Graphs are as described in Figure 6.6.

6.2.4 Short length strut

Previous studies (van der Neut, 1969; Koiter & Pignataro, 1976a) have shown that short length struts exhibit an approximately neutral post-buckling behaviour after the secondary bifurcation point. Therefore, the main focus presently is to determine the axial stiffness reduction factor η for the whole cross-section due to local buckling and the load at the secondary bifurcation point. The current variational model for short struts shows excellent comparisons with the FE model before the secondary bifurcation, as shown in Figure 6.14. However, after the secondary bifurcation, the variational model exhibits stable post-buckling behaviour, even though there are several snap-backs. The FE model shows an approximately neutral, in fact weakly unstable, post-buckling behaviour and there are also several snap-backs observed. Although the variational model shows a relatively stiffer response after the secondary bifurcation, the location of the secondary bifurcation point agrees very well with the FE model, as shown in Figure 6.14(d), which is meaningful for practical considerations in terms of ultimate load predictions.

It should be noted that even though the variational and FE models exhibit different post-buckling trends in the interactive buckling range, they show excellent comparisons for the local mode, *i.e.* the solutions for the normalized local out-of-plane displacement in the more compressed web w_{wc} , the less compressed web w_{wt} (Figure 6.15) and the cross-section deformation profile at mid span (Figure 6.16). In a similar fashion to the intermediate length strut, the ratio w_2/w_1 increases alongside the increase of q_s , leading to the transition

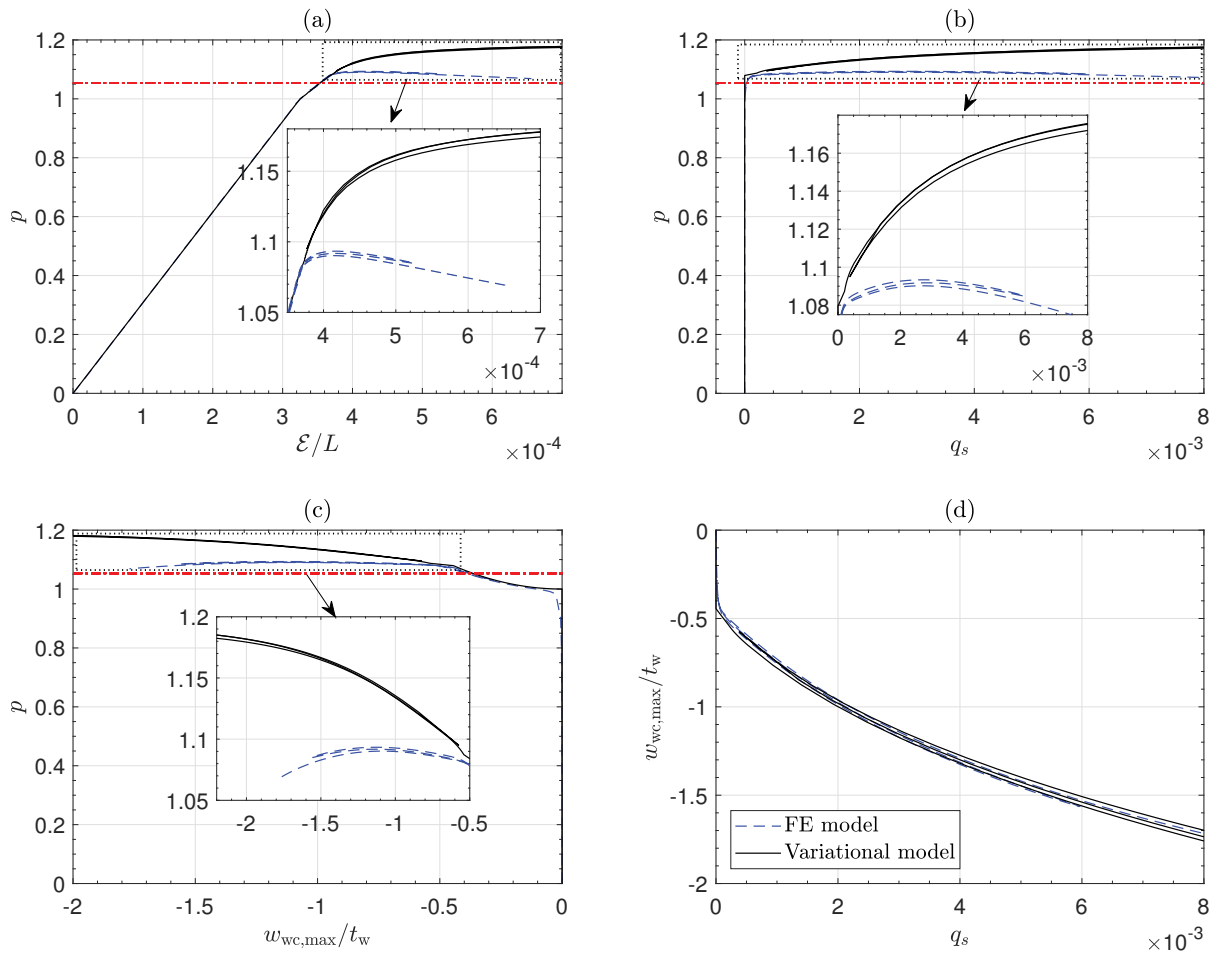


Figure 6.14: Nonlinear equilibrium paths for the short length strut with $L = 3600$ mm from the variational and FE models. Graphs (a–d) are as described in Figure 6.4. The dot-dashed line in (a–c) represents the normalized effective global buckling load $\eta P_o^C / P_1^C = 1.051$, where η is the axial stiffness reduction factor for the whole cross-section due to the local buckling. Insets in (a)–(c) present close-ups of graphs that show the snap-backs in the interactive post-buckling range.

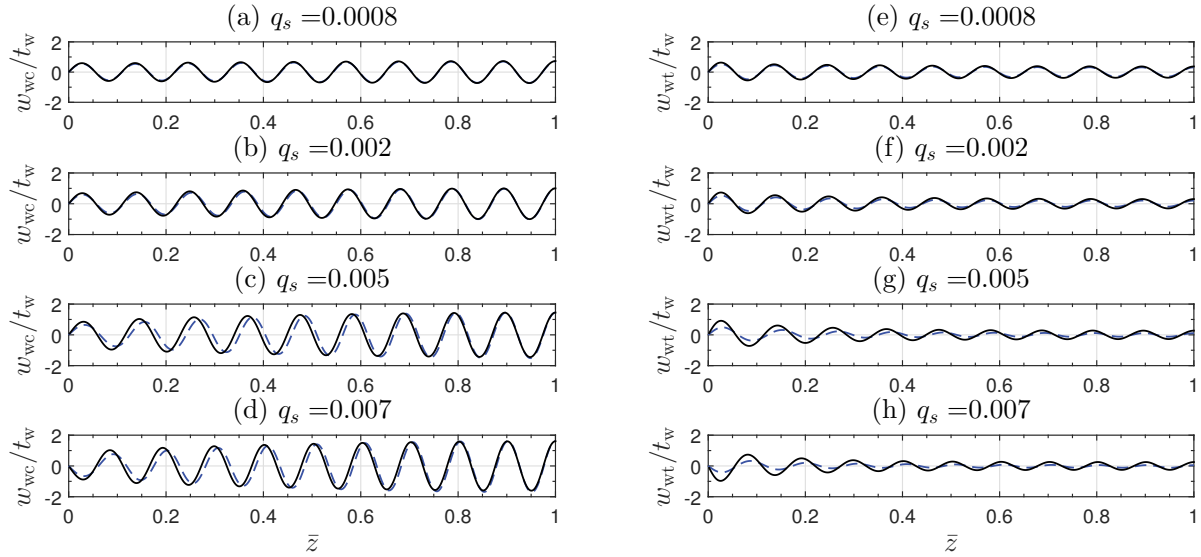


Figure 6.15: Evolution of the numerical solutions for (a–d) w_{wc}/t_w and (e–h) w_{wt}/t_w for the short length strut with $L = 3600$ mm. Graphs are as described in Figure 6.5. Note that w_{wc}/t_w is the same order of magnitude as w_{wt}/t_w .

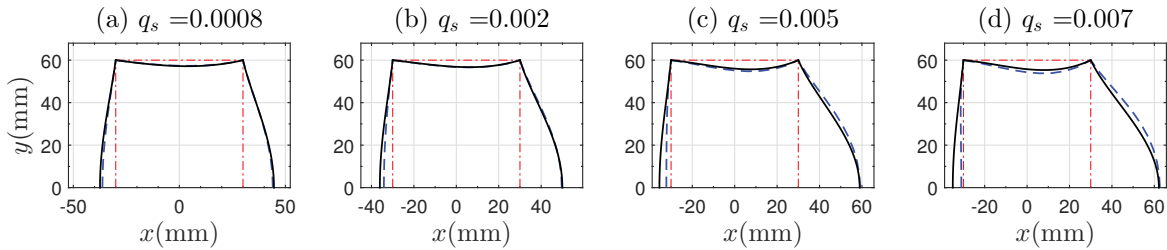


Figure 6.16: Local deformation of the cross-section at mid-span for the short length strut with $L = 3600$ mm with the increase of q_s . Graphs are as described in Figure 6.6.

of w_{wc} from being initially distributed to localized and the decay of the w_{wt} amplitude. Moreover, a change in the number of peaks and troughs is also observed, which corresponds to the snap-back in the equilibrium path, as shown in Figure 6.14. As for the cross-section deformation at mid-span, a profile transition from that dominated by mode 1 to one being dominated by mode 2 is also observed.

Compared with the other example struts, the strain level is much higher at and beyond the secondary bifurcation point, which makes the assumptions that are applicable to slender struts less valid. All the reasons leading to the stiffer post-buckling response in the transitional and intermediate length struts can also be used to explain the relatively stiffer

response of the strut predicted by the variational model. Moreover, it should be recalled that any explicitly transverse displacements within the cross-section are omitted in the current variational model and only Poisson's ratio effects are accounted in those directions. However, the corner joints of the cross-section would move with the progress of mode interaction, even though the magnitude is quite small, as illustrated in Figure 6.17. The effects become more significant in the short length struts, as shown in Figure 6.18.

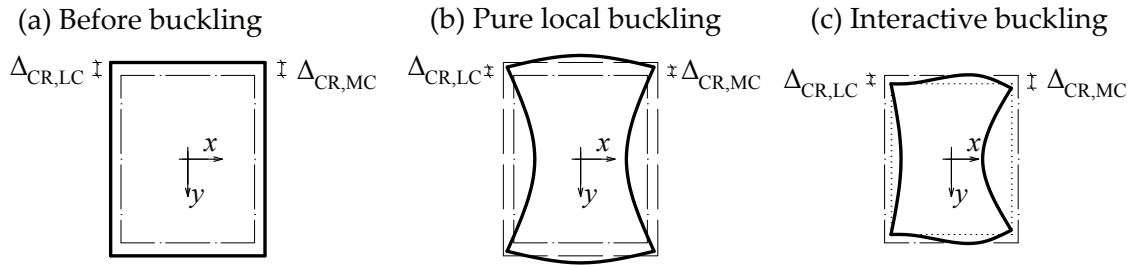


Figure 6.17: In-plane displacements within the cross-section. (a) Expansion due to the Poisson's ratio effect before local buckling occurs. (b) Symmetrical contraction due to pure local buckling. (c) Asymmetrical contraction due to interactive buckling. The thick solid line and the dot-dashed line represent the deformed and undeformed shape respectively. The dashed line in (b) represents the deformed shape before buckling. Also shown are the vertical displacements of the more and less compressed web-flange joints $\Delta_{CR,MC}$ and $\Delta_{CR,LC}$. The small reduction in the overall cross-section depth and width would account for some reduction in the post-buckling stiffness.

which presents results from the FE model. The omission of the explicitly transverse displacements has also been discussed recently in a related study (Garcea *et al.*, 2017). To capture the full post-buckling path accurately, a local mode description that includes the cross-section in-plane displacement field, *i.e.* the transverse displacements in both flanges and webs, would be required (Garcea *et al.*, 2017), but this would complicate the current variational formulation considerably.

From the FE results and previous studies (Bai & Wadee, 2016), it has been shown that the strut is approximately neutrally stable after the secondary bifurcation. Therefore, locating the secondary bifurcation point is in fact sufficient for practical strength prediction. Moreover, since the variational model shows excellent agreement with the FE model before the secondary bifurcation, the stiffness reduction factor η can be obtained precisely from

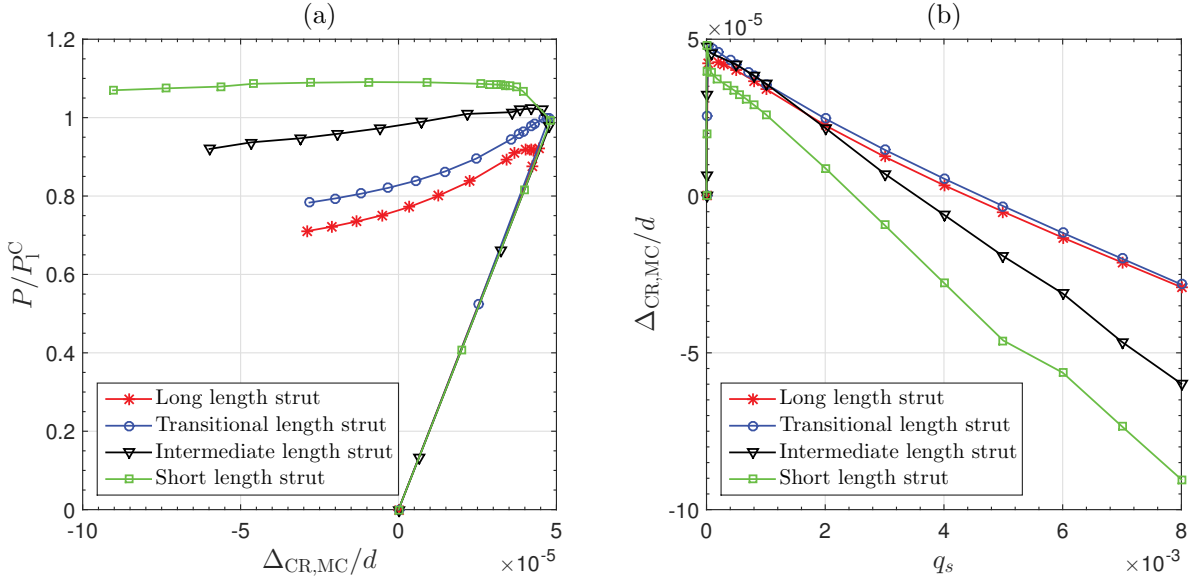


Figure 6.18: Normalized vertical in-plane displacement in the more compressed web $\Delta_{CR,MC}/d$ at mid-span (see Figure 6.17) versus (a) normalized load P/P_1^C and (b) q_s for struts with different lengths from the FE results. The variational model currently omits this displacement.

the load–end-shortening relationship, thus:

$$\eta = \frac{(dP/d\mathcal{E})_{\text{post}}}{(dP/d\mathcal{E})_{\text{pre}}} = 0.645. \quad (6.1)$$

Therefore, the Euler buckling load for the locally buckled strut ηP_o^C can be calculated and is plotted with the dot-dashed line in Figure 6.14. In comparison with the ultimate load from the FE model, $P_{u,FE}$, the variational model provides a safe, yet accurate strength prediction where $\eta P_o^C/P_{u,FE} = 0.976$. Hence, it may be concluded that the developed variational model has been satisfactorily verified for all the zones considered and may now be investigated further.

6.3 Discussion and comparison with Van der Neut's model

A parametric study is now presented to determine the respective boundaries for the four distinct length domains using the developed variational model. The numerical results are presented in Figure 6.19 in the style of the classical Van der Neut curve that was shown

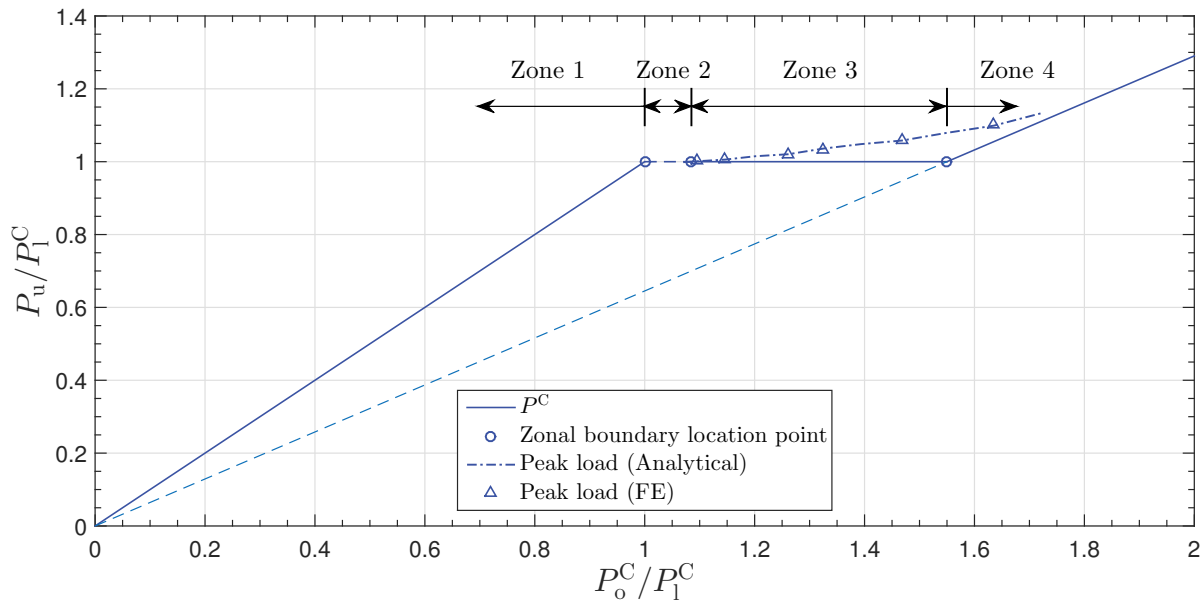


Figure 6.19: The numerically obtained Van der Neut curve for struts with cross-section properties presented in Table 4.1. It should be noted that the slope of dashed line is in fact equal to the axial stiffness reduction factor for the whole cross-section due to pure local buckling.

in Figure 6.1. The shape of the curve is very similar to previous similar results for stiffened panels (Koiter & Pignataro, 1976a; Wadee & Farsi, 2015) and I-section struts (Bai & Wadee, 2016; Liu & Wadee, 2016a). The ultimate load for perfect long and transitional length struts is the corresponding critical buckling load P^C . The triggering of mode interaction leads to unstable post-buckling behaviour. Particularly for transitional length struts (zone 2), since the critical and secondary bifurcations are practically coincident, reaching the ultimate load in practice may not be possible due to the inherently high degree of sensitivity to imperfections that would be expected (Thompson & Hunt, 1973; Thompson

([& Supple, 1973](#); [Tvergaard, 1973](#); [van der Neut, 1973](#); [Thompson & Hunt, 1974](#); [Wadee & Farsi, 2015](#); [Bai & Wadee, 2015a](#); [Liu & Wadee, 2016b](#)). For intermediate length struts (zone 3), stable post-buckling behaviour is exhibited after the critical bifurcation, as shown in Figure [6.11](#). Therefore, the ultimate load is higher than the critical (local) buckling load. For the ultimate load prediction, the variational model shows excellent agreement with the FE model, as shown in Figure [6.19](#). For the short length struts (zone 4), stable post-buckling behaviour is also exhibited after the critical bifurcation and approximately neutrally stable post-buckling behaviour after the secondary bifurcation. The variational model can also predict the ultimate load with good agreement compared to the FE model and ηP_o^C provides a safe, yet relatively accurate, prediction for the ultimate load.

Since the struts exhibit distinct behaviour in different zones, it is beneficial to determine the boundary between each zone for practical engineering purposes. The boundary between zones 1 and 2 is very straightforward since this is by definition where the global buckling load P_o^C and the local buckling load P_1^C precisely coincide.

The boundary between zones 2 and 3 corresponds to the competing mode between pure local and global buckling due to the cross-section bending stiffness reduction caused by local buckling of the compressed side of the cross-section, as shown in Figure [6.20](#). The buckling loads for the depicted modes (I) and (II) are the local buckling load P_1^C and the reduced global buckling load $\Phi_r P_o^C$ respectively, where Φ_r is the bending stiffness reduction factor due to local buckling of the more compressed web and flanges. At the zonal boundary, the ultimate load for the two competing modes would be the same, *i.e.* $\Phi_r P_o^C = P_1^C$, which leads to the value $P_o^C/P_1^C = 1/\Phi_r$.

For the ideal two-flange model originally presented by Van der Neut, Φ_r can be obtained from Engesser's so-called 'double modulus' theory ([Bažant & Cedolin, 1991](#)). The current variational formulation cannot in fact replicate the results of Van der Neut's idealization precisely since shear strain is neglected in the latter. However, a simplified rectangular hollow section strut model with pinned corners within the cross-section, which is very sim-

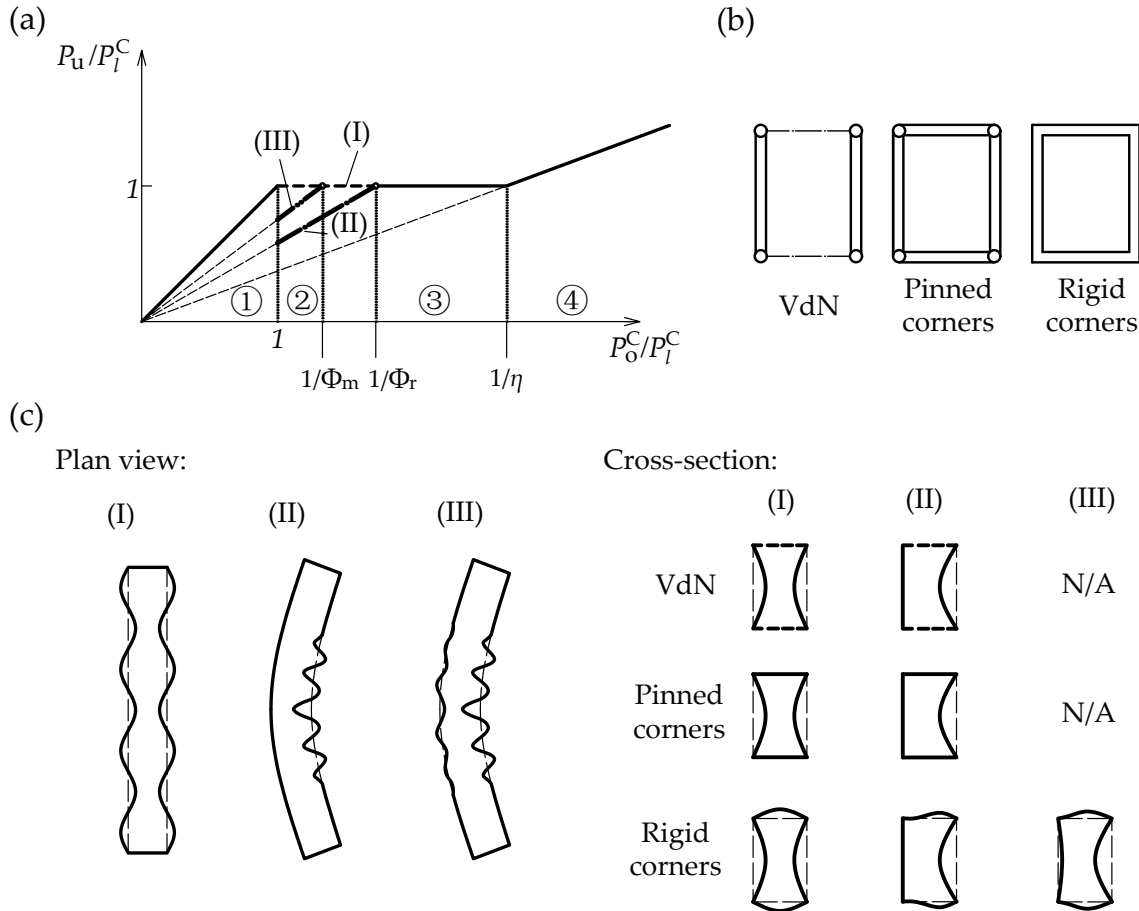


Figure 6.20: (a) The Van der Neut-type curve sketched with the competing buckling modes in zone 2. (b) Cross-section flange–web conditions for Van der Neut’s model (VdN), a rectangular hollow section with pinned corners and a rectangular hollow section with rigid corners. (c) Competing buckling modes in zone 2 for three different models: (I) pure local buckling; (II) global buckling from the cross-section bending stiffness reduction caused by local buckling in the compressed web and flanges; (III) transitional state between (I) and (II). The bending stiffness reduction factor due to local buckling in the more compressed web and flanges is Φ_r and the equivalent reduction factor for the transitional state (III) is Φ_m .

ilar to van der Neut’s ideal model, may be used for validation and illustration purposes, as shown in Figure 6.20(b). Since each corner within the cross-section is pinned, the web and flange plates buckle independently. In zone 2, when global buckling is triggered, only the more compressed web remains buckled, as shown in Figure 6.20(c), and the corresponding effective cross-section stiffness distribution is shown in Figure 6.21(a). Based on the cross-section stiffness distribution, using the double modulus theory, the details of which are in Appendix B, by setting $\eta_f(x)$ in Eqs. (B.2) and (B.8) to unity, the following expression for

Φ_r is obtained:

$$\Phi_r = \frac{[(\bar{\eta}_w + 1)^2 t_w^2 + 12b^2 \bar{\eta}_w] \phi_c^2 + 2[(\bar{\eta}_w + 1) t_w^2 + 4(\bar{\eta}_w + 1) b^2] \phi_c \phi_t + 4b^2 \phi_t^2}{2[2\phi_t + (1 + \bar{\eta}_w) \phi_c] [(3b^2 + t_w^2) \phi_c + b^2 \phi_t]}. \quad (6.2)$$

For the strut with the same cross-section and material properties as the example struts in the current chapter, $1/\Phi_r = 1.462$, which is very close to the value computed using the variational model, where $P_o^C/P_1^C = 1.461$; this verifies the effectiveness of the double modulus theory for predicting the boundary between zones 2 and 3 for such cases. Moreover, it should also be noted that the value is much smaller than that obtained by van der Neut, where $\bar{\eta}_w = 0.408$ and $1/\Phi_r = (1 + \bar{\eta}_w)/(2\bar{\eta}_w) = 1.725$, even though the equivalent axial stiffness reduction factor $\bar{\eta}_w$ in the more compressed web is adopted as the same value due to the pinned corners within the cross-section. The difference arises owing to the inclusion of both flanges, which contribute the full elastic modulus E .

For the hollow section with rigid flange–web joints, which is the most widely applicable for engineering practice, the axial stiffness distribution in the cross-section for the competing mode is not as straightforward as the pinned corner case due to the interaction of the flanges and webs within the cross-section. Therefore, three different stiffness distribution candidate schemes are considered, as shown in Figure 6.21, and the corresponding

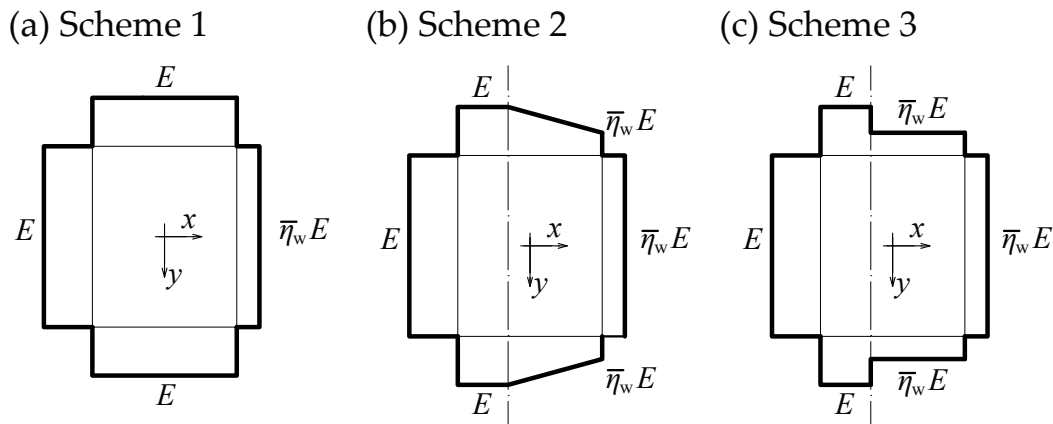


Figure 6.21: Cross-section axial stiffness distribution schemes where the stiffness is directly proportional to the material Young’s modulus E and $\bar{\eta}_w$ is the equivalent axial stiffness reduction factor due to local buckling of the more compressed web.

relationship between $1/\Phi_r$ and $\bar{\eta}_w$ can be established using Eq. (B.8). Figure 6.22 shows

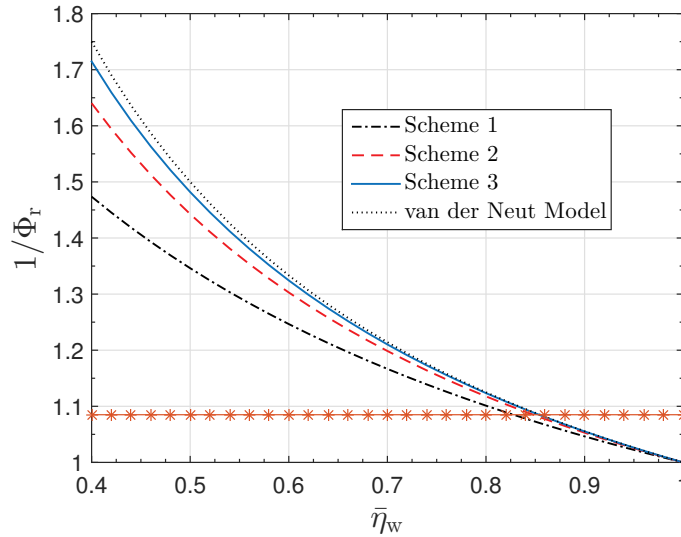


Figure 6.22: Relationship between $1/\Phi_r$ and $\bar{\eta}_w$ for the cross-section stiffness distributions presented in Figure 6.21 and the expression proposed by Van der Neut. The asterisk line represents the equivalent $1/\Phi_r$ for the example struts obtained from the current variational model results that are verified by FE.

the relationship for the strut with the same cross-section and material properties as the example struts. The value of $1/\Phi_r$, *i.e.* the ratio P_o^C/P_1^C at the boundary between zones 2 and 3, increases with the reduction of the effective axial stiffness of the whole section from schemes 1 to 3 as well as with the reduction of the equivalent axial stiffness of the more compressed web $\bar{\eta}_w$. Since the actual effective axial stiffness of the more compressed side of the flanges for the competing mode would be reduced due to local buckling, as shown in Figures 6.23 and B.1(b), scheme 1 would provide the lowest limiting prediction for $1/\Phi_r$ if the double modulus approach were to be applicable for the cross-section case with rigid flange–web joints.

However, the parametric study (see Figure 6.19) shows that the value of P_o^C/P_1^C at the boundary of zones 2 and 3 for the example struts with rigid joints between flanges and webs is 1.085, which corresponds to the asterisk line in Figure 6.22. Since it has been noted that scheme 1 provides the lowest limiting prediction of $1/\Phi_r$, the corresponding value of $\bar{\eta}_w$ for the more compressed web should be even larger than 0.8, as shown in Figure 6.22. Even

though the rigid flange–web joints can provide more restraint to the more compressed web, thus leading to a higher post-buckling stiffness, the value of $\bar{\eta}_w$ for the more compressed web using the isolated more compressed web model is 0.46 (Shen *et al.*, 2017). Therefore, it would seem that including the contribution of the flanges and the rigid flange–web joints not only introduces additional stiffness when compared to the pinned cross-section case but also potentially more competing modes, which diminishes the validity of the double modulus approach in such cases.

It should be stressed that in both the Van der Neut model and the case where the cross-section has pinned corners, the effective axial stiffness in the more compressed web remains approximately the same before and after the transition from the pure local buckling mode to local–global interactive buckling due to the simply-supported boundary condition of the unloaded edges, as shown in Figure 6.20(c). However, for the rigid flange–web joint case, there is a reduction in the deformation of the more compressed side after the transition, which is particularly apparent in the flanges, as can be seen from Figure 6.23. It suggests

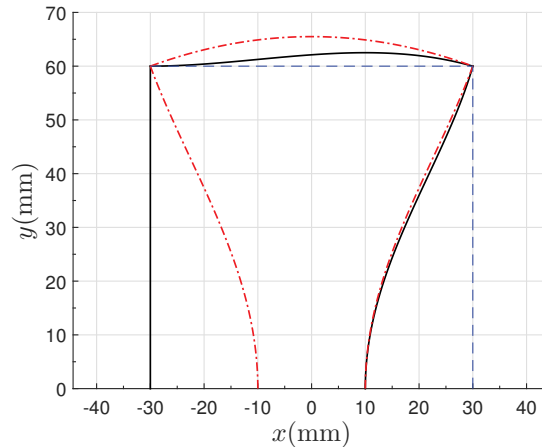


Figure 6.23: Cross-section deformation for the pure local buckling case (dot-dashed line) using Eqs. (5.2) and (5.3) and the global buckling induced local buckling case (solid line) using Eqs. (5.9)–(5.11). The deformation has been amplified by a factor of 20 to aid visualization.

that the unloading of the less compressed web and flanges affects the stiffness distribution in the more compressed side of the cross-section, which does not occur in Van der Neut’s

ideal model and the case of the cross-section with pinned corners. It implies that there is an increase in the axial stiffness of the more compressed side of the cross-section and it can thus resist higher compressive stresses. The condition for the boundary between zones 2 and 3 can thus be written as $P_1^C = \Phi_r P_o^C + \delta P$, where δP is the load increase due to the stiffness redistribution in the cross-section caused by the less compressed side of the cross-section. Therefore, there should be an additional transitional stage (III) between these two more distinct states, as shown in Figure 6.20. This is also confirmed by the numerical results of the cross-section deformation shape for the transitional length strut. The existence of this further transitional stage moves the boundary between zones 2 and 3 to the left when compared with stage (II), as shown in Figure 6.20(a), where P_o^C/P_1^C is equal to $(1 - \delta P/P_1^C)/\Phi_r$. This finding is also in accord with results from previous work on stiffened panels (Koiter & Pignataro, 1976a; Wadee & Farsi, 2015) and I-section struts (Bai & Wadee, 2016; Liu & Wadee, 2016a). Since the unstable range is notorious for its imperfection sensitivity (Bai & Wadee, 2015a; Wadee & Farsi, 2015), a somewhat reduced imperfection sensitivity range may be expected for such struts; these matters are investigated further in the subsequent chapters.

The boundary between the intermediate length struts (zone 3) and the short length struts (zone 4) is the same as that in Van der Neut's curve, where $P_o^C/P_1^C = 1/\eta = 1.550$. From Figure 6.14(a-c), with the decrease of the strut length, the peak load would converge to ηP_o^C , as shown in Figure 6.19. However, it should be noted that the straight line in zone 4 would in fact be curved with a decreasing slope due to the decreasing stiffness reduction factor caused by the effects of large deflections in plates; a similar effect would occur if a yield stress were introduced into the material model (Liu & Wadee, 2016a).

Finally, it should be stressed that the factors listed for the movement of the boundary between zones 2 and 3 also affect the value of P_o^C/P_1^C at the boundary of zones 3 and 4. However, since the local buckling mode is more developed before mode interaction is triggered, the effects of stiffness redistribution would be much smaller. Moreover, adopting

η as the bending stiffness reduction factor would provide an accurate, yet safe ultimate load prediction.

6.4 Concluding remarks

The nonlinear variational model in Chapter 5 has been adopted to analyse the interactive buckling behaviour of perfect elastic thin-walled rectangular hollow section struts with different lengths under pure compression. Numerical examples, considering four representative lengths corresponding to distinct parts of the Van der Neut curve, have been presented and verified using the commercial FE package ABAQUS. Using the verified variational model, the boundaries of four distinct length-dependent domains have been identified for realistic cross-section characteristics for the first time.

Unstable post-buckling behaviour due to mode interaction was observed in long, transitional and intermediate length struts. Potentially dangerous behaviour, *i.e.* a sharp drop in the load capacity immediately after the ultimate load is reached, has been identified where the global buckling load is close to the local buckling load. A progressive change in the local buckling mode is observed within the nonlinear post-buckling range in all struts. In particular, for intermediate and short length struts, snap-backs that correspond to the change in the number of troughs and peaks in the local mode that are akin to cellular buckling, are observed. The parametric study on strut length shows that the notoriously unstable post-buckling range for rectangular hollow-section struts is in fact significantly smaller than that predicted by Van der Neut's idealized model and the stiffness reduction factor is also considerably higher. The reason for this difference has been identified as being derived from the interaction between the individual plates due to the rigid corners within the cross-section, which lead to some stiffness redistribution. This is in contrast with the assumption that the corners are pinned where the web and flange plates behave independently.

The highly unstable post-buckling behaviour of struts in the transitional range between zones 1 and 2 and the whole range of zone 2 indicate that they may be very sensitive to initial imperfections, *i.e.* a tiny imperfection may lead to significant erosion in the load-carrying capacity. Therefore, in the following chapter, the variational model is adopted to investigate the imperfection sensitivity of such struts exhibiting local–global mode interaction.

Chapter 7

Imperfection sensitivity

The previous chapter investigated the effect of the strut length on the nonlinear interactive buckling behaviour of perfect thin-walled RHS struts. However, there are always imperfections in real structures, either in the geometry or in the loading. More importantly, thin-walled plated structures susceptible to interactive buckling tend to be highly sensitive to imperfections (Koiter & Pignataro, 1976a; Thompson *et al.*, 1976; Loughlan, 1983; Goltermann & Möllmann, 1989; Wadee, 2000; Bai & Wadee, 2015a; Wadee & Farsi, 2015; Liu & Wadee, 2016b); a tiny imperfection may lead to a significant erosion in the load-carrying capacity evaluated from a linear analysis.

In the current chapter, the effects of geometric imperfections on the ultimate load and equilibrium behaviour of thin-walled RHS struts is investigated using the full variational model developed in Chapter 5. In a similar way to Chapter 6, the developed system of nonlinear ordinary differential and integral equations subject to boundary conditions is solved using the numerical continuation software AUTO-07P. The resulting equilibrium paths are presented for various different cases and the erosion in the load-carrying capacity due to imperfections is observed. The results from the variational model show good comparisons with the numerical results from GNIA using the nonlinear FE method developed

in Chapter 3. A simplified method to calculate the pitchfork bifurcation load where mode interaction is triggered for struts with global imperfections is developed for the first time. The relative significance of global and local imperfections for struts with different lengths is investigated. Based on the numerical results, the simplified method is calibrated to predict the ultimate load for struts with tolerance level global imperfections and combined local and global imperfections. The current work provides an improved understanding of the imperfection sensitivity of thin-walled rectangular hollow section struts exhibiting mode interaction, which will allow the establishment of more rational and robust design guidance for such structural components in Chapter 9.

7.1 Numerical results, verification and discussion

Chapter 6 demonstrated that there is a redistribution of stiffness across the cross-section in the transition from the pure local buckling mode to the global buckling induced interactive mode, as shown in Figure 6.23. Specifically, owing to the rigid connection between each individual plates, the less compressed web provides additional restraint to the more compressed side (Bijlaard & Fisher, 1953; Hancock, 1981; Young & Rasmussen, 1997; Shen & Wadee, 2018b). Hence, there is an effective increase in the axial stiffness of the more compressed web and flanges, thus leading to a higher resistance to compressive stresses. It implies that the mono-symmetric cross-section imperfection profile would be effectively more severe than the doubly-symmetric case. Therefore, in the current chapter, only the mono-symmetric cross-section deformation profile, as shown in Figure 5.2(b), is used as the cross-section component for the local imperfection. Therefore, the local out-of-plane imperfection, Eq. (5.13), can be reduced to:

$$w_{f0}(x, z) = f_{2f}(x)w_0(z), \quad w_{wc0}(y, z) = f_{2wc}(y)w_0(z), \quad w_{wt0}(y, z) = f_{2wt}(y)w_0(z), \quad (7.1)$$

where the cross-section components f are the same as described in Eqs. (5.9)–(5.11).

Previous studies on the imperfection sensitivity of thin-walled struts (van der Neut, 1969; Koiter & Pignataro, 1976a; Bai & Wadee, 2015a; Wadee & Farsi, 2015; Liu & Wadee, 2016a) found that the maximum erosion in the load-carrying capacity principally occurs within the range where the global buckling load is close to the local buckling load, *i.e.* the transitional range between zones 1 and 2 and the whole range of zone 2, as shown schematically in Figure 7.1. Therefore, the imperfection sensitivity of two typical length

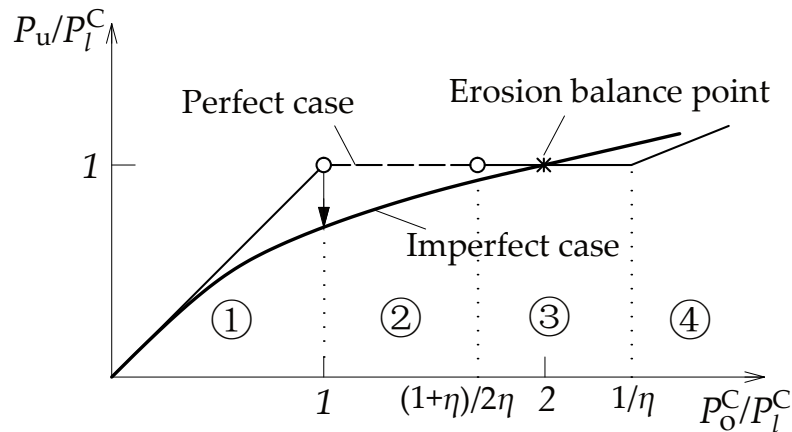


Figure 7.1: The Van der Neut curve for the geometrically perfect and imperfect cases (van der Neut, 1969). The quantity η is the stiffness reduction factor due to the local buckling of the flanges. The imperfect case line shows that within zones 1–3, there is a reduced ultimate load compared to the perfect case. There is also an ‘erosion balance point’ marked where the curve for the imperfect case intersects with the perfect case.

struts, where global and local buckling are critical respectively but the ratio of the global and local buckling loads is close to unity in both cases, are analysed in detail. The cross-section geometry and material properties of the example struts are the same as that in Chapter 6. Table 7.1 summarizes the strut lengths, the buckling loads and corresponding zones, as defined in Chapter 6. The effects of global imperfections, local imperfections and their combination on the nonlinear equilibrium path and load-carrying capacity of the two example struts are investigated. The solution of the governing equilibrium equations is obtained within the numerical continuation and bifurcation software AUTO-07P.

Typical equilibrium paths for perfect and imperfect example struts alongside the numerical continuation procedures to solve the equilibrium paths using AUTO are shown diagram-

Table 7.1: Theoretical values of the global and local buckling loads for the two separate lengths studied.

L (mm)	P_o^C (kN)	$P_{1,AUTO}^C$ (kN)	$P_{1,ABAQUS}^C$ (kN)	P_o^C/P_1^C	Zone	Length description
4800	22.67	24.61	24.57	0.92	1	‘Long’
4500	25.79	24.61	24.58	1.05	2	‘Transitional’

matically in Figure 7.2. For the case where only the global imperfection exists two stages

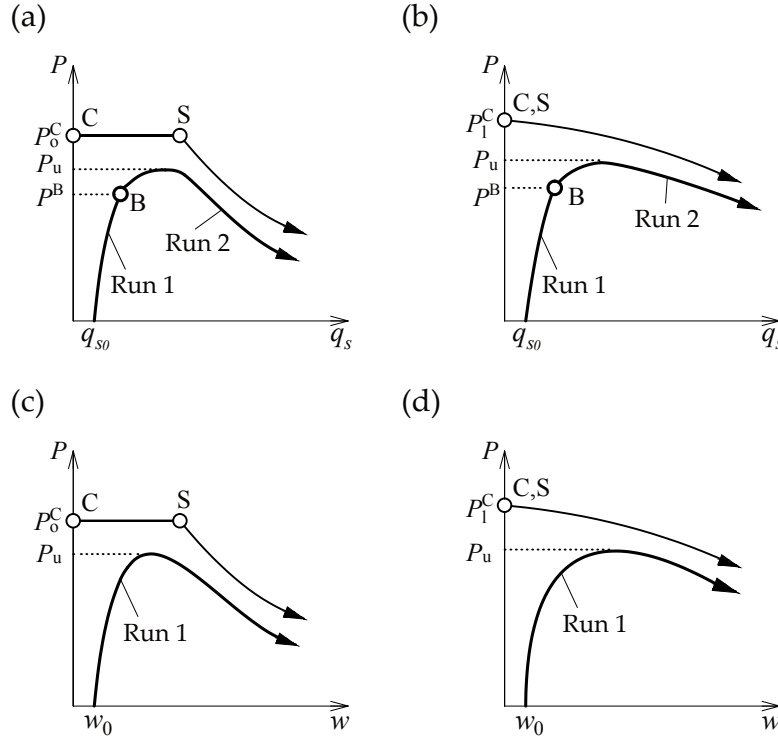


Figure 7.2: Sketches of the equilibrium paths and their numerical continuation procedures for imperfect struts primarily in zones 1 and 2. (a) Global buckling being critical with an initial out-of-straightness global imperfection q_{s0} only; (b) local buckling being critical with q_{s0} only; (c) global buckling being critical with a mono-symmetric local imperfection w_0 only or with both w_0 and q_{s0} ; (d) local buckling being critical with w_0 only or with both w_0 and q_{s0} . The thicker and thinner lines represent the imperfect and perfect systems respectively. Circles represent critical (C) and secondary (S) bifurcation points for the perfect systems and a pitchfork bifurcation point (B) for the imperfect system; P^B represents the load at the pitchfork bifurcation point.

are required to obtain the whole equilibrium path, as shown in Figure 7.2(a–b). Branch switching is necessary at the pitchfork bifurcation point (B) (Glendinning, 1994), which is the generic term for a conventional symmetric (stable or unstable) bifurcation (Thompson & Hunt, 1973), where local and hence interactive buckling is triggered, to trace the post-

buckling equilibrium path. For the cases with pure local imperfections and with combined local and global imperfections, only one run is required to obtain the whole equilibrium path, as shown in Figure 7.2(c, d). The mono-symmetric local imperfection immediately breaks the symmetry as the numerical run begins and therefore q_s and q_t are introduced without the need for branch switching.

7.1.1 Global imperfections ($q_{s0} \neq 0, w_0 = 0$)

In this section, the effects of a purely global imperfection are studied. Only initial sway and tilt imperfections, *i.e.* q_{s0} and q_{t0} , which satisfy the relationship from Eq. (5.37), are introduced. A set of values for the normalized initial sway imperfection amplitude q_{s0} ranging from 10^{-4} to 10^{-3} is selected for analysis. Figures 7.3 and 7.4 show a family of equilibrium paths with increasing global imperfection size and the relationship between the ultimate load and the global imperfection amplitude for the long (zone 1) and transitional length (zone 2) struts respectively. It is clearly observed that the ultimate load decreases as the imperfection size increases. For $q_{s0} = 1/1000$, which is the tolerance level for global imperfections recommended in the relevant part of Eurocode 3 (EN-1993-1-3:2006E, 2006), the erosion in the load-carrying capacity is approximately 25% compared with the critical buckling load of the perfect system for both struts. From the equilibrium path, the transition from highly unstable to approximately neutral post-buckling behaviour can be observed with the increase of the global imperfection size q_{s0} . Specifically, the snap-back and the sharp load drop at the secondary bifurcation in the load-end-shortening relationship for the perfect case disappear gradually with the increase of the imperfection size. It can also be seen that all equilibrium paths converge asymptotically to the same state, as would be expected from classical studies (Thompson & Hunt, 1973).

Moreover, for the perfect case and the cases where the imperfection size is vanishingly small, the triggering of local buckling represents the ultimate state, which is followed by

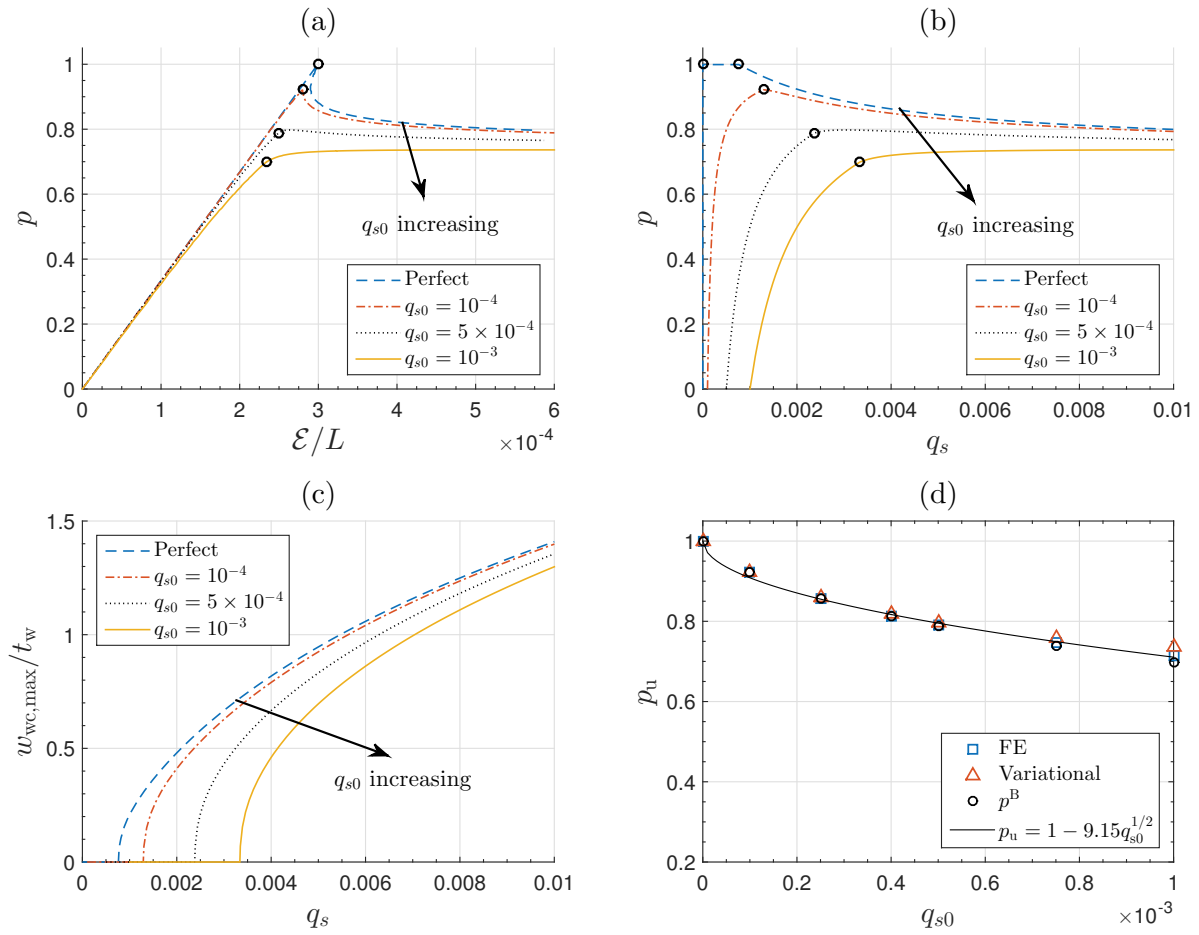


Figure 7.3: Equilibrium paths and the imperfection sensitivity graph for the long length strut ($L = 4800$ mm) with different global imperfection sizes q_{s0} . Graphs of the normalized load ratio $p = P/P^C$, where P^C is the critical buckling load for the perfect strut, versus (a) the normalized end-shortening \mathcal{E}/L , and (b) the normalized amplitude of the sway mode q_s ; (c) shows the normalized maximum amplitude of the local buckling deflection in the more compressed web $w_{wc,max}/t_w$ versus q_s ; (d) shows the normalized ultimate load $p_u = P_u/P^C$ from both the FE and variational models and the normalized load at the pitchfork bifurcation point for the imperfect system $p^B = P^B/P^C$ against q_{s0} showing the sensitivity to initial global imperfections. Circles in (a) and (b) represent bifurcation points.

unstable post-buckling behaviour. However, with increasing imperfection size, there is a further increase in the load-carrying capacity after local buckling in the more compressed web is triggered, as shown in Figures 7.3 and 7.4, which has also been reported previously (van der Neut, 1969; van der Neut, 1973; Bai & Wadee, 2016; Liu & Wadee, 2016b). Therefore, it would seem that determining the load at the pitchfork bifurcation point P^B

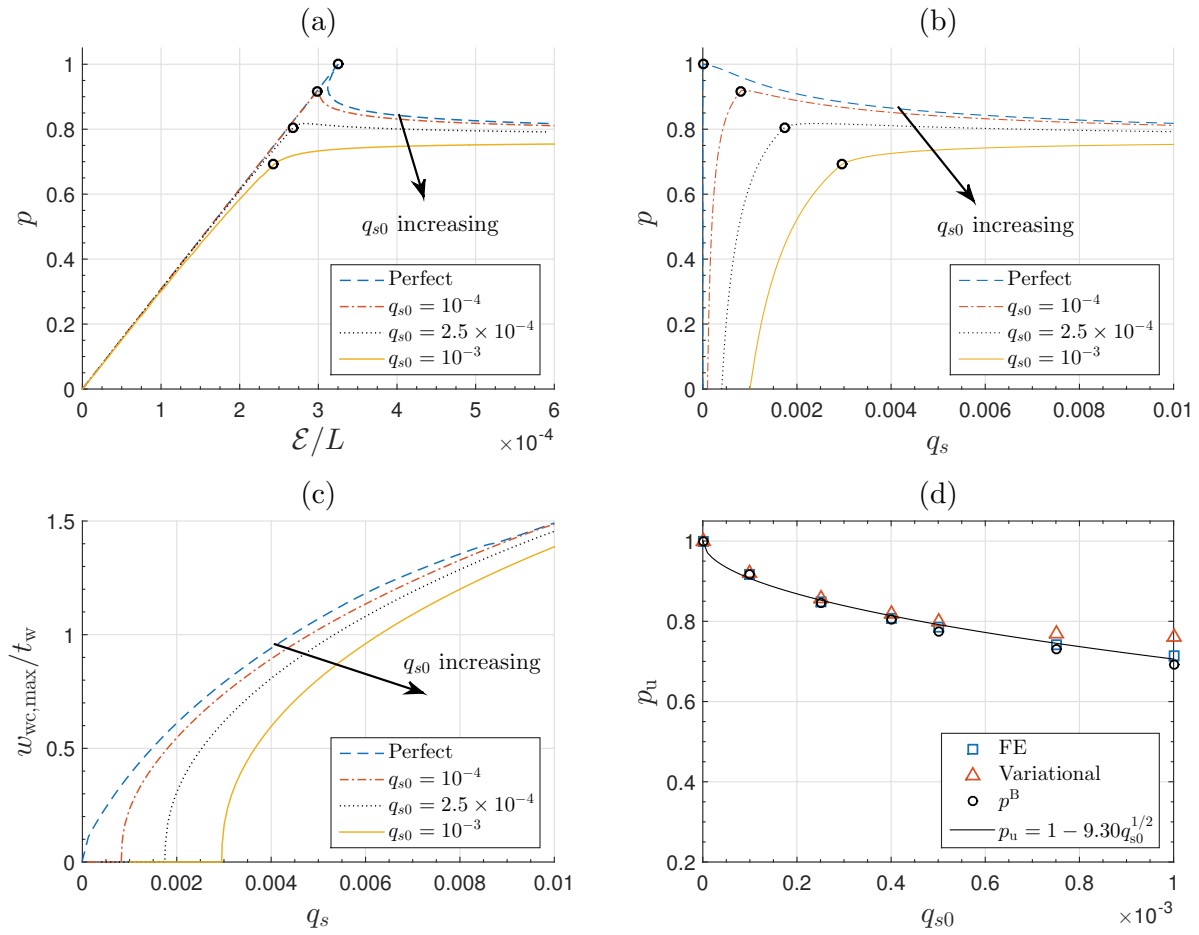


Figure 7.4: Equilibrium paths and the imperfection sensitivity graph for the transitional length strut ($L = 4500$ mm) with different global imperfection sizes q_{s0} . Graphs (a)–(d) are as described in Figure 7.3.

would provide a safe, yet accurate, method to predict the ultimate load for struts with purely global imperfections.

As shown in Figure 7.5(a) and (c), the global imperfection size also affects the profile of the interactive buckling mode in the proximity of the pitchfork bifurcation point. For the long length strut, the interactive buckling mode becomes more localized with increasing imperfection size. As for the transitional length strut, the global imperfection immediately breaks the symmetry, making the profile change from approximately periodically distributed along the length to localized at mid-span. The increasing imperfection size also increases the degree of localization of the interactive buckling mode as that for the long

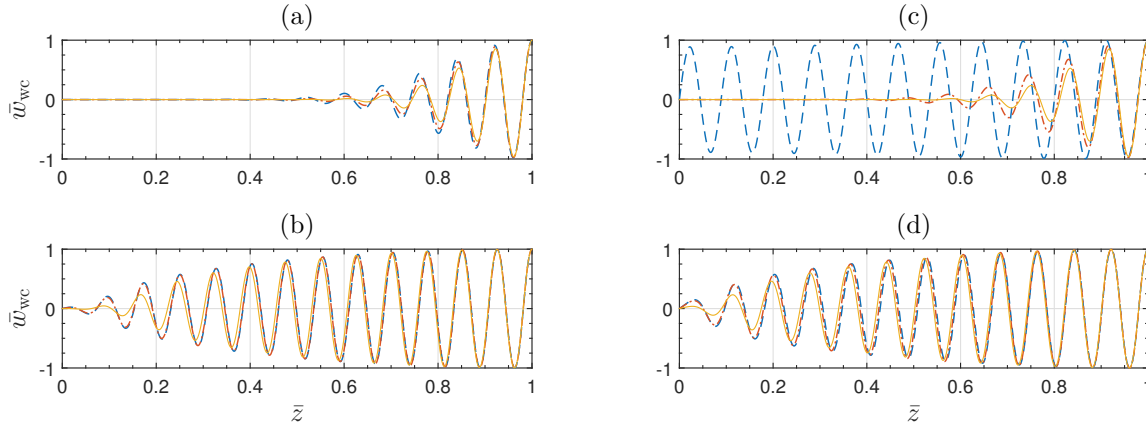


Figure 7.5: Numerical solutions of the longitudinal profile of the local out-of-plane displacement in the more compressed web $\bar{w}_{wc} = w_{wc}/w_{wc}(\bar{z} = 1)$ at (a, c) the pitchfork bifurcation point and (b, d) where $q_s = 8 \times 10^{-3}$ for the long length strut (a–b) and the transitional length strut (c–d) respectively. The dashed, dot-dashed and solid lines represent the cases with perfect and imperfect ($q_{s0} = 10^{-4}$ and 10^{-3}) geometries respectively. Note that the longitudinal coordinate is normalized with respect to half of the strut length $\bar{z} = 2z/L$.

length strut. It should be noted that in both cases the increase in the degree of localization is accompanied by a reduction in the wavelength. With the progress of mode interaction, the post-buckling mode spreads towards the boundary and becomes distributed along the whole length of the strut, as shown in Figure 7.5(b, d). It can be concluded that, in a similar way to the equilibrium path, the post-buckling mode also converges approximately to the same profile in the far-field post-buckling range.

7.1.2 Local imperfections ($w_0 \neq 0$, $q_{s0} = 0$)

For the study where only local imperfections exist, the global imperfection parameters q_{s0} and q_{t0} are set to zero. The cross-section profile of the local imperfection is assumed to be mono-symmetric and defined by Eqs. (5.9)–(5.11). The longitudinal component of the local imperfection w_0 is determined based on fitting the longitudinal component of the first local buckling mode from the FE models using Eq. (5.14). The profile of the imperfection is shown in Figure 7.6. For the long length strut, it is determined that $\alpha = 4.314$ and

$\beta = 47$; whereas for the transitional length strut, $\alpha = 5$ and $\beta = 47$. A set of values for

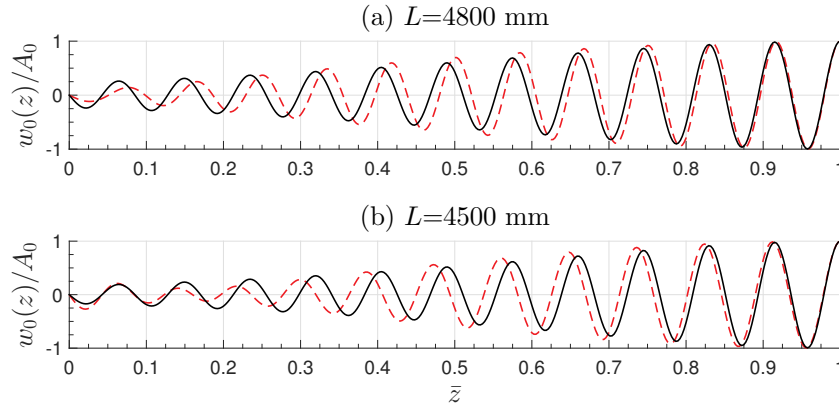


Figure 7.6: Longitudinal component of initial local imperfections for (a) the long length strut and (b) the transitional length strut. Solid and dashed lines represent fitting functions and the first local buckling mode from FE respectively. Note that the longitudinal coordinate is defined as in Figure [7.5](#).

the normalized local imperfection amplitude A_0/t_w ranging from 0.01 to 0.6 is selected for analysis.

Figures [7.7](#) and [7.8](#) show a family of equilibrium paths with increasing local imperfection sizes and the relationship between the ultimate load and the local imperfection amplitude for the long and transitional length struts respectively. The ultimate load drops substantially with increasing local imperfection amplitude. For $A_0/t_w = 0.6 = d/(200t_w)$, which is the tolerance level for local imperfections recommended in Eurocode 3 ([EN-1993-1-3:2006E, 2006](#)), the erosion in the load-carrying capacity is greater than 20% compared with the perfect case for both struts considered. As for the equilibrium paths, in a similar way to the global imperfection case, a transition from highly unstable to mildly stable behaviour is observed in both struts with increasing local imperfection size. Specifically, for the perfect case and the cases where the imperfection size is vanishingly small, reaching the ultimate load is accompanied by potentially unstable behaviour, *i.e.* snap-backs in the load–end-shortening relationship and a simultaneous sharp load drop may be expected. However, for the cases with larger imperfection sizes, the behaviour is relatively stable, *i.e.* the stiffness decreases with an increase of the applied load but remains positive and the

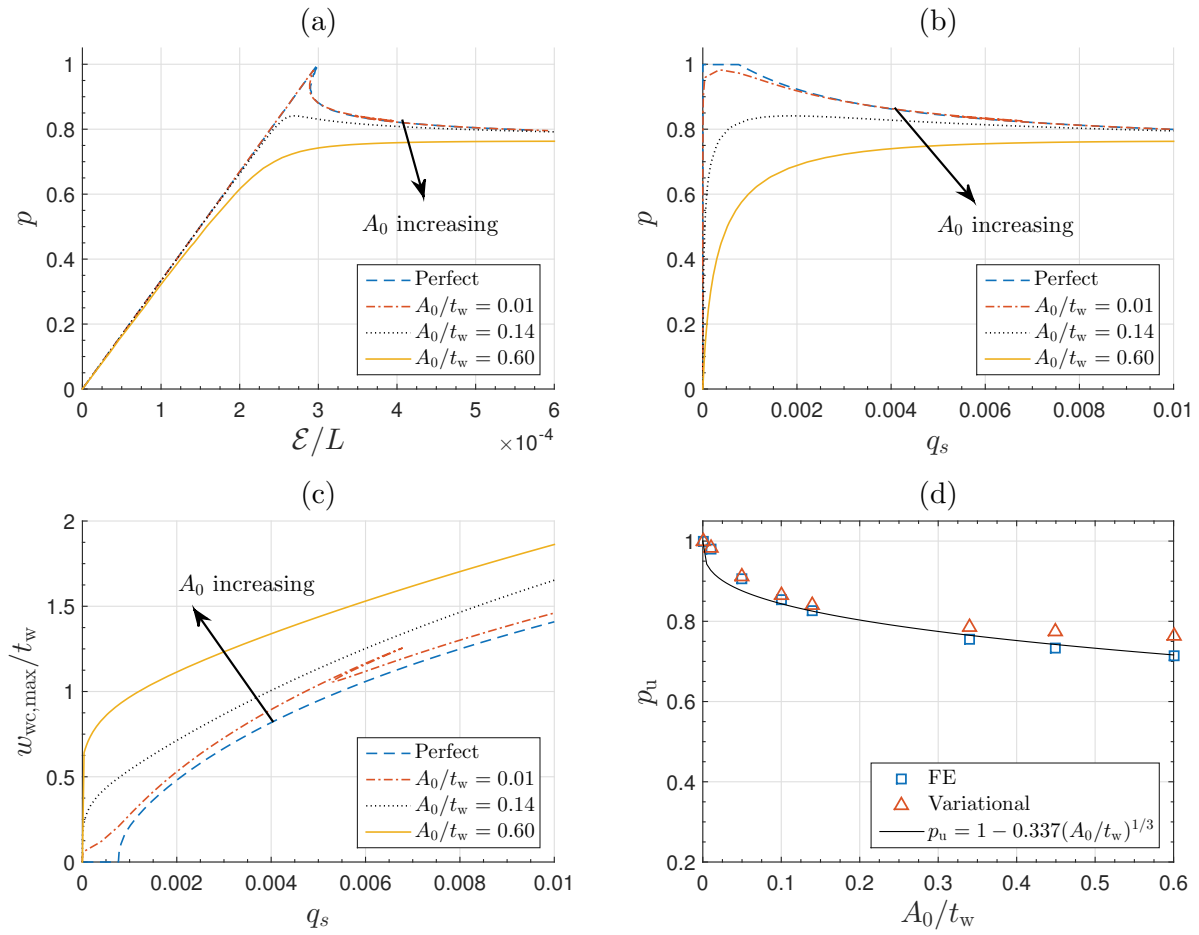


Figure 7.7: Equilibrium paths and the imperfection sensitivity graph for the long length strut with different local imperfection amplitudes A_0 . Graphs (a–c) are as described in Figure 7.3. Graph (d) shows the normalized ultimate load p_u from both FE and variational models against A_0 showing the sensitivity to initial local imperfections.

deformation level at the ultimate load is relatively large.

It should be noted that there is a snap-back in the q_s – w_{wc}/t_w relationship for the long length strut with a normalized local imperfection amplitude $A_0/t_w = 0.01$, as shown in Figure 7.7(c). It corresponds to a jump in the local mode, as shown in Figure 7.9. Before the mode jump occurs at $q_s = 0.002$, the number of peaks and troughs in the form of w_{wc} with $A_0/t_w = 0.01$ is the same as that for the strut with $A_0/t_w = 0.14$, which is determined by the pre-defined local imperfection function, as shown in Figures 7.6(a) and 7.9(a). However, after the mode jump, there are more peaks and troughs for the strut

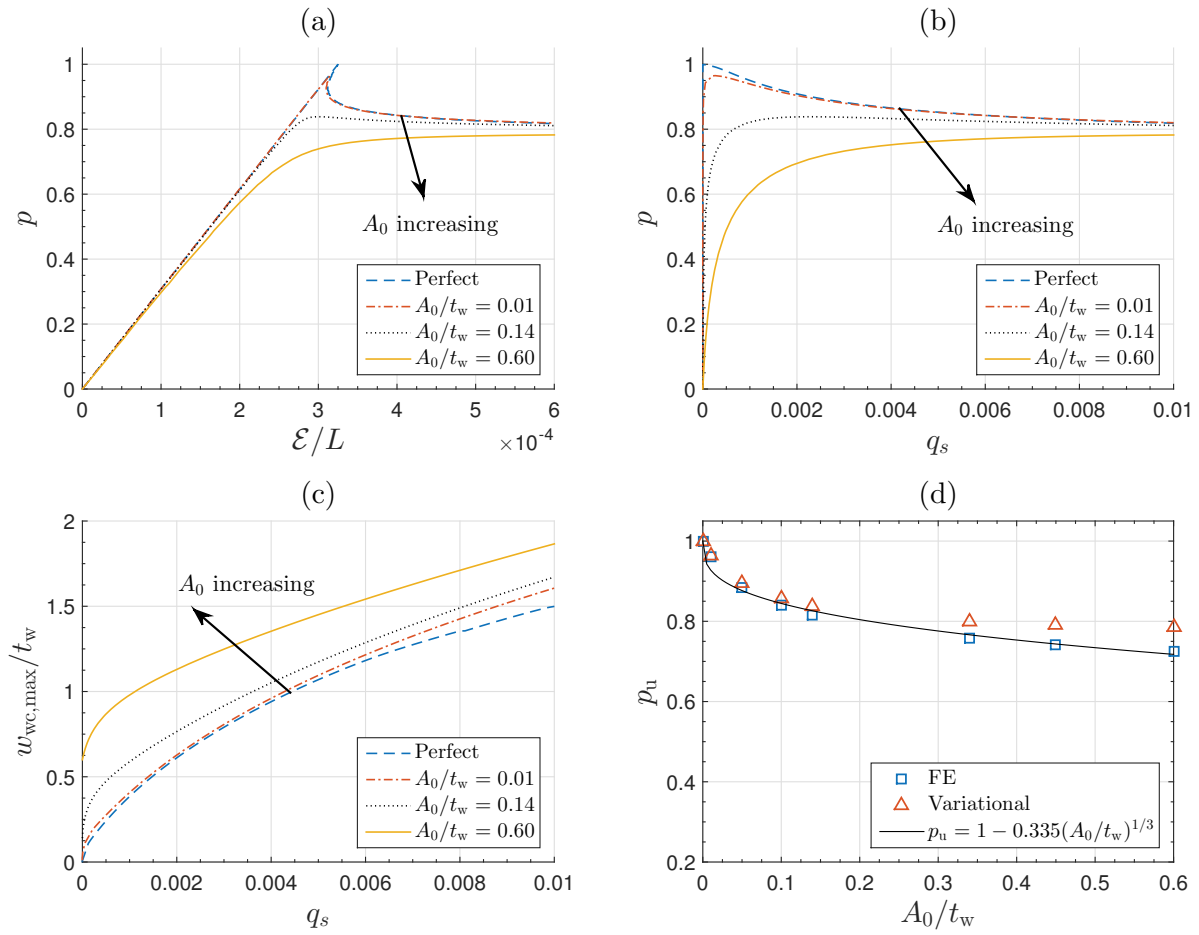


Figure 7.8: Equilibrium paths and the imperfection sensitivity graph for the transitional length strut with different local imperfection amplitudes A_0 . Graphs (a)–(d) are as described in Figure 7.7.

with $A_0/t_w = 0.01$ and the number is the same as that for the perfect case, as shown in Figure 7.9(b); this finding is also in accord with previous studies (Bai & Wadee, 2015a; Wadee & Farsi, 2015). With increasing local imperfection size, the formation of new peaks or troughs requires more membrane strain energy, which would necessitate a longer snap-back path. This, perhaps, explains why no mode jump is observed for the cases with larger imperfection sizes in the current deformation range, *i.e.* where $q_s < 10^{-2}$. It should also be noted that the mode jumping phenomenon is not observed in the transitional length strut with the same imperfection size ($A_0/t_w = 0.01$) while $q_s \lesssim 10^{-2}$, which in fact occurs at $q_s = 1.2 \times 10^{-2}$. This may, in turn, be explained by the fact that local buckling is critical in

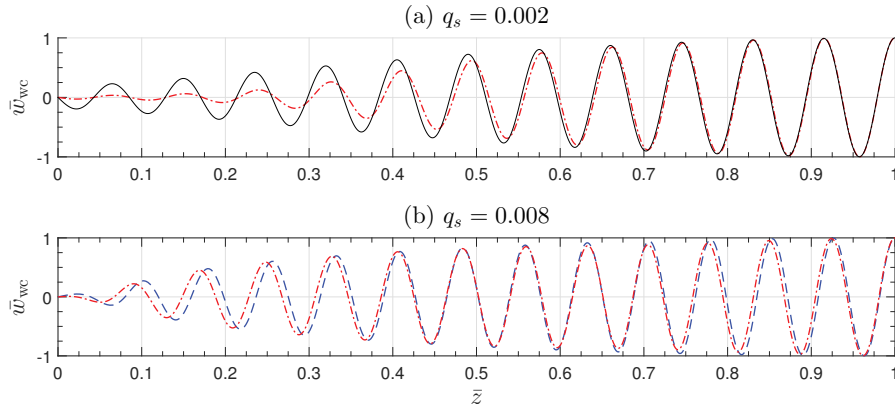


Figure 7.9: Evolution of the numerical solutions for the normalized local out-of-plane displacement in the more compressed web where (a) $q_s = 0.002$ and (b) $q_s = 0.008$ for the long length strut with different local imperfection amplitudes A_0 . The solid, dot-dashed and dashed lines represent where $A_0/t_w = 0.14$, $A_0/t_w = 0.01$ and the perfect case respectively.

that case and the local mode defined by the imperfection is well developed, thus requiring an excessive amount of strain energy (and hence a longer snap-back path) to trigger any jump in the post-buckling mode.

7.1.3 Combined imperfections ($q_{s0} \neq 0$, $w_0 \neq 0$)

The effects of combining local and global imperfections are now studied. As mentioned earlier, according to Eurocode 3 (EN-1993-1-3:2006E, 2006; Degée *et al.*, 2008), the tolerance levels for global and local imperfections are $q_{s0,tol}L = L/1000$ and $A_{0,tol} = d/200$ respectively. Hence, the imperfection combination selected currently is set to be proportional to and also normalized with respect to this combination, which is defined as $\mathbf{W}_{\mathcal{E}0} = \bar{W}_{\mathcal{E}0}\{q_{s0,tol}L, A_{0,tol}\}$, where $\bar{W}_{\mathcal{E}0}$ is a non-dimensional scaling factor.

Figures 7.10 and 7.11 show the nonlinear equilibrium paths and the imperfection sensitivity relationship for both example struts. With increasing imperfection size, a transition from highly unstable to mildly stable behaviour is also observed. It should be noted that there remains a snap-back in the relationship between the local and global mode amplitudes for

the long length strut with $\bar{W}_{\mathcal{E}0} = 1/60$, where the global and local imperfection amplitudes are $L/60000$ and $d/12000$ respectively; this implies that there is a jump in the local mode.

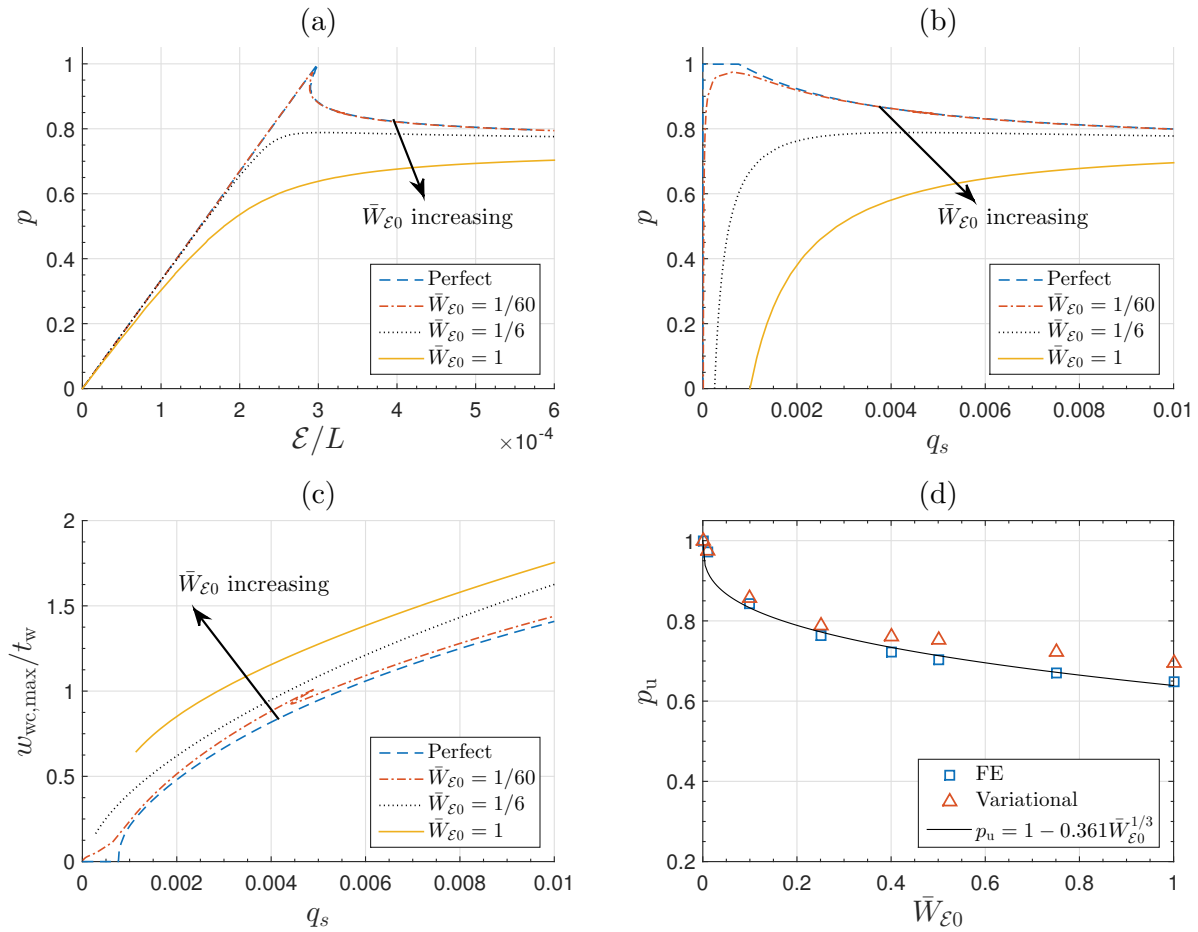


Figure 7.10: Equilibrium paths and the imperfection sensitivity graph for the long length strut with different normalized combined imperfection sizes $\bar{W}_{\mathcal{E}0}$. Graphs (a)–(c) are as described in Figure 7.3. Graph (d) shows the normalized ultimate load p_u from both the FE and variational models against $\bar{W}_{\mathcal{E}0}$ showing the sensitivity to the combined local and global imperfections. Note that $\bar{W}_{\mathcal{E}0} = 1$ corresponds to the global imperfection amplitude $q_{s0}L$ being $L/1000$ and the local imperfection amplitude A_0 being $d/200$.

Moreover, compared with purely global or local imperfection cases, the introduction of the other imperfection-type leads to a further 10% load drop. For the imperfections at the Eurocode 3 tolerance levels ($\bar{W}_{\mathcal{E}0} = 1$), the load-carrying capacity erosion in comparison with the perfect case is over 30% for both struts. According to the definition suggested

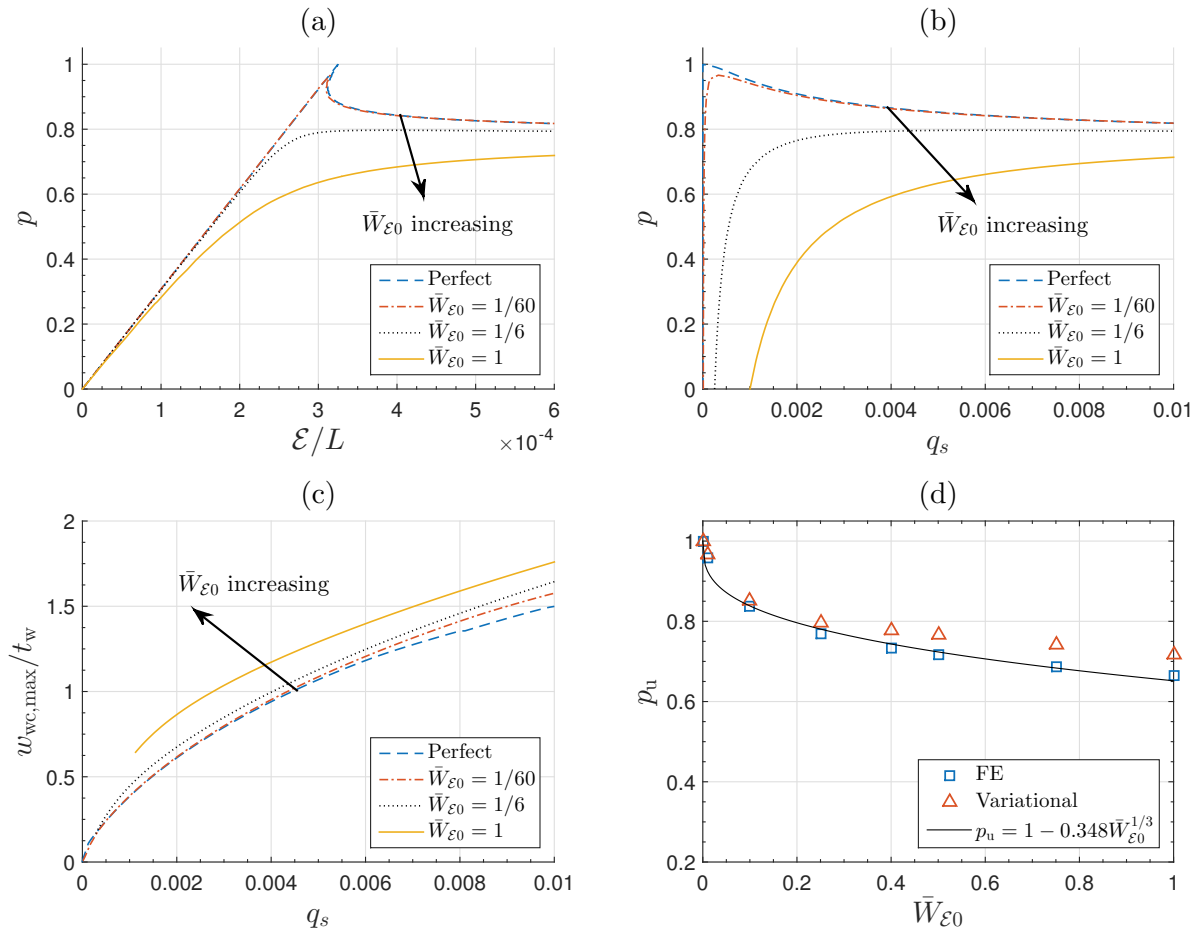


Figure 7.11: Equilibrium paths and the imperfection sensitivity graph for the transitional length strut with different normalized combined imperfection sizes \bar{W}_{ϵ_0} . Graphs (a)–(d) are as described in Figure 7.10.

by Gioncu (1994b), this may be classified as a strong interaction. A larger load-carrying capacity erosion would be expected for the cases where P_o^C/P_1^C is approximately unity.

7.1.4 Verification and discussion

The FE model developed in Chapter 3 is adopted to verify the variational model using GNIA. The comparison of the ultimate load from the FE and the variational models are shown in (d) of Figures 7.3–7.4, 7.7–7.8, 7.10–7.11 (inclusive). The results from the variational models generally show good comparisons with those from the FE models, with

the variational models generally predicting slightly higher ultimate loads. The discrepancy increases with increasing imperfection size and the maximum relative difference $(P_u - P_{u,FE})/P_{u,FE}$, which occurs at the tolerance imperfection combination case ($\bar{W}_{\varepsilon 0} = 1$) for the transitional length strut, is slightly below 8%.

The reasons for the stiffer response or higher ultimate load prediction of the variational model for the perfect case have been discussed in §6.2 and also apply currently. Firstly, when the more compressed web buckles, the neutral axis for strut flexure would move to the less compressed side, thus introducing an additional bending moment to the strut. The effect becomes more significant with the progression of interactive post-buckling, which facilitates the load reaching the ultimate value and subsequently dropping. To consider this effect, an additional displacement function would need to be introduced in the current model to describe the movement of the neutral axis. Secondly, in the current formulation, it is assumed that the effect of local buckling on the transverse stress in each plate is negligible, which leads to the relationship $\varepsilon_x = -\nu\varepsilon_z$ in the flanges and $\varepsilon_y = -\nu\varepsilon_z$ in the webs. In fact, this assumption is valid only when the local out-of-plane displacement of the plate is small. In the advanced post-buckling range, the assumption would be no longer valid, as demonstrated in Figure 7.12. The assumption also simplifies the transverse displacement field, *i.e.* the in-plane displacement field across the cross-section (see Figure 6.17), which may lead to a ‘locking’ problem (essentially, a stiffer response), as reported by a recent study (Garcea *et al.*, 2017). Moreover, the in-plane cross-section displacement would also reduce the effective flexural rigidity of the strut. To resolve the problem, an independent local mode to describe the transverse in-plane displacement field in both flanges and webs would be required, but this would complicate the variational model considerably.

Thirdly, in the current formulation, the cross-section component of the direct in-plane displacement field is assumed to be the same as that of the out-of-plane one. Although this assumption satisfies the kinematic boundary conditions, it does not represent the actual cross-sectional displacement field very well. To describe the cross-section component of

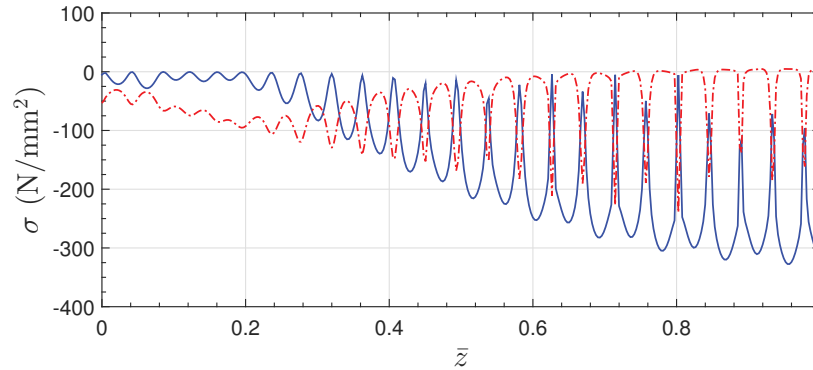


Figure 7.12: Membrane stress distributions along the strut corner line of the more compressed web at the ultimate load from FE for the transitional length strut with the tolerance imperfection combination ($\bar{W}_{\varepsilon_0}=1$). Solid and dot-dashed lines represent the longitudinal and transverse stresses respectively, showing that the transverse stresses are definitely not zero.

the direct in-plane displacement field better, the solutions from classical theory (Koiter, 1945) could be adopted with the introduction of more functions to describe the variation of the cross-section component along the strut length. However, the positive comparison of the current model versus the FE model suggests that any advantage would be minor and be mostly offset by the additional model complexity. Finally, the cross-section profile of the local mode is assumed to remain unchanged along the length of the strut and also throughout the progression of mode interaction with the only variable being the modal amplitude, as can be seen in Eq. (5.1). However, the profile is affected by the ratio of axial force and bending moment, which varies along the length and also throughout the entire loading history. Furthermore, some higher order effects, such as the bending effects on the cross-section profile as presented in Figure 6.7, would also affect the cross-section profile. All of these factors taken together lead to the stiffer response of the variational model, thus overestimating the ultimate load especially in the cases where the imperfection size is close to the recommended tolerance levels within the Eurocode. However, the errors are within generally acceptable bounds and the variational model does provide a better insight into the system mechanics.

Based on the FE results, curves have been fitted to describe the ultimate load-normalized

imperfection size relationship, as shown in (d) of Figures 7.3–7.4, 7.7–7.8, 7.10–7.11 (inclusive). For the pure global imperfection case, the expressions for both example struts indicate approximately a 1/2 power law relationship to leading order; for the pure local imperfection and combined imperfection cases, the expressions for both example struts indicate approximately a 1/3 power law relationship, which is also observed in I-section struts susceptible to mode interaction (Liu, 2016). Moreover, the transitional length strut exhibits relatively more sensitivity to global imperfections and the long length strut exhibits relatively more sensitivity to pure local and combined imperfections.

7.2 Variational model application and parametric study

7.2.1 Simplified method to predict load at pitchfork bifurcation

$$(q_{s0} \neq 0, w_0 = 0)$$

From the numerical results hitherto, it was demonstrated that for the case where only a global imperfection exists, the load at the pitchfork bifurcation point P^B can be used to predict the ultimate load that is safe and compares very well to the FE model, as shown in Figures 7.3(d) and 7.4(d). Therefore, a simplified method to predict P^B is proposed based on the method developed in §4.5, which determined the local buckling load of the more compressed web undergoing global buckling and the corresponding global buckling amplitude at the secondary bifurcation point for perfect thin-walled rectangular section struts exhibiting global–local mode interaction.

Equation (5.36) provides the governing equation for the relationship between q_s , q_t and P along the equilibrium path. By setting the terms related to the local mode to be zero, the first two expressions of Eq. (5.36) can be written as:

$$\frac{\partial V}{\partial q_s} = \pi^2 G t_f b L [(q_s - q_t) - (q_{s0} - q_{t0})] + \frac{\pi^4 E I_w (q_s - q_{s0})}{L} - P \frac{\pi^2 L q_s}{2} = 0, \quad (7.2)$$

$$\frac{\partial V}{\partial q_t} = \frac{\pi^4 E t_f b^3}{4L} \left(\frac{1}{3} + \frac{\phi_c}{\phi_t} \right) (q_t - q_{t0}) - \pi^2 G t_f b L [(q_s - q_t) - (q_{s0} - q_{t0})] = 0. \quad (7.3)$$

Substituting Eq. (7.3) into Eq. (7.2) to remove the shear term and using the relationship in Eq. (5.37) gives the following expression:

$$P = P_o^C \left(\frac{q_s - q_{s0}}{q_s} \right). \quad (7.4)$$

If no local buckling occurs, P would increase with q_s and tend towards P_o^C in the limit.

However, the bending stiffness would drop due to local buckling in the more compressed web and flanges. Since the transverse stress component is neglected currently, the direct stress in the more compressed web σ_{wc} before local buckling occurs can be written thus:

$$\sigma_{wc} = E \varepsilon_{wc} = - \frac{\pi^2 E b (q_t - q_{t0})}{2L} \sin \frac{\pi z}{L} - \frac{P}{A_g}, \quad (7.5)$$

where $A_g = 2(bt_f + dt_w)$ is the gross cross-sectional area. From the numerical results shown in Figures 7.5(a, c), the local mode is initially localized. Instead of analysing the whole web with the entire strut length, it was demonstrated in §4.6 that when σ_{wc} at mid-span reaches the local buckling stress of the more compressed web σ_{wc}^C , interactive buckling can be assumed to have been triggered. The expression for the local buckling stress of the more compressed web element restrained by both flanges is given by:

$$\sigma_{wc}^C = \frac{k_p \pi^2 E}{12(1 - \nu^2)(d/t_w)^2} \quad (7.6)$$

and the plate buckling coefficient k_p can be determined by Eq. (4.63). For the practically significant case where the cross-section has a uniform wall thickness ($\phi_t = 1$), the expression for k_p was determined by Eq. (4.68). By substituting Eqs. (5.37) and (7.4) into Eq. (7.5),

the relationship between P^B and the global imperfection size q_{s0} is obtained:

$$P^B = \frac{A_g}{2} \left[\frac{\pi^2 E b q_{s0}}{2(1+s)L} + \frac{P_o^C}{A_g} + \sigma_{wc}^C - \sqrt{\left(\frac{P_o^C}{A_g} - \sigma_{wc}^C \right)^2 + \frac{\pi^2 E b q_{s0}}{2(1+s)L} \left(\frac{\pi^2 E b q_{s0}}{2(1+s)L} + \frac{2P_o^C}{A_g} + 2\sigma_{wc}^C \right)} \right]. \quad (7.7)$$

Figure 7.13 shows the comparison of the normalized load $p^B = P^B/P^C$ obtained from Eq.

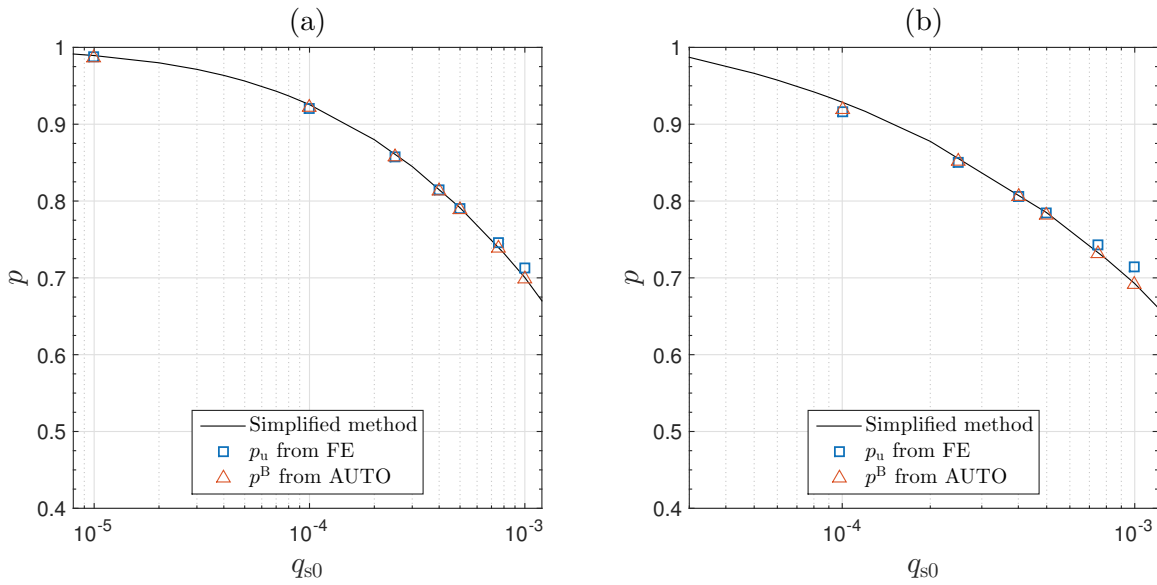


Figure 7.13: Comparison of the normalized load p^B using the simplified method and the full variational model against the normalized ultimate load p_u from the FE models for (a) the long length strut and (b) the transitional length strut. Note that only global imperfections are included in both example struts.

(7.7) and the full variational model against the normalized ultimate load $p_u = P_u/P^C$ from the FE model for example struts with purely global imperfections for different imperfection sizes. For the long length strut, the simplified method shows excellent comparisons with the full variational model for P^B , as shown in Figure 7.13(a). For the transitional length strut, the comparison is good for the cases where the global imperfection size is larger than 10^{-4} . For tiny global imperfections, the simplified method would overestimate P^B . This is caused by the fact that when the imperfection size is vanishingly small, the system would behave very similarly to the perfect system, *i.e.* the less compressed web would

also buckle, as shown in Figure 6.10. Therefore, the restraints on the more compressed web would be smaller, which leads to a smaller value of k_p . In general, for the current two example struts, the simplified method provides a safe, yet accurate prediction of the ultimate load for different imperfection sizes. Finally, it should be mentioned that if the material yield stress f_y replaced σ_{wc}^C in Eq. (7.7), the equation would revert to the classical Perry–Robertson formula (Trahair *et al.*, 2007) for the failure load of an imperfect column.

7.2.2 Simplified method to predict the ultimate load ($q_{s0} = 10^{-3}$, $w_0 = 0$)

Figure 7.14 presents the relationship between the ultimate and pitchfork bifurcation loads for different length struts with tolerance level global imperfections ($q_{s0} = 10^{-3}$). In the

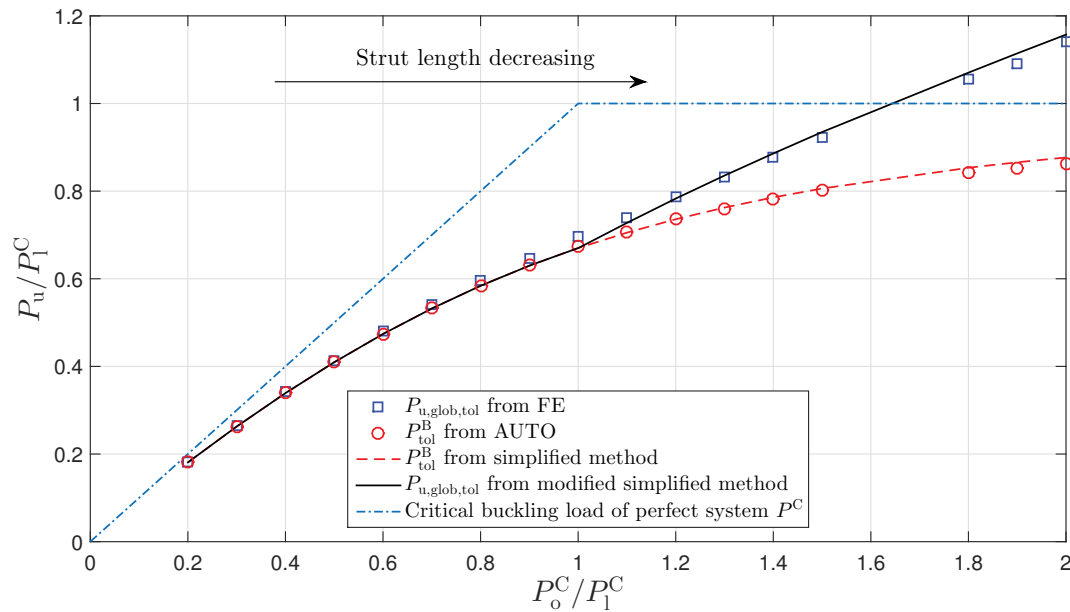


Figure 7.14: Length effects on the ultimate and pitchfork bifurcation load of thin-walled RHS struts with purely tolerance level global imperfections ($q_{s0} = 10^{-3}$). Note that the cross-section and material properties of the struts are the same as the example struts in previous section.

range where global buckling is critical ($P_o^C/P_1^C < 1$), the ultimate load is approximately the same as the pitchfork bifurcation load. Therefore, Eq. (7.7) can be used as an accurate

prediction of the ultimate load for such cases. However, in the range where local buckling is critical, the pitchfork bifurcation load is significantly smaller than the ultimate load and the difference increases with decreasing strut length, which implies that the triggering of local–global mode interaction in such cases does not lead to unstable post-buckling behaviour.

The prerequisite of the simplified method for predicting the ultimate load is that the effective global buckling load $\Phi_r P_o^C$ is less than or very close to P^B , where Φ_r is the bending stiffness reduction factor due to local buckling of the more compressed web and flanges and is given by Eq. (B.8). Otherwise, the load would still increase beyond P^B with a reduced stiffness and would tend to $\Phi_r P_o^C$, even though mode interaction is triggered, as shown in Figures 7.3 and 7.4. Therefore, more calibration parameters could be introduced in Eq. (7.7) to fit it for the whole length range. An equation is proposed based on the FE results in the range where $P_o^C/P_1^C \leq 4$:

$$P_{u, \text{glob, tol}} = \begin{cases} P_{\text{tol}}^B & \text{for } P_o^C/P_1^C \leq 1, \\ P_{\text{tol}}^B [0.32 (P_o^C/P_1^C - 1) + 1] & \text{for } 1 < P_o^C/P_1^C \leq 4. \end{cases} \quad (7.8)$$

The average ratio of Eq. (7.8) to $P_{u, \text{FE, glob, tol}}$ is 0.998 and the coefficient of variation (COV) is 0.96%, which represents an excellent fit. However, it should be noted that the equation is only valid for the current geometric parameter space; an extensive parametric study on geometric properties, *i.e.* plate width–thickness ratio and cross-section aspect ratio, would be required to make the equation more generic. This will be left for future study.

7.2.3 Simplified method to predict the ultimate load ($q_{s0} = 10^{-3}$, $A_0 = d/200$)

In the current subsection, the ultimate load for thin-walled RHS struts with purely tolerance level local imperfections, purely tolerance level global imperfections and their combi-

nations for different length struts is investigated. The aim is to establish the relationship between the ultimate load for the cases with purely tolerance level global imperfections and those with tolerance level combined imperfections alongside calibrating Eq. (7.8) to be valid for the latter cases.

Figure 7.15(a) shows the ultimate load for thin-walled RHS struts with purely tolerance level local imperfections, purely tolerance level global imperfections and their combinations in the range: $P_o^C/P_1^C=[0.2, 2.0]$. It can be observed that the struts exhibit sensitivity to

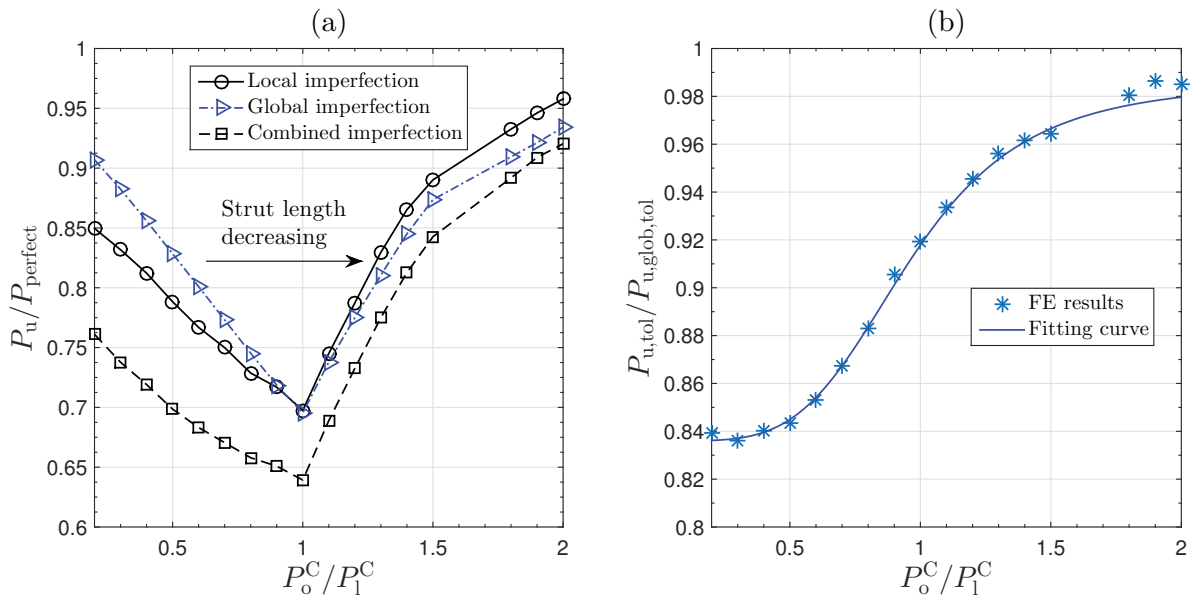


Figure 7.15: (a) Effects of tolerance level local imperfections, global imperfections and their combination on the ultimate load for thin-walled RHS struts with different lengths. (b) Ratio of $P_{u,\text{tol}}$ to $P_{u,\text{glob,tol}}$ versus the strut length, where $P_{u,\text{tol}}$ and $P_{u,\text{glob,tol}}$ represent the ultimate load with tolerance level combined imperfections and tolerance level global imperfections respectively. Note that local imperfection profiles are affine to the lowest local buckling mode from linear buckling analysis using FE models.

both local and global imperfections and the load erosion is most significant at the point where $P_o^C/P_1^C=1$. For the current example struts with the cross-section properties as presented in Table 4.1 and the imperfection tolerance level ($A_0/t=0.6$ and $q_{s0}=10^{-3}$) selected, the ultimate load erosion due to purely tolerance level local and global imperfections is nearly equal at the point where $P_o^C/P_1^C=1$. Therefore, an opportunity to determine the relative significance of both imperfection types on the ultimate load erosion for different

length ranges is provided. The principal finding from Figure 7.15(a) is that the ultimate load with purely local imperfections is lower than that with purely global imperfections in the range where global buckling is critical and vice versa. This observation implies that struts where global buckling is critical are more sensitive to local imperfections than global imperfections and vice versa.

The underlying mechanism of the critical buckling mode dependent imperfection sensitivity may be explained based on the interactive buckling behaviour of perfect systems. No matter to which type the critical buckling mode belongs, the failure of perfect thin-walled RHS struts is controlled by the symmetry breaking action of mode interaction (Supple, 1967; Shen & Wadee, 2018b). In the perfect case or the case with imperfections purely in the shape of the primary buckling mode, the secondary buckling mode would be triggered when the primary mode is fully developed. Since the primary mode is stable or neutral, the imperfect system would approximate to the perfect case in the purely elastic scenarios. The imperfections with interactive post-buckling mode profiles would have an immediate destabilization effect on the system, *i.e.* a reduction in stiffness, which would facilitate the triggering of the secondary mode and expedite the reaching of the ultimate state (Supple, 1967).

As for the effects of superposing a tolerance level global imperfection on a local imperfection, the ratio of the ultimate load for struts with purely tolerance level local imperfections to that of struts with combined imperfections, $P_{u,loc,tol}/P_{u,tol}$, almost remains constant in the range where global buckling is critical, with the average and the COV being 0.896 and 1.2% respectively. It should be noted that the value is very close to the strength reduction factor 0.877 of the nominal strength for slender elastic columns from the current Direct Strength Method (DSM) (Schafer, 2008). In the range where local buckling is critical, $P_{u,loc,tol}/P_{u,tol}$ increases with increasing P_o^C/P_1^C , with $P_{u,loc,tol}/P_{u,tol}=0.965$ at $P_o^C/P_1^C=2$. The ratio remains approximately constant beyond the point. As for the effects of superposing a tolerance level local imperfection on struts with a tolerance level global imperfection,

$P_{u, \text{glob, tol}}/P_{u, \text{tol}}$ increases with the increasing P_o^C/P_1^C from 0.839 at $P_o^C/P_1^C=0.2$ to 0.985 at $P_o^C/P_1^C=2$, as shown in Figure 7.15(b), and the ratio converges gradually to unity beyond this point.

As shown in Figure 7.15(b), a curve is fitted based on the numerical results to describe the relationship between $P_{u, \text{tol}}$ and $P_{u, \text{glob, tol}}$:

$$P_{u, \text{tol}} = \left[0.836 + \frac{0.18}{1.2 + (P_o^C/P_1^C)^{-4.24}} \right] P_{u, \text{glob, tol}}. \quad (7.9)$$

The average ratio of Eq. (7.9) to FE results in the range $P_o^C/P_1^C=[0.2, 4]$ is 1.000 and the COV is 0.63%. In a similar way to Eq. (7.8), the current equation is also limited to the current geometric space and further parametric studies are necessary to make it apply to a wider range of cases.

7.3 Concluding remarks

Based on the nonlinear variational model developed in Chapter 5, the imperfection sensitivity of axially-loaded thin-walled rectangular hollow section struts with initial global and local geometric imperfections is investigated. Numerical examples, focusing on cases where the global buckling load is close to the local buckling load, have been presented and verified using the FE model developed in Chapter 3. The sensitivity of two example struts exhibiting mode interaction to initial geometric imperfections has been quantified. With the increase of the geometric imperfection size, a transition from highly unstable to neutrally or mildly stable post-buckling behaviour is observed. A progressive change in the local buckling mode is identified in terms of both wavelength and amplitude. In particular, mode jumping within the interactive buckling mode, *i.e.* the change in the number of troughs and peaks of the local mode and snap-backs in the equilibrium path, is also observed in the cases where the local imperfection size is vanishingly small. A simplified

method to predict the load at the pitchfork bifurcation point, where interactive buckling is triggered, is proposed for struts with purely global imperfections based on the verified variational model; it is demonstrated to be simple, yet safe and accurate for the cases studied.

A parametric study on the effects of global tolerance imperfections, local tolerance imperfections and their combinations on the ultimate load for struts with different lengths was conducted. It was revealed that for struts with tolerance level global imperfections, the post-buckling behaviour after the pitchfork bifurcation point is unstable and stable for struts with global buckling and local buckling being critical respectively. It was also found that local imperfections are more significant than global imperfections for struts with global buckling being critical and global imperfections are more significant for struts with local buckling being critical. This is attributed to the characteristic behaviour where the alternative imperfection type would facilitate the necessary symmetry breaking to trigger interactive buckling. Based on the parametric study results, the simplified method to predict the pitchfork bifurcation load is calibrated to calculate the ultimate load for struts with tolerance level global and combined imperfections.

It should be stressed that, in the current chapter, only one type of local imperfection profile was investigated, *i.e.* a mono-symmetric cross-section profile with the longitudinal component based on fitting the eigenmode from linear buckling analysis. This may not represent the most severe imperfection profile. Therefore, the effects of imperfection profiles on the ultimate load is investigated in the following chapter.

Chapter 8

Sensitivity to manufacturing tolerance level imperfections

The current chapter is a continuation of the preceding one on the imperfection sensitivity of thin-walled RHS struts susceptible to interactive buckling. However, it focuses on the behaviour of such struts with imperfections, the sizes of which are related to the recommended manufacturing tolerances. A measurement method for different local imperfection profiles based on the concept of equal local bending strain energy is proposed. A procedure to terminate the nonlinear analysis within ABAQUS when certain failure criteria are met is developed, which makes an automated parametric study more efficient. The effects of the imperfection profile, *i.e.* cross-section profile, the longitudinal wavelength and the degree of localization, on the ultimate load and equilibrium path of four characteristic length struts are investigated and the most severe local imperfection forms are identified. The effects of localized imperfections on the behaviour of struts are also discussed. A parametric study on the wavelength of the most severe imperfection profile is conducted and a semi-empirical relationship to determine the corresponding wavelength is proposed. The mechanism of global buckling in struts with tolerance level doubly-symmetric local imperfections is discussed and an explicit equation to calculate the global buckling load is

proposed.

8.1 Imperfection description and modelling

Since the variational model exhibits a relatively stiffer response where the imperfection size is close to the tolerance level, all the analyses in the current chapter were conducted using the FE model developed in Chapter 3. In order to model bespoke imperfection profiles, MATLAB was used to generate the nodal coordinates input file for the FE model with pre-defined global and local imperfections. As shown in Figure 8.1, the geometric imperfection description follows the same principles as presented in §5.2 for the variational model, which is based on the local and global buckling mode description. These modal functions have been demonstrated to be capable of describing purely local and global buckling modes, as well as the interactive buckling mode, for perfect struts with different lengths very well. Specifically, the global and local imperfections are defined by Eq. (5.12) and Eq. (5.13) respectively. However, it should be noted that the set of functions for the

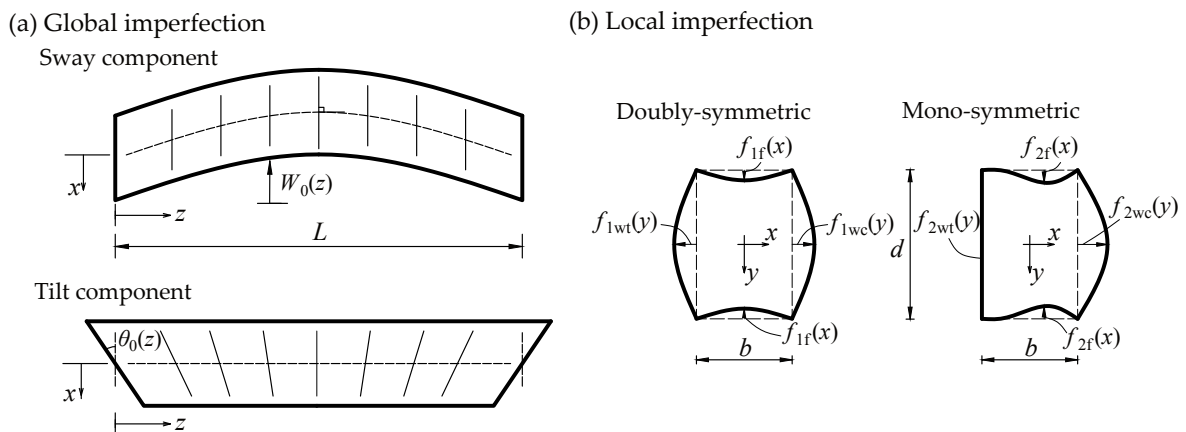


Figure 8.1: Imperfection descriptions. (a) Global imperfection bending about weak axis y : sway and tilt components. (b) Cross-section component of local imperfections: doubly-symmetric and mono-symmetric profiles.

doubly-symmetric cross-section profile in the local mode, *i.e.* Eqs. (5.2) and (5.3), is only valid for rectangular hollow section struts with relatively large cross-section aspect ratios,

i.e. $d/b \geq 1.5$. Therefore, a new set of functions is used, which is valid from a square to a rectangular hollow section. These expressions are derived from a semi-analytical method, the details of which may be found in Appendix C. The longitudinal component of the local imperfection $w_{i0}(z)$ has the same format as Eq. (5.14). As shown in Figure 5.4, the degree of localization and the number of half-waves in the local imperfection profile can be varied by adjusting the parameters α_i and β_i respectively.

8.2 Unified local imperfection measurement criterion

Since A_{i0} , β_i and α_i in Eq. (5.14) are parameters that have various different combinations, purely using the imperfection amplitude A_{i0} as the sole measurement of imperfection size inevitably neglects important features and does not provide meaningful comparisons. Previous studies (Wadee, 2000; Bai & Wadee, 2015a; Wadee & Farsi, 2015; Liu & Wadee, 2016b) adopted the concept of the total end-shortening arising from introducing the local imperfection to measure various different longitudinal distributions of local imperfections:

$$\mathcal{E}_{i0} = \frac{1}{2} \int_0^L \dot{w}_{i0}^2 dz, \quad (8.1)$$

which includes the contribution from all the parameters in Eq. (5.14). However, this 1-D approach is not easily adaptable for the comparison of the doubly-symmetric and mono-symmetric cross-section imperfection profiles in the current case. Hence, a 3-D approach based on the local bending energy is proposed currently. It should be noted that a similar methodology was also adopted previously in an investigation on the effects of local imperfection profiles in the response of simply-supported rectangular plates (Sadovský *et al.*, 2005). From classical plate bending theory (Bulson, 1970) and the energy formulation in preceding chapters, the total local bending energy stored in the entire strut due to the

initial local imperfections $U_{b,1}^0$ can be expressed as:

$$\begin{aligned}
U_{b,1}^0 &= U_{b,lf}^0 + U_{b,lwc}^0 + U_{b,lwt}^0 \\
&= D_f \int_0^L \int_{-b/2}^{b/2} \left\{ \left(\frac{\partial^2 w_{f0}}{\partial z^2} + \frac{\partial^2 w_{f0}}{\partial x^2} \right)^2 \right. \\
&\quad \left. - 2(1-\nu) \left[\frac{\partial^2 w_{f0}}{\partial z^2} \frac{\partial^2 w_{f0}}{\partial x^2} - \left(\frac{\partial^2 w_{f0}}{\partial z \partial x} \right)^2 \right] \right\} dx \, dz \\
&\quad + \frac{D_w}{2} \int_0^L \int_{-d/2}^{d/2} \left\{ \left(\frac{\partial^2 w_{wc0}}{\partial z^2} + \frac{\partial^2 w_{wc0}}{\partial y^2} \right)^2 \right. \\
&\quad \left. - 2(1-\nu) \left[\frac{\partial^2 w_{wc0}}{\partial z^2} \frac{\partial^2 w_{wc0}}{\partial y^2} - \left(\frac{\partial^2 w_{wc0}}{\partial z \partial y} \right)^2 \right] \right\} dy \, dz \\
&\quad + \frac{D_w}{2} \int_0^L \int_{-d/2}^{d/2} \left\{ \left(\frac{\partial^2 w_{wt0}}{\partial z^2} + \frac{\partial^2 w_{wt0}}{\partial y^2} \right)^2 \right. \\
&\quad \left. - 2(1-\nu) \left[\frac{\partial^2 w_{wt0}}{\partial z^2} \frac{\partial^2 w_{wt0}}{\partial y^2} - \left(\frac{\partial^2 w_{wt0}}{\partial z \partial y} \right)^2 \right] \right\} dy \, dz,
\end{aligned} \tag{8.2}$$

where $U_{b,lf}^0$, $U_{b,lwc}^0$, $U_{b,lwt}^0$ are the local bending energies due to the initial local imperfections in both flanges, the more compressed web and the less compressed web respectively; $D_f = Et_f^3/[12(1-\nu^2)]$ and $D_w = Et_w^3/[12(1-\nu^2)]$ are the flexural rigidities of the flanges and webs respectively.

By substituting w_{f0} , w_{wc0} and w_{wt0} from Eq. (5.13) into Eq. (8.2), the local bending energy due to local imperfections with the doubly-symmetric ($i = 1$) and mono-symmetric ($i = 2$) cross-sectional components can be expressed thus:

$$\begin{aligned}
U_{b,i}^0 &= D_w \int_0^L \left[\left(\frac{2t_f}{t_w} \{f_{if}^2\}_x + \{f_{iwc}^2\}_y + \{f_{iwt}^2\}_y \right) \ddot{w}_{i0}^2 \right. \\
&\quad + \left(\frac{2t_f}{t_w} \{f_{if}''^2\}_x + \{f_{iwc}''^2\}_y + \{f_{iwt}''^2\}_y \right) w_{i0}^2 \\
&\quad + 2\nu \left(\frac{2t_f}{t_w} \{f_{if} f_{if}''\}_x + \{f_{iwc} f_{iwc}''\}_y + \{f_{iwt} f_{iwt}''\}_y \right) \ddot{w}_{i0} w_{i0} \\
&\quad \left. + 2(1-\nu) \left(\frac{2t_f}{t_w} \{f_{if}'^2\}_x + \{f_{iwc}'^2\}_y + \{f_{iwt}'^2\}_y \right) \dot{w}_{i0}^2 \right] dz,
\end{aligned} \tag{8.3}$$

where dots represent differentiation with respect to z ; primes denote differentiation with respect to x and y for flanges and webs respectively. From Eqs. (8.2) and (8.3), it can be seen that the variation of local imperfections in both cross-sectional and longitudinal dimensions can be considered. Moreover, the advance in imperfection measurement facilities (Zhao *et al.*, 2015) has made it possible to obtain the 3D distribution of local imperfections. Using numerical integration, the corresponding local bending energy can be obtained, which can be adopted as a reference value to compare different imperfection profiles.

It should be noted that from the perspective of linear buckling theory (Timoshenko & Gere, 1961), the local bending strain energy in struts due to local imperfections is equal to the work done by load due to local imperfections at the initial instability. Therefore, the current method based on the equal local bending energy is essentially equivalent to previous concepts based on the equal work done by load or equal end-shortening (Wadee, 2000).

8.3 Effects of local imperfection profiles

Chapter 6 has demonstrated that there are four distinct length-dependent zones for thin-walled RHS struts, which exhibit different post-buckling behaviour, as shown in Figures 6.2 and 6.19. Therefore, four representative example struts with the same material and geometric properties as those in Table 6.1 are adopted. Table 8.1 presents the strut length and the corresponding number of half-waves β_0 in the local buckling mode. It should be noted

Table 8.1: Number of half-waves β_0 in the local buckling mode for the struts in four characteristic length-dependent zones. The theoretical values of global and local buckling loads as well as the length description for the struts can be found in Table 6.1.

Zone	1	2	3	4
$L(\text{mm})$	4800	4500	4000	3600
β_0	49	45	41	37

that the number of half-waves β_0 in the pure local buckling mode from both analytical and FE models are the same for all four characteristic struts, even though the profiles are periodic and modulated for the analytical and FE models respectively.

For each characteristic length strut, four different imperfection cases are studied, as presented in Table 8.2. For the first one, the imperfection profile is the critical local buckling

Table 8.2: Initial local imperfection parameters for the most severe local imperfection case study. Note that ‘Eval’ in the table represents quantities evaluated based on the other input parameters and the number of half-waves $\beta_i = \beta_0$.

Case	$U_{b,i}^0$	A_{i0}^0	Cross-section profile f_i	Notes
1	N/A	$d/200$	doubly-symmetric	Linear buckling mode
2	$U_{b,12}^0$	$d/200$	mono-symmetric	$A_{10}^0=0, A_{20}^0=d/200$
3	$U_{b,12}^0$	Eval	doubly-symmetric	$U_{b,1}^0$ is equal to that in case 2
4	Eval	$d/200$	doubly-symmetric	$A_{10}^0=d/200, A_{20}^0=0$

mode obtained from linear buckling analysis using the FE model and the corresponding imperfection amplitude is $d/200$, which is the tolerance level for the local imperfection amplitude, as recommended by Eurocode 3 (EN-1993-1-3:2006E, 2006). It is used as a reference to compare with the imperfection profiles in other cases. The second case adopts the mono-symmetric cross-section imperfection profile, with the number of half-waves along the strut length β_0 being equal to those listed in Table 8.1 and the initial imperfection amplitude A_{i0}^0 also being $d/200$. The third case adopts the doubly-symmetric cross-section imperfection profile and the local bending energy due to local imperfections is equal to that in the second case, which aims to study the more severe case between the mono-symmetric and doubly-symmetric ones with the same local bending energy stored from the initially imperfect geometry. The fourth case adopts the doubly-symmetric cross-section imperfection profile, with β_0 and A_{i0}^0 being the same as those in the second case; this aims to study the more severe case between the mono-symmetric and doubly-symmetric cases with the same local imperfection amplitude. Moreover, it should be stressed that the global imperfection is not included in the example struts in the current section. For convergence purposes, a global perturbation distribution defined by Eq. (5.12) with the normalized

amplitude $q_{s0}=10^{-6}$ is introduced.

8.3.1 Algorithm for determining most severe local imperfection profile

The investigation to determine the most severe local imperfections comprises two stages, as shown in Figure 8.2. A similar methodology has already been adopted for studying the

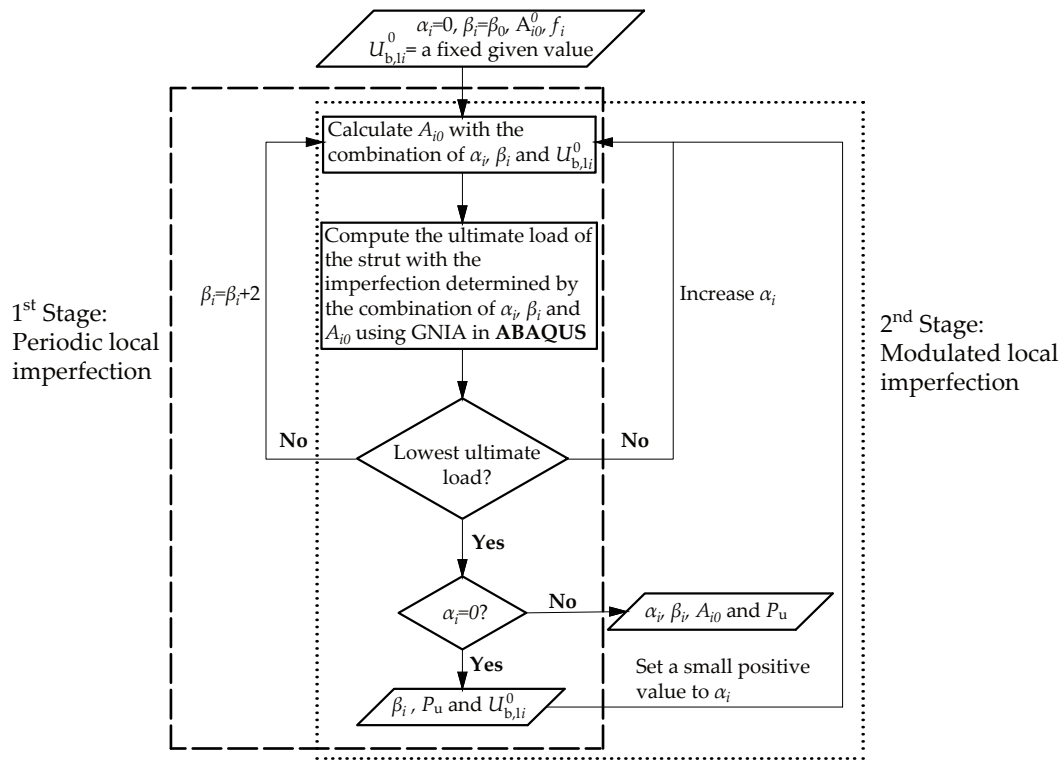


Figure 8.2: Algorithm for determining the most severe case periodic and modulated local imperfections under the constraint of the equal local bending energy of the initially imperfect geometry.

most severe local imperfection profile in sandwich panels (Wadee, 2000), I-section struts (Bai & Wadee, 2015a; Liu & Wadee, 2016b) and stiffened plates (Wadee & Farsi, 2015):

1. Periodic imperfections are investigated by adopting β_i as the principally varying parameter. Initially, the value of $U_{b,li}^0$ is determined and fixed based on the combination

of $\alpha_i = 0$, β_i being the number of half waves of the pure local buckling mode β_{i0} from the variational model in Chapter 6, A_{i0}^0 being the local imperfection amplitude tolerance level value adopted from Eurocode 3 (EN-1993-1-3:2006E, 2006). Then, the quantity β_i is varied as the principal parameter and increased from a sufficiently small but reasonable odd integer while the value of α_i remains zero. Note that the value of β_i only takes odd integer values to satisfy the boundary and symmetry conditions. The amplitude A_{i0} is varied accordingly to keep $U_{b,li}^0$ at the selected value; hence, increasing β_i would naturally lead to a decrease in A_{i0} . GNIA is conducted to obtain the ultimate load of the strut with each combination of β_i and A_{i0} . In particular, the combination of β_i and A_{i0} that gives the lowest ultimate load P_u is recorded and used for the modulated imperfection study.

2. Modulated local imperfections are investigated by adopting α_i as the principally varying parameter. The quantities β_i and $U_{b,li}^0$ are the same as those corresponding to the lowest ultimate load in stage 1. The localization parameter α_i is set as the principally varying parameter and the amplitude A_{i0} is varied accordingly to keep $U_{b,li}^0$ constant; increasing α_i naturally leads to a higher value of A_{i0} ; GNIA is also conducted to obtain the ultimate load of the strut with each imperfection combination of α_i and A_{i0} . In particular, the combination of α_i and A_{i0} that gives the lowest ultimate load P_u is recorded.

Automated termination of nonlinear analysis in Abaqus

In order to make the process presented in Figure 8.2 automated, the principal challenge is to terminate the nonlinear analysis automatically once certain failure criteria are met, since current versions of ABAQUS do not provide such a functionality satisfactorily. As mentioned in §3.3.2, there are some existing FORTRAN codes using an ABAQUS user subroutine (Sadowski *et al.*, 2017a) that are able to terminate the nonlinear Riks arc-length analysis automatically once certain criteria are met.

Currently, the main body of the program, as presented in Figure 8.2, is developed within MATLAB, such as the determination of key imperfection related parameters (*i.e.* A_{i0} , α_i , β_i and $U_{b,i}^0$), FE model creation, nonlinear analysis job submission and data post-processing and output. In order to make the program self-consistent, a function is developed within MATLAB to terminate the nonlinear analysis once the failure criteria are met, the algorithm of which is presented in Figure 8.3. Based on the equilibrium paths obtained in previous chapters, two failure criteria are adopted in the function, as shown in Figure 8.4. The first one represents the cases where there is a clear maximum load in the load–end-shortening relationship, as shown in Figure 8.4(a). This failure mode can be easily determined when the incremental load proportionality factor (LPF) becomes negative or smaller than the tolerance value (10^{-7}). In ABAQUS, the LPF of each step is output in the ‘.sta’ file. Therefore, by monitoring the incremental LPF in the ‘.sta’ file, the limit point can be easily detected. Once the negative incremental LPF is detected, the nonlinear analysis can be terminated using the system command in MATLAB.

The second failure criterion mainly deals with the cases where the post-buckling behaviour is essentially neutral, as shown in Figure 8.4(b). In such cases, it may take over hundreds of steps to reach the point where the incremental LPF becomes negative or smaller than the tolerance value (10^{-7}). Moreover, in practice, reaching the plateau can be treated as the failure of a column, since a tiny increase in the load capacity would lead to a large structural deformation. To improve the computational efficiency, the Modified Southwell (MS) method (Doerich & Rotter, 2011; Sadowski *et al.*, 2017a) is adopted to determine the termination point.

For illustration purposes, the equilibrium path of the short length strut with a tolerance level mono-symmetric cross-section profile local imperfections is presented, as shown in Figure 8.5. Firstly, the load and end-shortening are extracted from the ‘odb’ file by running the post-processing python script within MATLAB. Then, the equilibrium path is transformed into the Modified Southwell (MS) plot, as shown in Figure 8.5(b), which com-

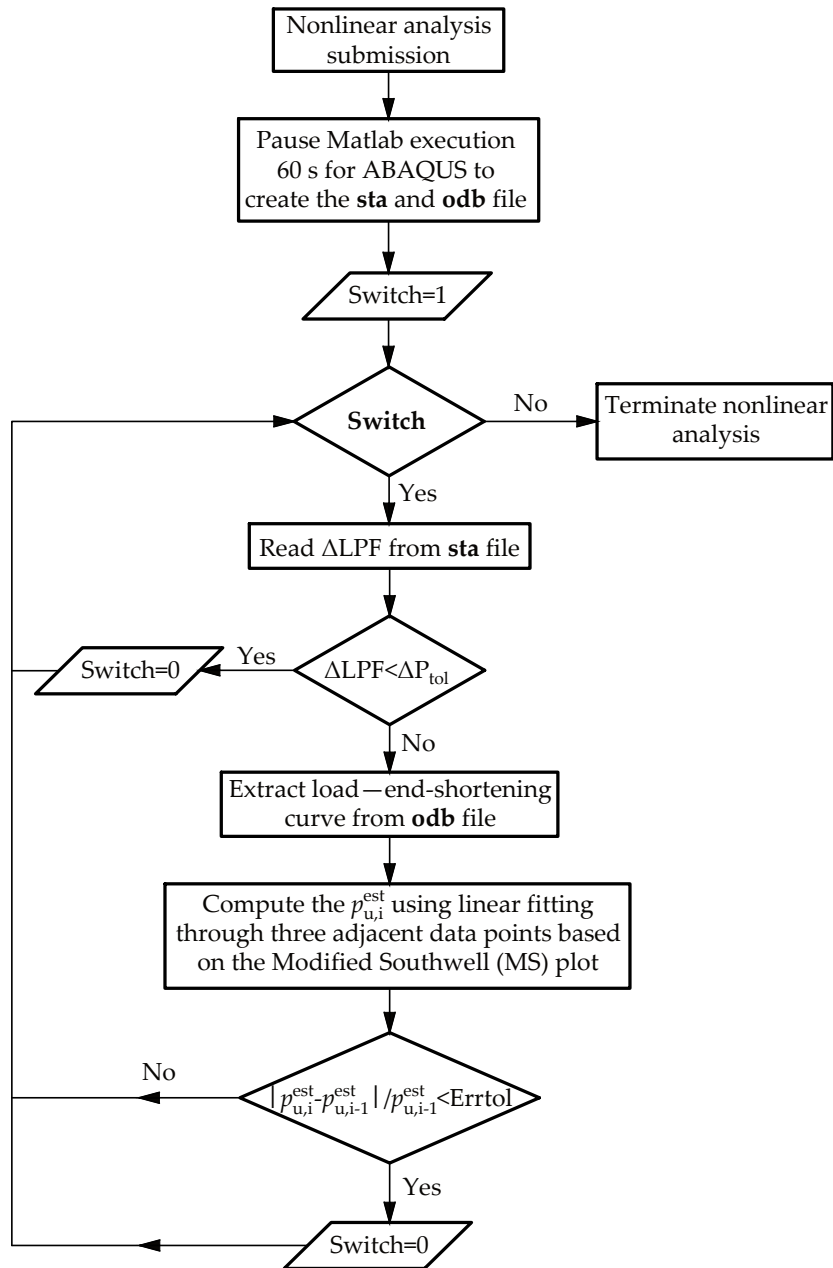


Figure 8.3: Algorithm for function to terminate the nonlinear analysis when the load begins to drop or the load–end-shortening curve reaches the plateau. Note that ΔLPF represents the incremental load proportionality factor; ΔP_{tol} is the tolerance value for ΔLPF ; $p_{u,i}^{est}$ represents the estimated ultimate load at the i^{th} step; ‘Errtol’ is the error tolerance for the difference between the estimated ultimate loads. Note also that the ‘odb’ file is ABAQUS output database and stores the entirety of the computed nodal and element variables; the ‘sta’ file is the ABAQUS status output file and stores the status of increment summaries of nonlinear analysis.

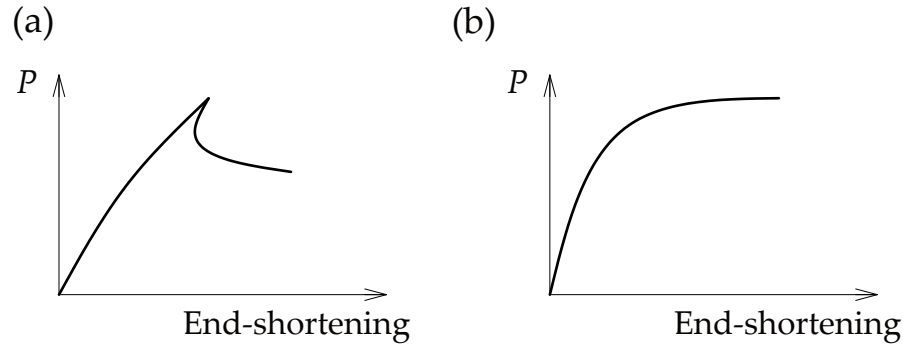


Figure 8.4: Sketch of two typical equilibrium paths describing failure for thin-walled RHS struts: (a) clearly unstable post-buckling behaviour; (b) weakly stable post-buckling behaviour.

prises a nearly vertical part at the start corresponding to the nearly linear response and a plateauing part corresponding to the global buckling of locally buckled struts. The estimated ultimate load $p_{u,i}^{\text{est}}$ is computed by the tip of the non-vertical portion of the MS curve on the vertical axis, which can be determined by linear fitting through the three adjacent data points on the MS curve. If the absolute relative difference between any two adjacent estimated ultimate loads is below the error tolerance, which is set as 0.05% currently, it is assumed that the plateau has been reached and the command is sent to the ABAQUS/Standard solver to terminate the nonlinear analysis. Currently, $p_{u,i}^{\text{est}}$ is only used for convergence judgement purposes and the load corresponding to the final step before the analysis termination is adopted as the ultimate load in such cases. Moreover, the failure criterion is used when the ultimate load is not reached within 100 steps, which can also avoid the effect of vertical portion in the MS plot. It should be noted that there may be some jumps in the $|p_{u,i}^{\text{est}} - p_{u,i-1}^{\text{est}}|/p_{u,i-1}^{\text{est}}$ due to the piecewise numerical solution, as shown in Figure 8.5(c), but the absolute difference decreases with the increase of load increment steps generally. As shown in Figure 8.5(a), the termination point determined by the second criterion can detect the plateau well.

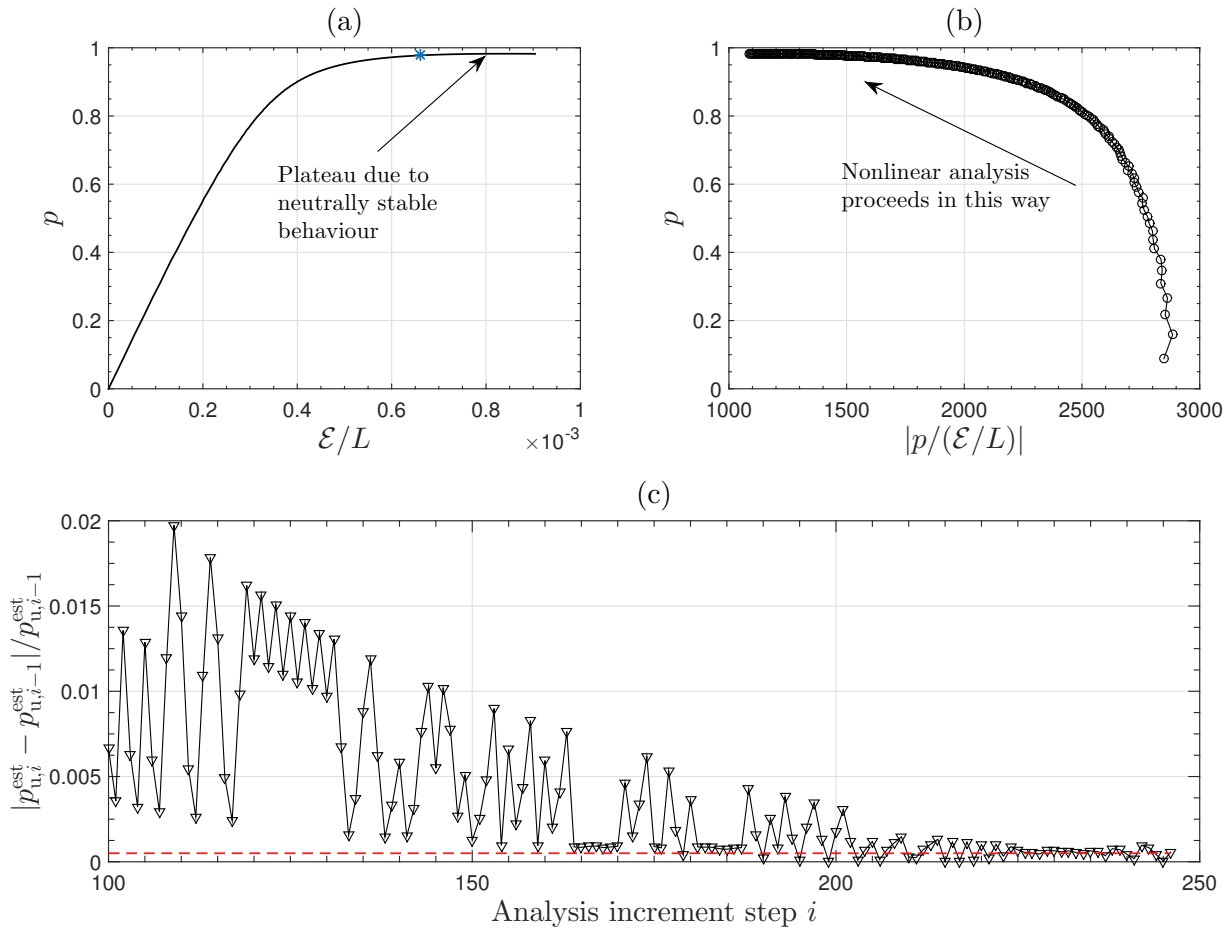


Figure 8.5: Numerical illustration example for the Modified Southwell (MS) method to estimate the failure load from partial nonlinear analysis data and terminate the nonlinear analysis once certain failure criterion is met. (a) The normalized load–end-shortening relationship. Symbol (*) represents the termination point determined based on the current failure criterion. (b) Modified Southwell (MS) plot from (a). Note that the curve is nearly vertical at the initial stage of loading. (c) Convergence and the termination criterion. The quantities $p_{u,i}^{\text{est}}$ and $p_{u,i-1}^{\text{est}}$ represent the estimated ultimate load using the MS method at step i , which are determined based on a linear fit through the three most recent adjacent data points in (b). The dashed line represents the error tolerance for the absolute relative difference between any two adjacent estimated ultimate loads through MS method, *i.e.* 0.05%.

8.3.2 Effects of number of sinusoidal half-waves β_i

The imperfection sensitivity of struts with various different local periodic imperfection profiles is shown in Figure 8.6. With the increase of the number of half-waves β_i , the

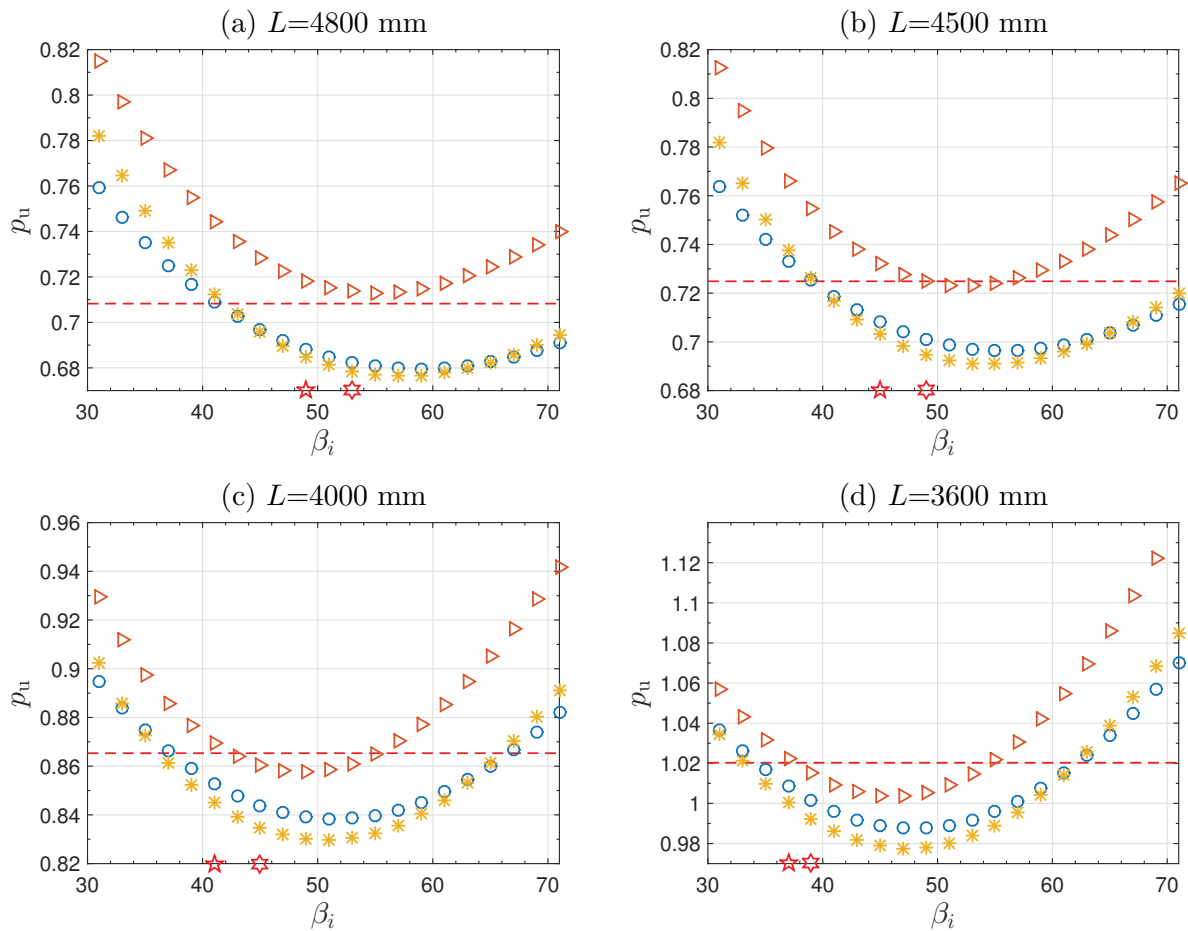


Figure 8.6: Normalized ultimate load of struts $p_u = P_u/P^C$ versus number of half-waves β_i with different local imperfection cases presented in Table 8.2 for different length struts. Symbols \circ , \triangleright , $*$ represent cases 2, 3 and 4 respectively; the dashed line represents case 1. The pentagram and hexagram on the horizontal axis represent the number of half-waves in the pure local buckling mode and in the local–global interactive post-buckling mode of the perfect struts respectively; recall that the interactive post-buckling mode has a naturally modulated amplitude.

normalized ultimate load $p_u = P_u/P^C$, where P^C is the critical buckling load for the perfect strut, decreases and then increases again. This trend resembles the relationship between the plate length to width aspect ratio and the critical buckling load of simply-supported

rectangular plates under axial compression (Bulson, 1970). It should be noted that under the equal local bending energy constraint, the imperfection amplitude naturally decreases with increasing β_i , as shown in Figure 8.7. Therefore, the amplitude of the most severe

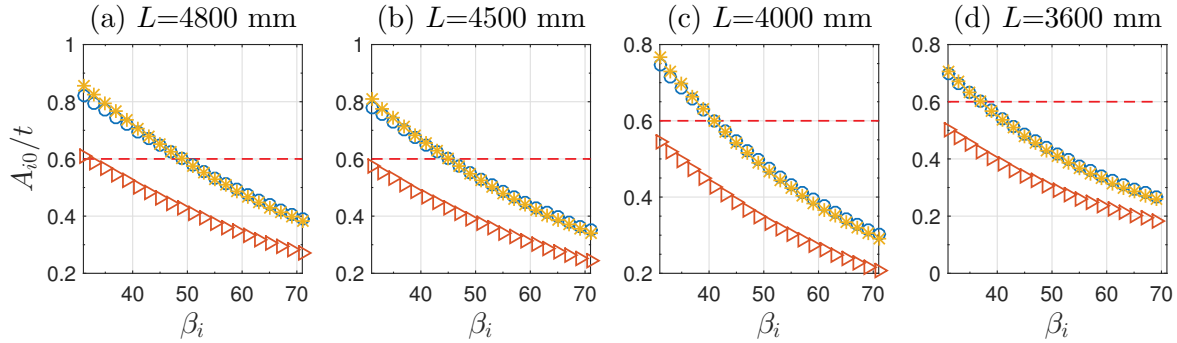


Figure 8.7: Normalized amplitude of local imperfections versus number of half-waves β_i for different imperfection cases presented in Table 8.2. The symbols in the graphs are the same as described in Figure 8.6. Note that the value of β_i at the intersection of \circ and $*$ symbols with the dashed line is the number of half-waves in the longitudinal direction of the pure local buckling mode.

imperfection profile is smaller than that of imperfection profiles with fewer half-waves, which correspond to a much higher ultimate load. It is therefore demonstrated that the imperfection amplitude itself only cannot be used as the unique reference for determining the most severe imperfection profile.

For all four different length struts, the most severe imperfection profile is from the doubly-symmetric cross-section profile imperfection (case 4) with the second most severe being from the mono-symmetric cross-section profile imperfection (case 2). The differences between these two cases are within 1%. It should be noted that the relationship of the imperfection amplitude and the number of half-waves is very close to each other for these two cases, as shown in Figure 8.7. However, the local bending strain energy due to the local imperfection in case 4 is nearly double of that in case 2. When the local bending energy is equal, *i.e.* taking cases 2 and 3, the mono-symmetric cross-section local imperfection profile is more severe than the doubly-symmetric one. Specifically, the difference is approximately 5% for the long length strut with $L = 4800$ mm, while the difference

becomes smaller with decreasing strut length. It should also be noted that the ratio of the local imperfection amplitude for cases 2 and 3 is approximately 1.4 in the range of β_i , as presented in Figure 8.7. It reveals that the ultimate load is principally affected by the local imperfection profiles, *i.e.* the number of half-waves and amplitude, in the more compressed web. Moreover, the difference in p_u for cases 3 and 4 also decreases as the strut length decreases, which implies that short struts with relatively larger values of P_o^C/P_1^C would exhibit relatively less sensitivity to local imperfections. This finding is also in accord with that presented in Figure 7.15.

As for the number of half-waves in the most severe case, it is larger than that in the pure local buckling mode and the local–global interactive post-buckling mode for perfect cases from Chapter 6, as shown in Figure 8.6. Moreover, cases 3 and 4 have the same cross-section imperfection profiles but different imperfection amplitudes, *i.e.* different local bending energy levels due to local imperfections. The values of β_i corresponding to the lowest ultimate load are different for these two cases, which implies that the most severe imperfection profile is also related to the imperfection amplitude. This finding is in accord with previous studies on the most severe local imperfection profile of I-section struts (Bai & Wadee, 2015a) and stiffened panels (Wadee & Farsi, 2015). However, it should be stressed that a small increase or decrease in the value of β_i would only lead to a tiny change in the ultimate load, which has also been reported in a study on the imperfection sensitivity of open-section storage rack columns (Trouncer & Rasmussen, 2015).

Figure 8.6 also shows the ultimate load of struts with imperfection profiles corresponding to the lowest local buckling mode from linear buckling analysis using the FE model. The difference with the most severe case decreases from approximately 5.4% for the long length strut to approximately 4.3% for the short length strut, as shown in Table 8.3. Therefore, it may be concluded that the lowest local buckling mode does not always represent the most severe imperfection profile.

Table 8.3: Ultimate load and local imperfection amplitude of the most severe local periodic imperfection profile. Note that for case 1, $P_u/P_{u,LBA,FE}=1.0$ by definition and $A_{i0}/t=0.6$ for all lengths.

L	$P_u/P_{u,LBA,FE}$			A_{i0}/t			
	case 2	case 3	case 4	case 1	case 2	case 3	case 4
4800	0.959	1.007	0.955	0.6	0.494	0.377	0.508
4500	0.961	0.998	0.953		0.488	0.358	0.480
4000	0.969	0.991	0.959		0.475	0.349	0.467
3600	0.968	0.984	0.958		0.463	0.323	0.455

8.3.3 Effects of the degree of localization α_i

As described in Figure 8.2, the study on the effect of localization is based on the results of the immediately preceding section. The number of half-waves β_i for each case is kept to the value corresponding to the lowest ultimate load as presented in Figure 8.6. The equivalent local bending energy due to local imperfections $U_{b,1}^0$ also remains the same in each case. The relationship of the normalized imperfection amplitude A_{i0}/t versus α_i under the constraint of equal local bending energy is shown in Figure 8.8. In contrast with the

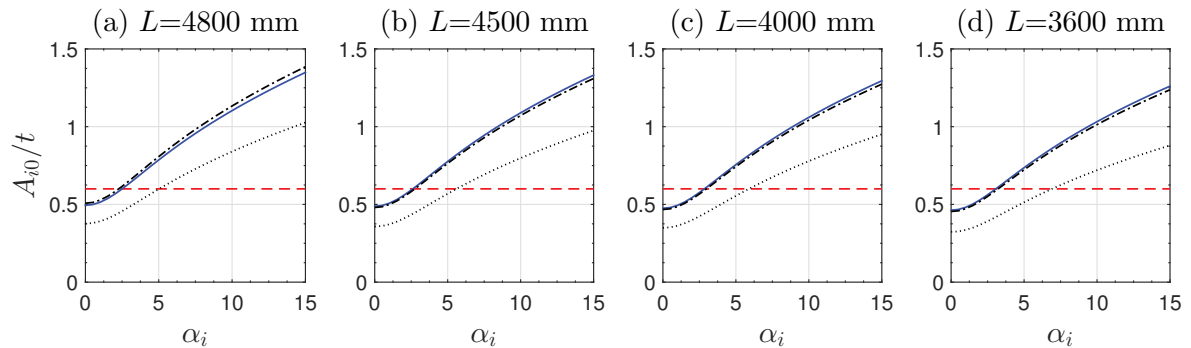


Figure 8.8: Normalized amplitude of the local imperfection versus the degree of localization α_i for different imperfection cases as presented in Table 8.2. The dashed, solid, dotted and dot-dashed lines represent the imperfection profiles from cases 1, 2, 3 and 4 respectively.

A_{i0}/t versus β_i relationship, the increase in α_i would lead to an increase in A_{i0}/t under the equal local bending energy constraint. However, the A_{i0}/t versus α_i relationships for cases 2 and 4 are still very close to each other, as they were in the A_{i0}/t versus β_i relationship, see Figure 8.7.

The relationship between the normalized ultimate load p_u and the degree of localization α_i for different length struts is shown in Figure 8.9. Initially, the ultimate load decreases from

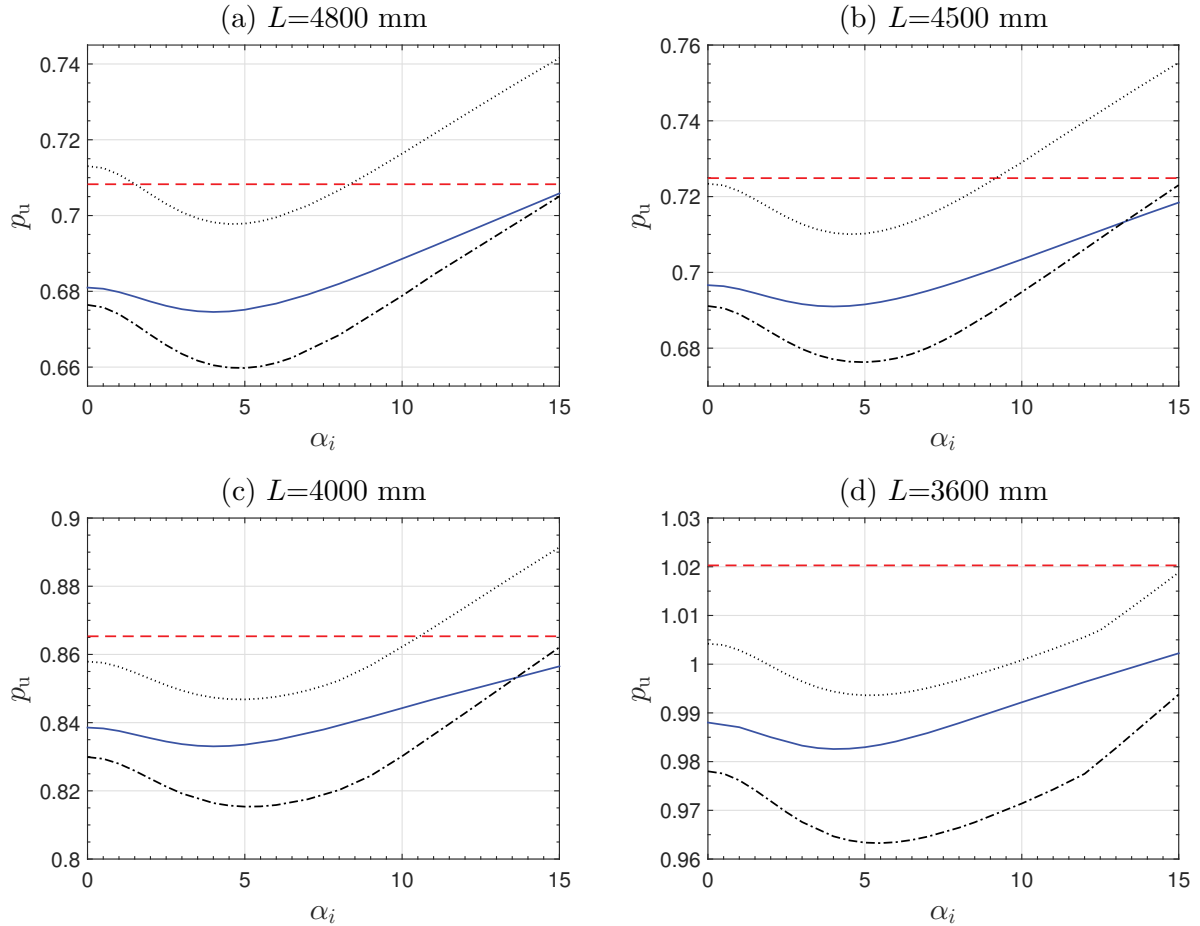


Figure 8.9: Normalized ultimate load of the strut $p_u = P_u/P^C$ versus the degree of localization α_i for different local imperfection cases presented in Table 8.2. Line types in the graphs represent the same cases as those described in Figure 8.8.

the periodic profile to the localized one in all four cases. The modulation of the longitudinal profile does affect the ultimate load but the effects are relatively small. Specifically, the modulation only leads to a further 0.6% to 2.6% drop in the ultimate load. Among cases 2–4, the effect is most minor for the mono-symmetric case, where the further drop is below 0.8%. With further increase in the degree of localization, the ultimate load begins to increase, even though the imperfection amplitude increases. This, again, demonstrates that the imperfection amplitude is not suitable to be used as the unique criterion for

imperfection measurement. Moreover, at least for the current purely elastic case, a highly localized local imperfection with a large imperfection amplitude does not represent the most severe imperfection profile.

The comparison of the lowest ultimate load and the normalized imperfection amplitude for each case with the profile that is affine to the lowest linear buckling mode from FE models is shown in Table 8.4. For all four cases, the largest and the second largest differences in

Table 8.4: Ultimate load and local imperfection amplitude of the most severe local modulated imperfection profile.

L	$p_u/p_{u,LBA,FE}$			A_{i0}/t			
	case 2	case 3	case 4	case 1	case 2	case 3	case 4
4800	0.952	0.985	0.932	0.6	0.711	0.570	0.817
4500	0.953	0.980	0.933		0.702	0.542	0.776
4000	0.963	0.979	0.942		0.684	0.555	0.756
3600	0.963	0.974	0.944		0.666	0.514	0.770

the ultimate load occur in cases 4 and 2 respectively, with the largest percentage difference value being 6.8% in case 4 for the long length strut. However, the corresponding imperfection amplitude in cases 2 and 4 is larger than that of the linear buckling mode profile, *i.e.* the tolerance level value.

For all four characteristic length struts, the values of α_i corresponding to the lowest ultimate load for doubly-symmetric imperfection cases are very close and are slightly larger than that for the mono-symmetric imperfection case. The longitudinal component of the most severe imperfection profiles in cases 3 and 4 for the long length strut are shown in Figure 8.10 (a, b). For comparison purposes, the longitudinal component of the local buckling mode from linear buckling analysis and the interactive buckling mode in the advanced post-buckling range of the perfect system from Chapter 6 are also shown in Figure 8.10 (c, d) respectively. As identified in the preceding subsection, the wavelength of the most severe imperfection profile is considerably shorter than the linear buckling mode and slightly smaller than the interactive post-buckling mode in the advanced post-buckling range.

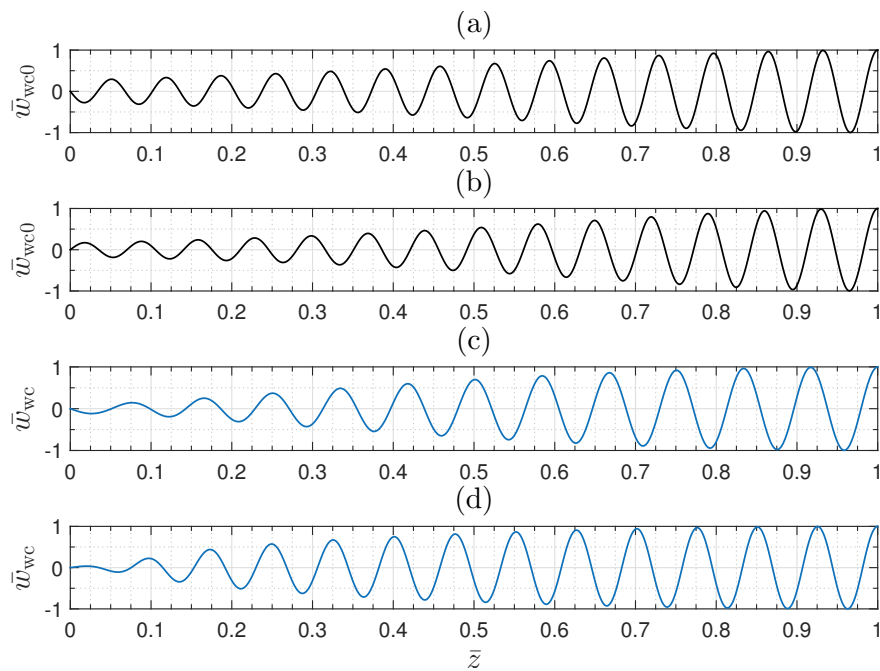


Figure 8.10: Normalized longitudinal profile in the more compressed web of (a) most severe imperfection profile for the mono-symmetric imperfection (case 2), (b) most severe imperfection profile for the doubly-symmetric imperfection (case 4), (c) local buckling mode from linear buckling analysis and (d) interactive mode in the advanced post-buckling range of the perfect system where $q_s = 0.009$ for the long length strut with $L = 4800$ mm. Note that $\bar{w}_{wc0} = w_{wc0}/w_{wc0,max}$ and $\bar{w}_{wc} = w_{wc}/w_{wc,max}$.

8.3.4 Equilibrium paths for struts with the most severe imperfection profile

Figure 8.11 presents the nonlinear equilibrium paths of example struts with the most

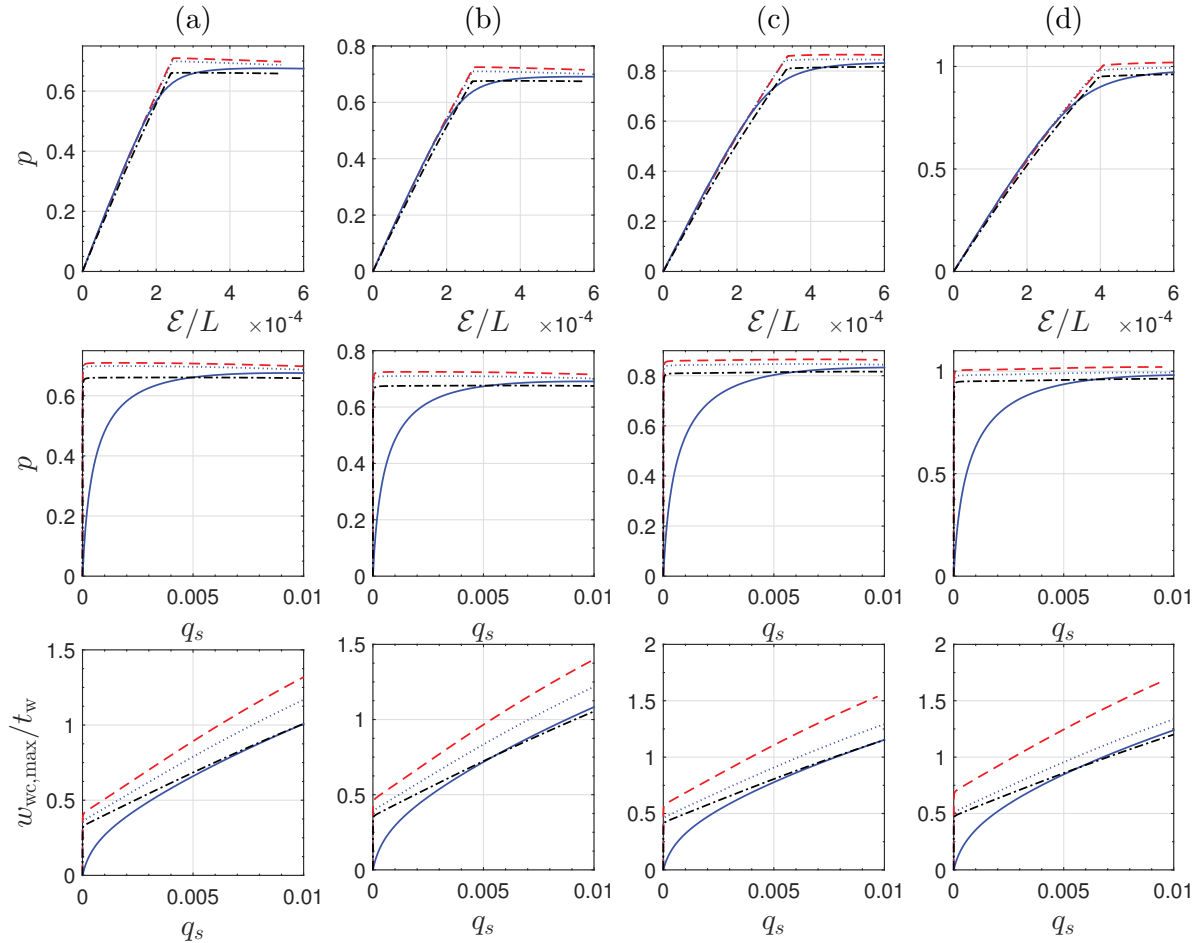


Figure 8.11: Equilibrium paths of example struts in zones 1–4 presented in columns (a)–(d) respectively, with the most severe imperfection profiles of the four cases presented in Table 8.2. Graphs of normalized load ratio $p = P/P^C$ versus normalized end-shortening \mathcal{E}/L in the first row and the normalized global amplitude q_s in the second row; the third row shows the normalized maximum amplitude of local deflection in the more compressed web $w_{wc,max}/t_w$ versus q_s . Line types in the graphs correspond to the same cases as described in Figure 8.8.

severe local imperfection profiles for each case described in Table 8.2. Unlike the perfect case, where the equilibrium paths for four example struts are qualitatively different, the struts with tolerance level local imperfections exhibit approximately the same behaviour,

i.e. column-like weakly stable, practically neutral, post-buckling behaviour. This is also reported in previous work using simplified models (van der Neut, 1969; Gilbert & Calladine, 1974) and experimental studies (Gilbert & Calladine, 1974).

For cases with doubly-symmetric cross-section imperfection profiles, the symmetry in the deformation remains until mode interaction is triggered and the interaction leads to the approximately neutral post-buckling behaviour. For the case with the mono-symmetric imperfection profile, the symmetry in the deformation is broken from the start, *i.e.* the global mode is introduced at the beginning of the numerical run, thus making the initial bending stiffness much lower than those in the doubly-symmetric cases. However, the equilibrium path converges to the doubly-symmetric case when the global mode is fully developed, *i.e.* when $q_s > 0.005$. Therefore, it may be inferred that the ultimate behaviour of such struts with tolerance level imperfections would be governed by eventual material failure, rather than the cases where imperfection size is tiny and a drop in stiffness due to mode interaction governs as reported in Chapter 6. Moreover, it is concluded that determining the global buckling load of struts with tolerance level local imperfections may provide a good approximation for the ultimate load in such cases.

8.4 Discussion

In a similar way to the local imperfection amplitude, the equivalent local bending energy of imperfection profiles also cannot be used as the sole criterion to determine the severity of imperfection profile. However, it gives an insight into how the imperfection profiles affect the ultimate load. Therefore, it can still be used as an important reference to judge the severity of local imperfections.

In this subsection, a discussion is presented that considers why very localized local imperfections with high imperfection amplitudes exhibit higher ultimate loads than the periodic

ones with the same local bending energy. Moreover, the most severe imperfection profile and the wavelength under the constraint of the manufacturing tolerance level is discussed, as is the effect of global imperfections on the most severe local imperfection profiles.

8.4.1 Effects of localization on tangent stiffness and ultimate load

As shown in Figure 8.9, struts with very localized imperfections exhibit considerably higher ultimate loads than periodic imperfections, even though the corresponding amplitude is much larger than that of the periodic case. These findings are similar to those in earlier work on thin plates (Dow & Smith, 1984).

Since the global buckling load of struts with doubly-symmetric cross-section imperfection profiles is related to the axial stiffness distribution, the axial tangent modulus of the cross-section versus load relationship is analysed. It should be stressed that the relationship for different lengths is approximately the same before global buckling is triggered. Therefore, the relationship of the tangent axial stiffness and the normalized axial load for the perfect short length strut and the short length strut with periodic ($\alpha_1 = 0$) and highly localized local imperfections ($\alpha_1 = 20$) with the cross-section profile being doubly-symmetric are presented in Figure 8.12(a) for illustration. It should also be noted that the cross-section imperfection profiles, the number of half-waves and initial local bending energy due to local imperfections for both imperfect struts are the same as that for case 4 in Figure 8.11(d).

The strut with localized imperfections exhibits a higher tangent stiffness than the periodic case from the commencement of loading. This is attributed to the fact that the local out-of-plane displacement in the webs is affine to the localized imperfection profile and that there is no out-of-plane displacement at the loaded end before the local buckling load is reached, as shown in Figure 8.12(b). It implies that there is no progression of the local out-of-plane displacement from the localized to being more distributed, as seen in the local-global interactive buckling for the perfect case. The zero displacement in the

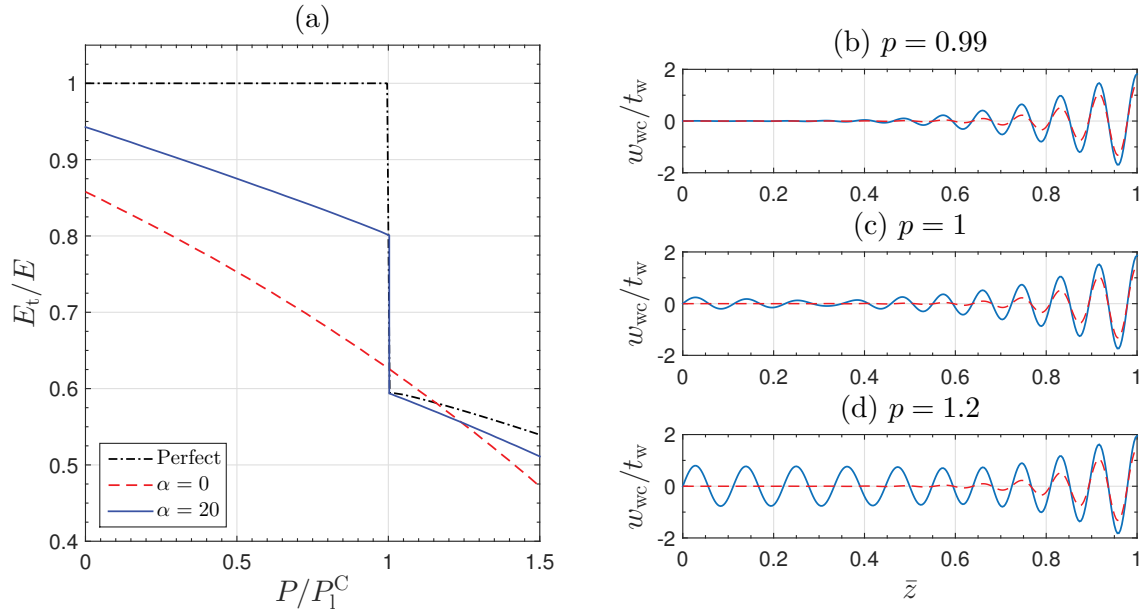


Figure 8.12: (a) Cross-sectional axial tangent modulus of the short length strut with increasing load level. (b–d) Longitudinal component of the local buckling mode in the webs (solid line) at different load levels and the initial imperfection (dashed line), where $p = P/P_1^C$. Note that the cross-section profile of the local imperfections is doubly-symmetric and global imperfections are not included.

plate represents no loss in the axial stiffness, which helps to explain the relatively higher tangent axial stiffness compared to the periodic imperfection case. When the load reaches the local buckling load of the strut, there is a sharp drop in the axial stiffness, which is also observed in the perfect case. This corresponds to local buckling of the unbuckled plate near the loaded-end, as shown in Figure 8.12(c). After that, the out-of-plane displacement in the webs becomes more distributed. However, it should be noted that the wavelength near the loaded end is relatively larger than at mid-span, which is determined by the imperfection, as shown in Figure 8.12(d). Moreover, it is worth mentioning that although struts with highly localized local imperfection profiles exhibit higher ultimate loads, there is a tiny drop in the load capacity afterwards and it converges to that of the periodic case with the lowest ultimate load, which implies that the post-buckling behaviour is weakly unstable. This is also observed in plates with localized imperfections (Dow & Smith, 1984). However, it should also be mentioned that the current discussion only applies for purely elastic cases. As reported by Gardner & Nethercot (2004a), the localization of deformation

profile could well lead to the premature failure of material. A study on the most severe imperfection profile where the effects of the material nonlinearity are included is left for future work.

8.4.2 Most severe imperfection profile under amplitude tolerance constraint

As presented in Figure 8.9 and Table 8.4, the most severe imperfection profile for each strut corresponds to case 4 with the modulated longitudinal components, *i.e.* the doubly-symmetric cross-section with $\alpha_1 \neq 0$ (see Eqs. (5.13) and (5.14) for the definition of the modulated imperfection). However, since current manufacturers principally adopt the tolerance level of imperfection amplitude as the quality control, the worst profile determined in §8.3.3 would be practically insignificant owing to its excessive amplitude, as shown in Table 8.4. Therefore, based on the algorithm presented in Figure 8.2, the value of α_1 that makes the imperfection amplitude be the tolerance value under the constraint of equal local bending energy is determined using the interval bisection method. It should be noted that the value of α_1 purely corresponds to the horizontal coordinate at the intersection of the dashed line and the dot-dashed line in Figure 8.8, where the amplitude of the imperfection is equal to the tolerance level under the equal local bending energy constraint. The longitudinal component of the most severe imperfection profile under the amplitude tolerance constraint is presented as the solid line in Figure 8.13.

It should be stressed that the modulated imperfection profiles are relatively complex to model when compared with the periodic imperfection profiles, the latter of which can be obtained directly from some software, such as CUFEM (Schafer, 2006a). Moreover, as can be seen from Table 8.5, the ultimate load for struts with a periodic imperfection profile is lower than the corresponding modulated imperfection with the same amplitude. Therefore, for modelling convenience, the periodic imperfection profile with the tolerance

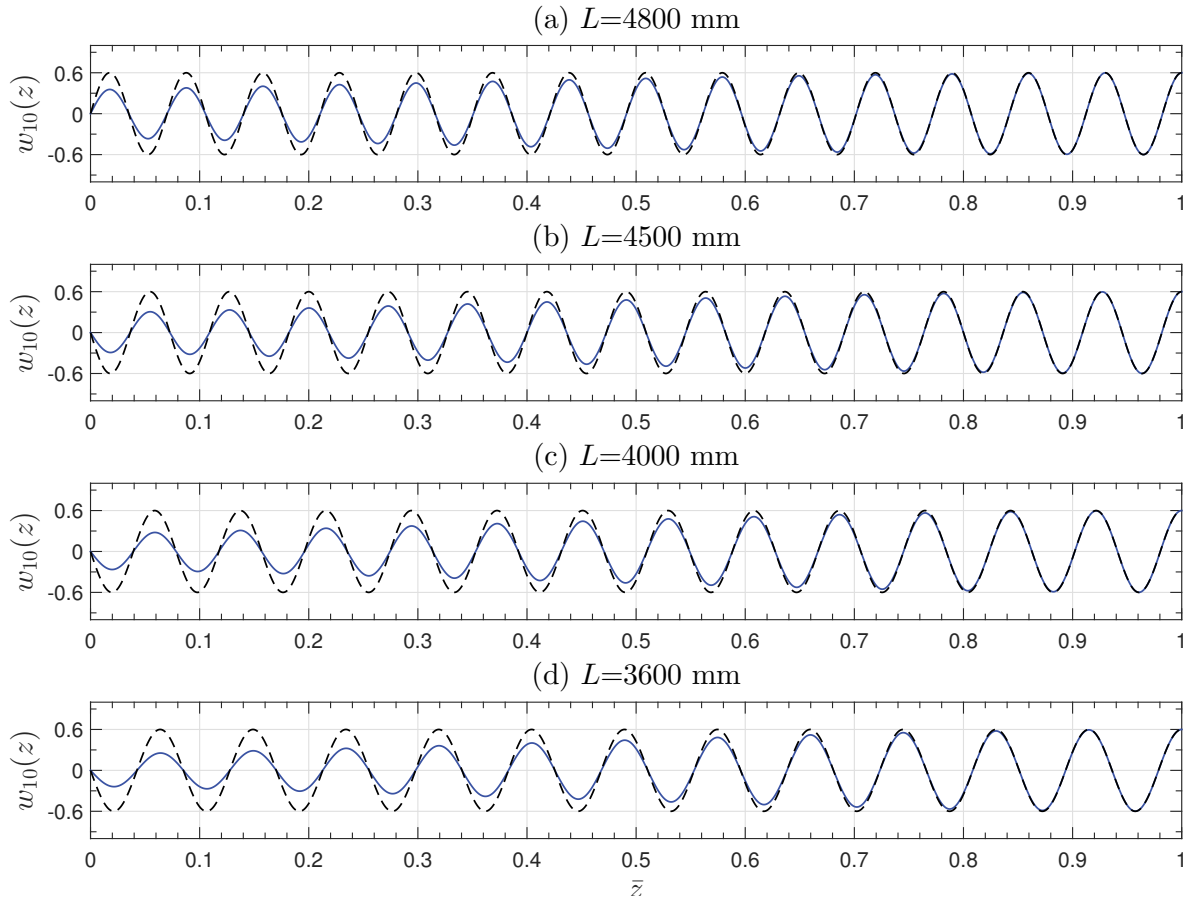


Figure 8.13: Longitudinal component of the most severe imperfection profile (case 4) w_{10} under the amplitude tolerance constraint (solid line), with the degree of localization parameter α_1 being (a) 2.269, (b) 2.742, (c) 2.977 and (d) 3.213 respectively for different length struts. Dashed lines represent the periodic imperfection profile with the amplitude being the tolerance value, which is currently used for a safe approximation of the most severe imperfection profile.

Table 8.5: Normalized ultimate loads of struts with the most severe modulated local imperfection and approximations using periodic profiles under the amplitude tolerance constraint; $P_{u,LBA,An}$ represents the ultimate load of struts with periodic imperfection profiles from linear buckling analysis using the analytical model presented in Appendix C with tolerance level imperfections.

L (mm)	$P_u/P_{u,LBA,FE}$		$P_{u,LBA,An}/P_{u,LBA,FE}$
	Modulated	Periodic	
4800	0.944	0.932	0.967
4500	0.941	0.925	0.970
4000	0.949	0.929	0.977
3600	0.949	0.927	0.980

level amplitude could be adopted as a safe approximation of the most severe imperfection profile, as presented with the dashed line in Figure 8.13. The following discussion and parametric study focuses on local imperfection profiles with doubly-symmetric cross-section and periodic longitudinal components.

8.4.3 Effects of superposing tolerance level global imperfections

In the preceding sections, the most severe local imperfection profile is determined based on the cases with pure local imperfections. In order to investigate whether the most severe local imperfection profile would change with the inclusion of tolerance level global imperfections, a parametric study on the most severe local imperfection is conducted for the cases where both tolerance level local and global imperfections exist using the algorithm presented in Figure 8.2.

The normalized wavelength of the most severe imperfection profile for the two cases are shown in Figure 8.14. Compared with the pure local imperfection cases (hollow circles), the introduction of the global imperfection (solid circles) leads to a further decrease in the wavelength. However, the increase and decrease in the number of waves near the most severe imperfection profiles β_{worst} has minor effects on the ultimate load. Specifically, for the example struts in the current paper, ± 4 half-waves would lead to errors within 0.5% for both cases, which are shown in Figure 8.14. Therefore, the range between $\beta_{\text{comb, worst}} - 4$ and $\beta_{\text{loc, worst}} + 4$, *i.e.* the range enclosed by the dashed lines in Figure 8.14, is the overlap of the two cases, which can be used for the approximation of the most severe imperfection profile with excellent accuracy for both cases, as outlined above. It may therefore be concluded that the most severe imperfection profile determined in the case with purely local imperfections is still valid for the cases with both local and global imperfections.

Moreover, instead of determining β_{worst} for each characteristic strut length individually using the iterative process, it is postulated that a fixed reduced wavelength can be used

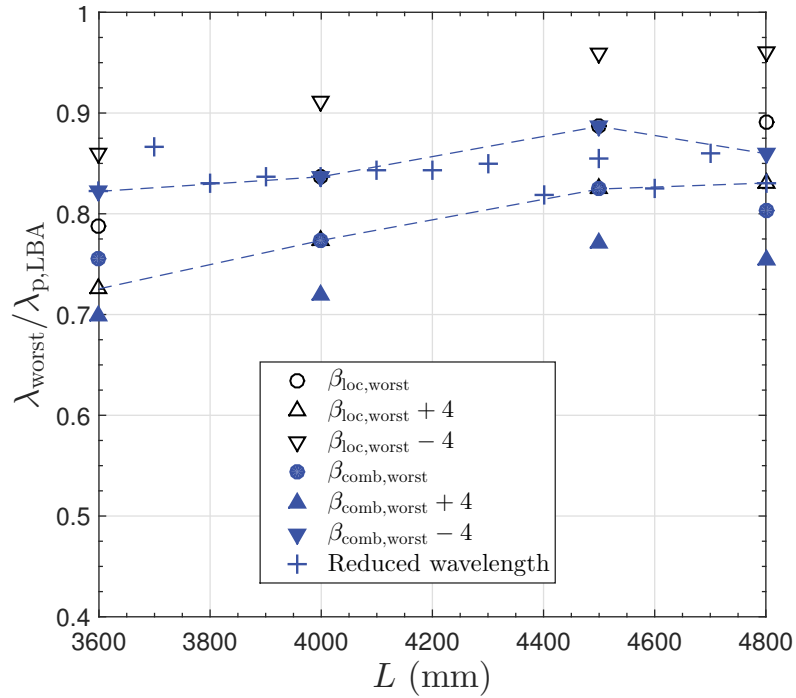


Figure 8.14: Normalized wavelength of the most severe local imperfection profile with a doubly-symmetric cross-section profile for different length struts. The quantity $\lambda_{p,LBA}$ represents the wavelength of the lowest local buckling mode, which is determined using Eq. (C.21); quantities $\beta_{\text{loc,worst}}$ and $\beta_{\text{comb,worst}}$ represent the number of half-waves of the most severe imperfection profile with purely local imperfections and combined local and global imperfections respectively. Range enclosed by the dashed line represents the overlap of the two cases, which can estimate the most severe local imperfection profile with good accuracy.

to approximate the most severe profile for the current case. Specifically, if a reduced wavelength $\lambda_{\text{worst}} = 0.825\lambda_{\text{p,LBA}}$ is adopted, which are shown as the plus (+) symbols in Figure 8.14, the largest differences in the corresponding ultimate load with the lowest ultimate load is 0.33% among the four example struts. Therefore, in the following section, an explicit expression is proposed to determine the wavelength of the worst imperfection profile based on the results of the parametric study.

8.5 Application and parametric study

8.5.1 Wavelength of most severe local imperfection profile

The parametric study in this section comprises two parts: the first part focuses on the effects of geometric properties and the second part focuses on the effects of imperfection size. In the first part, parametric studies on the wavelength of the most severe local imperfection profile for struts with different geometric properties, *i.e.* cross-section aspect ratios $\phi_c = [1, 2.5]$ and web depth to thickness ratios $\phi_{\text{dt}} = [60, 240]$, are conducted. The web width is fixed to 120 mm as that of the example struts in the preceding section. Since the ultimate load erosion is most significant in the range where $P_o^C/P_1^C \approx 1$, the strut length is determined based on the condition that $P_o^C/P_1^C=1$. Moreover, the initial local imperfection amplitude A_{i0}^0 is $0.6t$.

Figure 8.15(a) shows the normalized wavelength of the most severe imperfection profile determined using the algorithm presented in Figure 8.2. The variation of the wavelength is small in the range, *i.e.*, the average value is $0.836\lambda_{\text{p,LBA}}$ and the coefficient of variation (COV) is 2.14%. It implies that the normalized wavelength of the most severe imperfection profile can be treated to be constant for different ϕ_c and ϕ_{dt} cases. Moreover, the effects of the strut length varying ($P_o^C/P_1^C = 0.6, 1.0$ and 1.5) are also investigated; it is revealed that the average value almost remains the same with a slight increase in the COV to be

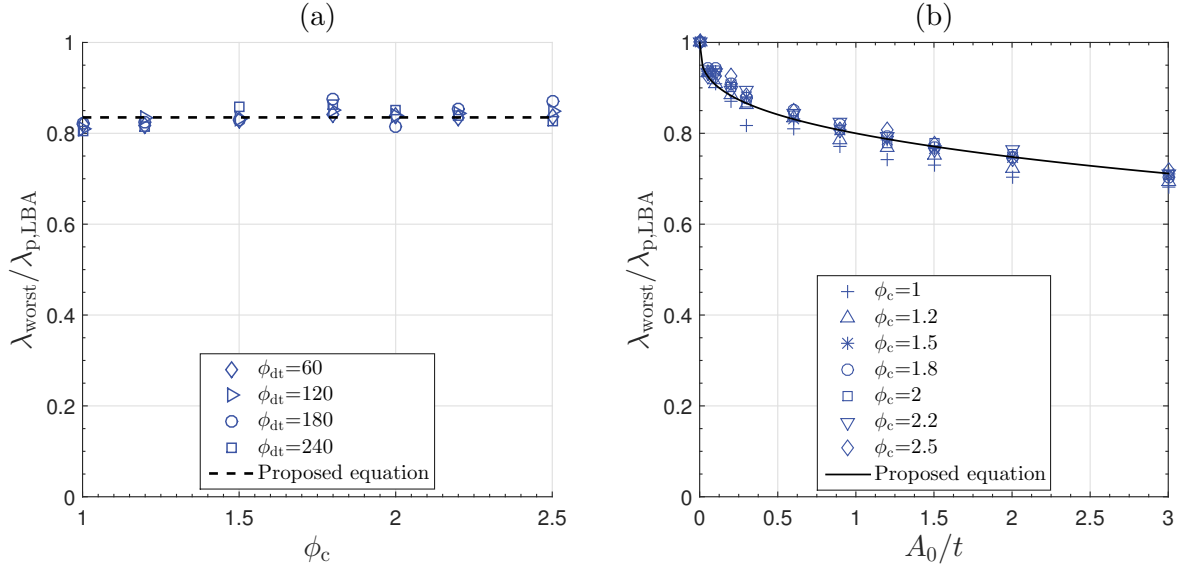


Figure 8.15: (a) Normalized wavelength of the most severe imperfection profile $\lambda_{\text{worst}}/\lambda_{\text{p,LBA}}$ for struts with different cross-section aspect ratios and different plate width to thickness ratios. (b) Relationship of $\lambda_{\text{worst}}/\lambda_{\text{p,LBA}}$ and the normalized imperfection size A_0/t for struts with different aspect ratios. Note that the length of all struts is determined based on the condition $P_o^C/P_1^C=1$.

3.36%. This may be attributed to the constraint that the number of half-waves should be an integer; for the cases where the number of half-waves is small, ± 2 half-waves along the length would lead to a relatively larger variation in the wavelength.

Since it has been demonstrated that the wavelength of the most severe imperfection profile decreases with the increase of imperfection size, a parametric study on the effects of imperfection size is conducted based on the results in the first part. The web depth and plate thickness are fixed to 120 mm and 1 mm respectively as those of the example struts in preceding section. It should be noted that the manufacturing tolerance of local imperfections is expressed as a ratio of plate width, *i.e.* $d/200$, in Eurocode 3 (EN-1993-1-3:2006E, 2006). However, a theoretical study (Supple, 1970) demonstrated that the imperfection related parameter in the governing equations for the buckling of imperfect plates can be normalized with respect to plate thickness A_0/t . Therefore, the dimensionless quantity A_0/t is adopted as the varying imperfection parameter.

The results of the parametric study are presented in Figure 8.15(b). With the increase of imperfection size, the wavelengths of the most severe imperfection profiles decrease. For a fixed value of imperfection size, the maximum COV in the wavelength for struts with different cross-section aspect ratios among all cross-section aspect ratio cases is found to be only 2.83%. Therefore, an equation is fitted based on the least squares method to describe the relationship between the most severe wavelength and the imperfection size:

$$\lambda_{\text{worst}}/\lambda_{\text{p,LBA}} = 1 - 0.2 \left(\frac{A_0}{t} \right)^{0.36}. \quad (8.4)$$

The average ratio of the FE results to that predicted by Eq. (8.4) is 1.002 and the COV is 2.14%, which represents an excellent fit.

8.5.2 Global buckling loads of struts with tolerance level doubly-symmetric cross-sectional local imperfections

A simplified method to calculate the load at the pitchfork bifurcation point (Glendinning, 1994), which is a generic term for a symmetric bifurcation point, of thin-walled RHS struts with purely global imperfections was proposed in §7.2.1. This has been demonstrated to provide a safe prediction with excellent accuracy. Currently, attempts are made to understand the mechanism of the global buckling of struts with tolerance level doubly-symmetric cross-sectional local imperfections and develop a simplified method to calculate the buckling load. The latter would also be a good approximation of the ultimate load since the post-buckling behaviour has been shown to be weakly stable in such cases.

As shown in Figure 8.12(a), local buckling leads to the axial stiffness dropping to below 60% of the pre-buckling value for the perfect strut. The post-buckling axial stiffness is much larger than that in Van der Neut's model (approximately 40%), where the compressed plates are simply-supported and there is no interaction between individual plates within the

cross-section (van der Neut, 1969). However, after local buckling is triggered, the tangent axial stiffness does not remain constant but drops further with increasing deformation. Specifically, the cross-section profile would not remain in the initially buckled shape but bulge out gradually, as shown in Figure 6.16. This finding is also reported in Young & Rasmussen (1997) and Loughlan *et al.* (2011), but has been omitted in other previous studies (Bijlaard & Fisher, 1953; van der Neut, 1969; Koiter & Pignataro, 1976a; Graves Smith, 1972) owing to technical complexity. As for the imperfect case, the tangent axial stiffness is lower than that of the perfect case at the start of loading and decreases as further loading is applied. When the load exceeds the local buckling load, the tangent stiffness of the imperfect strut would converge to that of the perfect strut.

In Van der Neut's idealized model (van der Neut, 1969), where there are only two simply-supported flanges contributing to the bending rigidity through their axial stiffness, the corresponding global buckling load for the locally buckled strut is ηP_o^C , which can be determined using double-modulus theory (Bažant & Cedolin, 2010), as discussed in Chapter 6. The stiffness reduction factor η can be determined from the normalized tangent stiffness E_t/E of purely local buckling struts directly because both flanges are parallel to the neutral axis of bending and thus E_t/E represents the actual stiffness reduction ratio in both flanges.

In the current case, however, the normalized tangent stiffness E_t/E from the load versus end-shortening relationship only represents the general stiffness reduction of the whole cross-section in the purely local buckling case. The transition from the purely local buckling mode to the global-local interactive post-buckling mode involves a stiffness redistribution across the entire cross-section due to the interaction of individual plates (Bijlaard & Fisher, 1952; Hancock, 1981; Shen & Wadee, 2018b). This implies that the tangent stiffness distribution would be different from that of the purely local buckling case at the same load level. Moreover, the restraint from both flanges on the webs also decreases with increasing load and thus the actual stiffness distribution profile is also affected by the load level,

i.e. it is related to the strut length. In order to obtain the corresponding global buckling load for the locally buckled struts, the actual tangent stiffness distribution at the pitchfork bifurcation point is required (Rasmussen, 1997). The problem itself is highly complex and requires geometrically nonlinear analysis to solve.

A systematic parametric study is conducted currently to investigate the key parameters that may affect the global buckling load of thin-walled RHS struts with purely tolerance level local imperfections \bar{P}_o^C . This is used to develop an expression to determine the value of \bar{P}_o^C . Firstly, the effect of geometric properties is investigated. The principal varying parameters are the cross-section aspect ratio ϕ_c , web depth to thickness ratio ϕ_{dt} , and the strut length P_o^C/P_1^C . The web depth is fixed to the value of 120 mm and the dimensionless local imperfection size is fixed to $A_0/t = 0.6$. The cross-section profile of local imperfections is doubly-symmetric and determined using Eqs. (C.2) and (C.3); the longitudinal component is periodic and the wavelength is determined using Eqs. (8.4) and (C.21).

The results from the parametric study on geometric properties are presented in Figure 8.16. As can be seen, \bar{P}_o^C/P_o^C decreases with decreasing strut length. It reflects that the tangent stiffness of the cross-section decreases with increasing load level, as shown in Figure 8.12(a). Moreover, \bar{P}_o^C/P_o^C decreases with increasing cross-section aspect ratio ϕ_c at a fixed value of P_o^C/P_1^C , but the difference is small and reduces with decreasing strut length, as seen in Figure 8.16(a). This may be attributed to the fact that the interaction between each individual plate becomes weaker with increasing load level. Compared with the cross-section aspect ratio ϕ_c , the effect of the plate width to thickness ratio ϕ_{dt} is much smaller, as shown in Figure 8.16(b). This is reasonable since the thickness has a relatively minor effect on the cross-section second moment of area for thin-walled section members. Therefore, it may be concluded that the effect of cross-section aspect ratio and web depth to thickness ratio on the relationship between \bar{P}_o^C/P_o^C and P_o^C/P_1^C may be safely neglected.

The second part of the parametric study focuses on the effect of local imperfection size. The

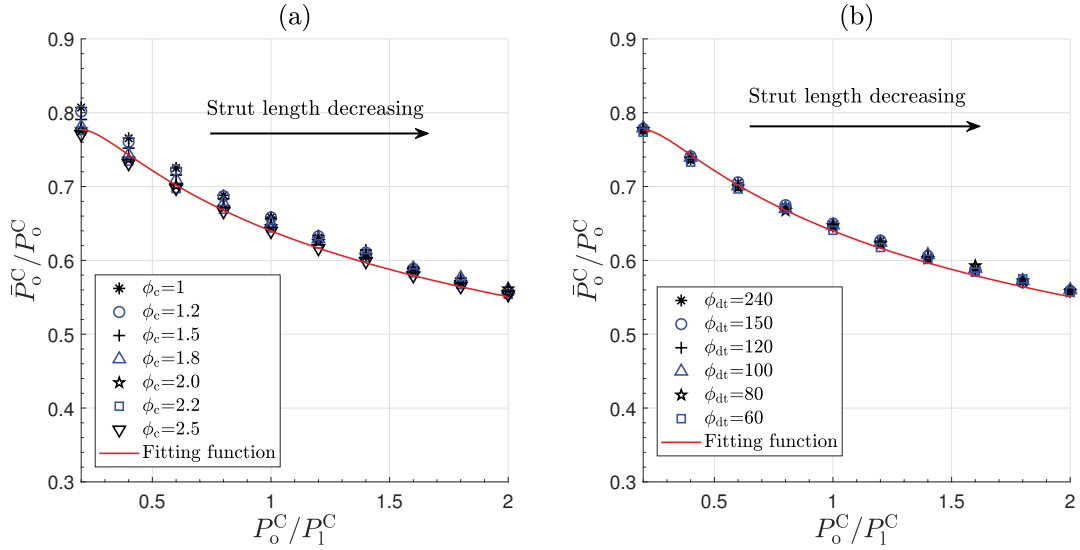


Figure 8.16: Reduced global buckling load of struts \bar{P}_o^C/P_o^C with dimensionless local imperfection size $A_0/t = 0.6$ versus P_o^C/P_1^C from FE results and Eq. (8.5) for different (a) ϕ_c values and (b) ϕ_{dt} values. Note that the web depth d is fixed to 120 mm; the plate thickness t is fixed to 1 mm in (a); in (b) ϕ_c is fixed to 2.

imperfection profiles are determined in the same way as the parametric study on geometric properties, which, in turn, is based on the parametric study on the worst imperfection profile. The cross-section geometric properties of the struts are the same as the example struts in §8.3, with the results presented in Figure 8.17(a). It is observed clearly that with increasing imperfection size, the value of \bar{P}_o^C/P_o^C decreases. In particular, the drop is much larger when global buckling is critical, *i.e.* where $P_o^C/P_1^C < 1$, which implies that struts with global buckling being critical are more sensitive to local imperfections. The difference in the reduced normalized global buckling load for different length struts becomes small when the normalized imperfection size A_0/t is large.

The following equation is fitted based on the results of the two-part parametric study using the least squares method:

$$\frac{\bar{P}_o^C}{P_o^C} = \left(C_1 - C_2 \sqrt{\frac{P_1^C}{P_o^C}} \right) \left(\frac{P_1^C}{P_o^C} \right)^{C_3}, \quad (8.5)$$

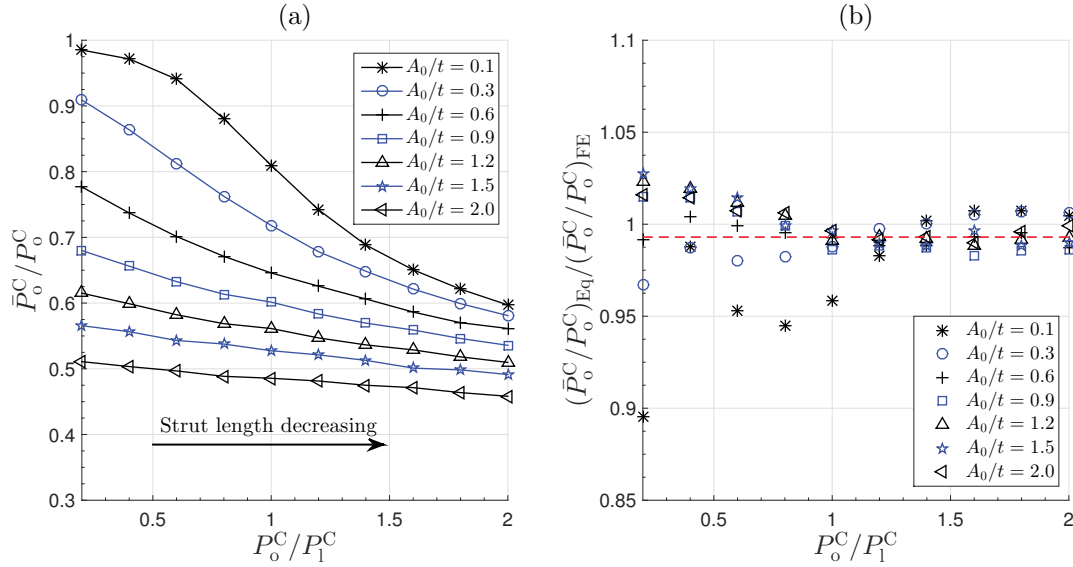


Figure 8.17: (a) Relationship of the normalized reduced global buckling load \bar{P}_0^C/P_0^C versus P_0^C/P_1^C at different imperfection amplitude levels. (b) Ratio of the normalized reduced global buckling load of struts with different imperfection sizes from FE results and Eq. (8.5); the dashed line represents the average with the value being 0.993.

where C_1 , C_2 and C_3 are imperfection size related parameters, thus:

$$C_1 = 4.67 - 4(A_0/t)^{0.05}, \quad C_2 = 0.15 - 0.24(A_0/t)^{-0.3}, \quad C_3 = 5.02 - 4.8(A_0/t)^{0.03}. \quad (8.6)$$

As shown in Figures 8.16(a) and (b), the average ratios of Eq. (8.5) to the FE results for struts with different geometric properties are 0.998 and 1.000 respectively, and the COVs are 1.20% and 0.46% respectively. As for imperfection size effects, as shown in Figure 8.17(b), the average ratio is 0.993 and the COV is 1.71%. It implies that Eq. (8.5) provides excellent agreement with FE models for the reduced global buckling load of thin-walled RHS struts with different geometric properties and imperfection sizes.

8.6 Concluding remarks

The behaviour of thin-walled RHS struts with tolerance level imperfections was investigated using GNIA based on the FE model developed in Chapter 3 alongside findings from the

variational model in Chapter 7. Focus has been on the effect of local imperfection profiles on the ultimate load and equilibrium behaviour.

A unified local imperfection measurement based on equal local bending energy has been proposed. An algorithm for determining the most severe local imperfection profile is proposed. A function to terminate the nonlinear analysis automatically once certain failure criteria is developed within MATLAB, which greatly improves the computational efficiency. Within the automated computational framework, the most severe local imperfection profiles for struts with different lengths have been determined. The study revealed that the ultimate load is principally affected by the imperfection in the more compressed web. The wavelength of the most severe periodic local imperfection was found to be smaller than that of the purely local buckling mode or the local–global interactive post-buckling mode for the perfect case, which implies that the lowest local buckling mode from linear buckling analysis does not necessarily represent the most severe local imperfection profile. Introducing a modulated amplitude in the local imperfection profile leads to a further decrease in the ultimate load. However, struts with highly localized local imperfection profiles exhibit a relatively stiffer response, thus leading to a higher ultimate load. Moreover, it was revealed that under the constraint of the manufacturing imperfection tolerance level, the most severe imperfection profile can be safely approximated using the case with doubly-symmetric cross-section initial deformation and periodic longitudinal components. An equation to approximate the corresponding wavelength has been proposed based on the results of the parametric study.

As for the equilibrium behaviour, the example struts with doubly-symmetric cross-section local imperfections with a tolerance level amplitude exhibit approximately neutral or weakly stable responses after the local–global mode interaction is triggered. This is different from the perfect case, where there are four representative length-related ranges that exhibit distinct interactive post-buckling responses. Although the mono-symmetric cross-section imperfection profile breaks the symmetry of the strut deformation at the beginning,

the equilibrium path converges to the doubly-symmetric case when the global mode is fully developed. An explicit equation to predict the global buckling load of thin-walled RHS struts with tolerance level doubly-symmetric cross-section imperfections has been proposed and shows excellent agreement with the FE results for different plate width to thickness ratios, cross-section aspect ratios and imperfection size levels.

Hitherto, the behaviour of perfect and imperfect purely elastic RHS struts have been investigated. In the next chapter, the effect of material nonlinearity on the behaviour of RHS struts susceptible to local–global mode interaction is investigated. Moreover, a systematic and extensive parametric study on geometric properties, material yielding stress levels, and residual stresses is conducted to understand the behaviour of RHS struts in practical scenarios.

Chapter 9

Parametric study

The previous chapters introduced a series of variational models and identified unstable interactive post-buckling behaviour, length effects and imperfection sensitivity of thin-walled rectangular hollow section struts susceptible to mode interaction. In the current chapter, systematic parametric studies on geometric properties (cross-section aspect ratio and plate width–thickness ratio), material yielding stress levels, imperfections (geometric imperfections and residual stresses) are conducted using the validated FE models in Chapter 3. Moreover, the numerical results are compared with the current design guidelines. Recommendations on the designing of such specimen are provided at the end.

9.1 Algorithm for Automated GMNIA

In the current chapter, a multitude of nonlinear analyses are required so as to understand the effects of different parameters on the interactive buckling behaviour of RHS struts. Processing so many nonlinear FE models is time-consuming and the volume of data generated can be very large. Moreover, the traditional nonlinear analysis procedure requires Linear Buckling Analysis (LBA) to acquire the geometric perturbation or imperfection

profile into the model for nonlinear analysis. The computational burden is therefore quite high, particularly for short columns with high P_o^C/P_1^C ratios, where a large number of unrelated eigenmodes would be produced simultaneously in order to obtain the global buckling mode. A post-processing script would have to be written to distinguish the desired eigenmode automatically. The whole process would have been quite cumbersome.

Therefore, based on the findings in preceding chapters, an algorithm to automate the Geometric and Material Nonlinear Analysis with Imperfection (GMNIA) is proposed, as presented in Figure 9.1. Since the global and local buckling modes for struts with different geometric properties have been defined using Eq. (4.1) and Eqs. (C.2)–(C.3) and (C.21) respectively, which showed good comparisons with that from LBA, the nonlinear FE model for struts with predefined geometric imperfections is developed directly based on these analytical expressions and thus the nonlinear analysis can be conducted directly without LBA. Moreover, the function developed in Chapter 8, as shown in Figure 8.3, is adopted to terminate the nonlinear analysis automatically once a certain failure criterion is met. Moreover, the post-processing is conducted immediately afterwards to extract the ultimate load and the equilibrium path (if required) using a Python script generated together with the model input file. After that, the capacious output database (.odb) file, which stores all details of model information and analysis results, is deleted to save memory storage since they are no longer used. The automated GMNIA process makes it possible to conduct a systematic and extensive parametric study.

9.2 Geometric parameter

In preceding chapters, the cross-section geometry of the example struts remains constant in most cases and the principal varying parameter is the strut length. In this section, the effects of plate width–thickness ratio and cross-section aspect ratio on the profile of the Van der Neut-type curve are investigated.

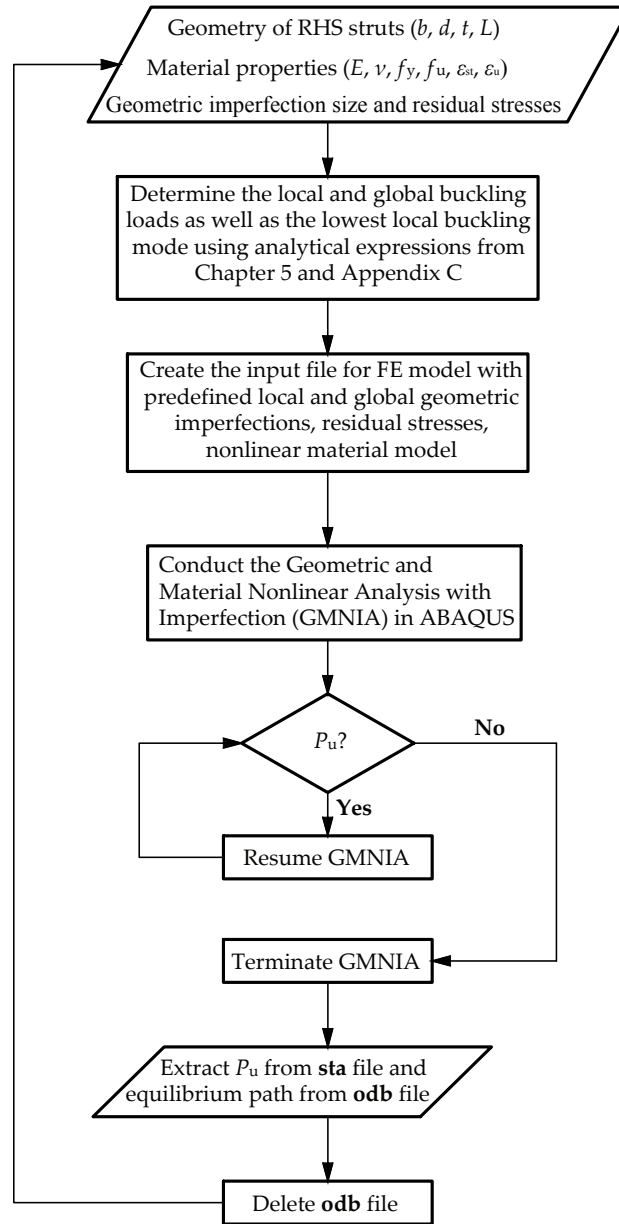


Figure 9.1: Algorithm for automated GMNIA for RHS struts. Codes were developed in MATLAB to achieve the entire process.

9.2.1 Plate width–thickness ratio

The flange width and web depth are fixed as presented in Table 4.1. The principally varying parameter is the plate thickness. The Van der Neut type curves of perfect RHS struts and struts with tolerance level geometric imperfections with different plate width–thickness ratios are shown in Figure 9.2. For both perfect and imperfect cases, the effect

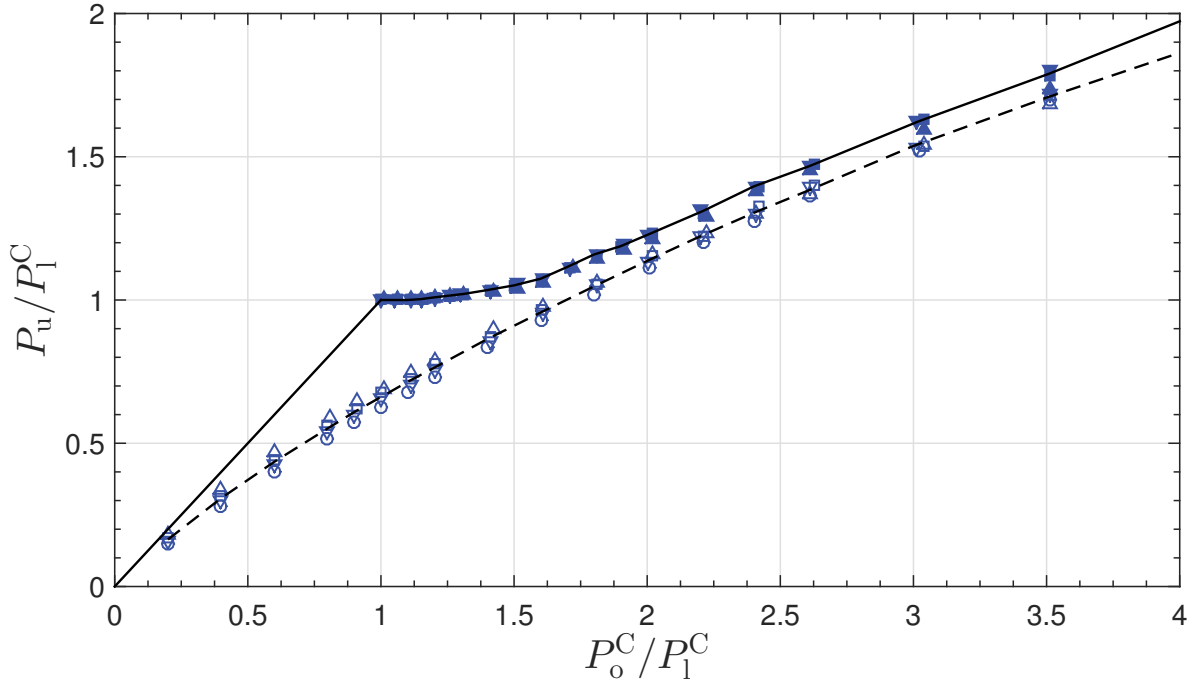


Figure 9.2: The effect of plate width–thickness ratio on the Van der Neut type curve for perfect rectangular hollow section struts and struts with tolerance level imperfections. Solid and hollow symbols represent the ultimate load of perfect struts and struts with tolerance level imperfections respectively. Solid and dashed lines represent the average ultimate load of perfect and imperfect struts with different d/t ratios. Symbols \circ , ∇ , \square and \triangle represent the web depth–thickness ratio being 120, 80, 60 and 40 respectively. Note that the width depth and flange width are fixed being 120 mm and 60 mm respectively.

of web depth–thickness ratios on the curve is small. Specifically, the COVs with respect to the corresponding average value ranges from 0.13% to 1.76% for the perfect and 0.68% to 3.82% imperfect cases respectively.

Specifically, for the perfect case, with the decrease of plate width–thickness ratio, the normalized ultimate load P_u/P_1^C decreases. The effect is very small in zones 2 and 3 and the difference increases with increasing P_o^C/P_1^C . As for the zonal boundary between zones 2 and 3, the differences are negligible. For illustration purposes, a simplified model presented in Figure 6.20, where the corners of the four plates are pin connected, is adopted. Figure 9.3(a) presents the effect of plate width–thickness ratio on the zonal boundary of such strut using Eq. (B.8) based on the double modulus theory. It can be seen that the effect of d/t on the zonal boundary is tiny. Moreover, it should be stressed that there is

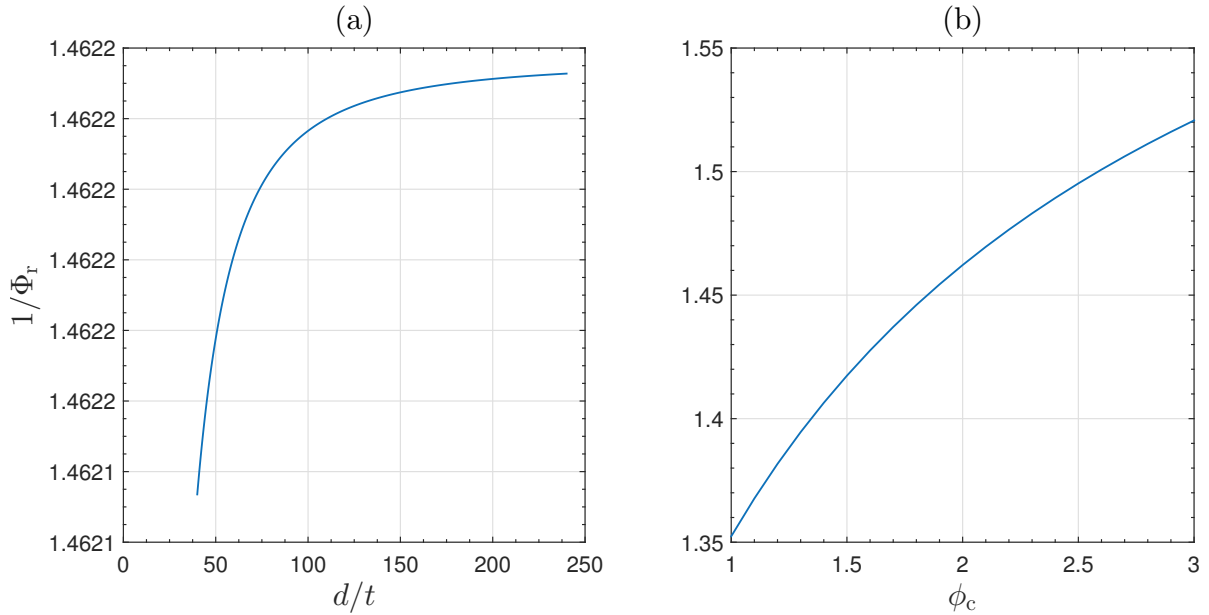


Figure 9.3: Effect of the cross-section aspect ratio and web depth–thickness ratio on the zonal boundary of zones 2 and 3 for rectangular hollow section struts with pinned corners. Note that web depth and flange width are 120 mm and 60 mm respectively in (a); the web depth and plate thickness are 120 mm and 1 mm respectively in (b). The stiffness reduction factor in the more compressed web is 0.408.

stiffness re-distribution in the rigid joint case, which may further alleviate the difference.

For the case with tolerance level imperfections, the trend seems to be to the contrary of that for the perfect case, particularly in the range where global buckling is critical. This may be attributed to the fact that the effect of the local imperfection on the ultimate load is essentially governed by the dimensionless parameter A_0/t (Supple, 1970; Little, 1980). However, in the current study, the amplitude of the tolerance level local imperfections is set to $d/200$. Therefore, A_0/t for sections with larger d/t is relatively higher and the corresponding erosion on the ultimate load would be more significant. Moreover, as demonstrated in Chapter 7, the effect of local imperfections is more significant in the range where global buckling is critical. This may explain why the trend is to the contrary of the range where global buckling is critical and becomes similar to that of the perfect case when P_0^C/P_1^C becomes large.

9.2.2 Cross-section aspect ratio

The parametric study on the cross-section aspect ratio is based on parametric study on the plate width–thickness ratio in the preceding subsection. The plate thickness and web depth are fixed to 1 mm and 120 mm respectively. The cross-section aspect ratio varies from 1 to 2.5. As shown in Figure 9.4, the change in the cross-section aspect ratios also has a small effect on the Van der Neut type curves for both perfect and imperfect struts. Specifically, the COVs for the ultimate load with respect to the average values within the

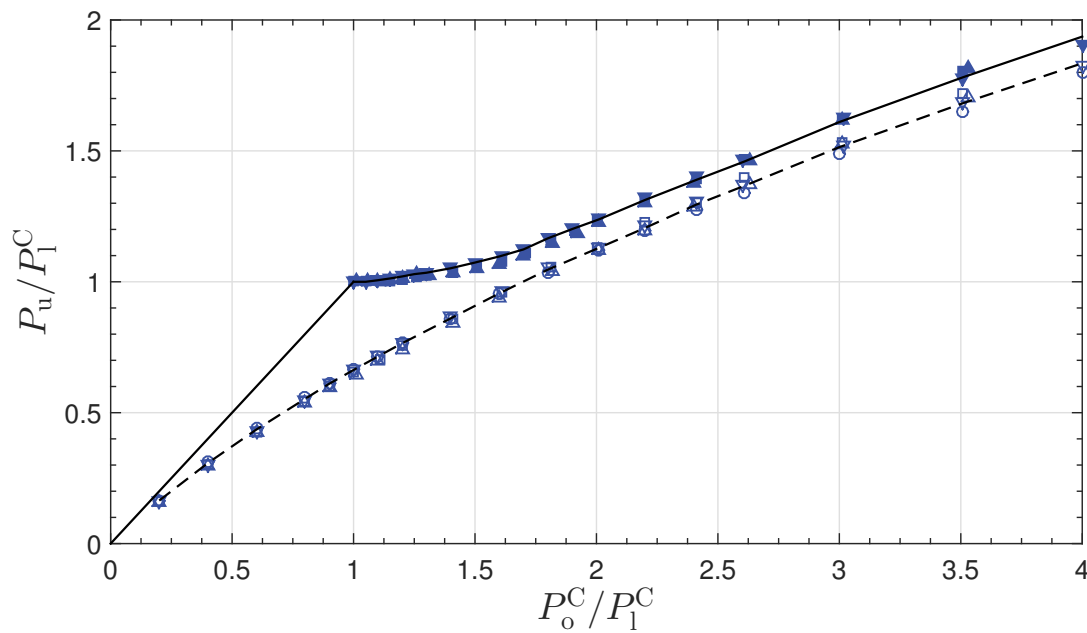


Figure 9.4: The effect of cross-section aspect ratio on the Van der Neut type curve. Solid and hollow symbols represent the ultimate load of perfect struts and struts with tolerance level geometric imperfections respectively. Symbols \circ , ∇ , \square and \triangle represent the cross-sections with aspect ratio being 1, 1.5, 2, and 2.5 respectively. The solid and dashed lines represent the average ultimate load of perfect and imperfect cases with different cross-section aspect ratios.

ranges shown are from 0.5% to 2.53% for the perfect struts and from 0.81% to 2.41% for the struts with tolerance level imperfections.

However, it should be noted that the zonal boundary value of P_o^C / P_1^C for zones 2 and 3 for the perfect struts increases with the increasing cross-section aspect ratio d/b . For illustration purposes, the simplified RHS strut model with the corners of four plates being

pin connected is adopted once again. As shown in Figure 9.3(b), with the increase of the cross-section aspect ratio for the pinned connection case, the value of P_o^C/P_1^C at the zonal boundary increases. It should be noted again that there is stiffness redistribution in the rigid connection case, which may alleviate the difference, but the simplified model can generally describe the trend.

From the parametric study on the plate width–thickness ratio and cross-section aspect ratio, it can be seen that the effects of these two parameters on the Van der Neut-type curve are minor, at least for the purely elastic case. It provides support to the Direct Strength Method (DSM) for the ultimate load prediction of RHS struts exhibiting mode interaction where the effects of cross-section geometry are excluded.

9.3 Material properties

In the current section, the effects of the yielding stress level on the profile of Van der Neut type curve and imperfection sensitivity as well as the effect of material strain-hardening on the ultimate load is investigated.

9.3.1 Yielding stress levels

Effect on the Van der Neut-type curve profile

The principally varying parameter in the study is the yielding stress level. As shown in Figure 9.5, the normalized ultimate load P_u/P_1^C decreases with the decreasing yielding stress levels. The ultimate load drop is not significant in the range where global buckling is critical but it becomes increasingly significant with the increase of P_o^C/P_1^C in the range where local buckling is critical. This finding is in accord with the previous study on the effect of yielding stress level on the Van der Neut model (Becque, 2014).

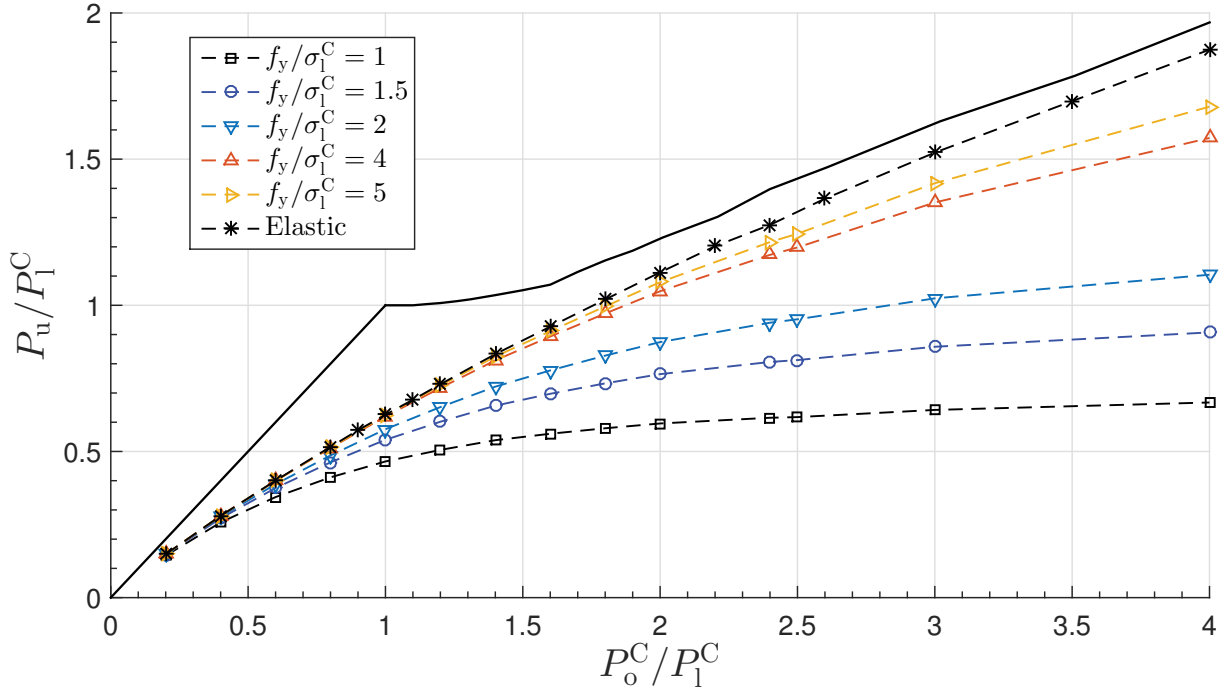


Figure 9.5: The effect of yielding stress levels on the Van der Neut-type curve of strut with tolerance level geometric imperfections. The solid line represents the ultimate load of elastic and perfect RHS struts. Note that the cross-section properties of the struts are presented in Table 4.1.

Effect on the strut imperfection sensitivity

An imperfection sensitivity study is conducted on the four characteristic length struts, as presented in Table 6.1, at different material yielding stress levels. In particular, four typical yielding stress levels are selected, *i.e.* $f_y/\sigma_1^C = \{1, 1.5, 2, 4\}$ and the corresponding normalized local slenderness $\bar{\lambda}_p = \sqrt{f_y/\sigma_1^C} = \{1, 1.225, 1.414, 2\}$ respectively (Trahair *et al.*, 2007). Moreover, four different imperfection cases are investigated:

1. local imperfection $A_0 = 0$, but global imperfection $q_{s0} \neq 0$ to investigate the sensitivity to global imperfections;
2. $A_0 \neq 0$, but $q_{s0} = 0$ to investigate the sensitivity to local imperfections;
3. $A_0 \neq 0$ and $q_{s0} \neq 0$ to investigate the sensitivity to combined imperfections. In particular, the combined imperfections are proportional to the tolerance level local and

global imperfections recommended in EC3, *i.e.* $\mathbf{W}_{\varepsilon_0} = \bar{W}_{\varepsilon_0}\{q_{s0,tol}L, A_{0,tol}\}$, where \bar{W}_{ε_0} is a non-dimensional scaling factor, $q_{s0,tol} = 1/1000$ and $A_{0,tol}/d = 1/200$.

4. $q_{s0} = 10^{-3}$ and $A_0 \neq 0$ to investigate the local imperfection sensitivity of struts with a tolerance level global imperfection.

For case 1, as shown in Figure 9.6(a), the global imperfection sensitivity of all struts increases with the decreasing $\bar{\lambda}_p$. In order to describe the imperfection sensitivity better, as

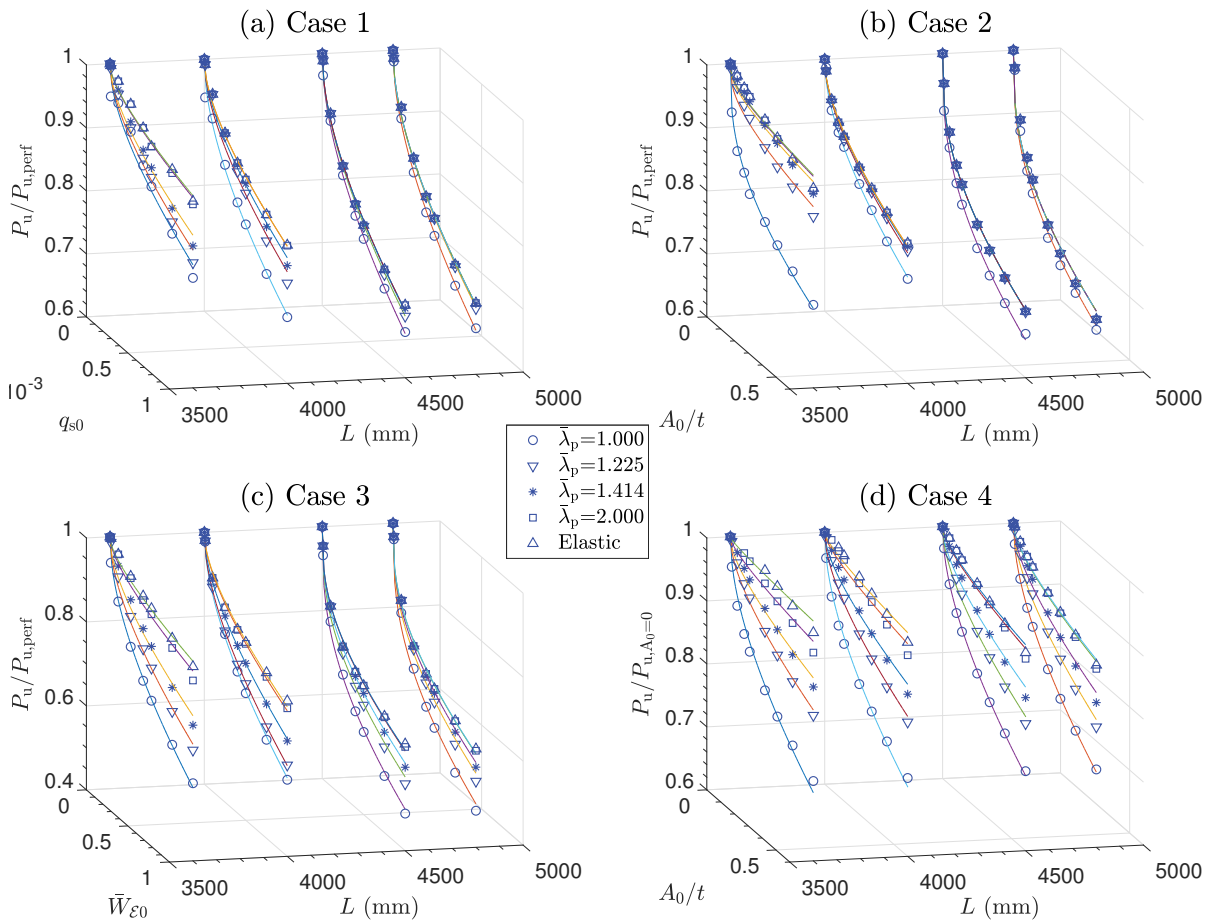


Figure 9.6: Imperfection sensitivity of four characteristic length struts to geometric imperfections at different cross-sectional local slenderness $\bar{\lambda}_p$ levels. Also shown are the fitted imperfection sensitivity curves, the details of which may be found in Table 9.1. Each family of curves represent zones 1 to 4 in sequence from right to left.

well as understanding the underlying mechanism, curves are fitted based on the numerical

results with the following function:

$$p_{u,\epsilon_0} = 1 - a_{\epsilon_0} (\epsilon_0)^{b_{\epsilon_0}}, \quad (9.1)$$

where p_{u,ϵ_0} is the normalized ultimate load of imperfect struts with respect to that of the perfect struts or struts without certain types of imperfection; ϵ_0 is the normalized imperfection, which is, for example, q_{s0} for case 1; a_{ϵ_0} and b_{ϵ_0} are constants determined using the least squares method. As presented in Table 9.1, the sensitivity to purely global imperfections indicates approximately a 1/2 power law relationship to leading order for all four characteristic length struts at different cross-sectional local slendernesses, which is in accord with the finding in (Shen & Wadee, 2018a) for the purely elastic system. At the same cross-sectional local slenderness level, struts in zones 3 and 4 exhibit less imperfection sensitivity compared to struts in zones 1 and 2. However, the imperfection sensitivity for struts in zones 3 and 4 is quite dependent on cross-sectional local slenderness levels. For instance, the imperfection sensitivity constant a_{ϵ_0} at $\bar{\lambda}_p = 1$ is approximately double of that at $\bar{\lambda}_p = 2$. On the contrary, the effects of $\bar{\lambda}_p$ on the imperfection sensitivity for struts in zones 1 and 2 are relatively small. Specifically, for the example struts in zones 1 and 2, the nonlinear behaviour is almost identical for $\bar{\lambda}_p = 2$ and the purely elastic cases. It implies that the strut failure in such cases is governed by stiffness loss due to instability rather than material failure. Moreover, the example strut in zone 2 also shows a relatively higher sensitivity to imperfections than struts in other zones owing to the severely unstable post-buckling behaviour that is intrinsic in such struts (Shen & Wadee, 2018b).

As for the sensitivity to purely local imperfections (case 2), as shown in Figure 9.6(b), similar trends are observed as that for the purely global imperfection case (case 1). The fitted imperfection sensitivity curves show a 1/3 power law relationship, as presented in Table 9.1. In particular, the short length strut in zone 4 exhibits mild imperfection sensitivity in the range where $\bar{\lambda}_p \geq 1.414$. This kind of imperfection sensitivity behaviour is most desirable for structural applications according to Chilver's stability design concept

Table 9.1: Constants for the fitted imperfection sensitivity curves and their comparison with FE results for four characteristic struts. Note that an average below unity represents a safe estimation by the fitted curve.

Imperfection type	$\bar{\lambda}_p$	$L = 3600$ mm (zone 4)		$L = 4000$ mm (zone 3)		$L = 4500$ mm (zone 2)		$L = 4800$ mm (zone 1)	
		$a_{\epsilon 0}$	$b_{\epsilon 0}$	$a_{\epsilon 0}$	$b_{\epsilon 0}$	$a_{\epsilon 0}$	$b_{\epsilon 0}$	$a_{\epsilon 0}$	$b_{\epsilon 0}$
Case 1: pure global imperfection	1	6.469		9.211		10.435		10.431	
	1.225	5.732		7.051		9.558		9.275	
	1.414	4.982	1/2	6.343	1/2	9.343	1/2	9.162	1/2
	2	3.102		5.768		9.284		9.151	
	Elastic	2.999		5.761		9.284		9.151	
$p_{u,Eq}/p_{u,FE}$	Average	0.997		0.998		0.998		0.997	
	COV	1.36%		1.15%		0.87%		0.81%	
Case 2: pure local imperfection	1	0.325		0.246		0.403		0.383	
	1.225	0.133		0.206		0.347		0.355	
	1.414	0.086	1/3	0.199	1/3	0.347	1/3	0.355	1/3
	2	0.076		0.196		0.347		0.355	
	Elastic	0.073		0.195		0.347		0.355	
$p_{u,Eq}/p_{u,FE}$	Average	0.995		0.993		0.998		0.995	
	COV	1.02%		1.31%		1.12%		2.29%	
Case 3: combined imperfection	1	0.425		0.413		0.501		0.496	
	1.225	0.322		0.384		0.424		0.424	
	1.414	0.254	1/2	0.320	1/2	0.391	1/3	0.398	1/3
	2	0.148		0.254		0.363		0.377	
	Elastic	0.124		0.244		0.360		0.376	
$p_{u,Eq}/p_{u,FE}$	Average	0.997		0.999		0.997		0.995	
	COV	1.47%		1.04%		1.95%		2.66%	
Case 4: $q_{s0} = 10^{-3}$, varying A_0	1	0.377		0.374		0.363		0.362	
	1.225	0.207		0.230		0.241		0.255	
	1.414	0.141	1/2	0.164	1/2	0.181	1/2	0.199	1/2
	2	0.067		0.081		0.102		0.135	
	Elastic	0.025		0.058		0.094		0.131	
$p_{u,Eq}/p_{u,FE}$	Average	0.996		0.996		0.995		0.996	
	COV	1.03%		0.91%		0.84%		0.73%	

(Chilver, 1976). However, when $\bar{\lambda}_p$ becomes close to unity, the strut becomes increasingly sensitive to imperfections owing to the interaction of material yielding and local buckling. Moreover, it should be noted that for the example struts in zones 1 and 2, the imperfection sensitivity relationship is almost identical compared to the purely elastic cases when $\bar{\lambda}_p > 1.225$. This bound is much smaller than that for case 1. This is reasonable since the local imperfection has a direct and immediate destabilization effect on the strut stiffness

in zones 1 and 2, which facilitates the stiffness-governed failure mode.

Figure 9.6(c) presents the sensitivity of struts to the combined imperfections (case 3). It also reveals that the sensitivity increases with the decrease of $\bar{\lambda}_p$ and the effect is most significant in the example strut that lies in zone 4. The fitted imperfection sensitivity curves exhibit a 1/2 power law for example struts in zones 3 and 4 and a 1/3 power law for struts in zones 1 and 2, as presented in Table 9.1. It implies that the struts in zones 3 and 4 are more sensitive to global imperfections and those in zones 1 and 2 are more sensitive to local imperfections. This finding is also in accord with the finding for purely elastic struts with tolerance level imperfections (Shen & Wadee, 2018a). Moreover, unlike the previous two cases, the struts in zones 1 and 2 become sensitive to the cross-sectional local slenderness, *i.e.* a gradual increase in the imperfection sensitivity is observed with the decrease of $\bar{\lambda}_p$.

The effects of cross-sectional local slenderness on the imperfection sensitivity in case 4 are presented in Figure 9.6(d). The fitted imperfection sensitivity curves exhibit a 1/2 power law relationship for all example struts, as presented in Table 9.1. Relatively mild imperfection sensitivity is observed in the example struts in zones 2, 3 and 4 in the purely elastic case, but the severity of imperfection sensitivity increases dramatically with the decrease of $\bar{\lambda}_p$. For the example strut in zone 4, the trend is the same as that in case 2. However, for the example struts in zones 2 and 3, the results are very different from any previous case. Moreover, an increasing sensitivity to the yielding stress level is also observed in the example strut in zone 1. All these findings imply that material yielding may be the governing failure mechanism in the current case for all four example struts. This is reasonable owing to the following facts: (1) the relatively large initial global imperfection would lead to a relatively large degree of bending in the strut; (2) as found in (Shen & Wadee, 2018c), the introduced local imperfection further undermines the effective axial stiffness of the cross-section, thus leading to increased global deflection. The latter may also explain why the imperfection sensitivity curves satisfy a 1/2 power law, the same as

for the purely global imperfection case.

Effect on equilibrium paths

Since Degée *et al.* (Degée *et al.*, 2008) suggested that the equivalent geometric imperfection combination for struts, where the residual stresses are not explicitly modelled, is $q_{s0} = 1/1000$ and $A_0/d = 200$, this particular combination is now adopted. As shown in Figure 9.7, all four example struts exhibit highly unstable behaviour after the ultimate load

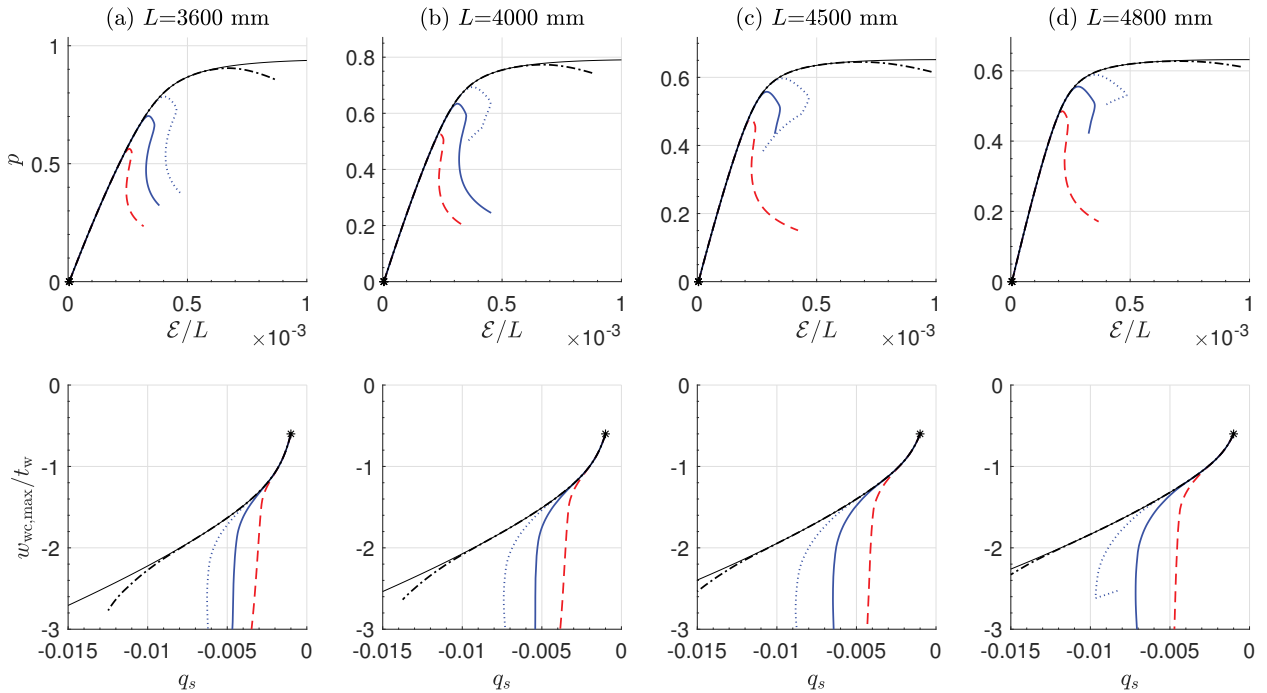


Figure 9.7: Equilibrium paths of four characteristic length struts with purely geometric imperfections with $q_{s0} = 1/1000$ and $A_0/d = 1/200$ at different $\bar{\lambda}_p$ levels. Dashed, solid, dotted and dot-dashed lines represent $\bar{\lambda}_p = 1, 1.225, 1.414,$ and 2 respectively; the outer thin dark solid line represents the purely elastic case. Graphs of normalized load ratio $p = P/P^C$ versus normalized end-shortening \mathcal{E}/L in the first row; the second row shows the normalized maximum amplitude of local deflection in the more compressed web $w_{wc,max}/t_w$ versus the normalized global amplitude q_s . Note that the point where loading commences is marked by ‘*’.

point when $\bar{\lambda}_p = 1$ due to the coupling of plate local buckling and material yielding. The severity of unstable behaviour is mollified with the increase of $\bar{\lambda}_p$. It may help explain the reason why the imperfection sensitivity of struts decreases with the increase of $\bar{\lambda}_p$. For the

practically significant range, *i.e.* the serviceability limit $|q_s| < 0.01$, $\bar{\lambda}_p = 2$ can be treated to be the same as the purely elastic case, particularly for the long length and transitional length struts. Moreover, from the $w_{wc,max}/t_w - q_s$ relationship, it can be determined that the final failure mechanism is due to the localized failure of the more compressed web at mid-span.

In order to understand the failure mechanism better, a simply-supported plate with the same geometric and material properties as well as initial geometric imperfections as the more compressed web is selected for illustration purposes. Figure 9.8 presents the relationship between the normalized axial tangent stiffness of the plate and the normalized axial load level. For the case where $\bar{\lambda}_p$ is small, the tangent stiffness decreases dramatically

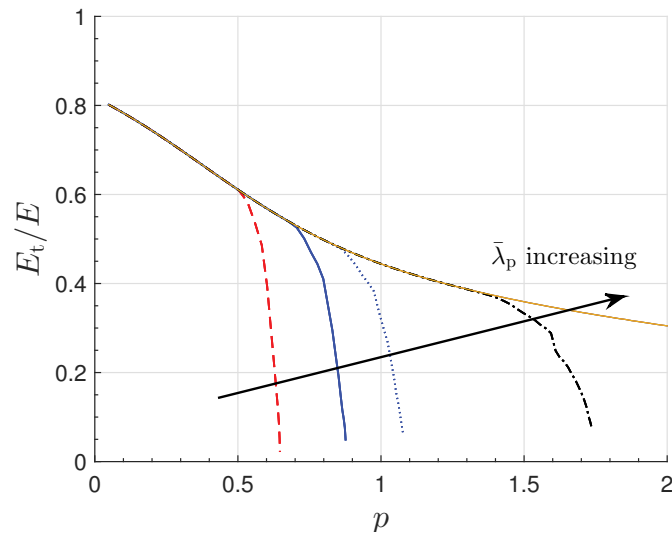


Figure 9.8: Axial tangent modulus of a simply-supported plate with $d = 120$ mm, $t = 1$ mm and initial imperfection size $A_0 = d/200$ with increasing axial load level. Line types in the graphs correspond to the same cases as described in Figure 9.7.

with a tiny increase of the axial load after the first yield. This is quite similar to the stiffness drop in the more compressed web owing to the local buckling in perfect struts in Chapter 6, which leads to highly unstable post-buckling behaviour after the secondary bifurcation point and a commensurate high degree of sensitivity to imperfections. It can explain the highly unstable behaviour of struts with relatively small $\bar{\lambda}_p$. With the increase of $\bar{\lambda}_p$, this severity is mollified. Specifically, for the case $\bar{\lambda}_p = 2$, the decrease in E_t/E is

accompanied by an obvious increase in p . This can, in turn, explain the mildly unstable behaviour of struts with $\bar{\lambda}_p = 2$. However, it should be noted that the actual boundary condition of the more compressed web is not simply-supported. A study on the effect of rotational restraints from both flanges, which may quantify the tangent axial stiffness change in the more compressed web, is left for future study.

9.3.2 Effect of material strain-hardening

Three different material models are adopted to investigate the effects of strain-hardening with the parameters shown in Table 9.2. Type 1 corresponds to an elastic–perfectly plastic

Table 9.2: Parameters for different elastic–plastic material models. Note that the definitions of the parameters n and E_h can be found in Figure 3.6.

Type	n	E_h/E	σ_u/f_y	Note
1	0	0	1	Elastic–perfectly plastic
2	0	1/50	1.2	Elastic–linear strain-hardening
3	9	1/50	1.2	Elastic–linear strain-hardening with plastic flow

model, where there is no strain–hardening. Type 2 corresponds to the elastic–linear strain-hardening model but there is no plastic flow. The material model represented by type 3 is more realistic particularly for carbon steel (Sadowski *et al.*, 2017b; Yun & Gardner, 2017), where there is a yield plateau before the linear strain-hardening. In particular, for types 2 and 3, the same strain-hardening modulus $E_h = 1/50$ is adopted. Moreover, the strain at the beginning of strain-hardening $(1 + n)\epsilon_y$ is taken to be $10\epsilon_y$. These values are chosen based on the material model for hot-rolled steel recommended by ECCS (1984).

Figure 9.9 presents the effect of material strain-hardening on the ultimate load for the four characteristic length struts with tolerance level combined imperfections. The ultimate load ratios of types 1 and 3 material model are almost the same for all four example struts, which implies that the strain-hardening after the plastic flow has no practical effect on the ultimate load for the current case. For the strain-hardening model without plastic

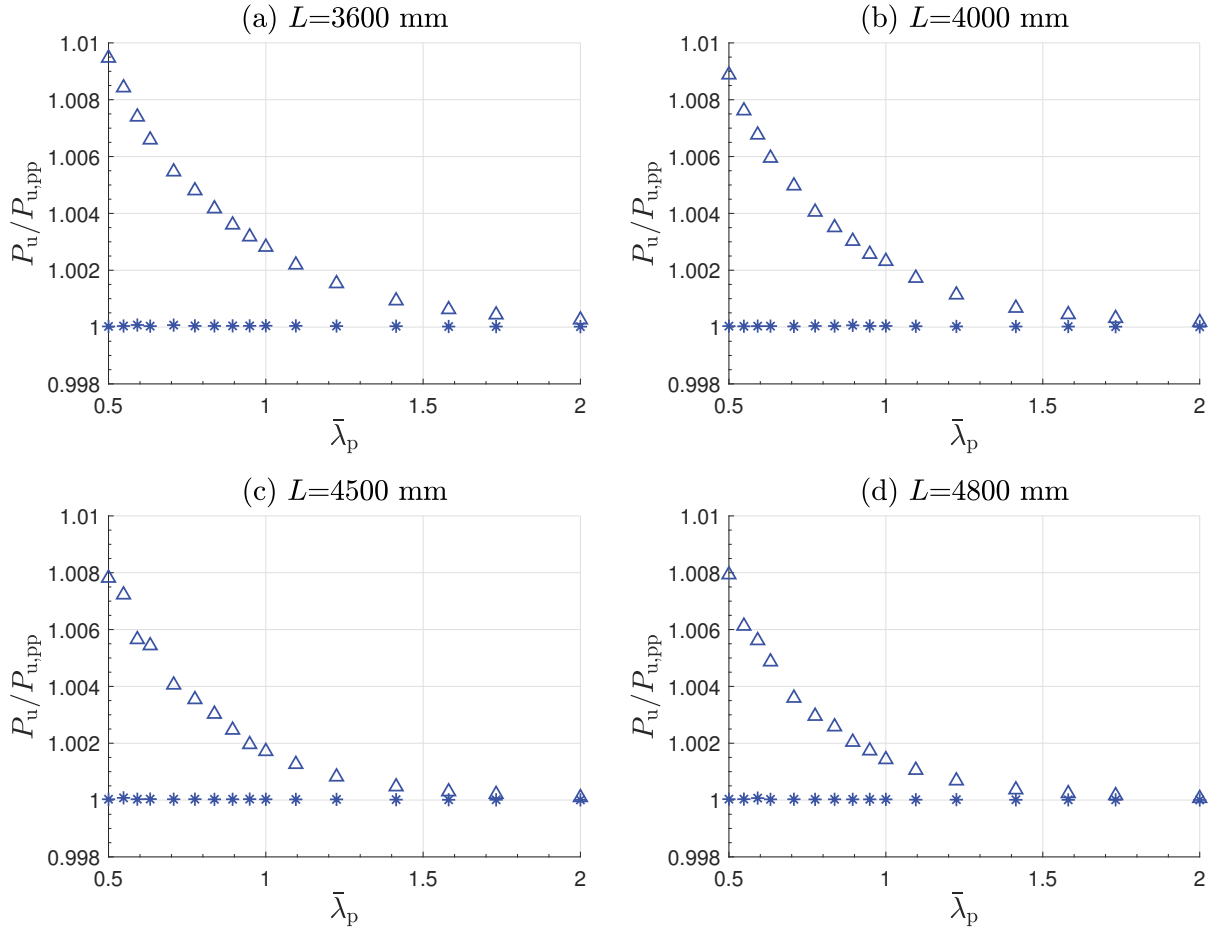


Figure 9.9: Effect of strain-hardening on the ultimate load of struts with tolerance level imperfections at different material yielding stress levels. Symbols \triangle and $*$ represent non-linear material types 2 and 3 in Table 9.2; the ordinate in each graph is normalized with respect to the ultimate load found from type 1, *i.e.* the elastic–perfectly plastic case; the abscissa $\bar{\lambda}_p = \sqrt{f_y/\sigma_1^C}$, where $\sigma_1^C = P_1^C/A_g$ with A_g being the gross cross-sectional area.

flow (type 2), the ultimate load is relatively higher due to the material strain-hardening, but the percentage increase is tiny, *i.e.* less than 1% at $\bar{\lambda}_p = 0.5$. Moreover, it should be noted that the increment in the ultimate load decreases with the increasing cross-sectional slenderness as well as the strut length. Therefore, it may be concluded that the effect of material strain-hardening on the ultimate load is tiny and it can be neglected currently.

9.4 Residual stress

In this section, the effects of residual stresses on the equilibrium path and imperfection sensitivity of struts are investigated. Unlike the stocky welded sections, the compressive residual stresses in slender sections would lead to premature local buckling at a lower external load level. Therefore, the ratio of the compressive residual stress σ_{rc} to the plate local buckling stress σ_1^C versus the plate width–thickness ratio d/t is investigated. By transforming Eq. (3.5), the relationship between the compressive residual stress σ_{rc} and the local buckling stress σ_1^C in the ECCS residual stress distribution model for welded box-section members can be expressed as:

$$\frac{\sigma_{rc}}{\sigma_1^C} = \left(\frac{3d_t}{d - 3d_t} \right) \frac{\sigma_{rt}}{\sigma_1^C} = \frac{3d_t d^2}{(d - 3d_t)t^2} \left[\frac{(1 - \nu^2)\sigma_{rt}}{k_p \pi^2 E} \right]. \quad (9.2)$$

For illustration purposes, the σ_{rc}/σ_1^C – d/t relationship for a heavily welded cross-section with an aspect ratio of 2 is presented in Figure 9.10. As shown in Figure 9.10(a), for a

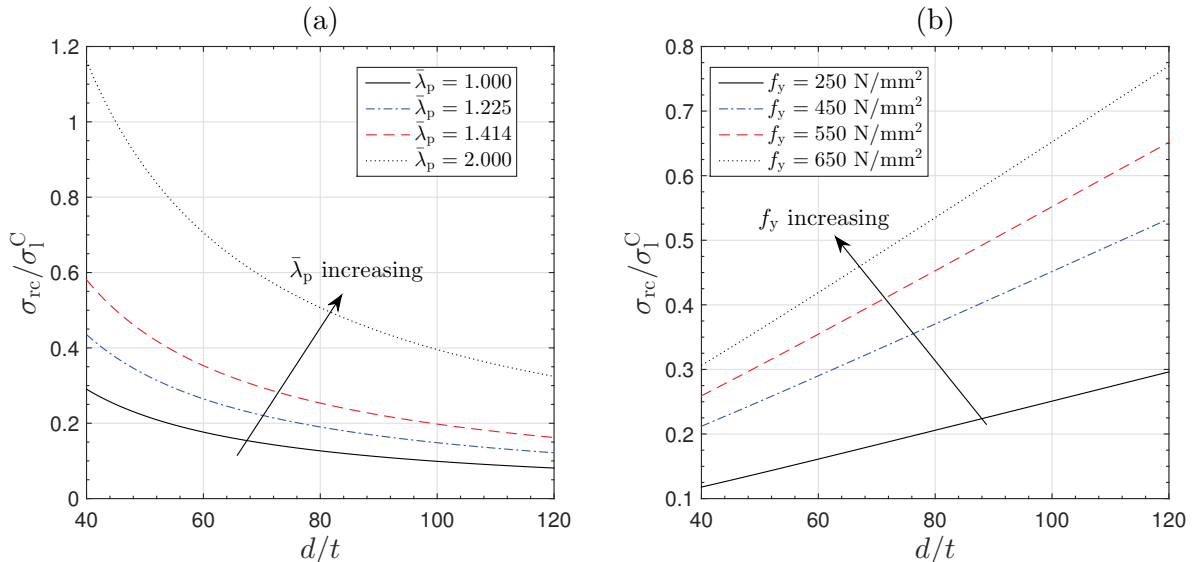


Figure 9.10: Ratio of compressive residual stresses σ_{rc} to local plate buckling stresses σ_1^C versus plate width–thickness ratios d/t in heavily welded box-section members for different (a) cross-sectional local slendernesses and (b) practical yielding stress levels. Note that the buckling coefficient for the local buckling stress is adopted with the cross-section aspect ratio being 2.

fixed value of the normalized local slenderness $\bar{\lambda}_p$, σ_{rc}/σ_1^C decreases with the increase of d/t ; for a fixed value of d/t , σ_{rc}/σ_1^C increases with the increase of $\bar{\lambda}_p$. Figure 9.10(b) presents the σ_{rc}/σ_1^C - d/t relationship at some practical yielding stress levels. It can be seen that σ_{rc}/σ_1^C increases with d/t as well as with increasing yielding stress levels. In particular, for high strength steel components ($f_y \geq 460$ N/mm²), the compressive residual stress in cross-sections with a high d/t ratio is larger than 50% of the local buckling stress.

9.4.1 Effects on imperfection sensitivity

Based on the numerical results, the effects of residual stress on the imperfection sensitivity are now investigated. Emphasis is placed on the local imperfection sensitivity of struts with the normalized global imperfection size q_{s0} being 1/1000, *i.e.* case 4 in §9.3.1. Moreover, the same four characteristic length struts are selected, as presented in Table 6.1. As for the residual stress distribution, the ECCS model is again adopted. Two different cases for the length of the uniform tensile range are considered. The first case, where $d_t = 3t$, corresponds to the ECCS model for heavily welded box-section members. Since the plate width–thickness ratio d/t for the web of the current example strut is 120, σ_{rc}/σ_1^C only varies from 0.081 to 0.324 in the range of $\bar{\lambda}_p = [1, 2]$, as shown in Table 9.3. Therefore, the second case, where $d_t = 6t$, is adopted to understand the effects of residual stresses at high σ_{rc}/σ_1^C levels, which reflects the effects of residual stress in relatively stocky sections.

Table 9.3: Ratio σ_{rc}/σ_1^C for the example struts with the ECCS residual stress distribution model for welded box-section members with two different uniform tensile range lengths at different plate slenderness levels.

$\bar{\lambda}_p$	σ_{rc}/σ_1^C	
	case 1: $d_t = 3t$	case 2: $d_t = 6t$
1	0.081	0.176
1.225	0.122	0.265
1.414	0.162	0.353
2	0.324	0.706

Figure 9.11 presents the sensitivity of four characteristic length struts to local geometric

imperfections for cases 1 and 2. In both cases, the imperfection sensitivity decreases with the increase of $\bar{\lambda}_p$, which is very similar to those cases with no residual stresses, as presented in Figure 9.6(d). Imperfection sensitivity curves are fitted to describe the imperfection sensitivity relationship, which exhibit a 1/2 power law relationship for all example struts, as presented in Table 9.4. This is also the same as for the struts without residual stresses. However, compared with the residual stress-free case, the imperfection sensitivity decreases with the increase of σ_{rc}/σ_1^C . For instance, the parameter a_{e0} of the imperfection sensitivity curve for the long length strut ($L = 4800$ mm) with $\bar{\lambda}_p = 2$ is 0.135 for the residual stress-free case, 0.098 for the case where $d_t = 3t$ and 0.039 for the case where $d_t = 6t$ respectively. Moreover, struts in case 2 with $\bar{\lambda}_p = 2$ exhibit relatively moderate sensitivity to imperfections, as shown in Figure 9.11(b) and Table 9.4.

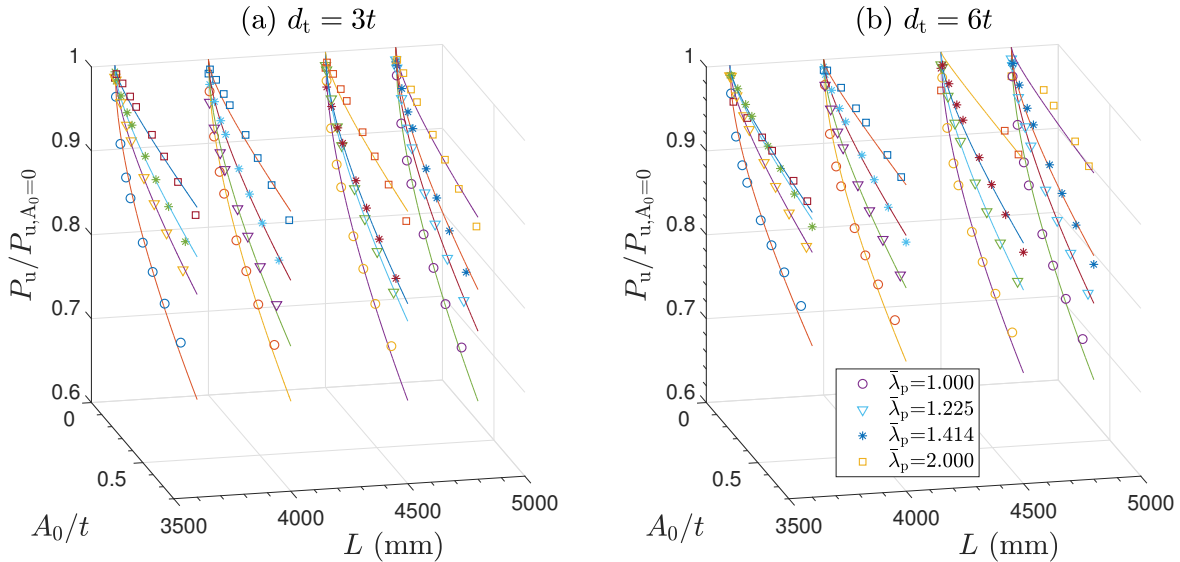


Figure 9.11: Local imperfection sensitivity relationship for four characteristic length struts with residual stresses and the normalized global imperfection amplitude q_{s0} being 1/1000 at different $\bar{\lambda}_p$ levels. Also shown are the fitted imperfection sensitivity curves, the details of which may be found in Table 9.4.

Table 9.4: Constants for the fitted imperfection sensitivity curves Eq. (9.1) and their comparison with FE results for four characteristic struts with ECCS welding residual stress distributions.

Imperfection type	$\bar{\lambda}_p$	$L = 3600$ mm (zone 4)		$L = 4000$ mm (zone 3)		$L = 4500$ mm (zone 2)		$L = 4800$ mm (zone 1)	
		$a_{\epsilon 0}$	$b_{\epsilon 0}$	$a_{\epsilon 0}$	$b_{\epsilon 0}$	$a_{\epsilon 0}$	$b_{\epsilon 0}$	$a_{\epsilon 0}$	$b_{\epsilon 0}$
Case 1: $d_t = 3t$	1	0.317		0.327		0.336		0.343	
	1.225	0.177	1/2	0.254	1/2	0.231	1/2	0.250	1/2
	1.414	0.127		0.166		0.207		0.195	
	2	0.061		0.074		0.084		0.098	
$p_{u,Eq}/p_{u,FE}$	Average	1.000		1.000		1.000		1.000	
	COV	0.91%		1.14%		0.86%		0.77%	
Case 2: $d_t = 6t$	1	0.246		0.274		0.300		0.315	
	1.225	0.121	1/2	0.176	1/2	0.189	1/2	0.213	1/2
	1.414	0.077		0.106		0.127		0.149	
	2	0.068		0.039		0.015		0.039	
$p_{u,Eq}/p_{u,FE}$	Average	1.000		1.000		1.000		1.000	
	COV	1.15%		0.92%		1.40%		1.17%	

9.4.2 Effects on equilibrium paths

In order to understand the underlying mechanism of the effects of residual stress on the imperfection sensitivity better, the effects of residual stresses on the equilibrium paths of struts are investigated. The equilibrium paths for the four characteristic length struts with a global imperfection $q_{s0} = 1/1000$ and a local imperfection $A_0/d = 1/1000$, which are recommended in previous studies (Degée *et al.*, 2008; Pavlovčič *et al.*, 2012) as a reasonable geometric imperfection combination for welded box-section struts with residual stresses being explicitly modelled, are presented in Figures 9.12 and 9.13. The general trends of the equilibrium paths are very similar to those in the residual stress-free case as presented in Figure 9.7. All four characteristic example struts exhibit similar responses, *i.e.* struts with $\bar{\lambda}_p = 2$ exhibit weakly stable behaviour and struts with lower $\bar{\lambda}_p$ values exhibit unstable behaviour after the ultimate load point. However, compared with the residual stress-free case, the severity of the behaviour after the ultimate load point is mollified with the increase of σ_{rc}/σ_1^C . This may help explain the decreasing imperfection sensitivity of struts with increasing σ_{rc}/σ_1^C .

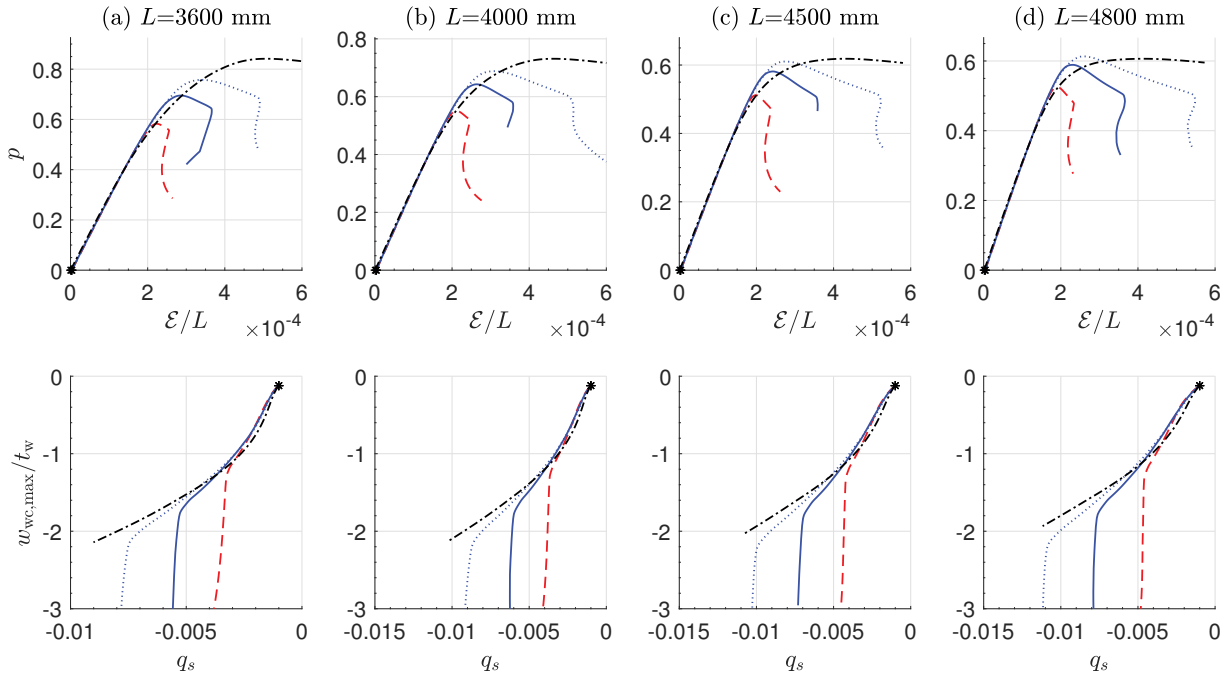


Figure 9.12: Equilibrium paths of four characteristic length struts with the ECCS residual stress distribution for welded box-section members with $d_t = 3t$ at different yielding stress levels. Note that the global and local imperfection sizes are $q_{s0} = 1/1000$ and $A_0/d = 1/1000$ respectively. Graphs (a)–(d) and the line types are the same as described in Figure 9.7, except there is no purely elastic case.

The residual stress also leads to an erosion in the ultimate load, as can be seen from Figure 9.14, which presents the equilibrium paths for intermediate length struts with different yielding stress magnitudes at various cross-section slenderness levels. A summary of the load capacity erosion of the four example struts is presented in Table 9.5. It should be noted that the length effects on the erosion percentage is tiny. Therefore, only the average value and COV are presented. Moreover, struts with a higher σ_{rc}/σ_1^C ratio exhibit stiffness erosion at a relatively lower load level. This is attributed to the fact that the compressive residual stress facilitates premature buckling of the more compressed web at a relatively lower external axial load level, thus leading to the loss of strut stiffness. For illustration purposes, the normalized tangent stiffness E_t/E of a simply-supported plate at different load levels are presented in Figure 9.15. The geometric properties, local imperfection size and the residual stress distributions are the same as for the more compressed web of the short length strut. It can be seen that the compressive residual stresses lead to an erosion

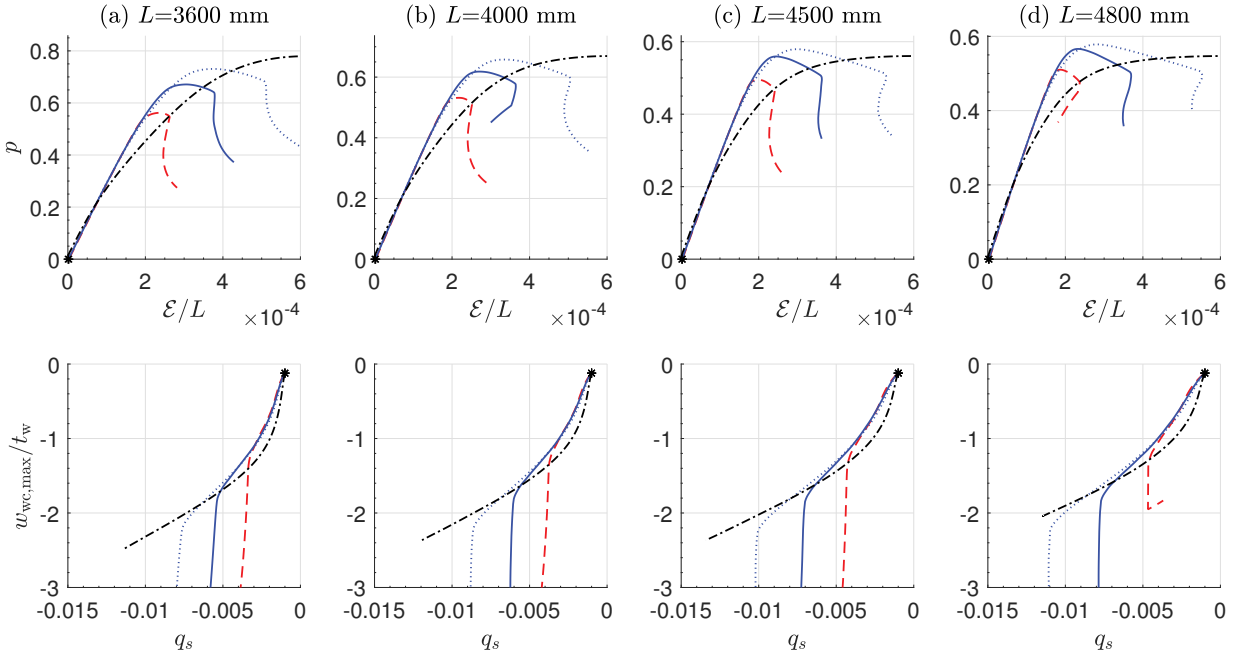


Figure 9.13: Equilibrium paths of four characteristic length struts with the ECCS residual stress distribution for welded box-section members with $d_t = 6t$ at different yielding stress levels. Graphs (a)–(d) and the line types are the same as described in Figure 9.7, except there is no purely elastic case.

in the axial tangent stiffness of the example plate. For the current case, the erosion is most significant in the case with $\bar{\lambda}_p = 2$, where σ_{rc}/σ_1^C is 0.324 and 0.706 for cases 1 ($d_t = 3t$) and 2 ($d_t = 6t$) respectively. Moreover, it should be noted that there is no material yielding in the case with $\bar{\lambda}_p = 2$ before $E_t/E = 0.40$, which is the tangent stiffness value within the initial post-buckling range of a simply-supported plate. The difference in p with respect to the residual stress-free case at the point is equal to the corresponding σ_{rc}/σ_1^C for each case respectively. However, it should be noted that Figure 9.15 is only for qualitative illustration purposes. A more refined model that includes the effects of rotational restraint from both flanges is required to quantify the actual axial tangent stiffness change, but this is left for future study.

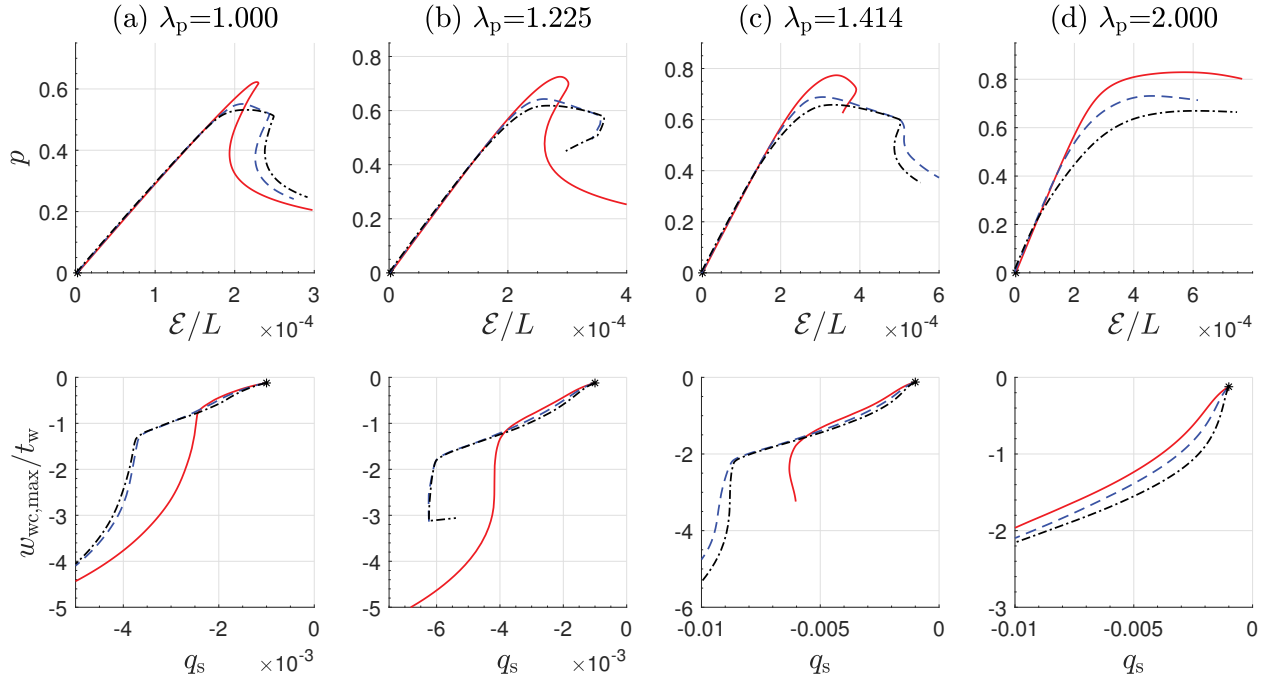


Figure 9.14: Equilibrium paths of the intermediate length strut ($L = 4000$ mm) with no residual stress (solid line), with the ECCS residual stress distribution with $d_t = 3t$ (dashed line) and $6t$ (dot-dashed line). Note that the global and local imperfection sizes are $q_{s0} = 1/1000$ and $A_0/d = 1/1000$ respectively and the point where loading commences is marked by ‘*’.

Table 9.5: Effect of residual stress on the ultimate load of example struts with global imperfection $q_{s0} = 1/1000$ and local imperfection $A_0/d = 1/1000$. Note that $p_{u,case0}$, $p_{u,case1}$ and $p_{u,case2}$ represent the cases with no residual stress, with the ECCS residual stress distribution with $d_t = 3t$ and $6t$ respectively; the ratio σ_{rc}/σ_1^C for each case is presented in Table 9.3.

$\bar{\lambda}_p$	$p_{u,case1}/p_{u,case0}$		$p_{u,case2}/p_{u,case0}$		$p_{u,case2}/p_{u,case1}$	
	Average	COV	Average	COV	Average	COV
1	0.890	0.89%	0.860	1.18%	0.967	0.30%
1.225	0.894	1.55%	0.860	1.46%	0.962	0.12%
1.414	0.897	1.86%	0.855	0.96%	0.953	0.91%
2	0.883	0.75%	0.806	0.49%	0.913	1.22%

9.4.3 Simplified method to determine initial local imperfection amplitude A_0^0

As illustrated in Figure 3.11, the initial imperfection amplitude A_0^0 introduced in the FE model is amplified owing to the compressive residual stresses after the self-equilibrating

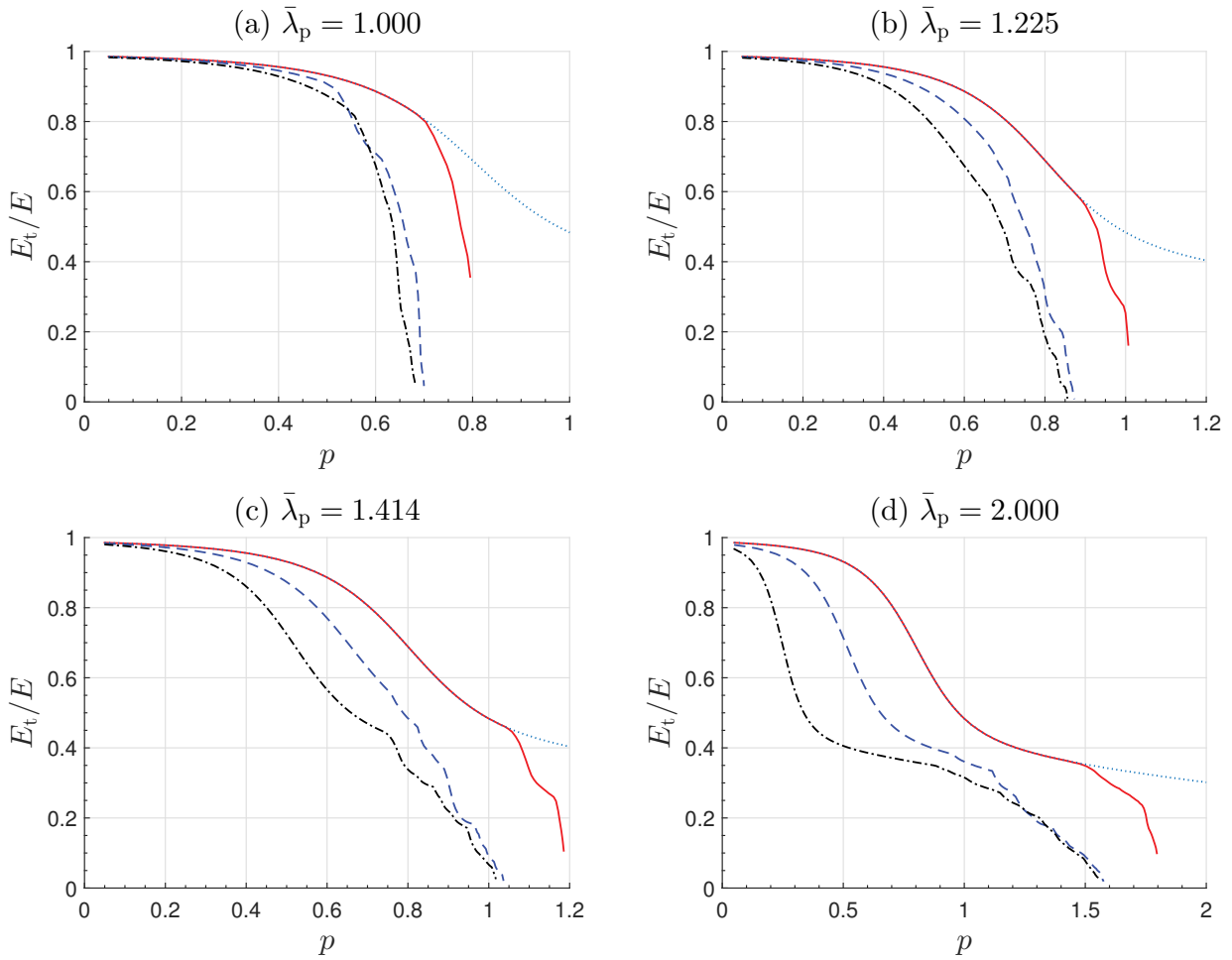


Figure 9.15: Effects of residual stresses on the axial tangent modulus–axial load relationship of a simply-supported plate with $d = 120$ mm and $t = 1$ mm. Note that the initial geometric imperfection size $A_0 = d/1000$. The dotted line represents the purely elastic case with no residual stress; the other line types in the graphs correspond to the same cases as described in Figure 9.14.

step. Since the self-equilibrating step involves geometric nonlinearity, an iterative solution process is required to determine the initial imperfection amplitude A_0^0 , such that A_0 is equal to the desired value after the self-equilibrating step. However, this process is very cumbersome, even though an automated solution searching program has been developed within MATLAB in conjunction with ABAQUS. Currently, an investigation is conducted to understand the amplification of the amplitude at different σ_{rc}/σ_1^C levels and propose a simplified equation to describe the relationship.

The self-equilibrating process is essentially an equilibrium problem of an initially deformed plate under initial residual stresses. From the perspective of linear theory, the total potential energy of an initially deformed plate under pure compression can be expressed as:

$$\begin{aligned}
 V &= U - P\mathcal{E} \\
 &= \frac{D}{2} \int_0^L \int_{-d/2}^{d/2} \left\{ \left[\frac{\partial^2 (w - w_0)}{\partial z^2} + \frac{\partial^2 (w - w_0)}{\partial y^2} \right]^2 - 2(1 - \nu) \left[\frac{\partial^2 (w - w_0)}{\partial z^2} \frac{\partial^2 (w - w_0)}{\partial y^2} \right. \right. \\
 &\quad \left. \left. - \left(\frac{\partial^2 (w - w_0)}{\partial z \partial y} \right)^2 \right] \right\} dy \, dz - \frac{P}{2} \int_0^L \int_{-d/2}^{d/2} \left[\left(\frac{\partial w}{\partial z} \right)^2 - \left(\frac{\partial w_0}{\partial z} \right)^2 \right] dy \, dz,
 \end{aligned} \tag{9.3}$$

where D is the plate flexural rigidity; L and d are length and width of the plate respectively; z and y are the longitudinal and transverse coordinates respectively. By assuming that the total out-of-plane deflection $w = Qf(y)w(z)$ and the initial out-of-plane deflection $w_0 = Q_0f(y)w(z)$, the relationship between Q , Q_0 and P can be obtained by applying the stationary potential energy condition for equilibrium $\partial V/\partial Q = 0$ and can be expressed thus:

$$\frac{Q_0}{Q} = 1 - \frac{P}{P_{\text{cr}}}, \tag{9.4}$$

where P_{cr} is the critical buckling load of the plate. It should be noted that Eq. (9.4) is a general expression that is independent of the selected functions for $f(y)$ and $w(z)$ and its format is practically identical to the load–deflection amplitude relationship for initially imperfect columns (Timoshenko & Gere, 1961). However, since plates have a considerable post-buckling stiffness compared with columns, this expression may only be valid for cases where the deflection and load levels are small, otherwise strain energy contributions from membrane stresses would need to be included.

Figure 9.16 presents the ratio of the initial imperfection amplitude A_0^0 to the imperfection amplitude $A_0 = d/1000$ after the self-equilibrating step at different $\sigma_{\text{rc}}/\sigma_1^{\text{C}}$ levels. The cross-section aspect ratio is fixed to 2 and the web depth is 120 mm; $\bar{\lambda}_{\text{p}}$ ranges from 1 to 2. It can be seen that with the increase of $\sigma_{\text{rc}}/\sigma_1^{\text{C}}$, A_0^0/A_0 decreases. A linear function is

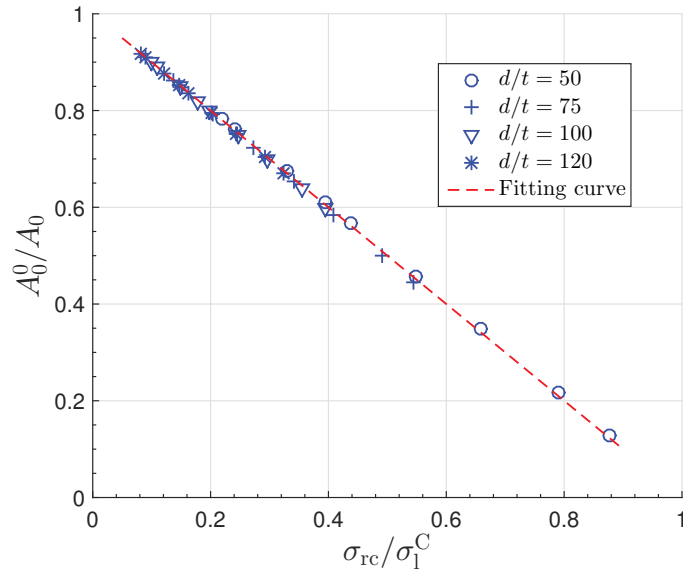


Figure 9.16: Relationship of the imperfection amplitude ratio before and after the self-equilibrating step A_0^0/A_0 and σ_{rc}/σ_1^C . Note that the cross-section aspect ratio is 2, the web depth d is fixed to 120 mm, and the ECCS residual stress distribution model for heavily welded box-section members is adopted; the targeted A_0 value is $d/1000$.

fitted based on the numerical results:

$$\frac{A_0^0}{A_0} = 1 - \frac{\sigma_{rc}}{\sigma_1^C}. \quad (9.5)$$

The mean ratio from the FE results to the fitting equation in the parameter range shown is 1.000 and the COV is 1.33%. It can be seen that this relationship is essentially identical to Eq. (9.4).

A more extensive study is conducted to establish the sensitivity of Eq. (9.5) to other parameters, such as the cross-section aspect ratio, plate width–thickness ratio and targeted imperfection size A_0 . As shown in Figure 9.17, Eq. (9.5) shows good comparisons with the FE results for the cases where σ_{rc}/σ_1^C is small and A_0 is relatively small. The difference increases with the increase of σ_{rc}/σ_1^C and A_0 . This is reasonable since Eq. (9.5) is essentially based on linear theory, which is only valid for small deflections.

However, Table 9.4 shows that the sensitivity of struts to local imperfections decreases

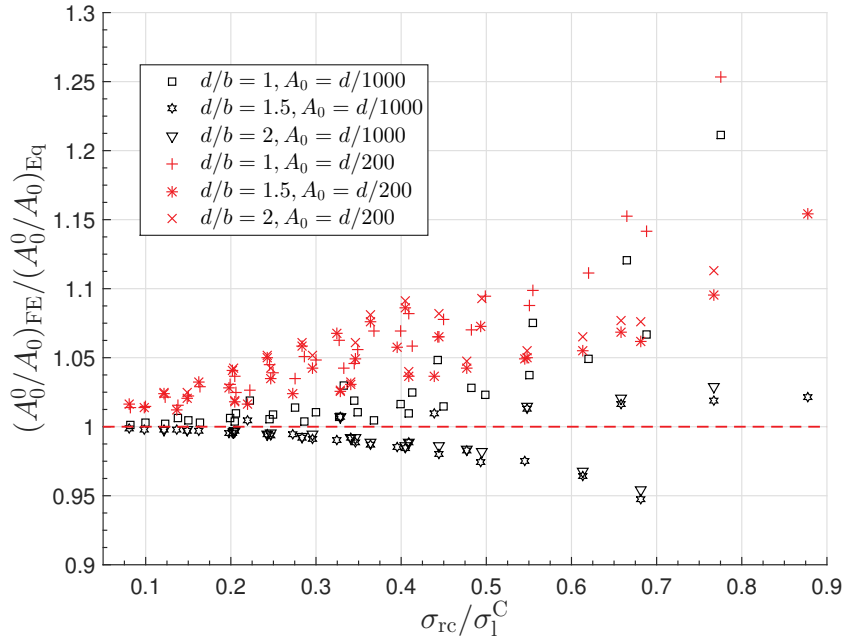


Figure 9.17: Comparison of FE results with Eq. (9.5) for different cross-section aspect ratios, targeted imperfection sizes and compressive residual stress levels.

commensurately with $\bar{\lambda}_p$ and struts exhibit only moderate sensitivity to local imperfections when $\bar{\lambda}_p = 2$. Figure 9.18 presents the envelope of two curves (solid line) defined by $\bar{\lambda}_p = 2$ (dashed line) and $f_y = 690 \text{ N/mm}^2$ (dot-dashed line) based on Eq. (9.2) with $d_t = 3t$, which represents heavily welded sections. The range below the envelope is practically

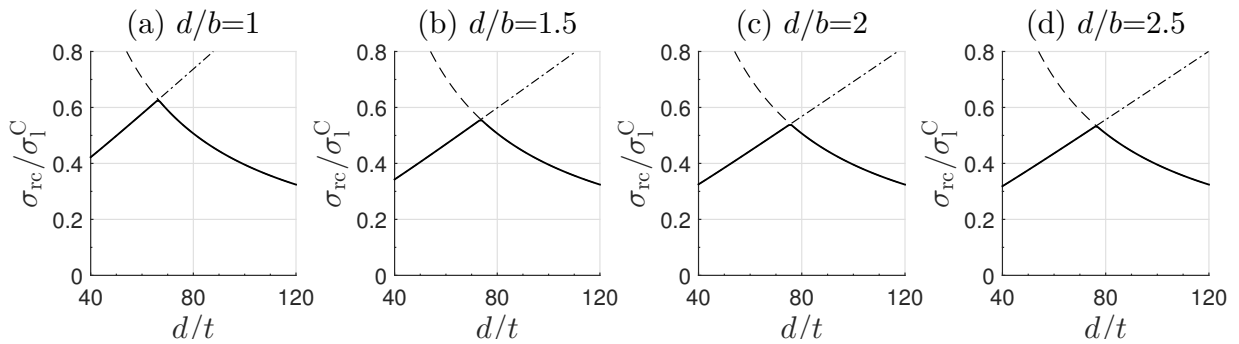


Figure 9.18: Ratio σ_{rc} / σ_1^C at the boundary of local geometric imperfection sensitivity range for practically realistic box-section members. The solid line envelope is defined by $\bar{\lambda}_p = 2$ (dashed line) and $f_y = 690 \text{ N/mm}^2$ (dot-dashed line) by Eq. (9.2), as illustrated in Figure 9.10 for the case where $d/b = 2$.

significant. It can be seen that σ_{rc} / σ_1^C is generally less than 0.6 for most cases, where

Eq. (9.5) can provide a relatively accurate estimation of A_0^0 , as shown in Figure 9.17. Specifically, for the target $A_0 = d/1000$, which is the local geometric imperfection size recommended in previous work (Degée *et al.*, 2008; Pavlovčič *et al.*, 2012) for numerical modelling of welded box-section members with residual stresses being explicitly modelled, $A_{0,FE}^0/A_{0,Eq}^0$ varies between 0.95 and 1.05. As for higher strength steels, previous studies (Ban *et al.*, 2013; Somodi & Kövesdi, 2018) have reported that the width of the uniform tensile zone would decrease with the increase of steel strength grade. This would make the size of the envelope decrease with the increase of the steel strength grade. Therefore, it may be concluded that Eq. (9.5) provides a simple yet relatively accurate estimation of the initially introduced imperfection size A_0^0 for the cases where residual stresses are explicitly accounted within the FE model.

9.5 Comparison with the current design guidelines and reliability analysis

Based on the findings in preceding sections, an extensive parametric study on geometric parameters, material yielding stress levels, as well as strut length is conducted and the results are placed in the context of the current design methodologies, *i.e.* the Effective Width Method (EWM) and the Direct Strength Method (DSM). The principal parameters and their ranges are presented in Table 9.6. As for imperfections introduced in the model,

Table 9.6: Principal parameters and their ranges for the parametric study for the guideline reliability assessment. Note that the critical buckling load ratio is altered by varying the strut length.

Principal parameters	Range
Cross-section aspect ratio d/b	$1 \rightarrow 2.5$
Critical buckling load ratio P_o^C/P_1^C	$0.6 \rightarrow 4$
Cross-sectional slenderness $\bar{\lambda}_p$	$0.6 \rightarrow 2$
Welding options d_t	$1.5t$ and $3t$

the combination recommended by Degée *et al.* (Degée *et al.*, 2008) is adopted, *i.e.* the

global imperfection being $L/1000$, the local imperfection being $d/1000$ and the ECCS residual stress distribution model for welded box-section members. The comparisons with the existing experimental results are shown in Figure 9.19. It can be seen that the FE

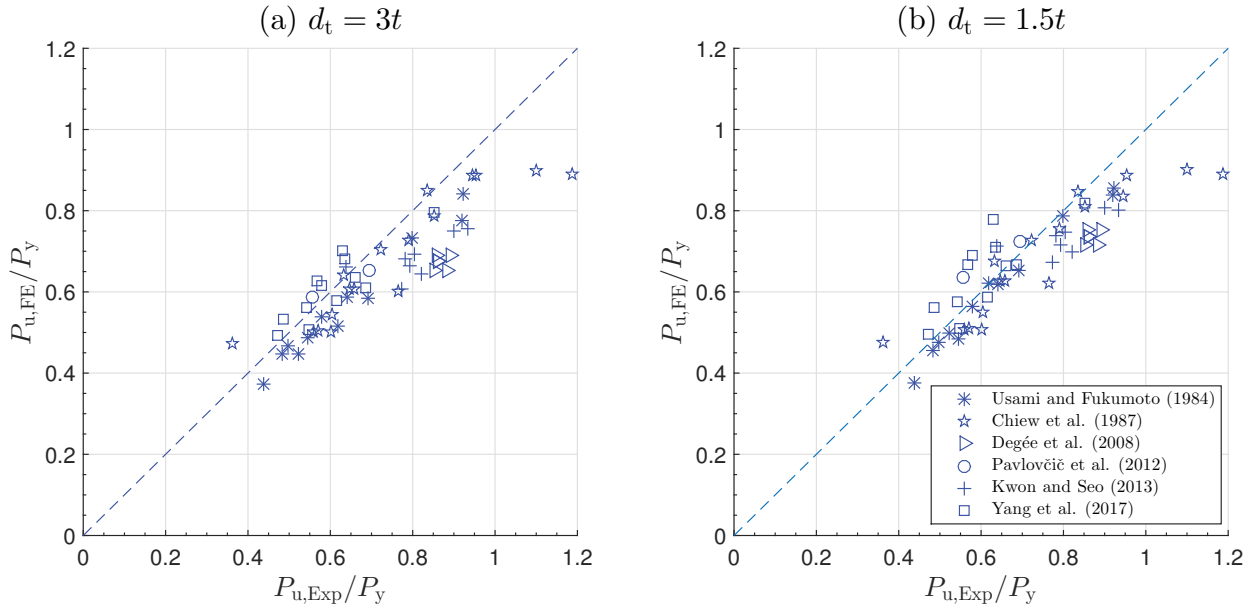


Figure 9.19: Comparison of ultimate loads between the experimental and FE results using the imperfection combination recommended by Degée *et al.* (Degée *et al.*, 2008).

model with the imperfection combination can provide a reasonably safe ultimate load prediction for welded box-section members exhibiting mode interaction. Specifically, the average of $P_{u,FE}/P_{u,Exp}$ is 0.914 with the COV being 12.07% for $d_t = 3t$ and 0.960 with the COV being 11.88% for $d_t = 1.5t$ respectively. This is attributed to the fact that the amplitudes of the currently chosen imperfections are generally larger than those of specimens in tests, particularly for the compressive residual stress level. In most cases, the compressive residual stress level is much closer to the ECCS model for lightly welded sections. Therefore, in the reliability analyses that follow, a variability term $V_{FE} = 0.1144$, determined by considering the deviation of the current numerical models to actual welded specimens, is adopted to add artificial variability to the numerical results. The procedure to determine V_{FE} is precisely the same as that presented in Bock *et al.* (Bock *et al.*, 2015), which was also adopted by a later study (Wang & Gardner, 2017) to consider the deviation of the numerical model. Currently, V_{FE} is determined based on the correlation between

the experimental results and the FE model with the lightly welded residual stress model and it is assumed that it also applies to the cases in heavily welded members, since there is a lack of available experimental data.

9.5.1 Assessment of the Effective Width Method in EC3 and reliability analysis

In the current version of EC3 (EN-1993-1-1:2006E, 2006; EN-1993-1-5:2006E, 2006), the column buckling curves for generally welded and heavily welded sections are recommended as b and c respectively, as shown in Table 2.4. The comparisons of the FE results for lightly welded and heavily welded members are presented in Figure 9.20. It can be seen that the current design approach based on the EWM can generally provide a good prediction for the ultimate load of thin-walled welded RHS struts susceptible to mode interaction. Specifically, for lightly welded struts, the average of $P_{u,FE+tests}/P_{u,EC3}$ is 1.001 and the COV is 9.24%; for heavily welded struts, the average and its COV are 1.011 and 9.96% respectively.

However, in some parameter ranges, the current design guidelines may give unsafe predictions. Therefore, a reliability analysis is conducted within the framework of the first order reliability method (FORM) in Annex D of EN 1990 (BS EN 1990, 2002). The objective of reliability analysis is to ensure that the probability of failure P_f is below a certain level, *i.e.*:

$$P_f = \Pr[(R - E_a) \leq 0] = \phi(-\beta_r), \quad (9.6)$$

where R is the resistance and E_a represents the action effects; ϕ is the cumulative distribution function of the standardized normal distribution; β_r is the total reliability index, which is equal to 3.8 for the ultimate limit state design of building structural members

with a 50-year design life (BS EN 1990, 2002).

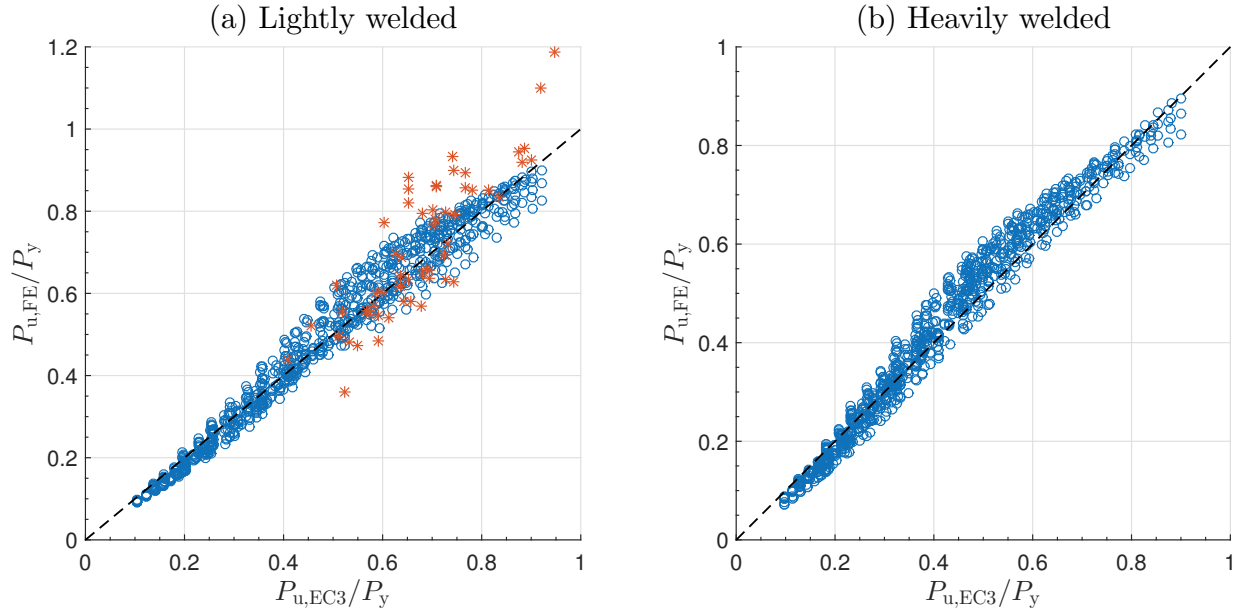


Figure 9.20: Comparison of the ultimate loads for lightly welded and heavily welded struts from the validated FE model and the design equation from EC3. Symbols ‘o’ and ‘*’ represent FE and experimental data respectively. Note that the column buckling curves for lightly and heavily welded struts are adopted as ‘b’ and ‘c’ respectively, as presented in Table 2.5.

In the FORM, the variabilities of the load effects and resistance functions are assessed separately. As for design resistance R_d , the probability of the resistance of structural members being smaller than R_d is given thus:

$$\Pr(R \leq R_d) = \phi(\alpha_r \beta_r) \approx 0.001, \quad (9.7)$$

where α_r is the sensitivity factor and is adopted to be 0.8. The principal task in reliability analysis is to determine the partial safety factor γ_M defined thus:

$$\gamma_M = r_n / r_d, \quad (9.8)$$

where r_n is the nominal resistance determined from the design resistance equation using the nominal geometric and material properties; r_d is the design resistance determined from the

reliability analysis procedure using the actual or measured data from tests. The detailed procedure to determine γ_M can be found in design guidelines (BS EN 1990, 2002) and previous studies (Afshan *et al.*, 2015; Bock *et al.*, 2015):

1. Compare the ultimate load from the FE model and design equation to obtain the mean value of the correction factor b and the corresponding COV of the error terms V_δ ;
2. Define the COVs for the basic variables V_{X_i} in the resistance function and calculate the COV of the resistance function V_{rt} as well as the COV of the FE model V_{FEM} ;
3. Calculate the combined COV V_r^2 such that: $V_r^2 = V_\delta^2 + V_{rt}^2 + V_{FEM}^2$;
4. Determine the design resistance value r_d using the expression given in Annex D of EN 1990 (BS EN 1990, 2002), which is a function of V_r , V_δ and V_{rt} ;
5. Calculate the nominal resistance value r_n using the nominal geometric and material properties;
6. Calculate the partial safety factor using Eq. (9.8).

Compared with previous studies, the key challenge in the current study is to determine the deviation of the resistance function V_{rt}^2 defined thus:

$$V_{rt}^2 = \frac{\text{Var}[g_{rt}(\underline{X})]}{g_{rt}^2(\underline{X}_m)} \approx \frac{1}{g_{rt}^2(\underline{X}_m)} \cdot \sum_{i=1}^j \left(\frac{\partial g_{rt}}{\partial X_i} \cdot V_{X_i} \right)^2, \quad (9.9)$$

where g_{rt} is the resistance function; \underline{X} and \underline{X}_m represent the variables in the resistance function and their respective mean values; V_{X_i} is the COV of variable X_i , which is generally determined based on prior knowledge. The COVs of basic variables in the current study are presented in Table 9.7. However, the current resistance function, *i.e.* Eqs. (2.22)–(2.24), is not a continuous function and comprises two parts, which means that a continuous and explicit expression may be difficult to obtain. Moreover, the value of V_{rt}^2 is not a

constant but varies with the geometric properties and yielding stress levels (Afshan *et al.*, 2015). Therefore, the resistance function is developed as a function in MATLAB and V_{rt}^2 is evaluated numerically for each specimen. Figure 9.21 presents the relationship of V_{rt}^2 versus P_o^C/P_1^C at different cross-section local slenderness levels for heavily welded RHS struts with $d=120$ mm, $b = 60$ mm and $t = 1$ mm. It can be seen that V_{rt}^2 increases with

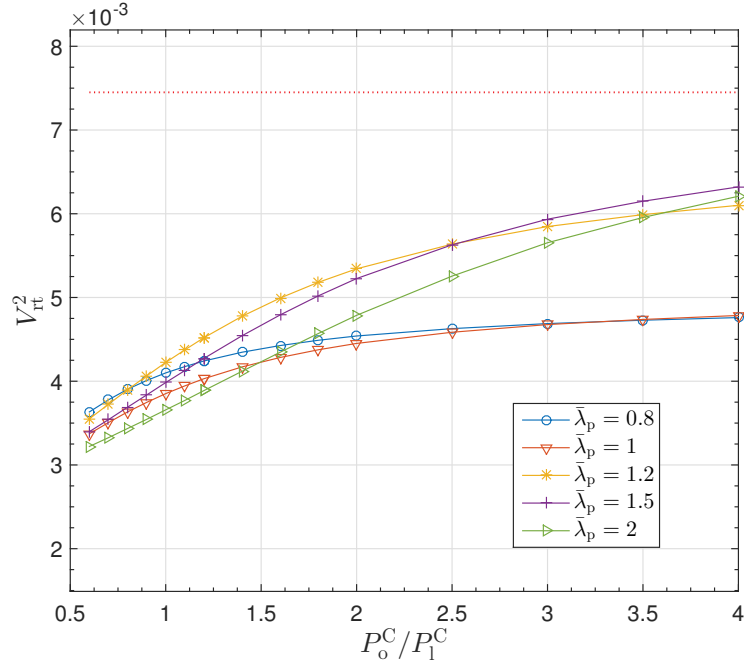


Figure 9.21: Relationship between V_{rt}^2 and P_o^C/P_1^C at different plate slendernesses determined based on Eq. (9.9) for heavily welded RHS struts with $d = 120$ mm, $b = 60$ mm and $t = 1$ mm. The dotted line represents the value of V_{rt}^2 determined based on a mean square formula (Schillo, 2017). Note that the coefficients of variation of geometric and material properties are presented in Table 9.7.

the increase of P_o^C/P_1^C and also varies with the local slenderness $\bar{\lambda}_p$. The variation is caused by the change of $\partial g_{rt}/\partial X_i$ in different parametric ranges, which reflects the corresponding governing failure mechanism of struts (Afshan *et al.*, 2015).

As for the calculation of the nominal resistance r_n , it is assumed that the mean to nominal yielding strength ratio $f_{y,mean}/f_{y,nominal} = 1.135$ (Wang & Gardner, 2017). Based on the $r_{n,i}$ and $r_{d,i}$ values for each specimen, the overall γ_{M1} is determined based on least squares

Table 9.7: Coefficient of variation (COV) for geometric and material property parameters based on the data presented in (Schillo, 2017).

Parameter	COV
Plate thickness (t_f, t_w)	0.05
Plate width (b, d)	0.005
Strut length (L)	0.005
Material yielding stress (f_y)	0.07

regression:

$$\gamma_{M1} = \frac{\sum_{i=1}^n r_{n,i}^2}{\sum_{i=1}^n r_{n,i} r_{d,i}}. \quad (9.10)$$

A summary of the results of the reliability analysis is presented in Table 9.8. For both

Table 9.8: Summary of reliability analysis results for the Effective Width Method in EC3. Note that $k_{d,n}$ is the fractile factor, which is related to the number of tests in each data set; b_m and V_δ are the mean value and the COV of the correction factor for the ultimate load from the tests, FE models and design equation.

Welding option	No. of simulations or tests	$k_{d,n}$	b_m	V_δ	γ_{M1}
Light	790 FE models + 57 tests	3.102	1.013	0.087	1.138
Light	57 tests	3.271	1.056	0.136	1.386
Heavy	885 FE models	3.101	1.036	0.102	1.172

cases, the values of γ_{M1} are larger than unity, where unity is the recommended value in EC3 for member buckling. It implies that the current design equation may fail to meet the Eurocode reliability requirement if $\gamma_{M1} = 1$ is adopted. However, it should be noted that the current parametric study includes extensive geometric and material property ranges, some of which may not be practically significant and may also contribute to the relatively higher values of γ_{M1} . A further parametric study on struts with practically significant geometric and material properties is required to assess the reliability of the design equation further but this is left for future study.

9.5.2 Assessment of the Direct Strength Method (DSM) and reliability analysis

The comparisons of the FE results and the DSM prediction are presented in Figure 9.22. Since the DSM was proposed based on systematic experimental and numerical studies specifically on cold-formed steel sections, it is not entirely surprising that the current DSM generally provides an overprediction for the ultimate load of thin-walled welded RHS struts. Specifically, for lightly welded struts, the average of $P_{u,FE+tests}/P_{u,DSM}$ is 0.887 and the COV is 7.77%; for heavily welded struts, the average and COV are 0.823 and 7.28% respectively. Following the same procedure presented in the preceding section as well as

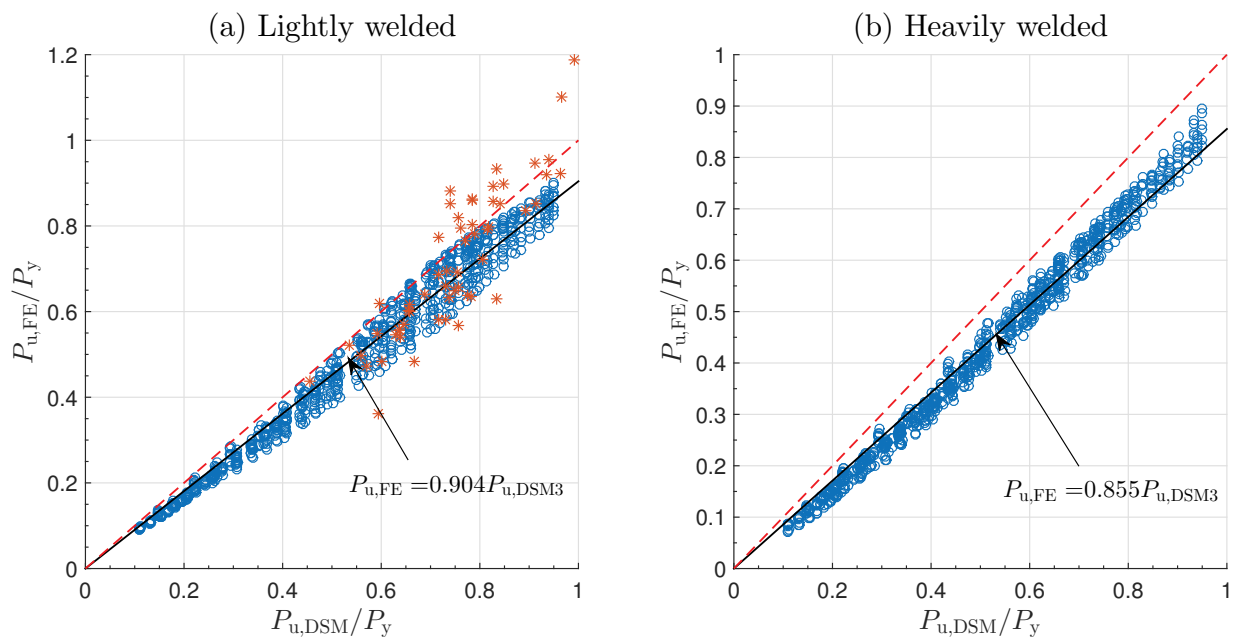


Figure 9.22: Comparison of the ultimate loads for lightly welded and heavily welded struts from the validated FE model and the DSM. Also shown are the correction factor functions fitted based on least squares.

adopting the same COVs for the basic parameters, reliability analysis has been conducted and a summary of results is presented in Table 9.9.

Table 9.9: Summary of reliability analysis results for the DSM with quantities being defined in Table 9.8.

Welding option	No. of simulations or tests	$k_{d,n}$	b_m	V_δ	γ_{M1}
Light	790 FE models + 57 tests	3.102	0.904	0.070	1.223
Light	57 tests	3.271	0.962	0.132	1.495
Heavy	885 FE models	3.101	0.855	0.075	1.319

9.6 Proposal and reliability analysis of a modified DSM procedure

Because the current DSM method cannot be applied directly to the ultimate load prediction of thin-walled welded RHS struts, efforts have been made currently to propose a new design equation. As presented in Table 9.9, the effects of welding options should be considered and separate equations need to be adopted for each case. Currently, the EC3 column curves for lightly welded and heavily welded members are b and c respectively (EN-1993-1-1:2006E, 2006). The column buckling curve adopted in the current DSM lies in the range between buckling curves a and b (see Table 2.5), as shown in Figure 9.23. This is an additional

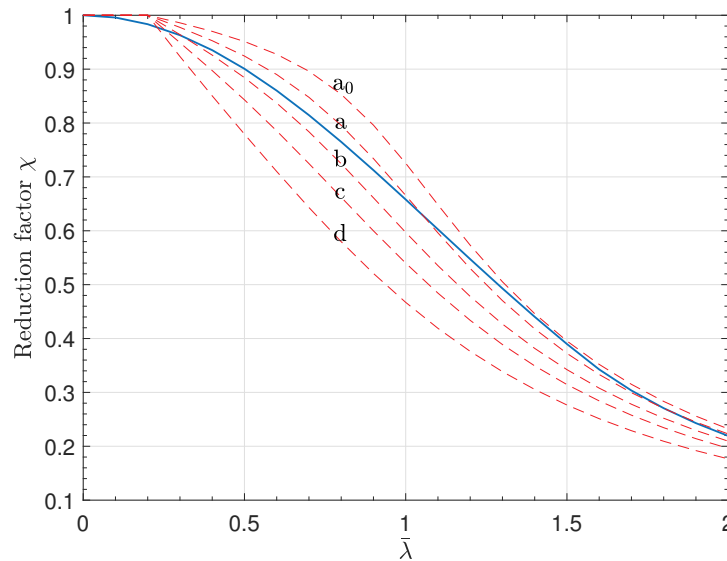


Figure 9.23: Column buckling curves. Solid and the dashed lines represent the column strength curve in the DSM and the five curves, a_0 –d, in EC3 respectively.

reason why the ultimate load prediction is on the unsafe side. Therefore, in the proposed modified DSM, the column buckling curves b and c from EC3 are adopted for the lightly welded and heavily welded members respectively to determine the nominal global failure load $P_{ne,N}$, *i.e.*:

$$P_{ne,N} = \chi A_g f_y, \quad (9.11)$$

with χ defined as that in Eq. (2.23) and the gross cross-sectional area being adopted to determine the relevant quantities in Eq. (2.24). The imperfection factors α for lightly welded and heavily welded members are 0.34 and 0.49 respectively, as presented in Table 2.5. As for local buckling, the nominal axial strength, $P_{nl,N}$ is given by:

$$\frac{P_{nl,N}}{P_{ne,N}} = \begin{cases} 1 & \text{for } \bar{\lambda}_{l,N} \leq 0.536, \\ \left[1 - 0.21 (P_1^C/P_{ne,N})^{0.6}\right] (P_1^C/P_{ne,N})^{0.46} & \text{for } \bar{\lambda}_{l,N} > 0.536, \end{cases} \quad (9.12)$$

where $\bar{\lambda}_{l,N} = \sqrt{P_{ne,N}/P_1^C}$ with $P_{ne,N}$ being defined in Eq. (9.11). The nominal axial strength, $P_{n,N}$, is the minimum of $P_{ne,N}$ and $P_{nl,N}$.

The comparisons of the modified DSM with the FE and experimental results are presented in Figure 9.24. Compared with the current DSM equations, the modified DSM equations provide a superior prediction of the ultimate loads. Specifically, for lightly welded struts, the average of $P_{u,FE+tests}/P_{u,NDSM}$ is 1.006 and the COV is 8.04%; for heavily welded struts, the average and its COV are 1.005 and 8.41% respectively. Moreover, a reliability analysis has been conducted and a summary of the results is presented in Table 9.10.

Table 9.10: Summary of reliability analysis results for the modified DSM equations with quantities being defined in Table 9.8.

Welding option	No. of simulations or tests	$k_{d,n}$	b_m	V_δ	γ_{M1}
Light	790 FE models + 57 tests	3.102	1.013	0.074	1.105
Light	57 tests	3.270	1.055	0.140	1.404
Heavy	885 FE models	3.101	1.029	0.087	1.135

The modified DSM takes advantage of the EC3 column buckling curves to consider the

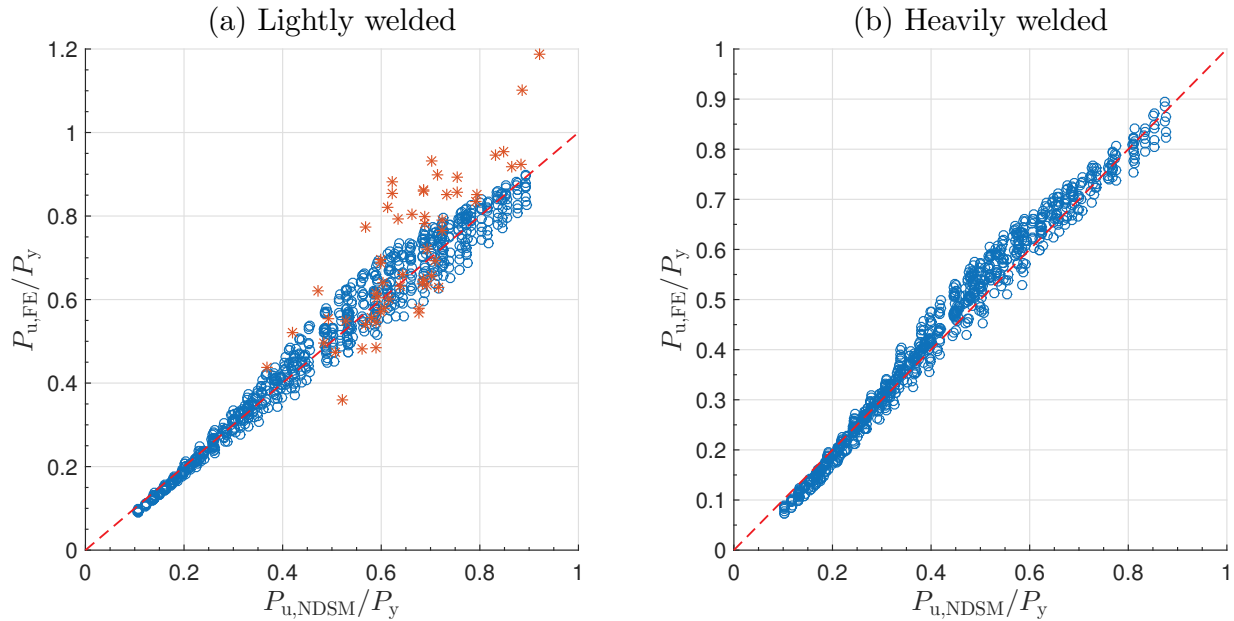


Figure 9.24: Comparison of the ultimate load for lightly and heavily welded struts from the validated FE model and the modified DSM. Graphs (a) and (b) are as described in Figure 9.20.

effects of welding options but remains within the framework of the DSM, which makes the calculation process relatively simple. More importantly, compared with the current DSM and EWM, it is demonstrated to provide superior accuracy and reliability for the ultimate load prediction, in terms of mean b_m and the partial safety factor γ_{M1} . Therefore, it may be concluded that the proposed modified DSM provides a simple and reliable approach in designing welded thin-walled RHS members.

9.7 Concluding remarks

In the current chapter, the effects of cross-section geometry, material properties, residual stress on the behaviour of thin-walled RHS struts exhibiting mode interaction were investigated using the validated FE model developed in Chapter 3 but also drawing on the developments presented in the subsequent chapters. An assessment of the current design guidelines was made by means of structural reliability analysis in accordance with Annex

D of EN1990.

Firstly, a program that could automatically generate, submit, terminate and process geometric and material nonlinear analyses with imperfections (GMNIA) was developed in MATLAB. With the program, an extensive parametric analysis can be conducted efficiently and systematically.

The parametric study on the cross-section geometry, *i.e.* plate width to thickness ratio and cross-section aspect ratio, showed that they generally have minor effects on the profile of the Van der Neut-type curve in the purely elastic case. It also indicated that the Direct Strength Method (DSM) can be used for the ultimate load prediction in such cases. Moreover, for perfect struts, the extent of the notoriously unstable range, *i.e.* zone 2, was observed to increase with the increase of cross-section aspect ratio, while there was little effect found from varying the plate width to thickness ratio.

The effects of the yielding stress level on the Van der Neut-type curve were also investigated. With the decrease of material yielding stress level, the Van der Neut-type curve was curtailed. The load-carrying capacity drop is not significant in the range where global buckling is critical but it becomes increasingly significant with the increase of P_o^C/P_1^C in the range where local buckling is critical. Based on the results, the imperfection sensitivity of four representative length struts at different yielding stress levels was investigated. In particular, four typical imperfection cases were studied, *i.e.* with purely a global imperfection, purely a local imperfection, a combined local and global imperfection with amplitudes normalized to the tolerance value combination and a varying local imperfection with the global imperfection being at the tolerance level. Curves were fitted to describe the imperfection sensitivity based on numerical results for different cases. It was found that the leading power law relationship order is not affected by the yielding stress level but the imperfection sensitivity increases with the decrease of the yielding stress level, particularly for ‘short’ struts. Moreover, it was found that the leading order in the power law relationship is related to the strut failure mechanism. Following that, the effects of ma-

terial yielding stress level on the equilibrium path of the four characteristic length struts were investigated. For struts with lower cross-sectional slenderness, the final failure mechanism is localized failure of the more compressed web at mid-span and the failure mode is highly unstable. With the increase of cross-sectional slenderness, the severity of the unstable behaviour is mollified, which helps explain the imperfection sensitivity of struts with different yielding stress levels. The failure mechanism of struts was explained using the axial tangent stiffness versus axial load relationship of a simply-supported plate under pure compression. Moreover, the study on the effect of material strain-hardening showed that the effect of strain-hardening slope in practical steels on the ultimate load of struts susceptible to local–global mode interaction is tiny and may be neglected.

As for the effect of residual stress, the local imperfection sensitivity of struts with the normalized global imperfection size q_{s0} being 1/1000 was investigated. The example struts exhibited a 1/2 power law relationship, which is the same as the residual stress-free case. With the increase of the ratio of the compressive residual stress to local buckling stress, mollification in the imperfection sensitivity was observed. The effects of residual stress on the equilibrium path of the four characteristic length struts with different normalized cross-section slenderness were investigated. Erosion in the load-carrying capacity was observed in all four example struts compared with the residual stress-free case and it was also found that the length effect on the erosion is negligible. Moreover, a reduction in the initial strut stiffness, as well as a mollification in the severity of unstable behaviour owing to the coupling of plate local buckling and material failure, were observed. This is attributed to the fact that the compressive residual stress promotes premature buckling of the more compressed web at a relatively lower external axial load level, thus leading to the loss of strut stiffness.

Since the initial imperfection size A_0^0 would be amplified after the self-equilibrating step for the cases where residual stresses are explicitly accounted within the FE model, a simplified method was proposed to determine A_0^0 . Parametric studies showed that it does provide a

simple yet relatively accurate estimation of A_0^0 .

Finally, based on the numerical results, an assessment of the current design rules for thin-walled welded RHS struts, *i.e.* the effective width method (EWM) in EC3 and the DSM, were made by means of reliability analysis in accordance with Annex D of EN1990. It revealed that the EWM can generally provide a good ultimate load prediction but may be unsafe in some parametric ranges; the DSM generally gives an unsafe ultimate load prediction. Partial safety factors γ_{M1} were determined for both cases such that make the current design equations meet the Eurocode reliability requirement. Moreover, a modified DSM equation has been proposed based on the numerical and experimental results and it is shown to provide a better ultimate load prediction than it does at present.

Chapter 10

Conclusions and future work

10.1 Conclusions

The current thesis has presented a series of variational and finite element (FE) models, describing the local–global mode interaction of thin-walled rectangular hollow section struts. The effects of flange–web joint rigidity, strut length and geometric imperfections were investigated using the developed variational model and verified by FE models. The highly unstable post-buckling behaviour and imperfection sensitivity due to interactive buckling have been highlighted. The behaviour of RHS struts exhibiting mode interaction in more practically realistic scenarios, which include material nonlinearity and residual stresses, were also investigated using FE models validated from existing experimental results, highlighting that particular attention should be paid while designing such structural members.

Firstly, nonlinear FE models using shell elements were developed in the commercial FE package ABAQUS. The classical solutions from linear theory for the buckling of simply-supported plates under pure compression and the Euler buckling load of simply-supported columns were used to verify the FE model and showed good comparisons. Moreover, experimental results on local–global mode interaction of welded box-section columns under

pure compression from two independent studies were used to validate the effectiveness of the nonlinear material modelling, geometric imperfections and residual stress modelling as well as the nonlinear solution strategy in the current FE model. Good comparisons were also observed.

The analytical study started with the focus on the global buckling induced local–global mode interaction of thin-walled RHS struts with semi-rigid flange–web joints. Unstable post-buckling behaviour due to mode interaction was observed. A progressive change in the local buckling mode was identified in terms of both the wavelength and the amplitude. As far as the author is aware, it is the first time that this has been demonstrated in rectangular hollow section struts. With the increase of the cross-section joint rigidity, a transition from highly unstable to more mildly unstable post-buckling behaviour was observed. The results from the variational model showed excellent comparisons with the FE results, which verified the effectiveness of the presented methodology. A simplified method to predict the local buckling coefficient in the more compressed web and the global buckling amplitude at the secondary bifurcation point was proposed based on the verified variational model; it was demonstrated to be simple, yet safe and accurate for the cases studied.

The variational model was then extended to describe the interactive buckling of elastic thin-walled RHS struts in scenarios where local buckling may be critical as well as the existence of both local and global geometric imperfections. Two independent sets of in-plane and out-of-plane local displacement fields, which represent the pure local buckling mode and global buckling induced interactive buckling mode respectively, were introduced to describe the interactive buckling mode of struts with different lengths. In particular, the cross-section components of these local modes were approximated by applying approximate kinematic boundary conditions for each plate in conjunction with Rayleigh–Ritz method. Global and local imperfections, the profiles of which correspond to the global and local modal descriptions adopted in the variational model, were introduced. The total

potential energy was determined based on the modal description and introduced geometric imperfections. By performing the calculus of variations on the total potential energy, the governing equations for the longitudinal components of the local post-buckling modes subject to boundary and integral conditions were obtained.

Based on the developed variational model, a parametric study on strut length was conducted. Numerical examples, considering four representative lengths corresponding to distinct parts of the Van der Neut curve, were presented and verified using the validated FE model developed in Chapter 3. Using the verified variational model, the boundaries of four distinct length-dependent domains were identified for realistic cross-section characteristics for the first time. Unstable post-buckling behaviour due to mode interaction was observed in long, transitional and intermediate length struts. Potentially dangerous behaviour, *i.e.* a sharp drop in the load-carrying capacity immediately after the ultimate load is reached, has been identified where the global buckling load is close to the local buckling load. A progressive change in the local buckling mode was observed within the nonlinear post-buckling range in all struts. In particular, for so-called ‘intermediate’ and ‘short’ length struts, snap-backs that correspond to the change in the number of troughs and peaks in the local mode that are akin to cellular buckling, were observed. The parametric study on strut length also showed that the notoriously unstable post-buckling range for rectangular hollow-section struts is in fact significantly smaller than that predicted by Van der Neut’s idealized model and the stiffness reduction factor is also considerably higher. The reason for this difference has been identified as being derived from the interaction between the individual plates due to the rigid corners within the cross-section, which lead to some stiffness redistribution. This is in contrast with the assumption that the corners are pinned where the web and flange plates behave independently.

Following the study of perfect systems, the imperfection sensitivity of thin-walled RHS struts with initial global and local geometric imperfections was investigated. Numerical examples, focusing on cases where the global buckling load is close to the local buckling

load, were presented and verified using the FE model developed in Chapter 3. The sensitivity of two example struts exhibiting mode interaction to initial geometric imperfections was quantified. With the increase of the geometric imperfection size, a transition from highly unstable to neutrally or mildly stable post-buckling behaviour was observed. A progressive change in the local buckling mode was identified in terms of both wavelength and amplitude. In particular, mode jumping within the interactive buckling mode, *i.e.* the change in the number of troughs and peaks of the local mode and snap-backs in the equilibrium path, was also observed in the cases where the local imperfection size is vanishingly small. Curves were fitted to describe the ultimate load versus normalized imperfection size relationship. For the purely global imperfection case, the expressions for both example struts indicated approximately a $1/2$ power law relationship to leading order; for the purely local imperfection and combined imperfection cases, the expressions for both example struts indicated approximately a $1/3$ power law relationship. A simplified method to predict the load at the pitchfork bifurcation point, where interactive buckling is triggered, was proposed for struts with purely global imperfections based on the verified variational model; it was demonstrated to be simple, yet safe and accurate for the cases studied.

A further parametric study on the effects of tolerance level global imperfections, local imperfections and their combinations on the ultimate load for struts with different lengths was conducted. It was revealed that for struts with tolerance level global imperfections, the post-buckling behaviour after the pitchfork bifurcation point is unstable and stable for struts with global buckling and local buckling being critical respectively. It was also found that local imperfections are more significant than global imperfections for struts where global buckling is critical and global imperfections are more significant for struts where local buckling is critical. This was attributed to the characteristic behaviour where the alternative imperfection type would facilitate the necessary symmetry breaking to trigger interactive buckling. Based on the parametric study results, the simplified method to predict the pitchfork bifurcation load was calibrated to calculate the ultimate load for struts with tolerance level global and combined imperfections.

Based on the FE model developed in Chapter 3 alongside findings from the variational model in Chapter 7, the behaviour of thin-walled RHS struts with tolerance level imperfections was investigated using the Geometric Nonlinear Analysis with Imperfections (GNIA). Focus was on the effect of local imperfection profiles on the ultimate load and equilibrium behaviour. A unified local imperfection measurement based on equal local bending energy was introduced, which could provide a consistent and meaningful comparison between different imperfection profiles. An algorithm for determining the most severe local imperfection profile was proposed. A function, which can terminate the nonlinear analysis automatically once certain failure criteria is met, was also developed within MATLAB. This greatly improved the computational efficiency and made an efficient parametric study feasible. Within the automated computational framework, the most severe local imperfection profiles for struts with different lengths were determined. The study revealed that the ultimate load is principally affected by the imperfection in the more compressed web. The wavelength of the most severe periodic local imperfection was found to be smaller than that of the purely local buckling mode or the local–global interactive post-buckling mode for the perfect case, which implies that the lowest local buckling mode from linear buckling analysis does not necessarily represent the most severe local imperfection profile. Under the equal local bending energy constraint, introducing a modulated amplitude in the local imperfection profile leads to a further decrease in the ultimate load. However, struts with highly localized local imperfection profiles exhibited a relatively stiffer response, thus leading to a higher ultimate load. Moreover, it was determined that under the constraint of the manufacturing imperfection tolerance level, the most severe imperfection profile can be safely approximated using the case with doubly-symmetric cross-section initial deformation and periodic longitudinal components. An equation to approximate the corresponding wavelength was proposed based on the results of the parametric study.

As for the equilibrium behaviour, the example struts with doubly-symmetric cross-section local imperfections with a tolerance level amplitude exhibit approximately neutral or weakly stable responses after the local–global mode interaction is triggered. This is differ-

ent from the perfect case, where there are four representative length-related ranges that exhibit distinct interactive post-buckling responses. Although the mono-symmetric cross-section imperfection profile breaks the symmetry of the strut deformation at the beginning, the equilibrium path converges to the doubly-symmetric case when the global mode is fully developed. An explicit equation to predict the global buckling load of thin-walled RHS struts with tolerance level doubly-symmetric cross-section imperfections was proposed and showed excellent agreement with the FE results for different plate width to thickness ratios, cross-section aspect ratios and imperfection size levels.

Finally, based on findings in preceding chapters, a program that can automatically generate, submit, terminate and process geometric and material nonlinear analyses with imperfections (GMNIA) was developed in MATLAB. With the program, an extensive parametric analysis was conducted in an efficient and systematic way. The parametric study on the cross-section geometry, *i.e.* plate width to thickness ratio and cross-section aspect ratio, showed that they generally have minor effects on the profile of the Van der Neut-type curve in the purely elastic case. It also indicated that the Direct Strength Method (DSM) can be used for the ultimate load prediction in such cases. Moreover, for perfect struts, the length of the notoriously unstable range, *i.e.* zone 2, was observed to increase in size with the increase of cross-section aspect ratio while there was little effect from varying the plate width to thickness ratio.

The effects of the yielding stress level on the Van der Neut-type curve have been investigated. With the decrease of material yielding stress level, the Van der Neut-type curve was curtailed. The load-carrying capacity drop is not significant in the range where global buckling is critical but it becomes increasingly significant with the increase of P_o^C/P_1^C in the range where local buckling is critical. Based on the results, the imperfection sensitivity of four representative length struts at different yielding stress levels was investigated. In particular, four typical imperfection cases were studied. Curves were fitted to describe the imperfection sensitivity based on numerical results for different cases. It was found that the

leading power law relationship order is not affected by the yielding stress level but the imperfection sensitivity increases with the decrease of the yielding stress level, particularly for ‘short’ struts. Moreover, it was found that the leading order in the power law relationship is related to the failure mechanism. Following that, the effects of material yielding stress level on the equilibrium path of the four characteristic length struts were investigated. For struts with lower cross-sectional slenderness, the final failure mechanism is localized failure of the more compressed web at mid-span and the failure mode is highly unstable. With the increase of cross-sectional slenderness, the severity of the unstable behaviour is mollified, which helps explain the imperfection sensitivity of struts with different yielding stress levels. The failure mechanism of struts was explained using the axial tangent stiffness versus axial load relationship of a simply-supported plate under pure compression. Moreover, the study on the effect of material strain hardening showed that the effect of strain-hardening slope in practical steels on the ultimate load of struts susceptible to local–global mode interaction is tiny and may be neglected.

As for the effect of residual stress, the local imperfection sensitivity of struts with the normalized global imperfection size q_{s0} being 1/1000 was investigated. The example struts exhibited a 1/2 power law relationship, which is the same as the residual stress-free case. With the increase of the ratio of compressive residual stress to the local buckling stress, mollification in the imperfection sensitivity was observed. The effects of residual stress on the equilibrium path of the four characteristic length struts with different normalized cross-section slenderness were investigated. Erosion in the load-carrying capacity was observed in all four example struts compared with the residual stress-free case and it was also found that the length effect on the erosion is negligible. Moreover, a reduction in the initial strut stiffness, as well as a mollification in the severity of unstable behaviour owing to the coupling of plate local buckling and material failure, were observed. This is attributed to the fact that the compressive residual stress promotes premature buckling of the more compressed web at a relatively lower external axial load level, thus leading to the loss of strut stiffness. Since the initially introduced imperfection size A_0^0 would be amplified after

the self-equilibrating step for the cases where residual stresses are explicitly accounted within the FE model, a simplified method was proposed to determine A_0^0 . Parametric studies showed that it does provide a simple yet relatively accurate estimation of A_0^0 .

Finally, based on the numerical results, an assessment of the current design rules for thin-walled welded RHS struts, *i.e.* the effective width method (EWM) in EC3 and the DSM, were made by means of reliability analysis in accordance with Annex D of EN1990. It revealed that the EWM can generally provide a good ultimate load prediction but may be unsafe in some parametric ranges; the DSM generally gives an unsafe ultimate load prediction. Partial safety factors γ_{M1} were determined for both cases such that make the current design equations meet the Eurocode reliability requirement. Moreover, a modified DSM equation has been proposed based on the numerical and experimental results and it is shown to provide a better ultimate load prediction than it does at present.

10.2 Future work

Following the work presented in the current thesis, the following subsections outline areas for further investigation.

10.2.1 Further enhancements of variational model

Modal description scheme As noted in preceding chapters, some simplifications have been made in the modal descriptions in the variational models, which account for the relatively over-stiff response of the variational model. Therefore, in order to simulate and predict the mode interaction behaviour more accurately, the following enrichment can be made in the modal description:

1. Introduce an independent set of transverse displacement field functions to consider

the effects of transverse stress in plates, which have been assumed to be zero in the current formulation.

2. Introduce higher order terms in the cross-section profile of the local buckling mode, which could capture the progressive change in the cross-section profile owing to the increasing compressive strain levels as well as the global inward deformation in the less compressed web due to global bending effects in the far-field post-buckling range.
3. Re-define the cross-section components of the direct in-plane displacement field based on the solutions from classical theory (Koiter, 1945) and results from FE models so that the actual in-plane displacements can be better simulated.

Material nonlinearity The current variational model only limits to the linear elastic material properties. However, as demonstrated in Chapters 8 and 9 as well as in the existing physical test results, the ultimate failure of the thin-walled RHS struts with practical imperfection levels is mainly governed by material failure. Therefore, including the nonlinear effects of the material in the variational model would help to understand the underlying mechanism in the failure of RHS structures in realistic scenarios better. The novel framework proposed by Köllner (2017), which extends the general elastic stability theory to certain non-conservative deformation processes, may be used to enhance the variational model. Moreover, the developed model may also be used to simulate mode interaction in thin-walled RHS struts made from nonlinear materials, such as stainless steel (Gardner & Nethercot, 2004b).

10.2.2 Inclusion of other factors

Cold-formed sections In the current thesis, mode interaction in welded RHS struts has been investigated using the FE method. In practice, cold-formed thin-walled RHS struts are also widely used. Compared with welded members, the process of cold working

leads to the enhancement of material strength at the corners. Moreover, the residual stress distribution pattern is also different (Schafer *et al.*, 2010; Quach *et al.*, 2010). Therefore, FE models considering these effects could be developed to investigate the mode interaction in cold-formed thin-walled RHS sections.

Boundary conditions of columns In the current thesis, the boundary condition of the columns are assumed to be simply-supported and the load is applied at the cross-section centroid. In practice, the boundary condition of column is always semi-rigid and the load condition is always a combination of axial load and bending moment. Therefore, a model including these factors would help better understand the effects of local–global mode interaction on the beam-column strength curves and provide suggestions for robust design guidelines.

10.2.3 Statistical analysis of geometric imperfections in welded RHS members

Chapters 7, 8 and 9 have demonstrated that the ultimate load of thin-walled RHS struts susceptible to mode interaction is sensitive to size of any geometric imperfections. Great efforts have been made to collect and analyse the geometric imperfections in cold-formed thin-walled members and some widely accepted equations to determine the statistically significant imperfection size have been proposed (Schafer & Peköz, 1998a; Schafer *et al.*, 2010). However, as far as the author is aware, there is no such kind of database for welded members. Therefore, a consistent and reasonable geometric imperfection size expression, which is based on the statistical analysis of the measured data and can reflect realistic imperfections, would be very helpful for developing a rational computational models for research and design purposes.

10.2.4 Extension of methodology to similar problems

Mode interaction in thin-walled RHS fibre-reinforced polymer struts Owing to its advantages over conventional structural materials (steel, concrete, wood, *etc.*), such as high strength-to-weight ratio, high failure stress and high corrosion resistance, fibre-reinforced polymer (FRP) members are gaining increasing popularity recently and this will probably continue (Barbero & Tomblin, 1994; Jones, 1998; Barbero, 2013). Since the FRP material remains linearly elastic for large strains, buckling is always the governing failure mode of such members (Barbero *et al.*, 2000). Therefore, thin-walled RHS struts with certain geometric properties would be susceptible to interactive buckling. Changing the isotropic material to an orthotropic material within the current model framework would make it possible to investigate mode interaction of such members. With the developed model, the effects of the lay-up of the laminates or orientation of the laminates on the local-global mode interaction, imperfection sensitivity, and Van der Neut-type curve can be investigated, which could be used to provide recommendations to design such members.

Mode interaction in thin-walled struts with other cross-section profiles As far as the author knows, the current methodology has not been used to investigate the local-global mode interaction in channel-section and polygonal section struts. The challenge in modelling these sections is a good local modal displacement scheme, which is more complex compared with that of RHS struts. More local mode components would have to be introduced to describe the actual local displacement field fully, which may make the formulation process very complex and cumbersome. Therefore, the automation of the formulation of the governing equations in the context of the symbolic computation package MAPLE (2017) is essential.

Appendix A

Expressions for ODEs, integral and boundary conditions

Currently, the extended expressions for the ODEs, integral and boundary conditions derived in Chapter 5 for struts with both local and global geometric imperfections ranging from local buckling being critical to global buckling being critical are presented. Moreover, it should be noted that by setting local and global imperfection related terms to zero, these expressions are the governing equations for the perfect struts presented in Chapter 6.

The fourth order ODE for w_1 and w_2 are given thus:

$$(A_{11}A_{22} - A_{12}A_{21})(\ddot{w}_1 - \ddot{w}_{10}) - A_{12}(C_{21} + C_{22}) + A_{22}(C_{11} + C_{12}) = 0, \quad (\text{A.1})$$

$$(A_{11}A_{22} - A_{12}A_{21})(\ddot{w}_2 - \ddot{w}_{20}) + A_{11}(C_{21} + C_{22}) - A_{21}(C_{11} + C_{12}) = 0, \quad (\text{A.2})$$

where

$$A_{11} = D_w \left(\frac{2D_f}{D_w} \{f_{1f}^2\}_x + \{f_{1wc}^2\}_y + \{f_{1wt}^2\}_y \right), \quad (\text{A.3})$$

$$A_{22} = D_w \left(\frac{2D_f}{D_w} \{f_{2f}^2\}_x + \{f_{2wc}^2\}_y + \{f_{2wt}^2\}_y \right), \quad (\text{A.4})$$

$$A_{12} = D_w \left[\frac{2D_f}{D_w} \{f_{1f}f_{2f}\}_x + \{f_{1wc}f_{2wc}\}_y + \{f_{1wt}f_{2wt}\}_y \right], \quad (\text{A.5})$$

$$A_{21} = D_w \left[\frac{2D_f}{D_w} \{f_{1f}f_{2f}\}_x + \{f_{1wc}f_{2wc}\}_y + \{f_{1wt}f_{2wt}\}_y \right], \quad (\text{A.6})$$

$$\begin{aligned} C_{11} = & 2D_w \nu \left[\frac{2D_f}{D_w} \{f_{1f}f''_{1f}\}_x + \{f_{1wc}f''_{1wc}\}_y + \{f_{1wt}f''_{1wt}\}_y \right] (\ddot{w}_1 - \ddot{w}_{10}) \\ & - 2D_w(1 - \nu) \left[\frac{2D_f}{D_w} \{f'_{1f}{}^2\}_x + \{f'_{1wc}{}^2\}_y + \{f'_{1wt}{}^2\}_y \right] (\ddot{w}_1 - \ddot{w}_{10}) \\ & + D_w \left[\frac{2D_f}{D_w} \{f''_{1f}{}^2\}_x + \{f''_{1wc}{}^2\}_y + \{f''_{1wt}{}^2\}_y \right] (w_1 - w_{10}) \\ & + Et_w \frac{\pi^2 b}{2L} (q_t - q_{t0}) \left[\frac{4t_f}{bt_w} \{x f_{1f}^2\}_x + \{f_{1wc}^2\}_y - \{f_{1wt}^2\}_y \right] \left(\frac{\pi}{L} \cos \frac{\pi z}{L} \dot{w}_1 + \sin \frac{\pi z}{L} \ddot{w}_1 \right) \\ & + Et_w \Delta \left[\frac{2t_f}{t_w} \{f_{1f}^2\}_x + \{f_{1wc}^2\}_y + \{f_{1wt}^2\}_y \right] \ddot{w}_1 \\ & - \frac{Et_w}{2} \left[\frac{2t_f}{t_w} \{f_{1f}^4\}_x + \{f_{1wc}^4\}_y + \{f_{1wt}^4\}_y \right] (3\dot{w}_1^2 \ddot{w}_1 - 2\dot{w}_{10} \ddot{w}_{10} \dot{w}_1 - \dot{w}_{10}^2 \ddot{w}_1) \\ & - Et_w \left[\frac{2t_f}{t_w} \{g_{1f}f_{1f}^2\}_x + \{g_{1wc}f_{1wc}^2\}_y + \{g_{1wt}f_{1wt}^2\}_y \right] (\ddot{w}_1 \dot{w}_1 + \dot{w}_1 \ddot{w}_1) \\ & - 2Gt_f \{f'_{1f}f_{1f}\}_x [(q_s - q_t) - (q_{s0} - q_{t0})] \frac{\pi^2}{L} \sin \frac{\pi z}{L} w_1 \\ & - Gt_w \left[\frac{2t_f}{t_w} \{g'_{1f}f'_{1f}f_{1f}\}_x + \{g'_{1wc}f'_{1wc}f_{1wc}\}_y + \{g'_{1wt}f'_{1wt}f_{1wt}\}_y \right] \dot{w}_1 w_1 \\ & - Gt_w \left[\frac{2t_f}{t_w} \{f'_{1f}{}^2 f_{1f}^2\}_x + \{f'_{1wc}{}^2 f_{1wc}^2\}_y + \{f'_{1wt}{}^2 f_{1wt}^2\}_y \right] (\ddot{w}_1 w_1^2 + \dot{w}_1^2 w_1 \\ & \quad - \ddot{w}_{10} w_{10} w_1 - \dot{w}_{10}^2 w_1), \end{aligned} \quad (\text{A.7})$$

$$\begin{aligned}
C_{22} = & 2D_w \nu \left[\frac{2D_f}{D_w} \{f_{2f} f''_{2f}\}_x + \{f_{2wc} f''_{2wc}\}_y + \{f_{2wt} f''_{2wt}\}_y \right] (\ddot{w}_2 - \ddot{w}_{20}) \\
& - 2D_w (1 - \nu) \left[\frac{2D_f}{D_w} \{f'_{2f}{}^2\}_x + \{f'_{2wc}{}^2\}_y + \{f'_{2wt}{}^2\}_y \right] (\ddot{w}_2 - \ddot{w}_{20}) \\
& + D_w \left[\frac{2D_f}{D_w} \{f''_{2f}{}^2\}_x + \{f''_{2wc}{}^2\}_y + \{f''_{2wt}{}^2\}_y \right] (w_2 - w_{20}) \\
& + Et_w \frac{\pi^2 b}{2L} (q_t - q_{t0}) \left[\frac{4t_f}{bt_w} \{x f_{2f}^2\}_x + \{f_{2wc}^2\}_y - \{f_{2wt}^2\}_y \right] \left(\frac{\pi}{L} \cos \frac{\pi z}{L} \dot{w}_2 + \sin \frac{\pi z}{L} \ddot{w}_2 \right) \\
& + Et_w \Delta \left[\frac{2t_f}{t_w} \{f_{2f}^2\}_x + \{f_{2wc}^2\}_y + \{f_{2wt}^2\}_y \right] \ddot{w}_2 \\
& - \frac{Et_w}{2} \left[\frac{2t_f}{t_w} \{f_{2f}^4\}_x + \{f_{2wc}^4\}_y + \{f_{2wt}^4\}_y \right] (3\dot{w}_2^2 \ddot{w}_2 - \dot{w}_{20}^2 \ddot{w}_2 - 2\dot{w}_{20} \ddot{w}_{20} \dot{w}_2) \\
& - Et_w \left[\frac{2t_f}{t_w} \{g_{2f} f_{2f}^2\}_x + \{g_{2wc} f_{2wc}^2\}_y + \{g_{2wt} f_{2wt}^2\}_y \right] (\dot{w}_2 \ddot{w}_2 + \dot{w}_2 \ddot{w}_2) \\
& - 2Gt_f \{f'_{2f} f_{2f}\}_x [(q_s - q_t) - (q_{s0} - q_{t0})] \frac{\pi^2}{L} \sin \frac{\pi z}{L} w_2 \\
& - Gt_w \left[\frac{2t_f}{t_w} \{g'_{2f} f'_{2f} f_{2f}\}_x + \{g'_{2wc} f'_{2wc} f_{2wc}\}_y + \{g'_{2wt} f'_{2wt} f_{2wt}\}_y \right] \dot{w}_2 w_2 \\
& - Gt_w \left[\frac{2t_f}{t_w} \{f'_{2f}{}^2 f_{2f}^2\}_x + \{f'_{2wc}{}^2 f_{2wc}^2\}_y + \{f'_{2wt}{}^2 f_{2wt}^2\}_y \right] (\ddot{w}_2 w_2^2 + \dot{w}_2^2 w_2 \\
& \quad - w_{20} \ddot{w}_{20} w_2 - \dot{w}_{20}^2 w_2),
\end{aligned} \tag{A.8}$$

$$C_{12} = C_{12,\text{bl}} + C_{12,\text{d}} + C_{12,\text{s}}, \tag{A.9}$$

$$\begin{aligned}
C_{12,\text{bl}} = & D_w \nu \left[\frac{2D_f}{D_w} \{f_{1f} f''_{2f}\}_x + \{f_{1wc} f''_{2wc}\}_x + \{f_{1wt} f''_{2wt}\}_x \right] (\ddot{w}_2 - \ddot{w}_{20}) \\
& - 2D_w (1 - \nu) \left[\frac{2D_f}{D_w} \{f'_{1f} f'_{2f}\}_x + \{f'_{1wc} f'_{2wc}\}_y + \{f'_{1wt} f'_{2wt}\}_y \right] (\ddot{w}_2 - \ddot{w}_{20}) \\
& + D_w \left[\frac{2D_f}{D_w} \{f''_{1f} f''_{2f}\}_x + \{f''_{1wc} f''_{2wc}\}_y + \{f''_{1wt} f''_{2wt}\}_y \right] (w_2 - w_{20}) \\
& + D_w \nu \left[\frac{2D_f}{D_w} \{f'_{1f} f_{2f}\}_x + \{f'_{1wc} f_{2wc}\}_y + \{f'_{1wt} f_{2wt}\}_y \right] (\ddot{w}_2 - \ddot{w}_{20}),
\end{aligned} \tag{A.10}$$

$$\begin{aligned}
C_{12,d} = & Et_w \frac{\pi^2 b}{2L} (q_t - q_{t0}) \left[\frac{4t_f}{t_w b} \{x f_{1f} f_{2f}\}_x + \{f_{1wc} f_{2wc}\}_y \right. \\
& \left. - \{f_{1wt} f_{2wt}\}_y \right] \left(\frac{\pi}{L} \cos \frac{\pi z}{L} \dot{w}_2 + \sin \frac{\pi z}{L} \ddot{w}_2 \right) \\
& + Et_w \Delta \left[\frac{2t_f}{t_w} \{f_{1f} f_{2f}\}_x + \{f_{1wc} f_{2wc}\}_y + \{f_{1wt} f_{2wt}\}_y \right] \ddot{w}_2 \\
& - Et_w \left[\frac{2t_f}{t_w} \{g_{2f} f_{1f}^2\}_x + \{g_{2wc} f_{1wc}^2\}_y + \{g_{2wt} f_{1wt}^2\}_y \right] (\ddot{w}_2 \dot{w}_1 + \dot{w}_2 \ddot{w}_1) \\
& - Et_w \left[\frac{2t_f}{t_w} \{g_{1f} f_{1f} f_{2f}\}_x + \{g_{1wc} f_{1wc} f_{2wc}\}_y + \{g_{1wt} f_{1wt} f_{2wt}\}_y \right] (\ddot{w}_1 \dot{w}_2 + \dot{w}_1 \ddot{w}_2) \\
& - Et_w \left[\frac{2t_f}{t_w} \{g_{2f} f_{1f} f_{2f}\}_x + \{g_{2wc} f_{1wc} f_{2wc}\}_y + \{g_{2wt} f_{1wt} f_{2wt}\}_y \right] (\ddot{w}_2 \dot{w}_2 + \dot{w}_2 \ddot{w}_2) \\
& - \frac{Et_w}{2} \left[\frac{2t_f}{t_w} \{f_{1f}^2 f_{2f}^2\}_x + \{f_{1wc}^2 f_{2wc}^2\}_y + \{f_{1wt}^2 f_{2wt}^2\}_y \right] (3\ddot{w}_1 \dot{w}_2^2 + 6\dot{w}_1 \dot{w}_2 \ddot{w}_2 \\
& \quad - 2\ddot{w}_{10} \dot{w}_{20} \dot{w}_2 - 2\dot{w}_{10} \ddot{w}_{20} \dot{w}_2 - 2\dot{w}_{10} \dot{w}_{20} \ddot{w}_2 - \dot{w}_{20}^2 \ddot{w}_1 - 2\dot{w}_{20} \ddot{w}_{20} \dot{w}_1) \\
& - \frac{Et_w}{2} \left[\frac{2t_f}{t_w} \{f_{1f}^3 f_{2f}\}_x + \{f_{1wc}^3 f_{2wc}\}_y + \{f_{1wt}^3 f_{2wt}\}_y \right] (6\dot{w}_1 \ddot{w}_1 \dot{w}_2 + 3\dot{w}_1^2 \ddot{w}_2 \\
& \quad - 2\ddot{w}_{10} \dot{w}_{20} \dot{w}_1 - 2\dot{w}_{10} \ddot{w}_{20} \dot{w}_1 - 2\dot{w}_{10} \dot{w}_{20} \ddot{w}_1 - \dot{w}_{10}^2 \ddot{w}_2 - 2\dot{w}_{10} \ddot{w}_{10} \dot{w}_2) \\
& - \frac{Et_w}{2} \left[\frac{2t_f}{t_w} \{f_{1f} f_{2f}^3\}_x + \{f_{1wc} f_{2wc}^3\}_y + \{f_{1wt} f_{2wt}^3\}_y \right] (3\dot{w}_2^2 \ddot{w}_2 - \dot{w}_{20}^2 \ddot{w}_2 \\
& \quad - 2\dot{w}_{20} \ddot{w}_{20} \dot{w}_2),
\end{aligned} \tag{A.11}$$

$$\begin{aligned}
C_{12,s} = & -2Gt_f \{f_{1f}f'_{2f}\}_x [(q_s - q_t) - (q_{s0} - q_{t0})] \pi \left(\frac{\pi z}{L} \sin \frac{\pi z}{L} w_2 - \cos \frac{\pi z}{L} \dot{w}_2 \right) \\
& - Gt_w \left[\frac{2t_f}{t_w} \{g'_{2f}f'_{1f}f_{1f}\}_x + \{g'_{2wc}f'_{1wc}f_{1wc}\}_y + \{g'_{2wt}f'_{1wt}f_{1wt}\}_y \right] (\dot{u}_2 w_1) \\
& - Gt_w \left[\frac{2t_f}{t_w} \{g'_{1f}f_{1f}f'_{2f}\}_x + \{g'_{1wc}f_{1wc}f'_{2wc}\}_y + \{g'_{1wt}f_{1wt}f'_{2wt}\}_y \right] (\dot{u}_1 w_2 + u_1 \dot{w}_2) \\
& - Gt_w \left[\frac{2t_f}{t_w} \{g'_{2f}f_{1f}f'_{2f}\}_x + \{g'_{2wc}f_{1wc}f'_{2wc}\}_y + \{g'_{2wt}f_{1wt}f'_{2wt}\}_y \right] (\dot{u}_2 w_2 + u_2 \dot{w}_2) \\
& - Gt_w \left[\frac{2t_f}{t_w} \{f'^2_{1f}f_{1f}f_{2f}\}_x + \{f'^2_{1wc}f_{1wc}f_{2wc}\}_y + \{f'^2_{1wt}f_{1wt}f_{2wt}\}_y \right] (w_1^2 \ddot{w}_2 \\
& \quad - \dot{w}_{10} \dot{w}_{20} w_1 - w_{10} \ddot{w}_{20} w_1 + w_{10} \dot{w}_{10} \dot{w}_2) \\
& - Gt_w \left[\frac{2t_f}{t_w} \{f'_{1f}f_{1f}^2 f'_{2f}\}_x + \{f'_{1wc}f_{1wc}^2 f'_{2wc}\}_y + \{f'_{1wt}f_{1wt}^2 f'_{2wt}\}_y \right] (\dot{w}_1^2 w_2 + 2w_1 \ddot{w}_1 w_2 \\
& \quad + 2w_1 \dot{w}_1 \dot{w}_2 - \ddot{w}_{10} w_{20} w_1 - \dot{w}_{10} \dot{w}_{20} w_1 - \ddot{w}_{10} w_{10} w_2 - \dot{w}_{10}^2 w_2 - w_{10} \dot{w}_{10} \dot{w}_2) \\
& - Gt_w \left[\frac{2t_f}{t_w} \{f'^2_{2f}f_{2f}f_{1f}\}_x + \{f'^2_{2wc}f_{2wc}f_{1wc}\}_y + \{f'^2_{2wt}f_{2wt}f_{1wt}\}_y \right] (2w_2 \dot{w}_2^2 + w_2^2 \ddot{w}_2 \\
& \quad - \dot{w}_{20}^2 w_2 - w_{20} \ddot{w}_{20} w_2 - w_{20} \dot{w}_{20} \dot{w}_2) \\
& - Gt_w \left[\frac{2t_f}{t_w} \{f_{1f}^2 f'^2_{2f}\}_x + \{f_{1wc}^2 f'^2_{2wc}\}_y + \{f_{1wt}^2 f'^2_{2wt}\}_y \right] (\dot{w}_1 w_2^2 + 2\dot{w}_1 w_2 \dot{w}_2 \\
& \quad - \ddot{w}_{10} w_{20} w_2 - \dot{w}_{10} \dot{w}_{20} w_2 - \dot{w}_{10} w_{20} \dot{w}_2) \\
& - Gt_w \left[\frac{2t_f}{t_w} \{f_{1f}f'_{1f}f_{2f}f'_{2f}\}_x + \{f_{1wc}f'_{1wc}f_{2wc}f'_{2wc}\}_y + \{f_{1wt}f'_{1wt}f_{2wt}f'_{2wt}\}_y \right] (2w_1 \dot{w}_2^2 \\
& \quad + 2w_1 w_2 \ddot{w}_2 - \dot{w}_{20}^2 w_1 - w_{20} \ddot{w}_{20} w_1 - \dot{w}_{10} \dot{w}_{20} w_2 - w_{10} \ddot{w}_{20} w_2 - w_{10} \dot{w}_{20} \dot{w}_2 \\
& \quad + \dot{w}_{10} w_{20} \dot{w}_2) \\
& - 2Gt_f \{f'_{1f}f_{2f}\}_x [(q_s - q_t) - (q_{s0} - q_{t0})] \pi \cos \frac{\pi z}{L} \dot{w}_2 \\
& + Gt_w \left[\frac{2t_f}{t_w} \{g'_{1f}f'_{1f}f_{2f}\}_x + \{g'_{1wc}f'_{1wc}f_{2wc}\}_y + \{g'_{1wt}f'_{1wt}f_{2wt}\}_y \right] u_1 \dot{w}_2 \\
& + Gt_w \left[\frac{2t_f}{t_w} \{g'_{2f}f'_{1f}f_{2f}\}_x + \{g'_{2wc}f'_{1wc}f_{2wc}\}_y + \{g'_{2wt}f'_{1wt}f_{2wt}\}_y \right] u_2 \dot{w}_2 \\
& + Gt_w \left[\frac{2t_f}{t_w} \{f'_{2f}f_{2f}^2 f'_{1f}\}_x + \{f'_{2wc}f_{2wc}^2 f'_{1wc}\}_y + \{f'_{2wt}f_{2wt}^2 f'_{1wt}\}_y \right] (w_2 \dot{w}_2^2 - w_{20} \dot{w}_{20} \dot{w}_2) \\
& + Gt_w \left[\frac{2t_f}{t_w} \{f'^2_{1f}f_{2f}^2\}_x + \{f'^2_{1wc}f_{2wc}^2\}_y + \{f'^2_{1wt}f_{2wt}^2\}_y \right] (w_1 \dot{w}_2^2 - w_{10} \dot{w}_{20} \dot{w}_2),
\end{aligned} \tag{A.12}$$

$$C_{21} = C_{21,bl} + C_{21,d} + C_{21,s}, \tag{A.13}$$

$$\begin{aligned}
C_{21,\text{bl}} = & D_w \nu \left[\frac{2D_f}{D_w} \{f''_{1f} f_{2f}\}_x + \{f''_{1wc} f_{2wc}\}_y + \{f''_{1wt} f_{2wt}\}_y \right] (\ddot{w}_1 - \ddot{w}_{10}) \\
& - 2(1 - \nu) D_w \left[\frac{2D_f}{D_w} \{f'_{1f} f'_{2f}\}_x + \{f'_{1wc} f'_{2wc}\}_y + \{f'_{1wt} f'_{2wt}\}_y \right] (\ddot{w}_1 - \ddot{w}_{10}) \\
& + D_w \left[\frac{2D_f}{D_w} \{f''_{1f} f''_{2f}\}_x + \{f''_{1wc} f''_{2wc}\}_y + \{f''_{1wt} f''_{2wt}\}_y \right] (w_1 - w_{10}) \\
& + D_w \nu \left[\frac{2D_f}{D_w} \{f_{1f} f''_{2f}\}_x + \{f_{1wc} f''_{2wc}\}_y + \{f_{1wt} f''_{2wt}\}_y \right] (\ddot{w}_1 - \ddot{w}_{10}),
\end{aligned} \tag{A.14}$$

$$\begin{aligned}
C_{21,\text{d}} = & Et_w \frac{\pi^2 b}{2L} (q_t - q_{t0}) \left[\frac{4t_f}{bt_w} \{x f_{1f} f_{2f}\}_x + \{f_{1wc} f_{2wc}\}_y \right. \\
& \left. - \{f_{1wt} f_{2wt}\}_y \right] \left(\frac{\pi}{L} \cos \frac{\pi z}{L} \dot{w}_1 + \sin \frac{\pi z}{L} \ddot{w}_1 \right) \\
& + Et_w \Delta \left[\frac{2t_f}{t_w} \{f_{1f} f_{2f}\}_x + \{f_{1wc} f_{2wc}\}_y + \{f_{1wt} f_{2wt}\}_y \right] \ddot{w}_1 \\
& - Et_w \left[\frac{2t_f}{t_w} \{g_{1f} f_{2f}^2\}_x + \{g_{1wc} f_{2wc}^2\}_y + \{g_{1wt} f_{2wt}^2\}_y \right] (\ddot{w}_1 \dot{w}_2 + \dot{w}_1 \ddot{w}_2) \\
& - Et_w \left[\frac{2t_f}{t_w} \{f_{1f} g_{2f} f_{2f}\}_x + \{f_{1wc} g_{2wc} f_{2wc}\}_y + \{f_{1wt} g_{2wt} f_{2wt}\}_y \right] (\dot{w}_1 \ddot{w}_2 + \ddot{w}_1 \dot{w}_2) \\
& - Et_w \left[\frac{2t_f}{t_w} \{g_{1f} f_{1f} f_{2f}\}_x + \{g_{1wc} f_{1wc} f_{2wc}\}_y + \{g_{1wt} f_{1wt} f_{2wt}\}_y \right] (\ddot{w}_1 \dot{w}_1 + \dot{w}_1 \ddot{w}_1) \\
& - \frac{Et_w}{2} \left[\frac{2t_f}{t_w} \{f_{1f}^2 f_{2f}^2\}_x + \{f_{1wc}^2 f_{2wc}^2\}_y + \{f_{1wt}^2 f_{2wt}^2\}_y \right] (3\dot{w}_1^2 \ddot{w}_2 + 6\dot{w}_1 \ddot{w}_1 \dot{w}_2 - \dot{w}_{10}^2 \ddot{w}_2 \\
& \quad - 2\dot{w}_{10} \ddot{w}_{10} \dot{w}_2 - 2\ddot{w}_{10} \dot{w}_{20} \dot{w}_1 - 2\dot{w}_{10} \ddot{w}_{20} \dot{w}_1 - 2\dot{w}_{10} \dot{w}_{20} \ddot{w}_1) \\
& - \frac{Et_w}{2} \left[\frac{2t_f}{t_w} \{f_{1f} f_{2f}^3\}_x + \{f_{1wc} f_{2wc}^3\}_y + \{f_{1wt} f_{2wt}^3\}_y \right] (6\dot{w}_1 \dot{w}_2 \ddot{w}_2 + 3\ddot{w}_1 \dot{w}_2^2 \\
& \quad - 2\ddot{w}_{10} \dot{w}_{20} \dot{w}_2 - 2\dot{w}_{10} \ddot{w}_{20} \dot{w}_2 - 2\dot{w}_{10} \dot{w}_{20} \ddot{w}_2 - \dot{w}_{20}^2 \ddot{w}_1 - 2\dot{w}_{20} \ddot{w}_{20} \dot{w}_1) \\
& - \frac{Et_w}{2} \left[\frac{2t_f}{t_w} \{f_{1f}^3 f_{2f}\}_x + \{f_{1wc}^3 f_{2wc}\}_y + \{f_{1wt}^3 f_{2wt}\}_y \right] (3\dot{w}_1^2 \ddot{w}_1 - \dot{w}_{10}^2 \ddot{w}_1 - 2\dot{w}_{10} \ddot{w}_{10} \dot{w}_1),
\end{aligned} \tag{A.15}$$

$$\begin{aligned}
C_{21,s} = & -2Gt_f \{f'_{1f} f_{2f}\}_x [(q_s - q_t) - (q_{s0} - q_{t0})] \pi \left(\frac{\pi z}{L} \sin \frac{\pi z}{L} w_1 - \cos \frac{\pi z}{L} \dot{w}_1 \right) \\
& - Gt_w \left[\frac{2t_f}{t_w} \{g'_{1f} f'_{2f} f_{2f}\}_x + \{g'_{1wc} f'_{2wc} f_{2wc}\}_y + \{g'_{1wt} f'_{2wt} f_{2wt}\}_y \right] (\dot{w}_1 w_2) \\
& - Gt_w \left[\frac{2t_f}{t_w} \{f'_{1f} g'_{2f} f_{2f}\}_x + \{f'_{1wc} g'_{2wc} f_{2wc}\}_y + \{f'_{1wt} g'_{2wt} f_{2wt}\}_y \right] (w_1 \dot{w}_2 + \dot{w}_1 w_2) \\
& - Gt_w \left[\frac{2t_f}{t_w} \{f'_{1f} g'_{1f} f_{2f}\}_x + \{f'_{1wc} g'_{1wc} f_{2wc}\}_y + \{f'_{1wt} g'_{1wt} f_{2wt}\}_y \right] (\dot{w}_1 w_1 + w_1 \dot{w}_1) \\
& - Gt_w \left[\frac{2t_f}{t_w} \{f_{1f} f'_{2f} f_{2f}\}_x + \{f_{1wc} f'_{2wc} f_{2wc}\}_y + \{f_{1wt} f'_{2wt} f_{2wt}\}_y \right] (\ddot{w}_1 w_2^2 \\
& \quad - \ddot{w}_{10} w_{20} w_2 - \dot{w}_{10} \dot{w}_{20} w_2 + w_{20} \dot{w}_{20} \dot{w}_1) \\
& - Gt_w \left[\frac{2t_f}{t_w} \{f'_{1f} f'_{2f} f_{2f}^2\}_x + \{f'_{1wc} f'_{2wc} f_{2wc}^2\}_y + \{f'_{1wt} f'_{2wt} f_{2wt}^2\}_y \right] (w_1 \dot{w}_2^2 \\
& \quad + 2w_1 w_2 \ddot{w}_2 + 2\dot{w}_1 w_2 \dot{w}_2 - \dot{w}_{10} \dot{w}_{20} w_2 - w_{10} \ddot{w}_{20} w_2 - \dot{w}_{20}^2 w_1 - w_{20} \ddot{w}_{20} w_1 \\
& \quad - w_{20} \dot{w}_{20} \dot{w}_1) \\
& - Gt_w \left[\frac{2t_f}{t_w} \{f_{1f}^2 f_{1f} f_{2f}\}_x + \{f_{1wc}^2 f_{1wc} f_{2wc}\}_y + \{f_{1wt}^2 f_{1wt} f_{2wt}\}_y \right] (2w_1 \dot{w}_1^2 \\
& \quad + w_1^2 \ddot{w}_1 - \dot{w}_{10}^2 w_1 - w_{10} \ddot{w}_{10} w_1 - w_{10} \dot{w}_{10} \dot{w}_1) \\
& - Gt_w \left[\frac{2t_f}{t_w} \{f_{1f}^2 f_{2f}^2\}_x + \{f_{1wc}^2 f_{2wc}^2\}_y + \{f_{1wt}^2 f_{2wt}^2\}_y \right] (w_1^2 \ddot{w}_2 \\
& \quad + 2w_1 \dot{w}_1 \dot{w}_2 - \dot{w}_{10} \dot{w}_{20} w_1 - w_{10} \ddot{w}_{20} w_1 - w_{10} \dot{w}_{20} \dot{w}_1) \\
& - Gt_w \left[\frac{2t_f}{t_w} \{f_{1f} f'_{1f} f_{2f} f'_{2f}\}_x + \{f_{1wc} f'_{1wc} f_{2wc} f'_{2wc}\}_y + \{f_{1wt} f'_{1wt} f_{2wt} f'_{2wt}\}_y \right] (2\dot{w}_1^2 w_2 \\
& \quad + 2w_1 \ddot{w}_1 w_2 - w_{10} \ddot{w}_{10} w_2 - \dot{w}_{10}^2 w_2 - \ddot{w}_{10} w_{20} w_1 - \dot{w}_{10} \dot{w}_{20} w_1 - \dot{w}_{10} w_{20} \dot{w}_1 \\
& \quad + w_{10} \dot{w}_{20} \dot{w}_1) \\
& - 2Gt_f \{f_{1f} f'_{2f}\}_x [(q_s - q_t) - (q_{s0} - q_{t0})] \pi \cos \frac{\pi z}{L} \dot{w}_1 \\
& + Gt_w \left[\frac{2t_f}{t_w} \{f_{1f} g'_{2f} f'_{2f}\}_x + \{f_{1wc} g'_{2wc} f'_{2wc}\}_y + \{f_{1wt} g'_{2wt} f'_{2wt}\}_y \right] \dot{w}_1 w_2 \\
& + Gt_w \left[\frac{2t_f}{t_w} \{g'_{1f} f_{1f} f'_{2f}\}_x + \{g'_{1wc} f_{1wc} f'_{2wc}\}_y + \{g'_{1wt} f_{1wt} f'_{2wt}\}_y \right] w_1 \dot{w}_1 \\
& + Gt_w \left[\frac{2t_f}{t_w} \{f'_{1f} f_{1f}^2 f'_{2f}\}_x + \{f'_{1wc} f_{1wc}^2 f'_{2wc}\}_y + \{f'_{1wt} f_{1wt}^2 f'_{2wt}\}_y \right] (w_1 \dot{w}_1^2 - w_{10} \dot{w}_{10} \dot{w}_1) \\
& + Gt_w \left[\frac{2t_f}{t_w} \{f_{1f}^2 f_{2f}^2\}_x + \{f_{1wc}^2 f_{2wc}^2\}_y + \{f_{1wt}^2 f_{2wt}^2\}_y \right] (\dot{w}_1^2 w_2 - \dot{w}_{10} w_{20} \dot{w}_1).
\end{aligned} \tag{A.16}$$

The detailed expressions of the ODEs for u_1 and u_2 are given thus:

$$(B_{11}B_{22} - B_{12}B_{21})\ddot{u}_1 - B_{12}(D_{21} + D_{22}) + B_{22}(D_{11} + D_{12}) = 0, \quad (\text{A.17})$$

$$(B_{11}B_{22} - B_{12}B_{21})\ddot{u}_2 + B_{11}(D_{21} + D_{22}) - B_{21}(D_{11} + D_{12}) = 0, \quad (\text{A.18})$$

where:

$$B_{11} = Et_w \left[\frac{2t_f}{t_w} \{g_{1f}^2\}_x + \{g_{1wc}^2\}_y + \{g_{1wt}^2\}_y \right], \quad (\text{A.19})$$

$$B_{22} = Et_w \left[\frac{2t_f}{t_w} \{g_{2f}^2\}_x + \{g_{2wc}^2\}_y + \{g_{2wt}^2\}_y \right], \quad (\text{A.20})$$

$$\begin{aligned} D_{11} = & -Et_w \frac{\pi^3 b}{2L^2} (q_t - q_{t0}) \left[\frac{4t_f}{bt_w} \{xg_{1f}\}_x + \{g_{1wc}\}_y - \{g_{1wt}\}_y \right] \cos \frac{\pi z}{L} \\ & + Et_w \left[\frac{2t_f}{t_w} \{g_{1f}f_{1f}^2\}_x + \{g_{1wc}f_{1wc}^2\}_y + \{g_{1wt}f_{1wt}^2\}_y \right] (\dot{w}_1\ddot{w}_1 - \dot{w}_{10}\ddot{w}_{10}) \\ & + 2Gt_f \{g'_{1f}\}_x [(q_s - q_t) - (q_{s0} - q_{t0})] \pi \cos \frac{\pi z}{L} \\ & - Gt_w \left[\frac{2t_f}{t_w} \{g_{1f}'^2\}_x + \{g_{1wc}'^2\}_y + \{g_{1wt}'^2\}_y \right] u_1 \\ & - Gt_w \left[\frac{2t_f}{t_w} \{g'_{1f}f'_{1f}f_{1f}\}_x + \{g'_{1wc}f'_{1wc}f_{1wc}\}_y + \{g'_{1wt}f'_{1wt}f_{1wt}\}_y \right] (\dot{w}_1w_1 - \dot{w}_{10}w_{10}), \end{aligned} \quad (\text{A.21})$$

$$\begin{aligned} D_{22} = & -Et_w \frac{\pi^3 b}{2L^2} (q_t - q_{t0}) \left[\frac{4t_f}{bt_w} \{xg_{2f}\}_x + \{g_{2wc}\}_y - \{g_{2wt}\}_y \right] \cos \frac{\pi z}{L} \\ & + Et_w \left[\frac{2t_f}{t_w} \{g_{2f}f_{2f}^2\}_x + \{g_{2wc}f_{2wc}^2\}_y + \{g_{2wt}f_{2wt}^2\}_y \right] (\dot{w}_2\ddot{w}_2 - \dot{w}_{20}\ddot{w}_{20}) \\ & + 2Gt_f \{g'_{2f}\}_x [(q_s - q_t) - (q_{s0} - q_{t0})] \pi \cos \frac{\pi z}{L} \\ & - Gt_w \left[\frac{2t_f}{t_w} \{g_{2f}'^2\}_x + \{g_{2wc}'^2\}_y + \{g_{2wt}'^2\}_y \right] u_2 \\ & - Gt_w \left[\frac{2t_f}{t_w} \{g'_{2f}f'_{2f}f_{2f}\}_x + \{g'_{2wc}f'_{2wc}f_{2wc}\}_y + \{g'_{2wt}f'_{2wt}f_{2wt}\}_y \right] (\dot{w}_2w_2 - \dot{w}_{20}w_{20}), \end{aligned} \quad (\text{A.22})$$

$$B_{12} = Et_w \left[\frac{2t_f}{t_w} \{g_{1f}g_{2f}\}_x + \{g_{1wc}g_{2wc}\}_y + \{g_{1wt}g_{2wt}\}_y \right], \quad (\text{A.23})$$

$$B_{21} = Et_w \left[\frac{2t_f}{t_w} \{g_{1f}g_{2f}\}_x + \{g_{1wc}g_{2wc}\}_y + \{g_{1wt}g_{2wt}\}_y \right], \quad (\text{A.24})$$

$$\begin{aligned}
D_{12} = & Et_w \left[\frac{2t_f}{t_w} \{g_{1f}f_{2f}^2\}_x + \{g_{1wc}f_{2wc}^2\}_y + \{g_{1wt}f_{2wt}^2\}_y \right] (\dot{w}_2\ddot{w}_2 - \dot{w}_{20}\ddot{w}_{20}) \\
& + Et_w \left[\frac{2t_f}{t_w} \{g_{1f}f_{1f}f_{2f}\}_x + \{g_{1wc}f_{1wc}f_{2wc}\}_y + \{g_{1wt}f_{1wt}f_{2wt}\}_y \right] (\ddot{w}_1\dot{w}_2 + \dot{w}_1\ddot{w}_2 \\
& \quad - \ddot{w}_{10}\dot{w}_{20} - \dot{w}_{10}\ddot{w}_{20}) \\
& - Gt_w \left[\frac{2t_f}{t_w} \{g'_{1f}g'_{2f}\}_x + \{g'_{1wc}g'_{2wc}\}_y + \{g'_{1wt}g'_{2wt}\}_y \right] u_2 \\
& - Gt_w \left[\frac{2t_f}{t_w} \{g'_{1f}f'_{2f}f_{2f}\}_x + \{g'_{1wc}f'_{2wc}f_{2wc}\}_y + \{g'_{1wt}f'_{2wt}f_{2wt}\}_y \right] (\dot{w}_2w_2 - \dot{w}_{20}w_{20}) \\
& - Gt_w \left[\frac{2t_f}{t_w} \{g'_{1f}f'_{1f}f_{2f}\}_x + \{g'_{1wc}f'_{1wc}f_{2wc}\}_y + \{g'_{1wt}f'_{1wt}f_{2wt}\}_y \right] (w_1\dot{w}_2 - w_{10}\dot{w}_{20}) \\
& - Gt_w \left[\frac{2t_f}{t_w} \{g'_{1f}f_{1f}f'_{2f}\}_x + \{g'_{1wc}f_{1wc}f'_{2wc}\}_y + \{g'_{1wt}f_{1wt}f'_{2wt}\}_y \right] (\dot{w}_1w_2 - \dot{w}_{10}w_{20}), \tag{A.25}
\end{aligned}$$

$$\begin{aligned}
D_{21} = & Et_w \left[\frac{2t_f}{t_w} \{f_{1f}^2g_{2f}\}_x + \{f_{1wc}^2g_{2wc}\}_y + \{f_{1wt}^2g_{2wt}\}_y \right] (\dot{w}_1\ddot{w}_1 - \dot{w}_{10}\ddot{w}_{10}) \\
& + Et_w \left[\frac{2t_f}{t_w} \{f_{1f}g_{2f}f_{2f}\}_x + \{f_{1wc}g_{2wc}f_{2wc}\}_y + \{f_{1wt}g_{2wt}f_{2wt}\}_y \right] (\dot{w}_1\ddot{w}_2 + \ddot{w}_1\dot{w}_2 \\
& \quad - \dot{w}_{10}\ddot{w}_{20} - \ddot{w}_{10}\dot{w}_{20}) \\
& - Gt_w \left[\frac{2t_f}{t_w} \{g'_{1f}g'_{2f}\}_x + \{g'_{1wc}g'_{2wc}\}_y + \{g'_{1wt}g'_{2wt}\}_y \right] u_1 \\
& - Gt_w \left[\frac{2t_f}{t_w} \{f_{1f}f'_{1f}g'_{2f}\}_x + \{f_{1wc}f'_{1wc}g'_{2wc}\}_y + \{f_{1wt}f'_{1wt}g'_{2wt}\}_y \right] (\dot{w}_1w_1 - \dot{w}_{10}w_{10}) \\
& - Gt_w \left[\frac{2t_f}{t_w} \{f_{1f}g'_{2f}f'_{2f}\}_x + \{f_{1wc}g'_{2wc}f'_{2wc}\}_y + \{f_{1wt}g'_{2wt}f'_{2wt}\}_y \right] (\dot{w}_1w_2 - \dot{w}_{10}w_{20}) \\
& - Gt_w \left[\frac{2t_f}{t_w} \{f'_{1f}g'_{2f}f_{2f}\}_x + \{f'_{1wc}g'_{2wc}f_{2wc}\}_y + \{f'_{1wt}g'_{2wt}f_{2wt}\}_y \right] (w_1\dot{w}_2 - w_{10}\dot{w}_{20}). \tag{A.26}
\end{aligned}$$

Moreover, equilibrium also requires the minimization of the total potential energy with respect to the generalized coordinates q_t , q_s and Δ , thus leading to three integral conditions:

$$\begin{aligned}
\frac{\partial V}{\partial q_t} = & Et_w \frac{\pi^4 b^2 d}{4L} (q_t - q_{t0}) \left[1 + \frac{t_f b}{3t_w d} \right] - Gt_f b L [(q_s - q_t) - (q_{s0} - q_{t0})] \pi^2 \\
& + 2\pi Gt_f \int_0^L \left[\{g'_{1f}\}_x u_1 + \{f'_{1f}f_{1f}\}_x (\dot{w}_1w_1 - \dot{w}_{10}w_{10}) + \{g'_{2f}\}_x u_2 \right. \\
& \quad + \{f'_{2f}f_{2f}\}_x (\dot{w}_2w_2 - \dot{w}_{20}w_{20}) + \{f'_{1f}f_{2f}\}_x (w_1\dot{w}_2 - w_{10}\dot{w}_{20}) \\
& \quad \left. + \{f_{1f}f'_{2f}\}_x (\dot{w}_1w_2 - \dot{w}_{10}w_{20}) \right] \cos \frac{\pi z}{L} dz
\end{aligned}$$

$$\begin{aligned}
& - \frac{\pi^2 E b t_w}{2L} \int_0^L \left[\left(\{g_{1wc}\}_y - \{g_{1wt}\}_y + \frac{4t_f}{bt_w} \{xg_{1f}\}_x \right) \dot{u}_1 \right. \\
& \quad + \left(\frac{1}{2} \{f_{1wc}^2\}_y - \frac{1}{2} \{f_{1wt}^2\}_y + \frac{2t_f}{bt_w} \{xf_{1f}^2\}_x \right) (\dot{w}_1^2 - \dot{w}_{10}^2) \\
& \quad + \left(\{f_{1wc}f_{2wc}\}_y - \{f_{1wt}f_{2wt}\}_y + \frac{4t_f}{bt_w} \{xf_{1f}f_{2f}\}_x \right) (\dot{w}_1\dot{w}_2 - \dot{w}_{10}\dot{w}_{20}) \\
& \quad + \left(\frac{1}{2} \{f_{2wc}^2\}_y - \frac{1}{2} \{f_{2wt}^2\}_y + \frac{2t_f}{bt_w} \{xf_{2f}^2\}_x \right) (\dot{w}_2^2 - \dot{w}_{20}^2) \\
& \quad \left. + \left(\{g_{2wc}\}_y - \{g_{2wt}\}_y + \frac{4t_f}{bt_w} \{xg_{2f}\}_x \right) \dot{u}_2 \right] \sin \frac{\pi z}{L} dz = 0, \quad (\text{A.27})
\end{aligned}$$

$$\begin{aligned}
\frac{\partial V}{\partial q_s} &= \pi^2 G t_f b L [(q_s - q_t) - (q_{s0} - q_{t0})] + \frac{\pi^4 E I_w (q_s - q_{s0})}{L} - P \frac{\pi^2 L q_s}{2} \\
& \quad - 2\pi G t_f \int_0^L \left[\{g'_{1f}\}_x u_1 + \{f'_{1f}f_{1f}\}_x (\dot{w}_1 w_1 - \dot{w}_{10} w_{10}) + \{g'_{2f}\}_x u_2 \right. \\
& \quad \quad + \{f'_{2f}f_{2f}\}_x (\dot{w}_2 w_2 - \dot{w}_{20} w_{20}) + \{f'_{1f}f_{2f}\}_x (w_1 \dot{w}_2 - w_{10} \dot{w}_{20}) \\
& \quad \quad \left. + \{f_{1f}f'_{2f}\}_x (\dot{w}_1 w_2 - \dot{w}_{10} w_{20}) \right] \cos \frac{\pi z}{L} dz = 0, \quad (\text{A.28})
\end{aligned}$$

$$\begin{aligned}
\frac{\partial V}{\partial \Delta} &= 2Et_w dL \Delta \left(1 + \frac{bt_f}{dt_w} \right) - Et_w \int_0^L \left[\left(\{g_{1wc}\}_y + \{g_{1wt}\}_y + \frac{2t_f}{t_w} \{g_{1f}\}_x \right) \dot{u}_1 \right. \\
& \quad + \left(\frac{1}{2} \{f_{1wc}^2\}_y + \frac{1}{2} \{f_{1wt}^2\}_y + \frac{t_f}{t_w} \{f_{1f}^2\}_x \right) (\dot{w}_1^2 - \dot{w}_{10}^2) \\
& \quad + \left(\{f_{1wc}f_{2wc}\}_y + \{f_{1wt}f_{2wt}\}_y + \frac{2t_f}{t_w} \{f_{1f}f_{2f}\}_x \right) (\dot{w}_1\dot{w}_2 - \dot{w}_{10}\dot{w}_{20}) \\
& \quad + \left(\frac{1}{2} \{f_{2wc}^2\}_y + \frac{1}{2} \{f_{2wt}^2\}_y + \frac{t_f}{t_w} \{f_{2f}^2\}_x \right) (\dot{w}_2^2 - \dot{w}_{20}^2) \\
& \quad \left. + \left(\{g_{2wc}\}_y + \{g_{2wt}\}_y + \frac{2t_f}{t_w} \{g_{2f}\}_x \right) \dot{u}_2 \right] dz - PL = 0. \quad (\text{A.29})
\end{aligned}$$

Two boundary conditions are obtained from the variational formulation process with regards to the in-plane strain, *i.e.* :

$$\left[\frac{\partial \mathcal{L}}{\partial \dot{u}_1} \delta u_1 \right] \Big|_0^L = 0 \quad \text{and} \quad \left[\frac{\partial \mathcal{L}}{\partial \dot{u}_2} \delta u_2 \right] \Big|_0^L = 0, \quad (\text{A.30})$$

which can be expressed thus:

$$\begin{aligned}
& - \left[\{g_{1wc}\}_y + \{g_{1wt}\}_y + \frac{2t_f}{t_w} \{g_{1f}\}_x \right] \Delta + \left[\{g_{1wc}^2\}_y + \{g_{1wt}^2\}_y + \frac{2t_f}{t_w} \{g_{1f}^2\}_x \right] \dot{u}_1(0) \\
& + \left[\frac{1}{2} \{g_{1wc}f_{1wc}^2\}_y + \frac{1}{2} \{g_{1wt}f_{1wt}^2\}_y + \frac{t_f}{t_w} \{g_{1f}f_{1f}^2\}_x \right] [\dot{w}_1^2(0) - \dot{w}_{10}^2(0)] \\
& + \left[\{g_{1wc}g_{2wc}\}_y + \{g_{1wt}g_{2wt}\}_y + \frac{2t_f}{t_w} \{g_{1f}g_{2f}\}_x \right] \dot{u}_2(0) \\
& + \left[\frac{1}{2} \{g_{1wc}f_{2wc}^2\}_y + \frac{1}{2} \{g_{1wt}f_{2wt}^2\}_y + \frac{t_f}{t_w} \{g_{1f}f_{2f}^2\}_x \right] [\dot{w}_2^2(0) - \dot{w}_{20}^2(0)] \quad (\text{A.31}) \\
& + \left[\{g_{1wc}f_{1wc}f_{2wc}\}_y + \{g_{1wt}f_{1wt}f_{2wt}\}_y + \frac{2t_f}{t_w} \{g_{1f}f_{1f}f_{2f}\}_x \right] [\dot{w}_1(0)\dot{w}_2(0) \\
& \quad - \dot{w}_{10}(0)\dot{w}_{20}(0)] \\
& + \frac{P}{2Et_w(b+d)} \left[2\{g_{1f}\}_x + \{g_{1wc}\}_y + \{g_{1wt}\}_y \right] = 0,
\end{aligned}$$

$$\begin{aligned}
& - \left[\{g_{2wc}\}_y + \{g_{2wt}\}_y + \frac{2t_f}{t_w} \{g_{2f}\}_x \right] \Delta + \left[\{g_{2wc}^2\}_y + \{g_{2wt}^2\}_y + \frac{2t_f}{t_w} \{g_{2f}^2\}_x \right] \dot{u}_2(0) \\
& + \left[\frac{1}{2} \{g_{2wc}f_{2wc}^2\}_y + \frac{1}{2} \{g_{2wt}f_{2wt}^2\}_y + \frac{t_f}{t_w} \{g_{2f}f_{2f}^2\}_x \right] [\dot{w}_2^2(0) - \dot{w}_{20}^2(0)] \\
& + \left[\{g_{2wc}g_{1wc}\}_y + \{g_{2wt}g_{1wt}\}_y + \frac{2t_f}{t_w} \{g_{2f}g_{1f}\}_x \right] \dot{u}_1(0) \\
& + \left[\frac{1}{2} \{g_{2wc}f_{1wc}^2\}_y + \frac{1}{2} \{g_{2wt}f_{1wt}^2\}_y + \frac{t_f}{t_w} \{g_{2f}f_{1f}^2\}_x \right] [\dot{w}_1^2(0) - \dot{w}_{10}^2(0)] \\
& + \left[\{g_{2wc}f_{2wc}f_{1wc}\}_y + \{g_{2wt}f_{2wt}f_{1wt}\}_y + \frac{2t_f}{t_w} \{g_{2f}f_{2f}f_{1f}\}_x \right] [\dot{w}_2(0)\dot{w}_1(0) - \dot{w}_{20}(0)\dot{w}_{10}(0)] \\
& + \frac{P}{2Et_w(b+d)} \left[2\{g_{2f}\}_x + \{g_{2wc}\}_y + \{g_{2wt}\}_y \right] = 0. \quad (\text{A.32})
\end{aligned}$$

Appendix B

Zone 2–3 boundary determination from double modulus theory

Van der Neut predicted the boundary between zones 2 and 3 using Engesser’s ‘double-modulus’ theory (Bažant & Cedolin, 1991). The same approach is adopted currently to predict the boundary for the rectangular hollow section strut.

It has been verified that global and local buckling is triggered simultaneously in zone 2. Prior to buckling ($w = 0$), the stress distribution is uniform, $\sigma_0 = P/A$. It has been assumed in the current work that plane cross-sections remain plane but not normal to the deflected centre line of the strut at the initial buckling stage. At the commencement of mode interaction, the compressed side of the strut would remain buckled and undergo further shortening, hence further loading, and the less compressed side would undergo relative extension, hence unloading. Somewhere within the cross-section, there is a neutral axis at which the axial strain would not change; its distance from the more and less compressed sides of the strut being denoted as b_1 and b_2 respectively, where $b_1 + b_2 = b$, as shown in Figure B.1(b). The effective axial stiffness in the more compressed side of the cross-section would drop due to plate buckling. It is assumed that the distribution of the

effective elastic axial stiffness is proportional to $\eta_f(x)E$ and $\eta_w(y)E$ in the flanges and the more compressed web respectively.

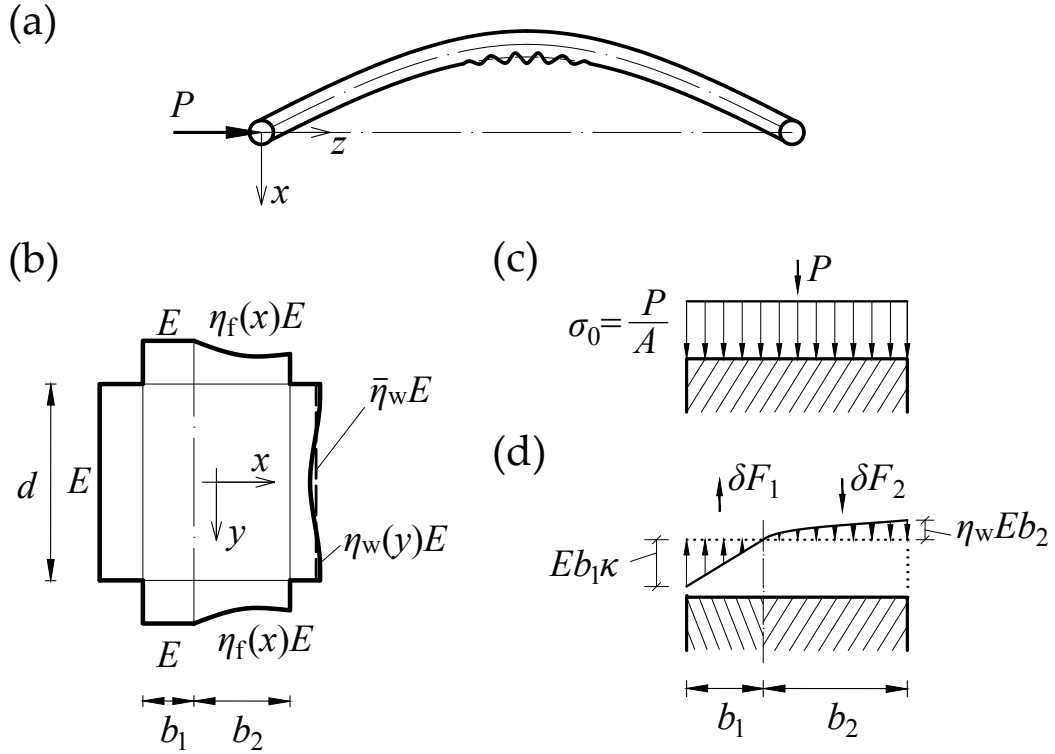


Figure B.1: (a) Local–global mode interaction in a simply-supported rectangular hollow section strut under the concentric axial load P . (b) Cross-section stiffness distribution at the starting point of the local–global mode interaction. The function $\eta_f(x)$ and $\eta_w(y)$ are the stiffness reduction factors for the flanges and the more compressed web respectively due to local buckling. (c) Normal stress distribution before mode interaction is triggered. (d) The variation in the normal stress due to mode interaction. The curvature due to global buckling is κ ; δF_1 and δF_2 are the relative load changes in the less and more compressed sides of the cross-section respectively, which include the unloading and loading of the flanges and webs.

According to the assumption of plane cross-sections remaining plane and the assumed effective axial stiffness distribution above, the incremental resultant force at the less compressed side δF_1 and more compressed side δF_2 can be obtained, thus:

$$\delta F_1 = \int_{-d/2}^{d/2} E t_w \varepsilon_{wt} dy + 2 \int_0^{b_1} E t_f \varepsilon_f dx = E b_1 \kappa (d t_w + b_1 t_f), \quad (\text{B.1})$$

$$\delta F_2 = \int_{-d/2}^{d/2} \eta_w(y) E \varepsilon_{wc} dy + 2 \int_0^{b_2} \eta_f(x) E t_f \varepsilon_f dx = E b_2 \kappa \left(\bar{\eta}_w dt_w + \frac{t_f}{b_2} \int_0^{b_2} x \eta_f(x) dx \right), \tag{B.2}$$

where $\varepsilon_{wt} = b_1 \kappa$ and $\varepsilon_{wc} = b_2 \kappa$ are the direct strains in the less compressed and more compressed webs respectively; $\varepsilon_f = x \kappa$ is the direct strain in the flanges; κ is the curvature due to global buckling; $\bar{\eta}_w = \int_{-d/2}^{d/2} \eta_w(y) dy$ is the equivalent stiffness reduction factor in the more compressed web.

The condition of constant axial load requires that the resultants δF_1 and δF_2 of the incremental normal stress in the more and less compressed sides must be of equal magnitudes, thus:

$$\delta F_1 = \delta F_2. \tag{B.3}$$

As for the moment M in the cross-section,

$$M = M_1 + M_2, \tag{B.4}$$

where:

$$\begin{aligned} M_1 &= \int_{b_1-t_w/2}^{b_1+t_w/2} \int_{-d/2}^{d/2} x E t_w \varepsilon_{wt} dy dx + 2 \int_0^{b_1} x E t_f \varepsilon_f dx \\ &= E \kappa \left(b_1^2 dt_w + \frac{dt_w^3}{12} + \frac{2b_1^3 t_f}{3} \right), \end{aligned} \tag{B.5}$$

$$\begin{aligned} M_2 &= \int_{b_2-t_w/2}^{b_2+t_w/2} \int_{-d/2}^{d/2} x \eta_w(y) E t_w \varepsilon_{wc} dy dx + 2 \int_0^{b_2} x \eta_f(x) E t_f \varepsilon_f dx \\ &= E \kappa \left[\bar{\eta}_w \left(b_2^2 dt_w + \frac{dt_w^3}{12} \right) + 2 \int_0^{b_2} x^2 \eta_f(x) t_f dx \right], \end{aligned} \tag{B.6}$$

this can be rewritten as:

$$M = \Phi_r E I \kappa, \tag{B.7}$$

where $I = b^3 t_f / 6 + b^2 dt_w + dt_w^3 / 6$ is the second moment of area about the weak neutral axis of the entire cross-section before buckling. Therefore, the bending stiffness reduction

factor due to local buckling in the more compressed side can be written as:

$$\begin{aligned}\Phi_r &= \frac{(M_1 + M_2)}{EI\kappa} \\ &= \frac{(b_1^2 dt_w + dt_w^3/12 + 2b_1^3 t_f/3) + \bar{\eta}_w (b_2^2 dt_w + dt_w^3/12) + 2 \int_0^{b_2} x^2 \eta_f(x) t_f dx}{b^3 t_f/6 + b^2 dt_w + dt_w^3/6},\end{aligned}\tag{B.8}$$

where b_1 and b_2 can be obtained explicitly using the constant axial force condition from Eq. (B.3). It should be noted that if $t_f \rightarrow 0$ and $b \gg t_w$, *i.e.* making both flanges having a negligible size, Φ_r would reduce to the expression developed by Van der Neut, where $\Phi_r = 2\bar{\eta}_w / (1 + \bar{\eta}_w)$.

Appendix C

Buckling load, wavelength and cross-section profiles of pure local buckling mode

Since the longitudinal component of the pure local buckling mode under compression is periodic, a plate element with length l_e , which is equal to the half wavelength of the local buckling mode in the longitudinal direction, is isolated for consideration, as shown in Figure [C.1\(a\)](#). The formulation begins with the definition of the buckling displacement field in the webs $w_w(y, z)$ and flanges $w_f(x, z)$:

$$w_w(y, z) = Qf_{1w}(y) \sin \frac{\pi z}{l_e}, \quad w_f(x, z) = Qf_{1f}(x) \sin \frac{\pi z}{l_e}, \quad (\text{C.1})$$

where Q is a generalized coordinate representing the amplitude of the local buckling mode; f_{1w} and f_{1f} are cross-sectional components of the local buckling mode in the webs and flanges respectively. The functions f_{1w} and f_{1f} , which are valid from square hollow sections to rectangular hollow sections, are derived based on a semi-analytical method. Since the pure local buckling mode is symmetric, symmetric shape functions are used for both flanges

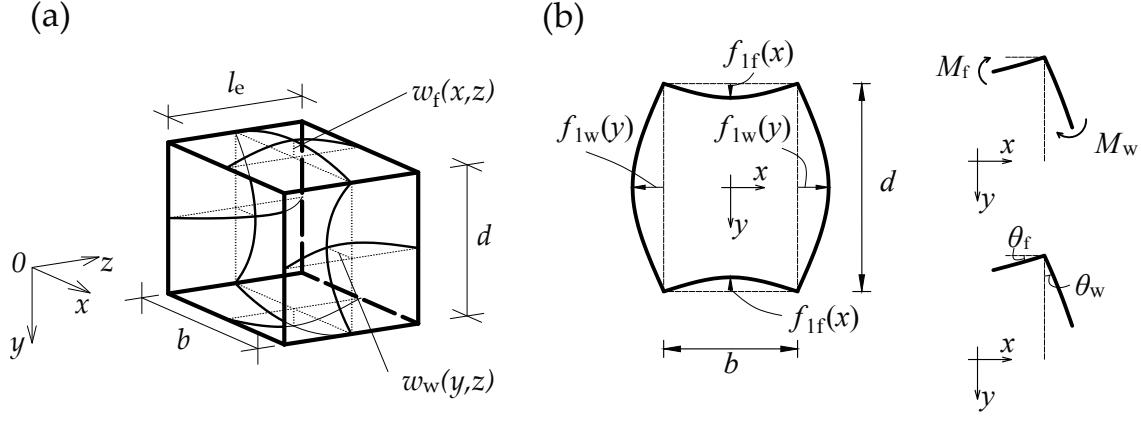


Figure C.1: (a) Deformed shape of an isolated thin-walled RHS strut element under pure compression. Effective length of the element is l_e with depth d and width b . The buckling displacement distributions in the webs and flanges are defined as $w_w(y, z)$ and $w_f(x, z)$ respectively. (b) Cross-section profile of the local buckling mode and the static and kinematic boundary conditions at the corner joint, where M and θ represent bending moments and rotations at the cross-section corners respectively.

and webs. For convenience, it is assumed that the amplitude of the buckling mode in the web is unity, thus:

$$f_{1w}(y) = B_0 \cos\left(\frac{\pi y}{d}\right) + (1 - B_0) \left(1 - \frac{4y^2}{d}\right), \quad (\text{C.2})$$

$$f_{1f}(x) = A_1 \left(1 - \frac{4x^2}{b}\right) + A_2 \cos\left(\frac{\pi x}{b}\right). \quad (\text{C.3})$$

Three boundary conditions are required for determining the three unknowns A_1 , A_2 and B_0 . However, there are only two available from the kinematic and static boundary conditions, as shown in Figure [C.1](#)(b):

$$M_f + M_w = 0, \quad (\text{C.4})$$

$$\theta_f = \theta_w, \quad (\text{C.5})$$

where:

$$M_f(x = b/2) = \left[D_f \left(\frac{\partial^2 w_f}{\partial x^2} + \nu \frac{\partial^2 w_f}{\partial z^2} \right) \right]_{x=b/2} = \left(D_f \frac{d^2 f_{1f}}{dx^2} \Big|_{x=b/2} \right) Q \sin \frac{\pi z}{l_e}, \quad (\text{C.6})$$

$$M_w(y = d/2) = \left[D_w \left(\frac{\partial^2 w_w}{\partial y^2} + \nu \frac{\partial^2 w_w}{\partial z^2} \right) \right]_{y=d/2} = \left(D_w \frac{d^2 f_{1w}}{dy^2} \Big|_{y=d/2} \right) Q \sin \frac{\pi z}{l_e}, \quad (\text{C.7})$$

$$\theta_f = - \frac{df_{1f}}{dx} \Big|_{x=b/2}, \quad \theta_w = \frac{df_{1w}}{dy} \Big|_{y=d/2}. \quad (\text{C.8})$$

The third condition is obtained in conjunction with data generated from the FE results. A parametric study was conducted to obtain the ratio of the amplitudes in the flange and the web for different cross-section aspect ratios, ranging from 1 to 3. The results are shown in Figure C.2 and a function describing the relationship is fitted:

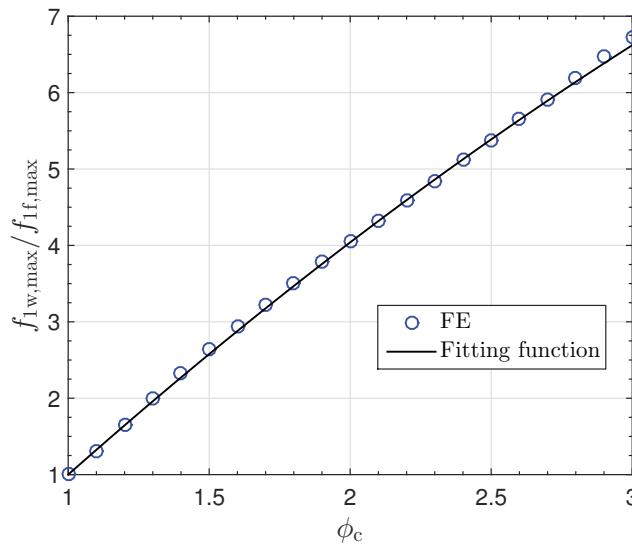


Figure C.2: Ratio of the local buckling modal amplitude in the web and flange for thin-walled RHS struts with different cross-section aspect ratios $\phi_c=d/b$.

$$\frac{f_{1w,max}}{f_{1f,max}} = \frac{1}{A_1 + A_2} = -0.23\phi_c^2 + 3.73\phi_c - 2.5, \quad (\text{C.9})$$

with $\phi_c = d/b$ being the cross-section aspect ratio. The mean ratio of the results from Eq. (C.9) to the FE results in the range shown is 0.993 and the maximum COV is 0.94%.

From Eqs. (C.4)–(C.5) and (C.9), the coefficients in Eqs. (C.2) and (C.3) can be deter-

mined:

$$A_1 = \frac{\pi (250 - 273\phi_c + 23\phi_c^2)}{\phi_c (214.60 - 105.58\phi_c - 300.44\phi_c^2 + 19.74\phi_c^3)}, \quad (\text{C.10})$$

$$A_2 = \frac{-3926.99 + 3859.07\phi_c - 790.49\phi_c^2}{5\phi_c (214.60 - 105.58\phi_c - 300.44\phi_c^2 + 19.74\phi_c^3)}, \quad (\text{C.11})$$

$$B_0 = \frac{214.60 + 679.81\phi_c - 1158.10\phi_c^2 + 92\phi_c^3}{214.60 - 105.58\phi_c - 300.44\phi_c^2 + 19.74\phi_c^3}. \quad (\text{C.12})$$

Based on the fitted functions for the webs and flanges in Eqs. (C.2) and (C.3), the linear buckling load and the corresponding wavelength is derived using small deflection theory (Timoshenko & Gere, 1961). The methodology used is very similar to that adopted in §4.5. The strain energy U in the strut element comprises the local bending energy in both flanges $U_{b,f}$ and webs $U_{b,w}$:

$$\begin{aligned} U &= U_{b,f} + U_{b,w}, \\ &= D_f \int_0^{l_e} \int_{-b/2}^{b/2} \left\{ \left(\frac{\partial^2 w_f}{\partial z^2} + \frac{\partial^2 w_f}{\partial x^2} \right)^2 \right. \\ &\quad \left. - 2(1 - \nu) \left[\frac{\partial^2 w_f}{\partial z^2} \frac{\partial^2 w_f}{\partial x^2} - \left(\frac{\partial^2 w_f}{\partial z \partial x} \right)^2 \right] \right\} dx dz \\ &\quad + D_w \int_0^{l_e} \int_{-d/2}^{d/2} \left\{ \left(\frac{\partial^2 w_{wc}}{\partial z^2} + \frac{\partial^2 w_{wc}}{\partial y^2} \right)^2 \right. \\ &\quad \left. - 2(1 - \nu) \left[\frac{\partial^2 w_{wc}}{\partial z^2} \frac{\partial^2 w_{wc}}{\partial y^2} - \left(\frac{\partial^2 w_{wc}}{\partial z \partial y} \right)^2 \right] \right\} dy dz. \end{aligned} \quad (\text{C.13})$$

The work done by the load term is given by the following standard expression:

$$P\Delta = \sigma_1^C t \left[\int_0^{l_e} \int_{-b/2}^{b/2} \left(\frac{\partial w_f}{\partial z} \right)^2 dx dz + \int_0^{l_e} \int_{-d/2}^{d/2} \left(\frac{\partial w_w}{\partial z} \right)^2 dy dz \right]. \quad (\text{C.14})$$

The total potential energy can thus be written:

$$V = U - P\Delta, \quad (\text{C.15})$$

and by setting $\partial V/\partial Q = 0$ for equilibrium, the following expression for the local buckling coefficient k_p of the more compressed web, where $\sigma_1^C = k_p \pi^2 E/[12(1 - \nu^2)(d/t)^2]$, can be obtained:

$$k_p = a_0 + a_1 \phi_1^2 + \frac{1}{\phi_1^2}, \quad (\text{C.16})$$

with $\phi_1 = l_e/d$ alongside a_0 and a_1 being constants that are functions of ϕ_c , A_1 , A_2 and B_0 , thus:

$$a_0 = \frac{10\phi_c (H_{01}\phi_c + H_{02})}{H_{03}\phi_c + H_{04}}, \quad a_1 = \frac{15\phi_c (H_{11}\phi_c^3 + H_{12})}{\pi (H_{03}\phi_c + H_{04})}, \quad (\text{C.17})$$

where:

$$\begin{aligned} H_{01} &= 32\pi A_1^2 + 192A_1A_2 + 3\pi^3 A_2^2, \\ H_{02} &= (3\pi^3 + 32\pi - 192) B_0^2 + (-64\pi + 192) B_0 + 32\pi, \\ H_{03} &= (31\pi^3 - 960) B_0^2 + (-32\pi^3 + 960) B_0 + 16\pi^3, \\ H_{04} &= 16A_1^2\pi^3 + 15A_2^2\pi^3 + 960A_1A_2, \\ H_{11} &= \pi^4 A_2^2 + 64\pi A_1A_2 + 128A_1^2, \\ H_{12} &= (\pi^4 - 64\pi + 128) B_0^2 + (64\pi - 256) B_0 + 128. \end{aligned} \quad (\text{C.18})$$

Defining $\phi_1 = (a_1)^{-1/4}$, an expression for the minimum value of k_p can be determined:

$$k_p = a_0 + 2\sqrt{a_1}, \quad (\text{C.19})$$

with the half-wavelength $l_e = \lambda_{p,\text{LBA}}/2 = d (a_1)^{-1/4}$.

The comparison between the analytical model expression obtained in Eq. (C.19) and the FE results is shown in Figure C.3(a). In the range of ϕ_c from 1 to 3, the average value of $k_{p,\text{FE}}/k_{p,\text{Eq}}$ is 1.001 and the COV is 0.04%, which demonstrates an excellent fit. Moreover, since Eq. (C.19) is relatively complex, an explicit expression was fitted:

$$k_p = 5.44 - 1.44\phi_c^{-2.54}, \quad (\text{C.20})$$

which is also shown in Figure C.3. The mean ratio of the results from Eq. (C.20) to the

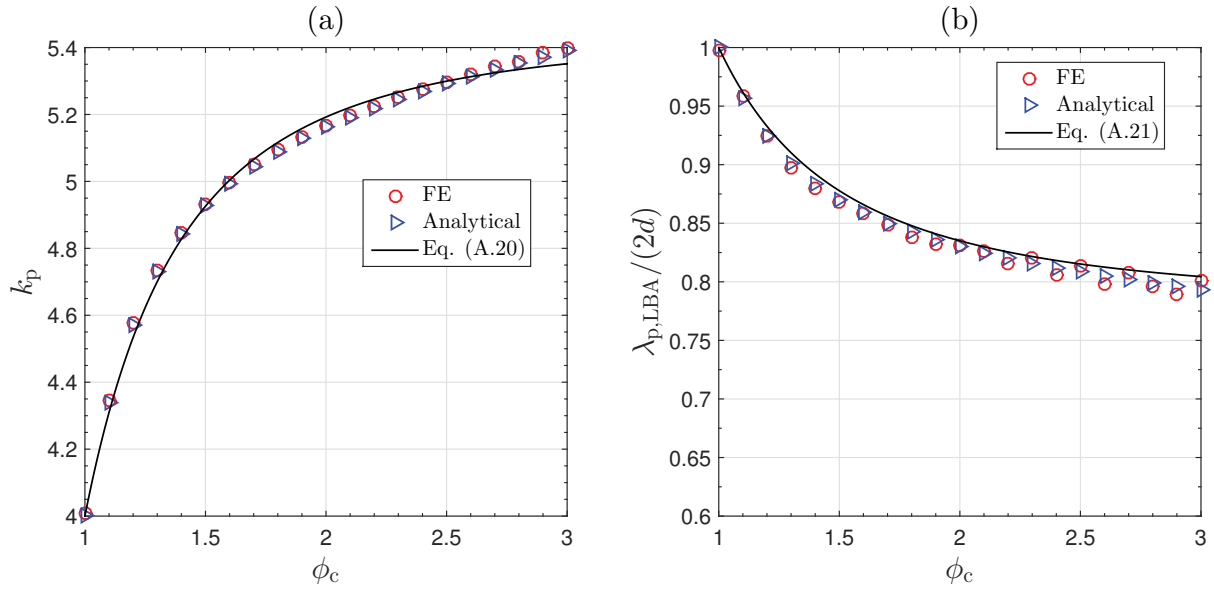


Figure C.3: (a) Relationship between local buckling coefficient k_p and cross-section aspect ratio ϕ_c for thin-walled rectangular hollow section struts from the fitted function Eq. (C.20) and FE results. (b) Relationship of normalized longitudinal wavelength versus ϕ_c from FE, analytical models and the fitted function Eq. (C.21).

FE results $k_{p,FE}$ is 0.999 and the COV is 0.50%.

Figure C.3(b) presents the relationship of the normalized wavelength of the pure local buckling mode versus the cross-section aspect ratio. The results from the analytical model show excellent comparisons with the FE model. It should be noted that the value of l_c is the length corresponding to the lowest k_p . However, the actual wavelength is also affected by the strut length since the number of half-waves should be an integer. This may explain the jump in the results when the cross-section aspect ratio is relatively large, *i.e.* when the wavelength is relatively large. A function is also fitted for the relationship:

$$\phi_l = \lambda_{p,LBA}/(2d) = 0.78 + 0.22\phi_c^{-2}. \quad (C.21)$$

The average ratio of ϕ_l from the fitted equation to the analytical model is 1.008 and the COV is 0.29%.

Figure C.4 presents the cross-section profile of the local buckling mode from FE and the

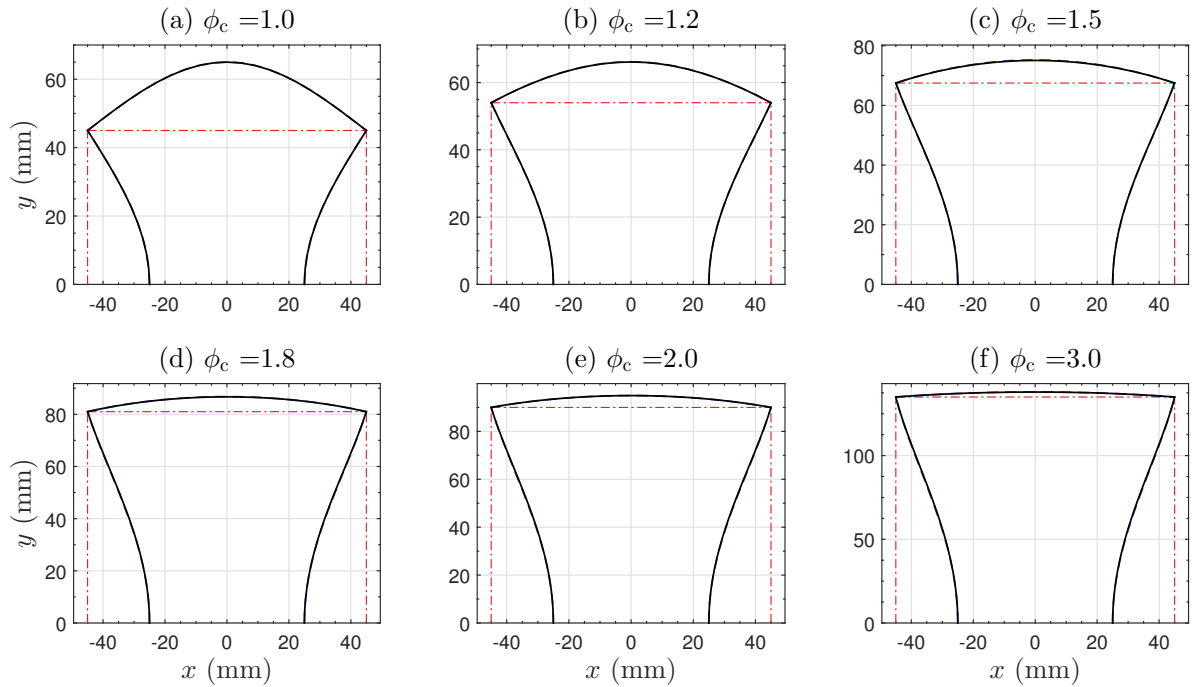


Figure C.4: Cross-section profile of the linear buckling mode for different cross-section aspect ratios ranging from 1 to 3. Dashed and solid lines represent the results from FE and analytical models respectively; the dot-dashed line represents the undeformed shape. Note that displacements shown have been amplified by a factor of 20 to aid visualization, but the differences are barely visible.

fitted functions, *i.e.* Eqs. (C.2) and (C.3), the differences being barely distinguishable. The excellent comparisons verify the effectiveness of the currently chosen cross-section functions.

References

- Abambres, M., & Quach, W. M. 2016. Residual stresses in steel members: a review of available analytical expressions. *Int. J. Struct. Integr.*, **7**(1), 70–94.
- ABAQUS. 2014. *Version 6.14*. Providence RI, USA: Dassault Systèmes.
- Afshan, S., Francis, P., Baddoo, N. R., & Gardner, L. 2015. Reliability analysis of structural stainless steel design provisions. *J. Constr. Steel. Res.*, **114**(Supplement C), 293–304.
- AISI:S100-2007. 2007. *North American specification for the design of cold-formed steel members*. American Iron and Steel Institute.
- Ali, M. A., & Sridharan, S. 1988. A versatile model for interactive buckling of columns and beam-columns. *Int. J. Solids Struct.*, **24**(5), 481–496.
- Ashby, M. 2011. *Materials selection in mechanical design (4th edition)*. Oxford: Butterworth-Heinemann.
- Augusti, G. 1964. *Some problems in structural instability with special reference to beam of I-section*. Ph.D. thesis, University of Cambridge.
- Bai, L. 2014. *Interactive buckling in thin-walled I-section struts*. Ph.D. thesis, Imperial College London.
- Bai, L., & Wadee, M. A. 2015a. Imperfection sensitivity of thin-walled I-section struts susceptible to cellular buckling. *Int. J. Mech. Sci.*, **104**, 162–173.

- Bai, L., & Wadee, M. A. 2015b. Mode interaction in thin-walled I-section struts with semi-rigid flange-web joints. *Int. J. Non-Linear Mech.*, **69**, 71–83.
- Bai, L., & Wadee, M. A. 2016. Slenderness effects in thin-walled I-section struts susceptible to local–global mode interaction. *Eng. Struct.*, **124**, 128–141.
- Bai, L., Wang, F., Wadee, M. A., & Yang, J. 2017. Nonlinear mode interaction in equal-leg angle struts susceptible to cellular buckling. *Proc. R. Soc. A*, **473**(2207), 20170583.
- Ban, H., Shi, G., Shi, Y., & Wang, Y. 2013. Residual stress of 460mpa high strength steel welded box section: Experimental investigation and modeling. *Thin-Walled Struct.*, **64**, 73–82.
- Barbero, E. J. 2013. *Finite element analysis of composite materials using abaqus*. CRC press.
- Barbero, E. J., & Tomblin, J. 1994. A phenomenological design equation for FRP columns with interaction between local and global buckling. *Thin-Walled Struct.*, **18**(2), 117–131.
- Barbero, E. J., Dede, E. K., & Jones, S. 2000. Experimental verification of buckling-mode interaction in intermediate-length composite columns. *Int. J. Solids Struct.*, **37**(29), 3919–3934.
- Basaglia, C., Camotim, D., & Silvestre, N. 2011. Non-linear gbt formulation for open-section thin-walled members with arbitrary support conditions. *Comput. Struct.*, **89**(21), 1906–1919.
- Bathe, K.-J. 2006. *Finite element procedures*. Prentice-Hall.
- Bažant, Z. P., & Cedolin, L. 1991. *Stability of structures: Elastic, inelastic, fracture, and damage theories*. Oxford: Oxford University Press.
- Bažant, Z. P., & Cedolin, L. 2010. *Stability of structures: Elastic, inelastic, fracture and damage theories*. World Scientific.

- Bebiano, R., Pina, P., Silvestre, N., & Camotim, D. 2008. *GBTUL-buckling and vibration analysis of thin-walled members*. Available from <http://www.civil.ist.utl.pt/gbt/>.
- Becque, J. 2008. *The interaction of local and overall buckling of cold-formed stainless steel columns*. Ph.D. thesis, University of Sydney.
- Becque, J. 2014. Local-overall interaction buckling of inelastic columns: A numerical study of the inelastic Van der Neut column. *Thin-Walled Struct.*, **81**, 101–107.
- Becque, J., & Rasmussen, K. J. R. 2009a. Experimental investigation of the interaction of local and overall buckling of stainless steel I-columns. *ASCE J. Struct. Eng.*, **135**(11), 1340–1348.
- Becque, J., & Rasmussen, K. J. R. 2009b. Numerical investigation of the interaction of local and overall buckling of stainless steel I-columns. *ASCE J. Struct. Eng.*, **135**(11), 1349–1356.
- Belytschko, T., Liu, W. K., Moran, B., & Elkhodary, K. 2000. *Nonlinear finite elements for continua and structures*. New York: Wiley.
- Benitot, R., & Sridharan, S. 1984. Mode interaction in thin-walled structural members. *J. Struct. Mech.*, **12**(4), 517–542.
- Bijlaard, P. P. 1951a. Analysis of the elastic and plastic stability of sandwich plates by the method of split rigidities-I. *J. Aeronaut. Sci.*, **18**(5), 339–349.
- Bijlaard, P. P. 1951b. Analysis of the elastic and plastic stability of sandwich plates by the method of split rigidities-II. *J. Aeronaut. Sci.*, **18**(12), 790–796.
- Bijlaard, P. P., & Fisher, G. P. 1952. *Interaction of column and local buckling in compression members*. Tech. rept. National Advisory Committee for Aeronautics.
- Bijlaard, P. P., & Fisher, G. P. 1953. *Column strength of H-sections and square tubes in postbuckling range of component plates*. Tech. rept. National Advisory Committee for Aeronautics.

- Bleich, F. 1952. *Buckling strength of metal structures*. New York: McGraw-Hill.
- Bock, M., Mirada, F.X., & Real, E. 2015. Statistical evaluation of a new resistance model for cold-formed stainless steel cross-sections subjected to web crippling. *Int. J. Steel Struct.*, **15**(1), 227–244.
- Brazier, L. G. 1927. On the flexure of thin cylindrical shells and other “thin” sections. *Proc. R. Soc. A*, **116**(773), 104–114.
- Brush, D. O., & Almroth, B. O. 1975. *Buckling of bars, plates, and shells*. McGraw Hill.
- BS EN 1990. 2002. *Basis of structural design*. British Standards Institution.
- Budd, C. J., Hunt, G. W., & Kuske, R. 2001. Asymptotics of cellular buckling close to the Maxwell load. *Proc. R. Soc. A*, **457**(2016), 2935–2964.
- Budiansky, B., & Hutchinson, J. W. 1979. Buckling: Progress and challenge. *Pages 93–116 of: Besseling, J. F., & van der Heijden, A. M. A (eds), Trends in solid mechanics: Dedicated to the 65th birthday of W. T. Koiter*. Delft, the Netherlands: Delft University Press.
- Bulson, P. S. 1970. *The stability of flat plates*. London, UK: Chatto and Windus.
- Byskov, E., & Hutchinson, J. W. 1977. Mode interaction in axially stiffened cylindrical shells. *AIAA J.*, **15**(7), 941–948.
- Cheung, Y. K. 1968. The finite strip method in the analysis of elastic plates with two opposite simply supported ends. *Proc. Inst. Civil Eng.*, **40**, 1–7.
- Chiew, S. P., Lee, S. L., & Shanmugam, N. E. 1987. Experimental study of thin-walled steel box columns. *ASCE J. Struct. Eng.*, **113**(10), 2208–2220.
- Chilver, A. H. 1976. Design philosophy in structural stability. *Pages 331–345 of: Budiansky, B. (ed), Buckling of Structures*. International Union of Theoretical and Applied Mechanics. Springer Berlin Heidelberg.

- Comac C919. 2014. *C919 fuselage section of first C919 aircraft delivered in Shanghai*. http://english.comac.cc/news/latest/201409/03/t20140903_1895735.shtml. [Online; accessed March 12, 2018].
- Cook, R. D. 1994. *Finite element modeling for stress analysis*. Wiley.
- Cook, R. D., David, S. M., & Michael, E. P. 2007. *Concepts and applications of finite element analysis*. New York: Wiley.
- Crisfield, M. A., & Wills, J. 1988. Solution strategies and softening materials. *Comput. Meth. Appl. Mech. Eng.*, **66**(3), 267–289.
- Cruise, R. B., & Gardner, L. 2006. Measurement and prediction of geometric imperfections in structural stainless steel members. *Struct. Eng. Mech.*, **24**(1), 63–89.
- Cruise, R. B., & Gardner, L. 2008. Residual stress analysis of structural stainless steel sections. *J. Constr. Steel. Res.*, **64**(3), 352–366.
- Davids, A. J., & Hancock, G. J. 1986. Compression tests of long welded I-section columns. *ASCE J. Struct. Eng.*, **112**(10), 2281–2297.
- Davids, A. J., & Hancock, G. J. 1987. Nonlinear elastic response of locally buckled thin-walled beam-columns. *Thin-Walled Struct.*, **5**(3), 211–226.
- De Boor, C., & Swartz, B. 1973. Collocation at Gaussian points. *SIAM J. Numer. Anal.*, **10**(4), 582–606.
- Degée, H., Boissonnade, N., & Rossi, B. 2007. Local and interactive post-buckling of RHS thin-walled members—comparing a new special beam finite element with shell FE models. *Int. J. Struct. Stab. Dyn.*, **7**(02), 213–241.
- Degée, H., Detzel, A., & Kuhlmann, U. 2008. Interaction of global and local buckling in welded RHS compression members. *J. Constr. Steel. Res.*, **64**(7), 755–765.

- Dewolf, J. T., Peokoz, T., & Winter, G. 1974. Local and overall buckling of cold-formed members. *J. Struct. Div. ASCE*, **100**(10), 2017–2036.
- Djubek, J., Kodnar, R., & Skaloud, M. 1983. *Limit state of the plate elements of steel structures*. Vol. 39. Birkhäuser.
- Doedel, E. J., & Oldeman, B. E. 2009. *AUTO-07p: Continuation and bifurcation software for ordinary differential equations*. Available from <http://indy.cs.concordia.ca/auto/>.
- Doerich, C., & Rotter, J. M. 2011. Accurate determination of plastic collapse loads from finite element analyses. *J. Pressure Vessel Technol.*, **133**(1), 011202–011202–10.
- Dow, R. S., & Smith, C. S. 1984. Effects of localized imperfections on compressive strength of long rectangular plates. *J. Constr. Steel. Res.*, **4**(1), 51–76.
- Dubina, D., & Ungureanu, V. 2002. Effect of imperfections on numerical simulation of instability behaviour of cold-formed steel members. *Thin-Walled Struct.*, **40**(3), 239–262.
- ECCS. TC 8. 1976. *Manual on stability of steel structures*. Tech. rept.
- ECCS. TC 8. 1984. *Ultimate limit state calculation of sway frames with rigid joints*. Tech. rept.
- EN, BS. 2008. 1090–2: 2008+ a1: 2011. *Execution of steel structures and aluminium structures. Technical requirements for steel structures*. London, UK: British Standards Institution, BSI.
- EN-1993-1-1:2006E. 2006. *Eurocode 3: Design of steel structures part 1-1. General rules and rules for buildings*.
- EN-1993-1-3:2006E. 2006. *Eurocode 3: Design of steel structures part 1-3. General rules—Supplementary rules for cold-formed members and sheeting*.

- EN-1993-1-5:2006E. 2006. *Eurocode 3: Design of steel structures part 1-5. Plated structural elements*.
- Euler, L. 1744. *Methodus inveniendi lineas curvas maximi minimive proprietate gaudentes*. (Appendix, De curvis elasticis), Marcum Michaellem Bousquet, Lausanne and Geneva.
- Fok, W. C., Walker, A. C., & Rhodes, J. 1976. Local buckling of outstands in stiffened plates. *Aeronaut. Quart.*, **27**, 277–291.
- Garcea, G., Leonetti, L., Magisano, D., Gonalves, R., & Camotim, D. 2017. Deformation modes for the post-critical analysis of thin-walled compressed members by a Koiter semi-analytic approach. *Int. J. Solids Struct.*, **110-111**, 367–384.
- Gardner, L., & Nethercot, D. A. 2004a. Experiments on stainless steel hollow sections – Part 2: Member behaviour of columns and beams. *J. Constr. Steel. Res.*, **60**(9), 1319–1332.
- Gardner, L., & Nethercot, D. A. 2004b. Experiments on stainless steel hollow sections–part 1: Material and cross-sectional behaviour. *J. Constr. Steel. Res.*, **60**(9), 1291–1318.
- Gilbert, R. B., & Calladine, C. R. 1974. Interaction between the effects of local and overall imperfections on the buckling of elastic columns. *J. Mech. Phys. Solids*, **22**(6), 519–540.
- Gioncu, V. 1994a. Consistent simplified theory for elastic coupled instability. *Thin-Walled Struct.*, **19**(2–4), 147–159.
- Gioncu, V. 1994b. General theory of coupled instabilities. *Thin-Walled Struct.*, **19**(2), 81–127.
- Glendinning, P. 1994. *Stability, instability and chaos: an introduction to the theory of nonlinear differential equations*. Cambridge Texts in Applied Mathematics, vol. 11. Cambridge University Press.

- Goltermann, P., & Møllmann, H. 1989. Interactive buckling in thin-walled beams: II. Applications. *Int. J. Solids Struct.*, **25**(7), 729–749.
- Gonçalves, R., & Camotim, D. 2004. Gbt local and global buckling analysis of aluminium and stainless steel columns. *Comput. Struct.*, **82**(17), 1473–1484.
- Graves Smith, T. R. 1968. The post-buckled strength of thin-walled columns. *Pages 311–320 of: IABSE congress report.*
- Graves Smith, T. R. 1972. The post-buckled behaviour of a thin-walled box beam in pure bending. *Int. J. Mech. Sci.*, **14**(11), 711–718.
- Graves Smith, T. R., & Sridharan, S. 1978. A finite strip method for the post-locally-buckled analysis of plate structures. *Int. J. Mech. Sci.*, **20**(12), 833–842.
- Guo, Y. L., & Chen, S. F. 1991. Elasto-plastic interaction buckling of cold-formed channel columns. *ASCE J. Struct. Eng.*, **117**(8), 2278–2298.
- Han, D. J., & Chen, W. F. 1983. Buckling and cyclic inelastic analysis of steel tubular beam-columns. *Eng. Struct.*, **5**(2), 119–132.
- Hancock, G. J. 1981. Nonlinear analysis of thin sections in compression. *J. Struct. Div. ASCE*, **107**(ST3), 455–471.
- Hancock, G. J., Davids, A. J., Key, P. W., Lau, S. C. W., & Rasmussen, K. J. R. 1990. Recent developments in the buckling and nonlinear analysis of thin-walled structural members. *Thin-Walled Struct.*, **9**(1), 309–338. Special Volume on Thin-Walled Structures: Developments in Theory and Practice.
- Hemp, W. S. 1945. *The theory of flat panels buckled in compression.* Reports and Memoranda No. 2178. Aeronautical Research Council.
- Howard, B. 2015. *Frame structure of BMW 7-series made from carbon fibre reinforced plastic (CFRP) along with aluminum and high-strength steel.*

- https://www.extremetech.com/extreme/209812-how-bmw-weaves-bakes-and-builds-the-carbon-fiber-7-series/attachment/bmw-7-series-lf-frame-p90176663_highres.
[Online; accessed March 12, 2018].
- Hunt, G. W. 1981. An algorithm for the nonlinear analysis of compound bifurcation. *Proc. R. Soc. A*, **300**(1455), 443–471.
- Hunt, G. W. 1989. Bifurcations of structural components. *Proc. Inst. Civil Eng.*, **87**, 443–467.
- Hunt, G. W., & Wadee, M. A. 1998. Localization and mode interaction in sandwich structures. *Proc. R. Soc. A*, **454**(1972), 1197–1216.
- Hunt, G. W., Da Silva, L. S., & Manzacchi, G. M. E. 1988. Interactive buckling in sandwich structures. *Proc. R. Soc. A*, **417**(1852), 155–177.
- Hunt, G. W., Bolt, H. M., & Thompson, J. M. T. 1989. Structural localization phenomena and the dynamical phase-space analogy. *Proc. R. Soc. A*, **425**(1869), 245–267.
- Hunt, G. W., Peletier, M. A., Champneys, A. R., Woods, P. D., Wadee, M. A., Budd, C. J., & Lord, G. J. 2000. Cellular buckling in long structures. *Nonlinear Dyn.*, **21**(1), 3–29.
- Johansson, B., Maquoi, R., Sedlacek, G., Müller, C., & Beg, D. 2007. *Commentary and worked examples to EN 1993-1-5 ‘Plated structural elements’*. Tech. rept. EUR 22898 EN.
- Jones, R. M. 1998. *Mechanics of composite materials*. CRC press.
- Keller, H. B. 1977. Numerical solution of bifurcation and nonlinear eigenvalue problems. In: Rabinowitz, P. H. (ed), *Applications of bifurcation theory*. New York, USA: Academic Press Inc.
- Kiyamaz, G. 2005. FE based mode interaction analysis of thin-walled steel box columns under axial compression. *Thin-Walled Struct.*, **43**(7), 1051–1070.

- Klöppel, K., & Schubert, J. 1971. The calculation of the carrying capacity in the postbuckling range of thin-walled box columns loaded by concentric and excentric compressive force. *Publications of the Institute for Statics and Steel Construction, Darmstadt*.
- Koiter, W. T. 1945. *On the stability of elastic equilibrium*. Ph.D. thesis, Delft University of Technology. (English translation available: NASA, Tech. Trans., F 10, 833, 1967.).
- Koiter, W. T., & Pignataro, M. 1976a. An alternative approach to the interaction between local and overall buckling in stiffened panels. *Pages 133–148 of: Budiansky, B. (ed), Buckling of Structures*. International Union of Theoretical and Applied Mechanics. Springer Berlin Heidelberg.
- Koiter, W. T., & Pignataro, M. 1976b. *A general theory for the interaction between local and overall buckling of stiffened panels*. Tech. rept. WTHD 83. Delft University of Technology, Delft, The Netherlands.
- Kołąkowski, Z. 1989. Some thoughts on mode interaction in thin-walled columns under uniform compression. *Thin-Walled Struct.*, **7**(1), 23–35.
- Kołąkowski, Z. 1993. Interactive buckling of thin-walled beam-columns with open and closed cross-sections. *Thin-Walled Struct.*, **15**(3), 159–183.
- Köllner, A. 2017. *An analytical framework for the structural stability analysis of damageable structures and its application to delaminated composites*. Ph.D. thesis, TU Berlin.
- Kwon, Y. B., & Seo, E. G. 2013. Prediction of the compressive strength of welded RHS columns undergoing buckling interaction. *Thin-Walled Struct.*, **68**, 141–155.
- Lanzo, A. D., & Garcea, G. 1996. Koiter's analysis of thin-walled structures by a finite element approach. *Int. J. Numer. Methods Eng.*, **39**(17), 3007–3031.
- Lay, M. G., & Ward, R. 1969. Residual stresses in steel sections. *J. Aust. Inst. Steel Construction*, **3**(3), 2–21.

- Little, G. H. 1979. The strength of square steel box columns: Design curves and their theoretical basis. *Struct. Eng.*, **57**(2), 49–61.
- Little, G. H. 1980. The collapse of rectangular steel plates under uniaxial compression. *Struct. Eng.*, **58B**(3), 45–61.
- Liu, E. 2016. *Interactive buckling in thin-walled I-section struts of uniform thickness*. Ph.D. thesis, Imperial College London.
- Liu, E. L., & Wadee, M. A. 2015. Interactively induced localization in thin-walled I-section struts buckling about the strong axis. *Structures*, **4**, 13–26.
- Liu, E. L., & Wadee, M. A. 2016a. Geometric factors affecting I-section struts experiencing local and strong-axis global buckling mode interaction. *Thin-Walled Struct.*, **109**, 319–331.
- Liu, E. L., & Wadee, M. A. 2016b. Mode interaction in perfect and imperfect thin-walled I-section struts susceptible to global buckling about the strong axis. *Thin-Walled Struct.*, **106**, 228–243.
- Lord, G. J., Champneys, A. R., & Hunt, G. W. 1997. Computation of localized post buckling in long axially compressed cylindrical shells. *Phil. Trans. R. Soc. Lond. A*, **355**(1732), 2137–2150.
- Loughlan, J. 1983. The ultimate load sensitivity of lipped channel columns to column axis imperfection. *Thin-Walled Struct.*, **1**(1), 75–96.
- Loughlan, J., Yidris, N., & Cunningham, P. R. 2011. The effects of local buckling and material yielding on the axial stiffness and failure of uniformly compressed I-section and box-section struts. *Thin-Walled Struct.*, **49**(2), 264–279.
- Maple. 2017. *version 2017.3*. Waterloo, ON Canada: Maplesoft Inc.

- Maquoi, R., & Massonnet, C. 1976. Interaction between local plate buckling and overall buckling in thin-walled compression members – theories and experiments. *Pages 365–382 of*: Budiansky, B. (ed), *Buckling of Structures*. International Union of Theoretical and Applied Mechanics. Springer Berlin Heidelberg.
- Martin, J. 2017. *The Steve Jobs Theater*. <http://solarhousehistory.com/blog/2017/12/18/apple-park-by-foster-partners>. [Online; accessed March 12, 2018].
- Martins, A. D., Camotim, D., Gonçalves, R., & Dinis, P. B. 2018. On the mechanics of local-distortional interaction in thin-walled lipped channel beams. *Thin-Walled Struct.*, **125**, 187–202.
- Mateus, A. F., & Witz, J. A. 2001. A parametric study of the post-buckling behaviour of steel plates. *Eng. Struct.*, **23**(2), 172–185.
- MATLAB. 2010. *version 7.10.0 (R2012a)*. Natick, Massachusetts: The MathWorks Inc.
- Menken, C. M., Groot, W. J., & Stallenberg, G. A. J. 1991. Interactive buckling of beams in bending. *Thin-Walled Struct.*, **12**(5), 415–434.
- Menken, C. M., Kouhia, R., & Groot, W. J. 1994. An investigation into non-linear interaction between buckling modes. *Thin-Walled Struct.*, **19**(2-4), 129–145.
- MISTRAS group. 2017. *Steel box girders A38 Thame Valley Viaduct*. <http://mistrasgroup.co.uk/projects-archive/structural-monitoring-tame-valley-viaduct/>. [Online; accessed March 12, 2018].
- Moen, C. D., Igusa, T., & Schafer, B. W. 2008. Prediction of residual stresses and strains in cold-formed steel members. *Thin-Walled Struct.*, **46**(11), 1274–1289.
- Møllmann, H., & Goltermann, P. 1989. Interactive buckling in thin-walled beams: I. Theory. *Int. J. Solids Struct.*, **25**(7), 715–728.
- Pastor, M. M., Bonada, J., Roure, F., & Casafont, M. 2013. Residual stresses and initial imperfections in non-linear analysis. *Eng. Struct.*, **46**, 493–507.

- Pavlovčić, L., Froschmeier, B., Kuhlmann, U., & Beg, D. 2010. Slender thin-walled box columns subjected to compression and bending. *J. Civ. Eng. Manag.*, **16**(2), 179–188.
- Pavlovčić, L., Froschmeier, B., Kuhlmann, U., & Beg, D. 2012. Finite element simulation of slender thin-walled box columns by implementing real initial conditions. *Adv. Eng. Softw.*, **44**(1), 63–74.
- Powercase Technology (Shenzhen) Co., Ltd. 2015. *Computer case PW-4*. <http://www.powercase.com.cn/product/pw-4/>. [Online; accessed March 12, 2018].
- Press, W. H., Teukolsky, S. A., Vetterling, W. T., & Flannery, B. P. 2007. *Numerical recipes: The art of scientific computing (3rd edition)*. Cambridge University Press.
- Quach, W. M., Teng, J. G., & Chung, K. F. 2004. Residual stresses in steel sheets due to coiling and uncoiling: a closed-form analytical solution. *Eng. Struct.*, **26**(9), 1249–1259.
- Quach, W. M., Teng, J. G., & Chung, K. F. 2010. Effect of the manufacturing process on the behaviour of press-braked thin-walled steel columns. *Eng. Struct.*, **32**(11), 3501–3515.
- Rasmussen, K. J. R. 1997. Bifurcation of locally buckled members. *Thin-Walled Struct.*, **28**(2), 117–154.
- Rasmussen, K. J. R., & Hancock, G. J. 1988. Geometric imperfections in plated structures subject to interaction between buckling modes. *Thin-Walled Struct.*, **6**(6), 433–452.
- Riks, E. 1979. An incremental approach to the solution of snapping and buckling problems. *Int. J. Solids Struct.*, **15**(7), 529–551.
- Rozvany, G. I. N. 2009. A critical review of established methods of structural topology optimization. *Struct. Multidisc. Optim.*, **37**(3), 217–237.
- Russell, R. D., & Christiansen, J. 1978. Adaptive mesh selection strategies for solving boundary value problems. *SIAM J. Numer. Anal.*, **15**(1), 59–80.

- Sadovskỳ, Z., Teixeira, A. P., & Soares, C. G. 2005. Degradation of the compressive strength of rectangular plates due to initial deflection. *Thin-Walled Struct.*, **43**(1), 65–82.
- Sadowski, A. J., & Rotter, J. M. 2013. On the relationship between mesh and stress field orientations in linear stability analyses of thin plates and shells. *Finite Elem. Anal. Des.*, **73**, 42–54.
- Sadowski, A. J., Fajuyitan, O. K., & Wang, J. 2017a. A computational strategy to establish algebraic parameters for the reference resistance design of metal shell structures. *Adv. Eng. Softw.*, **109**, 15–30.
- Sadowski, A. J., Rotter, J. M., Stafford, P. J., Reinke, T., & Ummenhofer, T. 2017b. On the gradient of the yield plateau in structural carbon steels. *J. Constr. Steel. Res.*, **130**(Supplement C), 120–130.
- Sarawit, A. T., Kim, Y., Bakker, M. C. M., & Peköz, T. 2003. The finite element method for thin-walled members-applications. *Thin-Walled Struct.*, **41**(2-3), 191–206.
- Schafer, B. W. 1997. *Cold-formed steel behavior and design analytical and numerical modeling of elements and members with longitudinal stiffener*. Ph.D. thesis, Cornell University.
- Schafer, B. W. 2006a. *CUFMS: elastic buckling analysis of thin-walled members by finite strip analysis*. Available from <http://www.ce.jhu.edu/bschafer/cufsm/>.
- Schafer, B. W. 2006b. Designing cold-formed steel using the direct strength method. *In: Proceedings of the Eighteenth International Specialty Conference on Cold-formed Steel Structures*.
- Schafer, B. W. 2006c. *Direct Strength Method design guide*. Tech. rept. American Iron and Steel Institute, Washington (DC).

- Schafer, B. W. 2008. Review: The Direct Strength Method of cold-formed steel member design. *J. Constr. Steel. Res.*, **64**(7–8), 766–778.
- Schafer, B. W., & Peköz, T. 1998a. Computational modeling of cold-formed steel: characterizing geometric imperfections and residual stresses. *J. Constr. Steel. Res.*, **47**(3), 193–210.
- Schafer, B. W., & Peköz, T. 1998b. Direct strength prediction of cold-formed steel members using numerical elastic buckling solutions. *In: Yu, W. W., & LaBoube, R. A. (eds), Fourteenth International Specialty Conference on Cold-formed Steel Structures.* Missouri S&T (formerly the University of Missouri-Rolla).
- Schafer, B. W., Li, Z., & Moen, C. D. 2010. Computational modeling of cold-formed steel. *Thin-Walled Struct.*, **48**(10), 752–762.
- Schardt, R. 1994. Generalized beam theory—an adequate method for coupled stability problems. *Thin-Walled Struct.*, **19**(2–4), 161–180.
- Schillo, N. 2017. *Local and global buckling of box columns made of high strength steel.* Ph.D. thesis, RWTH Aachen.
- Shanmugam, N. E., Chiew, S. P., & Lee, S. L. 1987. Strength of thin-walled square steel box columns. *ASCE J. Struct. Eng.*, **113**(4), 818–831.
- Shen, J., & Wadee, M. A. 2018a. Imperfection sensitivity of rectangular hollow section struts susceptible to interactive buckling. *Int. J. Non-Linear Mech.*, **99**, 112–130.
- Shen, J., & Wadee, M. A. 2018b. Length effects on interactive buckling in thin-walled rectangular hollow section struts. *Thin-Walled Struct.*, **128**, 152–170.
- Shen, J., & Wadee, M. A. 2018c. Sensitivity of elastic thin-walled rectangular hollow section struts to manufacturing tolerance level imperfections. *Eng. Struct.*, **170**, 146–166.

- Shen, J., Wadee, M. A., & Sadowski, A. J. 2015. Numerical study of interactive buckling in thin-walled section box columns under pure compression. *In: Camotim, D., Dinis, P. B., Chan, S. L., Wang, C. M., Goncalves, R., Silvestre, N., Basaglia, C., Landesmann, A., & Bebiano, R. (eds), Proceedings of the 8th International Conference on Advances in Steel Structures (ICASS' 2015)*. Paper number: 44.
- Shen, J., Wadee, M. A., & Sadowski, A. J. 2017. Interactive buckling in long thin-walled rectangular hollow section struts. *Int. J. Non-Linear Mech.*, **89**, 43–58.
- Shi, G., Zhou, W., Bai, Y., & Lin, C. 2014. Local buckling of 460mpa high strength steel welded section stub columns under axial compression. *J. Constr. Steel. Res.*, **100**(Supplement C), 60–70.
- Silvestre, N., & Camotim, D. 2003. Nonlinear generalized beam theory for cold-formed steel members. *Int. J. Struct. Stab. Dyn.*, **3**(04), 461–490.
- Silvestre, N., & Camotim, D. 2006. Local-plate and distortional postbuckling behavior of cold-formed steel lipped channel columns with intermediate stiffeners. *ASCE J. Struct. Eng.*, **132**(4), 529–540.
- Somodi, B., & Kövesdi, B. 2018. Residual stress measurements on welded square box sections using steel grades of S235–S960. *Thin-Walled Struct.*, **123**, 142–154.
- Sridharan, S. 1983. Doubly symmetric interactive buckling of plate structures. *Int. J. Solids Struct.*, **19**(7), 625–641.
- Sridharan, S., & Ali, M. A. 1986. An improved interactive buckling analysis of thin-walled columns having doubly symmetric sections. *Int. J. Solids Struct.*, **22**(4), 429–443.
- Supple, W. J. 1967. Coupled branching configurations in the elastic buckling of symmetric structural systems. *Int. J. Mech. Sci.*, **9**(2), 97–112.
- Supple, W. J. 1970. Changes of wave-form of plates in the post-buckling range. *Int. J. Solids Struct.*, **6**(9), 1243–1258.

- Svensson, S. E., & Croll, J. G. A. 1975. Interaction between local and overall buckling. *Int. J. Mech. Sci.*, **17**(4), 307–321.
- Tebedge, N., & Tall, L. 1973. *Residual stresses in structural steel shapes—a summary of measured values*. Tech. rept. Fritz Laboratory, Lehigh University.
- Tebedge, N., Alpsten, G., & Tall, L. 1973. Residual-stress measurement by the sectioning method. *Exp. Mech.*, **13**(2), 88–96.
- Teter, A. 2007. Static and dynamic interactive buckling of isotropic thin-walled closed columns with variable thickness. *Thin-Walled Struct.*, **45**(10-11), 936–940.
- Theofanous, M., & Gardner, L. 2009. Testing and numerical modelling of lean duplex stainless steel hollow section columns. *Eng. Struct.*, **31**(12), 3047–3058.
- Thompson, J. M. T. 1979. Stability predictions through a succession of folds. *Proc. R. Soc. A*, **292**(1386), 1–23.
- Thompson, J. M. T. 1982. Catastrophe theory in mechanics: progress or digression. *J. Struct. Mech.*, **10**(2), 167–175.
- Thompson, J. M. T., & Hunt, G. W. 1973. *A general theory of elastic stability*. London: Wiley.
- Thompson, J. M. T., & Hunt, G. W. 1974. Dangers of structural optimization. *Eng. Optimiz.*, **1**(2), 99–110.
- Thompson, J. M. T., & Hunt, G. W. 1984. *Elastic instability phenomena*. London: Wiley.
- Thompson, J. M. T., & Lewis, G. M. 1972. On the optimum design of thin-walled compression members. *J. Mech. Phys. Solids*, **20**(2), 101–109.
- Thompson, J. M. T., & Supple, W. J. 1973. Erosion of optimum designs by compound branching phenomena. *J. Mech. Phys. Solids*, **21**(3), 135–144.

- Thompson, J. M. T., Tulk, J. D., & Walker, A. C. 1976. An experimental study of imperfection-sensitivity in the interactive buckling of stiffened plates. *Pages 149–159 of: Budiansky, B. (ed), Buckling of Structures*. International Union of Theoretical and Applied Mechanics. Springer Berlin Heidelberg.
- Thompson, J. M. T., Tan, J. K. Y., & Lim, K. C. 1978. On the topological classification of postbuckling phenomena. *J. Struct. Mech.*, **6**(4), 383–414.
- Timoshenko, S. P., & Gere, J. M. 1961. *Theory of elastic stability*. New York: McGraw-Hill.
- Timoshenko, S. P., & Woinowsky-Krieger, S. 1959. *Theory of plates and shells*. New York: McGraw-Hill.
- Trahair, N. S., Bradford, M. A., Nethercot, D. A., & Gardner, L. 2007. *The behaviour and design of steel structures to EC3*. CRC Press.
- Trouncer, A. N., & Rasmussen, K. J. R. 2015. A rational procedure for modelling imperfections in advanced analysis of frames with locally unstable members. *Thin-Walled Struct.*, **96**, 183–201.
- Tvergaard, V. 1973. Imperfection-sensitivity of a wide integrally stiffened panel under compression. *Int. J. Solids Struct.*, **9**(1), 177–192.
- Usami, T., & Fukumoto, Y. 1982. Local and overall buckling of welded box columns. *J. Struct. Div. ASCE*, **108**(3), 525–542.
- Usami, T., & Fukumoto, Y. 1984. Welded box compression members. *ASCE J. Struct. Eng.*, **110**(10), 2457–2470.
- van der Neut, A. 1969. The interaction of local buckling and column failure of thin-walled compression members. *Pages 389–399 of: Proceedings of the 12th International Congress on Applied Mechanics*. Springer.
- van der Neut, A. 1973. The sensitivity of thin-walled compression members to column axis imperfection. *Int. J. Solids Struct.*, **9**(8), 999–1011.

- van der Neut, A. 1976. Mode interaction with stiffened panels. *Pages 117–132 of: Budiansky, B. (ed), Buckling of Structures*. International Union of Theoretical and Applied Mechanics. Springer Berlin Heidelberg.
- von Karman, T., Sechler, E. E., & Donnell, L. H. 1932. The strength of thin plates in compression. *ASME Trans.*, **54**(2), 53–57.
- Wadee, M. A. 1998. *Localized buckling in sandwich structures*. Ph.D. thesis, University of Bath.
- Wadee, M. A. 2000. Effects of periodic and localized imperfections on struts on nonlinear foundations and compression sandwich panels. *Int. J. Solids Struct.*, **37**(8), 1191–1209.
- Wadee, M. A. 2007. Nonlinear mathematics in structural engineering. *Mathematics Today*, **43**(3), 104–108.
- Wadee, M. A., & Bai, L. 2014. Cellular buckling in I-section struts. *Thin-Walled Struct.*, **81**, 89–100.
- Wadee, M. A., & Farsi, M. 2014a. Cellular buckling in stiffened plates. *Proc. R. Soc. A*, **470**(2168), 20140094.
- Wadee, M. A., & Farsi, M. 2014b. Local–global mode interaction in stringer-stiffened plates. *Thin-Walled Struct.*, **85**, 419–430.
- Wadee, M. A., & Farsi, M. 2015. Imperfection sensitivity and geometric effects in stiffened plates susceptible to cellular buckling. *Structures*, **3**, 172–186.
- Wadee, M. A., & Gardner, L. 2012. Cellular buckling from mode interaction in I-beams under uniform bending. *Proc. R. Soc. A*, **468**(2137), 245–268.
- Wadee, M. A., Yiatros, S., & Theofanous, M. 2010. Comparative studies of localized buckling in sandwich struts with different core bending models. *Int. J. Non-Linear Mech.*, **45**(2), 111–120.

- Wadee, M. K., Hunt, G. W., & Whiting, A. I. M. 1997. Asymptotic and Rayleigh–Ritz routes to localized buckling solutions in an elastic instability problem. *Proc. R. Soc. A*, **453**(1965), 2085–2107.
- Wadee, M. K., Wadee, M. A., Bassom, A. P., & Aigner, A. A. 2006. Longitudinally inhomogeneous deformation patterns in isotropic tubes under pure bending. *Proc. R. Soc. A*, **462**(2067), 817–838.
- Wang, J., & Gardner, L. 2017. Flexural buckling of hot-finished high-strength steel SHS and RHS columns. *ASCE J. Struct. Eng.*, **143**(6), 04017028.
- Weng, C. C., & Peköz, T. 1990. Residual stresses in cold-formed steel members. *ASCE J. Struct. Eng.*, **116**(6), 1611–1625.
- Winter, G. 1947. Strength of thin steel compression flanges. *Trans Am. Soc. Civil Eng.*, **112**(1), 527–554.
- Winter, G. 1968. Thin-walled structures, theoretical solutions and test results. *Pages 101–112 of: Preliminary Publication of the Eighth Congress, IABSE.*
- Wu, H.L., Yang, J., & Kitipornchai, S. 2016. Imperfection sensitivity of postbuckling behaviour of functionally graded carbon nanotube-reinforced composite beams. *Thin-Walled Struct.*, **108**, 225–233.
- Xie, Y. M., & Steven, G. P. 1993. A simple evolutionary procedure for structural optimization. *Comput. Struct.*, **49**(5), 885–896.
- Yang, L., Shi, G., Zhao, M., & Zhou, W. 2017. Research on interactive buckling behavior of welded steel box-section columns. *Thin-Walled Struct.*, **115**, 34–47.
- Yiatros, S., Marangos, O., Wadee, M. A., & Georgiou, C. 2015. Localized buckling in sandwich struts with inhomogeneous deformations in both face plates. *Compos. Struct.*, **133**, 630–641.

- Young, B., & Rasmussen, K. J. R. 1997. Bifurcation of singly symmetric columns. *Thin-Walled Struct.*, **28**(2), 155–177.
- Yuan, H. X., Wang, Y. Q., Gardner, L., & Shi, Y. J. 2014. Local-overall interactive buckling of welded stainless steel box section compression members. *Eng. Struct.*, **67**, 62–76.
- Yun, X., & Gardner, L. 2017. Stress-strain curves for hot-rolled steels. *J. Constr. Steel Res.*, **133**(Supplement C), 36–46.
- Zagari, G., Zucco, G., Madeo, A., Ungureanu, V., Zinno, R., & Dubina, D. 2016. Evaluation of the erosion of critical buckling load of cold-formed steel members in compression based on koiter asymptotic analysis. *Thin-Walled Struct.*, **108**, 193–204.
- Zeinoddini, V. M., & Schafer, B. W. 2012. Simulation of geometric imperfections in cold-formed steel members using spectral representation approach. *Thin-Walled Struct.*, **60**, 105–117.
- Zhao, X., Tootkaboni, M., & Schafer, B. W. 2015. Development of a laser-based geometric imperfection measurement platform with application to cold-formed steel construction. *Exp. Mech.*, **55**(9), 1779–1790.